Superconductor

edited by
Adir Moysés Luiz

SCIYO

Superconductor
Edited by Adir Moysés Luiz

Published by Sciyo
Janeza Trdine 9, 51000 Rijeka, Croatia

Publishing Process Manager Iva Lipovic
Technical Editor Teodora Smiljanic
Cover Designer Martina Sirotic
Image Copyright Creasence, 2010. Used under license from Shutterstock.com

First published October 2010
Printed in India

A free online edition of this book is available at **www.sciyo.com**
Additional hard copies can be obtained from **publication@sciyo.com**

Superconductor, Edited by Adir Moysés Luiz
p. cm.
ISBN 978-953-307-107-7

Contents

Preface

Superconductivity was discovered in 1911 by Kamerlingh Onnes. The history of superconductivity is full of theoretical challenges and practical developments. In 1986 the discovery of Bednorz and Müller of an oxide superconductor with critical temperature (Tc) approximately equal to 35 K has given a novel impetus to this fascinating subject. Since this discovery, there has been a great number of laboratories all over the world involved in researches of superconductors with high Tc values, the so-called "high-Tc superconductors". The discovery of a room temperature superconductor has been a long-standing dream of many scientists. The technological and practical applications of such a discovery should be tremendous. However, the actual use of superconducting devices is limited by the fact that they must be cooled to low temperatures to become superconducting. Currently, the highest Tc value is approximately equal to 135 K at 1 atm. The knowledge of the microscopic mechanisms of high-Tc superconductors should be a theoretical guide in the researches to synthesize a room temperature superconductor. However, up to the present time, the microscopic mechanisms of high-Tc superconductivity are unclear.

This book is a collection of works intended to study theoretical and experimental aspects of superconductivity. Here you will find interesting reports on low-Tc superconductors (materials with $Tc < 30$ K), as well as a great number of researches on high-Tc superconductors (materials with $Tc > 30$ K).

In Chapter 1 a model to study microscopic mechanisms in high-Tc superconductivity is discussed.

In Chapters 2 and 3 there are reports on low-Tc superconductors.

In Chapters 4-14 theoretical developments and experimental researches on high-Tc superconductors are described.

In Chapters 15-17 interesting works about theoretical aspects and other characteristic features of the phenomenon of superconductivity are presented.

I expect that this book will be useful to encourage further experimental and theoretical researches in superconducting materials.

Editor

Adir Moysés Luiz,
Instituto de Física, Universidade Federal do Rio de Janeiro, Brazil

1

A Model to Study Microscopic Mechanisms in High-T_c Superconductors

Adir Moysés Luiz
Instituto de Física, Universidade Federal do Rio de Janeiro
Brazil

1. Introduction

Superconductivity is a very curious phenomenon characterized by a phase transition at a critical temperature (T_c) in which the conducting phase is in equilibrium with the superconducting phase. The most important properties of the superconducting phase are: zero resistance, ideal diamagnetism (Meissner effect), magnetic flux quantization and persistent current in superconducting rings, cylinders or coils. On the other hand, many effects are found in superconducting constrictions as well as in junctions between two superconductors or in junctions between a superconductor and a conductor. These effects are known as "Josephson effects": (1) It is possible to occur tunneling of Cooper pairs across a thin insulator between two superconductors and thus a superconducting current may be maintained across the junction; (2) when we apply an electric field gradient across a Josephson junction an electromagnetic wave may be produced, (3) when a beam of electromagnetic waves is incident over a Josephson junction a variable electric potential difference may be produced.
Due to all the effects mentioned above, superconducting devices may be projected for an enormous number of practical applications. Superconducting wires can be used for power transmission and in other applications when zero resistance is required. A possible application of magnetic levitation is the production of frictionless bearings that could be used to project electric generators and motors. Persistent currents can be used in superconducting magnets and in SMES (superconducting magnetic energy storage). Devices based on the Josephson effects are actually been used in very sensitive magnetometers and appropriate devices based on these effects may give rise to a new generation of faster computers. Superconducting magnets are been used in particle accelerators and may also be used to levitate trains. Many of these devices are successfully been used and new devices are been developed. However, the actual use of these superconducting devices is limited by the fact that they must be cooled to low temperatures to become superconducting. Currently, the highest T_c is approximately equal to 135 K at 1 atm (Schilling & Cantoni, 1993). The discovery of a room temperature superconductor should trigger a great technological revolution. A book with a discussion about room temperature superconductivity is available (Mourachkine, 2004). The knowledge of the microscopic mechanisms of oxide superconductors should be a theoretical guide in the researches to synthesize a room temperature superconductor. However, up to the present time, the microscopic mechanisms of high-T_c superconductivity are unclear. In the present chapter we study microscopic mechanisms in high-T_c superconductors.

According to the type of charge carriers, superconductors can be classified in two types: n-type superconductors, when the charge carriers are Cooper pairs of electrons and p-type superconductors, when the charge carriers are Cooper pairs of holes.
We know that BCS theory (Bardeen et al., 1957) explains the microscopic mechanisms of superconductivity in metals. These materials are clearly n-type superconductors. According to BCS theory, electrons in a metallic superconductor are paired by exchanging phonons.
Microscopic mechanisms in some types of non-metallic superconductors, like MgB_2 (Nagamatsu et al., 2001), probably may be explained by BCS theory. However, according to many researchers (De Jongh, 1988; Emin, 1991; Hirsch, 1991; Ranninger, 1994), BCS theory is not appropriate to be applied to explain the mechanisms of superconductivity in oxide superconductors. Nevertheless, other models relying on a BCS-like picture replace the phonons by another bosons, such as: plasmons, excitons and magnons, as the mediators causing the attractive interaction between a pair of electrons and many authors claim that superconductivity in the oxide superconductors can be explained by the conventional BCS theory or BCS-like theories (Canright & Vignale, 1989; Prelovsek, 1988; Tachiki & Takahashi, 1988; Takada, 1993). In this chapter we discuss this controversy. That is, we discus the microscopic mechanisms to explain the condensation of the superconductor state of oxide superconductors. This discussion may be useful to study all types of oxide superconductors, that is, oxide superconductors containing copper, as well as oxide superconductors that do not contain copper. However, the main objective of this chapter is to discuss the role of double valence fluctuations in p-type oxide superconductors. In a previous work (Luiz, 2008) we have suggested a simple phenomenological model useful to calculate the optimal doping of p-type high-T_c oxide superconductors. In this chapter we study possible microscopic mechanisms in high-T_c superconductors in order to give theoretical support for that simple model.

2. Oxide superconductors

It is well known that there are metallic superconductors and non-metallic superconductors. Oxide superconductors are the most important non-metallic superconductors. An interesting review about oxide superconductors is found in the references (Cava, 2000). The history of oxide superconductors begins in 1933 with the synthesis of the superconductor NbO; with T_c = 1.5 K (Sleight, 1995). In 1975 it was discovered the oxide superconductor $BaPb_{0.7}Bi_{0.3}O_3$ (Sleight et al., 1975) with T_c = 13 K. In 1986, the oxide superconductor $Ba_{0.15}La_{1.85}CuO_4$ with T_c = 30 K has been discovered (Bednorz & Müller, 1986). The expression "high-T_c superconductors" has been generally used in the literature to denote superconductors with critical temperatures higher than 30 K. After this famous discovery many cuprate high-T_c superconductors have been synthesized. The cuprate superconductor $HgBa_2Ca_2Cu_3O_{8+x}$ (Hg-1223) has the highest critical temperature (T_c = 135 K) at 1 atm (Schilling & Cantoni, 1993). In 2008, a new type of high-T_c superconductor containing iron (without copper) has been discovered (Yang et al., 2008). In Table 1, we list in chronological order the most important discoveries of superconductors containing oxygen. In Table 1, T_c is expressed in Kelvin and x is a variable atomic fraction of the doping element.
The most relevant differences between the properties of oxide high-T_c superconductors and the properties of metallic superconductors can be summarized in the following points:

a. All metallic superconductors are isotropic (the so-called "S-wave superconductivity"). All high-T_c oxide superconductors are characterized by a very large anisotropy

manifesting itself in their layered structures with planes (a, b) perpendicular to the principal crystallographic axis (c-axis).

b. In a metallic superconductor the coherence length is isotropic and is of the order of 10^{-4} cm. In high-T_c superconductors, the coherence length is anisotropic and of the order of angstroms. For example, in the system Bi-Sr-Ca-Cu-O, the coherence length is approximately equal to 1 angstrom (10^{-10} cm) along the c-axis and approximately equal to 40 angstroms in the transverse direction (Davydov, 1990).

c. In high-T_c superconductors, the dependence of T_c on the concentration of charge carriers has nonmonotonic character, that is, T_c does not rise monotonically with the rise of the carrier concentration. In a metallic superconductor, T_c rises monotonically with the rise of the carrier concentration.

d. In a metallic superconductor, the energy gap can be predicted by BCS theory. However, the energy gap of oxide superconductors seems to be anisotropic and probably cannot be predicted by BCS theory.

The isotopic effect, predicted by BCS theory, is a fundamental characteristic of a metallic superconductor. However, the isotopic effect is not clearly observed in oxide superconductors.

Superconductor	Year	T_C	Reference
(1) NbO	1933	1.5	Sleight, 1995
(2) K_xWO_3	1967	6.0	Remeika et al., 1967
(3) $LiTi_{2+x}O_4$	1973	1.2	Johnston et al., 1973
(4) $BaPb_{1-x}Bi_xO_3$	1975	13	Sleight et al., 1975
(5) $La_{2-x}Ba_xCuO_4$	1986	30	Bednorz & Müller, 1986
(6) $YBa_2Cu_3O_{7-x}$	1987	90	Wu et al., 1987
(7) $Ba_{1-x}K_xBiO_3$	1988	30	Cava et al.,1988
(8) $BiSrCaCu_2O_{6+x}$	1988	105	Maeda et al., 1988
(9) $Tl_2Ba_2Ca_2Cu_3O_{9+x}$	1988	110	Shimakawa et al., 1988
(10) $HgBa_2Ca_2Cu_3O_{8+x}$	1993	130	Schilling & Cantoni, 1993
(11) $NdFeAsO_{1-x}$	2008	54	Yang et al., 2008

Table 1. Superconductors containing oxygen in chronological order

3. Double charge fluctuations

In Table 2, we show the electron configurations and the stable oxidation states of the most relevant metals that are used in the synthesis of the oxide superconductors listed in Table 1. The stable oxidation states reported in Table 2 have been summarized according to tables described in a textbook (Lee, 1991). In Table 2, the symbol [Ar] means the electron configuration of Ar, the symbol [Xe] means the electron configuration of Xe and the symbol [Kr] means the electron configuration of Kr. In Table 2 unstable oxidation states are not described.

Using Table 2 and considering the oxide superconductors listed in Table 1, we can verify that: in the superconductor (1) Nb may have the oxidation states Nb(+III) and Nb(+V); in the bronze superconductor (2) W may have the oxidation states W(+IV) and W(+VI); in the superconductor (3) Ti may have the oxidation states Ti(+II) and Ti(+IV); in the

superconductor (4) Pb may have the oxidation states: Pb(+II) and Pb(+IV) and Bi may have the oxidation states Bi(+III) and Bi(+V); in the copper oxide superconductors (5), (6), (8), (9) and (10) Cu may have the oxidation states Cu(+I) and Cu(+III).

Metal	*Electron configurations*	*Oxidation states*
As	$[Ar]3d^{10}4s^24p^3$	+III, +V
Bi	$[Xe]4f^{14}5d^{10}6s^26p^3$	+III, +V
Cu	$[Ar]3d^{10}4s^1$	+I, +II, +III
Fe	$[Ar]3d^64s^2$	+II, +III, +IV, +V
Nb	$[Kr]4d^35s^2$	+III, +V
Pb	$[Xe]4f^{14}5d^{10}6s^26p^2$	+II, +IV
Ti	$[Ar]3d^24s^2$	+II, +III, +IV
Tl	$[Xe]4f^{14}5d^{10}6s^26p^1$	+I, +III
W	$[Xe]4f^{14}5d^46s^2$	+IV, +V, +VI

Table 2. Electron configurations and oxidation states of some metals

Note also that in the superconductor (7) (without copper), Bi may have the oxidation states Bi(+III) and Bi(+V). In the superconductor (11), an example of the recent discovery of iron-based superconductors (Yang et al., 2008), we can verify that Fe may have the oxidation states Fe(+II) and Fe(+IV) and As may have the oxidation states As(+III) and As(+V).

Observe that in most high-T_c superconductors there are alkaline earth metals (such as Ca, Sr, and Ba). We know that the electron configuration of an alkaline earth metal is given by [noble gas] ns^2, where n is the number of the row in the periodic table. Thus, an alkaline earth atom may lose two paired external electrons (ns^2). According to Table 1, among the high-T_c oxide superconductors, $HgBa_2Ca_2Cu_3O_{8+x}$ (Hg-1223) has the highest critical temperature (T_c = 135 K) at 1 atm (Schilling & Cantoni, 1993). According to the tables in the textbook (Lee, 1991), the electron configuration of Hg is given by: [Xe] $4f^{14}$ $5d^{10}$ $6s^2$. Because all electrons are paired in a Hg atom, it is possible that an Hg atom may lose two paired electrons at the external level ($6s^2$). Therefore, alkaline earth metals atoms (such as Ca, Sr, and Ba) as well as Hg atoms may lose two paired electrons at the external level.

According to a number of authors the probable existence of double charge fluctuations in oxide superconductors is very likely (Callaway et al., 1987; Foltin, 1988; Ganguly & Hegde, 1988; Varma, 1988). Spectroscopic experiments (Ganguly & Hegde, 1988), indicate that double charge fluctuations is a necessary, but not sufficient, criterion for superconductivity. We argue that these charge fluctuations should involve paired electrons hoping from ions (or atoms) in order to occupy empty levels. That is, our basic phenomenological hypothesis is that the electrons involved in the hopping mechanisms might be paired electrons coming from neighboring ions or neighboring atoms.

Possible microscopic mechanisms for double charge fluctuations are: (1) hopping mechanisms (Foltin, 1989; Wheatley et al., 1988), (2) tunneling mechanisms (Kamimura, 1987), and (3) bipolaronic mechanisms (Alexandrov, 1999).

The discovery of Fe-based high-T_c superconductors (Yang et al., 2008) has reopened the hypothesis of spin fluctuations for the microscopic mechanisms of high-T_c superconductivity. However, it is interesting to note that Fe may have the oxidation states Fe(+II) and Fe(+IV). Thus, the conjecture of double charge fluctuations cannot be ruled out

in the study of the microscopic mechanisms in all Fe-based high-T_c superconductors. It is worthwhile to study the competition between double charge fluctuations and spin fluctuations in order to identify which phenomenon is more appropriate to investigate the microscopic mechanisms in the condensation of the superconducting state of Fe-based materials.

4. Valence skip

What is valence skip? About fifteen elements in the periodic table skip certain valences in all components they form. For example, according to Table 2, the stable oxidation states of bismuth are Bi(+III) and Bi(+V). The oxidation state Bi(+IV) is not stable. If the state Bi(+IV) is formed, occurs immediately a disproportionation, according to the reaction: 2Bi(+IV) = Bi(+III) + Bi(+V). In the compound $BaBiO_3$, the formal valence Bi(+IV) is understood as an equilibrium situation involving a mixture of equal amounts of the ions Bi(+III) and Bi(+V). Observing Table 2, other important examples of elements with valence skip are As, Pb and Tl. In (Varma, 1988) there is a discussion about the microscopic physics behind the phenomenon of valence skip.
Elements with valence skip, like Bi and Pb, are the most appropriate elements to study the hypothesis of double charge fluctuations. It has been stressed that all elements with valence skip may be used in the synthesis of superconductors (Varma, 1988).

5. D-wave superconductivity

Let us consider copper oxide high-T_c superconductors. We assume that the copper-oxygen planes are parallel to the plane x, y and that the z-axis is parallel to the crystallographic axis (c-axis).
In a weak crystal field, according to Hund's rule, the ion Cu(+III) is paramagnetic because the levels $3d(x^2 - y^2)$ and $3d(z^2)$ are half-filled. However, it has been shown that in a strong crystal field this ion becomes diamagnetic (McMurry & Fay, 1998). We know that the electron configuration of the ion Cu(+III) is $[Ar]3d^8$. Considering a strong crystal field, the ion Cu(+III) may give rise to a square planar complex. On the other hand, considering a strong crystal field, the spin-pairing energy P is smaller than the splitting energy Δ (McMurry & Fay, 1998). Thus, in this case, all electrons in a Cu(+III) ion should be paired and this ion should be diamagnetic. This hypothesis is consistent with a correlation between crystal field splitting and high transition temperatures (Zuotao, 1991).
If there are paired electrons in the nearest neighbors of the Cu(+III) ions, two neighboring paired electrons can be attracted by Coulomb interactions and eventually may occupy double empty energy levels. Because the orbital $3d(z^2)$ becomes filled, the electrons coming from +z and -z directions are strongly repelled. On the other side, electrons coming from the directions +x, -x, +y, -y are not repelled and, eventually, may jump to occupy the empty levels. These electrons are obviously d-electrons and these jumps may give rise to a collective wave function of d-electrons. This hypothesis is consistent with the so-called assumption of d-wave superconductivity. The probable existence of d-wave superconductivity in oxide superconductors is supported by a great number of experiments (Leggett, 1994; Scalapino, 1995; Shen & Dessau, 1995; Tanaka, 1994). This picture leads to the conclusion that the microscopic mechanism of the condensation of the superconducting state should be a Bose-Einstein condensation. In the next section we discuss the possibility of a direct Bose-Einstein condensation in oxide superconductors.

6. Bose-Einstein Condensation (BEC)

An important question concerning the microscopic mechanisms of high-T_c superconductivity is: how the electrons are paired to form the Cooper pairs that are necessary for the condensation of the superconducting state? An answer to this question might be provided by the following hypothesis: the superconducting state arises from a Bose-Einstein condensation (BEC) of existing paired electrons that jump to occupy the double empty 3d levels mentioned in the previous section. Because these electrons were previously paired in atoms or in ions, it is not necessary to assume external interactions (with phonons or other bosons) to account for the pairing energy P of these paired electrons.
Another question to analyze is: are these paired electrons in the spin-singlet or in the triplet state? By our hypothesis, these electrons were just paired in atoms or in ions; therefore, these existing pairs are in the spin-singlet state. This singlet state hypothesis is confirmed by Knight shift experiments (Scalapino, 1995).
Is BEC possible in oxide superconductors? According to (Chakraverty et al., 1998) BEC is impossible in oxide superconductors. However, we want to show that BEC in oxide superconductors cannot be ruled out.
Initially it is convenient to clarify some concepts regarding BEC. It is well known that a collection of particles (bosons) that follows the counting rule of Bose-Einstein statistics might at the proper temperature and density suddenly populate the collections ground state in observably large numbers (Silvera, 1997). The average de Broglie wavelength λ_{dB} which is a quantum measurement of delocalization of a particle, must satisfy this condition. We know that $\lambda_{dB} = h/p$, where h is Planck's constant and p is the momentum spread or momentum uncertainty of the wave packet. In the other extreme, for particles in the zero momentum eigenstate, the delocalization is infinite; i.e., the packet is spread over the entire volume V occupied by the system. It is generally accepted that BEC occurs when the interparticle separation is of the order of the delocalization λ_{dB} (Silvera, 1997).
The thermal de Broglie wavelength λ_{dB} is a measure of the thermodynamic uncertainty in the localization of a particle of mass M with the average thermal momentum. Thus, λ_{dB} is given by

$$\lambda_{dB} = h/[3MkT]^{1/2} \quad (1)$$

where k is Boltzmann's constant. Equation (1) shows that at a certain low temperature T or/and for a small mass M, λ_{dB} may be spread over great distances. In order to determine the critical temperature T_c at which the addition of more particles leads to BEC it is sufficient to calculate a certain critical density n = N/V, where N is the number of bosons. This calculation is performed using Bose-Einstein statistics; according to (Silvera, 1997) and considering M = 2m*, where m* is the effective mass of the electron, we obtain

$$T_c = 3.31h^2n^{2/3}/(4\pi^2kM) \quad (2)$$

The first application of BEC theory to explain ^{4}He superfluidity was realized in 1938 (London, 1938). In an important paper (Blatt, 1962), the BEC approach has been extended to give the same results predicted by BCS theory. Thus, it is reasonable to conclude that the conventional n-type superconductivity in metals (explained by BCS theory) is a special case that can also be considered as a phenomenon of BEC of Cooper pairs.
There are three possibilities of occurrence of BEC: (a) BEC involving just bosons, (b) BEC involving just fermions, and (c) BEC involving bosons and fermions simultaneously. In (a)

there is a direct BEC without the need of an interaction to bind the bosons. However, in the cases (b) and (c) BEC is possible only indirectly in two steps: in the first step it occurs the binding between pairs of fermions giving rise to bosons and, in the second step, BEC of these bosons may occur.

Because liquid ^{4}He is a system of bosons, the condensation of ^{4}He is a BEC of type (a). Superfluidity of ^{3}He (Lee, 1997) is an example of BEC of type (b). Because liquid ^{3}He is a system of fermions, in order to occur BEC, two particles must be binded to form a boson and, in he next step, a BEC of these bosons may occur. Another example of BEC of type (b) is the phenomenon of superconductivity in metals and alloys. On the other hand, BEC theory has been successfully applied in dilute atomic gases (Dalfovo et al., 1999), opening new applications involving the BEC concept.

We study now the possibility of occurrence of a Bose-Einstein condensation in an oxide material. If possible, this phenomenon should be a BEC of type (c) mentioned above, that is, the mechanism should involve bosons and fermions simultaneously. In order to verify if BEC is possible in oxide superconductors, it is sufficient to calculate the order of magnitude of the critical temperature T_c using Equation (2). According to Table 1 in the reference (De Jongh, 1988), in a p-type superconductor, the order of magnitude of the carrier density is $n = 10^{21}/cm^3$. Considering an effective mass $m^* = 12m$, where m is the rest mass of the electron, we obtain by Equation (2) the following approximated value: $T_c = 100$ K. This order of magnitude is reasonable because Equation (2) is based on an isotropic hypothesis. However, oxide superconductors are not isotropic. But the crude calculation based on Equation (2) is sufficient to show that BEC in oxide superconductors cannot be ruled out. A more appropriate formula to calculate T_c (supposing BEC) has been derived in (Alexandrov & Edwards, 2000).

7. Energy gap of High-T_c oxide superconductors

The energy gap is a controversial property of oxide superconductors. In order to study this fascinating subject it is instructive to clarify some concepts regarding the energy gap of superconductors. The excited states of a system may be decomposed in a superposition of elementary excitations, the so-called normal modes of excitations. The elementary excitations can be of two general classes (a) excitations of Bose-Einstein type, which can be created or destroyed individually, and (b) excitations of the Fermi-Dirac type, which can only be created or destroyed in pairs. In this case, the excitations are called quasiparticles and quasiholes, so that, in any state of the system, the number of quasiparticles is equal to the number of quasiholes.

The so-called "energy spectrum" is a function E(k) where k is the modulus of the wave propagator vector **k**. It is said that a given class of excitations has an energy gap E_g when the minimum value of E(k) is not zero. In the case of Bose-Einstein excitations there two possible E(k) curves: (a) an energy spectrum with an energy gap E_g that may represent an energy spectrum of plasma oscillations (plasmons) and (b) an energy spectrum without an energy gap that may represent an energy spectrum of lattice vibrations (phonons). The energy spectrum in the phenomenon of ^{4}He superfluidity is an example of the last case.

For Fermi-Dirac excitations in systems involving electrons, there are three possibilities: (1) In the case of a normal metal, an infinitesimal amount of energy is sufficient to excite a quasielectron and quasihole pair, in this case, the energy gap is equal to zero, (2) in a metallic superconductor, the minimum energy of excitation, always considering $k = k_F$, (that

is, on the Fermi surface), changes from zero to a certain value Δ (the energy gap parameter), and (3) in a semiconductor, the energy gap is the minimum energy necessary to excite a quasielectron and quasihole pair.

In the case of the Fermi excitations in metallic superconductors, the existence of an energy gap is always related to the binding energy of the fermions pairs. In this case, the energy gap is always temperature-dependent. At T = 0 K, the energy gap parameter Δ has a maximum value because all Cooper pairs are in the ground state. If the temperature is raised above absolute zero, pairs are broken up by thermal agitation and the energy gap begins to decrease. As the temperature rises, the number of quasiparticles increases and the energy gap continues to fall, until, finally, at $T = T_c$, the energy gap is equal to zero.

We discuss now the energy gap of oxide superconductors. By our phenomenological model, it is not necessary to assume mechanisms of pair binding involving virtual phonons. Thus, the above mentioned excitations should not exist. To break an existing pair it is necessary to give energy greater than P, where P is the pairing energy of the existing pair. Thermal energies, considering $T < T_c$, should not be pair breaking. Thus, as the temperature raises from T = 0 K until $T = T_c$, the above-mentioned excitations does not exist. Therefore, we conclude that the energy gap of oxide superconductors should be temperature-independent. This conclusion has also been obtained by another author, using a different approach (Alexandrov, 1998).

There are various experimental procedures to measure the energy gap: (a) specific heat measurements, (b) absorption of electromagnetic waves, (c) ultrasonic attenuation and (d) tunneling measurements using Josephson junctions. We discuss only the experimental procedures (b) and (d).

In metallic superconductors, the most direct energy gap measurement comes from tunneling measurements with Josephson junctions (SIS junctions). It is well known that a SIS junction is obtained with an insulator film between two superconductors. For metallic superconductors the width of the insulator film should be of the order of 10^4 angstroms. However, for high-T_c oxide superconductors, where the coherence length is of the order of the distance between two atoms, the order of magnitude of the width of the insulator film should be about one angstrom, and the production of this film should be a very difficult task. Therefore, tunneling measurements with SIS junctions are not very appropriate to measure the energy gap of high-T_c oxide superconductors. Thus, it seems that experimental methods such as optical spectroscopy and neutron scattering provide a better route for the investigation of the energy gap of high-T_c oxide superconductors.

We know that when a photon is absorbed by a metallic superconductor, we have:

$$h\nu = E_g + h\omega \tag{3}$$

where h is Plank' s constant, ν is the frequency of the photon and ω is the frequency of the phonon. However, according to recent experimental results of photon absorption (Carbotte et al., 1999; Munzar et al., 1999), it seems that for oxide superconductors, Equation (3) does not hold and, probably, the photon energy is used to break two paired electrons, according to the relation: $h\nu = 2E_g$.

By our phenomenological model, superconductivity is due to double charge fluctuations involving d-electrons and occurs in the a, b planes. Thus, we conclude that the energy gap of oxide superconductors should depend on the direction of the wave vector **k**, and there are many experimental evidences supporting the hypothesis of an anisotropic energy gap (Beasley, 1991; Sun et al., 1994; Maitra & Taraphder, 1999).

8. The pseudogap of High-T_c oxide superconductors

What is the so-called "pseudogap"? In the previous section we have discussed the question of the energy gap of high-T_c oxide superconductors. We have emphasized that spectroscopic methods are very appropriate to investigate the energy gap of high-T_c oxide superconductors. Using spectroscopic methods and other techniques it has been verified the opening of a gap in the electronic spectrum above the critical temperature of high-T_c oxide superconductors (Timusk & Statt, 1999). This energy gap has been denoted by "pseudogap". There is an interesting discussion in the literature about the origin of the pseudogap (Kugler et al., 2001). The existence of the pseudogap clearly reflects the possible presence of Cooper pairs above T_c and some experiments (Kugler et al., 2001), show that the order of magnitude of the pseudogap above T_c is approximately equal to the order of magnitude of the energy gap below T_c. If these experiments are confirmed, they should clearly indicate the presence of the same Cooper pairs above and below T_c. Thus, the hypothesis of Bose-Einstein condensation of Cooper pairs may be used to explain these experimental results (see Section 6). On the other hand, according to our phenomenological model, based on double charge fluctuations, these Cooper pairs should be paired electrons hoping from site to site to occupy double empty levels existing in neighboring ions or neighboring atoms (see Sections 3 and 5).

9. Oxygen doping of oxide superconductors

The most relevant doping procedures used for the synthesis of cuprate superconductors have been described in a review article (Rao et al., 1993). The first high-Tc oxide superconductor was the copper oxide $Ba_xLa_{2-x}CuO_4$ (Bednorz & Muller, 1986). This superconductor is synthesized by doping the parent material La_2CuO_4 with Ba atoms. Soon after this discovery, it was realized (Schirber et al., 1988) that doping the parent material La_2CuO_4 with oxygen, without the introduction of any Ba atomic fraction x, it is also possible to synthesize the superconductor La_2CuO_{4+x}. Thus, in this case, we conclude that the introduction of oxygen is responsible for the doping mechanism of the parent material La_2CuO_4 (Schirber et al., 1988).

Oxide materials may become superconductors when a parent material is doped by the traditional doping mechanism with cation (or anion) substitution or by a doping mechanism based on oxygen non - stoichiometry (De Jongh, 1988). If a certain oxide contains a metal with mixed oxidation numbers, by increasing (or decreasing) the oxygen content, the metal may be oxidized (or reduced) in order to maintain charge neutrality. Therefore, the synthesis of p-type superconductors may be obtained by doping the parent materials with an excess of oxygen atoms and the synthesis of n-type superconductors may be obtained by doping the parent materials with a deficiency of oxygen atoms. One famous example of oxygen doping is provided by the family of p-type oxide superconductors Y-Ba-Cu-O. It is well known that $YBa_2Cu_3O_{6+x}$, considering compositions x between x = 0.5 and x = 0.9 are superconductors with a maximum T_c with oxygen doping at a composition corresponding to x = 0.9. An important example of n-type superconductor is provided by the recent discovery of the superconductor $GdFeAsO_{1-x}$, a high-T_c superconductor with oxygen-deficiency; it has been shown that oxygen doping is a good and reliable procedure for the synthesis of a new family of iron-based high-T_c superconductors (Yang et al., 2008).

In the present chapter we shall study only oxygen doping of p-type oxide superconductors. It is well known that for p-type superconductors the optimal oxygen doping of high-T_c

oxide superconductors corresponds to a certain critical hole content. An under-doped superconductor is synthesized when the hole content is less than this critical value and an over-doped superconductor is synthesized when the hole content is greater than this critical value. The prediction of the optimal doping is an unresolved issue. In the next section we propose a simple model to estimate the optimal doping of p-type oxide superconductors.

10. Optimal oxygen doping of oxide superconductors

Our basic hypothesis is that the existence of double charge fluctuations involving paired electrons may be a key to study the microscopic mechanisms in oxide superconductors. The essential concept in this hypothesis is that the hopping mechanism involves two paired electrons, instead of the hopping of a single electron. Our hypothesis may be easily applied in the oxide superconductors containing Bi (without Cu) because, in this case, it is well known that Bi (III) and Bi (V) are the only stable oxidation states for the Bi ions. Thus, double charge fluctuations may occur between the ions Bi (III) and Bi (V).

To apply our hypothesis to a copper oxide superconductor (without Bi) it should be necessary to suppose the existence of Cu (I) because we are assuming double charge fluctuations between the states Cu(+I) and Cu(+III). In p-type Cu oxide superconductors, the existence of the oxidation state Cu(+III) is obvious by the consideration of charge neutrality. Thus, from an experimental point of view, it is very important to verify if the oxidation state Cu(+I) is present in the high-T_c Cu oxide superconductors. The probable existence of the states Cu(+I) and Cu(+III) has been verified in the works (Karppinen et al., 1993; Sarma & Rao, 1988).

It is generally believed that the microscopic mechanisms in a cuprate superconductor depends only on the ions Cu(+II) and Cu(+III). Let us suppose that the hopping mechanism involves just a single electron between Cu(+II) and Cu(+III); if this single charge fluctuation would be responsible for superconductivity, we should conclude that the enhancement of Cu(+III) ions should produce a continuous enhancement of the critical temperature T_c. However, it is well known that T_c decreases when the hole concentration is higher than a certain concentration (Zhang & Sato, 1993). This important property is the nonmonotonic dependence of T_c on the carrier concentration, a high-T_c characteristic feature mentioned in item (c) of Section 2. Thus, by this reasoning and considering the experimental results (Karppinen et al., 1993; Sarma & Rao, 1988), we can accept the presence of the mixed oxidation states Cu(+I), Cu(+II) and Cu(+III) in the copper oxide superconductors. On the other hand, this conjecture is well supported if we consider the copper disproportionation reaction (Raveau et al, 1988): 2Cu(+II) = Cu(+I) + Cu(+III).

What should be the optimal chemical doping of Cu oxide superconductors in order to obtain the maximum value of T_c? Initially we suppose an equal probability for the distribution of the copper ions states Cu (I), Cu (II) and Cu (III); thus, the initial concentrations of these ions should be (1/3)Cu(+I), (1/3)Cu(+II) and (1/3)Cu(+III). However, we may suppose that by oxidation reactions, (1/3)Cu(+II) ions may be completely converted to (1/3)Cu(+III) ions. In this case, the maximum concentration of the Cu(+III) ions should be: (1/3) + (1/3) = (2/3). Thus, the optimal doping should correspond to the following maximum relative concentrations: (1/3)Cu(+I) ions and (2/3)Cu(+III) ions. That is, the optimal doping, should be obtained supposing the following ratio: [(Cu(+III) ions)/(Cu(+I) ions)] = 2.

We apply this hypothesis to estimate the optimal doping of the famous cuprate superconductor $YBa_2Cu_3O_x$, where x is a number to be calculated. Using the relative values:

(1/3) for Cu(+I) ions and (2/3) for Cu(+III) ions, we may write the formula unit: $YBa_2Cu_1(+I)Cu_2(+III)O_x$. Considering the oxidation states Y(+III), Ba(+II) and O(-II) and using the charge neutrality condition, we get:

$$3 + (2 \times 2) + (1 \times 1) + (2 \times 3) - 2x = 0 \quad (4)$$

From Equation (4) we obtain:

$$x = 7.0 \quad (5)$$

The result (5) is in good agreement with the result (x = 6.9) reported in (Kokkallaris et al., 1999).
In the next section, using the above method, we estimate the oxygen content for optimal doping of the most important p-type copper oxide superconductors.

11. Results

Using the simple model described in the previous section, we estimate the necessary oxygen content to obtain the optimal doping of the most relevant p-type cuprate superconductors. It is important to note that the experimental determination of the oxygen content is a very difficult task. In Table 3 we have selected a number of works containing this experimental information.

Superconductor	*Predicted*	*Measured*	*REFERENCE*
$Ba_{0.15}La_{1.85}CuO_x$	x = 4.1	x = 4.0	Bednorz & Müller, 1986
La_2CuO_x	x = 4.2	x = 4.1	Schirber et al., 1988
$YBa_2Cu_3O_x$	x = 7.0	x = 6.9	Kokkallaris et al.,1999
$YBa_2Cu_4O_x$	x = 8.2	x = 8.0	Rao et al., 1993
Sr_2CuO_x	x = 3.17	x = 3.16	Hiroi et al., 1993
$Bi_2Sr_2CaCu_2O_x$	x = 8.3	x = 8.3	Babaei et al., 2003
$Tl_2Ba_2CuO_x$	x = 6.2	x = 6.0	Rao et al., 1993
$TlCa_2Ba_2Cu_3O_x$	x = 9.0	x = 9.0	Martin et al., 1990
$HgBa_2Ca_2Cu_3O_x$	x = 8.5	x = 8.4	Hung et al., 1997

Table 3. Comparison between the values of oxygen content predicted by our simple model and the experimental values reported in the literature

According to our model, we have used for the copper ions the following relative values: (1/3) for Cu(+I) ions and (2/3) for Cu(+III) ions. For the other elements in Table 3, we have considered the following stable oxidation states: La(+III), Y(+III), Ba(+II), Sr(+II), Bi(+III), Ca(+II), Tl(+III), Hg(+II) and O(-II). We verify that the results predicted by the simple model proposed here are in good agreement with the experimental results listed in Table 3.
In Table 3 we have considered only copper oxide superconductors. Our model may be extended to estimate the optimal doping of p-type oxide superconductors that do not contain Cu. For example, consider the material $Ba_{0.6}K_{0.4}BiO_x$, a famous superconductor without copper, with T_c approximately equal to 30 K (Cava et al., 1988). We shall suppose for the Bi ions the same proportionality assumed in the model just suggested for the cuprate superconductors, that is, for optimal doping, we assume that the relative concentrations

should be given by: (1/3)Bi(+III) and (2/3)Bi(+V). Considering the oxidation states Ba(+II) and K(+I) and using the charge neutrality condition, we have:

$$1.2 + 0.4 + (1/3)(3) + (2/3)(5) - 2x = 0 \quad (6)$$

From Equation (6) we obtain the result:

$$x = 2.95 \quad (7)$$

The result (7) is in good agreement with the value (x = 3) reported in the reference (Cava et al., 1988).

12. Discussion

We believe that the simple model proposed in this paper in the case of p-type oxide superconductors could also be extended to estimate the optimal doping of n-type oxide superconductors. However, in the case of n-type oxide superconductors, the reaction produced by oxygen doping is a reduction reaction instead of an oxidation reaction that occurs in p-type oxide superconductors. Since we have not found in the literature any experimental determination of the oxygen content in the case of n-type oxide superconductors we shall not discuss this issue here. This question will be addressed in a future work.

We have proposed a simple model to estimate the relative concentrations of the ions involved to estimate the oxygen content for optimal doping of p-type oxide superconductors. The predictions based on this model are in good agreement with experimental results reported in the literature (Table 3). However, we emphasize that this simple model is not a theoretical model, it is a phenomenological model. In Sections 5, 6, 7 and 8 we have discussed some questions in order to give theoretical support for this model.

13. Concluding remarks

In this chapter we have studied the most relevant questions about the microscopic mechanisms of superconductivity in oxide materials. Parts of our arguments may be found in the list of references in the next section. However, we believe that our ideas have been expressed in a clear form for the questions at hand.

Our conjectures can be used to explain some remarkable properties of high-T_c superconductors mentioned in Section 2: (a) the anisotropy is explained considering that the electrons involved in the hopping mechanisms are 3d-electrons (see Section 5); (b) the order of magnitude of the coherence length (the mean distance between two electron pairs) is in accordance with the order of magnitude of the distance between the electron clouds of two neighboring ions (see Section 2); (c) the nonmonotonic dependence of T_c on the carrier concentration is explained by the hypothesis of double charge fluctuations and optimal doping (Sections 3 and 11).

The theory of bipolaronic superconductivity (Alexandrov & Edwards, 2000) is similar to our phenomenological model. In the theory of bipolaronic superconductivity, bipolarons are formed supposing a mechanism to bind two polarons. However, by our hypothesis, it is not necessary to suppose the formation of bipolarons by the binding of two polarons. We have assumed that the preformed pairs are just pairs of electrons existing in the electronic configurations of the ions or atoms involved in double charge fluctuations. These pairs

should be, for example, lone pairs in atoms or ions or pairs of electrons in the electronic configurations obtained when Hund's rule is applied.

The simple model described here is not a theoretical model and cannot be used to account quantitatively for the microscopic mechanisms responsible for superconductivity in oxide materials. However, we believe that our assumptions are helpful to the investigations of the microscopic mechanisms in oxide superconductors. We expect that this simple model will also be useful to encourage further experimental and theoretical researches in superconducting materials. It is worthwhile to study the details of the role of double charge fluctuations in the microscopic mechanisms responsible for superconductivity in oxide materials.

Finally, we suggest some future researches. It is worthwhile to make experiments to verify if this model is correct. Supposing that this simple model works, it would be possible to calculate stoichiometric compositions in order to obtain the optimal doping in the researches to synthesize new oxide superconductors. It is well known that the most important method in semiconductor technology is obtained by ion implantation techniques. Similarly, we believe that ion implantation techniques probably will be important in superconductor technology as well. Thus, we hope that future researches based on ion implantation techniques could open a new route in the synthesis of high-T_c superconductors. These future researches, using ion implantation, should take advantage of the possibility of double charge hoping mechanisms, instead of single charge hoping mechanisms existing in the case of ion implantation in the semiconductor technology.

14. References

Alexandrov, A. S. (1998). D-wave Bose-Einstein condensate and tunneling in superconducting cuprates. *Physica C*, 312, 46-56

Alexandrov, A. S. (1999). Comment on "Experimental and theoretical constraints of bipolaronic superconductivity in high T_c materials: An impossibility". *Phys. Rev. Letters,* 82, 2620-2620

Alexandrov, A. S. & Edwards, P. P. (2000). High T_c cuprates: a new electronic state of matter? *Physica C*, 331, pp. 97-112

Babaei, M.; Ross, D. K.; Gorgiev, P. A.; Khoshenevisan, B. & Yazdani, A. (2003). Oxygen non-stoichiometry of bismuth-based $Bi_2Sr_2CaCu_2O_{8+\delta}$ (Bi-2212) high temperature superconductor. *Physica C: Superconductivity*, 391, 3, pp. 289-297

Bardeen, J.; Cooper, L. N. & Schrieffer, J. R. (1957). Theory of superconductivity. *Phys. Rev.* , 108, 5, pp. 1175-1204

Beasley, M. R. (1991). Tunneling and proximity effect studies of the high-temperature superconductors. *Physica C,* 185-189, 227-233

Bednorz, J. G. & Müller, K. A. (1986). Possible high T_c superconductivity in the Ba-La-Cu-O system. *Zeitschrift fur Physik B, Condensed Matter*, 64, 2, pp. 189-193

Blatt, J. M. (1962). Qualitative arguments concerning the Bose-Einstein condensation of fermion pairs. *Progress of Theoretical Physics*, 27, pp. 1137-1142

Callaway, J.; Kanhere, D. G & Misra, P. K. (1987). Polarization-induced pairing in high-temperature superconductivity. *Phys. Rev. B*, 3, 13, pp. 7141-7144

Canright, J. S. & Vignale, G. (1989). Superconductivity and acoustic plasmons in the two-dimensional electron gas. *Phys. Rev. B*, 39, 4, pp. 2740-2743

Carbotte, J. P.; Schachinger, E. & Basov, D.N. (1999). Coupling strength of charge carriers to spin fluctuations in high-temperature superconductors. Nature, 401, 6751, pp. 354-356

Cava, R. J.; Batlogg, B.; Krajewski, J. J.; Farrow, R.; Rupp Jr, L. W.; White, A. E.; Peck, W. E. & Kometani, T. (1988). Superconductivity near 30 K without copper: the $Ba_{0.6}K_{0.4}BiO_3$ system. *Nature*, 332, pp. 814-816

Cava, R. J. (2000). Oxide superconductors. *Journal American Ceramic Society*; 83, 1, pp. 5-28

Chakraverty, B. K.; Ranninger, J. & Feinberg, D. (1998). Experimental and Theoretical Constraints of Bipolaronic Superconductivity in High T_c Materials: An Impossibility. *Phys. Rev. Letters*, 81, pp. 433-436

Dalfovo, F.; Giorgini, S.; Pitaevskii, L. P. & Stringari. (1999). Theory of Bose-Einstein condensation in trapped gases. *Reviews of Modern Physics*, 71, 3, pp. 463-512

Davydov, A. S. (1990). Theoretical investigation of high-temperature superconductivity. *Physics Reports (Review Section of Physics Letters)*, 190, 4-5, pp. 191-306

De Jongh, L. J. (1988). A comparative study of (bi)polaronic (super)conductivity in high- and low-T_c superconducting oxides. *Physica C: Superconductivity*, 152, pp. 171-216

Emin, D. (1991). Large bipolarons and superconductivity. *Physica C: Superconductivity*, 185-189, Part 3, pp. 1593-1594

Foltin, J. (1988). Attractive interaction between electrons: An electron-pairing mechanism for superconductivity. *Phys. Review B*, 38, 15, pp. 10900-10902

Foltin, J. (1989). Difference in high temperature superconductivity of two families of cuprate oxides. *Physics Letters A*; 141, 8-9, pp. 427-428

Ganguly, P. & Hegde, M. S. (1988). Evidence for double valence fluctuation in metallic oxides of lead. *Phys. Rev. B*; 37, 10, pp. 5107-5111

Hiroi, Z.; Takano M.; Azuma, M. & Takeda, Y. (1993). A new family of copper oxide superconductors $Sr_{n+1}Cu_nO_{2n+1+\delta}$ stabilized at high pressure. *Nature*, 364, 6435, pp. 315-317

Hirsch, J. E. (1991). Bose condensation versus pair unbinding in short-coherence-length superconductors. *Physica C: Superconductivity*, 179, pp. 317-332

Hung, K. C.; Lam, C.; Shao, H. M.; Wang, S. D. & Yao, X. X.; (1997). Enhancement in flux pining and irreversibility field by means of a short time annealing technique for $HgBa_2Ca_2Cu_3O_{8.4}$ superconductor. *Superc. Science Technology*, 10, 11, pp. 836-842

Johnston, D. C.; Prakash, H.; Zachariessen, W. H. & Vishvanathan, B. (1973) High temperature superconductivity in the Li-Ti-O ternary system. *Materials Research Bulletin*; 8, 7, pp. 777-784

Kamimura, H. (1987). Cooperative bipolaron tunneling in high T_c copper oxide compounds and superconductivity. *Japanese Journal of Applied Physics*, 26, 5, pp. L627-L630

Karppinen, M.; Fukuoca, A.; Wang, J.; Takano, S.; Wakata, M.; Ikemachi, T. & Yamauchi, H. (1993). Valence studies on various superconducting bismuth and Lead cuprates and related materials. *Physica C: Superconductivity*, 208, pp. 130-136

Kokkallaris, S.; Deligiannis, K.; Oussena, M.; Zhukov, A. A.; Groot, P. A. J.; Gagnon, R. & Taillefer, L. (1999). Effect of oxygen stoichiometry on the out-of-plane anisotropy of $YBa_2Cu_3O_{7-\delta}$ single crystals near optimal doping. *Superconductor Science Technology*, 12, 10, pp. 690-693

Kugler, M.; Fischer, O.; Renner, Ch.; Ono, S. & Ando. Y. (2001). Scanning tunneling spectroscopy of $Bi_2Sr_2CuO_{6+\delta}$: New evidence for the common origin of the pseudogap and superconductivity. *Phys. Rev. Letters*, 86, 21, pp. 4911-4914

Lee, J. D. (1991). *Concise Inorganic Chemistry*. Chapman & Hall, London

Lee, D. M. (1997). The extraordinary phases of liquid ^{3}He. *Reviews of Modern Physics*, 69, pp. 645-666

Leggett, A. J. (1994). D-wave superconductivity: the lifetime problem. *Physica B*, 199-200, pp. 291-293

London, F. (1938). On the Bose-Einstein condensation. *Phys. Rev.*, 54, pp. 947-954

Luiz, A. M. (2008). A simple model to estimate the optimal doping of p-type oxide superconductors. *Mat. Research*, 11, 4, pp. 495-498

Maeda, H.; Tanaka, Y.; Fukutomi, M. & Asano, T. (1988). A new high-T_c oxide superconductor without a rare earth element. *Japanese Journal of Applied Physics*; 27, 2, pp. L209-L210

Maitra, T. & Taraphder, A. (1999). Gap anisotropy in the angle-resolved photoemission spectroscopy of $Bi_2Sr_2CaCu_2O_{8+\delta}$ *Physica C: Superconductivity*, 325, pp. 61-69

Martin, C.; Maignan, A.; Provost, J.; Michel, C.; Hervieu, M.; Tournier, R. & Raveau, B. (1990). Thalium cuprates: The critical temperature is mainly governed by the oxygen nonstoichiometry. *Physica C: Superconductivity*, 168, pp. 8-22

McMurry, R. C. & Fay, R. C. (1998). *Chemistry*. Prentice Hall, New Jersey

Mourachkine, A. (2004). *Room Temperature Superconductivity*. Cambridge International Science Publishers, Cambridge.

Munzar, D.; Bernhard, C. & Cardona, M. (1999). Does the peak in the magnetic susceptibility determine the in-plane infrared conductivity of YBCO? A theoretical study. *Physica C: Superconductivity*, 312, pp. 121-135

Nagamatsu, J.; Nacagawa, N.; Muranaka, T.; Zenitani, Y. & Akimitsu, J. (2001). Superconductivity at 39 K in magnesium diboride. *Nature*, 410, (March 2001), pp. 83-84

Prelovsek, P. (1988). Two band model for superconducting copper oxides. *Phys. Lett. A*, 126, 4, (January 1988), pp. 287-290

Ranninger, J. (1994). The polaron scenario for high T_c superconductivity. *Physica C: Superconductivity*, 235-240, Part 1, pp. 277-280

Rao, C. N. R.; Nagarajan R. & Vijayaraghavan, R. (1993). Synthesis of cuprate superconductors. *Superconductor Science Technology*, 6, 1, pp. 1-22

Raveau, B.; Michel, C.; Hervieu, M. & Provost, J. (1988). Crystal chemistry of perovskite superconductors. *Physica C: Superconductivity*, 153-155, pp. 3-8

Remeika, J. P.; Geballe, T. H.; Mathias, B. T.; Cooper, A. S.; Hull, G. W. & Kellye, M. (1967). Superconductivity in hexagonal tungsten bronzes. *Physics Letters A*, 24, 11, pp. 565-566

Sarma, D. D. & Rao, C. N. R. (1988). Nature of the copper species in superconducting $YBa_2Cu_3O_{7-\delta}$. *Sol. State Commun.*, 65, pp. 47-49

Scalapino, D. J. (1995). The case for $d(x^2 - y^2)$ pairing in the cuprate superconductors. *Physics Reports*, 250, pp. 329-325

Schilling, A. & Cantoni, M. (1993). Superconductivity above 130 K in the Hg-Ba-Ca-Cu-O system. *Nature*, 363, 6424, pp. 56-58

Schirber, J. E.; Morosin, B.; Merrill, R. M.; Hilava, P. F.; Venturinie L.; Kwak, J. F.; Nigrey, P. J.; Baughman, R. J. & Ginley, D. S. (1988). Stoichiometry of bulk superconducting $La_2CuO_{4+\delta}$: A superconducting superoxide? *Physica c,* 152, 1, 121-123

Shen, Z.-X. & Dessau, D. S. (1995). Electronic structure and photoemission studies of late transition metals – Mott insulators and high temperature superconductors. *Physics Reports*, 253, pp. 1-162

Shimakawa, Y.; Kubo, Y.; Manako, T.; Nakabayashi, Y. & Igarashi, H. (1988). Ritveld analysis of $Tl_2Ba_2Ca_{n-1}Cu_nO_{4+n}$ (n = 1, 2, 3) by powder X-ray diffraction. *Physica C: Superconductivity*, 156, 1 (1 August 1988), pp. 97-102

Silvera, I. F. (1997). Bose-Einstein condensation. *American Journal of Physics*, 65, 570-574

Sleight, A. W.; Gilson, J. L. & Bierstedt, P. E. (1975). High-temperature superconductivity in the $BaPb_{1-x}Bi_xO_3$ system. *Solid State Commun.*, 17, pp. 27-28

Sleight, A. W. (1995). Room temperature superconductivity. *Acc. Chem. Res.*, 28, pp. 103-108

Sun, A. G.; Gajewski, D. A.; Maple, M. P. & Dynes, R. C. (1994). Observation of Josephson pair tunneling between a high-T_c cuprate ($YBa_2Cu_3O_{7-\delta}$) and a conventional superconductor (Pb). *Phys. Rev. Letters*; 72, pp. 2267-2270

Tachiki, M. & Takahashi, S. (1988). Pairing interaction mediated by the Cu-O charge-transfer oscillations associated with LO phonons in oxide superconductors and their high-T_c superconductivity. *Phys. Rev. B*, 38, 1, pp. 218-224

Takada, Y. (1993). S- and p-wave pairings in the dilute electron gas: Superconductivity mediated by the Coulomb hole in the vicinity of the Wigner-crystal phase. *Phys. Rev. B*, 47, 9, pp. 5202-5211

Tanaka, Y. Josephson effect between s-wave and d($x^2 - y^2$) wave superconductors. (1994). *Phys. Rev. Letters*; 72, pp. 3871-3874

Timusk, T. & Statt, B. (1999). The pseudogap in high-temperature superconductors: an experimental survey. *Rep. Prog. Phys.*, 62, pp. 61-122

Varma, C. M. (1988). Missing valence states, diamagnetic insulators, and superconductors. *Phys. Rev. Letters*; 61, 23, pp. 2713-2716

Wheatley, J. M.; Hsu, T. C. & Anderson, P. W. (1988). Interlayer pair hopping: Superconductivity from the resonating-valence-bond state. *Phys. Rev. B*; 37, 10, pp. 5897-5900

Wu, M. K.; Ashburn J. R.; Torng, C. J.; Hor, P.H.; Meng, R. L.; Goa, L.; Huang, Z. J.; Wang, Y. Q. & Chu, C. W. (1987). Superconductivity at 93 K in a new mixed-phase Y-Ba-Cu-O compound system at ambient pressure. *Phys. Rev. Letters*, 58, 9, pp. 908-910

Yang, J.; Li, Z. C.; Lu, W.; Yi, W.; Shen, X. L.; Ren, Z. A.; Che, G. C.; Dong, X. L.; Sun, L. L.; Zhou, F. & Zhao, Z. X. (2008). Superconductivity at 53.5 K in $GdFeAsO_{1-\delta}$. *Superconductor Science Technology*, 21, 082001, pp. 1-3

Zhang, H. & Sato, H. (1993). Universal relationship between T_c and the hole content in p-type cuprate superconductors. *Phys. Rev. Letters*, 70, 11, pp. 1697-1699

Zuotao, Z. (1991). Coordination chemistry and superconductivity. *J. Phys. Chem. Solids*, 52, 5, pp. 659-663

2

The Discovery of Type II Superconductors (Shubnikov Phase)

A.G. Shepelev
National Science Center «Kharkov Institute of Physics and Technology»
Ukraine

"It is a fascinating testament to Shubnikov's great originality and to the terrible times that deprived him of his life and we all of the fruits of the science for so long. Even now, many do not really understand the breakthrough made in Kharkov."
From the letter of 31 December, 2008, written by Shubnikov Professor D. Larbalistier, Director of Applied Superconductivity Center, USA, on reprinting in English the article (Shubnikov et al., 1937) in 2008.

1. Introduction

At present, Type II superconductors enjoy wide applications in science and technology. It is worth noting that all the superconductors, from Nb_3Sn to cuprates, fullerenes, MgB_2, iron-based systems that have been discovered for the last 50 years, are Type II superconductors. It is of interest to trace back the intricate research carried out for 8 years from 1929 (De Haas & Voogd, 1929) to 1936 by experimenters in four countries out of the five, who had liquid helium at their laboratories at the time when L.V.Shubnikov, V.I.Khotkevich, G.D.Shepelev, Yu.N.Ryabinin (Schubnikow et al., 1936; Shubnikov et al., 1937; Shepelev, 1938) discovered experimentally in Kharkov the phenomenon of Type II superconductivity in single-crystal, single-phase superconducting alloys. A theoretical explanation of the phenomenon, based on experimental results (Shubnikov et al., 1937) and the Ginzburg-Landau theory (Ginzburg & Landau, 1950; Ginzburg, 1955), was given by A.A.Abrikosov only in 1957 (Abrikosov, 1957). The proposed publication lays out the recognition of the discovery of Type II superconductors by leading specialists in this area and indicates a role which this phenomenon plays in the science and technology. Unfortunately, neither L.D.Landau nor anyone of the pioneer-experimenters lived to witness the awarding the corresponding Nobel Prize 2003 when it was given to V.L.Ginzburg and A.A.Abrikosov.
All the superconductors are known to be of two types depending on the magnitude of the ratio:

$$æ=\lambda/\xi\,,$$

where æ – the Ginzburg-Landau parameter, λ - the penetration depth of magnetic field, ξ – the coherence length between electrons in Cooper pair (Fig.1). For the typical pure superconductors λ~500 Å, ξ~3000 Å, i.e. æ<<1. A critical value used to determine the superconductor type is the following: $æ_c = 1/\sqrt{2}$ (Ginzburg & Landau, 1950; Ginzburg, 1955).

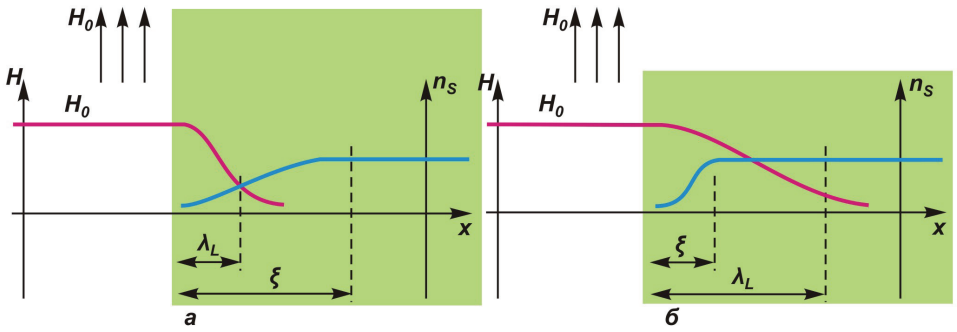

Fig. 1. Schematic diagram of interface between normal and superconducting phases: a) Type I superconductor; b) Type II superconductor. n_s – density of superconducting electrons (After Ginzburg & Andryushin, 2006).

Magnetic properties of these two superconductor types are essentially different (Fig.2). This phenomenon can be attributed to the fact that in the *Type I superconductors* (pure superconductors), where the Ginzburg-Landau parameter æ < $1/\sqrt{2}$ (Ginzburg & Landau, 1950; Ginzburg, 1955), the n-s interphase surface energy $\sigma_{ns} > 0$. For this reason, under the impact of magnetic field an intermediate state, as shown by L.D.Landau (Landau, 1937; Landau, 1943), is created in those superconductors of arbitrary shape (with the demagnetizing factor $n \neq 0$) where the layers of the normal and superconducting phases alternate.

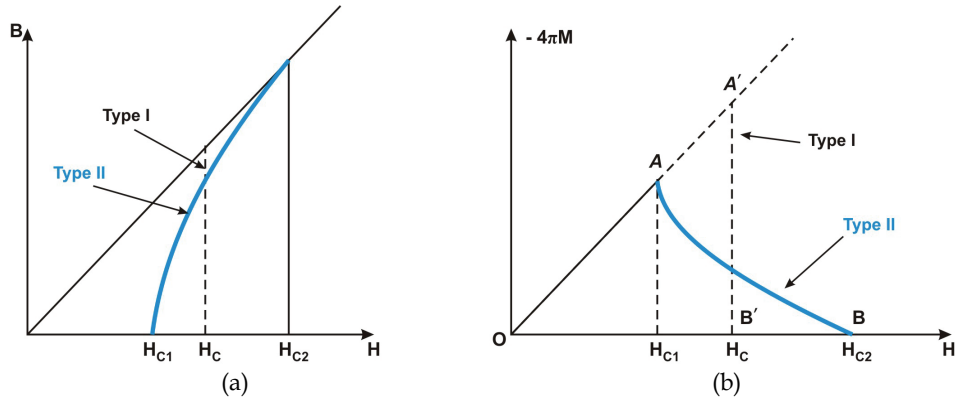

Fig. 2. (a) The induction in the long cylinder as a function of the applied field for Type I and Type II superconductors; (b) The reversible magnetization curve of a long cylinder of Type I and Type II superconductor (After De Gennes, 1966)

In *Type II superconductors* (superconducting alloys), where æ > $1/\sqrt{2}$, the n-s interphase surface energy $\sigma_{ns} < 0$ and magnetic field penetrates these superconductors in the form of the Abrikosov vortex lattice (Abrikosov, 1957). As indicated by A.A.Abrikosov (Abrikosov, 1957), the idea about the alloys turning into Type II superconductors at the value of the parameter æ > $1/\sqrt{2}$ was first brought forward by L.D.Landau.

Yet, it took about 30 years since the pioneering experimental research on superconducting alloys under applied magnetic field to understand fully the Type II superconductivity phenomenon.

The theory of Type II superconductors has been expounded in detail over the past 45 years in scores of reviews and monographs on superconductivity, the experimental side of the discovery of these superconductors, as far as the author knows, having been discussed only fragmentarily either at the early stages of the research (Burton, 1934; Wilson, 1937; Ruhemann, 1937; Shoenberg, 1938; Jackson, 1940; Burton et al., 1940; Ginzburg, 1946; Mendelssohn, 1946; Shoenberg, 1952) or later on (refer to the authoritative published papers (Mendelssohn, 1964; Mendelssohn, 1966; Goodman, 1966; De Gennes, 1966; Saint-James et al., 1969; Anderson, 1969; Chandrasekhar, 1969; Serin, 1969; Hulm & Matthias, 1980; Hulm et al., 1981; Pippart, 1987; Berlincourt, 1987; Dahl, 1992[1]; Dew-Hughes, 2001) and also to (Sharma & Sen, 2006; Slezov & Shepelev, 2008; Karnaukhov & Shepelev, 2008, Slezov & Shepelev, 2009)). Therefore, the way the real events took place is, quite regrettably, largely hidden from view to many of the International Scientific Community.

We shall remind that H.Kamerlingh Onnes (Physical Laboratory, University of Leiden), an outstanding physicist of those times, who discovered the phenomenon of superconductivity in *pure metals* in 1911 (Kamerlingh Onnes, 1911), was the first with his co-workers to take an interest beginning from 1914 in the effects of magnetic field on those superconductors (Kamerlingh Onnes, 1914; Tuyn & Kamerlingh Onnes, 1926; Sizoo et al., 1926; De Haas et al., 1926, De Haas & Voogd, 1931a). In particular, it was found that superconductivity in pure metals got suddenly disrupted when impacted by an applied magnetic field with a critical value H_c (in the case of the demagnetizing factor n = 0), which manifested itself in a sudden restoration of electrical resistance of the samples from zero to such value that corresponded to $T>T_c$ (Fig.3).

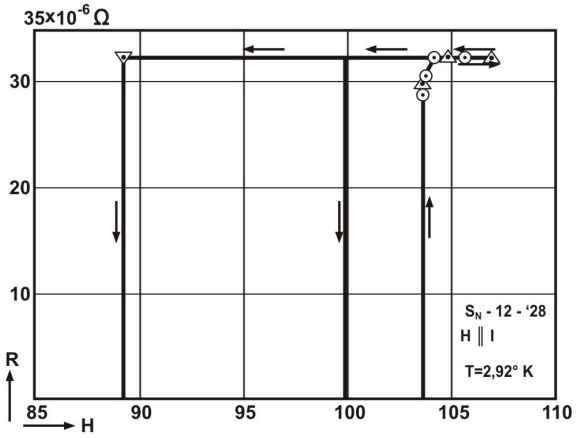

Fig. 3. Sudden change of electrical resistance of wire sample of single crystal tin at $T<T_c$, as caused by longitudinal magnetic field (After De Haas & Voogd, 1931a).

[1] In the interesting book, Dahl (Dahl, 1992) has erroneously ascribed the discovery of Type II superconductors to some other article from Kharkov. In reality, as is well known (see 4. Recognition), the world's leading specialists in superconductivity unanimously relate this discovery to the articles by L.V.Shubnikov V.I.Khotkevich, G.D.Shepelev, Yu.N.Ryabinin. (Schubnikow et al., 1936, Shubnikov et al., 1937).

It should be said that, aside from the feature of *electric properties* of Type I superconductors upon decreasing temperature below T_c (the steep fall of electrical resistance down to such resistivity which was smaller than 10^{-23} Ω·cm), the second fundamental characteristic of pure superconductors (*magnetic properties)* also had a peculiarity that was out of the ordinary. In 1933 W. Meissner and R. Ochsenfeld (Physikalische Technische Reichsanstalt) found (Meissner & Ochsenfeld, 1933) that a magnetic field which was smaller than H_c did not run through a *pure superconductor*, the magnetic induction in it being B = 0 (with the exception of a very thin surface layer ~ λ). Under the impact of an applied magnetic field with the value H_c the pure superconductor magnetization M and induction B also changed with a jump (Fig.4). These values are related via the following ratio:

$$M = (B - H) / 4\pi.$$

The exclusion of flux from the bulk of pure superconductor is called the Meissner effect.
Any discovery is generally preceded by a preparatory period. Then, some day or other, following the actual discovery the recognition is accorded. Some time after that one can look at final results and evaluate the prospects.

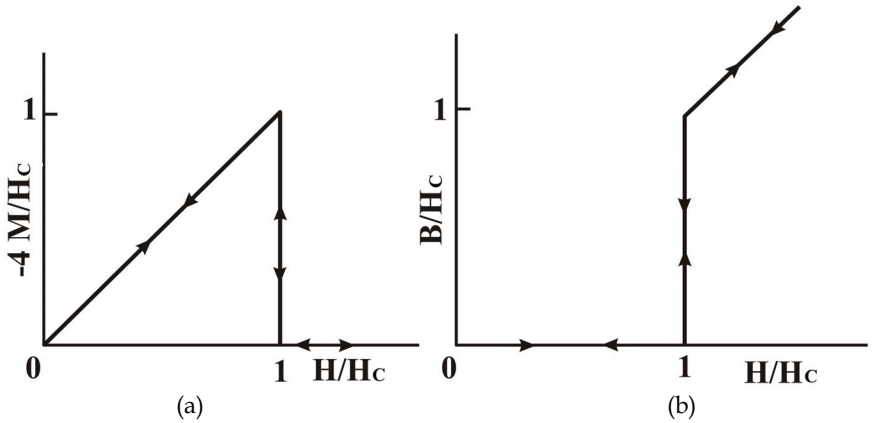

Fig. 4. a) Magnetization curve of a pure superconducting long cylinder in longitudinal magnetic field; b) B-H curve of a pure superconducting long cylinder in longitudinal magnetic field (After Shoenberg, 1938).

2. Preliminary stage

Interestingly enough, even before the Meissner effect was discovered, W.J.De Haas, J.Voogd (Kamerlingh Onnes Laboratory, University of Leiden) had discovered (De Haas & Voogd, 1929) a distinction between the behavior in applied magnetic field of *electrical resistance* of polycrystals of *superconducting alloys* and that of pure superconductors. It appeared that in rod specimens of the alloys Bi + 37.5at%Tl, Sn + 58wt%Bi, Sn +28.1wt%Cd (the latter two being close to the eutectic alloy) (De Haas & Voogd, 1929), in the alloy Pb + 66.7at%Tl, the eutectic Pb + Bi and in the alloys Pb-Bi (7wt%; 10wt%; 20wt%), Sn + 40.2wt%Sb (De Haas & Voogd, 1930), in the alloys Pb + 15wt%Hg, Pb + 40wt%Tl, Pb + 35wt%Bi, the eutectic Au-Bi (De Haas & Voogd, 1931b) the disruption of superconductivity occurred across a broad interval of magnetic fields irrespective of the orientation of the field running parallel, i.e. at

n=0 (Fig.5), or perpendicular (Fig.6) to the axis of cylindrical specimens, i.e. at n = ½ [2]. As D.Shoenberg noted (Shoenberg, 1938; Shoenberg, 1952), for superconducting alloys *"there is much less difference between the curves for a transverse and a parallel field than there is for a pure superconductor"*.

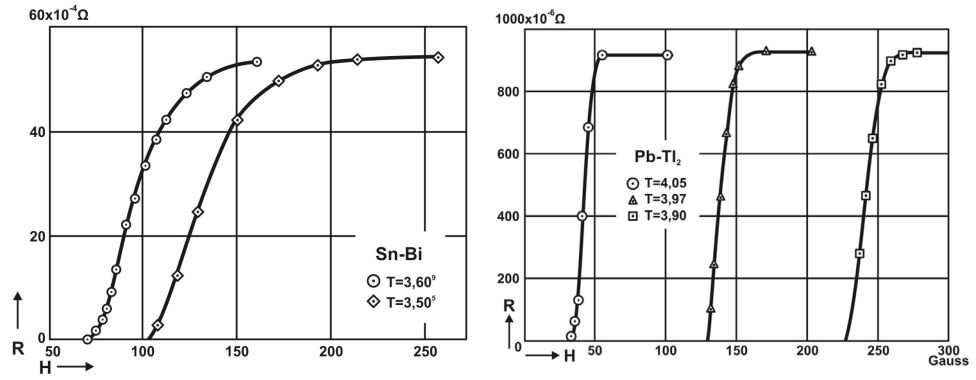

(a) (b)

Fig. 5. The resistance of superconducting long cylinder for polycrystalline Sn-Bi alloy (After De Haas & Voogd, 1929) and Pb-Tl alloy in longitudinal magnetic field (After De Haas & Voogd, 1930).

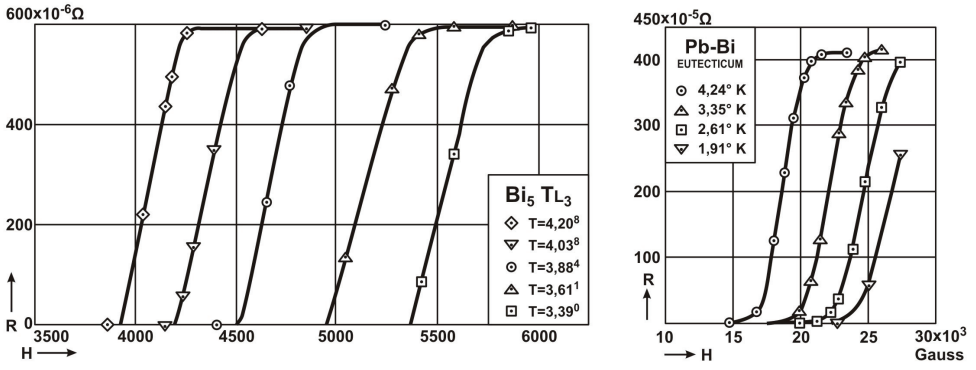

(a) (b)

Fig. 6. Variation of electrical resistance of cylindrical specimens of superconducting alloys Bi-Tl (After De Haas & Voogd, 1929), Pb-Bi (After De Haas & Voogd, 1930) in transverse magnetic field at various temperatures.

During studies on the electric properties of the eutectic Pb-Bi, while decreasing applied magnetic field from H_c to zero, (De Haas & Voogd, 1930) found a clear-cut hysteresis about

[2] The exact data about the composition of research alloy samples are given: for alloys Sn-Bi, Sn-Cd, Pb-Bi in (De Haas et al., 1929a), Pb-Tl in (De Haas et al., 1930), Sn-Sb in (Van Aubel et al., 1929), Au-Bi in (De Haas et al., 1929b).

which many authors wrote later so very many scientific papers. Much later, it was shown (Saint-James & DeGennes, 1963) that in the case of the magnetic field that ran parallel to the surface in the interval $H_{c2} < H < H_{c3} = 1{,}695H_{c2}$ a superconducting layer of the thickness on the order of ξ was formed on the surface of the sample. The problems of the hysteresis and "frozen-in" magnetic flux in such superconducting alloys that, as established later on, were strongly dependent on sample quality (compositional inhomogeneities, impurities, stresses) were discussed in minute detail in monographs by D.Shoenberg (Shoenberg, 1938; Shoenberg, 1952).

W.J.De Haas, J.Voogd noted quite reasonably (De Haas & Voogd, 1929), that the eutectic research samples were a mixture of two phases, one of which shunted the entire sample when the electrical resistance was taken. The difference in the disruption of superconductivity of the alloys, for instance Pb +66.7at% Tl and Pb +40wt% Tl, relative to pure superconductors was attributed by the above authors to the possible influence from inhomogeneities in the alloy samples (De Haas & Voogd, 1930; De Haas & Voogd, 1931b).

Unfortunately, in the early 20th century not all of the phase diagrams of the alloys were known precisely. According to data from such a prestigious source as (Massalski, 1987) (Fig.7 and 8) the majority of the alloys studied by W.J.De Haas, J.Voogd (De Haas & Voogd,

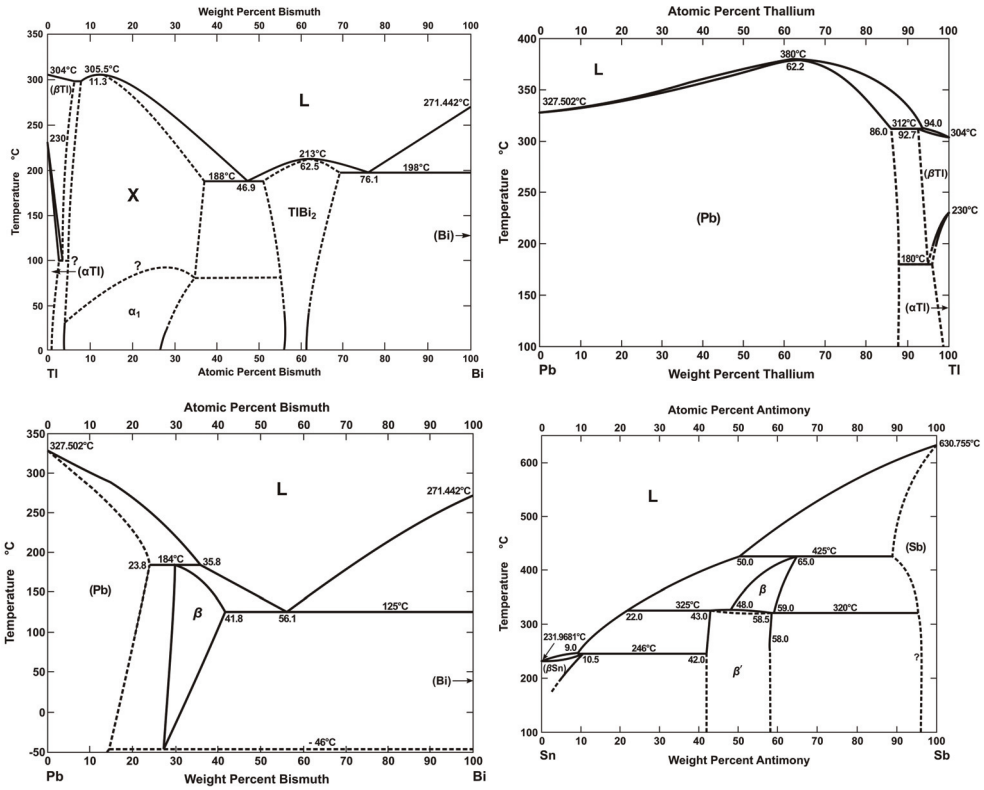

Fig. 7. Binary phase diagrams of the alloys Tl-Bi, Pb-Tl, Pb-Bi, Sn-Sb (After Massalski, 1987).

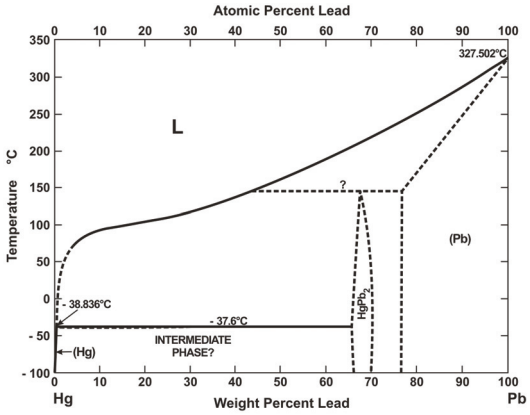

Fig. 8. Binary phase diagrams of the alloy Hg-Pb (After Massalski, 1987).

1929; De Haas & Voogd, 1930; De Haas & Voogd, 1931b) (except the alloys Pb+Tl, Pb+Bi (7wt%; 10wt%) and Pb+15wt%Hg) had more than one phase, i.e. they were distinctly inhomogeneous as were the alloys with the eutectics Sn-Bi, Sn-Cd, Pb-Bi, Au-Bi.

The discovery in the eutectic Pb-Bi of preservation of superconductivity under applied fields on the order of 2T allowed W.J.De Haas, J.Voogd (De Haas & Voogd, 1930) to bring back to life a dream that had been cherished by H.Kamerlingh Onnes about creating magnetic fields by using superconducting solenoids without wasting much energy. However, neither in Kharkov, nor in Leiden, nor in Oxford this dream was not to come true on account of the low value of the current that acted to disrupt the superconductivity (Rjabinin &Schubnikow, 1935a; Keesom, 1935; Mendelssohn, 1966). Thirty years on, K.Mendelssohn (Mendelssohn, 1964; Mendelssohn, 1966) reasoned that the resolution of this challenge, as it were, called for a change in mentality, a heretofore inconceivable progress in scientific engineering and scope of scientific research, as well as for considerable increases in the funding of the Science.

The subsequent experimental research indicated that not only the behavior of the electrical properties, but also that of the *magnetic ones*, in superconducting alloys were different to the properties of the pure superconductors. In the span of *1934-1936* there was a thrilling *"hurdle race"* in the studies on magnetic properties of superconducting alloys between scientists of four countries out of the five that had liquid helium at their laboratories at that moment. Considering that the superconductors possessed a large magnetic moment, the methods used in the works below were based on the standard magnetic measurements. Using a fluxmeter or a ballistic galvanometer, the measurements were made of magnetization-vs.-voltage characteristics in the coil that surrounded the sample: during sample cooling in constant pre-assigned magnetic field or after sample pulling out of the coil at constant temperatures and magnetic fields, or upon turning on and off the constant magnetic field, or during stepping up or down the magnetic field little-by-little across the entire range from zero to H_c and back.

Canadian scientists F.G.A.Tarr and J.O.Wilhelm (McLennan Laboratory, University of Toronto) submitted a paper for publication (Tarr & Wilhelm, 1935) *on September 14, 1934* which contained the results of their studies on magnetic properties of superconducting mercury, tin, tantalum, as well as the alloys with the eutectic Pb+Sn (40wt%; 63wt%; 80wt%) and the multiphase alloy Bi+27.1wt% Pb+22.9wt%Sn, observable under the impact of applied magnetic field. Fig.9 presents the phase diagram of the ternary alloy. In particular, a

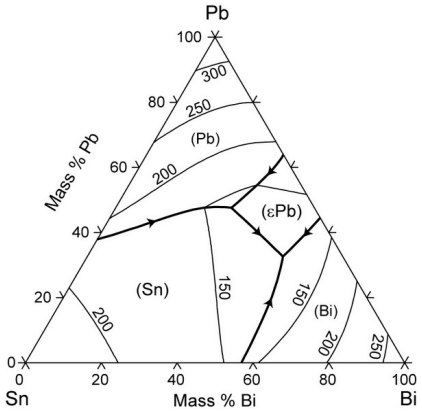

Fig. 9. Phase diagram of the alloy Bi-Pb-Sn (After Kattner, 2003).

study was made on decreasing the magnetic flux running through plane disklike samples during their cooling at a constant magnetic field which was perpendicular to the disk plane (n=1) from a temperature higher than T_c to the temperature corresponding to H_c. Whereas the magnetic flux was completely expelled from the pure mercury sample, in samples of the commercially produced tin, lead, tantalum (evidently of insufficient purity) the "frozen-in flux" was observable. There was no Meissner effect in the alloys that had more than one phase Pb+Sn (40wt%; 63wt%; 80wt%) and Bi+27.1wt% Pb+22.9wt%Sn at all.

T.C.Keeley, K.Mendelssohn, J.R.Moore (Clarendon Laboratory, Oxford University) in their paper (Keeley et al., 1934) submitted for publication on *October 26, 1934* and published on *November 17* of the same year presented the results of induction measurements in long cylindrical specimens of mercury, tin, lead and alloys Pb+Bi (1wt%; 4wt%; 20wt%), Sn+28wt%Cd, Sn+58wt%Bi (pre-cooled to a temperature below T_c) upon turning on and then off the longitudinal magnetic field (n = 0). It appeared that the "frozen in" magnetic flux, remaining in the sample («frozen in» induction) was zero for pure mercury, but a "*small addition of another substance has the effect of "freezing in" the entire flux which the rod contains at the Hc, when the external field is switched off*". The authors reported that at a temperature below T_c in samples of the said-alloys in longitudinal magnetic field "*it was observed in most cases that the change of induction did not seem to take place at a definite field strength but, at a constant temperature, extended over a field interval, amounting to 10-20 per cent of the threshold value field*". Let us say that a greater portion of the alloy compositions studied by these authors had been earlier investigated by W.J.De Haas, J.Voogd (De Haas & Voogd, 1929; De Haas & Voogd, 1930; De Haas & Voogd, 1931b); the single-phase alloys being only Pb+Bi (1wt%; 4wt%).

On December 22, 1934 in their report at a session of Royal Academy (Amsterdam) W.J.De Haas and J.M.Casimir-Jonker (De Haas & Casimir-Jonker, 1935a) reported the results of studies on magnetic properties of carefully prepared polycrystals of alloys Bi+37.5at.%Tl (multiphase alloy) and Pb+64.8wt%Tl. The samples were cylinders 35 mm long, 5 mm in diameter, with a narrow 1 mm dia. duct running along the axis; the applied magnetic field was incident perpendicular to the axis of the cylinders (n = ½). The measurement of the magnetic field inside the samples was made over measurement of the electrical resistance of a miniature bismuth wire placed in the middle of the duct. Apparently, for both alloys at temperatures below T_c the magnetic field began to penetrate the superconducting alloys only after attaining a certain value of the applied field (Fig.10).

In this way, it turned out that there were three characteristic fields in the superconducting alloy: a weak field of the incipient penetration of the magnetic flux into the alloy, a field of the onset of a gradual restoration of electrical resistance and a field of the complete transition of the alloy into the normal state (Fig.11). Articles covering those studies were submitted by W.J.De Haas and J.M.Casimir-Jonker on *December 7, 1934* to the prestigious "Nature" (which ran it on *January 5, 1935 (*De Haas & Casimir-Jonker, 1935b)) and to the sole low-temperature physics dedicated authority of those times "Communications from the Physical Laboratory of the University of Leiden» (De Haas & Casimir-Jonker, 1935c) (refer also to the paper (Casimir-Jonker & De Haas, 1935) submitted for publication on *July 29, 1935).*

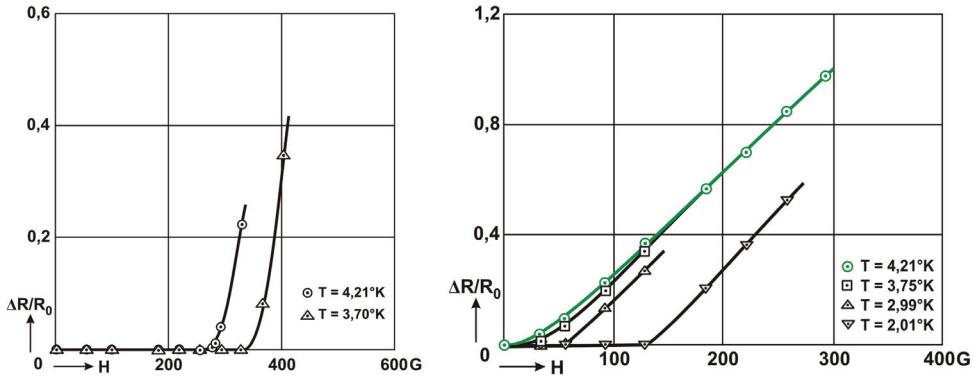

(a) (b)

Fig. 10. Penetration of magnetic field into the superconducting alloys Bi+37,5at.%Tl (left) and Pb+64,8wt%Tl (right). For alloy Pb+64,8wt%Tl curve at 4,21 K obtained for normal state ($T>T_c$) (After De Haas & Casimir-Jonker, 1935c).

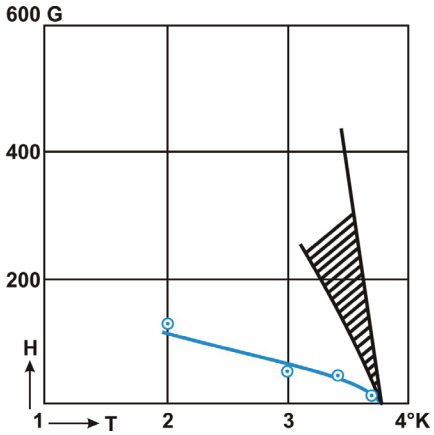

Fig. 11. Temperature dependence of the incipient penetration of magnetic field into the superconducting alloy Pb+64.8wt%Tl. The hatched region denotes the region of gradual flux penetration in magnetic field according to the electrical resistance measurement data (After De Haas & Casimir-Jonker, 1935a).

Fig. 12. Cryogenic Laboratory's Researchers, 1933. From left to right: (the first line) N.S.Rudenko (second), N.M.Zinn (third), O.N.Trapeznikova (fourth), Yu.N.Ryabinin (fifth), A.I.Sudovtsov (sixth), Dogadin (seventh); (the second line) G.D.Shepelev (third), L.V.Shubnikov (fourth), I.P.Korolyov (fifth), V.I.Khotkevich (sixth), V.A.Maslov (ninth).

L.V. Shubnikov, who was known to be working very successfully with W.J.De Haas from autumn of 1926 until summer of 1930 at Kamerlingh Onnes Laboratory (it was there exactly that the Shubnikov–De Haas Effect – the periodic magnetoresistance oscillations in pure metal at low temperatures – was discovered), knew well about his research into superconducting alloys. Having created at Ukrainian Physical-Technical Institute (UPhTI, now the National Science Center «Kharkov Institute of Physics and Technology» - NSC KIPT) the first Cryogenic Lab in the USSR (Fig.12), in 1934 he went into that research, too.
In paper submitted for publication on *January 27, 1935* (Rjabinin & Schubnikow, 1935a) (its summary published by the "Nature" on *April 13, 1935* (Rjabinin & Schubnikow, 1935b)) Yu.N. Ryabinin and L.V.Shubnikov supported the existence of the incipient penetration field (Fig.13) in a single crystal of the superconducting alloy Pb + 66.7at.%Tl and in the multiphase polycrystal Pb-35wt%Bi (samples of those alloys had been studied earlier by W.J.De Haas, J.Voogd (De Haas & Voogd, 1930; De Haas & Voogd, 1931b)) and designated it correspondingly as H_{c1}. It was confirmed that prior to the field H_{c1} there was the magnetic induction B=0 in the alloy Pb + 66.7at.%Tl, while in the interval of field strengths from H_{c1} to the field of total superconductivity disruption, which was designated by them as H_{c2}, the induction gradually increased with increasing applied field. The authors also measured the temperature relationship of H_{c1}, H_{c2} and field of critical current H_{cj} which acted to disrupt the superconductivity (Fig.14). It is noteworthy that Yu.N.Ryabinin and L.V.Shubnikov, as had done earlier W.J.De Hass and J.Voogd (Haas & Voogd, 1930; Haas & Voogd, 1931b), did not rule out a possibility that "*unusual behavior of alloys is caused by their inhomogeneity which may be due to the decomposition of the solid solution and the formation of a new very disperse phase*" (Rjabinin & Schubnikow, 1935a).

On *April 3, 1935* K. Mendelssohn and J.R.Moore (Mendelssohn & Moore, 1935) submitted a new article (published on *May 18, 1935)* in which they supported the existence of the incipient field of penetration into the multiphase alloy Pb+70wt%Bi. The article put forward a hypothesis about a "Mendelssohn Sponge" that suggested the existence in superconducting alloys of inhomogeneities of the composition, structure and internal stresses such that caused the formation of multiple-connection thin structures with anomalously high critical fields serving as current paths (for more detail, refer to the Mendelssohn report on *May 30, 1935,* in Discussion on Superconductivity and Other Low-Temperature Phenomena at Royal Society (London) (Mendelssohn, 1935), where he indicated *"that the amount of "frozen in" flux depended mainly on the purity, lead with 1%, 4%, 10% bismuth was investigated, and the results actually showed that the "frozen in" increased with the addition of the second component."*). Nonetheless, the existence of the Mendelssohn Sponge could not account for the magnetic field penetration at $H < H_c$ in Type II superconductors.

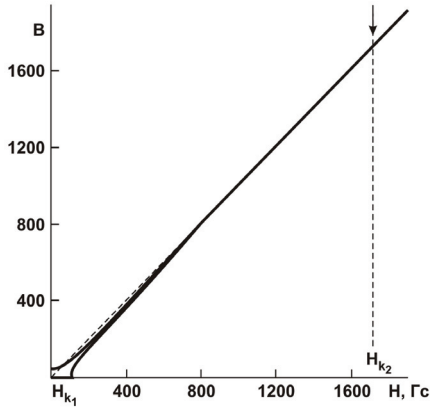

Fig. 13. B-H curve of long cylindrical sample of single crystal Pb+66,7at.%Tl in longitudinal field (Rjabinin & Shubnikow, 1935b).

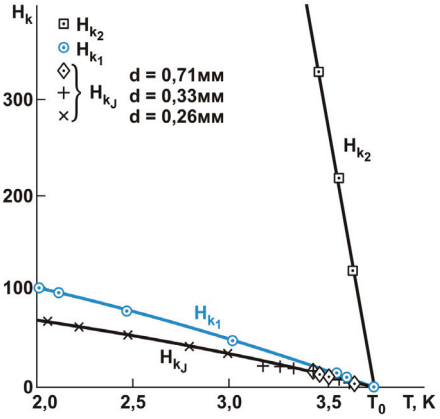

Fig. 14. Temperature dependents of H_{c1}, H_{c2}, H_{cj} for single crystal Pb+66,7at.% Tl (Rjabinin & Shubnikow, 1935a).

Note that in the same 1935 C.J.Gorter (Gorter, 1935) and H.London (London, 1935), while discussing the behavior of alloys with a large critical field in the absence of inhomogeneities, arrived at a conclusion that in magnetic field they had to be delaminated into thin (smaller than λ) superconducting laminae which ran parallel to the applied magnetic field and were separated by thin normal layers. An assessment of those efforts was quick to come in the first edition of the Shoenberg monograph (Shoenberg, 1938): "*De Haas and Casimir-Jonker* (*De Haas & Casimir-Jonker,1935b; De Haas & Casimir-Jonker,1935c*), *using the bismuth wire technique, showed that actually a magnetic field penetrated into an alloy long before it was large enough to restore the first trace of resistance, and that the penetration was very nearly complete at field strengths of the same order of magnitude as for pure elements. Similarly, Mendelssohn and Moore (Mendelssohn & Moore, 1935), and Rjabinin and Shubnikov (Rjabinin & Shubnikov, 1935a; Rjabinin & Shubnikov, 1935b), measuring the B-H curve of a long rod of superconducting alloy, found that B ceased to be zero, and approached the value of H, at fields much lower than those required to restore the first trace of resistance.*»

The Mendelssohn Sponge hypothesis was predominant for about 25 years used to explain the superconducting alloy properties. It would be just enough to mention a monograph "Superconductivity" by V.L.Ginzburg edited by L.D. Landau (Ginzburg, 1946) where it is said that "*The superconductor properties are strongly dependent on impurities, tensions and various inhomogeneities of their composition and structure. The properties of the alloys in which these inhomogeneities are actually always present are substantially different to those of the pure superconductors*". The Mendelssohn Sponge hypothesis was later found erroneous (refer, for instance, to (Goodman, 1964; Berlincourt, 1964; Morin et al., 1962; Berlincourt, 1987)).

We shall reiterate that nearly all of the alloy samples studied in all above works (except alloys Pb-Tl and Pb-Bi (1-10wt%)) had more than one phase, hence they were explicitly inhomogeneous.

Even though 9 out of 13 of the above-mentioned experimental studies on superconducting alloys pursued for 7 years by men of science from different countries W.J.De Haas, J.O. Wilhelm, K. Mendelsson, L.V. Shubnikov with co-workers (De Haas & Voogd, 1929; De Haas & Voogd, 1930; De Haas & Voogd, 1931b; De Haas & Casimir-Jonker, 1935a; De Haas & Casimir-Jonker, 1935b; De Haas & Casimir-Jonker, 1935c; Casimir-Jonker & De Haas, 1935; Tarr & Wilhelm, 1935; Keeley et al., 1934; Mendelsson & Moore, 1935; Mendelsson 1935; Yu.N. Ryabinin & Shubnikov, 1935a; Ryabinin & Shubnikov, 1935b) were published in high-rating journals ("Nature", "Commun. Phys. Lab. Univ. Leiden"), they were hardly referred to at a later time. Suffice it to say that the fundamental publication Handbuch der Physik of 1956 edition (Serin, 1956; Bardeen, 1956) did not mention any of the above-said research at all.

3. Discovery

Such was the status of research on magnetic properties of superconducting alloys around the globe by the time when the papers by L.V.Shubnikov, V.I.Khotkevich, G.D.Shepelev, Yu.N.Ryabinin (Schubnikow et al., 1936; Shubnikov et al., 1937) saw the light. Those papers submitted for publication on *April 11 and November 2, 1936,* respectively, contained the results of thorough studies across a broad temperature interval on magnetic properties of single-crystal metals and single crystals of single-phase alloys Pb-Tl (0.8; 2.5; 5; 15; 30; 50wt.%) and Pb-In (2; 8wt.%), which were very carefully annealed at the pre-melt temperatures.

Those are model alloys employed for research into Type II superconductors, since in a broad region of the impurity concentrations there is a region of the solid solution (Fig.7,15) which

was stable down to the cryogenic temperatures, thus opening up new vistas for making studies on the concentration effects.

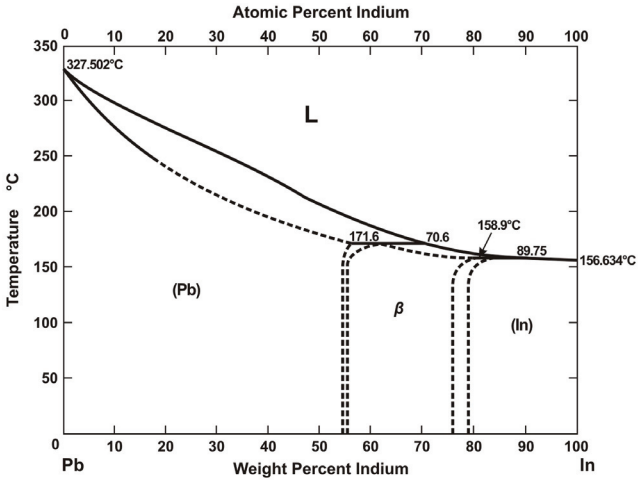

Fig. 15. Binary phase diagrams of the alloy Pb-In (After Massalski, 1987).

High-quality single-crystals of the alloys that had the length-to-diameter ratio ≥ 10 were grown according to the Obreimov-Shubnikov technique (Obreimow & Schubnikow, 1924). The magnetic moment of sample in a longitudinal homogeneous, constant pre-assigned magnetic field was measured over response of the ballistic galvanometer, while the sample was fast removed (or brought in) across the limits of a pickup coil connected to the galvanometer. The entire sample magnetization cycle went by the consecutive applied magnetic field variation.

In their articles (Schubnikow et al., 1936; Shubnikov et al., 1937) the authors implying the previous published papers (Rjabinin & Schubnikow, 1935a; Rjabinin & Schubnikow, 1935b) said again that "*In our first paper on the study of superconducting alloys we pointed out the possibility to explain the unusual magnetic properties of superconducting alloy by the disintegration of solid solutions at low temperatures*".

Besides, the authors indicated that: "*De Haas and Casimir-Jonker (De Haas & Casimir-Jonker, 1935b) found for the first time that, for* $PbTl_2$ *and* Bi_5Tl_8*, there exists the critical magnetic field which penetrates into the alloy but does not break up the superconductivity; that is why it is considerably lower than the critical magnetic field, at which the alloy acquires the ohmic resistance.*"

L.V.Shubnikov et al. (Schubnikow et al., 1936; Shubnikov et al., 1937) discovered that:

1. There was a boundary over the impurity concentration in the superconducting alloys before which their magnetic properties resembled the magnetic properties of pure superconductors – the total Meissner Effect at fields that were smaller than critical and a sudden disruption of the superconductivity upon further magnetic field increasing (Fig.16).
2. Upon increasing the impurity concentration beyond that boundary (within the present-day viewpoint: with the growth of the Ginzburg-Landau parameter æ) the magnetic properties of the alloys got to differ drastically from those of the pure superconductors: The Meissner Effect existed only as far as the magnetic field H_{c1}, and upon further field increasing the alloys remained superconducting as far as H_{c2}, with the magnetic field

gradually penetrating into the alloy. Fig.17,18 gives the results of research on alloys Pb-Tl, and Fig.19 does that for Pb-In.

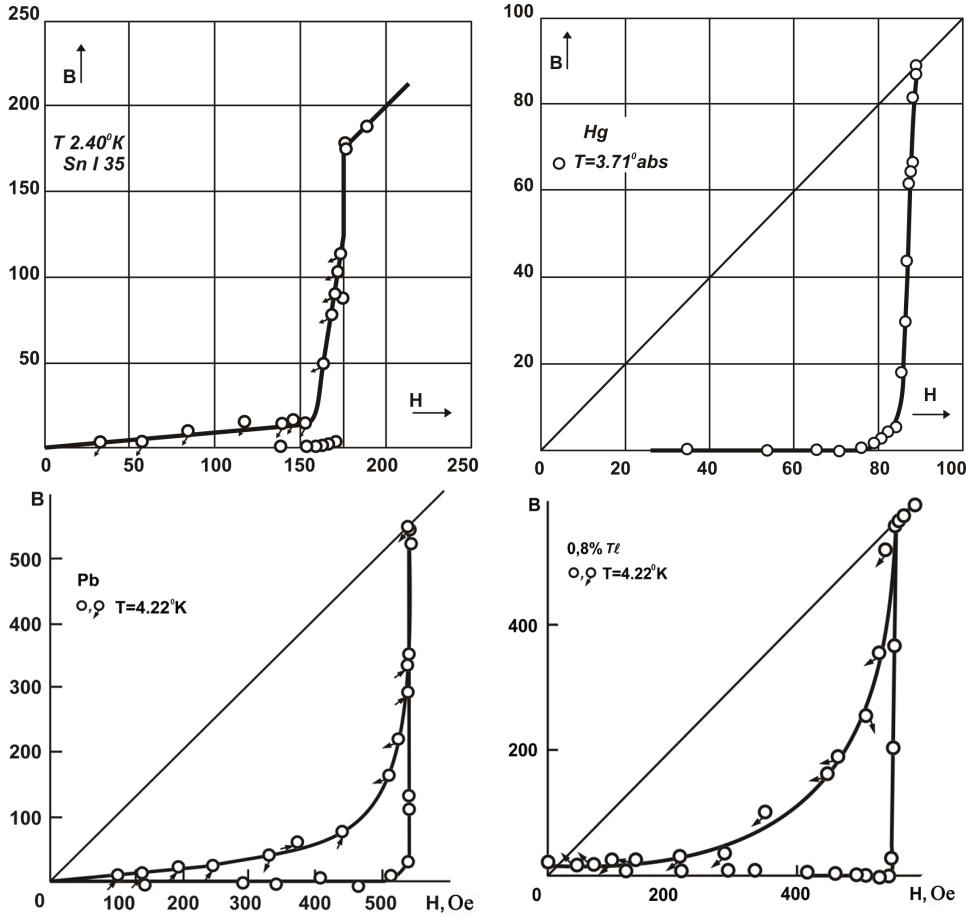

Fig. 16. The induction curve of long cylinders of pure single-crystal Sn, Hg, Pb and single-crystal alloy Pb+0,8wt%Tl in longitudinal magnetic field (After Schubnikow et al., 1936).

3. With increasing the impurity concentration (i.e. with a growing parameter æ) the interval between H_{c1} and H_{c2} broadened, i.e. H_{c1} got smaller, while H_{c2} grew. Fig. 20 presents data for alloys Pb-Tl.

4. The unusual properties found on the superconducting alloys could not be attributed to the hysteresis phenomena, since at high increasing and decreasing fields the phenomenon was well reversible, the hysteresis rather small.

5. The difference in free energy of magnetized and normal superconductors was given by the area of the curve:

$$\Delta F = \int M dH,$$

where M – the magnetization, while the entropy difference was produced by the derivative:

$$\Delta S = - (\partial F / \partial T)_B.$$

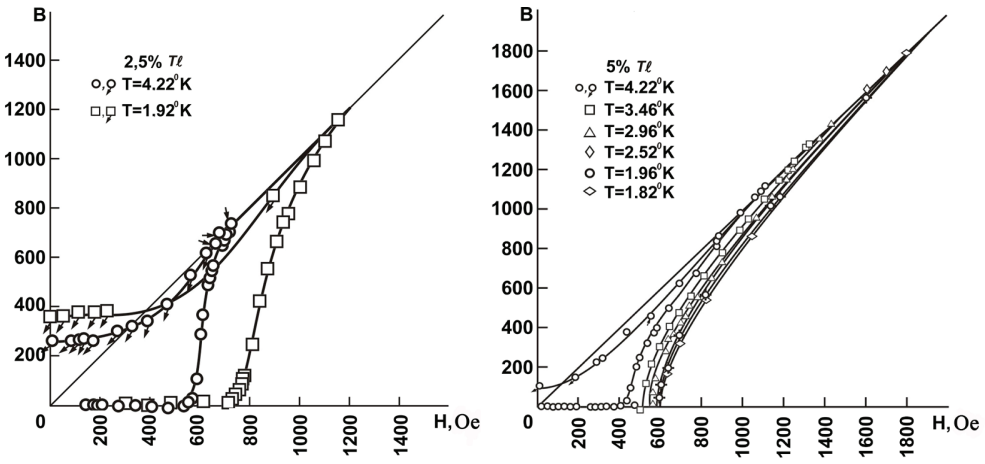

Fig. 17. The induction curve of long cylinders of single-crystals of alloys Pb+2,5wt%Tl; Pb+5wt%Tl (After Schubnikow et al., 1936).

The computation of the entropy difference made in reference (Schubnikow et al., 1936; Shubnikov et al., 1937) for these alloys indicated that in this case, as in the case of pure superconductors, the researchers dealt with magnitudes of the same order that were likewise dependent on temperature. For this reason, the jump in the heat capacity during the superconducting transition in zero magnetic field for the alloy was comparable to that of a pure superconductor.

6. The X-ray studies made on the superconducting alloys indicated that they had no solid solution disintegration going in them (the alloys were single-phase) which conflicted with the old ideas about their superconducting properties being related to the inhomogeneities.

In this way, it was exactly in the research papers by Shubnikov, Khotkevich, Shepelev, Ryabinin (Schubnikow et al., 1936; Shubnikov et al., 1937) that a well-substantiated and correct conclusion was made as to the existence of a new superconductor type. This conclusion clashed with all the preceding research that had explained the previously obtained results by compositional and structural inhomogeneities of samples.

Even though the published results by L.V.Shubnikov et al. (Schubnikow et al., 1936; Shubnikov et al., 1937) became instantly known abroad (Wilson, 1937; Ruhemann, 1937; Shoenberg, 1938; Jackson, 1940; Burton et al., 1940; Mendelssohn, 1946; Shoenberg, 1952), they were running long ahead of their time and their significance had not been appreciated for what they were for a very long time to come.

The reason for this was clearly stated in the Nobel Prize lecture by V.L.Ginzburg (Ginzburg, 2004) where he, while discussing his and Landau's phenomenological theory of superconductivity (Ginzburg & Landau, 1950), remarked that regarding the superconducting alloys: *"an understanding of the situation was lacking, and Landau and I, like many others, believed that alloys are an 'unsavory business', and did not take an interest in them, restricting ourselves to the materials with* $\text{æ} < \text{æ}_c$, *for which* $\sigma_{ns}>0$, *i.e. type I superconductors".*

Much later after the Ginzburg-Landau theory had been constructed (Ginzburg & Landau, 1950) an appreciation was given with reference to the studies made by Shubnikov and his co-workers (Schubnikow et al., 1936; Shubnikov et al., 1937) that *"The most spectacular application of the Ginzburg-Landau theory has been to a description of such superconductors"* (Chandrasekhar, 1969). Berlincourt (Berlincourt, 1987) noted very justifiably that Shubnikov et al. did not use in their research the C.J.Gorter (Gorter, 1935) and H.London's Theory (London, 1935). On the other hand, neither C.J.Gorter, nor H.London referred to Shubnikov's et al. results to support their theories. It would be very apt to cite the R.Kipling's "Oh, East is East, and West is West, and never the twain shall meet…".

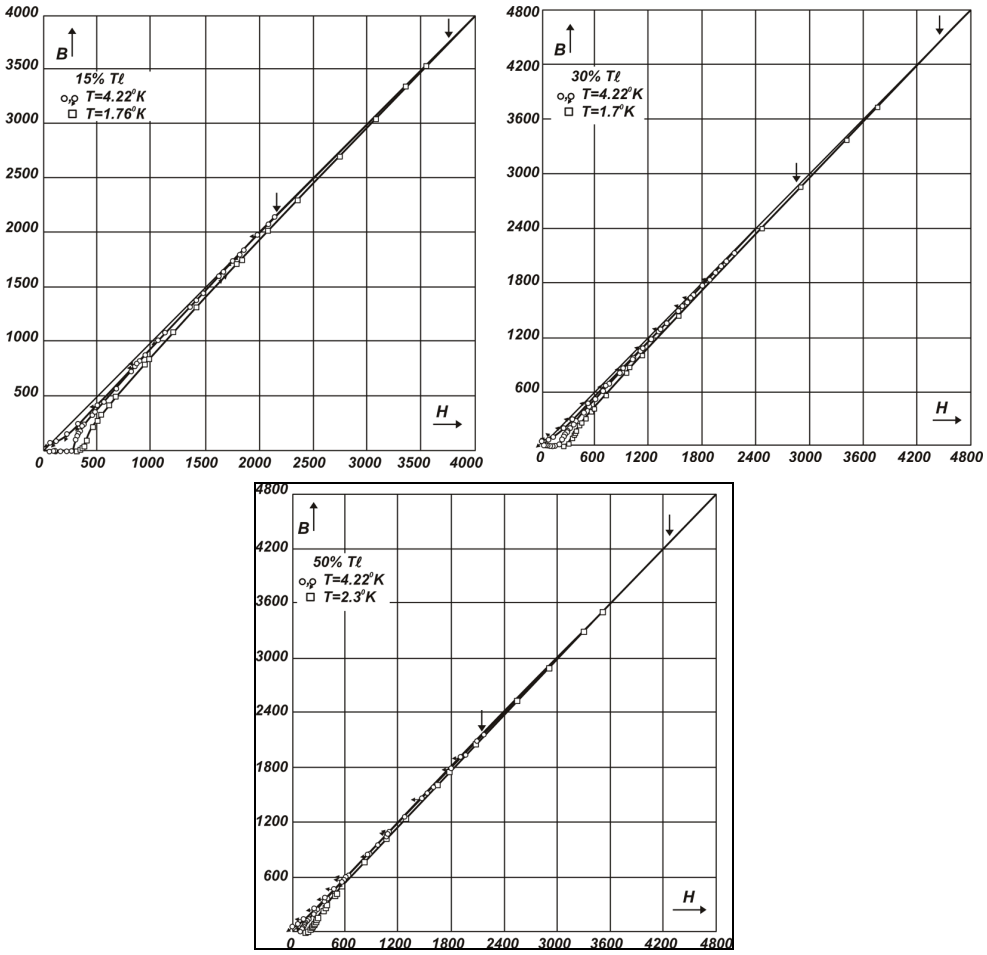

Fig. 18. The induction curve of long cylinders of single-crystals of alloys: Pb+15wt%Tl; Pb+30wt%Tl; Pb+50wt%Tl (After Schubnikow et al., 1936).

The discovery discussed above was accompanied by a dramatic conflict of creativity and a great human tragedy affecting the lives of two prominent scientists, L.D.Landau and

L.V.Shubnikov, and the directions the Big Physics might otherwise have taken. V.L.Ginzburg, a Nobel Laureate, addressing an International Conference of Fundamental Problems of High-Temperature Superconductivity (2004) had the following to say, *"Shubnikov and his students and colleagues accomplished a lot within only a few years, and I should specially mention his studies of superconducting alloys and a factual discovery of Type II superconductors. I am sure that Shubnikov would have achieved even greater success in science, and one cannot but feel bitterness about his untimely (at the age of only 36!), and quite guiltless death under the ax of Stalin's terror"* (Ginzburg, 2005).

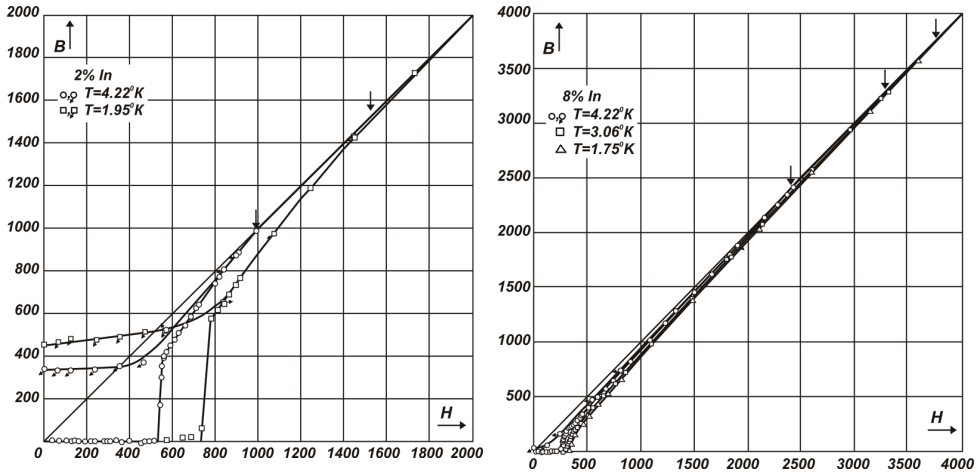

Fig. 19. The induction curve of long cylinders of single-crystals of alloy Pb+2wt%In; Pb+8wt%In (After Schubnikow et al., 1936).

The dramatic conflict of creativity concerned his close friend L.D. Landau with whom they had such lively discussions on all ongoing work at Shubnikov's Lab. L.D. Landau did not recognize the experimental discovery by L.V.Shubnikov and co-workers (Schubnikow et al., 1936; Shubnikov et al., 1937) either in 1936 (it is known as fact that the publishing of the articles (Schubnikow et al., 1936; Shubnikov et al., 1937) was delayed by more than 3 months, because Shubnikov failed to "run" them through Landau (Slezov et al., 2007)), or in 1950 when he and V.L.Ginsburg created the phenomenological theory of superconductivity (Ginzburg & Landau, 1950; Ginzburg, 1955) wherein the Ginzburg-Landau parameter æ was brought into the picture. In his paper published in 1997 and titled "Superconductivitry and superfluidity (what I could and could not do)", V.L.Ginzburg, discussing the theory (Ginzburg & Landau, 1950; Ginzburg, 1955) pointed out quite clearly, "*In this way, we actually overlooked the possibility of existence of Type II superconductors*" (Ginzburg, 1997).

The Great Human Tragedy was such that on August 6, 1937 L.V.Shubnikov was arrested without a warrant, and by the joint verdict of October 28, 1937, handed down by the odious functionaries of the Totalitarian Regime, Yezhov and Vyshinsky, he was shot dead (rehabilitated in 20 years) (Fig.21).

L.D.Landau was arrested on April 27, 1938, now as a staff scientist at Institute of Physical Problems, however in a year he was pulled out of jail by P.L.Kapitsa's intervention (L.D.Landau was also granted the pardon posthumously only in 1990). As a reminder, we

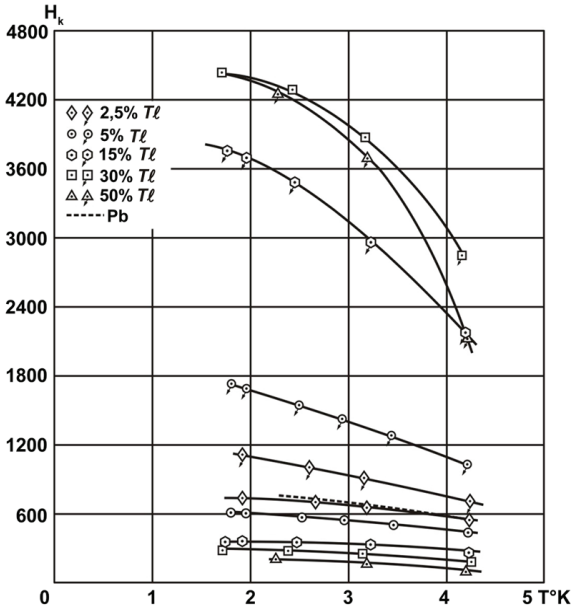

Fig. 20. Temperature dependence of H_{c1} and H_{c2} for single-crystals alloys Pb-Tl of the said concentrations and H_c for pure lead (After Schubnikow et al., 1936).

point out here that the Iron Curtain which was already hovering over the country slammed down hard on the scientific community, too: *"It should be recalled that Kirov was assassinated on December 1, 1934, and the whole country was in a wave of terror. Before, that, the Academy of Science was devastated for its unwillingness to take into its fold some scientists with party tickets, who had been recommended by the central committee of the All-Union Communist Party (Bolsheviks)" (*Rubinin, 1994). In summer 1930 L.V.Shubnikov was ordered by the Soviet authorities out of Kammerlingh Onnes Laboratory and to return to the USSR. In autumn 1934 P.L.Kapitsa was not permitted to come back for work at Mond Laboratory. The horrors of the Great Terror became known in the West from scientists who suffered through it in one way or another: E.Houtermans, K.F.Shteppa (Beck & Godin, 1951) and A.Weissberg-Cybulsky (Weissberg-Cybulsky, 1951) (see also (Pavlenko et al., 1998; Matricon & Waysand, 2003; Waysand, 2005)). Since the mid-thirties the scientific contacts with foreign scientists have been restricted. In 1936 Shubnikov was refused the permission to attend the International Conference on Low-Temperature Physics at the Hague, and such scientists of the world renown as W.J.De Haas and F.Simon were not granted the visa to visit Shubnikov's Cryo Lab (Trapeznikova, 1990). In the same year 1936 De Haas' fellow-scientist E.C.Wiersma who had been helping Shubnikov's Lab on behalf of W.J.De Haas and was eager to move to Kharkov to work at the Cryo Lab (he had sold all he had in Leiden for this purpose) was refused the admission to the USSR. In 1937 the bilingual "Physikalische Zeitschrift der Sowjetunion" and "Techical Physics of the USSR", published in German and in English in Kharkov and Leningrad, respectively, were closed down by the ruling of the powers-that-be. Similarly, in 1947 "J. of Physics of the USSR" that was published in Moscow in English was also closed down.

Выписка

из протокола № 13 решения Наркома Внутренних Дел СССР Генерального Комиссара Госбезопасности тов. ЕЖОВА и Прокурора Союза ССР тов. ВЫШИНСКОГО - от 28 октября 1937 года

Слушали: *Материалы на обвиняемых, представленные Управлением НКВД УССР по Харьковской области, в порядке приказа НКВД СССР за № 00439 от 25/VII - 1937 года.*

Постановили: Шубникова Льва Васильевича

расстрелять

Нарком Внутдел СССР Генеральный Комиссар Госбезопасности - ЕЖОВ

Прокурор СССР - ВЫШИНСКИЙ

ВЕРНО: ОПЕРУПОЛН Ш ОТД УГБ Лейтенан Госбезопасности /РЕШЕТНЕВ/

АМ
Тираж - 50л.

Форма № 30

Военная Коллегия Верховного Суда Союза ССР

1 июля 1957 г.

№ 4н-024554/56

Москва, ул. Воровского, д. 13.

СПРАВКА

Дело по обвинению ШУБНИКОВА Льва Васильевича, до ареста – 5 августа 1937 года – научный руководитель лаборатории низких температур Украинского физико-технического института, пересмотрено Военной коллегией Верховного Суда СССР 11 июня 1957 года.

Постановление НКВД СССР от 28 октября 1937 года в отношении ШУБНИКОВА Л.В. отменено и дело за отсутствием состава преступления прекращено.

ШУБНИКОВ Л.В. реабилитирован посмертно.

ПРЕДСЕДАТЕЛЬСТВУЮЩИЙ СУДЕБНОГО СОСТАВА ВОЕННОЙ КОЛЛЕГИИ ВЕРХОВНОГО СУДА СССР ПОЛКОВНИК ЮСТИЦИИ /А.КОСТРОМИН/

в.г.

Fig. 21. The unjust sentence upon L.V.Shubnikov in 1937 and the document about his rehabilitation of 1957 (After Pavlenko et al., 1998)

Yu.N.Ryabinin left UPhTI because of the conflict with L.V.Shubnikov and L.D.Landau. G.D.Shepelev who defended the first doctoral dissertation at Shubnikov's Cryo Lab (Shepelev, 1938) was placed at the head of this Lab. (Fig. 22). Then the Second World War broke out and interests of the scientists shifted en masse in other directions. After Germany's aggression against the USSR Shepelev volunteered to the front and was killed in action during the defense of Sevastopol at the age of 36.

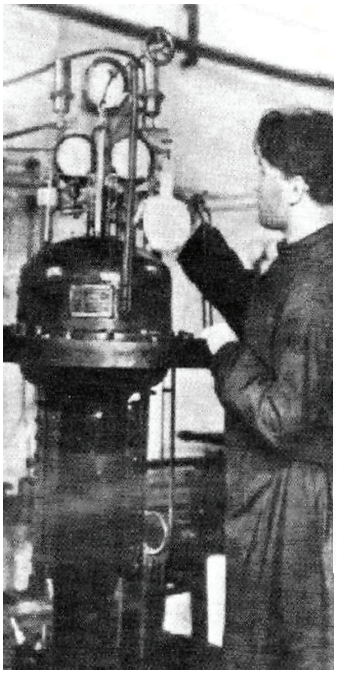

УРСР
Народний Комісаріат Освіти
ХАРКІВСЬКИЙ ДЕРЖАВНИЙ УНІВЕРСИТЕТ ім. О. М. Горького
№ 730/205 1938
м. Харків, вул. Військової Академії, № 14. Тел. № № 4-60-01, 4-60-08.

ПОСВІДЧЕННЯ

Видано Шепелеву Георгію Дмитриевичу
в тому, що за ухвалою Ради харківського Державного Університету ім. О. М. Горького від 26/12 сентября 193 8 р. (протокол засідання № 2)
надано вчену ступінь кандидата физико-математических наук после захисту на тему „Магнитные свойства сплавов"
Ректор ХДУ Бутинець
Проректор по науковій частині ХДУ

Fig. 22. G.D.Shepelev at the helium liquefier (Cryogenic Laboratory UPhTI, 1932) and the document about his defence (in 1938) of the Thesis "Magnetic Properties of Superconducting Alloys".

The very first reference to the research by Shubnikov, Khotkevich, Shepelev, Ryabinin (Shubnikov et al., 1937), acknowledging it as a pioneering one, was made in the paper written by A.A.Abrikosov (Abrikosov, 1957) which was published 20 years later. The author, acting on the basis of the experimental results by Shubnikov, Khotkevich, Shepelev, Ryabinin (Shubnikov et al., 1937) and the Ginzburg-Landau theory (Ginzburg & Landau, 1950; Ginzburg, 1955), constructed the Type II Superconductor Theory which now could describe, even quantitatively, these experimental results. It turned out that the thermodynamic critical field H_c was roughly equal to the geometric average of the fields H_{c1} and H_{c2}:

$$\frac{H_c}{H_{c_1}} \approx \frac{H_{c_2}}{H_c} \approx \sqrt{2} \cdot æ$$

Thus, the greater was the value æ, the smaller became H_{c1} and the greater became H_{c2}, which corresponded to Shubnikov and colleagues' experimental results (Schubnikow et al., 1936;

Shubnikov et al., 1937). Also, where in Type I superconductors the superconductivity disruption occurred according to the mechanism of phase transition of the first kind, in Type II superconductors, with H_{c1} and H_{c2} present, phase transitions of the second kind took place.

Abrikosov (Abrikosov, 1957) demonstrated that in the region between H_{c1} and H_{c2} the magnetic flux penetrated into the superconducting alloys in the form of a sort of vortex structure shaped as thin flux tubes with the dimension ξ (which was determined by the negative interphase surface energy) and not in layers, as in Type I superconductors (Landau, 1937; Landau, 1943). Each tube of the flux carried a quantum of the magnetic flux:

$$\Phi_0 = \frac{hc}{2e} = 2{,}07 \cdot 10^{-15}\,\text{Wb},$$

while around each tube of the flux, in the layer λ thick, the persistent currents were circulating.

4. Recognition

The Cold War Era and the McCarthyism in the US also impressed upon the recognition of this phenomenon. As Nobel Laureate in Physics P.W.Anderson (Anderson, 1969) stated: *"There followed a tragicomic period of over a decade which should be fascinating to the historians of science and to those concerned with the relationships between science and society, during which the interaction between Russia and the West in the subjects of superfluidity and superconductivity resembled a comic opera duet of two characters at cross purposes rather than a dialogue."* P.W.Anderson, noted that the experimental study (Schubnikow et al., 1936; Shubnikov et al., 1937) and A.A.Abrikosov's theory (Abrikosov, 1957) «*together founded and almost completed the science of type II superconductivity*» (Anderson, 1969).

The break-through in understanding the significance of L.V.Shubnikov and his colleagues' work (Schubnikow et al., 1936; Shubnikov et al., 1937) to take place in 1963 at International Conference on the Science of Superconductivity, which fact was noted by J.Bardeen, the Chairman of the Conference, who was the only one doubly-nominated Nobel Laureate in Physics, and by R.W. Schmitt, the Conference Secretary (Bardeen & Schmitt, 1964): *"It should be noted that our theoretical understanding of type II superconductors is due mainly to Landau, Ginsburg, Abrikosov, and Gor'kov, and that the first definitive experiments were carried out as early as 1937 by Shubnikov"*.

At the Superconductivity in Science and Technology Conference (1966) J.Bardeen indicated *"The phenomenon was discovered experimentally by a Russian physicist, Schubnikov (Shubnikov et al., 1937), around 1937."*(Bardeen, 1968).

Nobel Laureate in Physics P.G.De Gennes (De Gennes, 1966) was the first to introduce the notion "Shubnikov's phase" to describe the state of a superconductor between H_{c1} *и* H_{c2}, and after that this notion has come into use in literature.

K.Mendelssohn (Mendelssohn, 1966), a classic, estimated the 1936/1937 works as follows: *«The real trouble here is that it is extremely difficult to make a homogeneous alloy, containing no lattice faults. Of the laboratories engaged in low temperature research in the thirties, Shubnikov's group in Kharkov had evidently the best metallurgical know-how»*. By the way, when Mendelssohn met A.G.Shepelev at 10th International Conference on Low Temperature Physics (Moscow, 1966) and looked at his badge, he exclaimed at once: «Schubnikow, Chotkewitsch, Schepelew, Rjabinin!» - although 30 years have passed! So, it was necessary

to explain him that it was Shepelev-son, and that Shepelev-father was killed when defending Sevastopol. Mendelssohn expressed his deep regret and continued with high estimation of 1936/1937 works and Shubnikov's scientific achievements. He also said that his book (Mendelssohn, 1966) describing these works was about to come out.
In the well known two volumes "Superconductivity" B.Serin remarked: "The first fundamental experiments were done by Shubnikov and co-workers (Shubnikov et al., 1937, Schubnikow et al., 1936) in 1937" (Serin, 1969).
At the H.Kamerling Oness Symposium on the Origins of Applied Superconductivity – 75th Anniversary of the Discovery of Superconductivity T.G.Berlincourt estimated (Schubnikow et al., 1936, Shubnikov et al., 1937) as follows: "*Shubnikov et al. had done the crucial experiment and had interpreted it correctly"(*Berlincourt, 1987*).*

5. Final results and prospects

The concept of Type II superconductors elaborated by L.V.Shubnikov and co-workers (Schubnikow et al., 1936; Shubnikov et al., 1937) and by A.A.Abrikosov (Abrikosov, 1957) has joined the Golden Fund of the World Science, and it is described, in one way or another, in all dedicated monographs on superconductivity. The authors of the Ginzburg-Landau Theory of Superconductivity (Ginzburg & Landau, 1950; Ginzburg, 1955) and the related A.A.Abrikosov Type II Superconductor Theory (Abrikosov, 1957) that is based on the experimental results by Shubnikov, Khotkevich, Shepelev, Ryabinin (Schubnikow et al., 1936; Shubnikov et al., 1937), finally, received the Nobel Prize in Physics in 2003.
However, the insertion of this knowledge into "practical applications" took long years of intense research by many scientists in order to discover superconductors with high critical fields and temperatures (Hulm & Matthias, 1980; Hulm et al., 1981; Roberts, 1976; Roberts, 1978). Those efforts were crowned by success when in 1961 Kunzler et al. (Kunzler et al., 1961) found that the superconductivity in Nb_3Sn remained under large fields (~10 T) and at current densities $j_c \sim 10^5$ A/см^2. And those were exactly Nb_3Sn (Martin et al., 1963) and Nb-Ti (Coffey et al., 1964) alloys used not so long ago in 1963-1964 to have the first superconducting solenoids with magnetic fields greater than 10 T built with. Note that in the extreme Type II superconductors æ > 20 for Nb_3Sn and æ > 100 for cuprates.
Whereas the values of H_{c2} and T_c, generally speaking, are determined by the basic characteristics of material (being hard to predict to date), the value of j_c is strongly dependent on the pinning centers (crystal defects, impurities, second-phase precipitates and their dimensions and distribution) that impede the motion of the "Abrikosov vortices" under the action of the Lorentz force (Campbell & Evetts, 1972; Ullmair, 1975; Blatter, 1994; Brandt, 1995; Brandt, 2009). It took several decades for metallurgists to create the relevant microstructure of the superconductors by way of a complex metallurgical treatment (Dew-Hughes, 2001; Larbalestier et al., 2001; Slezov et al., 2005; Chen et al., 2009).
Type II superconductors are used widely in many areas of science and technology around the globe. The most notable among them are:

- Only 20 years ago, there were more than one thousand superconducting solenoids made of Nb-Ti with the aperture 1 m for NMRI scans of human body (Andrews, 1988) fig.23;
- About six years ago the US and Denmark introduced into operation three Bi-HTSC-based electric transmission lines (Chernoplekov, 2002);
- A remarkable progress has been achieved in engineering the MAGLEV trains, in December, 2003, Japan recorded the MAGLEV train speed of 581 km/h:

(http://www.rtri.or.jp/rd/maglev/html/english/maglev_frame_E.html);

- Not a single large magnetic system can be created without Type II superconductors. Just take the instances of the magnetic system already built and installed in place (more than 10 thousand various superconducting solenoids) of Large Hadron Collider which is 27 km long (Rossi, 2006) (Fig.24) and that of the world's largest superconducting solenoid which is 13 m long, with the internal diameter 6 m, magnetic field 4 T and stored energy 2.5 GJ (Barney & Lee, 2006) (Fig. 25) custom-made for the Muon Spectrometer. All of these solenoids were made of Nb-Ti superconductor.

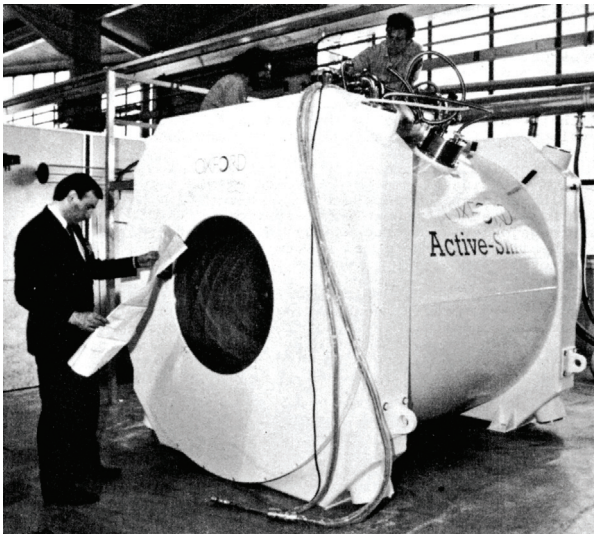

Fig. 23. Superconducting solenoids with the aperture 1 m for NMRI scans of human body (After Andrews, 1988).

Fig. 24. 1232 superconducting dipoles for Large Hadron Collider (After Rossi, 2006).

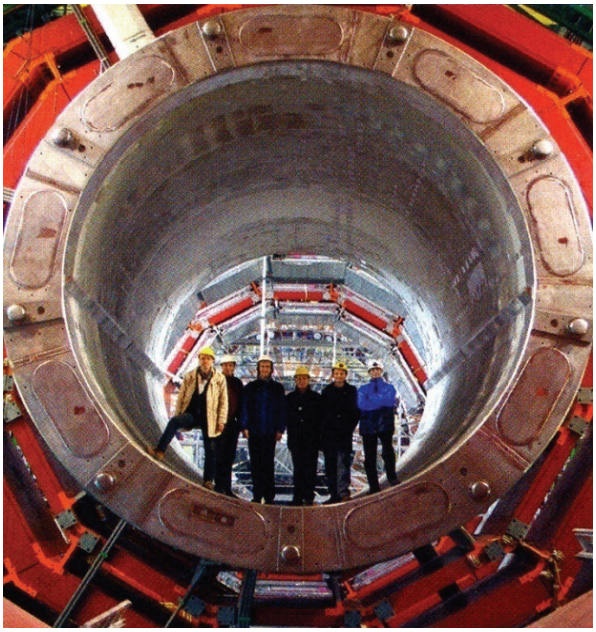

Fig. 25. Superconducting solenoid for the Muon Spectrometer (Barney & Lee, 2006).

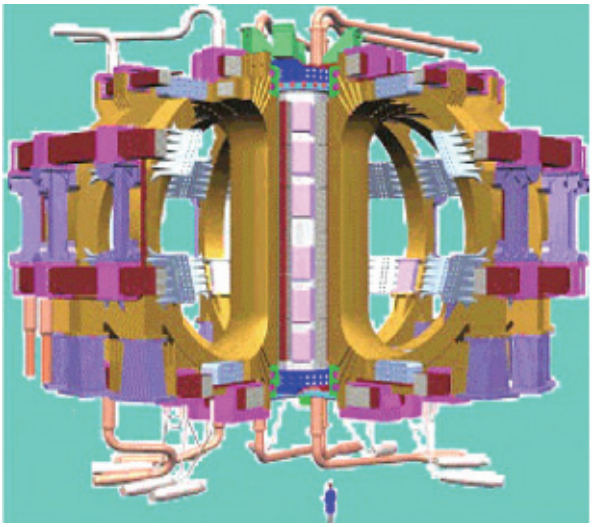

Fig. 26. Magnetic system of International Tokamak Reactor (ITER) (After Salpietro, 2006).

The sophisticated magnetic system of International Tokamak Reactor (ITER) (see, Fig.26), which is being built at the moment, is to comprise three sub-systems: the core solenoid, 18 toroidal field coils and 6 poloidal field coils. The core solenoid which is manufacturable from Nb_3Sn will create the field of 13,5 T, the toroidal magnetic field coils made of the same

superconductor will produce the axial magnetic field of 6 T (the maximum field about 12 T), while the Nb-Ti poloidal magnetic field coils will produce the field of 6 T (Salpietro, 2006). It is of interest to note here that the magnetic energy stored only in the toroidal magnetic field coils of this gigantic facility (around 30 m in diameter and in height) is 41 GJ!

Considering the importance of L.V. Shubnikov's scientific heritage for science and technology on the whole, the Presiding Council of National Academy of Sciences of Ukraine passed in 2001 an Ordinance about establishment of L.V.Shubnikov Prize for outstanding research in experimental physics.

As a remark, we shall also note here that the USA established an honorary degree of 'Shubnikov Professor' which has been bestowed on D.C.Larbalestier, Director of Applied Superconductivity Center.

The author acknowledges his sincere gratitude to the late Academician V.L.Ginzburg and to many colleagues for their interesting and stimulating discussions.

6. References

Abrikosov A.A. (1957). On the magnetic properties of second kind superconductors, *Sov.Phys.JETP.* V.5, №6, p.1174-1182.

Anderson P.W. (1969). *Superconductivity in past and future. In: Superconductivity* (ed.R.D.Parks), Marcel Dekker, Inc, N.Y., V.2, p.1343-1358.

Andrews D.E. (1988). *Magnetic resonance imaging in 1987. Adv. in Cryogenic Engineering* (ed. R.W.Fast), Plenum Press., N.Y.-London, v.33, p.1-7

Bardeen J. (1956). *Theory of superconductivity. In: Handbuch der Physik*, Bd.15. Kältephysik II. (ed. S.Flügge), Springer Verlag, Berlin, Göttingen, Heidelberg, S.274-369.

Bardeen J., Schmitt R.W. (1964). International conference on the science of superconductivity. *Revs. Mod. Phys.*, V.36, No.1. Pt.1, p.1-2.

Bardeen J. (1968). *Theory of superconductivity. In: Superconductivity in Science and Technology* (ed. M.H.Cohen), University of Chicago Press, Chicago&London, p.1-17.

Barney D., Lee C. (2006). CMS closes up for magnet test and cosmic challenge. *CERN Courier*. 2006. V.46, №6, p.28-29.

Beck F., Godin W. (1951). *Russian Purge and Extraction of Confession*, Hurst & Blackett Ltd, L.-N.Y.

Berlincourt T.G. (1964). Type II superconductivity. *Revs. Mod. Phys.*, V.36, No.1, Pt.1, p.19-26.

Berlincourt T.G (1987). Type II superconductivity: quest for understanding. *IEEE Trans. Magnetics*, V.MAG-26, №.2, p.403-412.

Blatter G., Feigel'man M.V., Geshkenbein V.B. et al. (1994). Vortices in high-temperature superconductors. *Revs. Mod. Phys.* V.66, №4, p.1125–1388.

Brandt E.H. (1995). The flux-line lattice in superconductors. *Repts.Prog.Phys.*, V.58, №11, p.1465-1594.

Brandt E.H. (2009). Vortices in superconductors: ideal lattice, pinning, and geometry effects. *Supercond. Science and Technology*, V.22, №3, p.1-9.

Burton E.F. (1934). *The phenomenon of superconductivity.* The University of Toronto Press, Toronto, p.75-78.

Burton E.F., Smith H.G., Wilhelm J.O. (1940). *Phenomena at the temperature of liquid helium*. Reinhold Publ. Corp., N.Y., p.307-310, 319.

Campbell A.M., Evetts J.E. (1972). *Critical currents in superconductors*. Taylor and Francis Ltd, London.

Casimir-Jonker J.M., De Haas W.J. (1935). Some experiments on a superconductive alloy in a magnetic field. *Physica*, V.2, №1-12, p.935-942.

Coffey H.T., Hulm J.K., Reynolds W.T. et.al. (1965). A protected 100 kG superconducting magnet. *J.Appl. Phys.*, V.36, №1, p.128-136.

Chandrasekhar B.S. (1969). *Early experiments and phenomenological theory. In: Superconductivity* (ed.R.D.Parks), Marcel Dekker Inc, N.Y., V.1, p.1-49.

Chen Z.J., Kametani F., Gurevich A. et al. (2009). Pinning, thermally activated depinning and their importance for tuning the nanoprecipitate size and density in high J_c $YBA_2CU_3O_7$-X films. *Physica C Superconductivity and its applications,* V. 469, №23-24, p.2021-2028.

Chernoplekov N.A. (2002). State of the art in applied high-current superconductivity. *Phys. Usp.*, V.45, №6, p.659-665.

Dahl P.F. (1992). *Superconductivity. Its historical roots and development from mercury to the ceramic oxides.* American Institute of Physics, N.Y., p.215-229, 231-234.

De Haas W.J., Sizoo G.J., Kamerlingh Onnes H. (1926). Measurements on the magnetic disturbance of the superconductivity with mercury. *Comm. Phys. Lab. Univ. Leiden,* V.16, №180d, p.57-103.

a - De Haas W.J., Van Aubel Edm., Voogd J. (1929). New superconductors. The resistance of alloys at the temperatures of liquid hydrogen and liquid helium. *Comm. Phys. Lab. Univ. Leiden,* V.18, №197b, p.11-20.

b - De Haas W.J., Van Aubel Edm., Voogd J. (1929). Supraleitern zusamenengesetzster Supraleiter. *Comm. Phys. Lab. Univ. Leiden,* V.18, №197a, S.3-8.

De Haas W.J., Van Aubel Edm., Voogd J. (1930). On the superconductivity of alloys. *Comm. Phys. Lab. Univ. Leiden,* V. 19, №208a, p.3-6.

De Haas W.J., Voogd J. (1929). Disturbance of the superconductivity of the compound Bi_5Tl_3 and of the alloys Sn-Bi and Sn-Cd by magnetic fields. *Comm. Phys. Lab. Univ. Leiden*, V.18, №199c, P.31-40.

De Haas W.J., Voogd J. (1930). The influence of magnetic fields on superconductors. C*omm. Phys. Lab. Univ. Leiden,* V.19, №208b, p.9-20.

a - De Haas W.J., Voogd J. (1931). The magnetic disturbance of the superconductivity of single-crystal wires of tin. *Comm. Phys. Lab. Univ. Leiden,* V. 19, №212c, p.29-36.

b - De Haas W.J., Voogd J. (1931). Further investigations on the magnetic disturbance of the superconducting state of alloys. *Comm. Phys. Lab. Univ. Leiden,* V.19, №214b, p.9-16.

a - De Haas W.J., Casimir-Jonker J.M. (1935). Penetration of magnetic field into superconductive alloys // *Proc. Roy. Acad. Amsterdam*, *Proc. Sec. Sci*., V.38, №1, p.2-7.

b -De Haas W.J., Casimir-Jonker J.M. (1935). Penetration of magnetic field into superconductive alloys // *Nature*, V.135, № 3401, p.30-31.

c -De Haas W.J., Casimir-Jonker J.M. (1935). Penetration of magnetic field into superconductive alloys // *Comm. Phys. Lab. Univ. Leiden.*, V. 21, №233c. p.1-7.

De Gennes P.G. (1966). *Superconductivity of metals and alloys*. W.A.Benjamin, Inc. N.Y., Amsterdam.

Dew-Hughes D. (2001). The critical current of superconductors: an historical review. *Low Temp. Phys*., V.27, №9-10, p.714-718.

Ginzburg V.L. (1946). *Superconductivity*. Publ. Acad. Sci. USSR, Moskow, p.117-121.

Ginzburg V.L., Landau L.D. (1950). On the theory of superconductivity. *Zh. Exper. Teor. Fiz.* (USSR). V.20, №12, p.1064-1982.

Ginzburg V.L. (1955). On the theory of superconductivity. *Nuovo Cimento*, V.2, №6, p.1234-1250.

Ginzburg V.L. (1997). Superconductivity and superfluidity (what was done and what was not). *Physics-Uspekhi,* V.40, №4, P.412.

Ginzburg V.L. (2004). On Superconductivity and Superfluidity (What I have and have not managed to do), As well as on the «Physical Minimum» at the beginning of the 21st century. *In:T.Frängsnyr (Ed.), Les Prix Nobel. The Nobel Prizes 2003 (Nobel Foundation, Stockholm),* p.103.

Ginzburg V.L. (2005). A few comments of superconductivity research. *Physics-Uspekhi,* V.48, №2, p.172.

Ginzburg V.L., Andryushin E.A. (2006). *Superconductivity (2nd ed.).* Alpha-M, Moskow.

Goodman B.B. (1964). Type II London s superconductors. *Revs. Mod. Phys.*, V.36, No.1., Pt.1. p.12-19.

Goodman B.B. (1966). Type II superconductors. *Repts.Progr.Phys.*, V.29, Pt.II, p.449.

Gorter C.J. (1935). Note on the superconductivity of alloys. *Physica*, V.2, No.1-12, p.449-452.

Gorter C.J. (1964). Some remarks on superconductivity of the second kind. *Revs.Mod.Phys.*, V.36, №1, Pt.1, p.27-29.

Hulm J.K., Matthias B.T. (1980). High-field, high-current superconductors. *Science*, V.208, №4446, p.881-887.

Hulm J.K., Kunzler J.E., Matthias B.T. (1981). The road to superconducting materials. *Physics Today*, V.34, №1, p.34-43.

Jackson L.C. (1940). Superconductivity. *Repts.Progr.Phys.* V.6, p.338.

Kamerlingh Onnes H. (1911). Further experiments with liquid helium. D. On the change of the electrical resistance of pure metals at very low temperatures, etc. V. The disappearance of the resistance of mercury. *Comm. Phys. Lab. Univ. Leiden,* V.12, №122b, p.13-15.

Kamerlingh Onnes H. (1914). The appearance of the resistance in superconductors, which are brought into a magnetic field, at a threshold value of the field. *Comm. Phys. Lab. Univ. Leiden,* V.13, №139f, p.65-71.

Kattner U. (2003). *Bi-Pb-Sn system*. Metallurgy Division of the Materials Science and Engineering Laboratory (MSEL) at the National Institute of Standards and Technology (NIST). http://matdl.org/repository/view/madtl:549

Karnaukhov I.M., Shepelev A.G. (2008). Type II superconductors are 70 years old. *Europhysicsnews*, V.39, №3, p.35-36.

Keesom W.H. (1935). On the disturbance of superconductivity of an alloy by an electric current. *Physica*, V.2, №1-12,p.35-36.

Keeley T.C., Mendelssohn K., Moore J.R. (1934). Experiments on supraconductors. *Nature*, V.134, №3394, p.773-774.

Kunzler J.E., Buehler E., Hsu F.S.L. et al. (1961). Superconductivity in Nb_3Sn at High Current Density in a Magnetic Field of 88 kgauss. *Phys. Rev. Lett.* V.6, Issue 3, p. 89–91.

Larbalestier D., Gurevich A., Feldman D.M. et al. (2001). A. High-T_c superconducting materials for electric power applications. *Nature,* v.414, №6861, p. 368-77.

Landau L.D. (1937). On the theory of superconductivity. *Zh. Exper. Teor. Fiz.* (USSR), V.7, №3, p.371-378.

Landau L.D. (1943). On the theory of intermediate state of superconductors. *Zh. Exper. Teor. Fiz.* (USSR), V.13, №11-12, p.377-387.

London H. (1935). Phase-equilibrium of superconductors in a magnetic field. *Proc. Roy. Soc.(London),* V.152A, No.877. p.650-663.

Massalski T.B., Editor-in-Chief. (1987). *Binary Alloy Phase Diagrams*. American Society for Metals, Metals Park, Ohio, in 2 vol., 2224p.

Martin D.L., Benz M.G., Bruch C.A. et. al. (1963). A 101000 Gaus niobium-tin superconducting solenoid. *Cryogenics,* V.3, №2, p.114.

Matricon J., Waysand G. (2003). *The cold wars: a history of superconductivity*. Rutgers University Press, New Jersey, p.80-100.

Meissner W., Ochsenfeld R. (1933). Ein neuer Effekt bei Eintritt der supraleitfähigkeit. *Naturwiss,* Bd.33, No.44. S.787-788.

Mendelssohn K. (1935). In Discussion on superconductivity and other low temperature phenomena. *Proc. Roy. Soc.(London),* V.152A, No.875, p.34-41.

Mendelssohn K., Moore J.R. (1935). Surpa-conducting alloys. *Nature,* V.135, No.3420. p.826-827.

Mendelssohn K. (1946). Superconductivity. *Repts.Progr.Phys.*, V.10, p.362-363.

Mendelssohn K. (1964). Prewar work on superconductivity as seen from Oxford. *Revs. Mod. Phys.*, V.36, №1, pt.1, p.9-12.

Mendelssohn K. (1966). *The Quest for Absolute Zero. The Meaning of Low Temperature Physics*. McGraw-Hill Book Company, N.Y., p.199-209.

Morin F.J., Maita J.P., Williams H.J. et al. (1962). Heat capacity evidence for a large degree of superconductivity in V_3Ga in high magnetic fields. *Phys. Rev.Letters*, V.8, Iss.7, p.275-277.

Obreimow I.W., Schubnikow L.W. (1924). Methode zur Herstellung einkristalliger Metalle. *Z. Phys.*, V.25, №1, S.31-36.

Pavlenko Yu.V., Ranyuk Yu.N., Khramov Yu.A. (1998). *The «case» of UPhTI, 1935-1938*. «Phoenix» Publishing House, Kiev.

Pippart A.B. (1987). Early superconductivity research (except Leiden). *IEEE Trans. Magnetics*, V.MAG-26, №.2, p.372-373.

a - Rjabinin J.N., Schubnikow L.W. (1935). Magnetic properties and critical currents of superconducting alloys. *Phys. Z. Sowjet.* V.7, No.1. p.122-125.

b - Rjabinin J.N., Schubnikow L.W. (1935). Magnetic properties and critical currents of superconducting alloys. *Nature.* V.135, No.3415. p.581-582.

Roberts B.W. (1976). Survey of superconductive materials and critical evaluation of selected prorepties. *J. of Phys. And Chem. Refer. Data*, V.5, №3, p.581-821.

Roberts B.W. (1978). *Properties of selected superconductive materials*. 1978 supplement. NBS Report, US Department of commerce, Govt. Print. Off., p.1-93.

Rossi L. (2006). The longest journey: the LHC dipoles arrive on time. *CERN Courier,* V.46, №8, p.28-32.

Rossi L. (2010). Superconductivity: its role, its success and its setbacks in the Large Hadron Collider of CERN. *Supercon. Science and Technology*, V.23, №3, p.1-18.

Rubinin P.E. (1994). Kapitsa P.L. and Kharkov. *Low Temp.Phys.*, V.20, №7, p.723.

Ruhemann M. and B. (1937). *Low Temperature Physics*. University Press, Cambridge, p.274-275; 287-288.

Saint-James D., DeGennes P.G. (1963). Onset of superconductivity in decresing fields. *Phys.Lett.*, V.7, №5, p.306-308.

Saint-James D., Thomas E.I., Sarma G. (1969) . *Type II Superconductivity*. Pergamon, N.Y.

Salpietro E. (2006). Status of the ITER magnets. *Supercond. Sci. Technol*. V.19, №3, p.84-89.

Serin B. (1956). *Superconductivity. Experimental part.* In: Handbuch der Physik Bd.15. Kältephysik II. (ed. S.Flügge), Springer Verlag, Berlin, Göttingen, Heidelberg, S.210-273.

Serin B. (1969). *Superconductivity. Experimental part.* In: Superconductivity (ed. R.D.Parks), Marcel Dekker Inc, N.Y., V.2, p.925-976.

Sharma H.P., Sen S.K. (2006). Shubnikov: A case of non-recognition in superconductivity research. *Current Science*, V.91, №11, p.1576-1578.

Schubnikow L.W., Chotkewitsch W.I., Schepelew J.D., Rjabinin J.N. (1936). Magnetische Eigenschaften supraleitender Metalle und Legierungen. *Sondernummer Phys.Z.Sowjet. Arbeiten auf dem Gebiete tiefer Temperaturen, Juni 1936*, S.39-66; Schubnikow L.W., Chotkewitsch W.I., Schepelew J.D., Rjabinin J.N. (1936). Magnetische Eigenschaften supraleitender Metalle und Legierungen. *Phys.Z.Sowjet*. Bd.10, H.2, S.165-192.

Shepelev G.D. (1938). Magnetic properties of superconducting alloys. *PhD Thesis (Kharkov State Univ.)*.

Shoenberg D. (1938). *Superconductivity*. University Press., Cambridge, p.79-86.

Shoenberg D. (1952). *Superconductivity (2nd ed.)*. University Press., Cambridge, p.39-47.

Shubnikov L.V., Khotkevich V.I., Shepelev Yu.D., Riabinin Yu.N. (1937). Magnetic properties of superconducting metals and alloys. *Zh. Exper. Teor. Fiz.* (USSR), V.7, №2, p.221-237; Shubnikov L.V., Khotkevich V.I., Shepelev Yu.D., Riabinin Yu.N. (2008). Magnetic properties of superconducting metals and alloys. *Ukrainian Journal of Physics,* 2008, V.53, Special Issue, p.42-52 (Reprinted in English).

Sizoo G.J., De Haas W.J., Kamerlingh Onnes H. (1926). Measurements on the magnetic disturbance of the superconductivity with tin. 1. Influence of elastic deformation. 2. Hysteresis phenomena. *Comm. Phys. Lab. Univ. Leiden,* V.16, №180c, p.29-53.

Slezov V.V., Chernyi O.V., Davydov L.N. (2005). Critical current density and magnetic pinning in Nb-Ti superconductor. *Supercond. Sci. Technol*. V.18, №5, p.747-752.

Slezov V.V., Papirov I.I., Shepelev A.G. (2007). Experimental discovery of type II superconductors at UPhTI. 70-years later: sum resalts and perspectives. *Universitates. Science and education*, V.3, p.38-45.

Slezov V., Shepelev A. (2008). Delayed recognition of Shubnikov. *Current Science* , V.94, №8, p.963.

Slezov V.V., Shepelev A.G. (2009). To the history of experimental discovery of Type II superconductors. *Research on history of physics and mechanics. 2008*. Physmatlit, Moskow, p.111-126.

Tarr F.G.A., Wilhelm J.O. (1935). Magnetic effects in superconductors. *Canad. J. Research*, V.12, №1, p.265-271.

Trapeznikova O. (1990). *In L.V.Shubnikov: Selected papers, memoirs*. Naukova dumka, Kiev, p. 287-289.

Tuyn W., Kamerlingh Onnes H. (1926). The disturbance of supra-conductivity by magnetic field and currents. The hypothesis of Silsbee. *Comm. Phys. Lab. Univ. Leiden,* V.16, №174a, p.3-39.

Van Aubel Edm., De Haas W.J., Voogd J. (1929). New super-conductors. *Comm. Phys. Lab. Univ. Leiden,* V.18, №193c, p.33-41.

Ullmair H. (1975). *Irreversible properties of type II superconductors*. Springer, Berlin, Heidelberg, N.Y.

Waysand G. (2005). Cold (and hot) wars: superconductivity and society, from Weissberg-Cibulsky 1931 to the 2003 Nobel prize. *Physica status solidi (c),* V.2, No.5, p.1566-1577.

Weissberg-Cybulsky A. (1951). *Hexensabbat. Russland im Schmelztiegel der Säuberungen.* Verlag der Frankfurter Hefte, Frankfurt am Main.

Wilson A.H. (1937). Superconductivity and the theory of metals. *Repts.Progr.Phys.*, V.3, p.267,268.

http://www.rtri.or.jp/rd/maglev/html/english/maglev_frame_E.html

3

Microstructure, Diffusion and Growth Mechanism of Nb_3Sn Superconductor by Bronze Technique

Aloke Paul[1], Tomi Laurila[2] and Vesa Vuorinen[2]
[1]*Department of Materials Engineering, Indian Institute of Science, Bangalore -560012*
[2]*Electronics Integration and Reliability, Department of Electronics, Helsinki University of Technology, FIN-02015 TKK*
[1]*India*
[2]*Finland*

1. Introduction

Nb-Ti is a widely used superconductor material. However, its use is limited to applications of magnetic field upto 8T (Sharma, 1987). At the present, Nb_3Sn intermetallic compound with A15 structure is considered to be one of the most suitable superconductors for the applications where field requirements go beyond the limit of Nb-Ti superconductors. However, intermetallic compounds are in general brittle and cannot be drawn as wire. To circumvent this problem, different manufacturing technologies have been developed for Nb_3Sn, such as bronze method, internal tin process, powder metallurgy route, Jelly roll process, ECN technique (Suenaga, 1981; Sharma, 1987) etc.
In this chapter, we shall discuss mainly the growth and diffusion mechanism of Nb_3Sn fabricated by the bronze technique. In this method, several Nb rods are inserted inside Cu(Sn) bronze alloy and drawn as a multifilamentary wire. The product phase Nb_3Sn is grown during the subsequent annealing by solid state diffusion. The efficiency of a superconductor wire largely depends on the presence of microstructural defects, such as grain boundaries and Kirkendall pores, grain size distribution, the variation of chemical composition over the cross section (Suenaga, 1981; Suenaga & Jansen, 1983; Lee & Larbalestier, 2005; Lee & Larbalestier, 2008) and so on. The application of pure Nb_3Sn compound has been found to be limited to magnetic fields of 12 T, since the increase in the field drastically reduces the critical current density, J_c. Further improvements have been achieved by alloying Nb_3Sn with different elements, such as Ti, Ta, Zr, Mg etc. (Suenaga et al., 1986). Thus, the aim of this chapter is to discuss and analyse various factors which affect the growth of the product phase by diffusion controlled process. The evolution of microstructure is detemined by the thermodynamics and kinetics of the system. The combined thermodynamic-kinetic approach will be discussed, which provides a feasible tool to rationalize the formation of the observed reaction structures.

2. Microstructural aspects

Grain boundaries play an important role on flux pinning and thus the critical current density is strongly influenced by the grain size distribution in a given multifilamentary

structure. Typical grain structure is shown in Fig. 1 (Flükiger et al., 2008). As explained by Müller & Schneider, 2008, mainly two different grain morphologies can be distinguished. Near the Nb core columnar grains are typically found, whereas near the Cu(Sn) bronze alloy equiaxed grains are generally seen. Further there can exist two types of equiaxed grains: small grains in the middle of the Nb_3Sn layer and coarse grains near to the Cu(Sn) alloy. Average grain size, as shown in Fig. 2, is found to increase with annealing time and temperature. However the average grain size does not define the distribution unambiguously, as shown in Fig. 3.

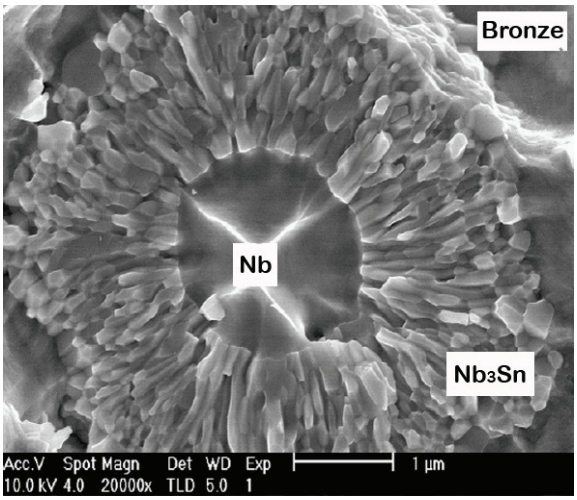

Fig. 1. Grain morphology of Nb_3Sn layer (Flükiger et al., 2008).

3. Diffusion mechanism

In the bronze technique, Nb rods are embedded in Cu(Sn) bronze alloy. Sn concentration in the alloy, in general, is kept within the solid solubility range of 6-8 at.%Sn in Cu. The composite structure is then drawn as a wire with the required dimensions. Subsequently, the multifilamentary wire is annealed in the temperature range of 600-800 ^{o}C. Nb_3Sn grows as product layer at the Cu(Sn)/Nb interface by interdiffusion process. The overall physical and mechanical properties of the structure depend on the thickness, composition and morphological evolution of the product phase (Suenaga, 1981; Sharma, 1987). Morphological evolution in the interdiffusion zone depends on many factors. Among them are the annealing temperature and time, relative mobilities of the species, number of nucleation sites and so on. Further increase in the grain size along with the growth of the product layer makes the whole process very complicated. It has also been reported that Kirkendall pores are formed near the Nb_3Sn/Cu(Sn) interface. This indicates that there must be a significant difference in the mobilities of the species (Sn and Nb) through the product layer. Vacancies flow opposite to the direction of the faster diffusing species and in general get consumed by different sites those act as sink, such as the edge dislocations, grain boundaries and interfaces. However, in some systems, because of unavailability of sufficient sites as sink, vacancies coalescence and form pores (Adda & Philibert, 1981). It can easily be understood

that the presence of pores can adversely affect the overall performance of the structure. The position of the pores indicates that Sn must be the faster diffusing species through the product phase. Cu is not considered to contribute to the growth process, since its concentration in Nb_3Sn is generally found to be negligible. This issue should, however, be confirmed, in order to better understand the interdiffusion behavior in Nb_3Sn.

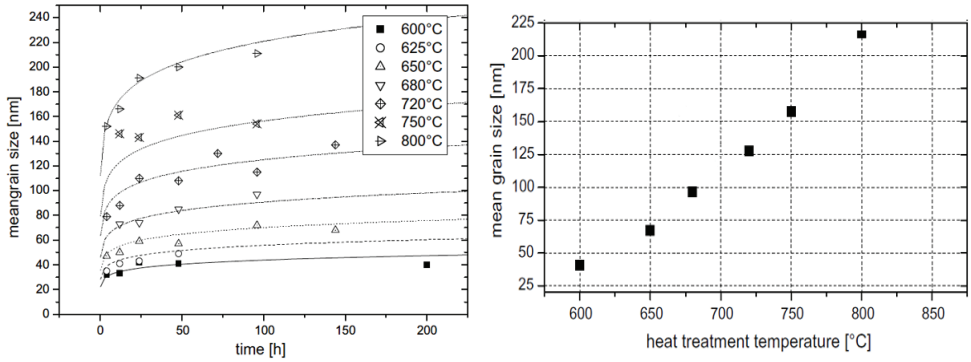

(a) (b)

Fig. 2. (a) The change in average grain size with the increase in annealing time at different temperatures is shown. (b) The increase in average grain size with temperature after fixed annealing time of 100 h is shown (Müller & Schneider, 2008).

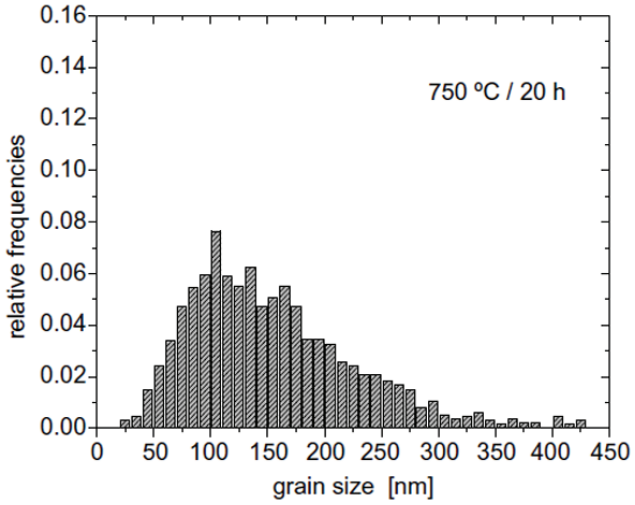

Fig. 3. Grain size distribution after annealing for 20 h at 750 °C (Müller & Schneider, 2008).

Hence, understanding the diffusion process is very important, since it is a key factor (together with thermodynamics) in the formation of microstructure, which ultimately controls the performance of the material. There are numerous studies published in order to understand the growth and diffusion mechanisms of Nb_3Sn, after the bronze method was developed to produce the superconductors (Sharma, 1987). However, the basic

understanding of the diffusion process is still lacking. This is not surprising since many times it is extremely difficult to draw any conclusion about the exact diffusion mechanism from simple diffusion couple experiments. Both lattice and grain boundary diffusion can be operative simultaneously and it is almost impossible to find the exact contribution from different mechanisms. To get rough idea about the diffusion mechanism, experiments are typically conducted at a particular temperature to measure the growth exponent. As stated earlier (Harrison, 1961), when the diffusion process is mainly controlled by lattice (Type A-kinetics) or grain boundary diffusion (Type C-kinetics), growth exponent is found to be of the order of 0.5. When contribution comes from lattice and grain boundary diffusion simultaneously, growth exponent is typically found to be around 0.25 (Type B-kinetics). Another way to evaluate the diffusion mechanism is by calculating the activation energy for diffusion by utilizing the Arrhenius equation. In general it is found that the activation energy for grain boundary diffusion is relatively low, since atoms need to cross the migration barrier only. On the other hand, the activation energy for lattice diffusion is found to be much higher, since the activation barrier for formation and migration of defects is added to the activation energy.

Several studies have concentrated in determining the growth exponent to evaluate the diffusion mechanism. For example, Farrel et al. (Farrel et al., 1974; Farrel et al., 1975) prepared multifilamentary wire by inserting Nb rods in the Cu(5at.%Sn) alloy. The rods were subsequenmtly drawn as wire with an approximate individual filament diameter of 25 μm. Multifilamentary wires were first annealed at two different temperatures, 700 and 800 ◦C for different annealing times to determine growth exponent. They noticed that layer was very wavy in nature. This is clear from the standard deviation of the average layer thickness shown in Fig. 4a. They found that the growth exponent is around 0.35±0.02. They also measured the temperature dependence of the growth of the phase in order to calculate the activation energy for diffusion, as shown in Fig. 4b. Activation energy was found to be around 12.4 kcal/mole (51.9 kJ/mol). Further study was conducted with higher Sn concentration in the bronze alloy and it showed that the growth rate becomes more sensitive to the Sn concentration starting from 7 at.%Sn and the growth exponent increases with increasing Sn concentration. Further, the growth rate became linear after certain annealing time, when bronze alloy had around 11.5 at.%Sn. As this is already beyond the solubility range of Sn in Cu, this result should be taken to be only indicative. They also found cracks in the Nb_3Sn phase after certain thickness. It was explained that the growth rate becomes linear because of the presence of cracks.

Reddi et al. (Reddi et al., 1983) carried out more systematic experiments to determine the change in the growth exponent along with the change in Sn concentration in the bronze alloy as well as a function of annealing temperature. Sn concentration was varied in the range of 2.01 to 10.87 wt.% (1.09 – 6.1 at.%). The diameter of the individual Nb rods in the multifilamentary wire was 0.12 mm. Experiments were conducted in the temperature range of 650–850 ◦C for 9 to 225 hrs. They reported that at 700 ◦C, growth exponent changes from 0.87 to 0.57 with the increase in Sn concentration from 7.29 to 10.87 wt.%. At 750 ◦C, as shown in Fig. 5a, the same changes from 0.80 to 0.57 with the change in Sn concentration from 3.30-10.87 wt.%. At 800 ◦C, as shown in Fig. 5b, it changes from 0.90 to 0.65 with the change in Sn concentration from 2.01-8.36 wt.%. They further noticed, as shown in Fig. 6a that the growth exponent mainly depends on the Sn concentration in the bronze alloy and more or less insensitive to the annealing temperature, as shown in Fig. 6b. The values were

further compared with the data available in the literature. They also calculated the activation energy for growth for the sample with 7 wt.%Sn (3.87 at.%) in the bronze alloy and found the value of 230 kJ/mol. It should be noted that this value is much higher than the value determined by Farrel et al. (Farrel et al., 1974). This is rather close to the value of 215-225 kJ/mol calculated by Larbalestier et al. (Larbalestier et al., 1975).

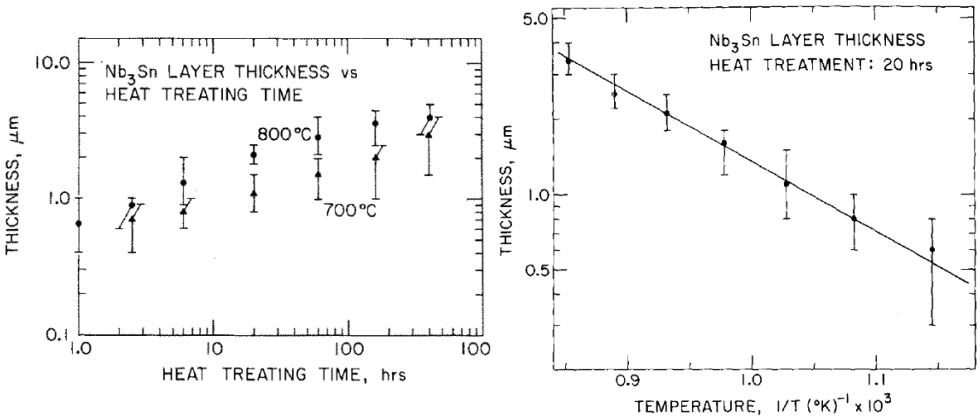

(a) (b)

Fig. 4. (a) The increase in layer thickness with annealing time at two different temperatures and (b) the layer thickness at different annealing temperatures, as reported by Farrel et al., 1974 and Farrel et al., 1975 are shown.

A more recent study (Muranishi & Kajihara, 2005) investigated the growth of the Nb_3Sn phase in the temperature range of 650-780 ◦C. They considered only 8.3 at.%Sn in the bronze alloy. They conducted experiments with diffusion couple technique with planar interfaces. There is an important difference between this and the earlier studies as will be discussed later on. Unlike the result of Reddi et al. (Reddi et al., 1983), they found that growth exponent is different at different temperatures. In the range of 650-700 ◦C, the growth exponent was found to be around 0.96 and decreased to 0.77 at 780 ◦C.

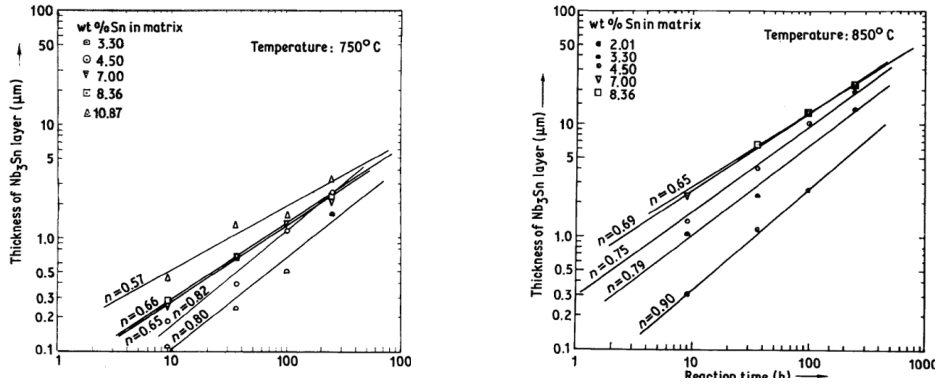

Fig. 5. The increase in layer thickness with annealing time and growth exponent at (a) 750 ◦C and (b) 850 ◦C as reported by Reddi et al., 1983 is shown.

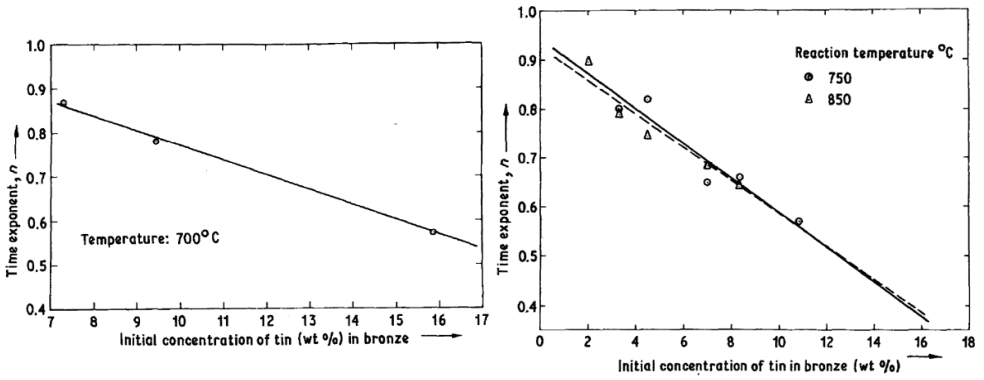

(a) (b)

Fig. 6. The variation of growth exponent with respect to Sn concentration in bronze alloy at (a) 700 ◦C and (b) 750 and 800 ◦C as reported by Reddi et al. is shown (Reddi et al., 1983).

What has been stated above clearly shows that it is very difficult to draw definite conclusions about the growth exponent of the Nb_3Sn phase. Outcome of different studies is found to be very different from each other. Further, a very common problem was found in most of the studies. To imitate the actual structure, experiments were mainly conducted with multi or monofilamentary structure, where Nb rods are surrounded by Cu(Sn) bronze alloy. However, the studies applied the growth kinetic relations derived for the sample geometries with planar interface. It should be noted that interdiffusion study with this geometry is rather complicated compared to the interdiffusion process in a specimen with planar interface. It is also not possible to use the laws developed for planar interface directly in the experimental results that are achieved from the experiments with cylindrical geometry, since the growth rate in this condition does not follow the same relation (van Loo, 1990). In a diffusion couple with planar interface, interfacial area does not change. However in a diffusion couple with cylindrical geometry, interfacial area continuously changes with the annealing time, as shown in Fig. 7a and growth deviates from linearity when plotted Δx vs. $\sqrt{t}$ as shown in Fig. 7b. Moreover because of waviness in the layer thickness, standard deviation is found to be very high. So it is very difficult to determine the exact growth exponent. Very few interdiffusion studies with planar interface have been reported (Muranishi & Kajihara, 2005; Hayase & Kajihara, 2006).

It is typically considered that Sn is virtually the only diffusing species through the product phase in the Nb/Cu(Sn) system. This is not an bad assumption, since the Kirkendall pores, which are formed because of unequal mobilities of the species, are found near the Cu(Sn)/Nb_3Sn interface (Easton & Kroeger 1979). This indicates that Sn must be the fastest diffusing species through the product layer.

To quantify the relative mobilities of the species during the growth of Nb_3Sn, Kirkendall marker experiments were carried out by Kumar & Paul (Kumar & Paul, 2009). Bronze alloys with the composition of 7 and 8 at.%Sn were prepared to couple with pure Nb. These compositions were selected, since according to Reddi et al. (Reddi et al., 1983) growth exponent was found to be close to 0.5, when Sn concentration in the bronze alloy was relatively high. After melting the alloys in an induction furnace in vacuum (~10^{-6} mbar), samples were annealed at 700 ◦C in vacuum for 48 h to achieve better homogeneity. The

average composition was further monitored by electron dispersive X-ray spectrometer (EDX). The experiments were conducted with planar interface geometry. TiO_2 particles of around 1 μm size were introduced at the initial contact plane, which acted as the inert Kirkendall markers. Experiments were done at three different temperatures of 700, 750 and 775 °C for 100-330 h. The cross-section from the (Cu-8at.%Sn)/Nb diffusion couple annealed at 775 °C for 330 h is shown in Fig. 8a. The composition profile measured by EDX is shown in Fig. 8b. Inert particles were found at the Cu(Sn)/Nb interface. Since the amount of Cu in the Nb_3Sn phase was negligible, it can be said that Sn is virtually the only mobile species through the product phase.

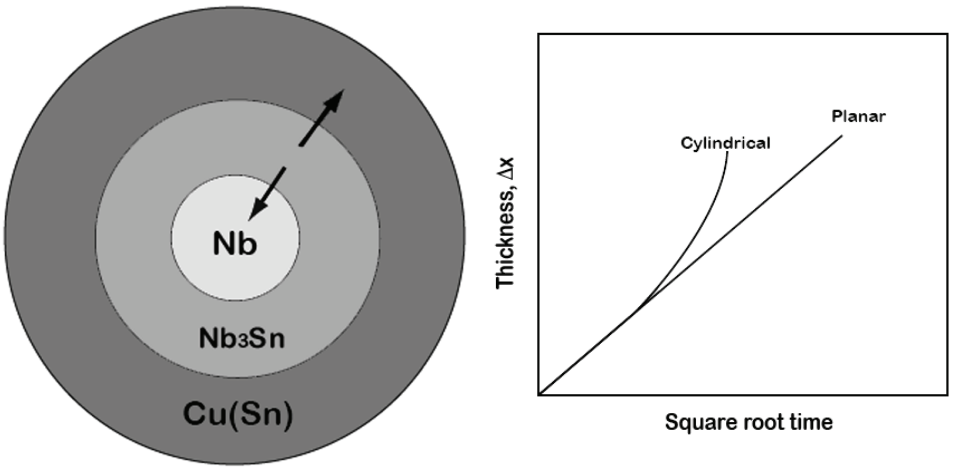

(a) (b)

Fig. 7. (a) The growth of Nb3Sn product phase in the sample with cylindrical geometry is shown. Arrows indicate the movement of the interfaces following which interfacial area changes. (b) The change in layer with square root of time in the case of sample with planar and cylindrical geometry is shown. Growth rate with planar interface will follow parabolic law in the case of diffusion controlled process; however, it will deviate in the case of growth in a sample with cylindrical geometry (van Loo, 1990).

Although Cu(Sn)/Nb diffusion couple experiment indicates that Sn is virtually only mobile species, it is rather surprising if one considers the crystal structure of the A15 Nb_3Sn intermetallic compound, as shown in Fig. 9. Sn atoms occupy the body corner and centre positions and two Nb atoms occupy each face of the cube. It can be clearly visualize that Sn atoms are surrounded by 12 Nb atoms. On the other hand, Nb atoms are surrounded by 10 Nb atoms and 4 Sn atoms. Since Nb has as its nearest neighbors Nb atoms, it can diffuse via its own sublattice if vacancies are available. In contrast, in a perfect (antisite defect free) crystal, there is no possibility for diffusion of Sn. If Sn jumps to a nearest neighbor sublattice position, it will be at a wrong place, since these sites should be occupied by Nb atoms and the jump is not allowed. However, certain amount of diffusion of Sn is still possible because of antisite and vacancies always present in the structure. According to theoretical analysis conducted by Besson et al. (Besson et al., 2007) as shown in Fig. 10a, there is a significant concentration of antisite defects in the compound, even at the stoichiometric composition.

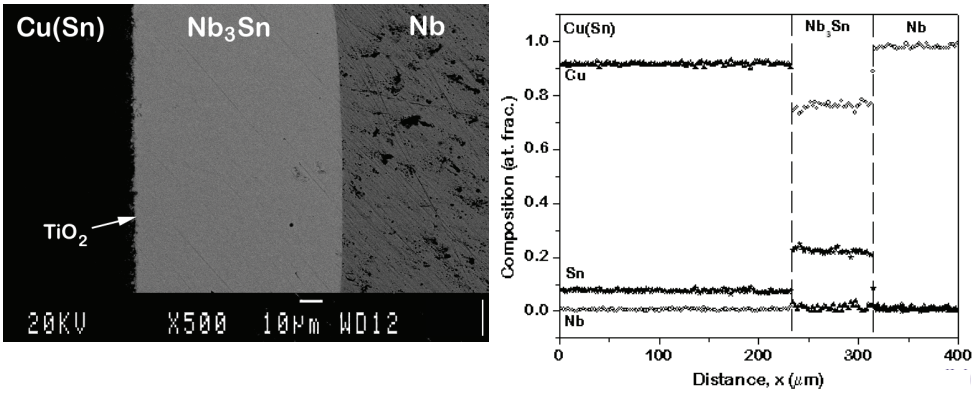

(a) (b)

Fig. 8. (a) The growth of the Nb3Sn phase and (b) corresponding composition profile are shown in a diffusion couple of Cu(8at.%Sn)/Nb at 775 °C annealed for 330 h (Kumar & Paul, 2009).

Following their calculation, the concentration of vacancies in Nb sublattice is much higher than the vacancies present in Sn sublattice. Nb can exchange position with the vacancies at its own sublattice. The presence of Nb antisite defects should further increase the diffusion rate of Nb. On the other hand, diffusion of Sn is possible only by the exchange of vacancies present on Nb sublattice with Sn antisite defects. This kind of jump is allowed since antisite Sn will move to Nb sublattice as antisite defects only. Nevertheless, the diffusion rate of Nb should always be higher than Sn in the Nb_3Sn compound, as shown in Fig. 10b based on the structural aspects alone. Of course, we are considering here only lattice diffusion. In the case of grain boundary diffusion, diffusion rate of Sn could be somewhat higher. Unfortunately, there is no experimental data available in the binary system Nb-Sn about the relative mobilities of the species in Nb3Sn phase to confirm these calculations. Till date experimental results on diffusion rates of elements are available only in two other A15 intermetallic compounds, V_3Ga (Bakker, 1985) and V_3Si (Kumar et al., 2009). In these cases, not surprisingly, diffusion rates of Ga and Si are found to be negligible compared to the diffusion rate of V. The well known Cu_3Au rule (d'Heurle & Gas, 1986) states that the if the ratio of major to minor element is equal or greater than 3 in an intermetallic compound, the major element will be the faster diffusing species. This empirical rule was developed based on the experimental data available in the literature. Hence, it is rather surprising to find that Sn is practically the only moving species in the Nb_3Sn compound growing between Nb/(Cu-Sn) diffusion couple.

Kumar and Paul (Kumar & Paul, 2009) did further experiments to study the effect of Sn content of the bronze alloy on the growth rate. Conventional diffusion couple experiments were conducted to study the growth of the phase with planar interface geometry. In a multifilamentary structure corrugated layer was always found, which resulted into a quite high standard deviation from the measured average layer thickness. Hayase & Kajihara (Hayase & Kajihara, 2006) argued that the corrugated structure is found because multifilamentary structure, which is cylindrical in geometry. They reported that the thickness of the uniform layer was similar to the one found by Kumar and Paul, as shown in Fig. 10a. However, if an uniform layer grows in a diffusion couple with a planar interface, then an uniform layer also should grow in the sample with a cylindrical geometry. The

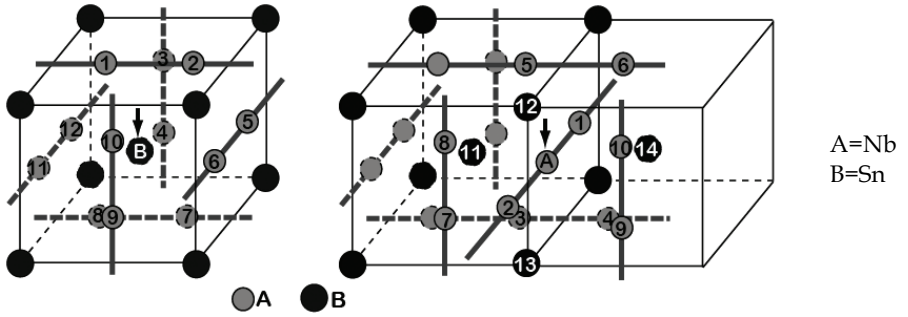

Fig. 9. A15 crystal structure is shown with the nearest neighbors of Nb and Sn.

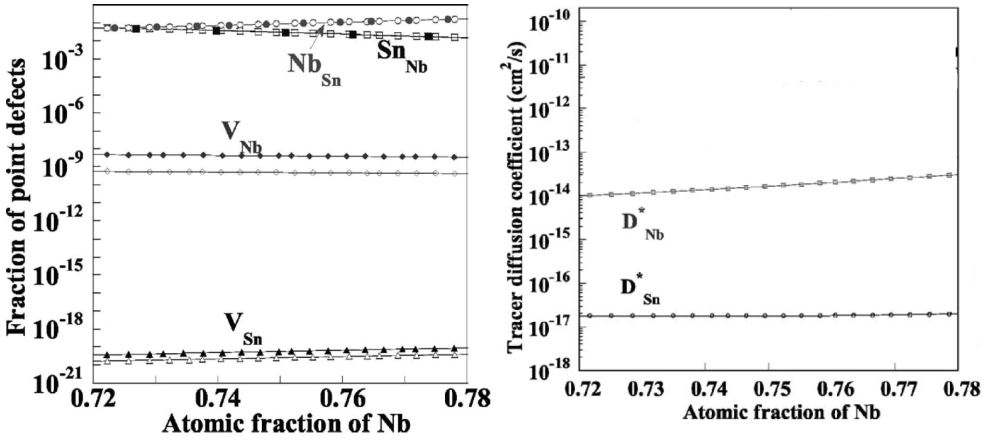

(a) (b)

Fig. 10. (a) Defect concentraions calculated by Besson et al. (Besson, 2007) in Nb_3Sn phase at 1000K. Data reported by open and closed symbols are calculated following local density approximation (LDA) and generalized gradient approximation (GDA). (b) Tracer diffusion coefficient of Nb (D^*_{Nb}) and Sn (D^*_{Sn}) calculated are shown.

radial distribution of the flux should be the same over the whole layer in the latter case. In fact, Kumar and Paul noticed that the layer grows uniform in thickness, but only locally. At different locations of the diffusion couple, large differences in the thickness of the product layer were found. As shown in the experimental results for Cu(8at.%Sn)/Nb diffusion couple annealed at 775 ^oC for 150 hrs in Fig. 11, the layer thickness varies over a wide range of 28.5-42 μm. On the otherhand, looking at one particular micrograph; it looks like Nb_3Sn phase grows more or less uniformly. In general, waviness in the product layer is found because of various reasons. For example, incubation period could be different at different places. Further, different diffusion rates because of different orientation of the grains also could cause waviness. In the present case, however, it might happen because of small inhomogeneity in the Cu(Sn) alloy. Following Farrel et al. (Farrel et al., 1974), small difference in Sn concentration can cause significant difference in the thickness of the product

layer. Despite the homogenization treatment, some inhomogeneity can still be present in the Cu(Sn) alloy, which may cause thickness variation at different locations of the diffusion couple.

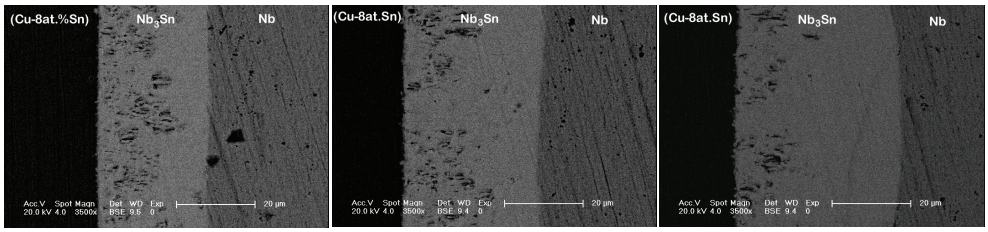

Fig. 11. Different layer thickness in the same diffusion diffusion couple annealed at 775 ^{o}C for 150 hrs at different locations is shown (Kumar and Paul, 2009).

Further the growth of the product phase for 7 and 8 at.%Sn in the Cu(Sn) alloy at different temperatures is shown in Fig. 12 a and b. The considerable deviation from the average values is evident from the standard deviation bar. It is very difficult to determine the exact

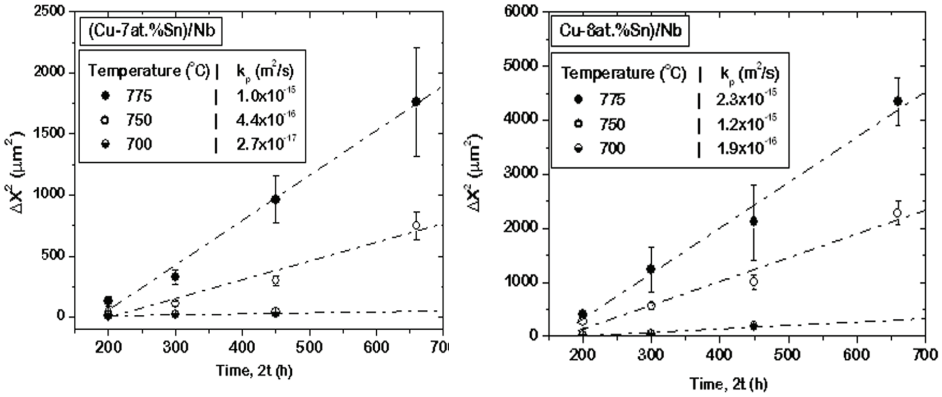

Fig. 12. The variation of layer thickness with annealing time and temperature is shown in (a) Cu(7at.%Sn)/Nb and (b) Cu(7at.%Sn)/Nb diffusion couple (Kumar & Paul, 2009).

growth exponent from these results and we have considered the parabolic growth of the phase. Following the parabolic growth constant can be calculated using

$$\left(\Delta x_{Nb_3Sn}\right)^2 = 2k_p\left(t - t_0\right) \tag{1}$$

where Δx_{Nb_3Sn} is the thickness of the Nb_3Sn phase layer and t is the total annealing time and t_0 is the incubation period. The activation energy for growth was further calculated from the Arrhenius equation

$$k_p = k_p^0 \exp\left(-\frac{Q}{RT}\right) \tag{2}$$

where k_p^0 is the pre-exponential factor, Q is the activation energy, R is the gas constant and T is the temperature in Kelvins. Fig. 13 shows the growth rate of the product phase in (Cu-7at.%Sn)/Nb and (Cu-8at.%Sn)/Nb diffusion couples at three different temperatures, 700, 750 and 775 °C. Following our analysis, we found that the activation energy for the growth of the phase in (Cu-7at.Sn)/Nb couple is 404 kJ/mole, whereas, in (Cu-8at.Sn)/Nb couple is 279 kJ/mole. It can be seen that there is a significant decrease in the activation energy for the diffusion along with a small change in the Sn concentration of the bronze alloy. By comparing the growth of the product phase for different Sn concentrations, as shown in Fig. 14, it was noticed that there was around 50 percent increase in the layer thickness with 1 at.% increase in the Sn concentration. In order to understand this behaviour, thermodynamic analysis was conducted to examine the change in the driving force for reactive diffusion with the change in the Sn content (Laurila et al., 2010).

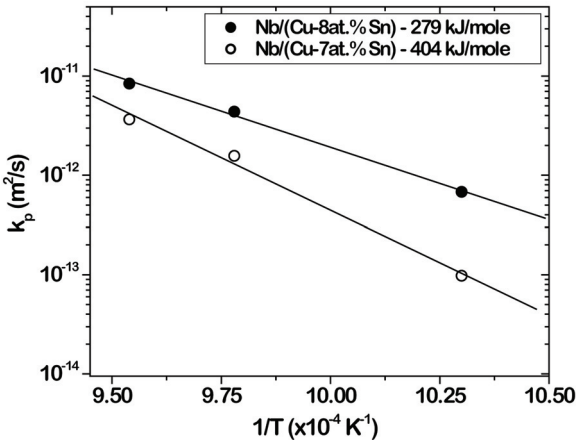

Fig. 13. The Arrhenius plot of the parabolic growth constant is shown (Kumar & Paul, 2009).

4. Thermodynamics, phase diagrams and driving force for diffusion

Thermodynamics of materials provide fundamental information both on the stability of various phases and on the driving forces for chemical reactions and diffusion processes in the system under investigation. Even though the complete (global) phase equilibrium is seldom met in practical applications, stable or metastable local or partial equilibria are generally attained at interfaces, which ensures that thermodynamics together with kinetic information provides a feasible method for analyzing the interfacial reactions in wide range of different material systems.

4.1 The Gibbs energy

The combined statement of the first and second laws of thermodynamics can be stated in terms of temperature (T) and pressure (p) with the Gibbs free energy as follows (in closed systems):

$$G \equiv U + pV - TS = H - TS \qquad 3)$$

where *U, V, H,* and *S* are the internal energy, the volume, the enthalpy and the entropy of the system, respectively. Given that $G = G(T,P,n_1, n_2,...)$ in an open system, with n_i being the number of moles of component *i*, the derivative of Eq. (1) yields:

$$dG = -SdT + Vdp + \sum_i \mu_i dn_i \tag{4}$$

where μ_i is the chemical potential of component *i*. At a constant value of the independent variables *P*, *T* and n_j $(j \neq i)$ the chemical potential equals the partial molar Gibbs free energy, $(\partial G/\partial n_i)_{P,T,j\neq i}$. The chemical potential has an important function analogous to temperature and pressure. A temperature difference determines the tendency of heat to flow from one body into another and a pressure difference on the other hand the tendency towards a bodily movement. A chemical potential can be regarded as the cause of a chemical reaction or the tendency of a substance to *diffuse* from one phase to another. This will be discussed further shortly.

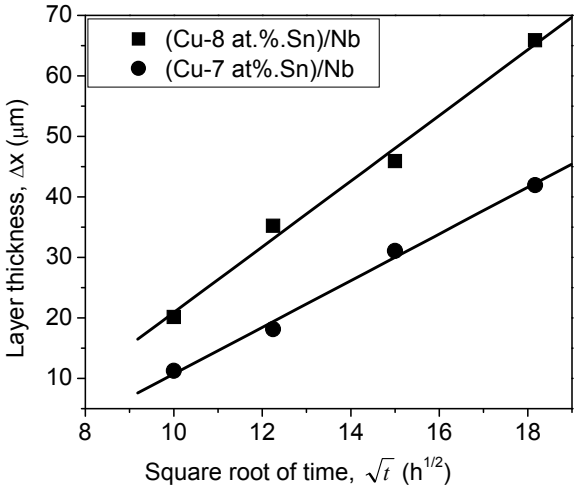

Fig. 14. The comparison between layer thicknesses at 775 °C is shown (Kumar & Paul, 2009).

With the help of the Gibbs free energy function the equilibrium state of the system can be investigated. The phase equilibria in any system are computed by summing up first all the Gibbs (free) energies of individual phases (i.e. solutions and compounds) and then minimizing - according to the second law of thermodynamics, the total energy of the system. At constant temperature and pressure the total Gibbs energy of n-component system can be written as

$$G_{tot} = \sum_{\varphi}\sum_{i}(G_i^{\varphi} n_i^{\varphi}) = \sum_{\varphi} y^{\varphi} \sum_{i=1}^{n}(x_i G_i^o + RT\sum_{i}^{n} x_i \ln x_i + G_m^E) \tag{5}$$

where y is the relative amount of a phase ϕ and x_i is a mole fraction of a component i in the system. The parameters G_i^o in Eq. 3 represent the partial molar Gibbs energies or chemical potentials of the pure components and are taken either from the SGTE databank (Dinsdale,

1991) or from the literature. G_m^E is the excess molar Gibbs energy taking into account the interactions of the constituents in all the phases to be considered.

4.2 Calculation of phase diagrams

Phase diagrams have some times been regarded as something that can only be determined experimentally. However, as phase diagram is a graphical manifestation of the state of equilibrium, it is possible to construct any kind of phase diagram if the equilibrium state of the system has been calculated. This in turn requires the evaluation of the thermodynamic properties of the corresponding system by assessing all the available experimental information in thermodynamic terms. Generally one is interested in equilibria under constant pressure and therefore the Gibbs free energy is the expedient thermodynamic function (Equation (5)). The procedure in a "nutt shell" is as follows: Analytical expressions for the free energy functions of all phases must be derived first. It is to be noted that the thermodynamic models used in the description of the Gibbs free energy of different phases are important, since successful and reliable calculation relies on the appropriate choice of model for each phase appearing in the system. Then by summing up all the Gibbs free energies of individual phases, the phase equilibria can be computed by minimizing the total Gibbs free energy of the system. The matemathical expressions for the Gibbs free energy of the individual phases contain parameters which have to be optimized to give the best fit to all the experimental information available. A major difficulty arises from the fact that the value of a parameter (which is used in the description of a simple system) will affect the evaluation of all the related higher systems. Thus, one should use as much information as possible from different sources in each optimisation process. The preceding approach is known as the CALculation of PHAse Diagrams (CALPHAD) method (Saunders & Miodownik, 1998; Kaufman & Bernstein, 1970).

The CALPHAD method is based on the axiom that complete Gibbs free energy versus composition curves can be constructed for all structures exhibited by the elements right across the whole alloy system. This involves the extrapolation of *(G,x)*-curves of many phases into regions where they are metastable and, in particular the relative Gibbs free energies for various crystal structures of the elements of the system must therefore be established. These are called as lattice stabilities and the Gibbs free energy differences between all the various potential crystal structures in which an element can exist need to be characterized as a function of temperature, pressure and volume. Information about the driving forces of different reactions in the system can also be obtained from the *(G,x)*-diagrams. This information is extremely useful, when, for example, diffusive phase growth is rationalized.

CALPHAD method is commonly used for evaluating and assessing phase diagrams. The power of the method is clearly manifested in its capability to extrapolate higher order systems from lower order systems, which have been critically assessed, thus reducing the number of experiments required to establish the phase diagram. The determination of binary equilibrium diagrams usually involves the characterization of only a few phases, and experimental thermodynamic data on each of the phases is generally available in various thermodynamic data banks as well as in the literature. However, when handling multicomponent systems or/and metastable conditions there is a need to evaluate the Gibbs free energies of many phases, some of which may be metastable over much of the composition space. Readers interested in the actual thermodynamic modelling procedures

and issues and problems associated with them are referred to vast amount of available literature, for example review articles and books (Saunders & Miodownik, 1998; Kaufman & Bernstein, 1970; Lukas et al., 2007; Ansara, 1990; Hillert, 1998).

4.3 Driving force for diffusion

The total Gibbs energy of the system can be expressed as a function of chemical potentials, which are related to the activities of the components as follows:

$$\mu_i^{\varphi} \equiv \mu_i^0(T) + RT \ln a_i \tag{6}$$

where μ_i and a_i are chemical potential and activity of element i. As explained above, the chemical potential of a component i will have the same value in all the equilibrated phases and therefore the difference in activity of a component (i.e. the driving force for its diffusion) will vanish at equilibrium. In the case of local equilibrium there are concentration gradients in the adjoining phases, but due to the chemical interaction between component atoms the diffusion is not necessarily driven by these gradients. Instead, the difference in chemical potential is the real driving force for diffusion as already discussed. A fundamental condition is that no atom can diffuse intrinsically against its own activity gradient (van Loo, 1990). If it would climb up its own activity profile, it would mean that the component moves from the region of lower chemical potential to a region of higher chemical potential – a process that does not spontaneously occur in nature. If a maximum is found experimentally in the activity profile of a component, the intrinsic movement of the other components causes it. This requirement can be used when movement of different species in a given reaction layer sequence are considered. To aid this analysis, another type of equilibrium diagrams – potential diagrams- can be utilized (Laurila et al., 2004).

5. Thermodynamic-kinetic analysis of the growth of Nb_3Sn

As already discussed there are basically three open questions concerning the growth of Nb_3Sn by the bronze technique:

1. Why Sn is the only diffusing species during the reaction?
2. Why there is such a drastic increase in the thickness of the Nb_3Sn grown under the same experimental conditions, when Sn content of the Cu(Sn) alloy is increased from 7 at.% to 8 at.%?
3. Is there solubility of Cu to Nb_3Sn?

What has been stated earlier indicates the thermodynamic-kinetic approach can be utilized to find answers to the above three questions.

With the aim to calculate the thermodynamic parameters to understand the diffusion process, the ternary phase diagram of the Cu-Nb-Sn system is calculated with the help of the assessed data from the references (Hämäläinen et al., 1990; Toffolon et al., 2002; Shim et al.,1996). In these calculations, all intermetallic compounds are modeled as binary compounds, since dissolution of ternary elements are found to be negligible based on the available information. In addition, no ternary compounds are known to exist in the Cu-Nb-Sn system. Isothermal section calculated at 700 °C is shown in Fig. 15. It is in general consistent with the very recent publication on the thermodynamic assesment of the Cu-Nb-Sn system (Li et al., 2009), except for two details. Firstly, in (Li et al., (2009) the Nb_6Sn_5 phase is stable already below 700 °C, different from our calculations and results of (Pan et al, 1980).

Secondly, there is also some ternary solubility to both Nb_3Sn and Nb_6Sn_5 in the diagram in (Li et al., 2009) contrary to our results and results by (Yamashina & Kajihara, 2006).

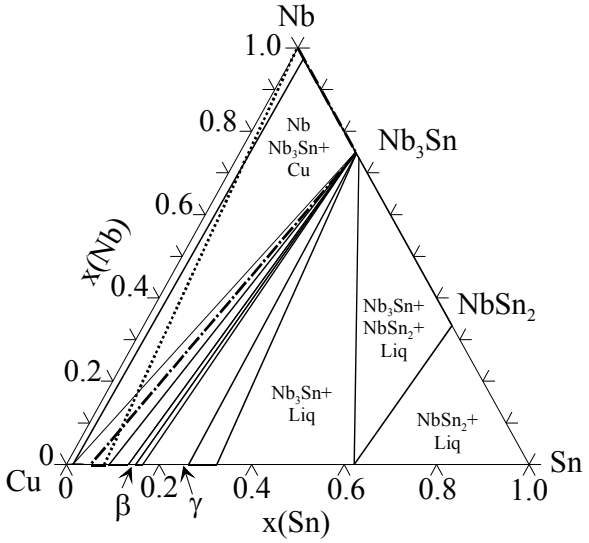

Fig. 15. Calculated Cu-Nb-Sn isothermal section at 700 °C. Dotted line is the contact-line (C.L.) between the end-members and the dashed-dotted line shows the diffusion path.

However, as the most relevant equilibrium to our analysis is the three-phase triangle Cu-Nb_3Sn-Nb, the occurrence of Nb_6Sn_5 phase that establishes equilibrium with the liquid phase, has no effect on the equilibria between Nb_3Sn and Cu, β or γ phases, even if it is stable already at 700 °C or below. Further, we have also induced ternary solubility to Nb_3Sn (up to 10 at.%) and it did not have any effect on the three-phase triangle of interest (Fig. 16) and did not markedly influence the values of chemical potentials of the species. Thus, from our analysis point of view these minor differences can be disregarded. With the same set of assessed thermodynamic data the values of driving forces for the diffusion (the difference in chemical potential between two moving interfaces, $\Delta\mu$ in the diffusion couple) of given species over Nb_3Sn layer at 700 °C, 750 °C and 775 °C, as a function of Sn content of 6, 7 and 8 at.% in Cu-Sn alloy were calculated. The results (interface I is Cu(Sn)/Nb_3Sn and interface II is Nb_3Sn/Nb) are tabulated in Table I. Following the data on driving force, it is clear that only the diffusion of Sn through the product layer is allowed from the thermodynamic point of view. If Nb or Cu would diffuse intrinsically they should move against their own activity gradient, which is not possible (van Loo, 1990). Now if we reconsider the possible atomic mechanism of diffusion, as discussed previously, the diffusion of Nb should be much easier than diffusion of Sn. However, from the thermodynamic point of view there is no possibility of diffusion of Nb (and Cu) in Nb_3Sn in Nb/Cu(Sn) diffusion couple, as there is no driving force. Thus, the only way for the product layer to grow is by diffusion of Sn. That is also the reason why the TiO_2 particles used as inert markers are found near the Cu(Sn)/Nb_3Sn interface. The fact that Sn must be the only *intrinsically* diffusing species in this reaction layer sequence, from the thermodynamic point of view, is evident also based on the isothermal section shown in Fig. 15, which shows also the diffusion path for the reaction

sequence under investigation. When we have a diffusion couple Cu(Sn)/Nb (the contact line connecting the end-members is drawn as dashed line) the diffusion path must proceed as drawn in Fig. 15. This is because of the requirement that the contact line between the end-members must be crossed at least once; as otherwise, the mass balance would not be fulfilled (van Loo, 1990). Thus, as can be seen from the figure, the diffusion path must always start from the Cu(Sn) end *towards* the Cu corner (i.e. towards higher activity of Cu) and then go to Nb_3Sn and finally to Nb. This also means that there should not be Cu inside Nb_3Sn, as in order to get there, it would have to move against its own activity gradient. Yamashina et al. (Yamashina & Kajihara, 2006) also calculated the activity diagram for Sn diffusion and concluded that the reaction product layer sequence can be produced by diffusion of Sn along its lowering activity, consistent with the present analysis. However, as they did not calculate the activity values for the other two component, they could not provide the reasons for the absence of movement of Nb and Cu.

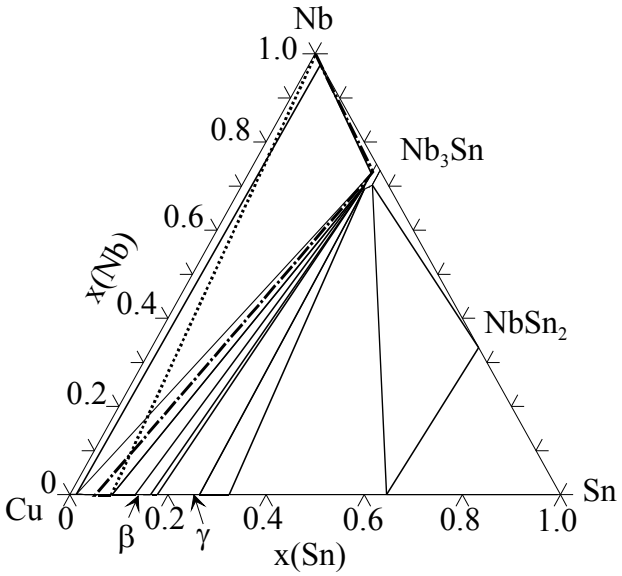

Fig. 16. Calculated Cu-Nb-Sn isothermal section at 700 °C, with 10 at-% Cu solubility induced to Nb_3Sn. Dotted line is the contact-line (C.L.) between the end-members and the dashed-dotted line shows the diffusion path.

Further from the experimental results, we have seen that there is considerable increase in the growth rate and decrease in activation energy just because of small increase in Sn content from 7 to 8 atomic percent in the Cu-Sn alloy. It does not look as surprising, when we consider the change in chemical potential between the two interfaces in the diffusion couple owing to the change in the Sn content. For example at 775 ^{o}C, the difference in the chemical potential of Sn changes from -14217 in Nb/(Cu-7at.%Sn) couple to -16008 J/mole in Nb/(Cu-8at.%Sn) at the same temperature. The change is around 12.5%. We can roughly consider that the flux of elements is linearly proportional to the driving force, if we neglect any other differences in the properties of the end members, which might be caused by the change in the Sn content. Thus we can estimate that the amount of Sn flux through the product layer (Nb_3Sn) will increase

approximately by 12.5%. Further, since one mole of Sn produces four moles of the product layer, we can expect that there will be at least 50% increase in the layer thickness because of the change in Sn content from 7 to 8 at.%. The results presented in the Fig. 14 are consistent with this calculation. So the increase in layer thickness because of such a small change in Sn content in the (Cu-Sn) alloy does not look surprising from the thermodynamic point of view. Since the change in driving force plays an important role in the activation energy, the considerable change in activation energy because of the change in Sn content is also rational. Consequently the high value of activation energy for the growth of Nb_3Sn is also acceptable, since it occurs by diffusion of Sn, which is dependent on the concentrations of antisite defects and vacancies present in the structure.

Temperature (°C)	Sn at.% in Cu(Sn) alloy	$\Delta\mu_{Sn}^{I\to II}$ (J/mol)	$\Delta\mu_{Cu}^{I\to II}$ (J/mol)	$\Delta\mu_{Nb}^{II\to I}$ (J/mol)
700	6	-15498	508	5634
	7	-17391	639	5765
	8	-19101	777	6336
750	6	-13464	487	4489
	7	-15402	621	5136
	8	-17150	762	5719
775	6	-12226	457	4076
	7	-14217	591	4740
	8	-16008	733	5338

Table I. The difference in chemical potential of elements between two different interfaces is listed.

6. Effect of alloying elements

There is always a demand to increase the critical temperatures, T_c, the critical current density, J_c, and the upper critical magnetics field, H_{c2}. It has been found that addition of alloying elements, such as, Ga, Ti, Ta, Zr, Hf etc. facilitates the use of the Nb_3Sn superconductor above 12 T (Sekine et a., 1979). The addition of around 3 at.% Ti to Nb increases the maximum critical current density measured at 20 T and at 1.8 as well as at 4.2 K. The addition of Ti in Nb is also found to increase the layer thickness of the product phase. Moreover, the Ti content of the Nb_3Sn is found to be more or less the same as the Ti content in the Nb alloy. Ta also has the same beneficial role and the maximum J_c was found with 4-5 at.%Ta in the Nb core (Suenaga et al. 1984). However, T_c decreases along alloying and with much faster rate because of Ti than Ta. Many times both Ti and Ta are added together to achieve maximum benefit (Flükiger et al., 2008). It was noticed that addition of Ga at the cost of Sn increases J_c, however, the growth rate of the product phase decreases (Dew-Hughes, 1977, Horigami et al., 1976, Sekine et al., 1979, Sekine et al. 1981). It is probable that because of the decrease of Sn content in the alloy, the activity of Sn is lowered, accordingly the driving force for the diffusion through the Nb_3Sn layer is diminished and thus the growth rate is decreased. It was also noticed that the addition of Hf and Zr in the Nb core increases both J_c and the growth rate of Nb_3Sn (Sekine et al., 1979, Sekine et al. 1981).

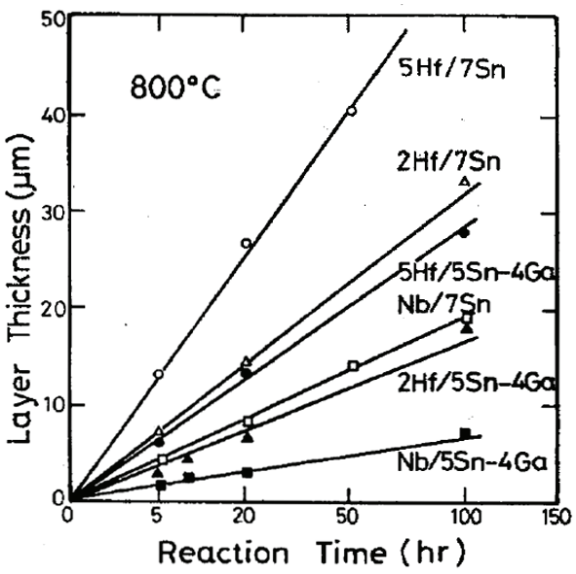

Fig. 17. The increase in layer thickness with the increase in annealing time at 800 °C with different Nb core and matrix Cu(Sn) bronze alloy is shown. Zr and Hf are added to the core and Ga is added to the matrix. 5Hf/7Sn means Nb-5at.%Hf/Cu-7at.%Sn (Sekine et al., 1981).

Sekine et al., 1981 and Takeuchi et al., 1981 studied the effect of addition of Ti, Zr and Hf in the Nb core and Ga in the Cu(Sn) matrix. The results reported in (Sekine et al., 1981) are shown in Fig. 17. It can be seen clearly that Ga addition at the cost of some Sn content decreases the growth rate of the product phase, although the content of (Sn+Ga) is higher than the Sn content of the bronze alloy without Ga. On the other hand, the addition of Hf increases the growth rate of the product phase drastically. The examination on grain structure revealed grain coarsening because of addition of Ga. On the other hand there was hardly any difference in the average grain size because of addition of Hf. Takeuchi et al., (Takeuchi et al., 1981), published a paper with similar studies and examined the effect of Ga content in the Cu(Sn) bronze alloy and Ti, Zr and Hf in the Nb core. They noticed that the addition of Zr and Hf beyond 10 and 5 at.%, respectively, created difficulties in workability to draw the material as a thin wire. The growth of the product phase with all investigated compositions was found to be parabolic with time, at least during the initial stage. Like in (Sekine et al., 1981; Takeuchi et al., 1981) they also found that there is a decrease in the growth rate because of Ga addition. However, the layer thickness increased considerably when Ti, Zr and Hf were added to the Nb core, as shown in Fig. 18. Composition analysis indicates that the Ti content in the Nb_3Sn phase was higher than that of the other elements. A Ga-rich phase was found to appear when Ga content was increased to 9 at.%. Likewise a Zr content of more than 5 at.% produced precipitates of Zr rich phase inside the Nb_3Sn phase. Close examination of the grain structure indicated the presence of finer grains because of addition of Ti, Zr and Hf. The grain structure did not change much with the increase of the alloying element content beyond 2 at.%. Ga addition, on the other hand, causes significant grain coarsening, as seen also in (Sekine et al., 1981 and Takeuchi et al., 1981).

Tachikawa et al. (1991) studied the effect of addition of Ge in the bronze alloy. They considered pure Nb and alloyed with Ta, Ti and Hf core. They found significant increase in the critical current density because of Ge addition. Grain refinement could be the reason to increase in J_c, however, the change in layer thickness because of addition of Ge is not reported.

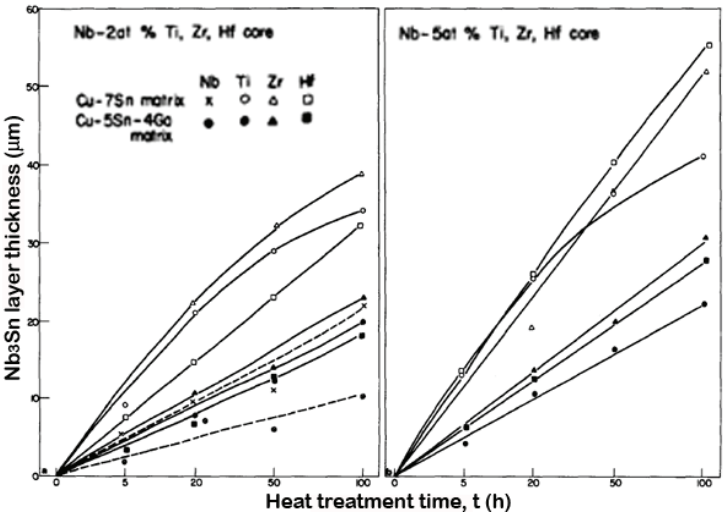

Fig. 18. The increase in layer thickness with the increase in annealing time at 800 °C is shown. (a) Nb-2at.%Ti, Zr and Hf core (b) Nb-5at.%Ti, Zr and Hf core (Takeuchi et al., 1981).

7. Conclusive remarks

It is clear from the results reported in various articles that it is very difficult to draw any definite conclusion about the growth and diffusion mechanism in Nb_3Sn based on the results available in the literature. It was found that the growth exponent is typically close to 0.5, when Sn content in the bronze alloy is relatively high. With the decrease in Sn content growth exponent deviates from this and this indicates that some other factors become important. Kirkendall marker experiments conducted by Kumar and Paul (2009) clearly indicated that Sn is almost the only mobile species. Further, very minor amount of Cu (Suenaga and Jansen, 1983) was found in the Nb_3Sn product phase and no Sn was found in Nb. Although thermodynamic analysis explains that there is no driving force for Cu to diffuse through the product layer, the trace amount of Cu was in mainly in grain boundaries (Suenaga and Jansen, 1983). There is always a chance that some amount could be added as impurity. It is quite possible that when Sn content is high in the Cu(Sn) bronze alloy, the process is controlled by the diffusion of Sn through the Nb_3Sn. At the later stage of the annealing or when the Sn content is initially low, the diffusion process may become much complicated because of lack of availability of Sn. Then the growth exponent could increase as was found in (Reddi et al., 1983).

Farrel et al. (1974 & 1975) argued that the growth of the Nb_3Sn phase mainly occurs because of grain boundary diffusion and developed a model to explain the diffusion process. They developed this model based on the growth exponent they calculated, which was found to

0.35 and the activation energy for growth, which was found to be 51.9 kJ/mol. However other researchers (Larbalestier et al. 1975; Reddi et al., 1983; Kumar & Paul, 2009) found much higher activation energy values (above 200 kJ/mol). It is in fact very difficult to find the exact diffusion mechanism from this kind of experiments. What we actually measure, is the apparent diffusion coefficient, which is a kind of average from the contribution from lattice and grain boundary diffusion. Nevertheless, the relatively high activation energy clearly indicates that there must be significant contribution from lattice diffusion. This might be the reason that even though Takeuchi et al. 1981 found that after addition of Ti, Zr and Hf beyond a certain limit did not change the grain morphology, however, there was significant increase in the growth rate. There might be significant increase in the driving force for diffusion with the increase in alloy content and there could also be increase in defect concentration (vacancies and antisites). However, further understanding is lacking because of unavailability of these information at the present. Further dedicated study is required to develop better understanding especially the effect of alloy additions on the growth of the product phase.

8. References

Adda, Y. and Philibert, J. (1981). *Atom movements and mass transport in solids*. Les Ulis: Les Éditions de Physique, 1991.

Ansara I.(1990). Thermodynamic modelling of solution phases and phase diagram calculations, *Pure Applied Chemistry*, **62**, (1990), 71-78.

Bakker H., *Diffusion in Solids: Recent developments*, edited by Dayananda MA and Murch GE. The Metallurgical society publication, Warrendale, PA (1985) 39-63.

Besson, R., Guyot, S. & Legris, A., Atomic scale study of diffusion in A15 Nb_3Sn. (2007) *Physical Review B* Vol. 75 (2007) 0541051- 0541057

Dew-Hughes, D. (1977) Effect of third element additions on the properties of bronze processed Nb_3Sn. *IEEE Transactions on Magnetics* Vol. 13 (1977) 651-654.

d'Heurle, FM., and Gas, P., (1986). Kinetics of formation of silicides: A review. *Journal Materials Research* Vol. 1 (1986) 205-221

Dinsdale A.T. (1991). SGTE data for pure elements, *Calphad*, **15,** (1991), 317-425.

Easton, DS. & Kroeger, DM. (1979). Kirkendall voids-A detriment to Nb_3Sn superconductors. *IEEE Transactions on Magnetics* Vol. 15 (1979) 178-181

Farrel, HH., Gilmer, GH. & Suenaga M. (1974) Grain boundary diffusion and growth of intermetallic layers:Nb_3Sn. *Journal of Applied Physics* Vol. 45 (1974) 4025-4035.

Farrel, HH., Gilmer, GH. & Suenaga M. (1975) Diffusion mechanisms for the growth of Nb_3Sn intermetallic layers. *Thin Solid Films* Vol. 25 (1975) 253-264.

Flükiger, R., Uglietti, D., Senatore, C. & Buta, F. (2008) Microstructure, composition and critical current density of superconducting Nb3Sn wires. *Cryogenics* Vol. 48 (2008) 293-307.

Hämäläinen M., Jaaskelainen K., Luoma R., Nuotio M., Taskinen P., and Teppo O, (1990). A thermodynamic analysis of the binary alloy systems Cu-Cr, Cu-Nb and Cu-V, *Calphad*, Vol. 14 (1990) 125-137.

Harrison, LG. (1961). Influence of dislocations on diffusion kinetics in solids with particular reference to the alkali halides *Transaction of Faraday Society* Vol. 57 (1961) 1191-1199.

Hayase, T. & Kajihara, M. (2006). Kinetics of reactive diffusion between Cu-8.1Sn-0.3Ti alloy and Nb. *Materials Science and Engineering A*, Vol. 433 (2006) 83-89.

Hillert M. (1998). *Phase Equilibria, Phase Diagrams and Phase Transformations : Their Thermodynamic Basis*, Cambridge Univ. Press, (1998).

Horigami, O., Luhman, T., Pande, CS. & Suenaga, M. (1976) Superconducting properties of $Nb_3(Sn_{1-x}Ga_x)$ by a solid-state diffusion process. *Applied Physics Letters* Vol. 28 (1976) 738-740.

Kaufman L. and Bernstein H. (1970). *Computer Calculation of Phase Diagrams*, Academic Press, New York, (1970).

Kumar, AK. & Paul, A. (2009) Interdiffusion and growth of the superconductor Nb_3Sn in Nb/Cu(Sn) diffusion couples. *Journal of Electronic Materials* Vol. 38 (2009) 700-705.

Kumar, AK., Laurila T., Vuorinen, V. and Paul, A. (2009). Determination of diffusion parameters and activation energy of diffusion in V_3Si phase with A15 crystal structure. *Scripta Materialia* vol. 60 (2009) 377-380.

Larbalestier, DC., Madsen, PE., Lee, JA., Wilson, MN., & Charlesworth, JP. (1975) Multifilamentary niobium tin magnet conductors. *IEEE Transactions on Magnetics* Vol. 11 (1975) 247-250.

Laurila, T., Vuorinen, V., Kumar, AK. & Paul A. (2010). Diffusion and growth mechanism of Nb_3Sn superconductor grown by bronze technique, *Applied Physics Letters* Vol. 96 (2010) 231910

Laurila T., Vuorinen V., and Kivilahti J.K. (2004). Analyses of interfacial reactions at different levels of interconnection, *Materials Science in Semicond. Processing* Vol. **7** (2004), 307-317.

Lee, PJ. & Larbalestier DC. (2001). Compositional and microstructural profiles across Nb3Sn filaments produced by different fabrication methods. *IEEE Transactions on Applied Superconductivity*. Vol. 11 (2001) 3671-3674.

Lee, PJ. & Larbalestier DC. (2005) Microstructure, microchemistry and the development of very high Nb_3Sn layer critical current density. *IEEE Transaction of Applied Superconductivity* Vol. 15 (2005) 3474-3477.

Lee, PJ. & Larbalestier DC. (2008). Microstructural factors important for the development of high critical current density Nb3Sn strand. *Cryogenics* Vol. 48 (2008) 283-292.

Li M., Du Z., Guo G. and Li C., (2009). Thermodynamic Optimization of the Cu-Sn and Cu-Nb-Sn Systems, *Journal Alloys Compounds* Vol. 477 (2009) 104-117.

Lukas H., Fries S., and Sundman B. (2007). Computational Thermodynamics- The Calphad Method, *Cambridge University Press* (2007).

Müller, H. & Schneider Th. (2008). Heat treatment of Nb_3Sn conductors. *Cryogenics* Vol. 48 (2008) 323-330.

Muranishi, Y. & Kajihara, M. (2005) Growth behavior of Nb3Sn layer during reactive diffusion between Cu-8.3Sn alloy and Nb. *Materials Science and Engineering A* Vol. 404 (2005) 33-41.

Pan V., Latysheva V., Litvinenko Y., Flis V. and Gorskiy V., (1980). The Phase Equilibria and Superconducting Properties of Niobium-Tin-Copper Alloys, The Physics of Metals and Metallography Vol. 49 (1980) 199-202.

Reddi, BV., Raghavan, V., Ray, S. & Narlikar, AV. (1983) Growth kinetics of monofilamentary Nb_3Sn and V_3Ga synthesized by solid-state diffusion. *Journal of Materials Science* Vol. 18 (1983) 1165-1173.

Saunders N. and. Miodownik A.P., (1998). CALPHAD, *Calculation of Phase Diagrams*, Pergammon Materials Series, Elsevier Science, (1998).

Sekine, H., Tachikawa, K. & Iwasa, Y. (1979). Improvements of current-carrying capacities of the composite-processed Nb_3Sn in high magnetic fields. *Applied Physics Letters* Vol. 35 (1979) 472-473.

Sekine, H., Takeuchi, T. and Tachikawa, K. (1981) Studies on the composite processed Nb-Hf/Cu-Sn-Ga high-field superconductors. *IEEE Transactions on Magnetics* Vol. 17 (1981) 383-386.

Sharma, RG. (1987). Review on the fabrication techniques of A-15 superconductors. *Cryogenics*, Vol. 27 (1987) 361-377

Shim J.H., Oh C.S., Lee B.J., Lee D.N., (1996). Thermodynamic Assessment of the Cu-Sn System, *Z Metallkunde* Vol. 87 (1996) 205-212.

Suenaga M. & Jansen W. (1983) Chemical compositions at and near the grain boundaries in bronze processed superconducting Nb_3Sn. *Applied Physics Letters* Vol. 43 (1983) 791-793.

Suenaga, M. & Jansen, W. (1983). Chemical compositions at and near the grain boundaries in bronze processed superconducting Nb3Sn. *Applied Physics Letters* Vol. 43 (1983) 791-793.

Suenaga, M. (1981) *Superconductor Materials Science: Metallurgy Fabrication and Applications*, Edited by Foner S. & Schwartz BB. Plenum, New York (1981) pp. 201

Suenaga, M., Tsuchiya, K. & Higuchi, N. (1984). Superconducting critical current density of bronze processed pure and alloyed Nb3Sn at very high magnetic fields (up to 24 T). *Applied Physics Letters* Vol. 44 (1984) 919-921.

Suenaga, M., Welch, D.O., Sabatini, RL., Kammere, OF. & Okuda, S. (1986). Superconducting critical temperatures, critical magnetic fields, lattice parameters and chemical compositions of "bulk" pure and alloyed Nb_3Sn produced by bronze process. *Journal of Applied Physics*, Vol. 59 (1986) 840-853.

Tachikawa, T., Terada, M., Endo, M. & Miyamoto, Y. (1992). Bronze processed Nb_3Sn with addition of Germanium to matrix. *Cryogenics* Vol. 33 (1993) 205-208.

Takeuchi, T., Asano, T., Iijima, Y. & Tachikawa, K. (1981). Effects of the IVa element addition on the composite-processed superconducting Nb_3Sn. *Cryogenics* Vol. 21 (1981) 585-589.

Toffolon C., Servant C., Gachon J. C., and Sundman B., (2002). Reassessment of the Nb-Sn system *Journal of Phase Equilibria*, 23, (2002) 134-139.

Van Loo, FJJ. (1990). Multiphase difusion in binary and ternary solid state systems. *Progress in Solid State Chemistry* Vol. 20, (1990) 47-99

Yamashina T. and Kajihara M., (2006). Quantitative Explanation for Uphill Diffusion of Sn During Reactive Diffusion Between Cu-Sn Alloys and Nb, *Materials Transaction* Vol. 47 (2006), 829-837.

4

Superconductor Properties for Silicon Nanostructures

Nikolay T. Bagraev[1], Leonid E. Klyachkin[1], Andrey A. Koudryavtsev[1], Anna M. Malyarenko[1] and Vladimir V. Romanov[2]
[1]Ioffe Physical-Technical Institute RAS, St.Petersburg, 194021,
[2]St.Petersburg State Polytechnical University, St.Petersburg, 195251,
[1,2]Russia

1. Introduction

Semiconductor silicon is well known to be the principal material for micro - and nanoelectronics. Specifically, the developments of the silicon planar technology are a basis of the metal-oxygen-silicon (MOS) structures and silicon-germanium (Si-Ge) heterojunctions that are successfully used as elements of modern processors (Macilwain, 2005). Just the same goals of future high frequency processors especially to resolve the problem of quantum computing are proposed to need the application of the superconductor nanostructures that represent the Josephson junction series (Nakamura & Tsai, 2000). Therefore the manufacture of superconductor device structures within frameworks of the silicon planar technology seems to give rise to new generations in nanoelectronics. Furthermore, one of the best candidate on the role of the superconductor silicon nanostructure appears to be the high mobility silicon quantum wells (Si-QW) of the p-type confined by the δ-barriers heavily doped with boron on the n-type Si (100) surface which exhibit the properties of high temperature superconductors (Bagraev et al., 2006a). Besides, the heavily boron doping has been found to assist also the superconductivity in diamond (Ekimov et al., 2004). Here we present the findings of the electrical resistance, thermo-emf, specific heat and magnetic susceptibility measurements that are actually evidence of the superconductor properties for the δ-barriers heavily doped with boron which appear to result from the transfer of the small hole bipolarons through the negative-U dipole centres of boron at the Si-QW – δ-barrier interfaces. These 'sandwich' structures, S-Si-QW-S, are shown to be type II high temperature superconductors (HTS) with characteristics dependent on the sheet density of holes in the p-type Si-QW. The transfer of the small hole bipolarons appears to be revealed also in the studies of the proximity effect that is caused by the interplay of the multiple Andreev reflection (MAR) processes and the quantization of the supercurrent.

2. Sample preparation and analysis

The preparation of oxide overlayers on silicon monocrystalline surfaces is known to be favourable to the generation of the excess fluxes of self-interstitials and vacancies that exhibit the predominant crystallographic orientation along a <111> and <100> axis, respectively (Fig. 1a) (Bagraev et al., 2002; 2004a; 2004b; 2005). In the initial stage of the oxidation, thin oxide

overlayer produces excess self-interstitials that are able to create small microdefects, whereas oppositely directed fluxes of vacancies give rise to their annihilation (Figs. 1a and 1b). Since the points of outgoing self-interstitials and incoming vacancies appear to be defined by the positive and negative charge states of the reconstructed silicon dangling bond (Bagraev et al., 2004a; Robertson, 1983), the dimensions of small microdefects of the self-interstitials type near the Si (100) surface have to be restricted to 2 nm. Therefore, the distribution of the microdefects created at the initial stage of the oxidation seems to represent the fractal of the Sierpinski Gasket type with the built-in self-assembled Si-QW (Fig. 1b) (Bagraev et al., 2004a; 2004b; 2005). Then, the fractal distribution has to be reproduced by increasing the time of the oxidation process, with the P_b centers as the germs for the next generation of the microdefects (Fig. 1c) (Robertson, 1983; Gerardi et al., 1986). The formation of thick oxide overlayer under prolonged oxidation results in however the predominant generation of vacancies by the oxidized surface, and thus, in increased decay of these microdefects, which is accompanied by the self-assembly of the lateral silicon quantum wells (Fig. 1d).

Although Si-QWs embedded in the fractal system of self-assembled microdefects are of interest to be used as a basis of optically and electrically active microcavities in optoelectronics and nanoelectronics, the presence of dangling bonds at the interfaces prevents such an application. Therefore, subsequent short-time diffusion of boron would be appropriate for the passivation of silicon vacancies that create the dangling bonds during previous oxidation of the Si (100) surface thereby assisting the transformation of the arrays of microdefects in the neutral δ - barriers confining the ultra-narrow, 2nm, Si-QW (Figs. 1e, f and g).

We have prepared the p-type self-assembled Si-QWs with different density of holes ($10^9 \div 10^{12}$ cm^{-2}) on the Si (100) wafers of the n-type within frameworks of the conception discussed above and identified the properties of the two-dimensional high mobility gas of holes by the cyclotron resonance (CR), electron spin resonance (ESR), scanning tunneling spectroscopy (STM) and infrared Fourier spectroscopy techniques.

Firstly, the 0.35 mm thick n- type Si (100) wafers with resistivity 20 Ohm·cm were previously oxidized at 1150°C in dry oxygen containing CCl_4 vapors. The thickness of the oxide overlayer is dependent on the duration of the oxidation process that was varied from 20 min up to 24 hours. Then, the Hall geometry windows were cut in the oxide overlayer after preparing a mask and performing the subsequent photolithography. Secondly, the short-time diffusion of boron was done into windows from gas phase during five minutes at the diffusion temperature of 900°C. Additional replenishment with dry oxygen and the Cl levels into the gas phase during the diffusion process provided the fine surface injection of self-interstitials and vacancies to result in parity of the kick-out and vacancy-related diffusion mechanism. The variable parameters of the diffusion experiment were the oxide overlayer thickness and the Cl levels in the gas phase during the diffusion process (Bagraev et al., 2004a). The SIMS measurements were performed to define the concentration of boron, $5 \cdot 10^{21}$ cm^{-3}, inside the boron doped diffusion profile and its depth that was equal to 8 nm in the presence of thin oxide overlayer. The Si-QWs confined by the δ - barriers heavily doped with boron inside the B doped diffusion profile were identified by the four-point probe method using layer-by-layer etching and by the cyclotron resonance (CR) angular dependencies (Figs. 2a and b).

These CR measurements were performed at 3.8 K with a standard Brucker-Physik AG ESR spectrometer at X-band (9.1-9.5 GHz) (Bagraev et al., 1995; Gehlhoff et al., 1995). The rotation of the magnetic field in a plane normal to the diffusion profile plane has revealed the anisotropy of both the electron and hole effective masses in silicon bulk and Landau levels

scheme in Si-QWs. This CR quenching and the line shifts for which a characteristic 180° symmetry was observed can be explained with the effect of the electrical field created by the confining potential inside p^+-diffusion profile and its different arrangement in longitudinal and lateral Si-QWs formed naturally between the δ - barriers heavily doped with boron (Figs. 2a and b). The observed different behavior of the heavy and light holes may be explained by lifting the degeneracy between the $J_z = \pm 3/2$ and $J_z = \pm 1/2$ valence bands for $k = 0$ due to the confining potential.

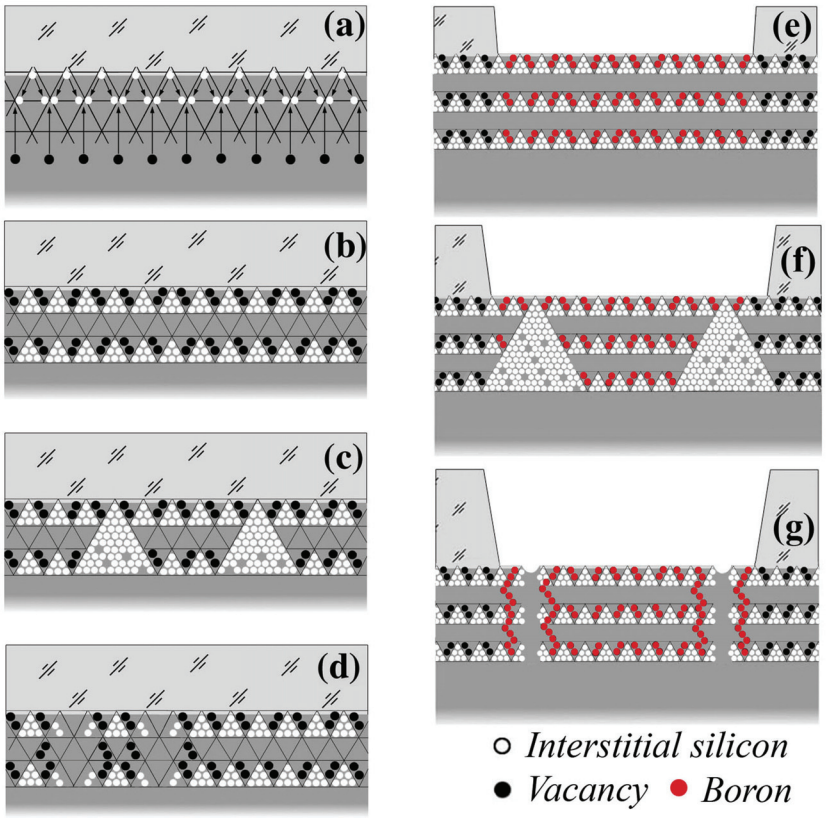

Fig. 1. A scheme of self-assembled silicon quantum wells (Si-QWs) obtained by varying the thickness of the oxide overlayer prepared on the Si (100) wafer. The white and black balls label the self-interstitials and vacancies forming the excess fluxes oriented crystallographically along a <111> and <100> axis that are transformed to small microdefects (a, b). The longitudinal Si-QWs between the alloys of microdefects are produced by performing thin oxide overlayer (b), whereas growing thick oxide overlayer results in the formation of additional lateral Si-QWs (d). Besides, medium and thick oxide overlayers give rise to the self-assembled microdefects of the fractal type (c). The atoms of boron replace the positions of vacancies in the process of subsequent short-time diffusion after making a mask and etching thereby passivating the alloys of microdefects and forming the neutral δ barriers that confine both the longitudinal (e, f) and lateral (g) Si-QWs.

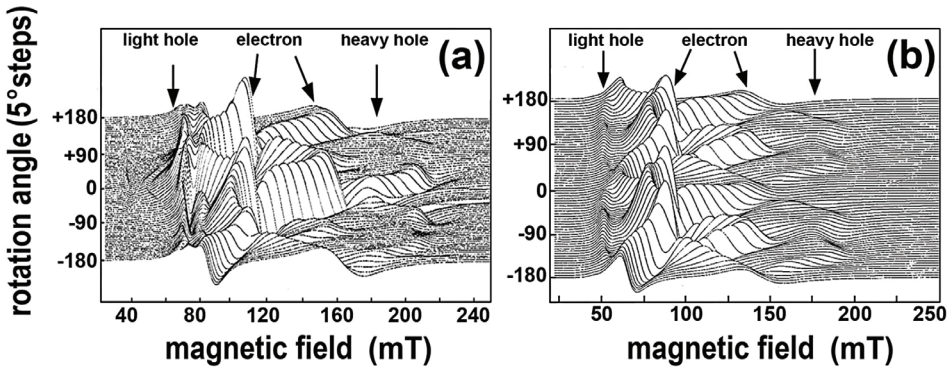

Fig. 2. Cyclotron resonance spectra for the ultra-shallow boron diffusion profiles obtained on the n - type silicon {100} surfaces at the diffusion temperatures of 900°C (*a*) and 1100°C (*b*) which consist of the δ - barriers confining the longitudinal (a) and lateral (b) Si-QW. Rotation of magnetic field *B* in a {110}-plane perpendicular to a {100}-surface of profiles (0° = $B \perp$ surface; ± 90° = $B \parallel$ surface), T= 3.8 K, ν = 9.45 GHz.

The energy positions of two-dimensional subbands for the light and heavy holes in the Si-QW studied were determined by studying the far-infrared electroluminescence spectra obtained with the infrared Fourier spectrometer IFS-115 Brucker Physik AG (Fig. 3a) as well as by measuring the high resolved CV characteristics (Fig. 4) (Bagraev et al., 2006a; 2007). The results obtained are in a good agreement with corresponding calculations following by Ref (Kotthaus & Ranvaud, 1977) if the width of the Si-QW, 2nm, is taken into account (Fig. 3b).

The STM technique was used to control the formation of the fractal distribution of the self-interstitials microdefects in the windows before and after diffusion of boron (Fig. 5a). The self-assembled layers of microdefects inside the δ - barriers that confine the Si-QW appear to be revealed by the STM method as the deformed potential fluctuations (DPF) after etching the oxide overlayer and after subsequent short-time diffusion of boron. The DPF effect induced by the microdefects of the self-interstitials type that are displayed as light poles in Fig. 4a is find to be brought about by the previous oxidation and to be enhanced by subsequent boron diffusion (Bagraev et al., 2000; 2004a). The STM images demonstrate that the ratio between the dimensions of the microdefects produced during the different stages of the oxidation process is supported to be equal to 3.3 thereby defining the self-assembly of microdefects as the self-organization of the fractal type (Figs. 5b and 1f). The analysis of the STM image in detail has shown that the dimension of the smallest microdefect observed in fractal series, ~2nm, is consistent with the parameters expected from the tetrahedral model of the Si_{60} cluster (Fig. 5c) (Bao-xing Li et al. 2000).

Thus, the δ - barriers, 3 nm, heavily doped with boron, 5 10^{21} cm^{-3}, represent really alternating arrays of the smallest undoped microdefects and doped dots with dimensions restricted to 2 nm (Fig. 5c). The value of the boron concentration determined by the SIMS method seems to indicate that each doped dot located between undoped microdefects contains two impurity atoms of boron. Since the boron dopants form shallow acceptor centers in the silicon lattice, such high concentration has to cause a metallic-like conductivity. Nevertheless, the angular dependencies of the cyclotron resonance spectra demonstrate that the p-type Si-QW confined by the δ - barriers heavily doped with boron

contains the high mobility 2D hole gas which is characterized by long momentum relaxation time of heavy and light holes at 3.8 K, $\tau \geq 5 \cdot 10^{-10}$ s (Figs. 2a and b) (Bagraev et al., 1995; Gehlhoff et al., 1995; Bagraev et al., 2005). Thus, the momentum relaxation time of holes in the ultra-narrow Si-QW appeared to be longer than in the best MOS structures contrary to what might be expected from strong scattering by the heavily doped δ - barriers. This passive role of the δ - barriers between which the Si-QW is formed was quite surprising, when one takes into account the high level of their boron doping. To eliminate this contradiction, the ESR technique has been applied for the studies of the boron centers packed up in dots (Bagraev et al., 2002; 2005).

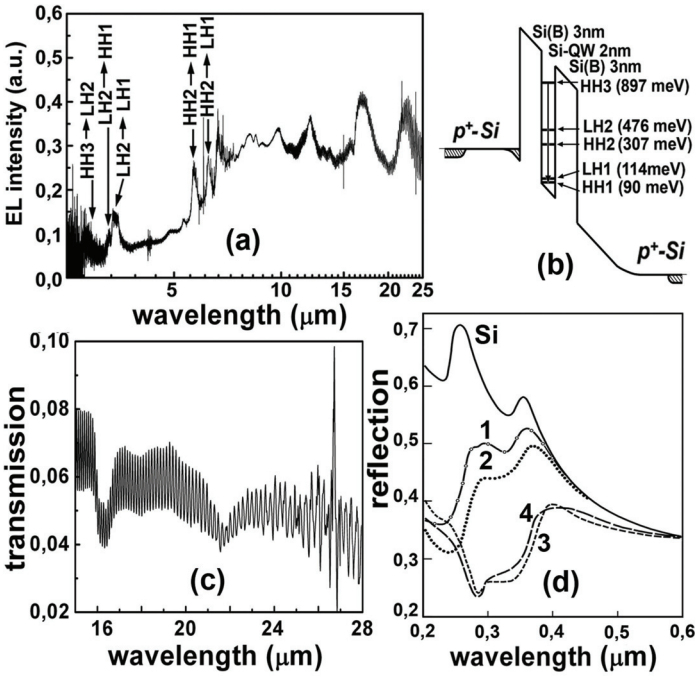

Fig. 3. Electroluminescence spectrum (a) that defines the energies of two-dimensional subbands of heavy and light holes in the p-type Si-QW confined by the δ - barriers heavily doped with boron on the n-type Si (100) surface (b). T=300K. (c) Transmission spectrum that reveals both the local phonon mode, λ = 16.4 μm, and the superconductor gap, λ = 26.9 μm, manifestation. (d) The reflection spectra from the n - type Si (100) surface and from the ultra-shallow boron diffusion profiles prepared on the n - type Si (100) surface that consist of the δ - barriers confining the ultra-narrow Si-QW. The curves 1-4 are related to the δ - barriers with different concentration of boron. The values of the concentration boron in different samples are characterized by the following ratio: curve 1 – 0.2, 2 – 0.3, 3 – 0.35, 4 -0.4. The concentration of boron in the sample characterized by the fourth curve is equal to $5 \cdot 10^{21}$ cm^{-3}. T=300K.

The angular dependences of the ESR spectra at different temperatures in the range 3.8÷27 K that reveal the trigonal symmetry of the boron dipole centers have been obtained with the same ESR spectrometer, the Brucker-Physik AG ESR spectrometer at X-band (9.1-9.5 GHz),

with the rotation of the magnetic field in the {110}-plane perpendicular to a {100}-interface (B_{ext} = 0°, 180° parallel to the Si-QW plane, B_{ext} = 90° perpendicular to the Si-QW plane) (Figs. 6a, b, c and d). No ESR signals in the X-band are observed, if the Si-QW confined by the δ - barriers is cooled down in the external magnetic field (B_{ext}) weaker than 0.22 T, with the persistence of the amplitude and the resonance field of the trigonal ESR spectrum as function of the crystallographic orientation and the magnetic field value during cooling down process at $B_{ext} \geq 0.22$ T (Figs. 6a, b and c). With increasing temperature, the ESR line observed changes its magnetic resonance field position and disappears at 27 K (Fig. 6d).

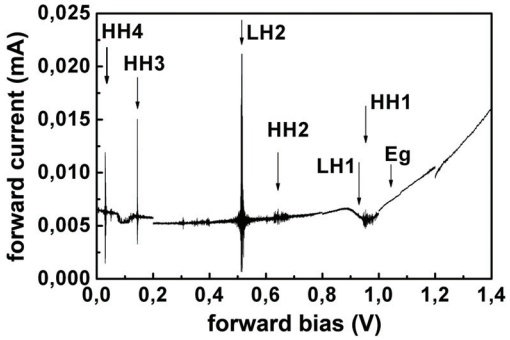

Fig. 4. The current-voltage characteristics under forward bias applied to the p-type Si-QW confined by the nanostructured δ-barriers heavily doped with boron on the n-type Si (100) surface. The energy position of each subband of 2D holes is revealed as a current peak under optimal tunneling conditions when it coincides with Fermi level. T=300K.

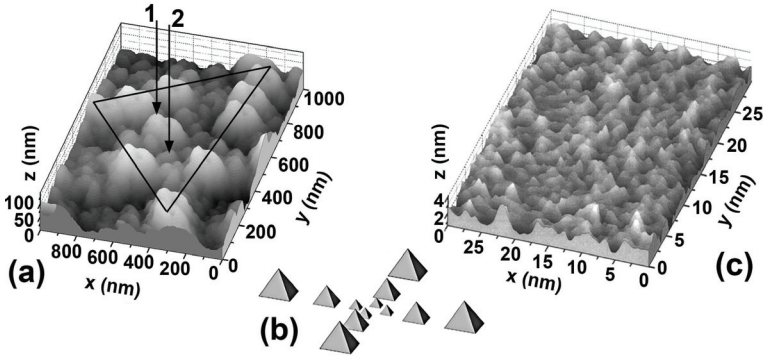

Fig. 5. (a) - STM image of the ultra-shallow boron diffusion profile prepared at the diffusion temperature of 800°C into the Si (100) wafer covered previously by medium oxide overlayer X||[001], Y||[010], Z||[100]. Solid triangle and arrows that are labeled as 1 and 2 exhibit the microdefects with dimensions 740 nm, 225 nm and 68 nm, respectively, which are evidence of their fractal self-assembly. (b) - The model of the self-assembled microcavity system formed by the microdefects of the fractal type on the Si (100) surface. (c) - STM image of the ultra-shallow boron diffusion profile prepared at diffusion temperature of 900°C into the Si (100) wafer covered previously by medium oxide overlayer. X||[001], Y||[010], Z||[100].

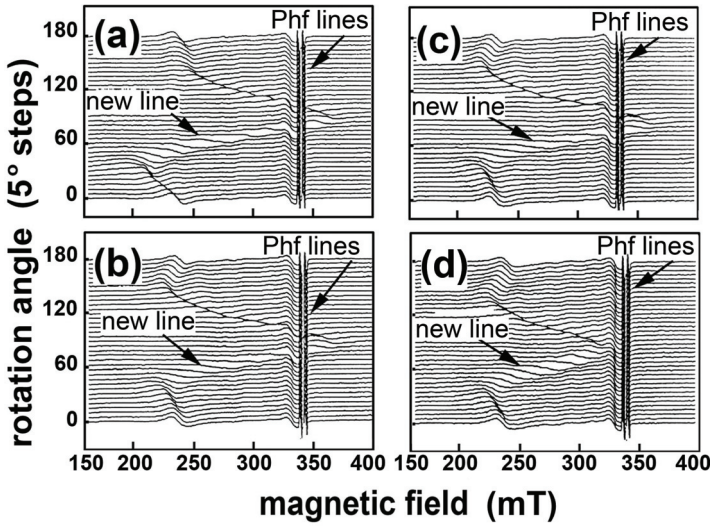

Fig. 6. The trigonal ESR spectrum observed in field cooled ultra-shallow boron diffusion profile that seems to be evidence of the dynamic magnetic moment due to the trigonal dipole centers of boron inside the δ - barriers confining the Si-QW which is persisted by varying both the temperature and magnetic field values. B_{ext} || <110> (a), || <112> (b), || <111> (c, d). Rotation of the magnetic field in the {110}-plane perpendicular to a {100}-interface (B_{ext} = 0°, 180° || interface, B_{ext} = 90° ⊥ interface), ν = 9.45 GHz, T = 14 K (a, b, c) and T=21 K (d).

The observation of the ESR spectrum is evidence of the fall in the electrical activity of shallow boron acceptors contrary to high level of boron doping. Therefore, the trigonal ESR spectrum observed seems to be evidence of the dynamic magnetic moment that is induced by the exchange interaction between the small hole bipolarons which are formed by the negative-U reconstruction of the shallow boron acceptors, $2B^0 \rightarrow B^+ + B^-$, along the <111> crystallographic axis (Fig. 7a) (Slaoui et al., 1983; Gehlhoff et al., 1995; Bagraev et al., 2002). These small hole bipolarons localized at the dipole boron centers, $B^+ - B^-$, seem to undergo the singlet-triplet transition in the process of the exchange interaction through the holes in the Si-QW thereby leading to the trigonal ESR spectrum (Figs. 6a, b, c and d). Besides, the sublattice of the hole bipolarons located between the undoped microdefects appears to define the one-electron band scheme of the δ - barriers as well as the transport properties for the 2D gas of holes in the Si-QW (Figs. 7b and 3b) (Bagraev et al., 2002).

In order to determine the one-electron band scheme of the δ - barriers that confine the Si-QW, the reflection spectra $R(\lambda)$ were studied using a UV-VIS Specord M-40 spectrophotometer with an Ulbricht sphere for the reflectivity measurements (Bagraev et al., 2000). Fig. 3d shows the spectra of the reflection from the δ - barriers with different concentration of boron. The decrease in $R(\lambda)$ compared with the data of the silicon single crystal and the drops in the position of the peaks at the wavelengths of λ=354 and 275 nm are observed. The above peaks are related to the transitions between Γ-L valleys and in the vicinity of the point X in the Brillouin zone, with the former of the above peaks being assigned to the direct transition $\Gamma'_{25} - \Gamma'_2$, whereas the latter peak is attributed to the transition $X_4 - X_1$ (Slaoui et al., 1983). An analysis of the spectral dependence of the

reflection coefficient shows that the presence of the microcavities formed by the self-assembled microdefects with medium size reduces $R(\lambda)$ most profoundly in the short-wavelength region of the spectrum (200-300 nm). It follows from the comparison of $R(\lambda)$ with the STM data that the position of the minima in the reflection coefficient in the spectral dependence $R(\lambda)$ and the microcavity size are interrelated and satisfy the Bragg condition, $x = \lambda/2n$, where x is the cavity size, λ is the wavelength, and n is the refractive index of silicon, n=3.4 (see Fig. 5a). The $R(\lambda)$ drop in the position of the Γ'_{25} - Γ'_2 and X_4 – X_1 transitions appears to be due to the formation of the wide-gap semiconductor layer with increasing the concentration of boron. These data substantiate the assumption noticed above that the role of the dot containing the small hole bipolaron is to establish the band structure of the δ - barrier with the energy confinement more than 1.25eV in both the conduction and the valence band of the Si-QW (Fig. 3d).

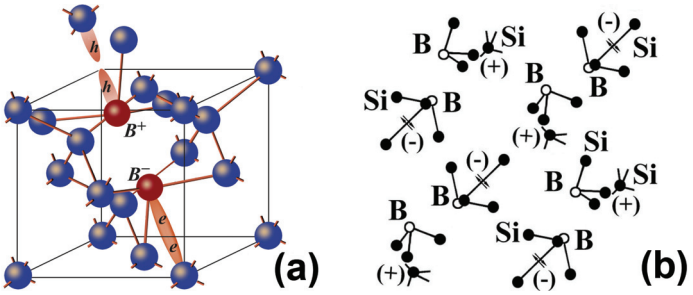

Fig. 7. (a) Model for the elastic reconstruction of a shallow boron acceptor which is accompanied by the formation of the trigonal dipole (B^+ - B^-) centers as a result of the negative-U reaction: $2B^o \rightarrow B^+ + B^-$. (b) A series of the dipole negative-U centers of boron located between the undoped microdefects that seem to be a basis of nanostructured δ - barriers confining the Si-QW.

3. Superconductor properties for δ – barriers heavily doped with boron

In common with the other solids that contain small onsite localized small bipolarons (Anderson, 1975; Watkins, 1984; Street et al., 1975; Kastner et al., 1976; Baraff et al., 1980; Bagraev & Mashkov, 1984; Bagraev & Mashkov, 1988**)**, the δ - barriers containing the dipole boron centres have been found to be in an excitonic insulator regime at the sheet density of holes in the Si-QW lower than 10^{15} m^{-2}. The conductance of these silicon nanostructures appeared to be determined by the parameters of the 2D gas of holes in the Si-QW (Bagraev et al. 2002; 2004b; 2006b). However, here we demonstrate using the electrical resistance, thermo-emf, specific heat magnetic susceptibility and local tunnelling spectroscopy techniques that the high sheet density of holes in the Si-QW (>10^{15} m^{-2}) gives rise to the superconductor properties for the δ - barriers which result from the transfer of the small hole bipolarons through the negative-U centers (Šimánek, 1979; Ting et al., 1980; Alexandrov & Ranninger, 1981; Chakraverty, 1981; Alexandrov & Mott, 1994) in the interplay with the multiple Andreev reflections inside the Si-QW (Andreev, 1964; Klapwijk, 2004; van Dam et al., 2006; Jarillo-Herrero et al., 2006; Jie Xiang et al., 2006).

The resistance, thermo-emf and Hall measurements of the device with high density of 2D holes, $6 \cdot 10^{15}$ m^{-2}, performed within Hall geometry were made in Special Design Electric and

Magnetic Measurement System with high precision bridge (Fig. 8a). The identical device was used in the studies of the local tunneling spectroscopy with the STM spectrometer to register the tunneling current as a function of the voltage applied between the STM tip and the Hall contacts (Fig. 8b). The measurements in the range 0.4-4 K and 1.2-300 K were carried out respectively in a He^3 and He^4 cryostat.

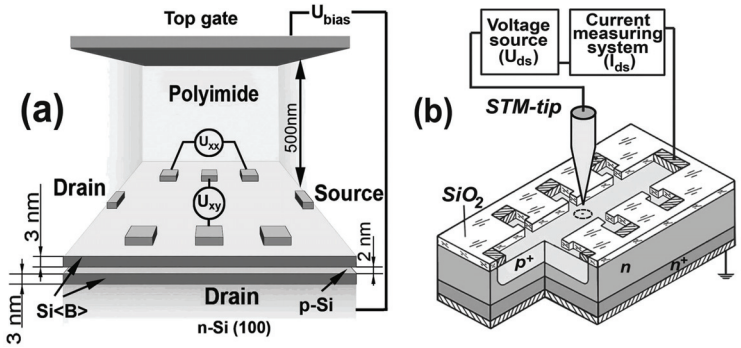

Fig. 8. (a) Schematic diagram of the devices that demonstrates a perspective view of the p-type Si-QW confined by the δ - barriers heavily doped with boron on the n-type Si (100) surface. The top gate is able to control the sheet density of holes and the Rashba SOI value. The depletion regions indicate the Hall geometry of leads. (b) Planar field-effect silicon transistor structure with the STM tip, which is based on an ultra-shallow p^+-diffusion profile prepared in the Hall geometry. The circle dashed line exhibits the point STM contact region.

The current-voltage characteristics (CV) measured at different temperatures exhibited an ohmic character, whereas the temperature dependence of the resistance of the device is related to two-dimensional metal only in the range 220-300 K (Fig. 9a). Below 220 K the resistance increases up to the value of 6.453 kOhm and then drops reaching the negligible value at the temperature of 145 K. The creation of the additional peak when the resistance begins to fall down seems to be evidence of the superconductor properties caused by the transfer of the small hole bipolarons. This peak shows the logarithmic temperature dependence that appears to be due to the Kondo-liked scattering of the single 2D holes tunneling through the negative-U boron dipole centres of boron at the Si-QW – δ-barrier interfaces.

As was to be expected, the application of external magnetic field results in the shift of the resistance drop to lower temperatures, which is accompanied by the weak broadening of the transition and the conservation of the peak values of the resistance (Fig. 9a). Since similar peaks followed by the drops of the Seebeck coefficient value are revealed also in the temperature dependences of the thermo-emf (Fig. 9b), the Kondo-liked scattering seems to be the precursor of the optimal tunneling of single holes into the negative-U boron centers of boron (Trovarelli et al., 1997). This process is related to the conduction electron tunneling into the negative-U centers that is favourable to the increase of the superconducting transition temperature, T_c, in metal-silicon eutectic alloys (Šimánek, 1979; Ting et al., 1980). The effect of single-hole tunneling is also possible to resolve some bottlenecks in the bipolaronic mechanism of the high temperature superconductivity, which results from the distance between the negative-U centers lesser than the coherence length (Alexandrov &

Ranninger, 1981; Alexandrov & Mott, 1994). Besides, two experimental facts are needed to be noticed. Firstly, the maximum value of the resistance, 6.453 kOhm ≈ $h/4e^2$, is independent of the external magnetic field. Secondly, applying a magnetic field is surprised to stabilize the δ-barrier in the state of the two-dimensional metal up to the temperature value corresponding to the shift of a transition to lower temperatures (Fig. 9a). Thus, the δ-barriers confining Si-QW seem to be self-organized as graphene (Geim & Novoselov, 2007) owing to heavily doping with boron which gives rise to the formation of the negative-U dipole centers.

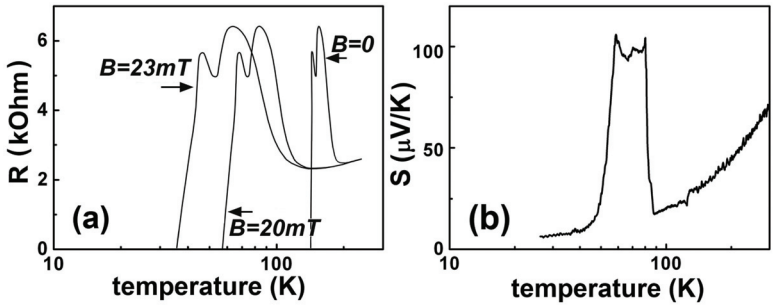

Fig. 9. The resistance (a) and thermo-emf (Seebeck coefficient) (b) temperature dependences that were observed in the ultra-shallow p^+ -diffusion profile which contains the p-type Si-QW confined by the δ-barriers heavily doped with boron on the n-type Si (100) surface.

The value of the critical temperature, T_c=145 K, the estimations of the superconductor gap, 2Δ=0.044 eV, and the T=0 upper critical field, H_{C2}=0.22 T, that were derived from the resistance and thermo-emf measurements using well-known relationships $2\Delta=3.52k_BT_c$ and $H_{c2}(0)=-0.69(dH_{c2}/dT\,|_{Tc})T_c$ (Werthamer et al., 1966) appear to be revealed also in the temperature and magnetic field dependencies of the static magnetic susceptibility obtained by the Faraday balance method (Fig. 10a, b and c).

These dependences were measured in the range 3.5-300 K with the magnetic balance spectrometer MGD312FG. High sensitivity, $10^{-9}\div10^{-10}$ CGS, should be noted to be provided by the $B\ dB/dx$ stability using this installation. Pure InP samples with the shape and size similar to the silicon samples studied here that are characterized by temperature stable magnetic susceptibility, $\chi = 313\cdot10^{-9}$ cm^3/g, were used to calibrate the $B\ dB/dx$ values.

The value of temperatures corresponding to the drops of the diamagnetic response on cooling is of importance to coincide with the drops of the resistance and the Seebeck coefficient thereby confirming the role of the charge correlations localized at the negative-U dipole centers in the Kondo-liked scattering and the enhancement of the critical temperature (Fig. 10). Just the same temperature dependence of the paramagnetic response observed after the field-in procedure exhibits the effect of the arrays of the Josephson transitions revealed by the STM image (Fig. 5c) on the flux pinning processes in the superconductor δ-barriers heavily doped with boron (Bagraev et al., 2006a). The plots of the magnetic susceptibility vs temperature and magnetic field shown in Fig. 10a result in the value of H_{C2}, H_{C2}=0.22 T, that corresponds to the data obtained by the measurements of the resistance and allow the estimation of the coherence length, ξ=39 nm, where $\xi = (\Phi_0/2\pi H_{C2})^{1/2}$, $\Phi_0 = h/2e$. This value of the coherence length appears to be in a good agreement with the estimations of the superconductor gap, 2Δ=0.044 eV, made if the value of the critical temperature, T_C=145

K, is taken into account, $\xi = 0.18\hbar v_F / k_B T_c$, where v_F is the Fermi velocity, and with the first critical magnetic field, H_{C1}=215 Oe, defined visually from Fig. 10a.

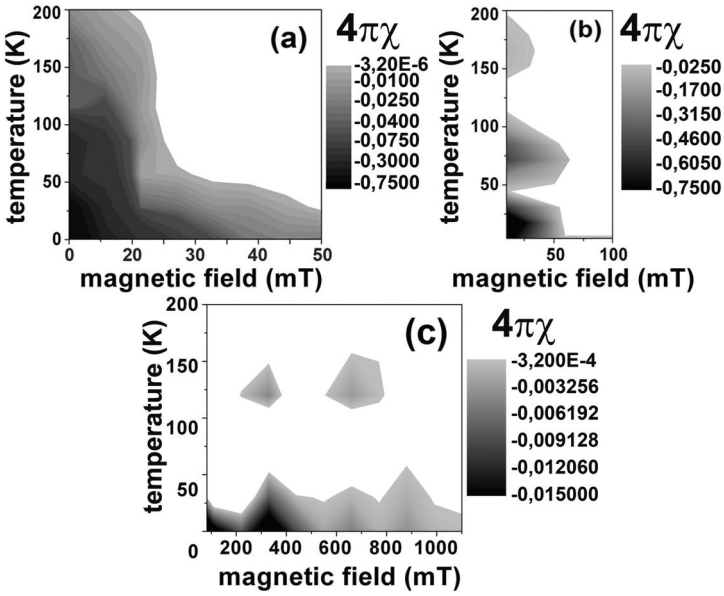

Fig. 10. Plots of static magnetic susceptibility vs temperature and magnetic field that was observed in field-cooled ultra-shallow p^+ -diffusion profile which contains the p-type Si-QW confined by δ-barriers heavily doped with boron on the n-type Si (100) surface. Diamagnetic response (a) revealed by field-out procedure demonstrates also the oscillations that seem to be related to the ratchet effect (b) and the quantization of the critical current (c).

The oscillations of the magnetic susceptibility value revealed by varying both the temperature and magnetic field value seem to be due to the vortex manipulation in nanostructured δ-barriers (Figs. 10b and c). Since the fractal series of silicon microdefects identified by the STM images is embedded in the superconductor δ-barrier, the multi-quanta vortex lattices are able to be self-organized (Vodolazov et al., 2007). These self-assembled pinning arrays that can be simulated as a series of anti-dots appear to capture in consecutive order several vortices and thus to enhance critical current (de Souza Silva et al., 2006; Vodolazov et al., 2007). Furthermore, the upper critical field, H_{C2}, is evidently dependent step-like on both temperature and magnetic field, because the critical current increases jump-like each time when the regular vortex is captured at such an anti-dot that is revealed by the corresponding oscillations of the diamagnetic response (Fig. 10c). The period of these oscillations that is derived from the plots in Fig. 10c appears to be due to the distance between the small microdefects in the fractal series identified by the STM image, ≈ 120 nm, with average dimensions equal to 68 nm (Fig. 5a): $\Delta B \cdot S = \Phi_0$, where ΔB is the period oscillations, $S = \pi d^2/4$, d is the distance between anti-dots (≈ 120 nm). The dependence $H_{C2}(T)$ is of importance to be in a good agreement with the value of this period, because each maximum of the diamagnetic response as a function of magnetic field is accompanied by the temperature satellite shifted by approximately 140 K (~T_C) to higher temperatures. In

addition to the oscillations of the magnetic susceptibility, the *B-T* diagram shown in figure 10b exhibits also the quantization of the critical current which seems to be caused by the vortex ratchet effect (de Souza Silva et al., 2006).

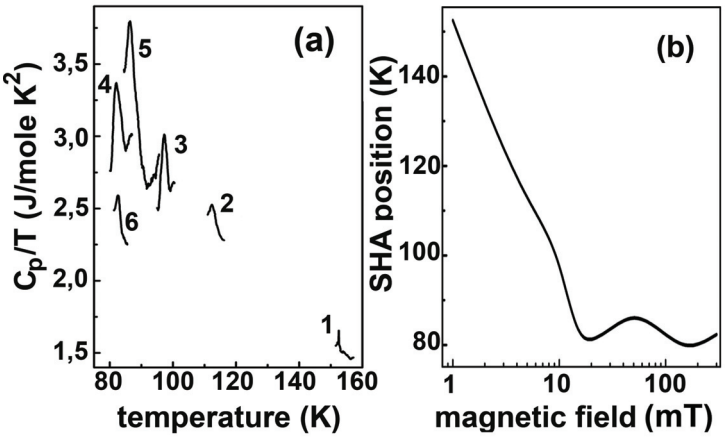

Fig. 11. (a) Specific heat anomaly as C/T vs T that seems to reveal the superconducting transition in field-cooled ultra-shallow p^+ -diffusion profile which contains the p-type Si-QW confined by δ-barriers heavily doped with boron on the n-type Si (100) surface. Magnetic field value: 1- 0 mT; 2 – 5 mT, 3 – 10 mT; 4 – 21.5 mT; 5 – 50 mT; 6 – 300 mT. (b) The oscillations of a specific heat anomaly as a function of external magnetic field that seem to be due to the quantization of the critical current.

The enhancement of the critical current due to the $N\,\Phi_0$ vortex capture at the anti-dots seems to result also from the studies of a specific heat anomaly at T_C (Figs. 11a and b). This anomaly arises at the temperature of 152 K (H=0) that is close to the value of the critical temperature derived from the measurements of the resistance and the magnetic susceptibility. With increasing external magnetic field, the position of the jump in specific heat is shifted to the range of low temperatures (Fig. 11a). The jump values in specific heat, ΔC, appear to be large if the abnormal small effective mass of heavy holes in these 'sandwich' structures, S-Si-QW-S, is taken into account to be analyzed within frameworks of a weak coupled BCS superconductor (Bagraev et al., 2008a). The oscillations of a specific heat anomaly as a function of external magnetic field are seen to be in a good agreement with the corresponding behavior of the diamagnetic response that corroborates additionally the important role of vortices in the superconductor properties of the nanostructured δ-barriers (Fig. 11b).

The values of the superconductor energy gap derived from the measurements of the critical temperature using the different techniques appear to be practically identical, 0.044 eV. Nevertheless, the direct methods based on the principles of the tunneling spectroscopy are necessary to be applied for the identification of the superconductor gap in the δ-barriers confining the Si-QW (Figs. 8a and b). Since the nanostructured δ-barriers are self-assembled as the dots containing a single dipole boron center that alternate with undoped silicon anti-dots shown in Fig. 5c, the tunneling current can be recorded by applying the voltage to the contacts prepared in the Hall geometry (Fig. 8a). The tunneling current-voltage

characteristic obtained is direct evidence of the superconductor gap that appears to be equal to 0.044 eV (Fig. 12a) (Bagraev et al., 1998). To increase the resolution of this experiment, a series of doped dots - undoped anti-dots involved in the sequence measured should not possess large discrepancies in the values of the superconductor energy gap. Therefore, the one-dimensional constriction is expediently to be prepared for the precise measurements of the tunneling current-voltage characteristics (Bagraev et al., 2002; 2004b; 2005; 2006a).

The other way for the definition of the superconductor energy gap is to use the techniques of the local tunneling spectroscopy (LTS) (Suderow et al., 2002; Bagraev et al., 2005; Fischer et al., 2007). The local density of states (LDOS) can be accessed by measuring the tunnelling current, while the bias voltage is swept with the tip held at a fixed vertical position (Fig. 8b) (Fischer et al., 2007). If a negative bias voltage is applied to the δ-barriers, holes will tunnel into unoccupied sample states, whereas at a positive bias voltage they will tunnel out of occupied sample states. Since the transport conditions inside the 'sandwich' structures, S-Si-QW-S, are close to ideal (Bagraev et al., 2002; 2004b; 2005; 2006b), the tunnelling conductance, $dI/dV(V)$, provides the measurements of the LDOS thereby allowing the precise definition of the superconductor energy gap. The LTS current-voltage characteristic shown in Fig. 12b that has been registered in the studies of the device structure identical discussed above demonstrates also the value of the superconductor energy gap equal to 0.044 eV which is in self-agreement with the measurements of the critical temperature and the upper critical magnetic field.

In order to identify the transfer of the small hole bipolarons as a possible mechanism of supeconductivity, the transport of holes in the S-Si-QW-S structures is followed to be studied at different orientation of the external magnetic field relatively the Si-QW plane. The dependences of the longitudinal and Hall voltages on the magnetic field value shown in Figs. 13a, b and c are evidence of the Zeeman effect that seems to be due to the creation of the triplet and singlet states of the small hole bipolarons localized at the dipole boron centers (Fig. 7b). The sign inversion of both U_{xx} and U_{xy} voltages is of importance to result from the change of the magnetic field direction to opposite. Thus, the transport of the small hole bipolarons that are able to capture and/or scattered on the dipole boron centers seems to be caused by the diamagnetic response induced by applying a magnetic field.

Besides, the magnetic field dependences of the U_{xx} and U_{xy} voltages considered within frameworks of the triplet, T^+, T^0, T^-, as well as the ground, S_0^+, S_0^-, and excited, S_1^+, S_1^-, states undergone by the Zeeman splitting appear to reveal the presence of the upper critical magnetic field H_{c2} and the oscillations of the critical current which are in a good agreement with the measurements of the magnetic susceptibility (see Fig. 13 and Figs. 10a, b, c). The resonance behaviour of the $U_{xx}(H)$ and $U_{xy}(H)$ dependences in the anti-crossing points of the triplet sublevels (T^+-T^0) is evidence of the spin polarization that results from the selective population or depopulation of the T^+ and T^- states relatively to the T^0 state in consequence of the partial removal of a ban on the forbidden triplet-singlet transitions (Laiho et al., 1998). The spin polarization of the bipolarons in the triplet state in the S-Si-QW-S structures should be of importance in the studies of the spin interference caused by the Rashba spin-orbit interaction in the quantum wires and rings (Bagraev et al., 2006b; 2008a). The creation of the excited singlet states in the processes of the bipolaronic transport is also bound to be noticed, because owing to the transitions from the excited to the ground singlet state of the small hole bipolarons these 'sandwich' structures seem to be perspective as the sources and recorders of the THz and GHz emission that is revealed specifically in the

electroluminescence spectra as a low frequency modulation (see Fig. 3a). The optical detection of magnetic resonance of the single impurity centers in the Si-QW confined by the δ-barriers heavily doped with boron was especially performed by the direct measurements of the transmission spectra under such an internal GHz emission in the absence of the external cavity resonator (Bagraev et al., 2003a; 2003b).

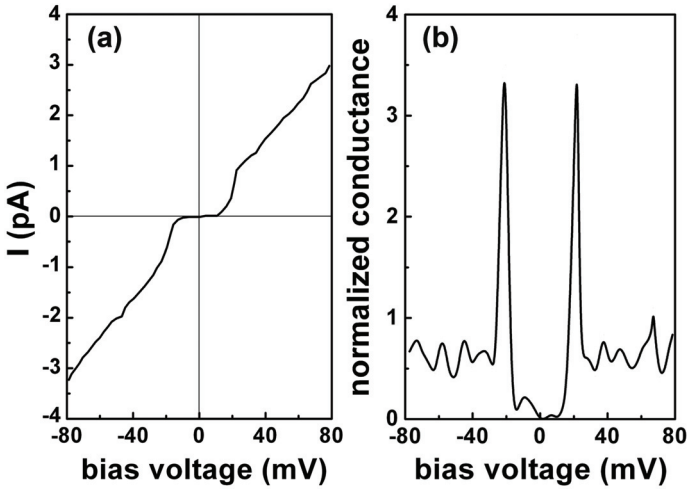

Fig. 12. The *I-U* (a) and *dI/dV(V)* (b) characteristics found by the current-voltage measurements (a) and using the STM point contact technique (b), which identify the superconductor energy gap in the nanostructured δ-barriers heavily doped with boron that confine the p-type Si-QW on the n-type Si (100) surface. (a) – 77 K; (b) – 4.2 K.

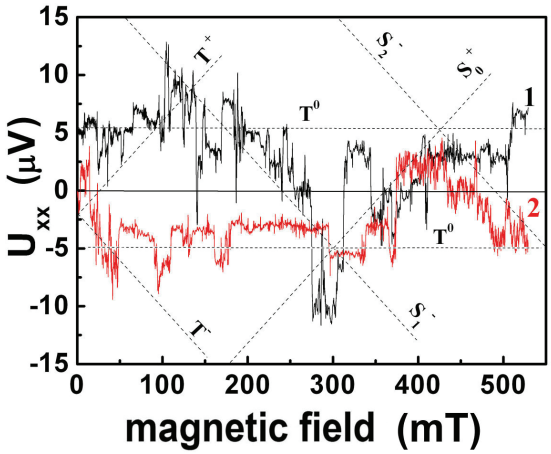

Fig. 13. U_{xx} vs the value of the magnetic field applied perpendicularly to the plane of the p-type Si-QW confined by the δ-barriers on the n-type Si (100) surface. I_{ds}=10 nA. T=77 K. Curves 1 and 2 measured for opposite orientations of a magnetic field reveal the sign of U_{xx} that corresponds to the diamagnetic response of the superconductor δ-barriers.

Thus, the extremely low value of the hole effective mass in the 'sandwich' S-Si-QW-S structures seems to be the principal argument for the bipolaronic mechanism of high temperature superconductor properties that is based on the coherent tunneling of bipolarons (Alexandrov & Ranninger, 1981; Alexandrov & Mott, 1994). The local phonon mode manifestation at λ = 16.4 μm that presents, among the superconductor gap, λ = 26.9 μm ⇔ 2Δ, in the transmission spectrum favours the use of this conception (Fig. 3c). High frequency local phonon mode, λ = 16.4 μm ⇔ 76 meV, appears to exist simultaneously with the intermediate value of the coupling constant, κ.

The value of the coupling constant, κ = *VN(0)*, is derived from the BCS formula $\Delta = 2\hbar\omega_D \exp(-1/\kappa)$ taking account of the experimental values of the superconductor energy gap, 2Δ = 0.044 eV, and the local phonon mode energy, $\hbar\omega_D$ = 76 meV. This estimation results in $\kappa \approx 0.52$ that is outside the range 0.1÷0.3 for metallic low-temperature superconductors with weak coupling described within the BCS approach. Therefore the superconductor properties of the 'sandwich' S-Si-QW-S structures seem to be due to the transfer of the mobile small hole bipolarons that gives rise to the high T_c value owing to small effective mass.

The results obtained, specifically the linear decay of the magnetic susceptibility with increasing a magnetic field revealed by the *B-T* diagram in Fig. 10a at high temperature and in weak magnetic fields, have a bearing on the versions of the high temperature superconductivity that are based on the promising application of the sandwiches which consist of the alternating superconductor and insulator layers (Ginzburg, 1964; Larkin & Ovchinnikov, 1964; Fulde & Ferrell, 1964; Little, 1971). In the latter case, a series of heavily doped with boron and undoped silicon dots that forms the Josephson junction area in nanostructured δ - barriers is of advantage to achieve the high T_c value, $T_c = (\hbar\omega_D / k_B)\exp(-N(0)V)$, because of the presence of the local high frequency phonon mode which compensates for relatively low density of states, *N(0)*.

Nevertheless, the mechanism of the bipolaronic transfer is still far from completely clear. This raises the question of whether the Josephson transitions dominate in the transfer of the pair of 2D holes in the plane of the nanostructured δ - barriers and in the proximity effect due to the tunneling through the Si-QW or the Andreev reflection plays a part in the bipolaronic transfer similar to the successive two-electron (hole) capture at the negative-U centers (Bagraev & Mashkov, 1984; Bagraev & Mashkov, 1988**)**.

4. Superconducting proximity effect

Since the devices studied consist of a series of alternating semiconductor and superconductor nanostructures with dimensions comparable to both the Fermi wavelength and the superconductor coherence length, the periodic modulation of the critical current can be observed in consequence with quantum dimensional effects (Klapwijk, 2004; van Dam et al., 2006; Jarillo-Herrero et al., 2006; Jie Xiang et al., 2006). Here the S-Si-QW-S structures performed in the Hall geometry are used to analyse the interplay between the phase-coherent tunneling in the normal state and the quantization of supercurrent in the superconducting state.

Firstly, the two-dimensional subbands of holes in the Si-QW identified by studying the far-infrared electroluminescence (EL) spectrum (Figs. 3a and b) appear to be revealed also by the I-V characteristic measured below the superconducting critical temperature of the δ-barriers

which exhibits the modulation of the supercurrent flowing across the junction defined as the Josephson critical current (Fig. 14). The modulation of supercurrent seems to be caused by the tuning of on- and off-resonance with the subbands of 2D holes relatively to the Fermi energy in superconductor δ-barriers (Jarillo-Herrero et al., 2006; Jie Xiang et al., 2006) (see Figs. 15a and b). The two-dimensional subbands of 2D holes are revealed by varying the forward bias voltage (Figs. 14 and 15a), whereas the reverse bias voltage involves the levels that result from the Coulomb charging effects in the Si-QW filled with holes (Figs. 14 and 15b). The spectrum of supercurrent in the superconducting state appears to correlate with the conductance oscillations of the $2e^2/h$ value in the normal state of the S-Si-QW-S structure (Figs. 16a and b). This highest amplitude of the conductance oscillations is evidence of strong coupling in the superconductor δ-barriers (Fig. 16b). The data obtained demonstrate also that the amplitude of the quantum supercurrent is within frameworks of the well-known relationship $I_cR_n=\pi\Delta/e$ (Klapwijk, 2004; Jie Xiang et al., 2006); where $R_n=1/G_n$ is the normal resistance state, 2Δ is superconducting gap, 0.044 eV. Besides, the strong coupling of on-resonance with the subbands of 2D holes which results from the $2e^2/h$ value of the conductance amplitude in the normal state is not related to the Kondo enhancement that is off-resonance (Cronenwett et al., 2002).

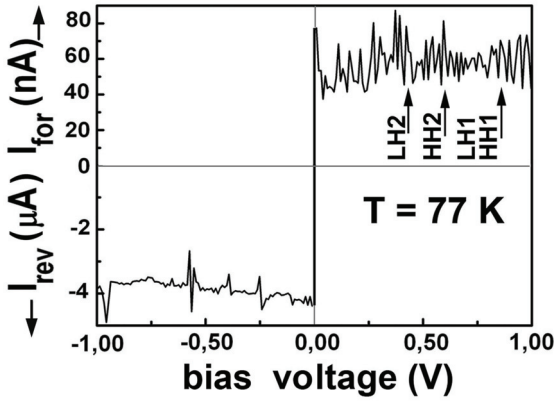

Fig. 14. *I-V* characteristic that demonstrates the modulation of the critical current with the forward and reverse bias applied to the p-type Si-QW confined by the δ-barriers on the n-type Si (100) surface.

Secondly, the spectrum of the supercurrent at low bias voltages appears to exhibit a series of peaks that are caused by multiple Andreev reflections (MARs) from the δ - barriers confining the Si-QW (Figs. 17a and b). The MAR process at the Si-QW - δ-barrier interface is due to the transformation of the 2D holes in a Cooper pair inside the superconducting δ-barrier which results in an electron being coherently reflected into the Si-QW, and vice versa, thereby providing the superconducting proximity effect (Figs. 18a and b) (Klapwijk, 2004). The single hole crossing the Si-QW increases its energy by eV. Therefore, when the sum of these gains becomes to be equal to the superconducting energy gap, 2Δ, the resonant enhancement in the supercurrent is observed (Figs. 17a and b). The MAR peak positions occur at the voltages $V_n = 2\Delta/ne$, where n is integer number, with the value n=1 related to the superconducting energy gap. It should be noted that the value of 2Δ, 0.033 eV, derived

from the MAR oscillations does not agree with the magnetic susceptibility data because of heating of the device by bias voltage at finite temperatures. The mechanism of disappearance of some MAR peaks by varying the applied voltage is still in progress (Klapwijk, 2004; Jarillo-Herrero et al., 2006; Jie Xiang et al., 2006). Nevertheless, the linear dependence of the MAR peak position on the value of $1/n$ was observed (Figs. 19a and b).

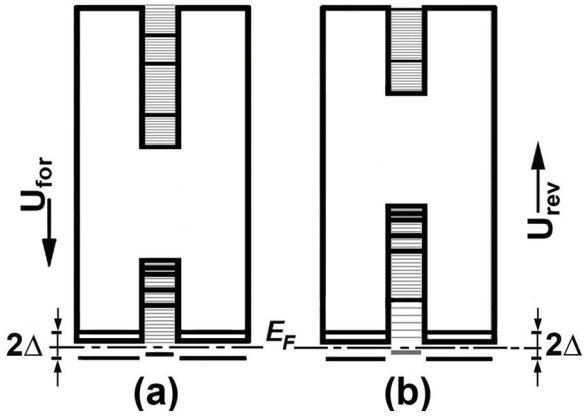

Fig. 15. The one-electron band scheme of the p-type Si-QW confined by the δ-barriers on the n-type Si (100) surface under forward (a) and reverse (b) bias, which depicts the superconducting gap, 2Δ, as well as the two-dimensional subbands of holes and the levels that result from the hole interference between the δ -barriers (a) and the Coulomb charging effects in the Si-QW filled with holes (b).

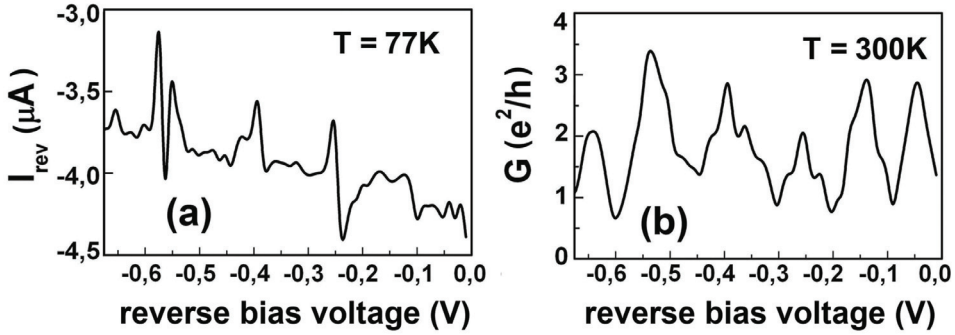

Fig. 16. Correlation between critical current (a) and normal state conductance (b) revealed by varying the reverse bias voltage applied to the sandwich structure, δ-barrier - p-type Si-QW - δ-barrier, on the n-type Si (100) surface.

The MAR processes are of interest to be measured in the regime of coherent tunneling (Eisenstein et al., 1991) in the studies of the device performed in frameworks of the Hall geometry, because the phase coherence is provided by the Andreev reflection of the single holes (electrons) at the same angle relatively to the Si-QW plane. In the device studied this angle is determined by the crystallographic orientation of the trigonal dipole centers of boron inside the δ-barriers (Figs. 7a and b). These MAR processes were observed as the

oscillations of the longitudinal conductance by varying the value of the top gate voltage, with the linear dependence of the MAR peak position on the value of $1/n$ (Fig. 20a and b).

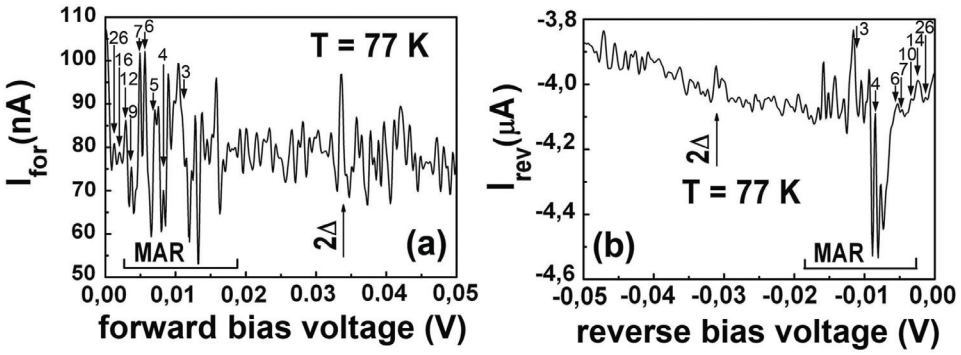

Fig. 17. Multiple Andreev reflections (MAR) with the forward (a) and reverse (b) bias applied to the sandwich structure, δ-barrier - p-type Si-QW - δ-barrier on the n-type Si (100) surface. The MAR peak positions are marked at $V_n = 2\Delta/ne$ with values n indicated. The superconducting gap peak, 2Δ, is also present. The difference in the values of critical current under forward and reverse bias voltage is due to non-symmetry of the sandwich structure.

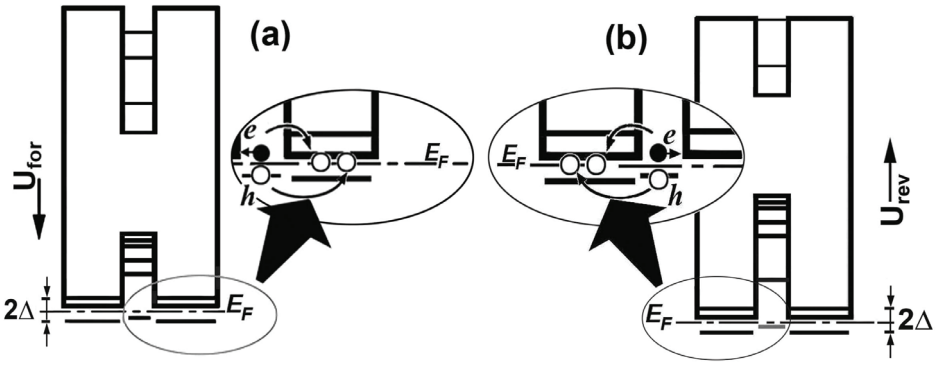

Fig. 18. The one-electron band scheme of the sandwich structure, δ-barrier - p-type Si-QW - δ-barrier, on the n-type Si (100) surface that reveals the multiple Andreev reflection (MAR) caused by pair hole tunneling into δ-barrier under forward (a) and reverse (b) bias.

The value of the superconducting energy gap, 0.044 eV, derived from these dependences was in a good agreement with the magnetic susceptibility data that is evidence of the absence of heating effects at the values of the drain-source voltage used in the regime of coherent tunneling. The amplitude of the MAR peaks observed, e^2/h, appeared to be independent of the value of the drain-source voltage that is also attributable to the coherent tunneling. Since the MAR processes are spin-dependent (Klapwijk, 2004), the effect of the Rashba SOI created at the same geometry by varying the value of the top gate voltage appears to be responsible for the mechanism of the coherent tunneling in Si-QW. In addition to the e^2/h amplitude of the MAR peaks, this concept seems to result from the stability of the

Fermi wave vector that was controlled in the corresponding range of the top gate voltage by the Hall measurements. Within frameworks of this mechanism of the coherent tunneling, the spin projection of 2D holes that take part in the MAR processes is conserved in the Si-QW plane (Klapwijk, 2004) and its precession in the Rashba effective field is able to give rise to the reproduction of the MAR peaks in the oscillations of the longitudinal conductance. Thus, the interplay of the MAR processes and the Rashba SOI appears to reveal the spin transistor effect (Bagraev et al., 2005; 2006b; 2008a; 2008c) without the injection of the spin-polarized carriers from the iron contacts as proposed in the classical version of this device.

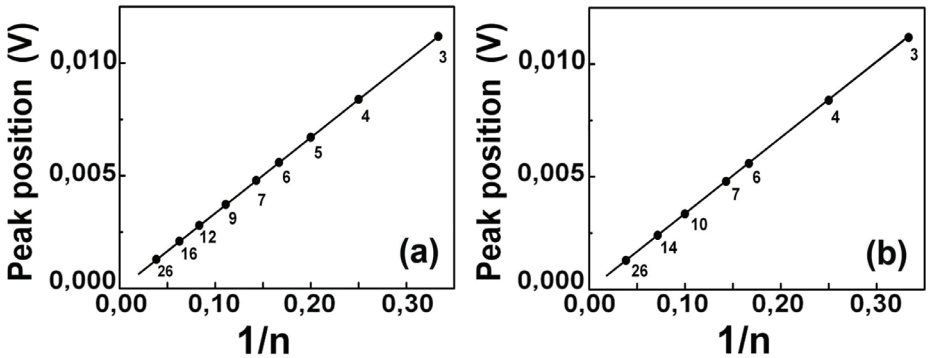

Fig. 19. Plot of the MAR peak position versus the inverse index 1/n with the forward (a) and reverse (b) bias applied to the sandwich structure, δ-barrier - p-type Si-QW - δ-barrier on the n-type Si (100) surface at 77 K.

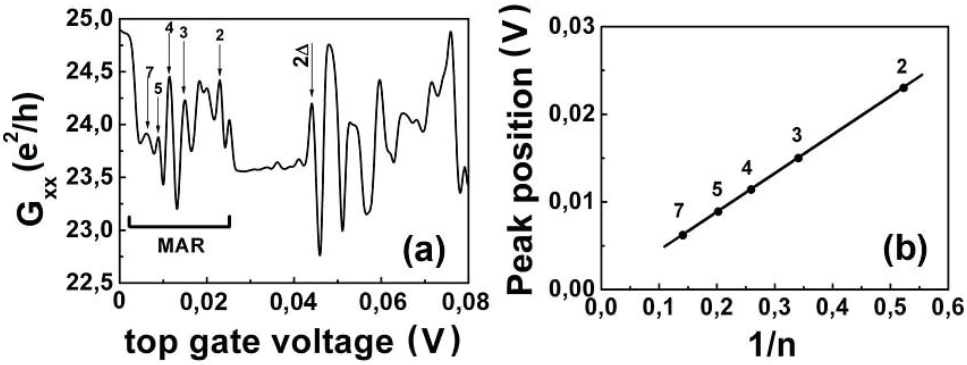

Fig. 20. (a) Multiple Andreev reflections (MAR) that are observed in the longitudinal conductance of the sandwich structure, δ-barrier - p-type Si-QW - δ-barrier, on the n-type Si (100) surface by varying the top gate voltage applied within frameworks of the Hall geometry (see Fig. 8a). I_{ds}=10 nA. T=77 K. The MAR peak positions are marked at $V_n = 2\Delta/ne$ with values n indicated. (b) Plot of the MAR peak position versus the inverse index 1/n.

Finally, the studies of the proximity effect in the 'sandwich' S-Si-QW-S structures have shown that the MAR processes are of great concern in the transfer of the small hole bipolarons both between and along nanostructured δ-barriers confining the Si-QW. Within MAR processes, the pairs of 2D holes introduced into the δ-barriers from the Si-QW seem to

serve as the basis for the bipolaronic transfer that represents the successive coherent tunneling of small hole bipolarons through the dipole boron centers up the point, of which an electron is coherently reflected into the Si-QW. The most likely tunneling through the negative-U centers appear to be due to the successive capture of two holes accompanied by their generation or single-electron emission in consequence with the Auger processes: $B^+ + B^- + 2h \Rightarrow B^+ + B^0 + h \Rightarrow B^0 + B^+ + h \Rightarrow B^- + B^+ + 2h$ or $B^+ + B^- \Rightarrow B^+ + B^0 + e \Rightarrow B^0 + B^0 + h + e \Rightarrow B^- + B^0 + 2h + e \Rightarrow B^- + B^+ + h + e$. Relative contribution of these processes determines the coherence length. Besides, the single-hole tunneling through the negative-U centers that is able to increase the critical temperature should be also taken into account (Šimánek, 1979; Ting et al., 1980). Thus, the charge and spin density waves seem to be formed along the δ-barrier – Si-QW interface with the coherence length defined by the length of the bipolaronic transfer that is dependent on the MAR characteristics.

5. Conclusion

Superconductivity of the sandwich' S-Si-QW-S structures that represent the p-type high mobility silicon quantum wells confined by the nanostructured δ - barriers heavily doped with boron on the n-type Si (100) surface has been demonstrated in the measurements of the temperature and magnetic field dependencies of the resistance, thermo-emf, specific heat and magnetic susceptibility.

The studies of the cyclotron resonance angular dependences, the scanning tunneling microscopy images and the electron spin resonance have shown that the nanostructured δ - barriers consist of a series of alternating undoped and doped quantum dots, with the doped dots containing the single trigonal dipole centers, $B^+ - B^-$, which are caused by the negative-U reconstruction of the shallow boron acceptors, $2B^0 \rightarrow B^+ + B^-$.

The temperature and magnetic field dependencies of the resistance, thermo-emf, specific heat and magnetic susceptibility are evidence of the high temperature superconductivity, T_c = 145 K, that seems to result from the transfer of the small hole bipolarons through these negative-U dipole centers of boron at the Si-QW – δ - barrier interfaces.

The oscillations of the upper critical field and critical temperature vs magnetic field and temperature that result from the quantization of the critical current have been found using the specific heat and magnetic susceptibility techniques.

The value of the superconductor energy gap, 0.044 eV, derived from the measurements of the critical temperature using the different techniques appeared to be practically identical to the data of the current-voltage characteristics and the local tunneling spectroscopy.

The extremely low value of the hole effective mass in the 'sandwich' S-Si-QW-S structures that has been derived from the measurements of the SdH oscillations seems to be the principal argument for the bipolaronic mechanism of high temperature superconductor properties that is based on the coherent tunneling of bipolarons. The high frequency local phonon mode that is revealed with the superconductor energy gap in the infrared transmission spectra seems also to be responsible for the formation and the transfer of small hole bipolarons.

The proximity effect in the S-Si-QW-S structure has been identified by the findings of the MAR processes and the quantization of the supercurrent. The value of the superconductor energy gap, 0.044 eV, appeared to be in a good agreement with the data derived from the oscillations of the conductance in normal state and of the zero-resistance supercurrent in superconductor state as a function of the bias voltage. These oscillations have been found to

be correlated by on- and off-resonance tuning the two-dimensional subbands of holes with the Fermi energy in the superconductor δ - barriers.
Finally, the studies of the proximity effect in the 'sandwich' S-Si-QW-S structures have shown that the multiple Andreev reflection (MAR) processes are of great concern in the coherent transfer of the small hole bipolarons both between and along nanostructured δ-barriers confining the Si-QW.

6. Acknowledgements

The work was supported by the programme of fundamental studies of the Presidium of the Russian Academy of Sciences "Quantum Physics of Condensed Matter" (grant 9.12); programme of the Swiss National Science Foundation (grant IZ73Z0_127945/1); the Federal Targeted Programme on Research and Development in Priority Areas for the Russian Science and Technology Complex in 2007–2012 (contract no. 02.514.11.4074).

7. References

Alexandrov, A. & Ranninger, J. (1981). Bipolaronic superconductivity, *Phys. Rev.,* B 24, 1164-1169.

Alexandrov, A.S., & Mott, N.F. (1994). Bipolarons, *Rep. Prog. Phys.,* 57, 1197-1288.

Altshuler, B.L., Aronov, A.G. & Spivak B.Z. (1981). The Aharonov-Bohm effect in disordered conductors, *JETP Lett.,* 33, 94-97.

Anderson, P.W. (1975). Model for the electronic structure of amorphous semiconductors, *Phys. Rev. Lett.,* 34, 953-955.

Andreev, A.F. (1964). The thermal conductivity of the intermediate state in superconductors, *Sov. Phys. JETP,* 19, 1228-1234.

Bagraev, N.T. & Mashkov, V.A. (1984). Tunneling negative-U centers and photo-induced reactions in solids, *Solid State Communications,* 51, 515-520.

Bagraev, N.T. & Mashkov, V.A. (1988). A mechanism for two-electron capture at deep level defects in semiconductors, *Solid State Communications,* 65, 1111-1117.

Bagraev, N.T., Gehlhoff, W. & Klyachkin, L.E. (1995). Cyclotron resonance in heavily doped silicon quantum wells, *Solid St. Phenomena,* 47-48, 589-594.

Bagraev, N.T., Bouravleuv, A.D., Gasoumyants, V.E., Gehlhoff, W., Klyachkin, L.E., Malyarenko, A.M., Naeser, A., Romanov, V.V., Rykov, S.A. & Vladimirskaya, E.V. (1998). Pair charge correlations in silicon nanostructures, *Proceedings of SPIE,* 3687, 105-111.

Bagraev, N.T., Bouravleuv, A.D., Klyachkin, L.E., Malyarenko, A.M. & Rykov, S.A. (2000). Self-ordered microcavities embedded in ultra-shallow silicon p-n junctions, *Semiconductors,* 34, 700-711.

Bagraev, N.T., Bouravleuv, A.D., Klyachkin, L.E., Malyarenko, A.M., Gehlhoff, W., Ivanov, V.K. & Shelykh, I.A. (2002). Quantized conductance in silicon quantum wires, *Semiconductors,* 36, 439–460.

Bagraev, N.T., Bouravleuv, A.D., Gehlhoff, W., Klyachkin, L.E., Malyarenko, A.M. & Romanov, V.V. (2003a). Electron-dipole resonance of impurity centers embedded in silicon microcavities, *Physica,* B 340-342, 1078-1081.

Bagraev, N.T., Bouravleuv, A.D., Gehlhoff, W., Klyachkin, L.E., Malyarenko, A.M. & Romanov, V.V. (2003b). Erbium-related centers embedded in silicon microcavities, *Physica,* B 340-342, 1074-1077.

Bagraev, N.T., Bouravleuv, A.D., Gehlhoff, W., Klyachkin, L.E., Malyarenko, A.M., Romanov, V.V. & Rykov, S.A. (2004a). Fractal self-assembled nanostructures on monocrystalline silicon surface, *Defect and Diffusion Forum,* 337-240, 1049–1054.

Bagraev, N.T., Ivanov, V.K., Klyachkin, L.E. & Shelykh, I.A. (2004b). Spin depolarization in quantum wires polarized spontaneously in a zero magnetic field, *Phys. Rev.,* B 70, 155315-9.

Bagraev, N.T., Bouravleuv, A.D., Klyachkin, L.E., Malyarenko, A.M., Gehlhoff, W., Romanov, Yu.I. & Rykov, S.A. (2005). Local tunneling spectroscopy of silicon nanostructures, *Semiconductors,* 39, 716-728.

Bagraev, N.T., Gehlhoff, W., Klyachkin, L.E., Malyarenko, A.M., Romanov, V.V. & Rykov, S.A. (2006a). Superconductivity in silicon nanostructures, *Physica,* C 437-438, 21-24.

Bagraev, N.T., Galkin, N.G., Gehlhoff, W., Klyachkin, L.E., Malyarenko, A.M. & Shelykh, I.A. (2006b). Spin interference in silicon one-dimensional rings, *J. Phys.:Condens. Matter,* 18, L1-L7.

Bagraev, N.T., Galkin, N.G., Gehlhoff, W., Klyachkin, L.E., Malyarenko, A.M. & Shelykh, I.A. (2007) Spin interference in silicon one-dimensional rings, *Journal of Physics: Conference Series,* 61, 56-60.

Bagraev, N.T., Galkin, N.G., Gehlhoff, W., Klyachkin, L.E., Malyarenko, A.M. & Shelykh, I.A. (2008a). Spin interference of holes in silicon one-dimensional rings, *Physica,* E 40, 1338-1340.

Bagraev, N.T., Galkin, N.G., Gehlhoff, W., Klyachkin, L.E. & Malyarenko, A.M. (2008b). Phase and amplitude response of '0.7 feature' caused by holes in silicon one-dimensional wires and rings, *J. Phys.:Condens. Matter,* 20, 164202-10.

Bagraev, N.T., Gehlhoff, W., Klyachkin, L.E., Kudryavtsev, A.A., Malyarenko, A.M., Oganesyan, G.A., Poloskin, D.S. & Romanov, V.V. (2008c). Spin-dependent transport of holes in silicon quantum wells confined by superconductor barriers, *Physica,* C 468, 840-843.

Bao-xing Li, Pen-lin Cao & Duam-lin Que. (2000). Distorted icosahedral cage structure of Si_{60} clusters, *Phys. Rev.,* B 61, 1685-1687.

Baraff, G.A., Kane, E.O. & Schlüter, M. (1980). Theory of the silicon vacancy: An Anderson negative-U system, *Phys. Rev.,* B 21, 5662 – 5686.

Chakraverty, B.K. (1981). Bipolarons and superconductivity, *J. Physique,* 42, 1351-1356.

Cronenwett, S.M., Lynch, H.J., Goldhaber-Gordon, D., Kouwenhoven, L.P., Marcus, C.M., Hirose, K., Wingreen, N.S. & Umansky, V. (2002). Low-temperature fate of the 0.7 structure in a point contact: a Kondo-like correlated state in an open system, *Phys. Rev. Lett.,* 88, 226805-4.

van Dam, J.A., Nazarov, Y.V., Bakkers, E.P.A.M., De Franceschi, S. and Kouwenhoven, L.P. (2006). Supercurrent reversal in quantum dots, *Nature,* 442, 667-672.

Eisenstein, J.P., Gramila, T.J., Pfeiffer, L.N. & West, K.W. (1991). Probing a two-dimensional Fermi surface by tunneling, *Phys. Rev.,* B 44, 6511-6514.

Ekimov, E.A., Sidorov, V.A., Bauer, E.D., Mel'nik, N.N., Curro, N.J., Thompson, J.D. & Stishov, S.M. (2004). Superconductivity in diamond, *Nature,* 428, 542–545.

Fischer, Ø., Kugler , M., Maggio-Aprile, I., Berthod, Ch. & Renner, Ch. (2007). Scanning tunneling spectroscopy of high-temperature superconductors, *Reviews of Modern Physics*, 79, 353-419.

Fulde, P. & Ferrell, R.A. (1964). Superconductivity in a strong spin-exchange field, *Phys. Rev.*, 135, A550-A563.

Gehlhoff, W., Bagraev, N.T. & Klyachkin, L.E. (1995). Shallow and deep centers in heavily doped silicon quantum wells, *Materials Sci.Forum,* 196-201, 467-472.

Geim, A.K. & Novoselov, K.S. (2007). The rise of grapheme, *Nature Materials,* 6, 183-191.

Gerardi, G.J., Poindexter, E.H., Caplan, P.J. & Johnson, N.M. (1986). Interface traps and Pb centers in oxidized silicon wafers, *Appl. Phys. Lett.,* 49, 348-350.

Ginzburg, V.L. (1964). On surface superconductivity, *Phys.Lett.,* 13, 101-102.

Jarillo-Herrero, P, van Dam, J.A. & Kouwenhoven, L.P. (2006). Quantum supercurrent transistors in carbon nanotubes. *Nature,* 439, 953-957.

Jie Xiang, Vidan, A., Tinkham, M., Westervelt, R.M. & Lieber, Ch. (2006). Ge-Si nanowire mesoscopic Josephson Junctions, *Nature-nanotechnology,* 1, 208-214.

Kastner, M., Adler, D. & Fritzsche, H. (1976). Valence-alternation model for localized gap states in lone-pair semiconductors, *Phys. Rev. Lett.,* 37, 1504-1507.

Klapwijk, T.M. (2004). Proximity effect from an Andreev perspective, *Journal of Superconductivity. Incorporating Novel Magnetism,* 17, 593-611.

Kotthaus, J.P. & Ranvaud, R. (1977). Cyclotron resonance of holes in surface space charge layers on Si, *Phys.Rev.,* B 15, 5758-5761.

Laiho, R., Afanasjev, M.M., Vlasenko, M.P. & Vlasenko, L.S. (1998). Electron exchange interaction in S=1 defects observed by levele crossing spin-dependent microwave photoconductivity in irradiated silicon, *Phys. Rev. Lett.,* 80, 1489-1492.

Larkin, A.I. & Ovchinnikov, Yu.N. (1964). Nonuniform state of superconductors, *Sov. Phys. JETP,* 47, 1136-1146.

Little, W.A. (1971). Higher temperatures: theoretical models, *Physica,* 55, 50-59.

Macilwain, C. (2005). Silicon down to the wire, *Nature,* 436, 22-23.

Nakamura, Y. & Tsai, J.S. (2000). Quantum-state control with a single-cooper pair box, *J. Low Temp. Phys.,* 118. 765-779.

Robertson, J. (1983). Electronic structure of amorphous semiconductors, *Advances in Physics,* 32, 361-409.

Slaoui, A., Fogarassy, E., Muller, J.C. & Siffert, P. (1983). Study of some optical and electrical properties of heavily doped silicon layers, *J. de Physique Colloq.*, C5 44, 65-71.

de Souza Silva, C.C., van de Vondel, J., Morelle, M. & Moshchalkov, V.V. (2006). Controlled multiple reversals of ratchet effect, *Nature,* 440, 651-654.

Street, R.A. & Mott, N.F. (1975). States in the gap in glassy semiconductors, *Phys. Rev. Lett.,* 35, 1293-1296.

Suderow, H., Bascones, E., Izquierdo, A., Guinea, F. & Vieira, S. (2002). Proximity effect and strong-coupling superconductivity in nanostructures built with an STM, *Phys. Rev.,* B 65, 100519-4.

Šimánek, E. (1979). Superconductivity at disordered interfaces, *Solid State Comm.,* 32, 731–734.

Ting, C.S., Talwar, D.N. & Ngai, K.L. (1980). Possible mechanism of superconductivity in metal-semiconductor eutectic alloys, *Phys. Rev. Lett.,* 45, 1213–1216.

Trovarelli, O., Weiden, M., Müller-Reisener, R., Gómez-Berisso, M., Gegenwart, P., Deppe, M., Geibel, C., Sereni, J.G. & Steglich, F. (1997). Evolution of magnetism and superconductivity in $CeCu_2(Si_{1-x}Ge_x)_2$, *Phys. Rev.,* B 56, 678–685.

Vodolazov, D.Y., Golubović, D.S., Peeters, F.M. & Moshchalkov, V.V. (2007). Enhancement and decrease of critical current due to suppression of superconductivity by a magnetic field, *Phys. Rev.,* B 76, 134505-7.

Watkins, G.D. (1984). Negative-U properties for defects in solids, *Festkoerperprobleme*, 24, 163-186.

Werthamer, N.R., Helfand, E. & Hohenberg, P.C. (1966). Temperature and purity dependence of the superconducting critical field H_{c2}. III. Electron spin and spin-orbit effects, *Phys. Rev.,* 147, 295–302.

5

MgB_2-MgO Compound Superconductor

Yi Bing Zhang and Shi Ping Zhou
Department of Physics, College of Science, Shanghai University, Shanghai 200444 China

1. Introduction

1.1 Superconductive materials

Since the first superconductor, mercury (Hg), was discovered in 1911 by H. Kamerlingh Onnes and his students, there are thousands of superconducting materials were reported up to now. By 1980 superconductivity had been observed in many metals and alloys. Most metals in the periodic table exhibit superconductivity, aside from the ferromagnetic transition metals and rare-earth and actinide metals. Several nonsuperconducting elements will also have a superconductive state under high pressure. Niobium (Nb) has the highest T_c (9.2 K) among all elements at normal pressure. The A-15 compound Nb_3Ge remained the highest transition temperature (T_c = 23.2 K) until the high-T_c cuprate superconductors discovered by Bednorz and Müller (Bednorz & Müller, 1986) in 1986.

The cuprate superconductors adopt a perovskite structure and are considered to be quasi-two dimensional materials with their superconducting properties determined by electrons moving within weakly coupled copper-oxide (CuO_2) layers. There are several families of cuprate superconductors, including $YBa_2Cu_3O_{7-\delta}$, $Bi_2Sr_2Ca_nCu_{n+1}O_{6+2n+\delta}$, $Tl_mBa_2Ca_nCu_{n+1}O_{4+m+2n+\delta}$ (m = 1, 2), $HgBa_2Ca_nCu_{n+1}O_{4+2n+\delta}$ etc., where n may be 0, 1, and 2. They raise T_c of superconductor to 92 K, 110 K, 125 K, and 135 K respectively. Usually, they are categorized by the elements that they contain and the number of adjacent copper-oxide layers in each superconducting block. For example, YBCO and BSCCO can alternatively be referred to as Y123 and Bi2201/Bi2212/Bi2223 depending on the number of layers in each superconducting block (L). The superconducting transition temperature has been found to peak at an optimal doping value (p = 0.16) and an optimal number of layers in each superconducting block, typically L = 3. The weak isotope effects observed for most cuprates contrast with conventional superconductors that are well described by BCS theory. Another difference of the high-temperature superconducting oxides from the conventional superconductors is the presence of a pseudo-gap phase up to the optimal doping.

The first superconducting oxide without copper element is an iron-based superconductor, LaFeOP, which was discovered in 2006 by Y. Kamihara et al. (Kamihara et al., 2006) at Tokyo Institute of Technology, Japan. It is gained much greater attention in 2008 after the analogous material LaFeAs(O,F) was found with superconductivity at 43 K (Kamihara et al., 2008; Takahashi et al., 2008) under pressure. Within just a few months, physicists in China found optimal electron and hole dopants then doubled T_c to 55 K (Ren et al., 2008). The iron-based superconductors contain layers of iron and a pnictogen such as arsenic or phosphorus, or chalcogens. This is currently the family with the second highest critical

temperature, behind the cuprates. Since the original discoveries, two main families of iron-based superconductors have emerged: the rare-earth (R) iron-based oxide systems $RO_{1-x}F_xFeAs$ (R = rare earth) and the $(Ca,Ba,Sr)_{1-x}KxFe_2As_2$. Most undoped iron-based superconductors show a tetragonal-orthorhombic structural phase transition followed at lower temperature by magnetic ordering, similar to the cuprate superconductors. However, they are poor metals rather than Mott insulators and have five bands at the Fermi surface rather than one. Strong evidence that the T_c value varies with the As-Fe-As bond angles has already emerged and shows that the optimal T_c value is obtained with undistorted FeAs tetrahedra.

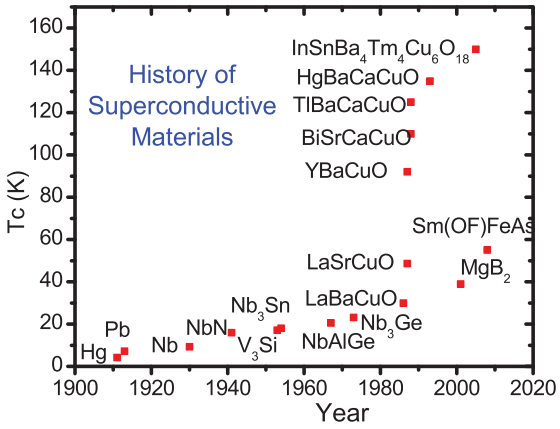

Fig. 1. Survey diagram for superconductive materials. $InSnBa_4Tm_4Cu_6O_{18+}$ is a multiphase superconductor with a possible superconductivity at 150 K (Patent No.: US60/809,267) and T_c of this family is up to about 250 K in 2010.

Fig. 1 shows the survey of superconductive materials. Other potential superconducting systems with a high transition temperature may also include fulleride superconductors, organic superconductors, and heavy fermion compounds. Theoretical work by Neil Ashcroft (Ashcroft, 1968) predicted that liquid metallic hydrogen at extremely high pressure should become superconducting at approximately room-temperature because of its extremely high speed of sound and expected strong coupling between the conduction electrons and the lattice vibrations. Scientists dream to find room-temperature superconductors but the survey of discovering superconductors indicates that only 1 ~ 2 K of T_c was increased per year from the first element superconductor to the first high- T_c cuprate oxide and after the discovery of TlBaCaCuO to now.

Even though new superconductive families and new T_c value are reported in the cuprate oxides, their structures become more and more complicated. Scientists expect new superconductors with simple structure for theory studying and device fabricating and well mechanic behavior for application. But the history stepping of superconductor discoveries seems to have its rule. In 2001 the discovery of superconductivity in magnesium diboride (Nagamatsu et al., 2001), a simple compound with only two elements and well metallic behavior, excite scientists again for studying alloy superconductors. It also opens an attractive application in the high power and superconductive electronics due to its transition

temperature (~ 40 K) far above liquid Helium, high critical current density (10^6 ~ 10^7 A/cm^2 at low temperatures and zero field), larger coherence length (ξ ~ 3 ~ 12 nm) than high temperature superconductors (HTSC), and the characteristic of transparent grain boundaries. Funnily, this compound had been synthesized in 1950s but its superconductivity was discovered until 2001. Fig. 2 shows the history diagram of discovering conventional superconductors, in which the points distribute closely along the fitting curve. Therefore it may be not surprising that the superconductivity of MgB_2 was disclosed until 2001 and superconductors with a transition temperature above liquid nitrogen boiling point may be found after 2060.

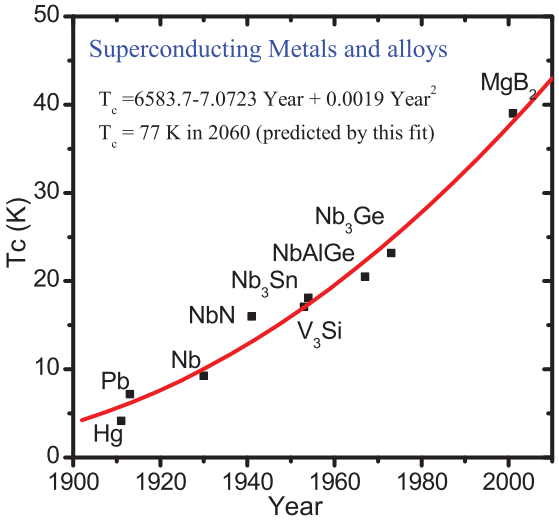

Fig. 2. The date dependence of critical temperature (T_c) for conventional superconductors.

1.2 Compound superconductors

Mixing one of superconductors mentioned above with other materials, we may obtain superconducting composite. Superconducting-nonsuperconducting composites or some granular superconducting materials with weak-link characteristics can be regarded as those composed of superconducting grains embedded in a non-superconducting host. The latter can be a normal metal, an insulator, a ferromagnet, a semiconductor, or a superconductor with lower transition temperature. Several reports suggested that these materials may exhibit novel properties (Shih et al., 1984; John & Lunbensky, 1985; Petrov et al., 1999; John & Lunbensky, 1986; Gillijns et al., 2007) different from their pure superconducting phases and be useful in practical applications. One striking feature of such materials is the existence of two superconductive transitions: a higher one at which the grains become superconducting but the matrix remains normal and a lower one at which the whole composite becomes superconducting but the critical current density is low. Another attractive feature is that the magnetic flux pinning and critical current density of superconducting composites are enhanced (Matsumoto et al., 1994; li Huang et al., 1996) at a low fraction of several non-superconductors. The most obvious application of these

materials is to make a superconducting fault current limiter (SFCL) because composite superconductors have a broad range of current-carrying capacity (Mamalis et al., 2001).
The superconducting material, MgB_2, which superconductivity at 39 K was discovered in 2001 by Akimitsu's group (Nagamatsu et al., 2001), has shown a huge potentiality of theory researches and applications for high-performance electronic devices and high-energy systems (Xi, 2008). Scientists believe that it will be the best material, up to now, to replace the traditional niobium (Nb) and Nb alloy superconductors working at the liquid helium temperature. Comparing with high-temperature superconducting oxides (HTSC), the glaring properties of MgB_2 include transparent boundaries without weak links (Larbalestier et al., 2001; Kambara et al., 2001), high carrier density, high energy gaps, high upper critical field, low mass density, low resistivity (Xi et al., 2007), and low anisotropy (Buzea & Yamashita, 2001). Owing to the strong links among MgB_2 grains, there is no much influence on its superconductivity when a sample was contaminated or doped by a small ratio. Experimental results reported by Wang's group (Wang et al., 2004) and Ma's group (Ma et al., 2006; Gao et al., 2008) showed that the critical current density and flux pinning in some doping were enhanced evidently. Several papers suggested also that there was no appreciable difference between a perfect MgB_2 sample and one with MgO or oxygen contamination, but the flux pinning was improved (Eom et al., 2001; Przybylski et al., 2003; Zeng et al., 2001; Liao et al., 2003). These characteristics interest us in studying compound MgB_2 superconductor. Mitsuta et al. (Matsuda et al., 2008) reported the properties of MgB_2/Al composite material with low and high fraction of MgB_2 particles and Siemons et al. (Siemons et al., 2008) demonstrated a disordered superconductor in MgB_2/MgO superstructures. But there are little data for superconducting MgB_2 composites when the content of non-superconducting phase is comparable to or even more than one of MgB_2 phase.

2. The synthesis and superconductivity of MgB_2-MgO compound superconductor

2.1 Structure, fabrication and physical properties of MgB_2

MgB_2 has a very simple AlB_2-type crystal structure, hexagonal symmetry (space group P6/mmm) with unit cell lattice parameters a = 3.08136(14) Å and c = 3.51782(17) Å, where the boron atoms form graphite-like sheets separated by hexagonal layers of Mg atoms. The magnesium atoms are located at the centre of hexagons formed by borons and donate their electrons to the boron planes. Similar to graphite, MgB_2 exhibits a strong anisotropy in the B-B lengths: the distance between the boron planes is significantly longer than the inplane B-B distance.
Magnesium diboride can be synthesized by a general solid phase reaction, by using boron and magnesium powders as the raw materials. However, there are two main problems to block the path for obtaining a high-quality MgB_2 superconducting material. Firstly, magnesium (Mg) has very high vapor pressure even below its melting point. Meanwhile there is a significant difference in the melting points between Mg and B (Mg: 651 ˚C and B: 2076 ˚C). Secondly, Mg is sensitive to oxygen and has a high oxidization tendency. On the other hand, the thermal decomposition at high temperature is also a problem in the synthesis of MgB_2. So a typical method is to wrap the samples with a metal foil, for example Ta, Nb, W, Mo, Hf, V, Fe etc., then sinter by high temperature and high Ar pressure.

Superconducting magnesium diboride wires are usually produced through the powder-in-tube (PIT) process.

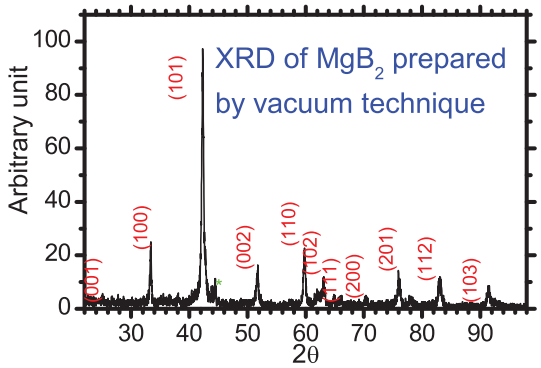

Fig. 3. X-ray diffraction pattern of superconducting MgB_2 sample synthesized by the vacuum technique.

Several reports showed that MgB_2 can be prepared by vacuum techniques rather than high-pressure atmosphere and metal wrapping. Fig. 3 shows the X-ray diffraction pattern of a superconducting MgB_2 sample synthesized by the vacuum technique in the authors' laboratory. It indicates that no MgO or other higher borides of magnesium (MgB_4, MgB_6, and MgB_{12}) are detected excluding the phase of MgB_2. Magnesium and boron powder were mixed at the mole ratio of Mg : B = 1 : 2, milled, pressed into pellets, then sintered in a vacuum furnace at about 5 Pa and 800 ˚C for 2 hours. The temperature dependence of resistance of the sample in the vicinity of transition temperature is shown in Fig. 4. The sample has well metallic behavior with a high transition temperature (39.2 K) and narrow transition width (0.3 K), a residual resistance ratio, RRR = R(300 K)/R(40 K) = 3.0, resistivity at 300 K estimated about 110 μΩ, and critical current density higher than 10^6 A /cm² at 5 K and zero field. These results indicate that high-quality superconducting MgB_2 bulks can be fabricated by the vacuum route. Comparing with high-temperature cuprate oxides and conventional superconductors, magnesium diboride exhibits several features listed below:

a. Highly critical temperature, T_c = 39 K, out of the limit of BCS theory.
b. High current carrier density: 1.7 ~ 2.8 × 10^{23} holes/cm^3, a value that is 2 orders higher than ones of YBCO and Nb_3Sn.
c. High and multiple energy gaps, $2\Delta_1$ = 17 ~ 19 meV, $2\Delta_2$ = 7 ~ 9 meV.
d. Highly critical current density, J_c (4.2 K, 0 T) > 10^7 A/cm^2.
e. Larger coherent lengths than HTSC, $\xi_{ab}(0)$ = 37 ~ 120 Å, $\xi_c(0)$ = 16 ~ 36 Å.
f. High Debye temperature, Θ_D ~ 900 K.
g. Negative pressure effect, dT_c/dp = – 1.1 ~ 2 K/GPa.
h. Positive Hall coefficient.
i. Very low resistivity at normal state.

These characteristics indicate that MgB_2 has the potentiality of superconductive applications in high-power field and electronic devices and will be the best material to replace the traditional niobium (Nb) and Nb alloy superconductors working at the liquid helium temperature.

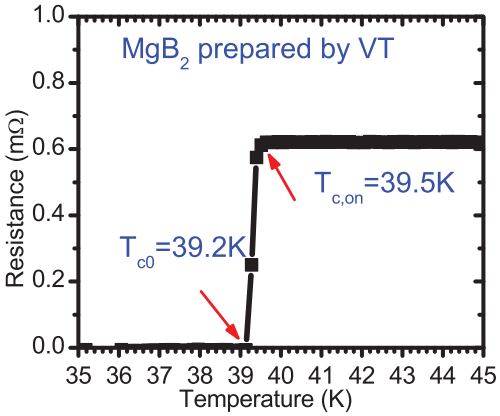

Fig. 4. The temperature dependence of resistance of superconducting MgB_2 sample synthesized by the vacuum technique in the vicinity of transition temperature.

2.2 Preparation of MgB_2-MgO compound superconductor

(Zhang et al., 2009)

Magnesium oxide (MgO) has the cubic crystal structure with a lattice parameter a=4.123 Å, which is close to one of MgB_2. Considering that MgO phase is easily to be formed in the process of preparing MgB_2 superconductor and a small amount of MgO contamination will not degrade evidently the superconductivity of MgB_2, the authors are interested in studying MgB_2-MgO Compounds. The superconducting MgB_2-MgO composite with about 75% mole concentration of MgO was synthesized *in situ* by a single-replacement reaction.

The magnesium powder (99% purity, 100 mesh) and B_2O_3 (99% purity, 60 mesh) were mixed at the mole ratio of Mg: B_2O_3=4:1, milled, and pressed into pellets with a diameter of 15 mm and thickness of 5 ~ 10 mm under a pressure of 100 MPa. These pellets were placed in a corundum crucible which was closed by an inner corundum cover, and then fired in a vacuum furnace by the sequential steps: pumping the vacuum chamber to 5 Pa, heating from room temperature to 400 °C and holding 2 hours, increasing temperature by a rate of greater than 5 °C/min to 600 °C and holding about 1 hour, then 800 °C × 1 hour for completing reaction, and, finally, cooling naturally to room temperature. A more detail of the synthesis processes can be found in China Patent No. ZL 200410017952.0, on July 19, 2006. That holding 2 hours at 400 °C was to vitrify B_2O_3 completely at a low temperature and 1 hour at 600 °C was to diffuse and mix Mg sufficiently with B_2O_3 below the melting point of magnesium. The furnace pressure was maintained at a value of lower than 5 Pa by a vacuum pump while sintering. The sample preparation can be described by a solid-state replacement reaction as follows:

$$4Mg + B_2O_3 = MgB_2 + 3MgO \quad (1)$$

The raw materials, Mg and B_2O_3, are available commercially and B_2O_3 powder is far cheaper than B. The small difference of melting points between Mg and B_2O_3 allows the sample synthesis without high pressure. The moderate reaction condition and the low-cost starting materials used in this method are favorable for practical application.

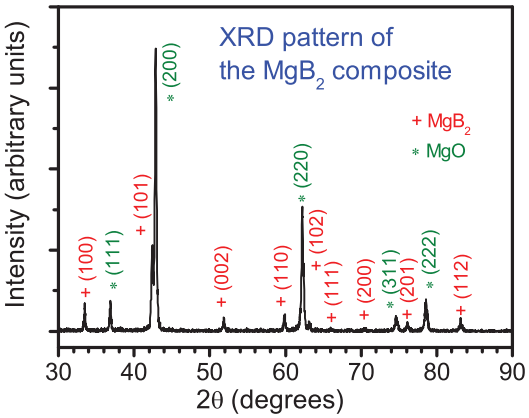

Fig. 5. X-ray diffraction pattern of superconducting MgB_2-MgO composite. Only diffraction peaks of MgB_2 and MgO phases were detected. The mass ratio of MgB_2 to MgO in the sample was calculated to 1:2.6.

The x-ray powder diffraction (XRD) pattern, as shown in Fig. 5, measured by Rigaku/D Max2000 x-ray diffractometer confirmed that only MgB_2 and MgO phases were detected in the composite and the mass ratio of MgB_2 to MgO was calculated to 1:2.6. Thus the mole fractions of MgB_2 and MgO in the composite were roughly 25% and 75% respectively. It means that the replacement reaction mentioned above was realized and complete. The samples exhibited black color, soft texture, and low density. The measured mass density was in the range of 1.4 ~ 2.3 g/cm^3, which is lower than the theoretical density, 2.625 g/cm^3 for MgB_2 and 3.585 g/cm^3 for MgO. The lattice parameters of MgB_2 calculated by XRD were a=3.0879 A° and c=3.5233 Å, which are consistent with ones of a pure MgB_2 sample.
The SEM image of the MgB_2-MgO sample at 15.0 kV and a magnification of 50,000 is shown in Fig. 6. The MgB_2 crystal grains, embedded dispersedly in MgO matrix, with a size of 100 ~300 nm can be observed obviously. MgO grains with a far smaller size than MgB_2 are filled in the boundaries and gaps among MgB_2 crystal grains. Such crystallite size and distribution indicate this is an ideal composite for studying the boundary and grain connection properties of MgB_2 superconductor.

2.3 Superconductivity in MgB_2 -MgO composite

(Zhang et al., 2009; 2010)
The resistance of the composite as a function of temperature was measured from 10 K to 300 K by the standard four-probe method in a close-cycle refrigeration system. Fig. 7 shows that the temperature dependence of resistance of the superconducting MgB_2-MgO composite and the pure MgB_2 bulk fabricated by the general solid reaction and vacuum sintering techniques. Comparing with the pure MgB_2 bulk, it is scientifically interesting that the composite exhibited an excellently electrical transport behavior and a narrow normal superconductive (N-S) transition. The onset transition temperature ($T_{c,on}$) and the critical transition temperature (T_c, at 50% of the onset transition resistance) were 38.0 K and 37.0 K respectively. The transition temperature width ΔT_c, which was calculated from 90% to 10%

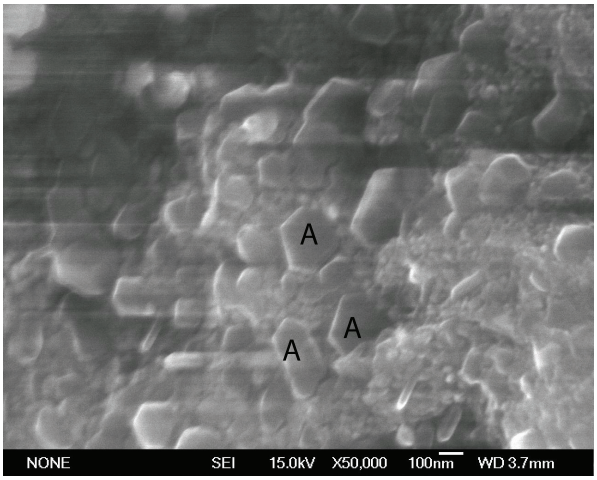

Fig. 6. (Zhang et al., 2009) Image of scanning electronic microscopy (SEM) of the superconducting MgB_2-MgO composite. Examples of MgB_2 crystal grains were labelled by the letter "A".

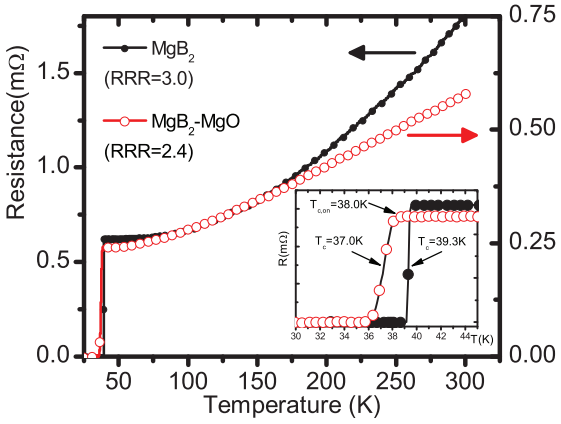

Fig. 7. (Zhang et al., 2010) Resistance vs temperature (R-T) curves of superconducting MgB_2-MgO composite and pure MgB_2 bulk. The inset shows their R-T curves in the vicinity of N-S transition.

of the onset transition resistance, was only 0.6 K. The residual resistance ratio, RRR=R(300 K)/R(40K), was 2.4, which was also comparable to the value (RRR=3.0) of our pure MgB_2 bulk samples.

Most experimental results showed that the transition temperature T_c of MgB_2 has weak dependence with the RRR value or high resistivity at normal state (Rowell, 2003), and the resistivity dependence with temperature at normal state can be pictured by the following formula.

$$\rho = \rho_0 + AT^n \quad (2)$$

The exponent n was measured to be 3 for a single crystal sample and ranged from 2 to 3 for the multicrystal. These R-T behaviors of MgB_2 at normal state may be explained by using the two-band model and considering π-band and σ-band contributions (Varshney, 2006). For our samples of pure MgB_2 multicrystal, the above formula is a good R-T expression and the exponent n was fitted to 2.3. But for the superconducting MgB_2-MgO composite, it seems not to be a proper approximation.

Zero resistance, which will be detected when continuous carrier's paths exist in a sample, may not mean the bulk superconducting characteristics. In Fig. 8, the temperature dependence of the real part (χ') and the imaginary one (χ'') of ac magnetic susceptibility is given at an ac field amplitude of 10 Oe and frequency of 777 Hz. It shows a diamagnetic transition at 37 K with a broad transition width. The imaginary part has a positive peak at 32 K and the saturation is observed at about 20 K. The diamagnetic transition at the temperature of 37 K is consistent with the R-T result. It means that the MgB_2-MgO composite is a bulk superconductor. Therefore, the composite may be utilized as a bulk superconductor or applied in superconductive function devices. One possible application is to make the superconducting fault current limiter (SFCL) because MgO has no obvious influence on the superconductivity of MgB_2 as well as the absence of chemical reaction between them. Composite superconductors have broad current carry and are considered the best material of SFCL (Mamalis et al., 2001). In addition, the composite implies a new potentiality of preparing MgB_2 superconductor when MgO is removed by some effective methods, for example, chemical wash or high-voltage static separation.

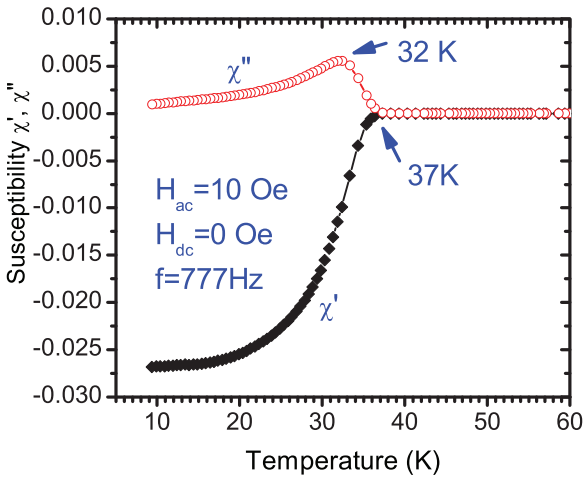

Fig. 8. Temperature dependence of the real component (χ') and the imaginary one (χ'') of ac magnetic susceptibility at the ac field amplitude 10 Oe and frequency 777 Hz. The magnitude of susceptibility was not normalized in this figure (Zhang et al., 2009).

3. Electric transport characteristics of MgB_2 -MgO composite

(Zhang et al., 2009; 2010)

3.1 Effective media and statistical percolation theories

MgO is an insulator and MgB_2 is a good conductor with low resistivity. The conductivity of MgB_2-MgO composite belongs to a metal-insulator transport problem. A metal-insulator conductance is generally pictured by effective media theories (EMT) (Nan, 1993) or percolation theories (PT) (Lux, 1993; Kirkpatrick, 1973). There are the following four typical expressions, symmetric Bruggeman (SB) approximation of EMT, Clausius-Mossotti (CM) function of EMT, statistical percolation (SP) model, and McLachlan (ML) phenomenological equation (McLachlan et al., 2003) to explain the electrical conductivity (σ_m) of a metal-insulator mixture.

$$\begin{cases} \sigma_m^{SB} = \dfrac{1}{2}[(3\phi-1)\sigma_i], \quad \phi > \dfrac{1}{3}, & \text{SBapprox.} \\ \sigma_m^{CM} = \dfrac{2\phi}{3-\phi}\sigma_i, \quad \phi >= 0, & \text{CMapprox.} \\ \sigma_m^{SP} = \sigma_i(\phi-\phi_c)^{\mu}, \quad \mu = 1.7 \sim 1.9, & \text{SPmodel} \\ \sigma_m^{ML} = \sigma_i \dfrac{(\phi-\phi_c)^t}{(1-\phi_c)^t}, \quad t = 1.5 \sim 3.1, & \text{MLequation} \end{cases}$$

Here ϕ is the volume fraction of the metal phase, ϕ_c is the critical volume fraction with a value of 0.16 ± 0.02 in the 3D lattice site percolation model (Zallen, 1983), σ_i is the electric conductivity of the metal phase, μ and t are critical exponents. Fig. 9 shows normalized conductivities of a metal-insulator composite as a function of volume fraction calculated by SB, CM, SP, and ML approximations. The inset gives the measured conductivity of W-Al_2O_3 composite (Abeles et al., 1975), and fitted data by the SP estimation and ML approximation. At a low volume fraction of the metal phase, the SP model gives the best explanation for the conductivity of a metal-insulator mixture. The effective media theories can only give qualitative results, owing to its simplicity. When the host phase is an insulator, McLachlan (ML) phenomenological equation shows accordant results with the statistical percolation (SP) model at low (ϕ -ϕ_c). In fact, ML conductivity function may be understood as the normalization expression of SP model.

3.2 Conductivity vs. temperature of MgB_2 composite

The electrical transport behavior of a metal-insulator composite can be described well by the statistical percolation model. But, as we know that the percolation model is a pure geometrical problem, it can not give a conductivity expression with temperature. However, if the temperature dependence of volume fraction, (ϕ -ϕ_c), could be obtained, we believe that SP model shall still be an simple and practical approach to understand the electrical transport behavior of a metal-insulator composite.

Thermal expansion measurements indicated that lattice parameters of MgB_2 have strong dependence on temperature, $\alpha_a \approx 5.4 \times 10^{-6}\,K^{-1}$, $\alpha_c \approx 11.4 \times 10^{-6}\,K^{-1}$, and $\alpha \approx 8 \times 10^{-6}\,K^{-1}$ for a multicrystal sample (Lortz et al., 2003; Jorgensen et al., 2001; Neumeier et al., 2005). It will result in the temperature dependence of (ϕ – ϕ_c) and then influence on the conductivity of

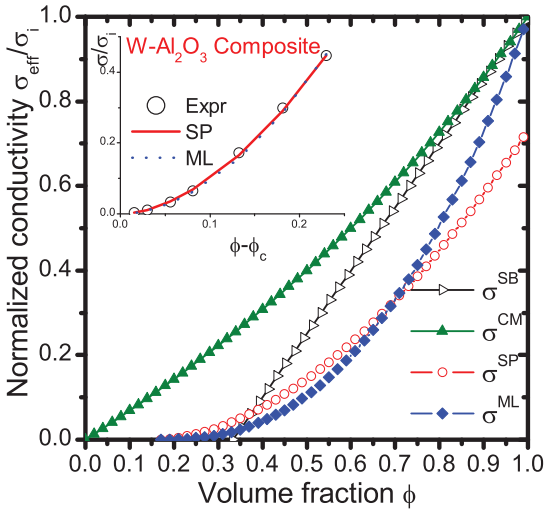

Fig. 9. The volume fraction dependence of composite's conductivity calculated by SB, CM, SP, and ML approximations. The inset shows the normalized conductivity of W-Al_2O_3 composite: "○" refers to the experimental data (Abeles et al., 1975), "—" SP result at μ=1.8, "…" ML approximation at t=1.8.

the metal-insulator mixture. According to measured mass density and the scanning electron microscope (SEM) image of the composite (Zhang et al., 2009), we noticed that the composite is not dense and the host phase is an insulator (MgO) with crystal grain sizes of far smaller than ones of the metal phase (MgB_2). Both of MgO particles and the holes in the composite can be regarded as an insulating background for superconducting MgB_2 grains to embed. The grain size variation of MgO is neglected and the grain size variation of MgB_2 with temperature has no influence on the whole volume of mixture. Thus a model of the temperature dependence of composite volume fraction is proposed and shown in Fig.10. Suppose V is the total volume of mixture, r_{i0} and $r_i(T)$ are the i^{th} grain's radius of MgB_2 at temperature 0 K and T K respectively.

Supposing all MgB_2 grains are spherical for simplifying calculation, then the volume fractions of metal phase at 0 K and T K are:

$$\phi_0 = \phi(0) = \frac{1}{V}\sum(\frac{4}{3}\pi r_{i0}^3); T = 0K \tag{3}$$

$$\phi = \phi(T) = \frac{1}{V}\sum_i(\frac{4}{3}\pi r_i^3(T)) \tag{4}$$

Grain radiuses of conductive phase satisfy with the normal distribution law.

$$n(r) = \frac{1}{r\sqrt{2\pi}\delta}\exp\left(-\left[\frac{\ln(r/r_0)}{\sqrt{2}\delta}\right]^2\right) \tag{5}$$

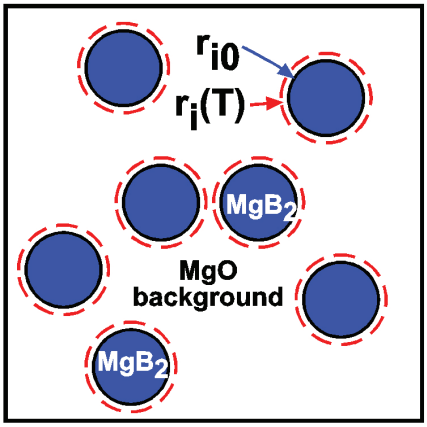

Fig. 10. Diagram of a simple model for the temperature dependence of composite volume fraction (Zhang et al., 2010).

Here r is the effective grain radius, r_0 is the effective mean radius, and δ is the standard deviation. Hence, the volume fraction can be calculated by the average radius: r_0 at 0 K and r at T K. Assume the grain number of the conductive phase is N and the grain number per volume is n, then

$$\phi_0 = \phi(0) = \frac{N}{V}\frac{4}{3}\pi r_0^3 = \frac{4}{3}n\pi r_0^3 \tag{6}$$

$$\phi = \phi(T) = \frac{N}{V}\frac{4}{3}\pi r^3(T) = \frac{4}{3}n\pi r^3(T) \tag{7}$$

The thermal expansion coefficient of MgB_2 satisfies well with Grüneisen relationship (Neumeier et al., 2005; Jorgensen et al., 2001; Xue et al., 2005):

$$\beta = 3\alpha = \gamma_G \kappa_T C_V / V \tag{8}$$

Where β is the volume expansivity of MgB_2, α is its linear expansivity, γ_G Grüneisen constant, κ_T isothermal compressibility and almost independence with temperature, C_V specific heat at constant volume. Specific heat C_V of MgB_2 at normal state as a function of temperature can be written as:

$$C_V = \gamma T + \beta_3 T^3 + \beta_5 T^5 \tag{9}$$

Here γ, β_3, β_5 are constant. Wang et al. (Wang et al., 2001) measured specific heat of MgB_2 from 2 K to 300 K and showed Sommerfeld constant $\gamma = 0.89 \pm 0.05$ mJ/K^{2}g (2.7 mJ/K^{2}mol). Obviously, the first term is the contribution of normal electrons and is important only at very low temperature. The second term is offered by phonons. The third one is small and influential only at high temperature. At the normal state of MgB_2, electron's term can be ignored.

Then

$$C_V \approx \beta_3 T^3 + \beta_5 T^5 \tag{10}$$

and

$$\alpha = \gamma_G \kappa_T C_V / (3V) \approx \frac{\gamma_G \kappa_T}{3V}(\beta_3 T^3 + \beta_5 T^5) . \tag{11}$$

Noticing that the grain radius variation is a small quantity, the temperature dependence of average grain radius, r(T), can be derived.

$$\frac{1}{r}\frac{\partial r}{\partial T} \approx \frac{\gamma_G \kappa_T}{3V}(\beta_3 T^3 + \beta_5 T^5) \tag{12}$$

$$r(T) \approx r_0 \left[1 + \frac{\gamma_G \kappa_T}{3V}\left(\frac{1}{4}\beta_3 T^4 + \frac{1}{6}\beta_5 T^6 \right) \right] \tag{13}$$

Here ρ_0 is the average radius at 0 K. Thus the volume fraction can be rewritten as,

$$\begin{aligned} \phi(T) &= \frac{4}{3} n\pi r^3(T) \\ &= \frac{4}{3} n\pi r_0^3 \left[1 + \frac{\gamma_G \kappa_T}{3V}\left(\frac{1}{4}\beta_3 T^4 + \frac{1}{6}\beta_5 T^6 \right) \right]^3 \\ &\approx \phi_0 \left[1 + \frac{\gamma_G \kappa_T}{V}\left(\frac{1}{4}\beta_3 T^4 + \frac{1}{6}\beta_5 T^6 \right) \right] \\ &\equiv \phi_0 (1 + \Delta\phi) \end{aligned} \tag{14}$$

Due to the volume fraction variation is very small ($\Delta\phi \ll 1$), the conductivity approximation of SP model is modified.

$$\begin{aligned} \sigma_m^{SPT} &= (\phi_0 - \phi_c)^{\mu} \sigma_i \left(1 + \frac{\Delta\phi}{\phi_0 - \phi_c} \right)^{\mu} \\ &\approx (\phi_0 - \phi_c)^{\mu} \sigma_i(T) \left[1 + \frac{\mu \gamma_G \kappa_T / V}{\phi_0 - \phi_c}\left(\frac{1}{4}\beta_3 T^4 + \frac{1}{6}\beta_5 T^6 \right) \right] \end{aligned} \tag{15}$$

We name this expression conductivity approximation of statistical percolation model with temperature (SPT) (Zhang et al., 2010) for a metal-insulator composite. Considering the electrical resistivity of normal-state MgB_2, we have resistivity expression of MgB_2-MgO composite as a function of temperature.

$$\rho_m^{SPT} \approx (\phi_0 - \phi_c)^{-\mu} \left(\rho_{i0} + bT^n \right) \left[1 - \frac{\mu \gamma_G \kappa_T / V}{\phi_0 - \phi_c}\left(\frac{1}{4}\beta_3 T^4 + \frac{1}{6}\beta_5 T^6 \right) \right] \tag{16}$$

If we define,

$$\begin{cases} \rho_0 = (\phi_0 - \phi_c)^{-\mu} \rho_{i0} \\ \alpha_n = (\phi_0 - \phi_c)^{-\mu} b \\ \alpha_e = -\dfrac{(\phi_0 - \phi_c)^{-\mu} \rho_{i0}}{4V(\phi_0 - \phi_c)} \mu \gamma_G \kappa_T \beta_3 \end{cases} \quad (17)$$

Then the temperature dependence of resistivity of the superconducting MgB_2-MgO composite has a simple power-law expression as,

$$\rho_m^{SPT} = \rho_0 + \alpha_n T^n + \alpha_e T^4 + \alpha_c T^6 \quad (18)$$

Where ρ_0 relates to the residual resistivity of composite, $\alpha_c T^6$ is a small correction term for the high-power terms of expression (18) and α_c is called as the correction parameter. Fig. 11 shows the fitting resistance vs. temperature of MgB_2 composite with the above expression. Its inset shows that the optimal exponent, n=2.3, which is well consistent with one in the resistivity expression for our MgB_2 multicrystal samples. The coefficient of determination (COD), R-square (R^2), is higher than 0.99996 and the reduced chi-square value, χ^2/DoF, is low to 3.83×10^{-7}. Therefore, the SPT approximation can picture well the conductivity of the superconducting MgB_2-MgO composite at its normal state. It will also be a proper conductivity expression for a metal-insulator composite in which the grain size of metal phase is far larger than the insulator.

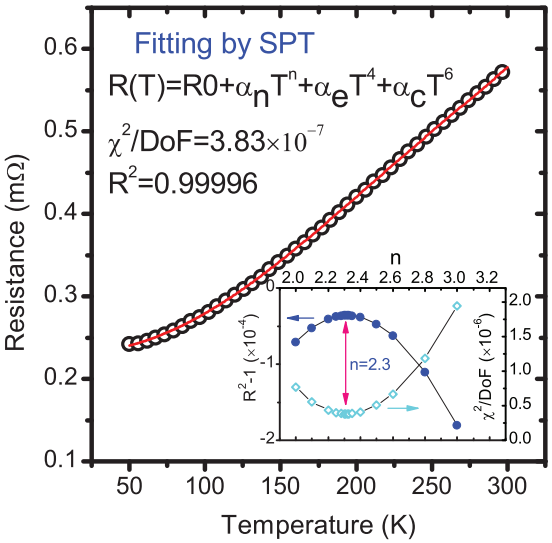

Fig. 11. Fitting the resistance-temperature data of superconducting MgB_2-MgO composite from 50 K to 300 K by the SPT approximation. Solid circle symbols refer to experimental values and the solid line refers to the fitting result. The inset is the fitting R-square and χ^2/DoF at n range from 2.0 to 2.4. The maximum R-square and minimum of χ^2/DoF were obtained at n=2.3 (Zhang et al., 2010).

4. Applications of superconducting MgB_2 composite

The fault current limiter (FCL) is an important components in the electric power system for running safely and stably. In general, it can be performed by power-electronic circuits or positive temperature coefficient (PTC) thermistors. But for a large current or fast response system, the superconducting fault current limiter (SFCL) is the best choice. A composite superconductor is more attractive than a pure-phase superconductor for the application of SFCL because of the broadly current-carrying capacity and mechanical performance by doping. Several superconducting composites have the so-called history effect (HE) in the current-voltage (IV) sweep curve. Using the history effect, a resistive type SFCL (RSFCL) can be easily realized by superconducting composites. HE refers to that the critical current density (j_c) of a superconductor has different values detected in a current sweeping cycle or magnetic field cycle. Fig. 12 shows the current-voltage characteristics of the MgB_2-MgO composite. An anticlockwise HE is observed obviously in the IV curve with two critical currents, I_{c+} = 220 mA and I_{c-}=180 mA.

The HE of the superconducting MgB_2-MgO composite can be understood using the Stewart-McCumber (SM) model for Josephson junctions. Using the history effect, a resistive type SFCL may be designed as shown in Fig. 13. Normally, system is working at a current far lower than the low critical current (I_{c-}) at the superconductive state. When a fault occurs then the transport current increases to exceed the up critical current (I_{c+}), the superconducting MgB_2-MgO composite becomes a normal conductor with a high resistance (R_{RSFCL}). The R_{RSFCL} will restrain the transport current to a limit value. After the system is recovering, the line current decreases to be lower than I_{c-} and the SFCL return to work at the superconductive state then the current is normal.

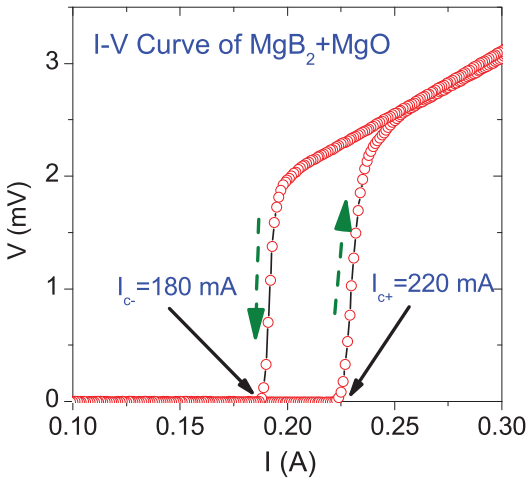

Fig. 12. The current-voltage characteristics of the MgB_2-MgO composite. The current sweeps from 0 mA to 400 mA by a step of 1 mA per 0.1 S, then returns from 400 mA to 0 mA by the same step.

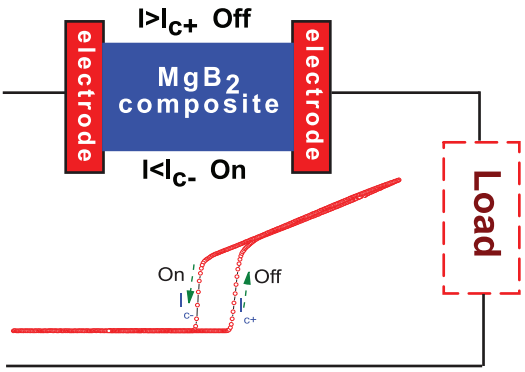

Fig. 13. Diagram for realizing the resistive type SFCL by the superconducting MgB_2-MgO composite.

5. Conclusions

In summary, this chapter introduce a composite superconductor, MgB_2-MgO, which was prepared by a solid-state replacement reaction and vacuum sintering technique. Even the mole fraction of MgO phase was estimated about 75%, the composite exhibited a metallic transport behavior with low resistivity and superconductivity at a high temperature (38.0 K) comparable to a pure-phased MgB_2 sample (39 K). The composite superconductor has the history effect in the current-voltage curve. The results indicate that MgB_2 superconductor can tolerance a high content of insulating contamination and the superconducting MgB_2 MgO composite can be utilized for the superconducting fault current limiter (SFCL). The electrical transport features of the composite are explained by using the statistical percolation model and a conductivity expression with temperature for the metal-insulator MgB_2 composite is given (Zhang et al., 2010),

$$\sigma_m^{SPT} = (\phi_0 - \phi_c)^{\mu}\sigma_i(T)[1 + \frac{\mu\gamma_G\kappa_T / V}{\phi_0 - \phi_c}(\frac{1}{4}\beta_3 T^4 + \frac{1}{6}\beta_5 T^6)].$$

It is considered to be proper for other metal-insulator compounds when the grain size or thermal expansivity of the insulator is far smaller than the metal grain.

6. References

Abeles, B., Pinch, H. L. & Gittleman, J. L. (1975). *Phys. Rev. Lett.* 35: 247.
Ashcroft, N. W. (1968). *Phys. Rev. Lett.* 21: 1748.
Bednorz, J. G. & Müller, K. A. (1986). *Z. Phys. B* 64: 189.
Buzea, C. & Yamashita, T. (2001). *Supercond. Sci. Technol.* 14: R115.
Eom, C. B., Lee, M. K., Choi, J. H., Belenky, L. J., Song, X., Cooley, L. D., Naus, M. T., Patnaik, S., Jiang, J., Rikel, M., Polyanskii, A., Gurevich, A., Cai, X. Y., Bu, S. D., Babcock, S. E., Hellstrom, E. E., Larbalestier, D. C., Rogado, N., Regan, K. A., Hayward, M. A., He, T., Slusky, J. S., Inumaru, K., Haas, M. K. & Cava, R. J. (2001). *Nature* 411: 558.

Gao, Z., Ma, Y., Zhang, X., Wang, D., Wang, J., Awaji, S., Watanabe, K. & Liu, B. (2008). *Supercond. Sci. Technol.* 21: 105020.

Gillijns, W., Aladyshkin, A. Y., Silhanek, A. V. & Moshchalkov, V. V. (2007). *Phys. Rev. B* 76: 060503(R).

John, S. & Lunbensky, T. C. (1985). *Phys. Rev. Lett.* 55: 1014.

John, S. & Lunbensky, T. C. (1986). *Phys. Rev. B* 34: 4815.

Jorgensen, J. D., Hinks, D. G. & Short, S. (2001). *Phys. Rev. B* 63: 224522.

Kambara, M., Babu, N. H., Sadki, E. S., Cooper, J. R., Minami, H., Cardwell, D. A., Campbell, A. M. & Inoue, I. H. (2001). *Supercond. Sci. Technol.* 14: L5.

Kamihara, Y., Hiramatsu, H., Hirano, M., Kawamura, R., Yanagi, H., Kamiya, T. & Hosono, H. (2006). *J. Am. Chem. Soc.* 128: 10012.

Kamihara, Y., Watanabe, T., Hirano, M. & Hosono, H. (2008). *J. Am. Chem. Soc.* 130: 3296.

Kirkpatrick, S. (1973). *Rev. Mod. Phys.* 45: 574.

Larbalestier, D. C., Cooley, L. D., Rikel, M., Polyanskii, A. A., Jiang, J., Patnaik, S., Cai, X. Y., Feldmann, D. M., Gurevich, A., Squitieri, A. A., Naus, M. T., Eom, C. B., Hellstrom, E. E., Cava, R. J., Regan, K. A., Rogado, N., Hayward, M. A., He, T., Slusky, J. S., Khalifah, P., Inumaru, K. & Haas, M. (2001). *Nature* 410: 186.

li Huang, S., Dew-Hughes, D., Zheng, D. N. & Jenkins, R. (1996). *Supercond. Sci. Technol.* 9: 368.

Liao, X. Z., Serquis, A., Zhu, Y. T., Huang, J. Y., Civale, L., Peterson, D. E., Mueller, F. M. & Xu, H. F. (2003). *J. Appl. Phys.* 93: 6208.

Lortz, R., Meingast, C., Ernst, E., Renker, B., Lawrie, D. D. & Frank, J. P. (2003). *J. Low Temp. Phys.* 131: 1101.

Lux, F. (1993). *J. Materials Science* 28: 285.

Ma, Y., Zhang, X., Nishijima, G., Watanabe, K., Awaji, S. & Bai, X. (2006). *App. Phys. Lett.* 88: 072502.

Mamalis, A. G., Ovchinnikov, S. G., Petrov, M. I., Balaev, D. A., Shaihutdinov, K. A., Gohfeld, D. M., Kharlamova, S. A. & Vottea, I. N. (2001). *Physica C* 364-365: 174.

Matsuda, K., Nishimura, K., Ikeno, S., Mori, K., Aoyama, S., Yabumoto, Y., Hishinuma, Y., Mullerova, I., Frank, L., Yurchenko, V. V. & Johansen, T. H. (2008). *J. Phys.: Conference Series* 97: 012230.

Matsumoto, K., Takewaki, H., Tanaka, Y., Miura, O., Yamafuji, K., Funaki, K., Iwakuma, M. & Matsushita, T. (1994). *Appl. Phys. Lett.* 64: 115.

McLachlan, D. S., Chiteme, C., Heiss, W. D. &Wu, J. (2003). *Physica B* 338: 261.

Nagamatsu, J., Nakagawa, N., Muranaka, T., Zenitani, Y. & Akimitsu, J. (2001). *Nature* 410: 63.

Nan, C.-W. (1993). *Progr. Mat. Sci.* 37: 1.

Neumeier, J. J., Tomita, T., Debessai, M., Schilling, J. S., Barnes, P.W., Hinks, D. G. & Jorgensen, J. D. (2005). *Phys. Rev. B* 72: 220505(R).

Petrov, M. I., Balaev, D. A., Gohfeld, D. M., Ospishchev, S. V., Shaihudtinov, K. A. & Aleksandrov, K. S. (1999). Physica *C* 314: 51.

Przybylski, K., Stobierski, L., Chmist, J. & Kolodziejczyk, A. (2003). *Physica C* 387: 148.

Ren, Z. A., Lu,W., Yang, J., Yi,W., Li, X. L. S. Z. C., Che, G. C., Dong, X. L., Sun, L. L., Zhou, F. & Zhao, Z. X. (2008). *Chin Phys. Lett.* 25: 2215.

Rowell, J. M. (2003). *Supercond. Sci. Technol.* 16: R17.

Shih,W. Y., Ebner, C. & Stroud, D. (1984). *Phys. Rev. B* 30: 134.

Siemons,W., Steiner, M. A., Koster, G., Blank, D. H. A., Beasley, M. R. & Kapitulnik, A. (2008). *Phys. Rev. B* 77: 174506.

Takahashi, H., Igawa, K., Arii, K., Kamihara, Y. & andH. Hosono, M. H. (2008). *Nature* 453: 376.

Varshney, D. (2006). *Supercond. Sci. Technol.* 19: 685.

Wang, X. L., Soltanian, S., James, M., Qin, M. J., Horvat, J., Yao, Q. W., Liu, H. K. & Dou, S. X. (2004). *Physica C* 408C410: 63.

Wang, Y., Plackowski, T. & Junod, A. (2001). *Physica C* 355: 179.

Xi, X. X. (2008). *Rep. Prog. Phys.* 71: 116501.

Xi, X. X., Pogrebnyakov, A. V., Xu, S. Y., Chen, K., Cui, Y., Maertz, E. C., Zhuang, C. G., Li, Q., Lamborn, D. R., Redwing, J. M., Liu, Z. K., Soukiassian, A., Schlom, D. G., Weng, X. J., Dickey, E. C., Chen, Y. B., Tian, W., Pan, X. Q., Cybart, S. A. & Dynes, R. C. (2007). *Physica C* 456: 22.

Xue, Y., Asada, S., Hosomichi, A., Naher, S., Xue, J., Kaneko, H., Suzuki, H., Muranaka, T. & Akimitsu, J. (2005). *J. Low Temp. Phys.* 138: 1105.

Zallen, R. (1983). *The physics of amorphous solids*, Wley, New York.

Zeng, X. H., Sukiasyan, A., Xi, X. X., Hu, Y. F.,Wertz, E., Li, Q., Tian,W., Sun, H. P., Pan, X. Q., Lettieri, J., Schlom, D. G., Brubaker, C. O., Liu, Z.-K. & Li, Q. (2001). *Appl. Phys. Lett.* 79: 1840.

Zhang, Y. B., Zeng, M., Gao, Z. S., Liu, J., Zhu, H. M. & Zhou, S. P. (2009). *J. Supercond. Nov. Magn.* 22: 729.

Zhang, Y. B., Zhou, D. F., Lv, Z. X., Deng, Z. Y., Cai, C. B. & Zhou, S. P. (2010). *J. Appl. Phys.* 107: 123907.

6

Superconducting Properties of Carbonaceous Chemical Doped MgB_2

Wenxian Li and Shi-Xue Dou
University of Wollongong
Australia

1. Introduction

The discovery of superconductivity in magnesium diboride (MgB_2: 39 K, in January 2001) (Nagamatsu et al., 2001) has generated enormous interest and excitement in the superconductivity community and the world in general, but especially among researchers into superconductivity in non-oxide and boron related compounds. MgB_2 possesses an AlB_2-type hexagonal structure (space group *P6/mmm*) with alternating boron honeycomb planes and magnesium triangular planes, as shown in Fig. 1. Each Mg atom is located at the center of a hexagon formed by boron, and it donates its electrons to the boron planes; hence, the B-B bonding is strongly anisotropic. The unit cell parameters are a = 0.3086 nm and c = 0.3524 nm at room temperature. These values of lattice parameters for MgB_2 are in the middle of the values of lattice parameters of AlB_2-type compounds. Owing to the simple hexagonal structure with space group *P6/mmm*, four optical modes at the Γ point of the Brillouin zone are predicted for MgB_2 (An & Pickett, 2001): a silent B_{1g} mode (at 87.1 meV, ~700 cm^{-1}), the E_{2g} Raman mode (at 74.5 meV, ~600 cm^{-1}), and the infrared active E_{1u} (at 40.7 meV, ~330 cm^{-1}) and A_{2u} (at 49.8 meV, ~400 cm^{-1}) modes. The E_{2g} mode is responsible for the high transition temperature, T_c, in MgB_2.

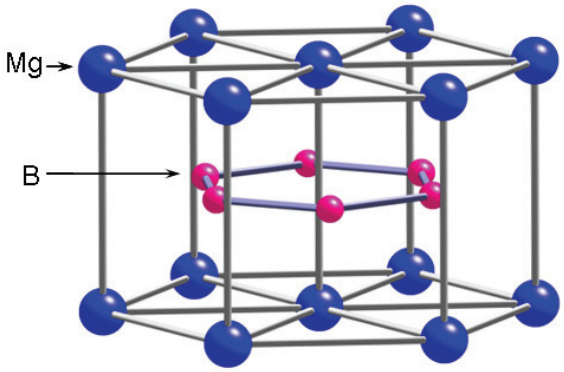

Fig. 1. Hexagonal structure of MgB_2 with space group *P6/mmm* (Nagamatsu et al., 2001)

Further studies based on a number of experimental techniques, such as angle-resolved photoemission spectroscopy (ARPES), the de Haas-van Alphen effect, and Hall resistivity

measurements, have found that MgB_2 exhibits a rich multiple-band structure. These results are in agreement with band structure calculations and reveal strongly two-dimensional $sp_xp_y(\sigma)$ bands, as well as three-dimensional $p_z(\pi)$ bands. The identification of MgB_2 as a two gap superconductor has resulted in much research associated with the spectroscopy of this material. It has become generally accepted that the larger gap is associated with the 2D σ bands arising from the boron planes, which has the value of $\Delta_\sigma \cong 7.069$ meV, while the 3D π bands have a gap of $\Delta_\pi \cong 2.70$ meV (Bouquet et al., 2001; Kortus et al., 2001).

MgB_2 has been fabricated in bulks, single crystals, thin films, tapes, and wires for different applications (Eisterer & Weber, 2009). In addition to the relatively high critical transition temperature, T_c, and the simple crystal structure, MgB_2 possesses a large coherence length, high critical current density, and transparency of grain boundaries to current flow. The *in-situ* route seems to be the most promising method to improve the upper critical field, H_{c2}, and the critical current density, J_c, performance of MgB_2. MgB_2 is a promising superconductor for high-magnetic field applications because of its already high J_c. The grain boundaries in MgB_2 do not significantly degrade J_c and even serve as pinning centers, which is different from the weak-link effects in high-T_c superconductors.

For single-gap dirty limit superconductors, the upper critical field $H_{c2}(0) = 0.69T_c(\mathrm{d}H_{c2}/\mathrm{d}T)_{Tc}$, and $(\mathrm{d}_{Hc2}/\mathrm{d}T)_{Tc} \propto \rho_n$, where ρ_n is the normal state resistivity (Werthame et al., 1966); therefore, H_{c2} increases with ρ_n, which can be achieved by adding impurities and defects into the superconductor. Gurevich pointed out that the two-band superconductor MgB_2 can be understood as a weakly-coupled bilayer in which two thin films corresponding to the σ and π bands are in contact through Josephson coupling (Gurevich, 2007). Using the dirty-limit, weak-coupling, multiband Bardeen Cooper Schrieffer (BCS) model and taking into account both interband and intraband scattering by nonmagnetic impurities, Gurevich showed that the temperature dependence of $H_{c2}(T)$ is influenced by whether the σ bands or π bands are dirtier, making it very different from the temperature dependence in the one-band theory (Gurevich, 2003). The global $H_{c2}(T)$ of the bilayer is dominated by the layer with the higher H_{c2}. If the π layer is dirtier, it will have higher H_{c2} at low temperature, even though its T_c is much lower. As a result, an upturn in the global $H_{c2}(T)$ occurs at low temperature. $H_{c2}(0)$ of MgB_2 can exceed $0.69T_c(\mathrm{d}H_{c2}/\mathrm{d}T)_{Tc}$ considerably because of the existence of the two bands. Considering the electron–phonon coupling effect, Gurevich argued that the strong coupling paramagnetic limit in MgB_2 can be as high as 130 T; thus, there is still room for further enhancement of H_{c2} by engineering the σ- and π-band scattering (Gurevich, 2007). The high H_{c2} in MgB_2 is very attractive for high-magnetic-field applications. The H_{c2} behavior described by Gurevich has been observed in experimental results. For example, Braccini et al. observed different types of temperature dependence of H_{c2}, including the anomalous upturn at low temperature, reflecting different multiband scattering in thin film samples from various groups, with disorder introduced in different ways. The value of H_{c2} in carbon-doped thin films has reached over 60 T at low temperature, approaching the BCS paramagnetic limit of 65 T (Braccini et al., 2005).

The depairing current density, J_d, is ~8.7×10^8 A/cm^2 for pure MgB_2, as estimated from the Ginzburg-Landau (GL) formula:

$$J_d = \Phi_0 / \left[3 / \left(\sqrt{3} \right) \pi \mu_0 \lambda^2(T) \xi(T) \right] \tag{1}$$

where Φ_0 is the flux quantum, μ_0 the permeability of vacuum, λ the penetration depth, and ξ the coherence length. The self-field critical current density, $J_c(0)$, in the best connected

samples indicates the ultimate current-carrying potential in the superconductor, which has been reported as 3.5×10^7 A/cm² at 4.2 K and 1.6×10^8 A/cm² at 2 K in clean films made by hybrid physical-chemical vapour deposition (HPCVD). These values are about 4% and 20% of the J_d values. Compared with these values, the $J_c(0)$ values in polycrystalline MgB_2 bulks and wires are very low and have great potential to be improved.

It was pointed out soon after the discovery of MgB_2 that clean grain boundaries are, in principle, no obstacles for supercurrents (Finnemore et al., 2001; Kawano et al., 2001). Such obstacles are known as weak links in the high temperature superconductors. Nevertheless, the connections between the grains remain delicate, since dirty grain boundaries potentially reduce the critical current. Insulating phases have been found at the grain boundaries, consisting of MgO, boron oxides, or boron carbide. Cracks, porosity, or normal conducting phases can further reduce the cross-section over which supercurrents effectively flow. The density of *in-situ* prepared MgB_2 is typically only about half (or less) of its theoretical value, which leads to high porosity.

The *in-situ* route seems to be the most promising method to improve the H_{c2} and J_c performance of MgB_2. Magnesium or MgH_2 reacts with boron after mixing and compacting of these precursor powders. MgB_2 samples with small grains of poor crystallinity can be obtained at low processing temperatures, resulting in strong pinning and high H_{c2}. The stoichiometry can be modified to yield samples with magnesium deficiency, which induces lattice strain, decreases T_c, and increases H_{c2}. An excess of magnesium in the starting powders may compensate the loss of magnesium due to evaporation or due to a reaction with other elements (e.g. with oxygen or with the sheath material). The precursor powders are very important for the properties of the final samples (Yamada et al., 2004). They should be clean to ensure good grain connectivity. The grain size is strongly influenced by the grain sizes of the precursor powders, especially of the boron powders. Ball milling or mechanical alloying of the precursor powders reduces the grain size and improves the critical current.

Chemical or compound doping changes the reaction kinetics and therefore influences the grain growth, the formation of secondary phases, the density, and the stoichiometry. Carbon doping can be easily performed by the addition of B_4C, carbon, carbon nanotubes, nanodiamonds, NbC, SiC, or organic compounds. SiC is by far the most popular dopant, because carbon can be doped into MgB_2 at low temperatures (600 °C), according to the dual reaction model (Dou et al., 2007). Higher processing temperatures are necessary for most of the other carbon sources, leading to more grain growth and worse pinning. However, comparable results have also been obtained with nanoscale carbon powder, stearic acid, and carbon nanotubes. It should be noted that the electromagnetic properties of MgB_2 are greatly dependent on the starting materials, shielding metals, processing techniques, and measurements. That is why the irreversibility field (H_{irr}), H_{c2}, and J_c values are different from one batch to another, even for pristine samples, as shown in the figures in this text. All the J_c values are based on the transport measurements reported in this chapter.

2. Nanosized carbon doping effects

The carbon atom has one more electron than boron, and the two-gap feature of MgB_2 can be modified if the extra electron is interposed properly into the system. Fortunately, the carbon atoms show strong substitution effects on the boron sites, both theoretically and experimentally, ranging from 1.225% to 30%. As a result, the enhancement of H_{irr}, H_{c2}, and J_c can be achieved by a controlled carbon doping. The T_c decreases monotonically with

increasing carbon content in the full investigated range of substitution. By adjusting the nominal composition, T_c of substituted crystals can be tuned over a wide temperature range between 10 and 39 K. However, carbon solubility and the effects of carbon doping on T_c vary significantly due to differences in the precursor materials, fabrication techniques, and processing conditions used, because polycrystalline carbon substituted samples may contain significant amounts of impurity phases and the nominal content is assumed most often to be equal to the actual one. Avdeev et al. first suggested the relationship between carbon concentration and lattice parameters. The level of C substitution, x, in the formula $Mg(B_{1-x}C_x)_2$, can be estimated as $x = 7.5\Delta(c/a)$, where $\Delta(c/a)$ is the change in c/a compared to a pure sample (Avdeev et al., 2003).

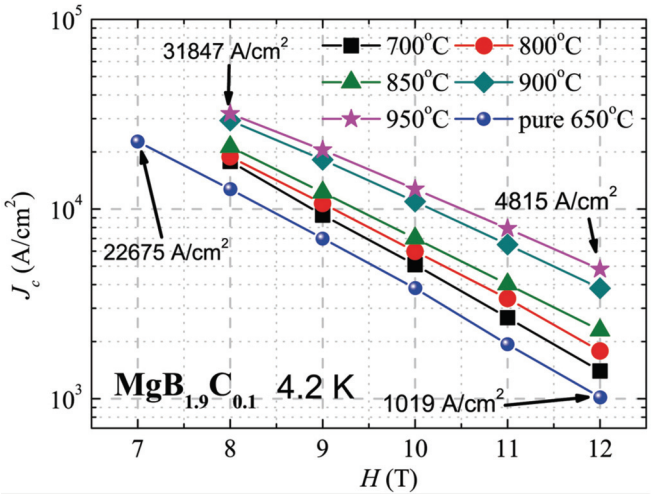

Fig. 2. The effects of sintering temperature on $J_c(H)$ performance of $MgB_{1.9}C_{0.1}$ (Yeoh et al., 2006b)

The J_c performance is greatly dependent on the sintering temperature, as shown in Fig. 2. High sintering temperature is essential for a strong flux pinning force because of the intensive carbon substitution effects. Under the optimum conditions, transport J_c has been enhanced by a factor of 5.7 at 12 T and 4.2 K as compared to the pure MgB_2 wire. The increased H_{c2} shown in Fig. 3 is in agreement with the high carbon substitution effects. $H_{c2}(0)$ of pure MgB_2 increased from 16.0 to 32.5 T in a carbon doped MgB_2 filament with slight depression of T_c from 39.2 to 36.2 K for 3.8% C substitution, using the chemical vapor deposition (CVD) method to co-deposit B together with carbon (Wilke et al., 2004). The carbon substitution effects on H_{c2} have shown an encouraging enhancement, with a range of enhanced H_{c2} values from 25 to 40 T at temperatures of 4.2 K and below (Masui et al., 2004; Ohmichi et al., 2004; Putti et al., 2004). Furthermore, H_{c2} with a value of 52–55 T has been commonly observed for carbon alloyed thin films at temperatures around 1.5–4.2 K (Ferdeghini et al., 2005; Ferrando et al., 2005). The enhancement of H_{c2} is in agreement with predictions of the model of two-band impurity scattering of charge carriers in MgB_2, which indicates increased intraband scattering via shortening of the electron mean free path, l (Gurevich, 2003). The coherence length, ξ, will be shortened according to the equation $1/\xi = 1/l + 1/\xi_0$, where ξ_0 is the coherence length at 0 K.

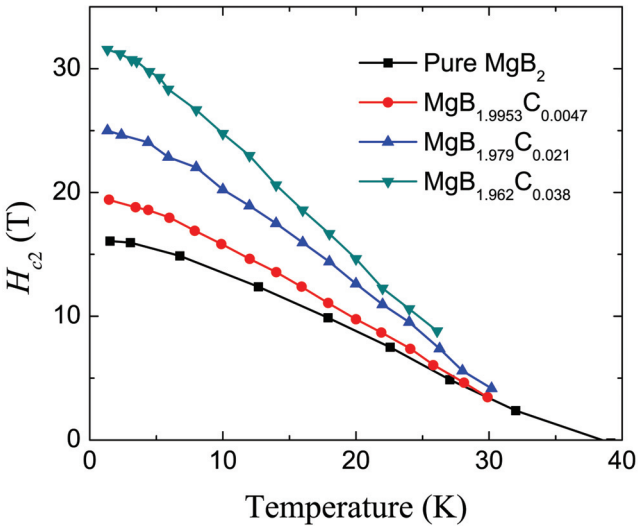

Fig. 3. H_{c2} dependence on carbon substitution content (Wilke et al., 2004)

3. Carbon nanotube (CNT) doping effects

Compared with other nano-carbon precursors, carbon nanotubes (CNTs) are particularly interesting because their special geometry (high aspect ratio and nanometer diameter) may induce more effective pinning centers. CNTs can form column-like strong pinning centers to enhance J_c in the Bi-based superconductors (Fossheim et al., 1995; Huang et al., 1999). The flux pinning force depends greatly on the geometry of the different CNTs. Furthermore, the CNT doping significantly improves heat transfer and dissipation during materials processing (Dou et al., 2006), due to the high thermal conductivity and stable electric conductivity of CNTs (Kim et al., 2001; Wei et al., 2001). With CNT properties of high axial strength and stiffness, approaching values for an ideal carbon fiber (Treacy et al., 1996), CNT doping can improve the current path and connectivity between the grains in MgB_2. Transmission electron microscope (TEM) images have shown that CNTs are easy to align in the wire processing direction, as shown in the TEM images in Fig. 4.

The doping effects of single-walled carbon nanotubes (SWCNTs) include amazing pinning effects in MgB_2 at 4.2 K, as shown in Fig. 4. Similarly to the case of ordinary carbon-doped MgB_2, the best performance in $J_c(H)$ was shown by SWCNT doping with sintering at 900 °C, where the high processing temperature encourages better carbon substitution compared to lower processing temperatures. The J_c(4.2 K) reached the values of ~51,000 and ~3500 A/cm^2 at 7 and 12 T, respectively, as shown in Fig. 5.

Multi-walled carbon nanotubes (MWCNT) have also shown positive effects on the J_c of MgB_2, however, the results are not as significant as with the SWCNTs. Furthermore, the J_c is dependent on the length of the MWCNTs: short MWCNTs give rise to a stronger flux pinning force than long ones. Yeoh et al. have shown that there is a correlation between the reactivity of the CNTs and the amount of carbon substitution in the MgB_2, with the substitution of carbon for boron only occurring after the carbon atoms break free from the CNT (Yeoh et al., 2007a). Longer CNTs tend to entangle and agglomerate, which results in

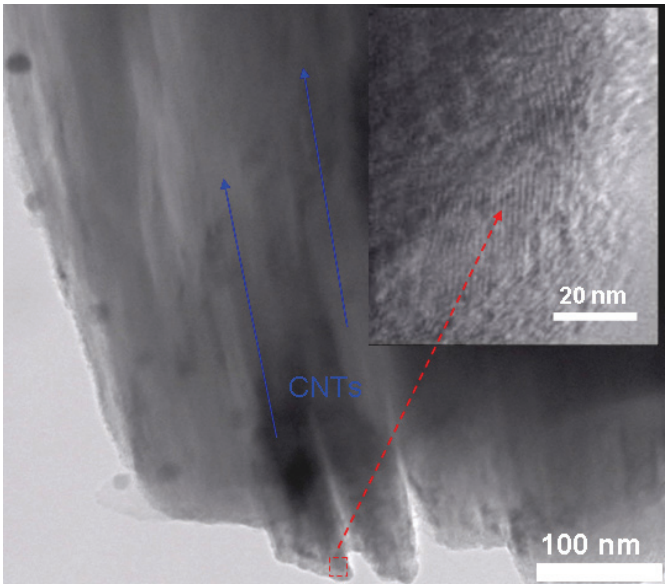

Fig. 4. TEM images of CNT doped MgB_2 show straightened CNTs in the same processing direction in the MgB_2 matrix. The inset is a high resolution image of a CNT (Dou et al., 2006)

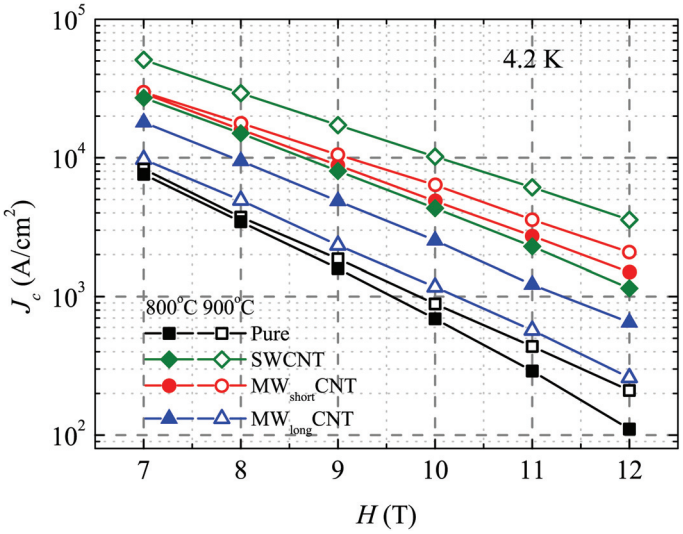

Fig. 5. Transport critical current at 4.2 K at fields up to 12 T for different CNT doped wires produced at sintering temperatures of 800 and 900 °C (Kim et al., 2006a)

inhomogeneous mixing of the CNTs with the precursor powder, blocking the current transport and suppressing the J_c (Yeoh et al., 2005). Ultrasonication of CNTs has been introduced to improve the homogenous mixing of the CNTs with the MgB_2 matrix, resulting in a significant enhancement in the field dependence of the critical current density (Yeoh et

al., 2006a). The J_c performance of different types of CNT doped MgB_2 is in agreement with the H_{c2} shown in Fig. 6.

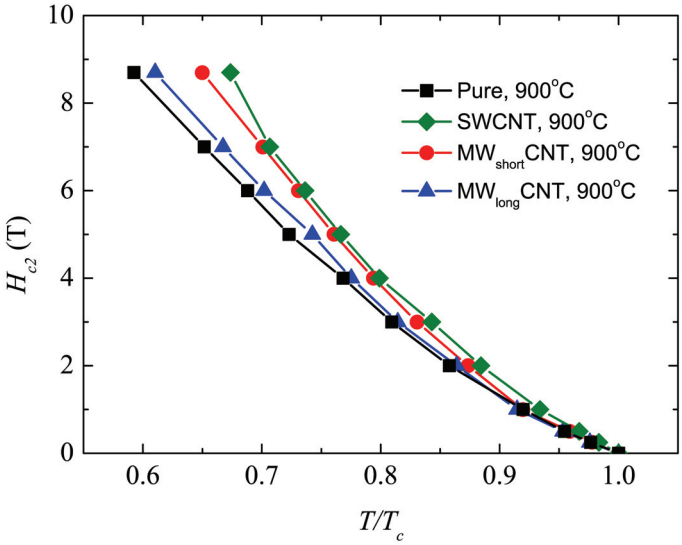

Fig. 6. The H_{c2} of different CNT doped MgB_2 samples sintered at 900 °C. The temperature has been normalized by T_c (Kim et al., 2006a)

4. Nanosized SiC doping effects

Nanosized doping centers are highly effective, as they are comparable with the coherence length of MgB_2 (Soltanian et al., 2003). MgB_2 has a relatively large coherence length, with $\xi_{ab}(0)$ = 3.7–12 nm and $\xi_c(0)$ = 1.6–3.6 nm (Buzea & Yamashita, 2001), so a strong pinning force can be introduced by nanoparticles that are comparable in size. Nanoscale SiC has been found to be the right sort of candidate, providing both second phase nanoscale flux pinning centers and an intensive carbon substitution source (Dou et al., 2002a; Dou et al., 2002b; Dou et al., 2003b). 10 wt% nano-SiC doped MgB_2 bulk samples showed $H_{irr} \approx 8$ T and $J_c \approx 10^5$ A cm^{-2} under 3 T at 20 K. The T_c reduction is not pronounced, even in heavily doped samples with SiC up to 30% (Dou et al., 2002b).

Fig. 7 compares the J_c values of pure MgB_2 and those of MgB_2 doped with 10 wt% nanosized SiC at different temperatures. There are crossover fields for the J_c at the same temperature for different samples, due to the different reductions in slope of the flux pinning force when the temperature is lower than 20 K. The carbon substitution effects in the SiC doped sample are very strong, and therefore, the J_c decreases steadily with increasing field. The J_c drops quickly when the temperature approaches T_c. An increase in H_{c2} from 20.5 T to more than 33 T and enhancement of H_{irr} from 16 T to a maximum of 28 T for an SiC doped sample were observed at 4.2 K (Bhatia et al., 2005). Matsumoto et al. showed that very high values of $H_{c2}(0)$, exceeding 40 T, can be attained in SiC-doped bulk MgB_2 sintered at 600 °C (Matsumoto et al., 2006). This result is considerably higher than for C-doped single crystal (Kazakov et al., 2005), filament (Wilke et al., 2004; Li et al., 2009a), or bulk samples (Senkowicz et al., 2005). Low temperature sintering is beneficial to both the H_{irr} and the H_{c2},

as shown in Fig. 8, which suggests that significant lattice distortion is introduced by alloying and by reaction at low temperature. This has important consequences for the application of MgB_2 wires and tapes in the cable and magnet industries.

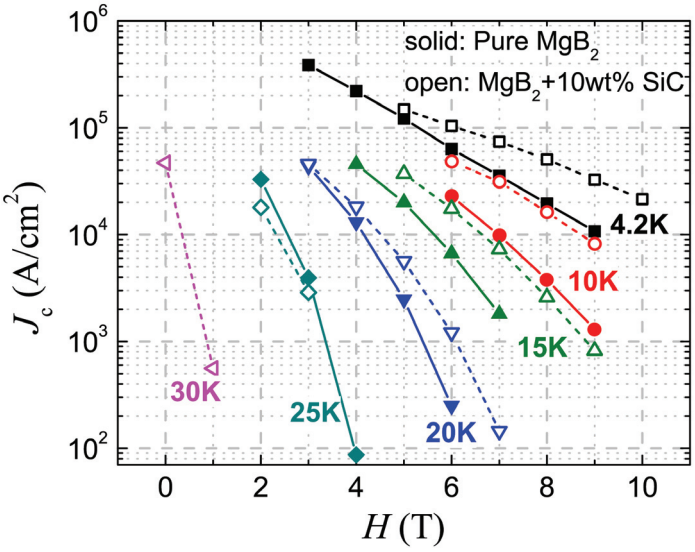

Fig. 7. Comparison of J_c of pure MgB_2 with that of a nanosized SiC doped sample at different temperatures (Dou et al., 2002b; Shcherbakova et al., 2006)

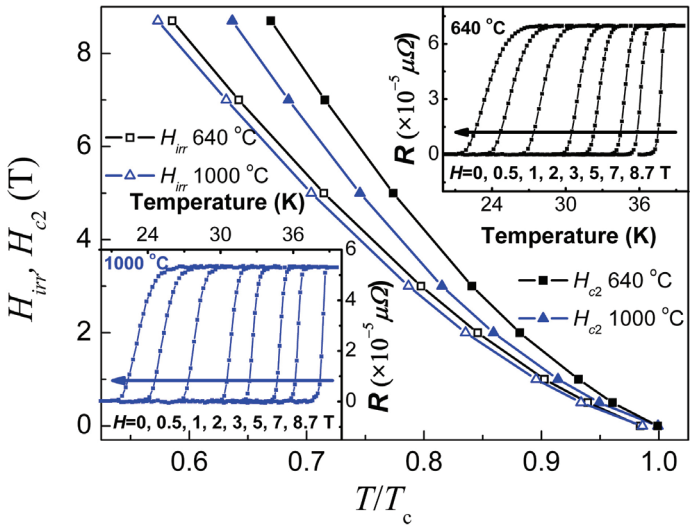

Fig. 8. The effects of sintering temperature on H_{c2} and H_{irr} of 10 wt%, ~15 nm SiC doped MgB_2 (Soltanian et al., 2005). The insets show the resistance as a function of temperature at different magnetic fields for samples sintered at 640 °C (upper right) and 1000 °C (lower left)

Fig. 9 shows the critical current density of MgB_2 in comparison with other commercial superconductor materials. It should be noted that the J_c of SiC-doped MgB_2 stands out very strongly, even at 20 K in low field, and that it is comparable to the value of J_c for Nb–Ti at 4.2 K, which is very useful for application in magnetic resonance imaging (MRI). At 20 K, the best J_c for the 10 wt% SiC doped sample was almost 10^5 A/cm² at 3 T, which is comparable with the J_c of state-of-the-art Ag/Bi-2223 tapes. These results indicate that powder-in-tube-processed MgB_2 wire is promising, not only for high-field applications at 4.2 K, but also for applications at 20 K with a convenient cryocooler. Fig. 10 shows TEM and high resolution TEM (HRTEM) images of 10 wt% nanosized SiC doped MgB_2. A high density of dislocations and different sizes of nano-inclusions can be observed in the MgB_2 matrix. Furthermore, the HRTEM images indicate that the MgB_2 crystals display nanodomain structures, which is attributed to lattice collapse caused by the carbon substitution.

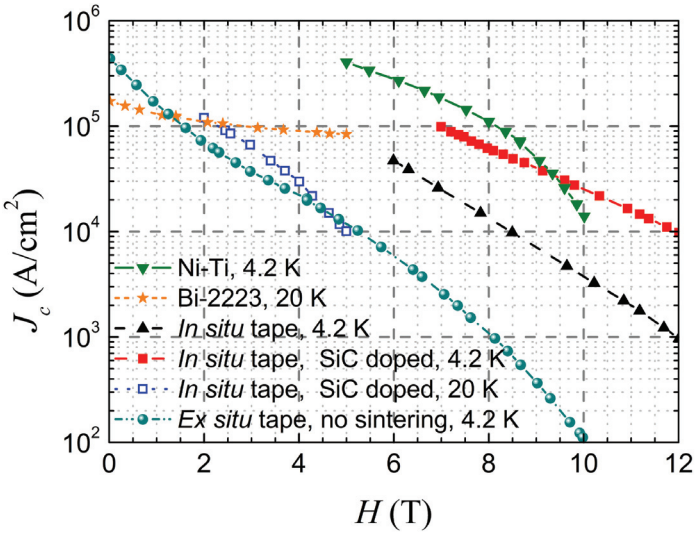

Fig. 9. Comparison of J_c of MgB_2 with those of other commercial superconducting wires and tapes (Yeoh & Dou, 2007)

However, similar to the doping effects of carbon and CNTs, the connectivity of nanosized SiC doped MgB_2 is quite low. To improve the connectivity, additional Mg was added into the precursor mixture (Li et al., 2009a; Li et al., 2009b). To explore the effects on connectivity of Mg excess, microstructures of all the samples were observed by scanning electron microscope (SEM), as shown in Fig. 11. The grains in the stoichiometric MgB_2 samples show an independent growth process, which is responsible for their isolated distribution. The grains in $Mg_{1.15}B_2$ have clearly melted into big clusters because the additional Mg can extend the liquid reaction time. The grain shapes in MgB_2 + 10 wt % SiC are different from those in pure, stoichiometric MgB_2 because the former crystals are grown under strain due to the C substitution effects. The strain is also strong in $Mg_{1.15}B_2$ + 10 wt % SiC, as long bar-shaped grains can be observed under SEM. The strain is released in the high Mg content samples (x > 1.20), judging from the homogeneous grain sizes and shapes. Compared with MgB_2 + 10 wt % SiC, the grain connectivity improved greatly with the increasing Mg addition. The

grains were merged into big particles, and grain boundaries have replaced the gaps between grains. However, more impurities are induced in forms such as residual Mg and MgO.

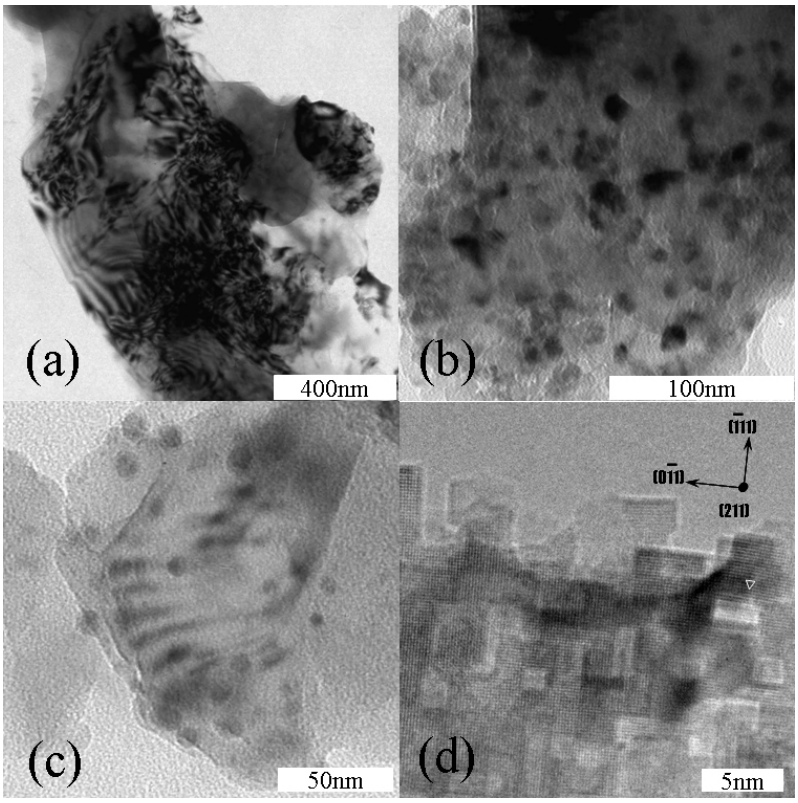

Fig. 10. TEM images of SiC-doped MgB_2 showing the high density of dislocations (a), inclusions larger than 10 nm (b), inclusions smaller than 10 nm (c), and HRTEM image of the nanodomain structure (d) (Dou et al., 2003a; Li et al., 2003)

The concept of the connectivity, A_F, was introduced to quantify this reduction of the effective cross-section, σ_{eff}, for supercurrents (Rowell, 2003; Rowell et al., 2003): $A_F = \sigma_{eff} / \sigma_0$, where σ_0 is the geometrical cross-section. The connectivity can be estimated from the phonon contribution to the normal state resistivity by

$$A_F = \Delta\rho_{ideal} / \Delta\rho(300\ \mathrm{K}) \tag{2}$$

where $\Delta\rho_{ideal} = \rho_{ideal}(300\ \mathrm{K}) - \rho_{ideal}(T_c) \approx 9\,\mu\Omega\cdot\mathrm{cm}$ is the resistivity of fully connected MgB_2 without any disorder, and $\Delta\rho(300\ \mathrm{K}) = \rho(300\ \mathrm{K}) - \rho(T_c)$. This estimate is based on the assumption that the effective cross-section is reduced equivalently in the normal and superconducting states, which is a severe simplification. The supercurrents are limited by the smallest effective cross-section along the conductor, and the resistivity is given more or less by the average effective cross-section. A single large transverse crack strongly reduces

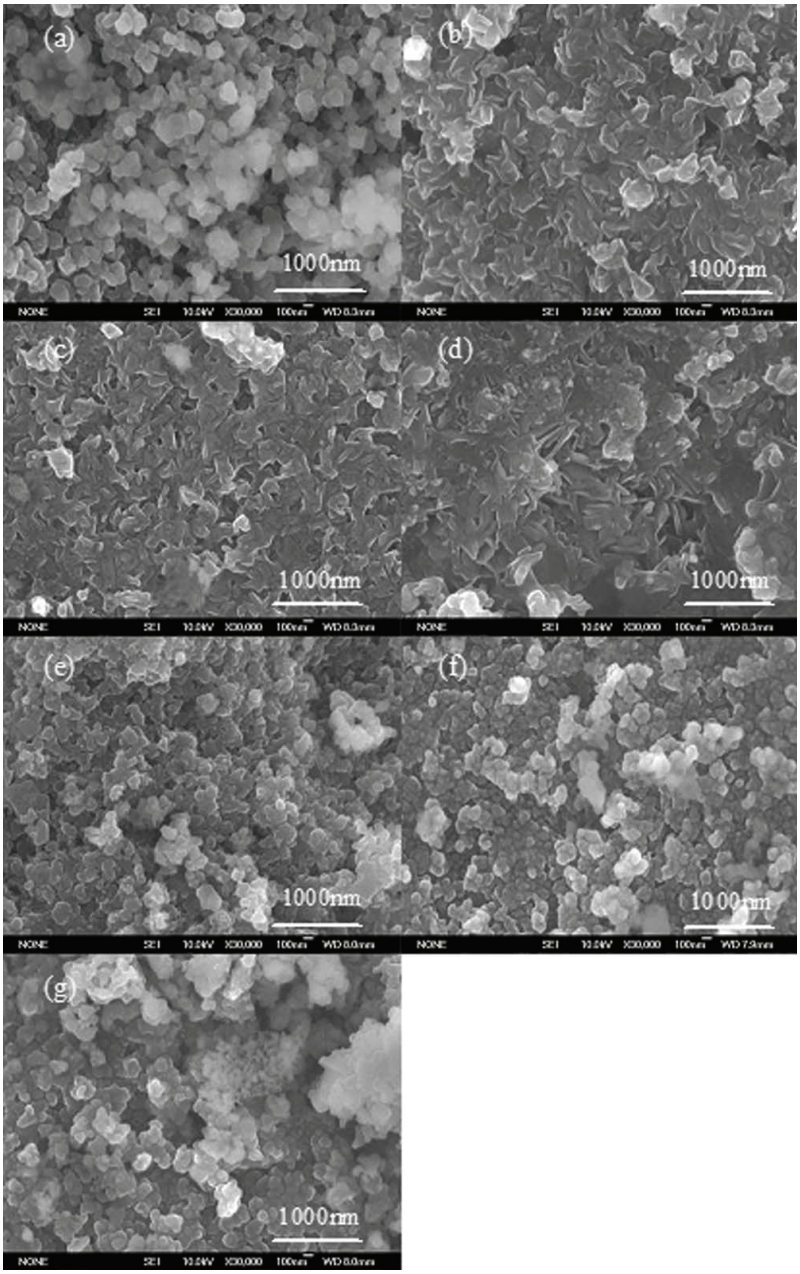

Fig. 11. SEM images of MgB_2 (a), $Mg_{1.15}B_2$ (b), MgB_2+10 wt % SiC (c), $Mg_{1.15}B_2$+10 wt % SiC (d), $Mg_{1.20}B_2$+10 wt % SiC (e), $Mg_{1.25}B_2$+10 wt % SiC (f), and $Mg_{1.30}B_2$+10 wt % SiC (g) (Li et al., 2009a)

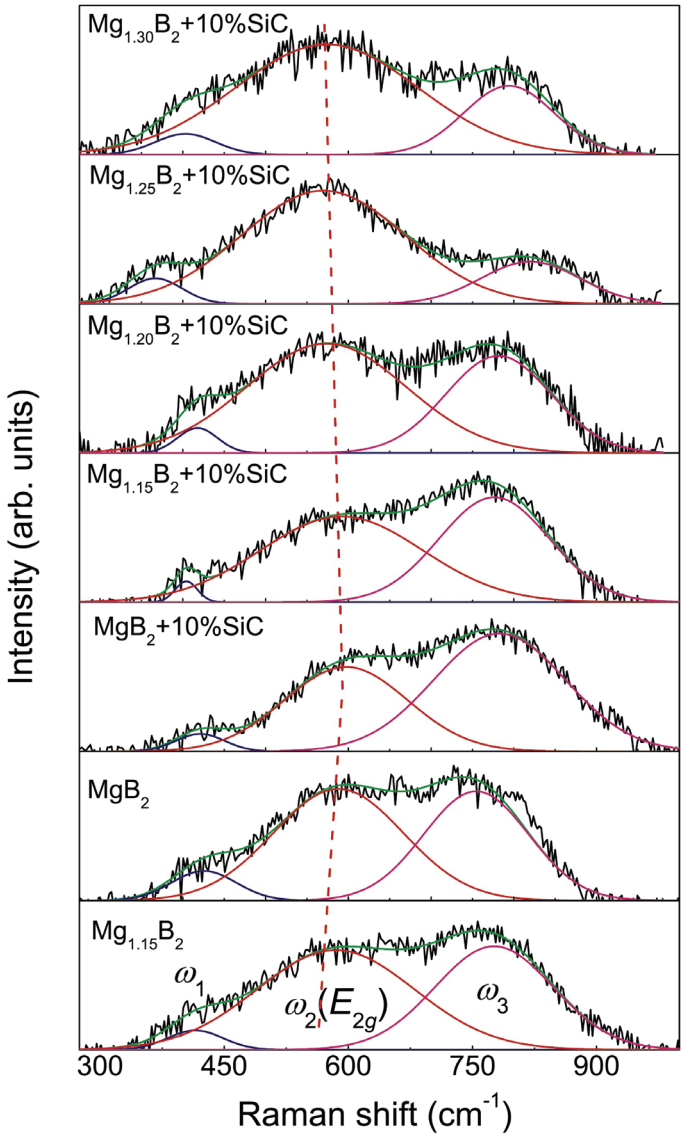

Fig. 12. (Color online) Ambient Raman spectra of MgB_2, $Mg_{1.15}B_2$, and Mg_xB_2+10 wt % SiC (x = 1.00, 1.15, 1.20, 1.25, and 1.30) fitted with three peaks: ω_1, ω_2, and ω_3. The dashed line indicates the vibration of the E_{2g} mode (ω_2) in different samples (Li et al., 2009a)

J_c, but only slightly increases the resistivity of a long sample. Un-reacted magnesium decreases $\Delta\rho$(300 K) (Kim et al., 2002) and the cross-section for supercurrents. Thin insulating layers on the grain boundaries strongly increase $\Delta\rho$(300 K), but might be transparent to supercurrents. Finally, $\Delta\rho_{ideal}$ within the grains can change due to disorder. Even a negative $\Delta\rho$(300 K) has been reported in highly resistive samples (Sharma et al.,

2002). Despite these objections, A_F is very useful, at least if the resistivity is not too high. A clear correlation between the resistivity and the critical current has been found in thin films (Rowell et al., 2003). Nevertheless, one should be aware of the fact that this procedure is not really reliable, but just a possibility for obtaining an idea about the connectivity.

It should be noted that the connectivity is far removed from that found in ideal crystals, as reflected by the low A_F values. Although the A_F values of pure and 10% SiC doped MgB_2 are just 0.106 and 0.062, additional Mg can improve them to 0.162 and 0.096 for 15 wt % Mg excess samples, respectively. High A_F values are the reflection of a broad channel of supercurrents, while impurities reduce the connectivity in large x samples. High connectivity improves the supercurrent channels because the currents can easily meander through the well-connected grains. The results show that excess Mg in $Mg_{1.15}B_2$ + 10 wt% SiC composite effectively improves the connectivity, as evidenced by its higher A_F. Its promising $J_c(H)$ is attributed to both the high connectivity and the improved H_{irr} and H_{c2}.

Raman scattering is employed to study the combined influence of connectivity and lattice distortion. Chemical substitution and lattice distortion are expected to modify the phonon spectrum, by changing the phonon frequency and the electron-phonon interaction. The effects of C substitution include an increase in impurity scattering and band filling, which reduces the density of states (DOS) and alters the shape of the Fermi surface. The E_{2g} phonon peak shifts to the higher energy side, and the peak is narrowed with increasing x in $Mg(B_{1-x}C_x)_2$ (Li et al., 2008). As a carbon source, nano-SiC shows a similar influence, due to its C atoms, on the J_c, H_{irr}, H_{c2}, and even Raman spectra in MgB_2. Figure 12 shows the Raman spectra fitted with three peaks: ω_1, ω_2, and ω_3. The ω_1 and ω_3 peaks are understood to arise from sampling of the phonon density of states (PDOS) due to disorder, while ω_2 is associated with the E_{2g} mode, which is the only Raman active mode for MgB_2 (Kunc et al., 2001). A reasonable explanation for the appearance of ω_1 and ω_3 is the violation of Raman selection rules induced by disorder. All three peaks are broad, as in previous results, due to the strong electron-phonon coupling. The influence of ω_1 on the superconducting performance is negligible compared with those of ω_2 and ω_3 because of its weak contribution to the Raman spectrum. The frequency and full width at half maximum (FWHM) of ω_2 and ω_3 are shown in Fig. 13. Both ω_2 and ω_3 are hardened with SiC addition. The ω_2 frequency is reduced with further Mg addition, whereas the ω_3 frequency remains almost stable. The frequencies of ω_2 for the $x \geq 1.20$ samples are even lower than for the pure, stoichiometric MgB_2. The FWHM of ω_2 decreases with SiC doping, while the Mg excess weakens this trend. On the contrary, the ω_3 FWHM increases with SiC addition and becomes narrow with more addition of Mg.

The Raman scattering properties are the direct reflection of the phonon behavior of MgB_2. The parameters of Raman spectra vary with the composition of MgB_2 crystals and the influence of their surroundings, which depends on both the connectivity and the disorder of the samples. Furthermore, the disorder should be considered as composed of intrinsic and extrinsic parts based on their different sources. The crystallinity and chemical substitution are believed to be responsible for the intrinsic disorder effects, while the grain boundaries and impurities are treated as responsible for the extrinsic disorder effects. The influences of intrinsic disorder on the basic characteristics of Raman spectra are significant because the physical properties of MgB_2 depend on the intrinsic disorder. The Raman parameters can also be tuned by the extrinsic disorder. Especially in samples with good connectivity, the influences of grain boundaries and impurities on the Raman spectra need to be taken into account because of their strain effects on the MgB_2 crystals (Zeng et al., 2009). The

differences between shifts and FWHMs in the Raman spectra for MgB_2, $Mg_{1.15}B_2$, MgB_2 + 10 wt % SiC, and $Mg_{1.15}B_2$ + 10 wt % SiC are mostly attributable to their intrinsic characteristics because of their different chemical compositions. The Raman spectra of Mg_xB_2 + 10 wt % SiC (x > 1.20) can be considered as gradual modifications of that of $Mg_{1.15}B_2$ + 10 wt % SiC. The weakened C substitution effects are responsible for the decreased frequencies and slightly increased FWHMs of ω_2 with Mg addition. Accordingly, the FWHMs of ω_3 decrease with increased Mg due to the weakened lattice distortion. Although the A_F values are quite low for Mg_xB_2 + 10 wt % SiC (x > 1.20), the effects of extrinsic disorder on Raman parameters are considerable, through the MgB_2–MgB_2 and MgB_2-impurity interfaces, and the connectivity deteriorates with the increased x values due to the decreased number of MgB_2–MgB_2 interfaces. A high FWHM value for ω_2 is correlated with high self-field J_c due to high carrier density, while a high FWHM value for ω_3 is correlated with strong high-field J_c because of the strong flux pinning force due to the large disorder. The FWHM behaviors show that high connectivity and strong disorder are best combined in $Mg_{1.15}B_2$ + 10 wt % SiC among all the samples.

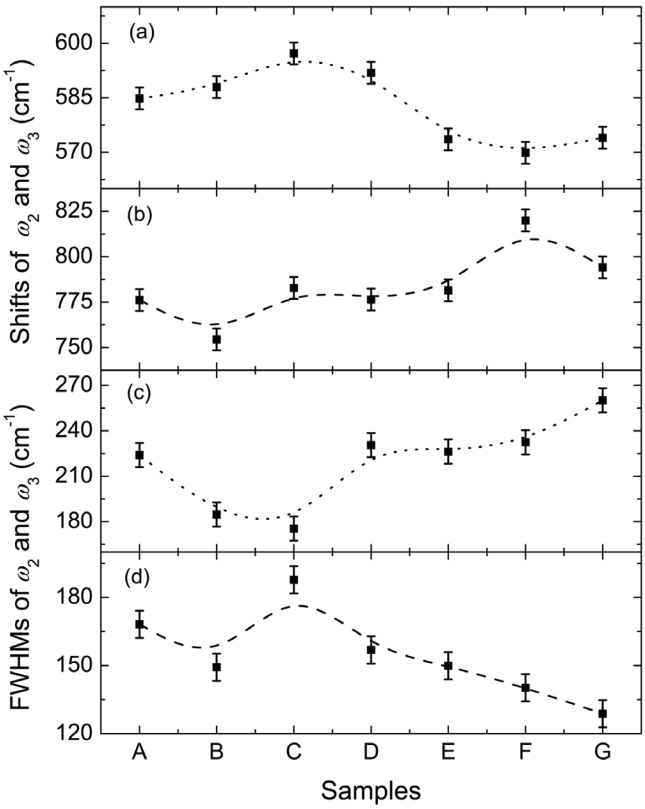

Fig. 13. Fitted parameters of Raman shifts for ω_2 (a) and ω_3 (b), and FWHMs for ω_2 (c) and ω_3 (d). The sample labels are defined as A for $Mg_{1.15}B_2$, B for MgB_2, C for MgB_2+10 wt % SiC, D for $Mg_{1.15}B_2$+10 wt % SiC, E for $Mg_{1.20}B_2$+10 wt % SiC, F for $Mg_{1.25}B_2$+10 wt % SiC, and G for $Mg_{1.30}B_2$+10 wt % SiC (Li et al., 2009a)

5. Organic dopants

Most dopants have been introduced into MgB_2 superconductors via solid state reaction using a dry mixing process, which is responsible for the common inhomogeneous distribution of dopants. Therefore, the soluble nature and low melting point of hydrocarbons and carbohydrates give these dopants advantages over the other carbon based dopants. The homogeneous distribution of hydrocarbons and carbohydrates results in high J_c values comparable with those from the best SiC nanoparticles (Kim et al., 2006b; Yamada et al., 2006; Li et al., 2007; Zhou et al., 2007).

Fig. 14 shows the J_c performance of MgB_2 doped with malic acid and sintered at different temperatures. Low temperature sintering has significant benefits for the J_c. Moreover, the malic acid ($C_4H_6O_5$) doping technique provides additional benefits to the $J_c(H)$ performance in low fields, that is, J_c at low fields is not degraded at certain doping levels as it is for any other C doping method. A cold, high pressure densification technology was employed for improving J_c and H_{irr} of monofilamentary *in-situ* MgB_2 wires and tapes alloyed with 10 wt% $C_4H_6O_5$. Tapes densified at 1.48 GPa exhibited an enhancement of J_c after reaction from 2 to 4 × 10^4 A cm^{-2} at 4.2 K/10 T and from 0.5 to 4 × 10^4 A cm^{-2} at 20 K/5 T, while the H_{irr} was enhanced from 19.3 to 22 T at 4.2 K and from 7.5 to 10.0 T at 20 K (Flukiger et al., 2009; Hossain et al., 2009). Cold densification also caused a strong enhancement of $H(10^4)$, the field at which J_c takes the value 1 × 10^4 A cm^{-2}. For tapes subjected to 1.48 GPa pressure, $H(10^4)||$ and $H(10^4)^{\perp}$ at 4.2 K were found to increase from 11.8 and 10.5 T to 13.2 and 12.2 T, respectively. Almost isotropic conditions were obtained for rectangular wires with aspect ratio a/b < 2 subjected to 2.0 GPa, where $H(10^4)||$ = 12.7 T and $H(10^4)^{\perp}$ = 12.5 T were obtained. At 20 K, the wires exhibited an almost isotropic behavior, with $H(10^4)||$ = 5.9 T and $H(10^4)^{\perp}$ = 5.75 T, with H_{irr}(20 K) being ~10 T. These values are equal to or higher than the highest values reported so far for isotropic *in-situ* wires with SiC or other carbon based additives. Further improvements are expected in optimizing the cold, high pressure densification process, which has the potential for fabrication of MgB_2 wires of industrial lengths.

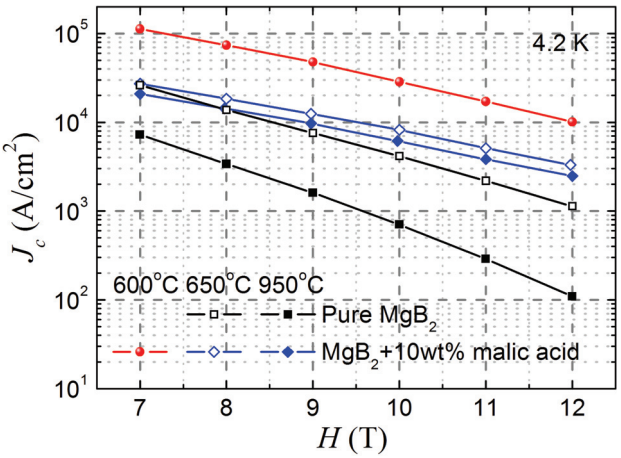

Fig. 14. Sintering temperature effects on the J_c performance of MgB_2 doped with malic acid (Kim et al., 2008)

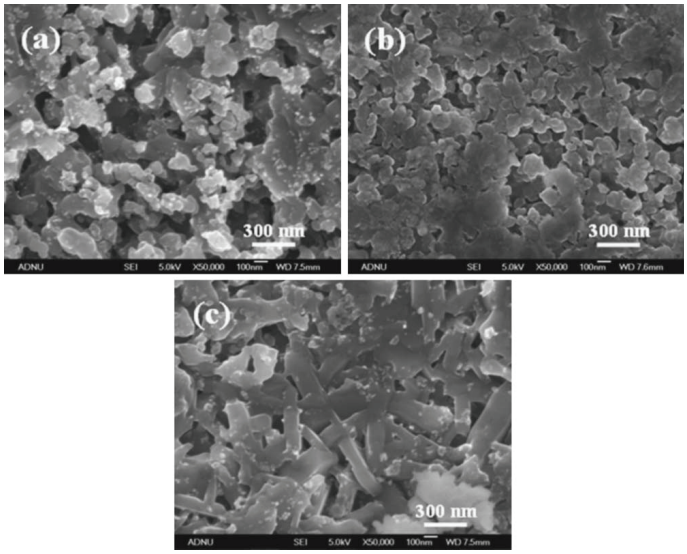

Fig. 15. Field emission SEM images: (a) pure MgB_2, (b) MgB_2 + 10 wt% malic acid, and (c) MgB_2 + 30 wt% malic acid (Kim et al., 2006b)

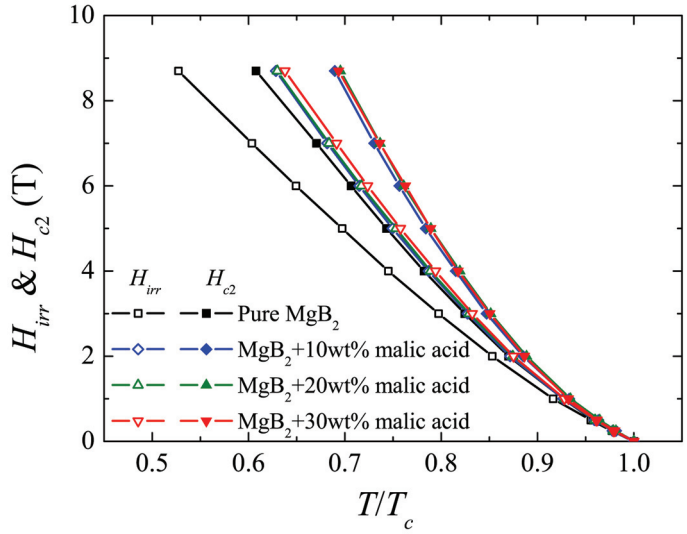

Fig. 16. H_{irr} and H_{c2} variations with doping content of malic acid in MgB_2 (Kim et al., 2006b)

Highly reactive and fresh carbon on the atomic scale can be introduced into the MgB_2 matrix because the organic reagents decompose at temperatures below the formation temperature of MgB_2. The carbon substitution is intensive at temperatures as low as the formation temperature of MgB_2. Microstructural analysis suggests that J_c enhancement is due to the substitution of carbon for boron in MgB_2, liquid homogenous mixing, and highly homogeneous and highly connected MgB_2 grains, as shown in Fig. 15. MgB_2 with

hydrocarbon-based carbonaceous compounds has also demonstrated great application potential due to the improvements in both J_c and H_{c2}, as shown in Fig. 16, while the T_c just decreases slightly. It should be noted that 30 wt% doping with malic acid is still effective for the improvement of H_{c2}, which benefits from the high density of flux pinning centers in the MgB_2 matrix.

6. Doping effects of other carbon sources

Diamond, Na_2CO_3, carbon nanohorns, graphite, and carbide compounds have also been employed as dopants to achieve flux pinning in MgB_2 (Zhao et al., 2003; Ueda et al., 2004; Xu et al., 2004; Ban et al., 2005; Yamamoto et al., 2006). All show positive effects on J_c performance. B_4C appears to be an ideal carbon source to avoid excessive carbonaceous chemical addition. Ueda et al. and Yamamoto et al. showed that C could substitute into the B sites when a mixture of Mg, B, and B_4C was sintered at 850 °C for bulk samples (Ueda et al., 2005; Yamamoto et al., 2005a; Yamamoto et al., 2005c). Substantially enhanced J_c properties under high magnetic fields were observed in the B_4C doped samples due to the relatively low processing temperature and carbon substitution effects. Lezza et al. successfully obtained a J_c value of 1×10^4 A cm^{-2} at 4.2 K and 9 T for 10 wt% B_4C powders added to MgB_2/Fe wires at a reaction temperature of 800 °C (Lezza et al., 2006). Despite the carbon substitution effects, the homogeneous microstructure of the dopants provides the MgB_2 composites with good grain connection for the MgB_2 phase and a high density of flux pinning centers.

7. Mechanism of doping effects — dual reaction model

Carbon substitution in the boron sites is the dominant factor for the enhancement of $J_c(H)$ and H_{c2} in all carbonaceous chemical doped MgB_2 because of the strong disorder effects. Furthermore, the defects, grain sizes, second phases, grain boundaries, and connectivity are also important for the superconducting properties. The study of reaction kinetics for different carbonaceous chemicals during the MgB_2 synthesis is a crucial issue for understanding the H_{irr}, H_{c2}, and J_c performance in MgB_2. A systematic correlation between the processing temperature, J_c, and H_{c2} has been observed in pure, nano-carbon, CNT, SiC, and hydrocarbon doped MgB_2 samples (Dou et al., 2007; Yeoh et al., 2007b). The processing temperature is believed to be the most important factor influencing the electromagnetic properties because both the carbon substitution intensity and the microstructure are dependent on it.

Fig. 17 shows the effects of sintering temperature on the J_c(H) for different carbon based dopants. The hydrocarbon and SiC doped MgB_2 show significant enhancement in J_c for the samples sintered at lower temperature, whereas the carbon and CNT doped MgB_2 need to be sintered at higher temperature for high J_c. The low sintering temperature results in small grain size, high concentrations of impurities and defects, and large lattice distortion, which are all responsible for a strong flux pinning force (Soltanian et al., 2005; Yamamoto et al., 2005b). Furthermore, the hydrocarbon and SiC can release fresh and active free carbon at very low temperature, which means that the carbon substitution effects take place simultaneously with the MgB_2 formation. A high sintering temperature will perfect the crystallization and decrease the flux pinning centers in the MgB_2 matrix. That is the reason why high sintering temperature degrades the J_c performance. Although high sintering

temperature has the same shortcomings in nanosized carbon and CNT doped MgB_2, the carbon substitution effects improve their J_c values. The high sintering temperature is necessary for carbon and CNT doped MgB_2 because the carbon and CNT are quite stable at low temperature and the substitution effects are absent if the sintering temperature is not high enough.

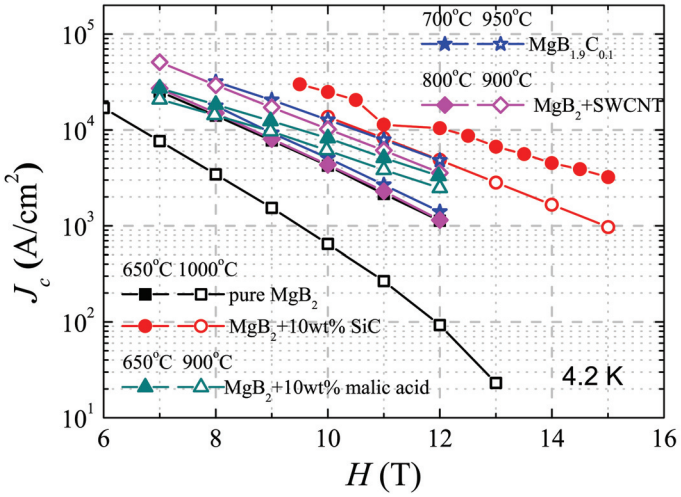

Fig. 17. The critical current density (J_c) at 4.2 K versus magnetic field for wires of pure MgB_2 and MgB_2 doped with C, SiC, SWCNTs, and malic acid that were sintered at different temperatures (Dou et al., 2002b; Yeoh et al., 2006b; Dou et al., 2007; Kim et al., 2008)

A dual reaction model has been suggested to explain the improvement of the superconducting properties in SiC doped MgB_2, based on the J_c dependence on the sintering temperature (Dou et al., 2007). The reaction of SiC with Mg at low temperature will release fresh and active carbon, which is easily incorporated into the lattice of MgB_2 at the same temperature. The reaction product Mg_2Si and excess carbon are also high quality nanosized flux pinning centers. The low temperature substitution is accompanied by small grain size, high density of grain boundaries, and high density of all kinds of defects, which are all favorable to the high superconducting performance. Another example for the dual reaction model is the high J_c malic acid doped MgB_2 shown in Fig. 14. The carbonaceous chemical doping effects on the superconducting performance can be predicted according to the dual reaction model as arising from the combination of defects and carbon substitution effects. Most dopants, such as TiC and NbC, show very small effects towards the enhancement of J_c compared with carbon, SiC, CNTs, and hydrocarbons because the substitution effects are very weak and there are no efficient flux pinning centers either.

8. Conclusions

The experimental results on H_{c2} and J_c strongly suggest that MgB_2 doped with carbonaceous sources shows remarkable enhancement of superconducting performance if the carbon substitution effects are intensive. In particular, nanosized SiC and malic acid are the most promising dopants to advance the high field J_c performance for practical application. The

enhancement of J_c, H_{irr}, and H_{c2} for MgB_2 with carbon substituted into boron sites is due to its intrinsic properties arising from the strong two-band impurity scattering effects of charge carriers. The carbonaceous chemical doping effects have been attributed to a dual reaction model, based on the sintering effects on superconducting properties for different kinds of carbonaceous chemicals. The fresh, active, and free carbon atoms are very easy to substitute onto B sites in the MgB_2 lattice if the carbonaceous decomposition temperatures are close to the formation temperature of MgB_2, ~650 °C. The dual reaction model can explain and predict the doping effects of carbonaceous chemicals on the superconducting properties very well. The high density of defects is another factor that improves the J_c, H_{irr}, and H_{c2}. However, the connectivity of the samples is also responsible for the low field J_c performance, which is free from the flux pinning force and can be attributed to the density of supercurrent carriers. Both microstructure observations and Raman scattering measurements have confirmed the great influence of connectivity on J_c behavior, as shown by the effects of extra Mg addition in nanosized SiC doped MgB_2. The proper Mg content will improve the connectivity greatly to improve the density of supercurrent carriers.

9. References

An, J. M. & Pickett, W. E. (2001). Superconductivity of MgB_2: Covalent bonds driven metallic. *Physical Review Letters*, 86(19): 4366-4369.

Avdeev, M.; Jorgensen, J. D.; Ribeiro, R. A.; Bud'ko, S. L. & Canfield, P. C. (2003). Crystal chemistry of carbon-substituted MgB_2. *Physica C - Superconductivity and Its Applications*, 387(3-4): 301-306.

Ban, E.; Sakaguchi, R.; Matsuoka, Y.; Goto, T.; Watanabe, K. & Nishijima, G. (2005). Carbon nanohorn doping in MgB_2 wire prepared by suspension spinning. *Physica C - Superconductivity and Its Applications*, 426-431(9): 1249-1253.

Bhatia, M.; Sumption, M. D. & Collings, E. W. (2005). Effect of various additions on upper critical field and irreversibility field of *in-situ* MgB_2 superconducting bulk material. *IEEE Transactions on Applied Superconductivity*, 15(2): 3204-3206.

Bouquet, F.; Fisher, R. A.; Phillips, N. E.; Hinks, D. G. & Jorgensen, J. D. (2001). Specific heat of (MgB_2)-^{11}B: Evidence for a second energy cap. *Physical Review Letters*, 87(4): 047001.

Braccini, V.; Gurevich, A.; Giencke, J. E.; Jewell, M. C.; Eom, C. B.; Larbalestier, D. C.; Pogrebnyakov, A.; Cui, Y.; Liu, B. T.; Hu, Y. F.; Redwing, J. M.; Li, Q.; Xi, X. X.; Singh, R. K.; Gandikota, R.; Kim, J.; Wilkens, B.; Newman, N.; Rowell, J.; Moeckly, B.; Ferrando, V.; Tarantini, C.; Marre, D.; Putti, M.; Ferdeghini, C.; Vaglio, R. & Haanappel, E. (2005). High-field superconductivity in alloyed MgB_2 thin films. *Physical Review B*, 71(1): 012504.

Buzea, C. & Yamashita, T. (2001). Review of the superconducting properties of MgB_2. *Superconductor Science & Technology*, 14(11): R115-R146.

Dou, S. X.; Horvat, J.; Soltanian, S.; Wang, X. L.; Qin, M. J.; Zhou, S. H.; Liu, H. K. & Munroe, P. G. (2003a). Transport critical current density in Fe-sheathed nano-SiC doped MgB_2 wires. *IEEE Transactions on Applied Superconductivity*, 13(2): 3199-3202.

Dou, S. X.; Pan, A. V.; Zhou, S.; Ionescu, M.; Liu, H. K. & Munroe, P. R. (2002a). Substitution-induced pinning in MgB_2 superconductor doped with SiC nano-particles. *Superconductor Science & Technology*, 15(11): 1587-1591.

Dou, S. X.; Pan, A. V.; Zhou, S.; Ionescu, M.; Wang, X. L.; Horvat, J.; Liu, H. K. & Munroe, P. R. (2003b). Superconductivity, critical current density, and flux pinning in $MgB_{2-x}(SiC)_{x/2}$ superconductor after SiC nanoparticle doping. *Journal of Applied Physics*, 94(3): 1850-1856.

Dou, S. X.; Shcherbakova, O.; Yoeh, W. K.; Kim, J. H.; Soltanian, S.; Wang, X. L.; Senatore, C.; Flukiger, R.; Dhalle, M.; Husnjak, O. & Babic, E. (2007). Mechanism of enhancement in electromagnetic properties of MgB_2 by nano SiC doping. *Physical Review Letters*, 98(9): 097002.

Dou, S. X.; Soltanian, S.; Horvat, J.; Wang, X. L.; Zhou, S. H.; Ionescu, M.; Liu, H. K.; Munroe, P. & Tomsic, M. (2002b). Enhancement of the critical current density and flux pinning of MgB_2 superconductor by nanoparticle SiC doping. *Applied Physics Letters*, 81(18): 3419-3421.

Dou, S. X.; Yeoh, W. K.; Shcherbakova, O.; Weyler, D.; Li, Y.; Ren, Z. M.; Munroe, P.; Chen, S. K.; Tan, K. S.; Glowacki, B. A. & MacManus-Driscoll, J. L. (2006). Alignment of carbon nanotube additives for improved performance of magnesium diboride superconductors. *Advanced Materials*, 18(6): 785-788.

Eisterer, M. & Weber, H. W. (2009). Application prospects of MgB_2 in view of its basic properties. *IEEE Transactions on Applied Superconductivity*, 19(3): 2788-2792.

Ferdeghini, C.; Ferrando, V.; Tarantini, C.; Bellingeri, E.; Grasso, G.; Malagoli, A.; Marre, D.; Putti, M.; Manfrinetti, P.; Pogrebnyakov, A.; Redwing, J. M.; Xi, X. X.; Felici, R. & Haanappel, E. (2005). Upper critical fields up to 60 T in dirty magnesium diboride thin films. *IEEE Transactions on Applied Superconductivity*, 15(2): 3234-3237.

Ferrando, V.; Orgiani, P.; Pogrebnyakov, A. V.; Chen, J.; Li, Q.; Redwing, J. M.; Xi, X. X.; Giencke, J. E.; Eom, C. B.; Feng, Q. R.; Betts, J. B. & Mielke, C. H. (2005). High upper critical field and irreversibility field in MgB_2 coated-conductor fibers. *Applied Physics Letters*, 87(25): 252509.

Finnemore, D. K.; Ostenson, J. E.; Bud'ko, S. L.; Lapertot, G. & Canfield, P. C. (2001). Thermodynamic and transport properties of superconducting MgB_2-^{10}B. *Physical Review Letters*, 86(11): 2420-2422.

Flukiger, R.; Hossain, M. S. A. & Senatore, C. (2009). Strong enhancement of J_c and B_{irr} in binary *in situ* MgB_2 wires after cold high pressure densification. *Superconductor Science & Technology*, 22(8): 085002.

Fossheim, K.; Tuset, E. D.; Ebbesen, T. W.; Treacy, M. M. J. & Schwartz, J. (1995). Enhanced flux-pinning in $Bi_2Sr_2CaCu_2O_{8+X}$ superconductor with embedded carbon nanotubes. *Physica C - Superconductivity and Its Applications*, 248(3-4): 195-202.

Gurevich, A. (2003). Enhancement of the upper critical field by nonmagnetic impurities in dirty two-gap superconductors. *Physical Review B*, 67(18): 184515.

Gurevich, A. (2007). Limits of the upper critical field in dirty two-gap superconductors. *Physica C - Superconductivity and Its Applications*, 456(1-2): 160-169.

Hossain, M. S. A.; Senatore, C.; Flukiger, R.; Rindfleisch, M. A.; Tomsic, M. J.; Kim, J. H. & Dou, S. X. (2009). The enhanced J_c and B_{irr} of in situ MgB_2 wires and tapes alloyed with $C_4H_6O_5$ (malic acid) after cold high pressure densification. *Superconductor Science & Technology*, 22(9): 095004.

Huang, S. L.; Koblischka, M. R.; Fossheim, K.; Ebbesen, T. W. & Johansen, T. H. (1999). Microstructure and flux distribution in both pure and carbon-nanotube-embedded

$Bi_2Sr_2CaCu_2O_{8+\delta}$ superconductors. *Physica C - Superconductivity and Its Applications*, 311(3-4): 172-186.

Kawano, K.; Abell, J. S.; Kambara, M.; Babu, N. H. & Cardwell, D. A. (2001). Evidence for high intergranular current flow in a single-phase polycrystalline MgB_2 superconductor. *Applied Physics Letters*, 79(14): 2216-2218.

Kazakov, S. M.; Puzniak, R.; Rogacki, K.; Mironov, A. V.; Zhigadlo, N. D.; Jun, J.; Soltmann, C.; Batlogg, B. & Karpinski, J. (2005). Carbon substitution in MgB_2 single crystals: Structural and superconducting properties. *Physical Review B*, 71(2): 024533.

Kim, J. H.; Dou, S. X.; Oh, S.; Jercinovic, M.; Babic, E.; Nakane, T. & Kumakura, H. (2008). Correlation between doping induced disorder and superconducting properties in carbohydrate doped MgB_2. *Journal of Applied Physics*, 104(6): 063911.

Kim, J. H.; Yeoh, W. K.; Qin, M. J.; Xu, X.; Dou, S. X.; Munroe, P.; Kumakura, H.; Nakane, T. & Jiang, C. H. (2006a). Enhancement of in-field J_c in MgB_2/Fe wire using single- and multiwalled carbon nanotubes. *Applied Physics Letters*, 89(12): 122510.

Kim, J. H.; Zhou, S.; Hossain, M. S. A.; Pan, A. V. & Dou, S. X. (2006b). Carbohydrate doping to enhance electromagnetic properties of MgB_2 superconductors. *Applied Physics Letters*, 89(14): 142505.

Kim, K. H.; Betts, J. B.; Jaime, M.; Lacerda, A. H.; Boebinger, G. S.; Jung, C. U.; Kim, H. J.; Park, M. S. & Lee, S. I. (2002). Mg as a main source for the diverse magnetotransport properties of MgB_2. *Physical Review B*, 66(2): 020506.

Kim, P.; Shi, L.; Majumdar, A. & McEuen, P. L. (2001). Thermal transport measurements of individual multiwalled nanotubes. *Physical Review Letters*, 87(21): 215502.

Kortus, J.; Mazin, I. I.; Belashchenko, K. D.; Antropov, V. P. & Boyer, L. L. (2001). Superconductivity of metallic boron in MgB_2. *Physical Review Letters*, 86(20): 4656-4659.

Kunc, K.; Loa, I.; Syassen, K.; Kremer, R. K. & Ahn, K. (2001). MgB_2 under pressure: phonon calculations, Raman spectroscopy, and optical reflectance. *Journal of Physics - Condensed Matter*, 13(44): 9945-9962.

Lezza, P.; Senatore, C. & Flukiger, R. (2006). Improved critical current densities in B_4C doped MgB_2 based wires. *Superconductor Science & Technology*, 19(10): 1030-1033.

Li, S.; White, T.; Laursen, K.; Tan, T. T.; Sun, C. Q.; Dong, Z. L.; Li, Y.; Zhou, S. H.; Horvat, J. & Dou, S. X. (2003). Intense vortex pinning enhanced by semicrystalline defect traps in self-aligned nanostructured MgB_2. *Applied Physics Letters*, 83(2): 314-316.

Li, W. X.; Li, Y.; Chen, R. H.; Zeng, R.; Dou, S. X.; Zhu, M. Y. & Jin, H. M. (2008). Raman study of element doping effects on the superconductivity of MgB_2. *Physical Review B*, 77(9): 094517.

Li, W. X.; Li, Y.; Zhu, M. Y.; Chen, R. H.; Xu, X.; Yeoh, W. K.; Kim, J. H. & Dou, S. X. (2007). Benzoic acid doping to enhance electromagnetic properties of MgB_2 superconductors. *IEEE Transactions on Applied Superconductivity*, 17(2): 2778-2781.

Li, W. X.; Zeng, R.; Lu, L.; Li, Y. & Dou, S. X. (2009a). The combined influence of connectivity and disorder on J_c and T_c performances in Mg_xB_2+10 wt % SiC. *Journal of Applied Physics*, 106(9): 093906.

Li, W. X.; Zeng, R.; Lu, L.; Zhang, Y.; Dou, S. X.; Li, Y.; Chen, R. H. & Zhu, M. Y. (2009b). Improved superconducting properties of in situ powder-in-tube processed $Mg_{1.15}B_2$/Fe wires with nano-size SiC addition. *Physica C - Superconductivity and Its Applications*, 469(15-20): 1519-1522.

Masui, T.; Lee, S. & Tajima, S. (2004). Carbon-substitution effect on the electronic properties of MgB_2 single crystals. *Physical Review B*, 70(2): 024504.

Matsumoto, A.; Kumakura, H.; Kitaguchi, H.; Senkowicz, B. J.; Jewell, M. C.; Hellstrom, E. E.; Zhu, Y.; Voyles, P. M. & Larbalestier, D. C. (2006). Evaluation of connectivity, flux pinning, and upper critical field contributions to the critical current density of bulk pure and SiC-alloyed MgB_2. *Applied Physics Letters*, 89(13): 132508.

Nagamatsu, J.; Nakagawa, N.; Muranaka, T.; Zenitani, Y. & Akimitsu, J. (2001). Superconductivity at 39 K in magnesium diboride. *Nature*, 410(6824): 63-64.

Ohmichi, E.; Komatsu, E.; Masui, T.; Lee, S.; Tajima, S. & Osada, T. (2004). Carbon-substitution effect on vortex order-disorder transition in MgB_2 single crystals. *Physical Review B*, 70(17): 174513.

Putti, M.; Braccini, V.; Ferdeghini, C.; Pallecchi, I.; Siri, A. S.; Gatti, F.; Manfrinetti, P. & Palenzona, A. (2004). Critical field of MgB_2: Crossover from clean to dirty regimes. *Physical Review B*, 70(5): 052509.

Rowell, J. M. (2003). The widely variable resistivity of MgB_2 samples. *Superconductor Science & Technology*, 16(6): R17-R27.

Rowell, J. M.; Xu, S. Y.; Zeng, H.; Pogrebnyakov, A. V.; Li, Q.; Xi, X. X.; Redwing, J. M.; Tian, W. & Pan, X. Q. (2003). Critical current density and resistivity of MgB_2 films. *Applied Physics Letters*, 83(1): 102-104.

Senkowicz, B. J.; Giencke, J. E.; Patnaik, S.; Eom, C. B.; Hellstrom, E. E. & Larbalestier, D. C. (2005). Improved upper critical field in bulk-form magnesium diboride by mechanical alloying with carbon. *Applied Physics Letters*, 86(20): 202502.

Sharma, P. A.; Hur, N.; Horibe, Y.; Chen, C. H.; Kim, B. G.; Guha, S.; Cieplak, M. Z. & Cheong, S. W. (2002). Percolative superconductivity in $Mg_{1-x}B_2$. *Physical Review Letters*, 89(16): 167003.

Shcherbakova, O.; Dou, S. X.; Soltanian, S.; Wexler, D.; Bhatia, M.; Sumption, M. & Collings, E. W. (2006). The effect of doping level and sintering temperature on $J_c(H)$ performance in nano-SiC doped and pure MgB_2 wires. *Journal of Applied Physics*, 99(8): 08M510.

Soltanian, S.; Wang, X. L.; Horvat, J.; Dou, S. X.; Sumption, M. D.; Bhatia, M.; Collings, E. W.; Munroe, P. & Tomsic, M. (2005). High transport critical current density and large H_{c2} and H_{irr} in nanoscale SiC doped MgB_2 wires sintered at low temperature. *Superconductor Science & Technology*, 18(5): 658-666.

Soltanian, S.; Wang, X. L.; Horvat, J.; Qin, M. J.; Liu, H. K.; Munroe, P. R. & Dou, S. X. (2003). Effect of grain size and doping level of SiC on the superconductivity and critical current density in MgB_2 superconductor. *IEEE Transactions on Applied Superconductivity*, 13(2): 3273-3276.

Treacy, M. M. J.; Ebbesen, T. W. & Gibson, J. M. (1996). Exceptionally high Young's modulus observed for individual carbon nanotubes. *Nature*, 381(6584): 678-680.

Ueda, S.; Shimoyama, J.; Yamamoto, A.; Katsura, Y.; Iwayama, I.; Horii, S. & Kishio, K. (2005). Flux pinning properties of impurity doped MgB_2 bulks synthesized by diffusion method. *Physica C-Superconductivity and Its Applications*, 426-431(2): 1225-1230.

Ueda, S.; Shimoyama, J. I.; Yamamoto, A.; Horii, S. & Kishio, K. (2004). Enhanced critical current properties observed in Na_2CO_3-doped MgB_2. *Superconductor Science & Technology*, 17(7): 926-930.

Wei, B. Q.; Vajtai, R. & Ajayan, P. M. (2001). Reliability and current carrying capacity of carbon nanotubes. *Applied Physics Letters*, 79(8): 1172-1174.

Werthame, N. R.; Helfand, E. & Hohenber, P. C. (1966). Temperature and purity dependence of the superconducting critical field, H_{c2}. III. Electron spin and spin-orbit effects. *Physical Review*, 147(1): 295-302.

Wilke, R. H. T.; Bud'ko, S. L.; Canfield, P. C.; Finnemore, D. K.; Suplinskas, R. J. & Hannahs, S. T. (2004). Systematic effects of carbon doping on the superconducting properties of $Mg(B_{1-x}C_x)_2$. *Physical Review Letters*, 92(21): 217003.

Xu, H. L.; Feng, Y.; Xu, Z.; Yan, G.; Cao, L. Z. & Li, X. G. (2004). Enhancement of critical current density in graphite doped MgB_2 wires. *Chinese Physics Letters*, 21(12): 2511-2513.

Yamada, H.; Hirakawa, M.; Kumakura, H. & Kitaguchi, H. (2006). Effect of aromatic hydrocarbon addition on in situ powder-in-tube processed MgB_2 tapes. *Superconductor Science & Technology*, 19(2): 175-177.

Yamada, H.; Hirakawa, M.; Kumakura, H.; Matsumoto, A. & Kitaguchi, H. (2004). Critical current densities of powder-in-tube MgB_2 tapes fabricated with nanometer-size Mg powder. *Applied Physics Letters*, 84(10): 1728-1730.

Yamamoto, A.; Shimoyama, J.; Ueda, S.; Horii, S. & Kishio, K. (2006). Reactivity of carbides in synthesis of MgB_2 bulks. *Physica C - Superconductivity and Its Applications*, 445-448: 801-805.

Yamamoto, A.; Shimoyama, J.; Ueda, S.; Iwayama, I.; Horii, S. & Kishio, K. (2005a). Effects of B_4C doping on critical current properties of MgB_2 superconductor. *Superconductor Science & Technology*, 18(10): 1323-1328.

Yamamoto, A.; Shimoyama, J.; Ueda, S.; Katsura, Y.; Iwayama, I.; Horii, S. & Kishio, K. (2005b). Universal relationship between crystallinity and irreversibility field of MgB_2. *Applied Physics Letters*, 86(21): 212502.

Yamamoto, A.; Shimoyama, J. I.; Ueda, S.; Katsura, Y.; Horii, S. & Kishio, K. (2005c). Doping effects on critical current properties of MgB_2 bulks synthesized by modified powder-in-tube method. *IEEE Transactions on Applied Superconductivity*, 15(2): 3292-3295.

Yeoh, W. K. & Dou, S. (2007). Enhancement of H_{c2} and J_c by carbon-based chemical doping. *Physica C - Superconductivity and Its Applications*, 456(1-2): 170-179.

Yeoh, W. K.; Horvat, J.; Dou, S. X. & Munroe, P. (2005). Effect of carbon nanotube size on superconductivity properties of MgB_2. *IEEE Transactions on Applied Superconductivity*, 15(2): 3284-3287.

Yeoh, W. K.; Horvat, J.; Kim, J. H.; Xu, X. & Dou, S. X. (2007a). Effect of carbon substitution on the superconducting properties of MgB_2 doped with multi-walled carbon nanotubes and nano carbon. *IEEE Transactions on Applied Superconductivity*, 17(2): 2929-2932.

Yeoh, W. K.; Horvat, J.; Kim, J. H.; Xu, X. & Dou, S. X. (2007b). Effect of processing temperature on high field critical current density and upper critical field of nanocarbon doped MgB_2. *Applied Physics Letters*, 90(12): 122502.

Yeoh, W. K.; Kim, J. H.; Horvat, J.; Dou, S. X. & Munroe, P. (2006a). Improving flux pinning of MgB_2 by carbon nanotube doping and ultrasonication. *Superconductor Science & Technology*, 19(2): L5-L8.

Yeoh, W. K.; Kim, J. H.; Horvat, J.; Xu, X.; Qin, M. J.; Dou, S. X.; Jiang, C. H.; Nakane, T.; Kumakura, H. & Munroe, P. (2006b). Control of nano carbon substitution for enhancing the critical current density in MgB_2. *Superconductor Science & Technology*, 19(6): 596-599.

Zeng, R.; Dou, S. X.; Lu, L.; Li, W. X.; Kim, J. H.; Munroe, P.; Zheng, R. K. & Ringer, S. P. (2009). Thermal-strain-induced enhancement of electromagnetic properties of SiC-MgB_2 composites. *Applied Physics Letters*, 94(4): 042510.

Zhao, Y.; Cheng, C. H.; Rui, X. F.; Zhang, H.; Munroe, P.; Zeng, H. M.; Koshizuka, N. & Murakami, M. (2003). Improved irreversibility behavior and critical current density in MgB_2-diamond nanocomposites. *Applied Physics Letters*, 83(14): 2916-2918.

Zhou, S. H.; Pan, A. V.; Wexler, D. & Dou, S. X. (2007). Sugar coating of boron powder for efficient carbon doping of MgB_2 with enhanced current-carrying performance. *Advanced Materials*, 19(10): 1373-1376.

7

Studies on the Gamma Radiation Responses of High Tc Superconductors

Carlos M. Cruz Inclán, Ibrahin Piñera Hernández,
Antonio Leyva Fabelo and Yamiel Abreu Alfonso
Center of Technological Applications and Nuclear Development, CEADEN
Cuba

1. Introduction

The Future applications of new solid state materials, electronic devices and detectors in radiation environments like Fission and Fusion new generation of Nuclear Reactors, as well as astronomical researches, require a well established understanding about the radiation response of all these items.

In addition to foregoing applications the Gamma Radiation (γR) combined effects of energy dependent displacement per atom (dpa) rates and high penetration strength might be attractive for getting a deeper understanding. In particular for high temperature superconductors (HTS) these are interesting for get a better comprehension about their superconducting mechanisms.

Quite controversial results have been reported in γR damage studies on HTS, especially on regard to the $YBa_2Cu_3O_{7-x}$ (YBCO) superconducting behavior. On this way, the papers dedicated to study gamma irradiation effects on the HTS properties are characterized for a lack of coincidence in criteria and results. Some authors have observed an improvement of the superconducting properties with dose increment (Boiko et at., 1988; Leyva et al., 1992), some others report exactly the opposite (Vasek et al., 1989; Elkholy et al., 1996), and other studies have not found any dependence (Bohandy et al., 1987; Cooksey et al., 1994). These contradictions have not been completely explained yet; some authors even attribute these behaviors to a "sample effect" (Polyak et al., 1990).

However, Belevtsev et al. (Belevtsev et al., 2000) has determined the relationship between the superconducting order parameter ξ_2 and the density of oxygen vacancy rate lower bound, expressed in displacement per atom, in order to achieve significant modification of the superconducting behavior. On this ground, by means of the Oen-Holmes-Cahn atom displacement calculation algorithm (Oen & Holmes, 1959; Cahn, 1959), they calculated the incoming gamma quanta total flux inducing a dpa rate of about 0.02. That makes the $YBa_2Cu_3O_{7-\delta}$ superconducting material mean intervacancies distance close to its superconducting coherence length or order parameter ξ_2, in which case the superconducting properties will be modified.

Consequently, a systematic behavior of HTS material properties upon γR must be expected to be observed, where superconducting intrinsic properties (crystal and electronic structures, critical superconducting temperature), as well extrinsic ones (critical

superconducting electrical current, electric resistivity at normal state) must show proper dependences on both, the induced dpa rates and the gamma radiation incident energies.
Present chapter is devoted presenting the research findings on regard the main physical issues characterizing the gamma radiation damages in high Tc superconductors, focusing to the induced superconducting and normal state physical properties modifications.
Firstly, in section 2 the basic concepts in gamma radiation damage studies on solids are presented, supported by an introduction to main approaches for calculating dpa rate distributions, which are discussed in section 3. Section 4 is devoted to simulations studies of gamma radiation transport in YBCO material, particularly those related to in-depth dpa profile distribution. Gamma radiation damage effects on the YBCO intrinsic properties are reported in section 5, involving the crystalline structure and superconducting critical temperature T_c behaviors under gamma irradiation. Finally, the γR damage effects on the YBCO extrinsic properties on regard to the superconducting critical electric current Jc and electrical resistivity in non superconducting normal state are discussed in section 6.

2. Basic concepts in gamma radiation damage studies on solids

Gamma rays transport in solid matrix involves multiple gamma quanta and secondary electrons interactions with host material valence and core atomic electrons as well with atomic nuclei leading to modifications of its crystal structure by the formation of an amount of point defects, like ionizations, color centers and atom displacements from crystalline sites. These defects modify the irradiated target microscopic and macroscopic properties in a specific way, which is usually referred as Gamma Radiation Damage.
A general measure of all these accounts related to Gamma Radiation Damage is the energy deposition at a given point in the target. Energy deposition spatial distribution can be calculated by means of Monte Carlo assisted gamma quanta transport codes, like EGS-4 (Nelson et al., 1985), EGSnr (Krawrakov & Rogers, 2003) or MCNP (Briesmeister, 2000). Alternatively, for measuring the intensity of the irradiation effects it has been applied the total incident gamma quanta fluence, as well as, the so called exposition doses.
However, from all point defects induced by gamma ray transport in solids, atom displacements might induce a large time scale target properties modification because of the huge time of life of induced vacancies and interstitial Frenkel pairs defect in target crystalline structure. Therefore, gamma radiation damage in solids is commonly described by the spatial dpa distribution. However, because of the insignificant photon transferred energies in their interactions with atoms, secondary electrons must be considered as the unique particles transferring enough recoil energy to the target atoms for leaving their crystalline sites leading to atom displacements processes in solids.
Consequently, high energy secondary electrons induced by gamma ray transport in solids might be considered its main radiation damage source through the basic atom displacements mechanism. This occurs as a result of high transferred recoil energy arising at high scattering angle electronic elastic collision with atoms. This is assumed to be truth whenever $T^k \geq T^k_d$ *(atom displacement main requirement)* (Corbett, 1966). Here T^k is the recoil kinetic energy transferred to the atomic specie A_k placed at a given crystallographic site and T^k_d is the corresponding atom displacement threshold energy value. T^k_d may depend on the crystallographic site and generally ranges between 20 eV to 40 eV. At a given initial electron kinetic energy E_i, T^k will be higher at lower atomic mass M_k and higher scattering angle θ ($\theta \rightarrow \pi$).

From the atom displacement main requirement, it follows that secondary electrons will induce atom displacements processes through the elastic atomic scattering for $E_i \geq E_C$ (Corbett, 1966; Piñera et al., 2007a), where

$$E_c = \sqrt{(mc^2)^2 + \tfrac{1}{2} M_k c^2 T_d^k} - mc^2 \tag{1}$$

For example, assuming for oxygen $T^O{}_d = 20\ eV$ (Piñera et al., 2007a), then $E_C = 130\ keV$ for oxygen in YBCO. However, for the O(5) YBCO crystalline sites, at the Cu-O chains at the crystal cell basis plane, Bourdillon & Tan had reported $T_d{}^{O(5)} = 3.45\ eV$, leading to a $E_c(O(5)) = 26\ keV$ (Bourdillon & Tan, 1995).

The removed atom as a result of an electron elastic atomic scattering is known as Primary Knock-on Atom (PKA). If any of these recoil atoms has a kinetic energy above the displacement threshold energy *Td*, the secondary atoms can be knocked-on by PKA and additional dpa cascades can be ascribed to the corresponding displaced atoms. Thus, these secondary atoms will enhance dpa rates on regard to PKA ones with an increasing contribution whenever $\boldsymbol{T^k \gg T^k_d}$.

Threshold energy $\boldsymbol{T^k_d}$ could be experimentally determined by high energy electron microscopy (over 200 keV), where the irradiating electron beam is applied for both, inducing and detecting vacancies when the electron beam incident energies is over $\boldsymbol{E_c}$ (Kirk et al. 1988; Frischherz, 1993; Kirk & Yan, 1999). Alternatively, spectroscopic methods like Electron Paramagnetic Resonance (EPR) and Hyperfine Interaction Methods may be applied indirectly for these purposes, by analyzing "off beam" electron or gamma quanta irradiated samples, searching for evidences of vacancies or other point defects induced on this way (Lancaster, 1973; Jin et al., 1997). The application of Mössbauer Spectroscopy in this framework is presented in section 5.1. For high symmetric and simple crystalline structures, like TiO_2, theoretical methods had been applying for threshold energy $\boldsymbol{T^k_d}$ determination, mainly through the application of the Molecular Dynamic approaches (Thomas et al., 2005).

3. Main approaches for calculating atom displacements rate distributions

3.1 Averaging methods following Oen – Holmes – Cahn algorithm

The mean number of electron elastic atomic scattering events leading to atom displacements processes along a given electron path can be calculated according to the expression

$$n_{dpa} = \sum\nolimits_{k,i} N^{e,k}_{dpa,i} = \sum\nolimits_{k,i} N^k_i \sigma^k_{dpa}(E_i) \Delta S_i \tag{2}$$

where $N^{e,k}_{dpa,i}$ is the number of atom displacements processes induced in a sectional electron path length ΔS_i, σ^k_{dpa} is the total electron elastic atomic scattering cross section (enhanced by the atom displacements contribution of secondary atoms ejected by PKA) ascribed to the k-th atomic specie with atomic density N^k_i for electron initial energies E_i at the beginning of the i-th sectional path, where it is assumed that $\sigma^k_{dpa}(E_i) = 0$ for $E_i \leq E^k_c$. In Fig. 1 is schematically represented a secondary electron scattering path.

Oen, Holmes and Cahn (Oen & Holmes, 1959; Cahn, 1959) had applied Eq. (2) by approaching the electron kinetic energy values at a given section path E_i as a continuous function of path length *S*,

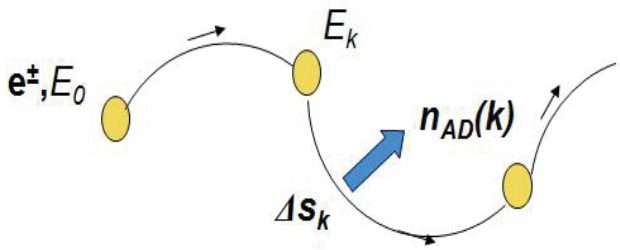

Fig. 1. A simplified physical picture of the electron transport in a solid matrix. Smooth movements along continuous path sections mostly prevail, representing an averaged multiple scattering events under low transferred energy and linear momentum values. These continuous sections delimited by single point like scattering events, where the electrons may suddenly change their kinetic energy and linear momentum values.

$$E(S) - E(0) = \int_0^S \left(-\frac{dE}{ds} \right) ds \tag{3}$$

where $\left(-\frac{dE}{ds} \right)$ is calculated following standard electron linear energy loss formula, as for example Bethe – Ashkin equation (Bethe & Ashkin, 1953), which represents a smoothed picture of the real fluctuating nature of high energy electron movements in a solid. Consequently, Eq.(2) is approached as

$$N_{dpa}^{e,k} = N_a \int_{E_c^k}^{E} \sigma_{dpa}^k (E(s'))ds' = N_a \int_{E_c^k}^{E} \frac{\sigma_{dpa}^k (E')}{\left(-\frac{dE}{ds'} \right)} dE' \tag{4}$$

where N_a is the number of atoms in the unit volume in the sample. Then, by assuming a mean energetic electron flux distribution $\Phi(E_i,z)$ in the neighborhood of a target sample point at a depth z, the Oen-Homes-Cahn algorithm calculates total number of displacement per atom N_{dpa} at the given point according to the expression

$$N_{dpa} = \sum_k \left(n_k \left(\sum_i N_{dpa,k}^e (E_i) \Phi(E_i, z) \Delta E_i \right) \right) \tag{5}$$

where n_k denotes the relative fraction of the *k*-atom in its crystalline sublattice. The Oen-Holmes-Cahn algorithm will be referred as the "atom displacements Classical Method calculation".

The applications of the Eq. (5) in the practice have been done mostly assuming a "model" dependence $\Phi(E_i,z)$ following an in depth exponential decay law as well as the Klein - Nishina energy distribution for electron emerging from a Compton interaction. This approach was applied by Belevtsev et al. to YBCO dpa calculations (Belevtsev et al., 2000). However, Piñera et al. had shown by means of Monte Carlo Methods assisted gamma quanta transport calculations in YBCO matrix, that $\Phi(E_i, z)$ does not follow such a "model" dependence on regard of both, E_i *and* z as it is shown in Fig. 2 (Piñera et al., 2007a).

In Fig.2 the kinetic energy distribution of electrons energy fluxes were calculated for YBCO ceramic sample with parallelepiped form. These distributions were determined in the central line voxel at a depth corresponding to the maximum energy deposition on which impact photons at different selected incident gamma energies. Monte Carlo method code MCNP-4C was used.

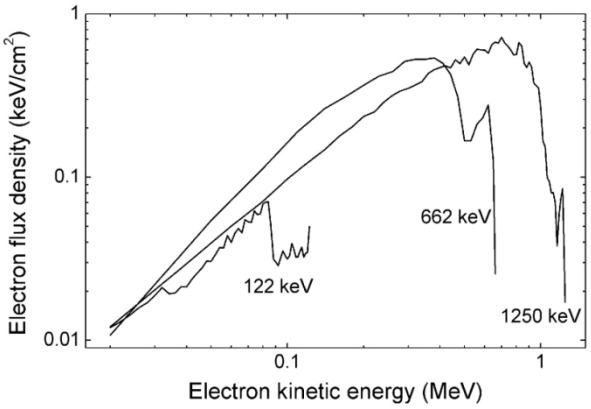

Fig. 2. Kinetic energy distribution of electrons energy flux in central voxel for different incident gamma energies. (Piñera et al., 2007a)

Two important facts arise from these kinetic energy distribution profiles $\Phi(E_i,z)$. Firstly, the ejected photoelectrons own the higher kinetic energies values ($\approx E_\gamma$) with an appreciable relative intensity, which can give an important contribution to dpa rate. On the second place, the continuous Compton electron contribution at lower energies becomes a broader unimodal distribution with a relative maximum near to the Compton electron maximum kinetic energy. This is an essentially different behavior, as predicted by Klein-Nishina scattering law for Compton scattered electrons ruled by electron multiple scattering relaxation processes (Klein & Nishina, 1929).

Therefore, this complex electron kinetic energy distribution behaviors seen before do not agreed with the starting assumptions taken in by Belevtsev et al. for the direct calculation of dpa rate in YBCO (Belevtsev et al., 2000), clearly supporting the introduction of a more realistic treatment for secondary electron transport as done in Monte Carlo based codes here applied. This is the aim of the Monte Carlo assisted Classical Method (MCCM) introduced by I. Piñera et al. (Piñera et al., 2007a, 2007b, 2008a, 2008b).

The MCCM consists in applying to the classical theories about atom displacements by electrons and positrons elastic scattering with atoms the flux $\Phi(E_i,z)$ distribution of these particles obtained from the Monte Carlo simulation. Oen-Holmes-Cahn Classical Method does not take into account the shower and cross linked nature of the gamma quanta and the secondary electron interactions happen at γR transport in solids. But this γR complex stochastic behavior can be nowadays very well simulated and described through calculation codes based on Monte Carlo method, modeling the transport of different types of radiations in substance. Thus, on this basis, it can be locally calculated the Energy Deposition distribution as well as the energy profile flux distributions of the transported particles, which might provide the calculation tools required for Radiation Damage evaluation.

By the application of Eq. (4) in MCCM,

$$\sigma_{dpa}^{k}(E) = \sigma_{PKA}^{k}(E) \cdot \nu(T) \tag{6}$$

where $\sigma_{PKA}^{k}(E)$ is the PKA cross section following the McKinley – Feshbach equation (McKinley & Feshbach, 1948)

$$\sigma_{PKA}^{k}(E) = \frac{\pi r_0^2 Z_k^2}{\beta^4 \gamma^2} \cdot \{\tau - 1 - \beta^2 \ln(\tau) \pm \pi\alpha\beta\left[2\sqrt{\tau} - \ln(\tau) - 2\right]\} \tag{7}$$

with Z_k being the atomic number of the k-atom, r_0 is the electron classic radius, $\alpha = Z_k/137$, $\boldsymbol{\beta}$ is the ratio of the electron velocity to the velocity of light, $\boldsymbol{\gamma}^2 = 1/(1 - \beta^2)$, $\boldsymbol{\pi} = T^k_{max}/T^k_d$, being $T^k_{max} = 2E(E + 2mc^2)/M_k c^2$ the maximum kinetic energy of the corresponding recoil atom with mass M_k and $\nu(T)$ is the damage function, which in the case of MCCM is implemented according to the Kinchin – Pease model (Khinchin & Pease, 1955)

$$\nu(T) = \begin{cases} 0, & T < T_d^k \\ 1, & T_d^k \le T \le 2T_d^k \\ \frac{T}{2T_d^k}, & T > 2T_d^k \end{cases} \tag{8}$$

This damage function introduces an enhancement factor in dpa calculations due to the atom displacement cascades phenomenon. To evaluate $\nu(T)$ in MCCM, the average value of the scattered atoms energies, $\boldsymbol{T}^k_{ave}$, is calculated through the expression

$$T_{ave}^{k} = \frac{\tau\ln(\tau) - \beta^2(\tau-1) \pm \pi\alpha\beta(1-\sqrt{\tau})^2}{\tau - 1 - \beta^2\ln(\tau) \pm \pi\alpha\beta\left[2\sqrt{\tau} - \ln(\tau) - 2\right]} \tag{9}$$

3.2 Monte Carlo Simulation of Atom Displacements

The basic ideas supporting the present description of the atom displacements processes induced by the electron transport in a solid matrix are represented in Fig. 3. As usually, in a macroscopic scale, the Monte Carlo Methods based simulation of the electron transport in solids is treated as a sectional smooth continuous path, delimited by discreet point like events arising at high transferred energy and linear momentum. In the present case, the atom displacements processes are only produced at elastic scattering discreet events at high scattering angles, where enough energy is transferred to an atom to be ejected from its crystalline site. It will also imply that atom displacements processes do not take place under the sectional continuous path.

As a reference point, in Fig. 3 is also represented the Fukuya's approach to atom displacements processes (Fukuya & Kimura, 2003), following the classical Oen-Holmes-Cahn dpa calculation algorithm. In this case, the continuous electron motion path lengths are sampled according to a Monte Carlo simulation of the gamma quanta and electron transport in a solid under which the electron elastic scattering events at high scattering angles are not involved. Consequently, atom displacements processes are essentially

calculated in Fukuya's approach on the basis of the continuous path lengths which really are connected to an averaged multiple quasi-continuous electron motions under small electron linear momentum and energy instantaneous changes.

Cruz et al. proposed a new approach involving the full Monte Carlo Simulation of Atom Displacements (MCSAD). In MCSAD the occurrence of single and multiple Elastic Scattering (ES) events is defined by the limiting scattering angle θ_l, according to Mott's criteria (Mott & Massey, 1952), at which the electron single and multiple ES probabilities become equals.

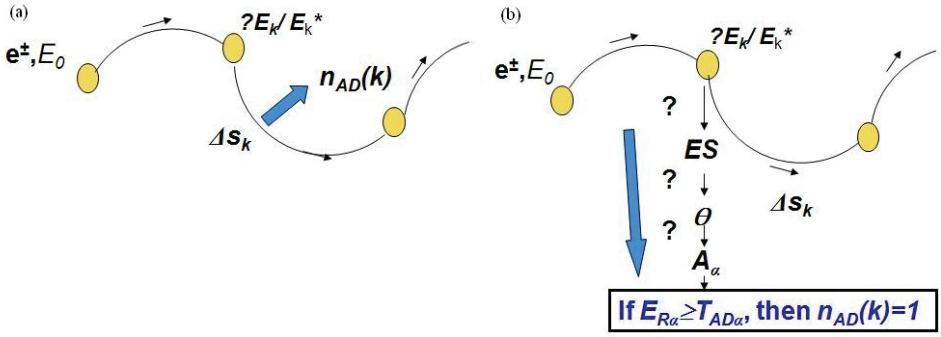

Fig. 3. (a) Fukuya's treatment of atom displacements processes (Fukuya & Kimura, 2003). (b) New MCSAD approach (Cruz et al., 2008). E_k denotes the electron kinetic energy; n_{dpa} is the number of atom displacements events. Solid bold balls represent the occurrence of single scattering events (Elastic Scattering, Moeller or Bremsstrahlung).

Electron multiple ES probability were calculated according to Moliere-Bethe Theory (Bethe, 1953). Thus, McKinley-Feshbach cross section was renormalized for the occurrence of single ES between π and θ_l according to the following expression for the total Macroscopic Cross Section $\Sigma_{ES}(\theta_l)$ of the discreet electron elastic atomic scattering processes

$$\sum_{ES}(\theta_i) = \frac{1}{4}\frac{\theta_c^2}{\Delta s}\xi^{-2}\left[1 \pm 2Z\pi\alpha\beta\xi\right] - (1 \pm 2Z\pi\alpha\beta)\xi^2 + 2\left(\beta^2 \pm Z\pi\alpha\beta\right)\xi^2 \ln(\xi) \qquad (10)$$

where $\xi = \sin(\theta_1/2)$, $\beta = (1 - E_0^2/E^2)$, $\theta_c^2 = (0.60089)Z_s(\frac{\rho\Delta s}{A})(\frac{c^2p^2}{E})^2$ and Z_s is defined in the EGS-4 user manual (Nelson et al., 1985). The positive sign is related to the electron scattering and the negative sign to the positron one.

The occurrence of an electron single ES event is sampled regarding the other competing interactions (Moeller electron scattering, Bremsstrahlung and Positron Annihilation). The emerging electron single ES angular distribution was described applying the McKinley – Feshbach cross section formula restricted to the scattering angles inside the interval $\theta_l \le \theta \le \pi$, which was consequently renormalized by the Total Macroscopic Cross Section $\Sigma_{ES}(\theta_l)$ value given by Eq. (10). This angular probabilistic distribution function was statistically sampled by the application of the combination and rejection methods.

On this way ES scattering angle θ was sampled and the occurrence of this event at a given constituting atom A_k will randomly arise by taking into the account to the relative weight of each atomic species in the total elastic scattering process. Consequently, a given atomic sort

A_k is sampled and the transferred energy $\boldsymbol{T^k}$ is determined. Following the atom displacement main request, if $\boldsymbol{T^k \geq T^k_d}$ hold for the stochastically chosen k-th atomic specie, then $n_{dpa} = 1$, which means that an atom displacement event takes place. Otherwise, single ES event leads to a phononic excitation of the solid.
Some partial results involving Monte Carlo gamma quanta and secondary electron simulations on regard atom displacements rates produced in YBCO are represented in Fig. 4 for different electrons initial energies. Fig. 4 shows that each atomic specie contributes to atom displacement processes only over a given critical electron kinetic energy E_c. A critical evaluation among MCSAD predictions with those previously obtained by Piñera et al. and Fukuya-Kimura is in course (Piñera et al., 2007a, 2007b, 2008a, 2008b; Fukuya & Kimura, 2003).

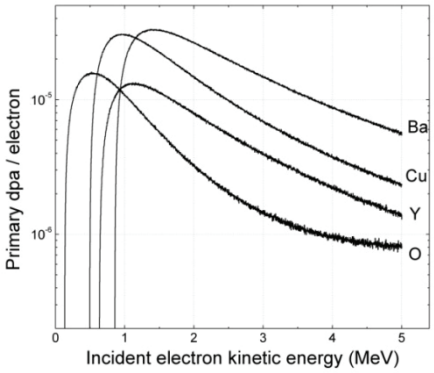

Fig. 4. Monte Carlo simulation of ES processes inducing Primary Knock-On Atomic Displacements in $YBa_2Cu_3O_{7-\delta}$ depending on electron initial energy at a given discreet event.

4. Monte Carlo numerical simulations of gamma radiation damage in YBCO

4.1 Gamma ray dpa in-depth distribution in YBCO

Some results of applying MCCM method on slab samples of the YBCO superconducting material are reported here. The MCNPX code (Hendricks et al., 2006) was used for simulation purposes, considering that it gives directly the flux energy distribution through its energy bin *F4 tally, separating contributions from electrons and positrons with the help of the FT card ELC option. Fig. 5 shows the calculated number of displacement per atom for electrons and positrons for incident gamma energies (E_γ) up to 10 MeV.
As it can easily observed, the shape of these profiles for electrons and positrons are very similar. Also, the *dpa* values are always higher at higher incident radiation energies in all the sample volume and the damage increases drastically with depth as the incident energy increases. Also, averaging the $N_{dpa}(z)$ values over the sample thickness, the total *dpa* for each E_γ is obtained. This was done in such a way that we could evaluate separate the contributions from electrons and positrons. These contributions are shown in Fig. 6a together with the total *dpa* distribution.
As can be seen from this figure, the contribution from electrons to the total *dpa* is greater up to about 8 MeV, beyond which the *dpa* induced by positrons begins to prevail. At E_γ = 10 MeV the positrons *dpa* contribute for 53.4%, almost 7% higher than the corresponding contribution induced by electrons. It is important to note that, when positrons are also

considered in the atom displacement process, the total *dpa* at 10 MeV of incident gamma radiation increase up to 2.15 times compared to the situation that only electron interactions are considered. The contribution from each atom to the total *dpa* value was also possible to be studied like it is shown in Fig. 6b. The contribution of the Cu-O_2 planes was considered, taking together the effects on the oxygen and the copper atoms in those sites. The results show that the contribution to the total damage from yttrium and barium atoms is smaller than the contribution from the Cu-O_2 planes. They have a maximum contribution of 11.7% (in case of Y) and 30.9% (in case of Ba) for 10 MeV of incident radiation. This result could support the fact that Y and Ba displacements are not decisive for the possible changes provoked in this material at low and medium energies (Belevtsev et al., 2000; Legris et al., 1993). Then, the main contribution to the total damage comes from the Cu-O_2 planar sites in the sample in the studied energy range.

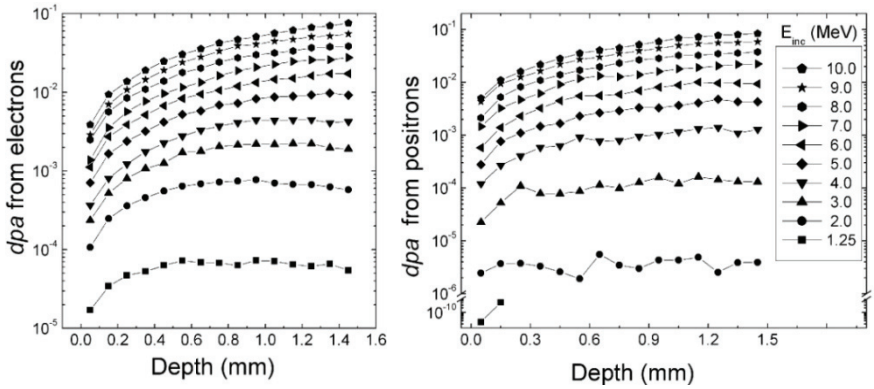

Fig. 5. *dpa* in-depth distributions due to electrons (left) and positrons (right) for different incident energies. Continuous lines are only visual guides.

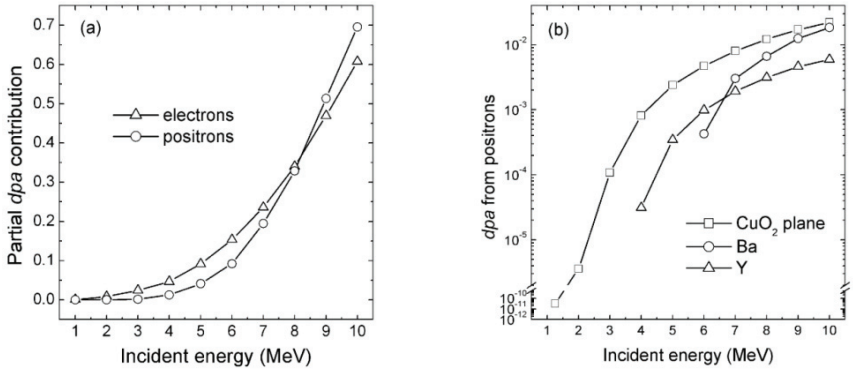

Fig. 6. (a) Number of *dpa* induced by electrons and positrons at different incident gamma energies. (b) Number of positrons *dpa* corresponding to each atom site at different incident gamma energies. All continuous lines are only visual guides.

The independent contributions from oxygen and copper atoms to the in-plane dpa could be also analyzed. The contribution from oxygen atoms diminishes with increasing the incident

energy while the contribution from copper atoms increases to 62% in the studied energy range. Another interesting observation is that the main dpa contribution with regard to the Cu-O_2 planes arises from O-displacements up to 4 MeV. But at higher energies, an increasing role of Cu-displacements is observed, reaching a maximum contribution of about 65% inside planes at E_γ = 10 MeV (Piñera et al., 2008a).
Similar analysis about these points can be made taking separately the contributions from positrons and electrons.

4.2 Dependency between dpa and energy deposition

Comparing the dpa distributions from Fig. 5 with the corresponding energy deposition profiles and taking some previous own-works as reference, was possible to study the dependence between both distributions (dpa and energy deposition), like that shown in Fig. 7a. It seems apparent from this figure that a nearly linear dependence may be established between the energy deposition and the number of atoms displaced by the gamma radiation at a given incident energy in the YBCO material. For this reason we carry out the linear fitting of these dependences, which can be analyzed in Fig. 7b, obtaining the dpa to energy deposition production rate η at each incident energy. Correspondingly, it can also be asserted that the Gamma Radiation energy deposition process in YBCO material supports better the atom displacement production at higher incident energies.

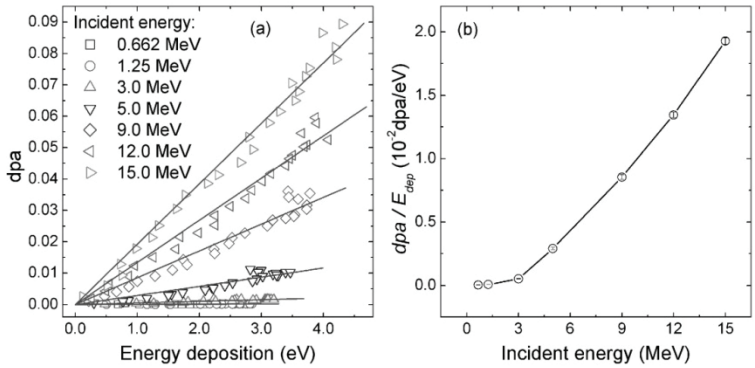

Fig. 7. (a) Dependence between dpa and energy deposition for each incident energy. Continuous lines represent the linear fitting. (b) Displacements to energy deposition rate as function of the incident energy. Continuous lines are visual guides.

Consequently, there exists a general local dependence among N_{dpa} and E_{dep} values, independently of the given target position,

$$N_{dpa} = \eta(E_\gamma) \cdot E_{dep} \tag{11}$$

where η is the dpa rate per deposited energy unit at any target position, which depends on the initial gamma ray value following Fig. 7b, as well as on the atomic composition of the target material (Piñera, 2006).
These particular behaviors should be expected, since secondary electrons play an important and decisive role on the general energy deposition mechanism and particularly on displacing atoms from their crystalline sites. On this basis, it must be reasonably to assume

that the previously findings reported by Leyva (Leyva, 2002) (see below section 5.2) on regard with the observed correlation among in-depth measured T_c and calculated E_{dep} values might be extrapolated to among the former one and the calculated dpa values.
On the other hand, exposition doses D_{exp}, is related to the total incident gamma ray quanta through the equation

$$\Phi = \frac{D_{\exp}}{E_\gamma} \cdot \frac{\rho_{air}}{\mu_a(E_\gamma)}, \tag{12}$$

where $\mu_a(E_\gamma)$ is the gamma air mass absorption coefficient at the incident energy E_γ and Φ is the incoming total gamma quanta. On this way, knowing the exposition dose D_{exp} from dosimetric measurements, Eq. (11) allows to calculate Φ. This is related with the number of histories of independent gamma ray transport to be calculated by means of any of the Monte Carlo based codes introduced above in sections 2 and 3. Then, E_{dep} and N_{dpa} distributions corresponding to a given irradiation experiment can be determined through theses D_{exp} values.

5. Gamma radiation damage effects on the YBCO intrinsic properties: crystalline structure and superconducting critical temperature T_c

5.1 Gamma ray influence on YBCO crystalline structure

The ideal well ordered orthorhombic $YBa_2Cu_3O_{7-x}$ unit crystal cell owing high Tc superconducting behaviour (Fig. 8a) is observed only for $\delta \leq 0.35$, where Oxygen site O(5) along the a axis are completely unoccupied (Santoro, 1991). For $\delta \geq 0.35$ this material undergoes an orthorhombic to tetragonal phase transition, which is shown in Fig. 8b through the temperature behavior by heating of the $YBa_2Cu_3O_{7-\delta}$ orthorhombicity parameter (ε), where $\varepsilon = (a-b)/(b+a)$. It is observed that at 950 K, $\varepsilon = 0$, which means that lattice constants *a* and *b* become equals, which corresponds to the tetragonal crystal structure.

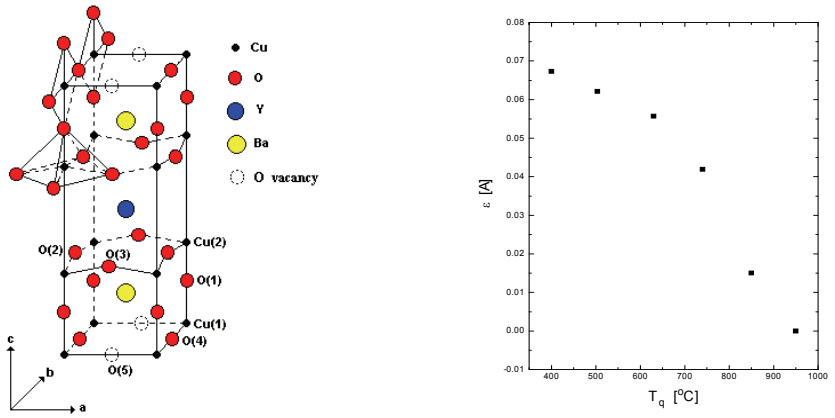

(a) (b)

Fig. 8. (a) YBCO orthorhombic crystal unit cell. (b) YBCO orthorhombicity temperature dependence.

In connection with YBCO crystal structure featuring, Cu(1)-O chains in the basal planes play an important role, since its YBCO non–stoichiometric behavior is related to existing Oxygen vacancies in these sites (O(4)). It modulates also its electrical conducting properties (Gupta & Gupta, 1991) for $\delta \leq 0.35$ it owns metallic conduction (it turns superconducting at $T \leq T_c$), while for $\delta \geq 0.35$ it reaches a semiconducting behavior, being the electronic conduction associated to Cu(2) – O_2 planes.

Though an ideal orthorhombic structure is accepted to be observed at $\delta = 0$, for $\delta > 0$ an $YBa_2Cu_3O_{7-\delta}$ oxygen disorder at its crystal unit cell basis plane take place: both, O(4) and O(5) sites, are partially and random occupies. Therefore, Cu(1) sites will be surrounded by different oxygen configurations, where the four neighbor oxygen positions O(4) and O(5) will be randomly occupied.

Fig. 9 shows the different oxygen nearest neighborhood around the Cu(1) sites, where the nomenclature OC. Nα idicates the oxygen coordination number N, oriented in the α direction. At the orthorhombic structure, $0 < \delta \leq 0.35$, O(4) sites will be preferably occupied, oxygen rich nearest neighbor configurations OC.4α, OC.4αβ, OC.5α are mostly to be expected. X- Ray Diffraction studies had shown the tendency, that higher O(4) occupation fraction leads to shorter Cu(1)-O(4) distance, while lower O(5) occupation fraction leads to higher Cu(1)-O(5) distance. On the contrary, at the tetragonal structure, $\delta > 0.35$, both, O(4) and O(5), are randomly, but equally occupied, pour oxygen nearest neighbor configuration only take place. In the limit of $\delta = 1$, which observed at annealing temperature over 1200 K, both oxygen basal plane positions remain unoccupied. The ordering of the atoms of oxygen in the chains plays an important role in the control of the charge carrier concentration in the CuO_2 planes (Gupta & Gupta, 1991), what must influence the superconducting intrinsic properties, like Tc.

YBCO samples exposed to ^{60}Co gamma irradiation does not follow the orthorhombic to tetragonal structural transition pattern observed by heating, as it can be easily observed by comparison of the ε orthorhombicity parameter behaviors shown in Figs. 8b and 10b.

YBCO samples were irradiated in a ^{60}Co gamma chamber and the orthorhombic lattice constants were measured by X-Ray Diffraction. The dose dependence of the experimentally determined lattice constants for one representative sample is shown in Fig. 10a. The values corresponding to the YBCO cell parameter obtained from (JCPDS, 1993) have been represented by dashed lines and will ascribed as YBCO ideal structure parameters with optimum superconducting properties.

The sample just after the synthesis process presents oxygen basal plane disorder in its structure as a result of the heat treatments, since its lattice parameters were found away from the ideal ones. With the beginning of the irradiation process a singular behavior of the lattice parameters is observed (see Fig. 10a). The *b* and *c* reach their optimum values at near the exposition dose $E_0 \approx 120$ kGy, beyond E_0 they diminish approaching to some intermediate value between the optimum and the initial ones. The lattice constant a changes monotonically, approaching for $E_{dose} \geq E_0$ to its optimum value. On the other hand, the orthorhombicity parameter ε oscillates around the YBCO optimum value.

It is clear from the lattice constants and crystal cell parameters behaviors under gamma irradiation shown in Fig. 10, that gamma ray induced YBCO crystal structure variations do not correspond to a deoxygenating process, as in thermal activated treatments at temperatures higher than 600 K, in which cases the non – stoichiometric parameter δ increases, provoking the $YBa_2Cu_3O_{7-\delta}$ orthorhombic to tetragonal phase transition. In any

case, it seems that the gamma exposition, specially at doses about E_0, has stimulated an population increase of the oxygen rich nearest neighbor configurations in the oxygen basis plane disorder picture , like the OC.4α, OC.4αβ, OC.5a ones, as it is expected from the a and b approaching tendency to $YBa_2Cu_3O_{7-\delta}$ ideal crystal structure values. At higher exposition doses, it seems that the oxygen rich nearest neighbor configuration population displace partially back from the optimum ones and tend to stabilize to a long range orthorhombic structure.

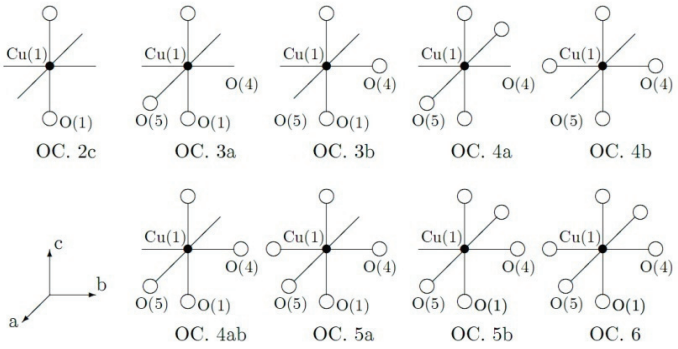

Fig. 9. Oxygen configurations (OC) formation considered around Cu(1) position.

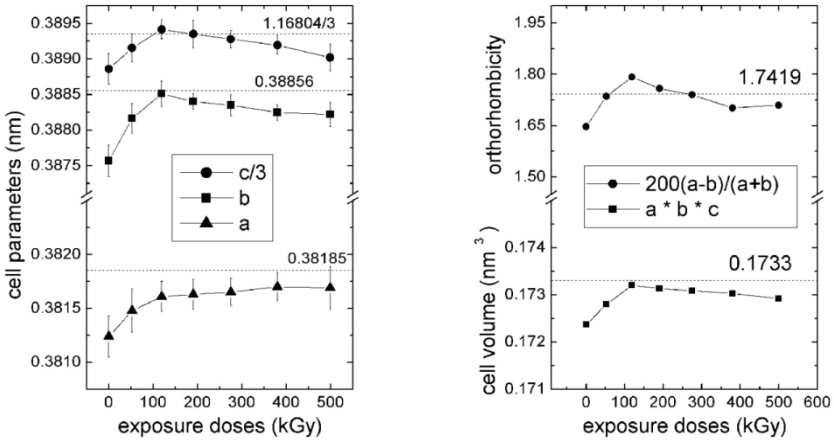

Fig. 10. ^{60}Co - γ dose exposition dependence of the YBCO elementary cell parameters, volume and orthorhombicity behaviors measured by X-Ray Diffraction. (a) Orthorhombic cell lengths a, b and c. (b) Elementary volume and orthorhombicity. Dashed lines represent the presupposed optimum values of YBCO cell parameters, volume and orthorhombicity.

It is possible to get deeper in the foregoing gamma radiation damage picture by means of the application of the magnetic resonance methods and the hyperfine interaction techniques, like the Mössbauer Spectroscopy, allowing a better understanding of the crystal short range order, especially defects properties, since in X-ray Diffraction studies long range crystal order is better evaluated. Therefore the gamma radiation impact on YBCO oxygen basis

plane disorder had been studied by ^{57}Fe Mössbauer Spectroscopy (Jin et al., 1997), in which case, ^{57}Fe very low doping contents were applied ($YBa_2(Cu_{0.97}Fe_{0.03})_3O_{7-\delta}$) and the Fe: YBCO doped samples were exposed with ^{60}Co gamma radiation up to 1 MGy.
The Mössbauer spectra were measured after and before irradiation; these spectra are characterized by four lines presented in Table 2; and the main effect they observe was that the D1 doublet relative area decreases and the D4 doublet relative area increases in correspondence. The variation on these magnitudes was around 5% and the created damage was reversible after some days. This radiation effects were ascribed to some oxygen coordination environment associated to D1, which becomes under irradiation in some other one related to D4 due to mainly atoms displacements and electron trapped in vacancies (color centers). This effect is different from the one observed by thermal activation oxygen hopping between the coordination structures of doublets D1 and D2 (Jin et al., 1997).

Doublet	IS (mm/s)	ΔE_Q (mm/s)	W (mm/s)	S (%)
D1	0.06	2.00	0.16	32
D2	0.03	1.10	0.25	53
D3	0.23	0.40	0.16	12.2
D4	0.24	0.16	0.10	4.8

Table 2. Isomer shift (IS), quadruple splitting (ΔE_Q), line width (W) and relative area (S) of ^{57}Fe subspectra in the Mössbauer spectra of $YBa_2(Cu_{0.97}Fe_{0.03})_3O_{7-\delta}$ samples (Jin et al., 1997).

To analyze these observations the correspondence between ^{57}Fe crystallographic sites and the Mössbauer subspectra should be take in to account; but some contradictions subsist in the interpretation of ^{57}Fe Mössbauer spectra in $YBa_2Cu_3O_{7-\delta}$ (Jin et al., 1997; Boolchand & McDaniel, 1992; Sarkar et al., 2001; Liu et al., 2005), reason that stimulated the reanalysis of this problem. In order to promote these aspects, a methodology developed by Abreu et al. (Abreu et al., 2009) was used to consider the structural defects influence in the quadruple splitting observed values; through the calculation of the electric field gradient (EFG) components in this situation by the point charge model (Abreu et al., 2009; Lyubutin et al., 1989). Specifically the point defects are taken in to consideration through different oxygen configurations, like cluster formation around the ^{57}Fe position and vacancies; and electron trapped in vacancies near this position too, like negative vacancies.
To take in to consideration the influence of crystallographic point defects in the Mössbauer probe atom neighborhood to the EFG, the methodology presented by Abreu et al. was applied (Abreu et al., 2009). The EFG values in the material with presence of vacancies and defects (V_{def}) could be consider as the ideal value (V_{ideal}), calculated following the point charge algorithm outside the first coordination sphere where the ^{57}Fe provoke the presence of oxygen atoms over the ideal composition; adding (V_{oc}), which is the EFG value inside the first coordination sphere, considering the formation of oxygen configurations (OC) due to the ^{57}Fe presence in the structure and the radiation damage process (Santoro, 1991).

$$V_{def} = V_{ideal} + V_{oc} \tag{13}$$

Parameters reported for the YBCO (Liu et al., 2005; Lyubutin et al., 1989; Santoro, 1991) were used to calculation the EFG values for the ideal tetragonal and orthorhombic structure. These calculations were made following point charge model algorithm; reaching a precision order in the sum of 10^{-6} for the atoms located inside a sphere with radius R = 380 A^o. The

ionic charges were taken mainly as nominal values: Y^{+3}, Ba^{+2}, O^{-2}, Cu^{+2} for Cu(2) positions; and in the Cu(1) position, Cu^{+1} for the tetragonal case and Cu^{+3} for the orthorhombic ones.
Since the interest is to evaluate the EFG and the corresponding ΔE_Q observed in the Mössbauer experiments of this superconducting material, the ^{57}Fe location will be consider only in the Cu(1) position as it was reported for doublets D1 and D4 (Jin et al., 1997; Boolchand & McDaniel, 1992; Santoro, 1991).
It is also interesting to analyze the influence of Iron atoms introduction in the $YBa_2Cu_3O_{7-\delta}$ crystalline structure. Santoro reported that in that case the oxygen content on the material is over ($7 - \delta \geq 7$); caused by oxygen vacancies population around the Cu(1) position, depending on iron ionization state (Santoro, 1991). For this reason the OC around the Cu(1) position shown in Fig. 9 were considered in the calculations.
Finally, it becomes necessary to obtain the corresponding splitting values due to the hyperfine quadruple interaction of the nuclear sublevels ΔE_Q, which are observed in the experiment. This magnitude could be calculated from the following expression (Abreu et al., 2009; Lyubutin et al., 1989)

$$\Delta E_Q = \frac{1}{2} e V_{zz} Q (1 - \gamma_\infty) \left[1 + \frac{1}{3} \eta^2 \right]^{\frac{1}{2}} \tag{14}$$

where e is the electron charge, Q is the nuclear quadruple momentum of Iron and $1 - \gamma_\infty$ is the Sternheimer anti-shielding factor. To evaluate ΔE_Q the following values of this parameters for the ^{57}Fe (I = 3/2) were used in all cases, Q = 0.16b and γ_∞ = −9.14 (Abreu et al., 2009; Lyubutin et al., 1989).
The calculation results are presented in Fig. 11 for all the oxygen configurations studied. From the ΔE_Q results could be assigned the doublet D1 to the OC. 5a for the orthorhombic structure and OC. 5a & 5b for the tetragonal, while the doublet D4 could be assigned to OC 6. Is clear from these assignations that an oxygen displacement event could move this atom to the vacant position present in the OC. 5; transforming it in the OC. 6. A negative vacancy (electron trapped) was also added to the OC. 5; and in both cases the ΔE_Q values changes as indicated by the vertical arrows; so the same effect is observed with negative vacancies and with oxygen atoms displacements events in the Cu(1) position first coordination neighborhood. With the obtained results the damage effects reported by (Jin et al., 1997) are confirmed. These findings agreed well with those previously reported X-ray Diffraction ones.
X-Ray Diffraction and Mössbauer Spectroscopy studies on ^{60}Co – γ quanta irradiated YBCO samples lead to the conclusion, that gamma radiation induced oxygen displacements in both, Cu(2)-O_2 planes and Cu(1)-O chains (Piñera et al., 2007a), as well as secondary electrons are eventually trapped in unoccupied O(4) and O(5) sites in crystal unit cell basis plane, provoking a strengthening of the orthorhombic structural phase, specially at relative low exposition dose E_0 ≈120 kGy.

5.2 Superconductive critical temperature Tc behavior on the gamma quanta exposition doses

The ^{60}Co-γ radiation induced reinforcement of the orthorhombic crystal structure properties at relative low exposition doses seems to correspond also to an enhancement of the YBCO superconducting properties. A maximum in the T_{on} with the dose dependence for YBCO and BSCCO samples was reported at $E_0 \sim 100$ *KGy* (Leyva et al., 1992). Upon irradiating thick YBCO films, a maximum in the dependence of T_c with E_0 ranging between 120-130 kGy was also observed (Leyva et al., 1995).

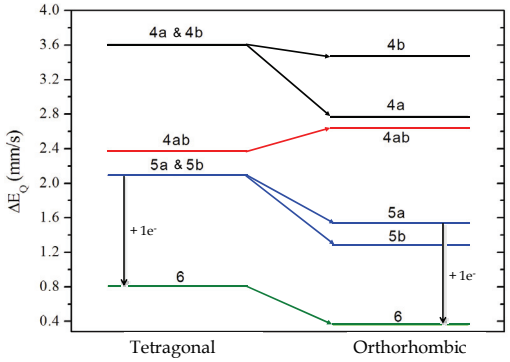

Fig. 11. ΔE_Q values obtained for the OC in the studied crystalline structures.

In Fig. 12 is schematically represented a ^{137}Cs gamma irradiation experiment on YBCO samples, where in depth Tc was measured at defoliated samples after irradiation, as it is shown in Fig. 13a.

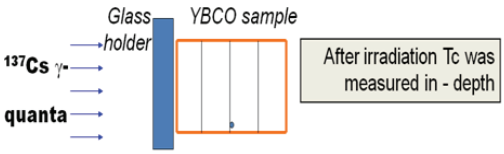

Fig. 12. ^{137}Cs gamma ray irradiation experimental and simulation applied for gamma radiation damage YBCO in depth studies.

The intact samples were placed within a glass container to preserve it from ambient conditions. The container was directly exposed to a ^{137}Cs source calibrated to a power dose of $1x10^{-3}$ Gyh^{-1} until a 0.265 Gy exposition dose was reached. The irradiation took place at room temperature.

For all samples, the transition temperatures were measured using the "four probe method", first placing the probes on the surface that later should be directly exposed to the radiation source and next on the opposite side.

Fig. 13a shows the results of the after irradiation measurements for one representative sample. Measurements made on the surface directly exposed to the source show an improvement of the superconducting properties. Its critical temperature increased in 2.24 K and the transition width decreased from 3.15 K to 1.44 K. The transition temperature values measured on the opposite surface practically did not change.

The in-depth gamma ray energy deposition profile were simulated by means of EGS-4 code, where in the simulation the real geometrical conditions were preserved and $1x10^8$ incidents 662 keV photons were taken in order to obtain a good statistics. The variance of each obtained value did not surpass 0.5 %.

The results of this experiment are very important, showing a positive correlation among in depth T_c measured values with the simulated deposited energy ones, as an increasing monotonic "*in situ*" relationship, since in previous gamma ray induced Tc enhancement reports, Tc were measured only on the irradiated sample surface and global irradiation effects by means of the exposition doses measurements were established. Furthermore, the Eq. (11) lead also to the conclusion, that such an in-depth correlation among Tc and the

energy deposition values must be worth among the former ones and the atom displacement rate N_{dpa}. This means that the upraise of induced vacancy concentration (relaying mainly for ^{137}Cs in changes in the oxygen distribution in YBCO basal plane) at the YBCO incident surface provokes a Tc increase, very close to the above reported ^{60}Co-γ radiation YBCO Tc enhancement and in excellent agreement with X-Ray Diffraction and Mössbauer Spectroscopy findings seen in section 5.1.

However, this YBCO Tc gamma radiation induced enhancement depends on the initial non-stoichiometric parameter δ (Leyva, 2002), as it is shown in Fig. 14. Here, YBCO samples with different non-stoichiometric parameter δ (and corresponding different initial Tc values) were irradiated with ^{60}Co gamma ray at different exposition doses.

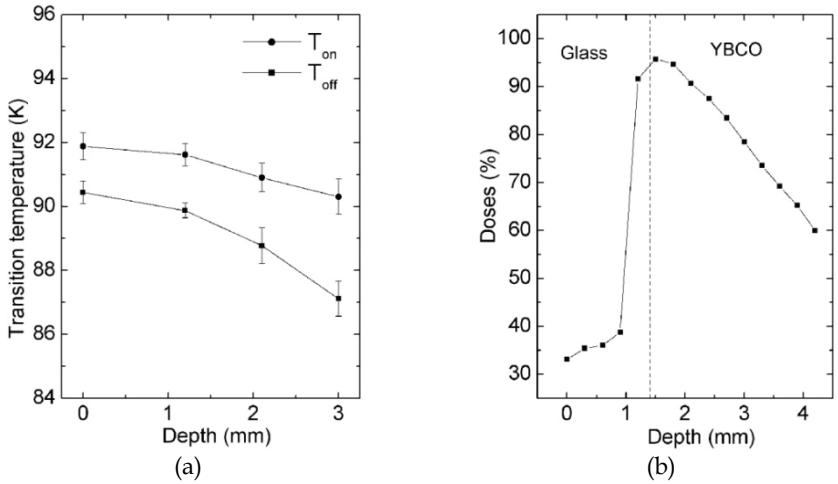

Fig. 13. (a) In-depth Tc profile in a ^{137}Cs gamma irradiated YBCO sample, Tc measurements were performed through step by step sample polishing. (b) Energy deposition distribution calculated for a model irradiation experiment by means of the EGS-4 code (Leyva et al., 2002a).

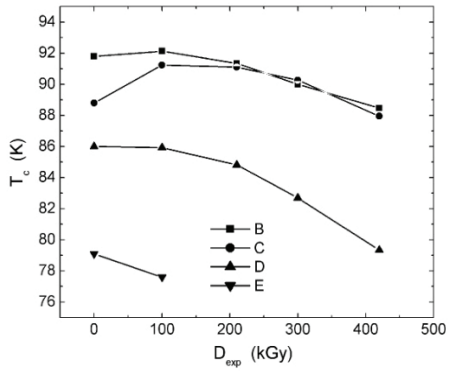

Fig. 14. YBCO superconducting transition temperature Tc dependence on ^{60}Co induced gamma ray exposition doses at different initial non-stoichiometric parameter δ values, 0.05, 0.09, 0.18 and 0.23 for A, B, C and D curves respectively.

6. Gamma radiation damage effects on the YBCO extrinsic properties: critical superconducting electrical current J_c and electrical resistivity

6.1 Critical superconducting electrical current J_c

Independently of the gamma radiation effect over the oxygen random distribution on the basis plane, specially over the Cu(1)-O chain sites, the electronic movement of the Cooper pairs ascribed to the YBCO superconducting properties takes place at the Cu(2)-O_2 planes. Gamma radiation with initial energies $E_\gamma \geq 129$ keV can provoke Oxygen displacements and for $E_\gamma \geq 489$ keV, Cupper displacement, as well, in the Cu(2)-O_2 planes. These effects can be well observed in YBCO thick films exposed to ^{60}Co gamma radiation (Leyva et al, 1995). The electrical resistivity at the normal state shows a nearly linear dependence on the exposition doses, which on the basis of Mathiessen rule, which is expected to be related to a gamma ray induced vacancy concentration upraise in the of the Cu(2)-O_2 planes. In relationship with superconducting transport properties, it had been proved that gamma radiation induces an enhancement of the vortex pinnig energy U_0, as it is shown in Fig. 15a, which should favors transport superconducting properties, like the critical superconducting electrical current J_C.

On the other side, ac susceptibilities superconducting transition measurements had shown that Tc is always over 85 K for the exposition doses up to 500 kGy, with a maximum at $E_0 \approx$ 120 kGy, as was shown pointed out in section 5.2, where in addition a monotonous superconducting volume fraction increasing was also observed (Leyva et al., 2005). However, Fig. 15b shows a J_C monotonous decreasing dependence on the exposition doses, with an inflexion between 150 to 250 kGy, which has been ascribed to the strengthening of the irradiated thick films superconducting properties at E_0, as well as to the vortex pinning energy U_0 upraised showed in Fig. 15a, the last one not being enough to maintain this transitional J_C value at higher exposition doses.

This peculiar J_C suppressing behavior at higher exposition doses, which is radiation damage dependent, seems to be relaying on some extrinsic electrical conduction properties connected with its percolative nature, but independent of atom displacement trials on the Cu(2)-O_2 planes.

In order to get deeper in this picture, ^{57}Co gamma irradiation experiments on YBCO ceramic samples were performed (Mora et al., 1995). Since maximal secondary electron kinetic energy is lower than the electron critical energy for inducing oxygen displacements on Cu(2)-O_2 planes , the atom displacements processes take place only on the Cu(1)-O chains. Fig. 16a shows the J_C dependence on the exposition doses at target temperature of 80 K, where J_C changes very weak under minor oscillatory changes (about 15% amplitude) with the exposition doses, what might be expected under the non occurrence of atom displacements processes at the Cu(2)-O_2 planes in this case.

It seem apparently that by ^{57}Co gamma irradiation on YBCO target cooled at 80 K there not exists any extrinsic effect, as those observed in ^{137}Cs irradiation on YBCO thick film samples. Since vacancy diffusion movements and recombination effects can be neglected at low temperature, it might be expected, that such J_C suppressing mechanism should be even weaker by target irradiation at room temperature. Consequently, the drastic J_C radiation suppressing effect presented in Fig. 16b by target irradiation at room temperature is a surprising one and has been explained by Mora et al. by a radiation conditioned increase of the weak linking Josephson junction thickness *d* (Mora et al., 1995). In Mora et al. model it was taking into the account the influence of the internal magnetic field acting on each superconducting Josephson junction when a critical electrical current fluxes in a

superconducting granular ceramic sample. It was concluded that the weak linking Josephson junction thickness d increase with the exposition doses following approximately a $(D_{exp})^{½}$ law leading to a monotonic J_C diminution with the exposition doses. It is important to note that the irradiated samples in this case showed the Meissner Effect even at exposition doses of 1 kGy, for which no superconducting transition was observed and J_C vanished.

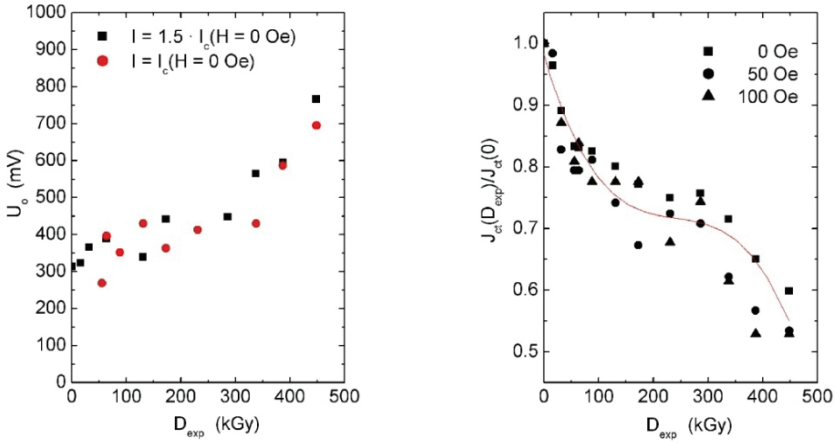

(a) (b)

Fig. 15. Transport properties in a YBCO thick film exposed to ^{60}Co gamma radiation. Vortex pinning energies (a) and superconducting electrical critical current (b) vs. exposition doses; the continuous curve is a visual guide. (Leyva et al, 1995)

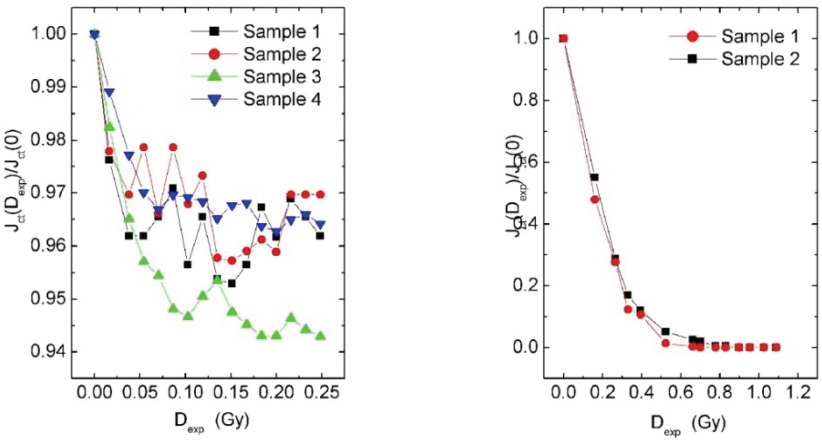

(a) (b)

Fig. 16. Dependence of the superconducting critical current dependence on the ^{57}Co gamma ray exposition doses at different target temperatures: (a) 80 K, (b) 300 K.

Such an exotic electrical conduction behavior have been observed also on regard of the electrical resistivity in the normal state (T > Tc) at relative low ^{57}Co gamma exposition dose,

as it is shown in Fig. 17. Here the electrical resistivity temperature dependence in metallic state has been described according the Mathiessen Law

$$\rho(T, D_{\exp}) = \rho_0(D_{\exp}) + \alpha'(D_{\exp})T \tag{15}$$

where $\rho_0(D_{\exp})$ is the residual electrical resistivity and $\alpha'(D_{\exp})$ is the thermal electrical resistivity coefficient. The Mathiessen Law Eq. (15) is a semiempirical statement which works well in metal and alloys, where ρ_0 has been related to electron elastic scattering processes, as for instance, point crystal defects, and the second term $\alpha'(D_{\exp})T$ represents inelastic electron scattering, like those with lattice phonon. Fig. 17 describes (a) ρ_0 and (b) $\alpha'(D_{\exp})$ dependences with the $D_{\exp}$ in terms of the experiment proportional coefficients $R_0(m\Omega)$ and $\alpha(m\Omega K^{-1})$.

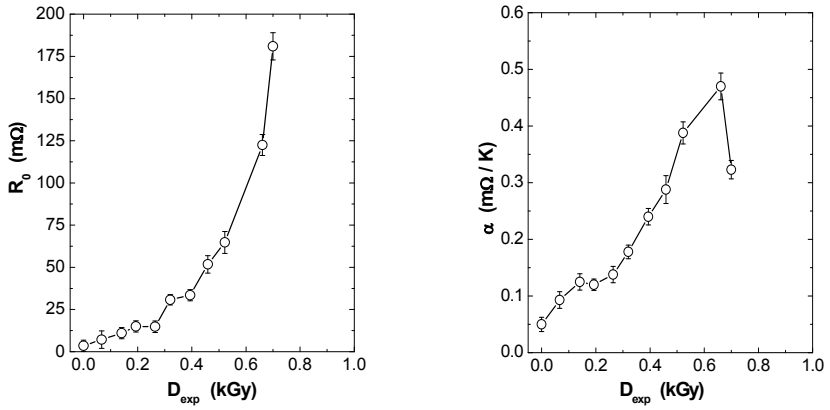

(a) (b)

Fig. 17. Exposition dose dependence of (a) residual resistivity R_0 in (mΩ) and (b) thermal electrical resistivity coefficient α (mΩK^{-1}) of ^{57}Co irradiated YBCO ceramic samples at room temperature.

According to the Mathiessen law, on one side, R_0 must increases proportionally with the exposition doses; on the other side, while α must remain constant, independent from the exposition doses. However, R_0 increases no linearly with the exposition doses, approximately as $1/(E_{MIT}\text{-}D_{exp})$ by approaching to the exposition dose $E_{MIT} \approx 0.7$ kGy, where at the same time α owns a maximum near to E_{MIT}. For $D_{exp} > E_{MIT}$, the samples undergo a kind of metal – insulator transition (at low temperature $T \gtrsim T_c$ semiconducting behavior, while at room temperature metallic one), and finally, at exposition doses higher than 1 kGy, no superconducting transition is observed ($J_C = 0$) and the samples behaves completely as a semiconductor.

Such electrical resistivity dependence with the ^{57}Co gamma exposition doses differs basically form the one corresponding to the ^{60}Co gamma radiation, since in this case, a nearly linear dependence with the exposition doses was observed following well the Mathiessen Law.

6.2 ^{57}Co gamma radiation induced enhanced vacancy diffusive movements in ceramic YBCO samples

The dependence of the Junction Thickness d of the Josephson Weak Linking on the ^{57}Co gamma exposition doses presented by Mora et al. (Mora et al., 1995) was analized taking into the account the following assumptions:

(A) The Junction Thickness d involves the intergrain space with superconductive depleted properties between two neighbour superconductive grains, as well as, the intragrain regions close to the external grain boundaries (GB), which contain high crystalline defects concentration, specially oxygen vacancies, in comparison with the internal intragrain volume defect concentration. This Josephson junction structure is schematically represented in Fig. 18.

(B) During the Gamma irradiation the induced secondary electron shower strongly modify the Activation Energy for intracrystalline oxygen diffusion. Therefore, at a given temperature during irradiation enhanced diffusion motions of atoms and vacancies take place. Due to the high vacancy concentration gradient at GB, the particle diffusive flux is mainly directed inwards to the internal grain regions, where diffusive motions among close YBCO grains can be neglected.

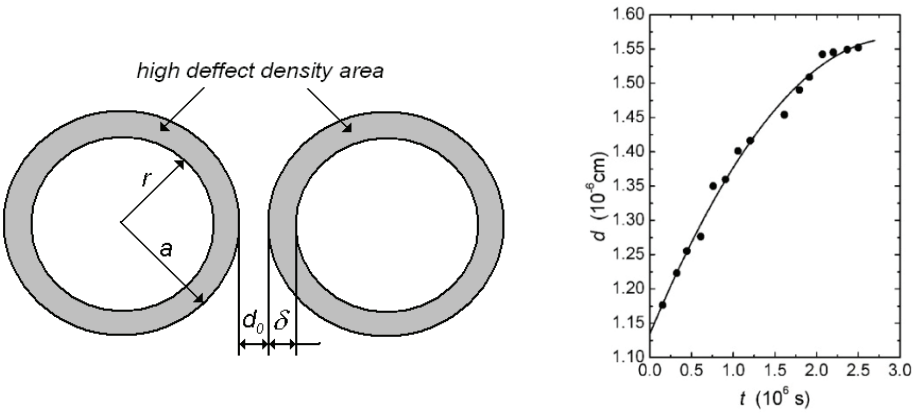

Fig. 18. Schematic representation of the YBCO superconducting weak intergrain linking: intragrain defect distribution and the intergrain junction thickness d (left). Evolution of the superconductive junction thickness d with the ^{57}Co irradiation time (right).

(C) An initial Gaussian Normal Vacancy Distribution, with its maximum value at the Grain Boundary for a supposed typical spherical shaped YBCO´s grain was taken for simplicity, where its thickness $\delta << a$, the grain radius. The Inhomogeneous Diffusion Equation with a constant source term due to Gamma Irradiation induced atomic displacements was applied and solved. Vacancy intergrain diffusion was neglected during irradiation.

From assumptions (A) and (B), following expression of the total Josephson junction thickness d was applied

$$d(t_{irr}) = d_0 + 2\delta(t_{irr}) \tag{16}$$

where d_0 is the intergrain separation (see Fig. 18, left) and the irradiation time was used as a dynamic variable instead of the exposition doses.

Note, that in the present gamma irradiation effect model, main effects arise from the existing high crystal defect concentration at the GB before the irradiation, which will remain higher than the gamma radiation induced crystal defects as a result of oxygen displacements or trapped secondary electrons in oxygen vacancies.
From these calculations it was concluded that $(\Delta d)^2 \propto t_{irr}$, a kind of Einstein's Random Walk dependence. Fig. 18(right) shows the following Mora et al. model calculated Josephson junction thickness d values for the corresponding irradiation times and their fitting according the enhanced vacancy diffusive movement model (Cruz, Leyva & Leyva, 2003). From this fitting the resulting YBCO oxygen vacancy diffusion constant was determined of about 10^{-20} cm/s^2, three orders higher than the value of the Oxygen Diffusion Constant at room temperature for this material at normal conditions. An increase of the Activation Energy of 0.36 eV was also estimated.
The extrapolated value D_{irrad} (77 K) was estimated to be approximately 10^{-60} cm/s^2, showing that on the basis of the mentioned enhanced diffusion mechanism the J_C drastic suppressing effect does not take place when irradiation are made at low temperatures in good agreement with $J_c(D_{exp})$ measured results at target temperature of 80 K (Fig. 16a).
Since gamma radiation damages on Cu(1)-O chain sites are always present due to their low atom displacements threshold energy, the mechanism of J_C drastic suppressing related to gamma radiation induced enhanced vacancy diffusive movements will superpose to other radiation effects taking place at higher gamma ray energies, as was observed in ^{60}Co gamma irradiation experiments presented in Fig. 15 (Leyva et al., 1995).

7. Conclusions

Important improvements have been accomplished recently concerning a detailed description and evaluation of the gamma radiation damage effects in solids, and particularly in high Tc superconductors, were Monte Carlo simulation tools have been introduced in different approaches. In Monte Carlo assisted Classical Method approach, MCCM, the Oen-Holmes-Cahn classical atom displacement rate calculation algorithm was expanded. For this, secondary electron in-depth energy profiles calculated by means of Monte Carlo based codes was introduced, particularly to YBCO superconducting material. On the other side, a new theoretical description of the conditions favoring the occurrence of single fast electron elastic scattering in solids has been developed. Further works in this field are in course, comparing this new atom displacements rate calculation algorithm with previous ones, like MCCM.
On the basis of MCCM approach, gamma quanta induced YBCO in-depth atom displacement rate distributions were calculated up to incident energies lower than 10 MeV. At very low incident energies, oxygen atom displacements take place on Cu(1)-O chain sites. With increasing incident energy, firstly Oxygen displacements in Cu(2)-O_2 planes and other crystalline sites, while at higher energies Cupper displacements are also induced, which begins to be dominant at about 4 MeV and reaches a maximum contribution of 65% at 10 MeV. The corresponding in-depth dpa profiles at different incident energies due to electrons and positrons were characterized as being very similar.
It was concluded, that gamma radiation induced oxygen displacements in both, Cu(2)-O_2 planes and Cu(1)-O chains, as well as secondary electrons are eventually trapped in unoccupied O(4) in Cu(1)-O chain sites in basal planes, favoring oxygen rich nearest neighbor configuration around the Cu(1) sites, provoking a strengthening of the

orthorhombic structural phase properties, specially at relative low exposition dose $E_0 \approx 120$ kGy, depending on the initial non–stiochiometry parameter. In particular, critical temperature enhancement induced by gamma rays at low exposition doses seems to the connected with foregoing changes on the oxygen basal plane disorder.
Electronic transport properties on the Cu(2)-O_2 in the superconducting state are favored by gamma radiation at higher energies, where an strengthening of vortex pinning energies has been observed. However, gamma radiation induces also a the drastic J_C radiation suppressing effect through enhanced vacancy diffusive movements in ceramic YBCO samples, which is sharply temperature dependent and in large scale modulates the supercoducting intergrain boundary properties and its percolative properties.
It may be concluded that gamma radiation induces on high Tc superconductor systhematically crystal structure and superconducting property changes, in a very peculiar way, which deserve future researches in order to get a better understanding of their influence on superconducting mechanisms.

8. References

Abreu, Y.; Cruz, C.M.; Piñera, I. & Leyva, A. (2009). Influencia del desorden cristalino en los espectros Mössbauer del $YBa_2Cu_{3-y}Fe_yO_{7-x}$. *Rev. Cub. Física*, Vol. 26, No. 2A, 179-185, ISSN 0253-9268.

Belevtsev, B.I.; Volchok, I.V.; Dalakova, N.D.; Dotsenko, V.I; Ivanchenko, L.G.; Kuznichenko A.V. & Lagvinov I.I. (2000). Effect of γ-Irradiation on Superconductivity in Polycrystalline $YBa_2Cu_3O_{7-\delta}$. *Phys. Stat. Sol. (a)*, Vol. 181, No. 2, 437-450.

Bethe, H.A. (1953). Molière's Theory of Multiple Scattering. *Phys. Rev.*, Vol. 89, No. 6, 1256-1266.

Bethe, H.A. & J. Ashkin, J. (1953). Passage of Radiations through Matter. In: *Experimental Nuclear Physics*, E. Segré (Ed.), 348, John Wiley & Sons, Inc., New York.

Bohandy, J.; Suter, J.; Kim, B.F.; Moorjani, K. & Adrian, F.J. (1987). Gamma radiation resistance of the high Tc superconductor $YBa_2Cu_3O_{7-\delta}$. *Appl. Phys. Letters*, 51, 25, 2161-2163.

Boiko, B.B.; Korshunov, F.P.; Gatalskii, G.V.; Akimov, A.I.; Gatalskaya, V.I.; Demyanov, S.E. & Stribuk, E.K. (1988). Radiation effect on the superconductivity in the Y-Sm-Ba-Cu-O ceramic system. *Phys. Stat. Sol. (a)*, 107, K139-K144.

Boolchand, P. & McDaniel, D. (1992). Progress in Mössbauer Spectroscopy of High-Temperature Superconductors. *Hyperfine Interactions*, Vol. 72, 125–152.

Bourdillon, A.J. & Tan, N.X. (1995). Displacement damage in supported $YBa_2Cu_3O_{7-x}$ thin films and finite-element simulations. *Supercond. Sci. Technol.*, Vol. 8, No. 7, 507-512.

Briesmeister, J.K. (ed.) (2000). *MCNP™ - A General Monte Carlo N-Particle Transport Code*. Los Alamos National Laboratory Report LA-13709-M, Version 4C.

Cahn, J.H. (1959). Irradiation Damage in Germanium and Silicon due to Electrons and Gamma Rays. *J. Appl. Physics*, Vol. 30, No. 8, 1310-1316.

Cooksey, J.A; Brown, W.D.; Ang, S.S.; Naseem, H.A.; Ulrich, R.K. & West, L. (1994). Gamma-ray and fast neutron radiation effects on thin film superconductors. *IEEE Trans. Nucl. Sci.*, Vol. 41, No. 6, 2521-2524.

Corbett, J.M. (1966). *Electron Radiation Damage in Semiconductors and Metals*, Academic Press, New York and London.

Cruz, C.; Leyva, Y. & Leyva, A. (2003). Ensanchamiento Inducido por la Radiación Gamma de la Frontera de los Granos en Cerámicas Superconductoras. Revista Cubana de Física. Vol. 20, No. 1, 39-43, ISCN: 0253-9268

Cruz, C.; Piñera, I.; Abreu, Y. & Leyva, A. (2008). Theoretical Foundations of Atom Displacements induced by Fast Electron Elastic Scattering in Solids. Proceedings of IEEE Nuclear Sciences Symposium, pp. 2542-2544, ISBN 978-1-4244-2714-7, Dresden, Germany, October 2008, IEEE.

Elkholy, M.M.; El-Deen, L.M.S.; El-Zaidia, M.M., El-Hamalawy, A.A. & Hussain, W.M. (1996). Response of YBCO superconductor doped with strontium after gamma irradiation. *Radiat. Phys. Chem.*, Vol. 47, No. 5, 691-694.

Frischherz, M.C.; Kirk, M.A.; Zhang, J.P. & Weber, H.W. (1993). Transmission electron microscopy of defect cascades in $YBa_2Cu_3O_{7-\delta}$ produced by ion irradiation. *Philosophical Magazine A*, Vol. 67, No. 6, 1347-1363.

Fukuya, K. & Kimura, I. (2003). Calculation of Gamma Induced Displacement Cross-sections of Iron Considering Positron Contribution and Using Standard Damage Model. *J. Nucl. Sci. Technol.*, Vol. 40, No. 6, 423-428.

Gupta, R.P. & Gupta, M. (1991). Order-disorder-driven change in hole concentration and superconductivity in $YBa_2Cu3O_{6.5}$. *Phys. Rev. B*, Vol. 44, No. 6, 2739-2746.

Hendricks, J.S., McKinney, G.W.; Trellue, H.R.; Durkee, J.W.; Finch, J.P.; Fensin, M.L.; James, M.R.; Pelowitz, D.B.; Waters, L.S.; Gallmeier, F.X. & David, J.C. (2006). *MCNPX™ Version 2.6.B*, Los Alamos National Laboratory report, LA-UR-06-3248 (June 2006).

JCPDS - Join Committee of Powder Diffraction Studies (1993). *Inorganic Index to the Powder Diffraction File*, 38-1433.

Jin, M.Z.; Liu, X.W.; Liu, M.L.; Xu, J.; Liu, R. & Jia, Y.Q. (1997). Mössbauer spectra of ^{57}Fe in thick film of $YBa_2(Cu_{0.97}Fe_{0.03})_3O_{7-x}$ irradiated by a large dose of γ-rays. *Physica C*, Vol. 288, 226-230.

Kawrakow, I. & Rogers, D.W.O. (2003). The EGSnrc Code System: Monte Carlo Simulation of Electron and Photon Transport. *NRCC Report* PIRS-701, Dec. Stanford Univ., California.

Kinchin, G.H. & Pease, R.S. (1955). The Displacement of Atoms in Solids by Radiation. *Rep. Prog. Phys.*, Vol. 18, 1-51.

Kirk, M.A.; Baker, M.C.; Lin, J.Z.; Lam, D.J. & Weber, H.W. (1988). Defect structures in $YBa_2Cu_3O_{7-x}$ produced by electron irradiation. In: *High Temperature Superconductors*, Brodsky, M.B.; Dynes, R.C.; Kitazawa, K. & Tuller, H.L. (Eds.), 209, MRS Symposia Proceedings No. 99, Material Research Society, Pittsburg.

Kirk, M.A. & Yan, Y. (1999). Structure and properties of irradiation defects in $YBa_2Cu_3O_{7-x}$. *Micron*, Vol. 30, 507-526.

Klein, O. & Nishina, Y. (1929). Über die Streuung von Strahlung durch freie Elektronen nach der neuen relativistischen Quantendynamik von Dirac. Zeitschrift für Physik A Hadrons and Nuclei, Vol. 52, No. 11-12, 853-868.

Lancaster, G. (1973). *Paramagnetische Elektronen Resonanz in Halbleitern*, Akademische Verlagsgesellschaft, Geest & Portig, Leipzig, Germany.

Legris, A.; Rullier-Albenque, F.; Radeva, E. & Lejay, P. (1993). Effects of electron irradiation on $YBa_2Cu_30_{7-\delta}$ superconductor. *J. Phys. I France*, Vol. 3, No. 7, 1605-1616.

Leyva, A.; Suárez, J.C.; Mora, M.; Cruz, C.M. & Quesada, D. (1992). AC Magnetic Susceptibility in High Temperature Superconductors Irradiated with γ-Rays. *Phys. Stat. Sol. (a)*, Vol. 134, No. 1, K29-K31.

Leyva, A.; Mora, M.; Martin, G. & Martinez, A. (1995). Irradiation effect of Co-60 gamma rays in YBCO thick films. Supercond. Sci. Technol., Vol. 8, No. 11, 816-821.

Leyva, A. (2002). Efectos de las radiaciones gammas en cerámicas superconductoras de interés en las tecnologías nucleares. PhD Thesis on Physics, University of Havana.

Leyva, A.; Alfonso, A. & Cruz, C. (2002). Transition temperature depth profiling of Cs^{137} gamma-irradiated YBCO ceramic. *Nucl. Instr. and Meth. B*, Vol. 174, No. 1-2, 222-224.

Leyva, A.; Cruz, C.M.; Mora, M.; Shtejer, K.; Diez, J.C.; Angurel, L.A.; Piñera, I. & Abreu, Y. (2005). The effects of ^{137}Cs and ^{60}Co γ radiation on the magnetic susceptibility of BSCCO textured thin rods. *Nucl. Instr. and Meth. B*, Vol. 239, No. 3, 281-285.

Liu, Y.H.; Che, G.C.; Li, K.Q. & Zhao, Z.X. (2005). Superconductivity and Mössbauer effect of $Fe_xCu_{1-x}Ba_2YCu_2O_{7-y}$ superconductors synthesized by high pressure. *Phys. Rev. B*, Vol. 71, 104503.

Lyubutin, I.S.; Terziev, V.G. & Dmitrieva, T.V. (1989). Lattice sum calculations and electric field gradients for orthorhombic and tetragonal phases of $YBa_2Cu_3O_x$. *Physics Letter A*, Vol. 137, No. 3, 144-148.

McKinley, W.A. & Feshbach, H. (1948). The Coulomb Scattering of Relativistic Electrons by Nuclei. Phys. Rev., Vol. 74, No. 12, 1759-1763.

Mora, M.; Cruz, C.M.; Leyva, A.; Suárez, J.C.; & Quesada, D. (1995). Influencia de la radiación γ del Co-57 sobre las uniones débiles intergranulares de las cerámicas superconductoras YBCO. *Nucleus*, Vol. 18, 21-24.

Mott, N.F. & Massey, H.S.W. (1952). *The Theory of Atomic Collisions*, 2nd Edition, Oxford University Press, England.

Nelson, W.R.; Hrayama, H.H. & Rogers, D.W.O. (1985). *The EGS-4 Code System*, SLAC-Report-225, Dec. Stanford Univ., California.

Oen, O.S. & Holmes, D.K. (1959). Cross Sections for Atomic Displacements in Solids by Gamma Rays. J. Appl. Phys., Vol. 30, No. 8, 1289-1295.

Piñera, I. (2006). Estudio del Daño Radiacional en materiales sólidos mediante la simulación de procesos físicos. Master Degree These on Nuclear Physics. High Institute on Technologies and Applied Sciences, InTEC, Havana City, December 2006.

Piñera, I.; Cruz, C. ; Abreu, Y. & Leyva, A. (2007a). Determination of Atom Displacements Distribution on YBCO superconductor induced by Gamma Radiation. *Phys. Stat. Sol. (a)*, Vol. 204, No. 7, 2279-2286.

Piñera, I.; Cruz, C.; Leyva, A. & Abreu, Y. (2007b). Displacement per atom calculation in YBCO superconductors through Monte Carlo simulation. *Nucl. Instrum. Meth. B*, Vol. 265, No. 2, 536-540.

Piñera, I.; Cruz, C.; Abreu, Y. & Leyva, A. (2008a). Monte Carlo simulation study of positron contribution to displacement per atom production in YBCO superconductors. *Nucl. Instr. and Meth. B*, Vol. 266, No. 22, 4899-4902.

Piñera, I.; Cruz, C.; Abreu, Y. ; Leyva, A.; Cabal, A.E. & Van Espen, P. (2008b). Monte Carlo Assisted Classical Method for the Calculation of *dpa* Distributions in Solid Materials. *Proceedings of IEEE Nuclear Sciences Symposium*, pp. 2557-2560, ISBN 978-1-4244-2714-7, Dresden, Germany, October 2008, IEEE.

Polyak, O.Yu.; Tukhvatulin, R.Kh.; Chan, K.G.; Gasanov, E.M. & Ibragimova, E.M. (1990). Effect of γ-Irradiation on $YBa_2Cu_3O_{7-x}$ Ceramics and Monocrystals in the Superconducting State. *Phys. Stat. Sol. (a)*, Vol. 122, No. 1, K45-K50.

Santoro, A. (1991). *Chemistry of Superconductor Materials,* Noyes Publications, Park Ridge, New Jersey, USA.

Sarkar, M.; Patel, N.V.; Mehta, P.K. & Somayajulu, R.S. (2001). Mössbauer Study of Multiple Substitutions in YBCO. *Hyperfine Interactions*, Vol. 136-137, 587-592.

Thomas, B.S.; Marks, N.A.; Corrales, L.R. & Devanathan, R. (2005). Threshold displacement energies in rutile TiO_2: A molecular dynamics simulation study. *Nucl. Instrum. Meth. B*, Vol. 239, No. 3, 191-201.

Vašek, P.; Smrčka, L.; Dominec, J.; Pešek, M.; Smrčková, O. & Sýkorová, D. (1989). Gamma irradiation of $YBa_{2Cu3O7-x}$ ceramics. Solid State Commun., Vol. 69, No. 1, 23-25.

8

Charged Particle Irradiation Studies on Bismuth Based High Temperature Superconductors & MgB_2; A Comparative Survey

S.K.Bandyopadhyay
Variable Energy Cyclotron Centre, 1/AF, Bidhan Nagar, Kolkata-700 064
India

1. Introduction

In the field of superconductivity, the discovery of Lanthanum Cuprate ($La_{2-x}Sr_xCuO_4$) ushered in a new era- the so called High Tc superconductors (HTSC). High Tc Cuprate Superconductors are quite intriguing and unique in their behaviour in contrast to their low Tc counterparts. Defects and disorder play a crucial role in controlling various physical properties like Tc, resistivity, Critical Current Density (Jc) etc. in these hole doped superconductors. The nonstoichiometries in these compounds, in particular, with respect to oxygen bring out fascinating properties, oxygen playing the role of hole carrier. These compounds are based on layered perovskite structure. Superconductivity essentially resides in CuO_2 plane, with other layers containing multivalent metal ions functioning as charge reservoir layers, pumping holes or, electrons to the superconducting CuO_2 layer and thereby controlling the Cu-O-Cu coupling and Tc. The cuprates are essentially quasi 2-dimensional systems with a weak interlayer coupling along c-direction between two CuO_2 layers residing in ab-plane. This also gives rise to anisotropy in various physical properties like conductivity, Jc etc. It is seen that Tc increases in general with more number of CuO_2 layers and with more anisotropy. This millennium saw a non cuprate system MgB_2 which is quite simple compared to cuprates, yet with a fairly high Tc of 40K. This has got some similarity with the conventional superconductors in that it is BCS type superconductor with holes in the antibonding band of Boron, coupling with phonons of E_{2g} vibrational mode. MgB_2 possesses hexagonal AlB_2 type structure with Mg ions sandwitched between boron hexagons. Boron is sp^2 hybridised with in plane σ-band primarily participating in superconductivity and the out of plane π-band taking the role of conductivity like graphite, though it is a two band superconductor. Intra and interband scattering play a great role in controlling the superconducting and transport properties.

Charged particle irradiation introduces various kinds of point defects, line defects, etc. which have wide manifestations. In case of HTSC, irradiation produces drastic change in Tc and resistivity. We had observed an increase in Tc in $Bi_2Sr_2CaCuO_2$ (Bi-2212) by α and proton irradiation, which could be explained by irradiation induced knock out of oxygen in overdoped system [1-3]. With this end in view, we carried out irradiations of textured polycrystalline Bi-2212 and $(Bi,Pb)_2Sr_2Ca_2Cu_3O_{10+x}$((Bi,Pb)-2223) with 40MeV α and 15MeV protons at various does. We have also irradiated MgB_2 with Neon ions of 160 MeV available

at Variable Energy Cyclotron Centre, Kolkata. Energies of particles were selected considering the optimisation of nuclear reaction of the projectile with the sample and the range of particles in the sample. In case of HTSC Bi-cuprates, the purpose was to investigate the knock-out of oxygen caused by particle irradiation and its effects on superconductivity. For MgB_2, heavy ion like Neon was chosen to have effective damage as it was seen to be fairly insensitive to particle irradiation. In this article, we are highlighting the salient features of charged particle irradiation effects on HTSC and MgB_2 and analysing the remarkable differences.

The presentation is divided into following sections. The section 2 briefly describes irradiation effects on solids and in particular, the superconductors. In section 3, we describe the effects on Tc and resistivity of Bi-2212 and Bi-2223 and their qualitative difference due to light charged particle (proton and alpha particles) irradiation in the light of oxygen knock-out. Manifestation of this difference with respect to irradiation induced oxygen knock-out is in the nature and size of irradiation induced defects and their pinning potentials which control the enhancement of Jc due to irradiation. These aspects are discussed in section 4 with respect to proton irradiation on these systems. In section 5, we have dealt with heavy ion irradiation studies on MgB_2 and have brought out comparative studies.

2. Irradiation effects on solids

High energy charged particles interact with solids through two main processes-elastic and inelastic. Elastic collisions with solid target nuclei cause nuclear energy loss leading to displacement of atoms. Inelastic or electronic energy loss causes ionisation and excitation of atoms. The dissipation energy (-dE) of the incident particle of energy E for the distance (dx) traversed in solid target is expressed as:

$$(-dE/dx)_{total} = (-dE/dx)_{nuclear} + (-dE/dx)_{electronic} \quad (1)$$

The cross-sections of two processes depend on the energy and nature of the incident particle. Thus, for protons of energy 1MeV, electronic energy loss is ~$2x10^4$ times the nuclear energy loss, whereas for Argon ions of same energy, both are of comparable magnitude [4]. For low energy or, medium energy projectile, it is the displacement of atoms caused by nonionising energy loss (NIEL) through elastic collisions that are of most concern in condensed matter physics. If S_n is the energy deposited due to elastic collisions and E_d is the displacement energy of the target atom, then the number of displaced atoms is $S_n/2E_d$ [5]. If N is the total no. of atoms, the number of displacements that each atom suffers is $(S_n/2E_d)/N$. This is called the displacement per atom (d.p.a.) and is a measure of the nonionising energy deposited. For a particular irradiation, d.p.a. is proportional to the fluence or dose of irradiation. Moreover, it depends on the energy and the nature of the projectile as well as the atomic number of the target material. Thus, for same energy, heavy ions will have larger d.p.a. compared to light atoms. For a typical dose of $1x10^{15}$ particles/cm^2, d.p.a. for 40 MeV α-particles and 15 MeV protons in BSCCO are $1.26x10^{-4}$ and ~$1.2x10^{-5}$ respectively. D.P.A. is a measure of defect concentration.

In electronic energy loss, target atoms get ionised or, excited. During the deexcitation, heat is generated due to transfer of energy to vibrational modes of target atoms. This gives rise to amorphisation due to local heating effects. In case of high energy heavy ions, there is extensive amorphisation along the track of the projectile, giving rise to so called columnar defects. These are much effective as pinning centres in case of superconductors, particularly HTSC.

In the interaction of projectile particle with target atoms, we are concerned with the fates of the scattered projectile particle and the recoil atoms after collision. The projectile loses energy by collisions with the target atoms. Similarly, the target atoms with high recoil energy collide with other target atoms and in turn lose energy.
It is obvious that estimation of the total damage created by a single projectile necessitates following every collision that a projectile undergoes until it almost stops. Hence comes the need of some simulation program. The Monte Carlo method as applied in simulation techniques is more advantageous than the analytical formulations based on transport theory. The most commonly used simulation program is the one developed by Biersack et al [6] called TRIM (TRansport of Ions in Matter). In this program, the nuclear and electronic energy losses are assumed to be independent of each other. Particles lose energy in discrete amounts in nuclear collisions and continuously in electronic interactions.

2.1 Effects of irradiation induced defects on superconductors:

In case of superconductors, nonionising energy loss (NIEL) causing displacement of atoms plays a significant role in controlling physical properties like critical temperature, resistivity, critical current density etc. In conventional superconductors, point defects generated by radiation induced atomic displacements change electronic density of states around Fermi surface, causing thereby depression of Tc [7,8]. In case of high Tc superconductors also, it has been seen that atomic displacements caused by NIEL of incident particle control the change of Tc as a function of fluence [9,10]. NIEL causes anionic (oxygen) and cationic displacements and both play important roles in the change of Tc and resistivity by varying the carrier concentration. As discussed earlier, these superconductors are non-stoichiometric with respect to oxygen which controls the hole concentration in conducting CuO_2 planes. Thus, irradiation induced change in oxygen content is expected to bring forth change in carrier concentration resulting in changes in Tc and resistivity. Moreover, the irradiation induced knock-out would cause oxygen vacancies which can act as effective pinning centres, thereby causing enhancement of Jc. This makes the study of irradiation induced knock-out of oxygen so fascinating.
In YBCO system, particle irradiation generally causes knock-out of oxygen from Cu-O-Cu chain and leads to orthorhombic to tetragonal phase transition with oxygen deficiency. At high dose, metallic to semiconducting phase transition occurs [11]. These oxygen vacancy defects act as flux pinning centres. Activation energy for flux creep decreases with oxygen deficiency [12].

3. Charged particle irradiation effects on HTSC:

X-ray Diffraction patterns of some α-irradiated Bi-2212 and Bi-2223 samples along with the unirradiated ones are presented in Figs. 1 and 2 respectively. The characteristic reflection lines of the unirradiated samples are present in the irradiated samples. There have been slight shifts of 00l peaks in α-irradiated Bi-2212 samples towards lower angles compared to those of the unirradiated sample. There is an increase in c-parameter in the irradiated Bi-2212 samples. Normally, the holes or, oxygen causes an increase in positive character of the copper in CuO_2 plane. Thereby attraction of copper to apical oxygen atoms increases and decrease in c-parameter occurs. Also, Cu-O bond length decreases causing a decrease in a-parameter. In case of Bi-2212 irradiated with 40 MeV α, the increase in c-parameter can be

explained by the irradiation induced knock-out of oxygen. Thereby the hole carrier concentration in CuO_2 plane decreases, causing increases in both a and c-parameters. On the other hand, in case of Bi-2223, there has not been any change in c-parameter.

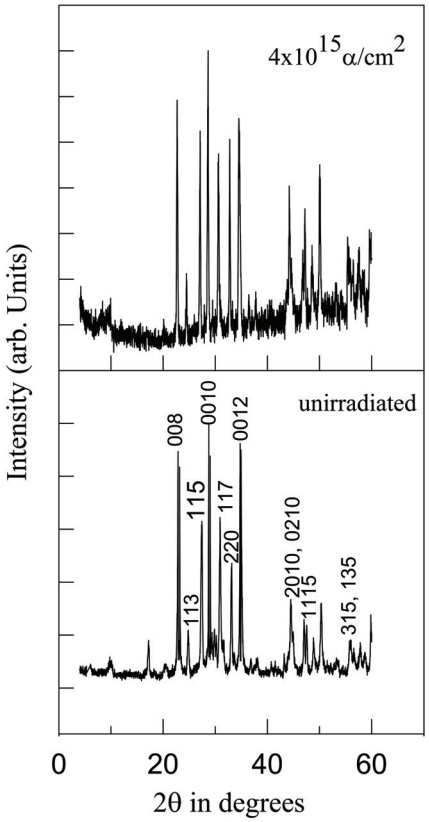

Fig. 1. XRD pattern of unirradiated and $4x10^{15}$ α/cm² polycrystalline of Bi-2212.

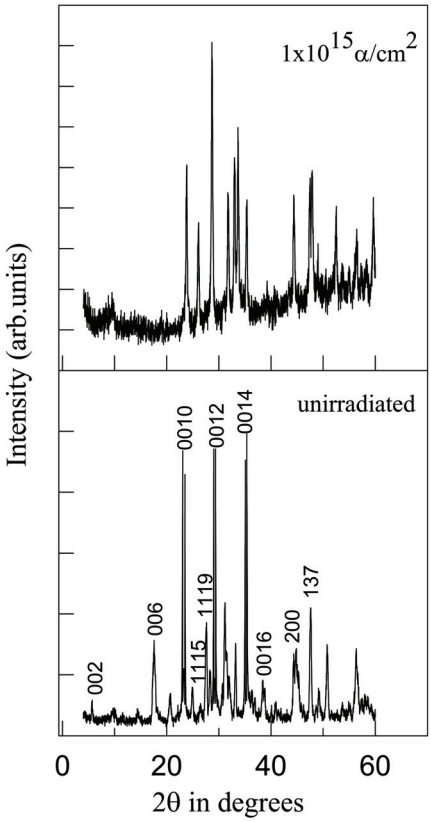

Fig. 2. XRD pattern of unirradiated and $1x10^{15}$ α/cm² polycrystalline of Bi-2223.

Resistivity versus temperature plots of some irradiated samples of 40MeV α-irradiated Bi-2212 polycrystal as compared to the unirradiated samples are presented in Figures. 3(a and b). Table-I shows the values of Tc(R=0), Tc(onset) and excess oxygen (determined by iodometry) as a function of fluence.

In case of Bi-2212 polycrystalline samples, oxygen contents have decreased with dose. The unrradiated polycrystalline Bi-2212 of Tc=73K has x value (i.e. oxygen content in excess to that of stoichiometry) of 0.204 as evident from iodometric estimations. Excess oxygen is the source of the hole carrier in these cuprates. Tc is related to the hole carrier density and hence excess oxygen content(x). In Bi-2212, Tc increases initially with x, goes to a maximum and then decreases with the increase of x following a typical dome shaped curve [13]. The excess oxygen contents corresponding to the peak values of Tc vary from 0.15 to 0.16 [13,14]. The excess oxygen in unirradiated polycrystalline Bi-2212 (0.204) corresponded to the right or the overdoped side of the Tc versus oxygen dome-shaped

curve [13]. As oxygen content of the unirradiated sample was in excess to that (~0.16) corresponding to the maximum Tc, it is expected that there would be an increase in Tc on reduction of oxygen content. Thus, the increase in Tc for the irradiated samples was due to the loss of excess oxygen. The peak of Tc(R=0) corresponds to a dose of ~$6x10^{15}\alpha/cm^2$ and the equivalent oxygen content is 0.10.

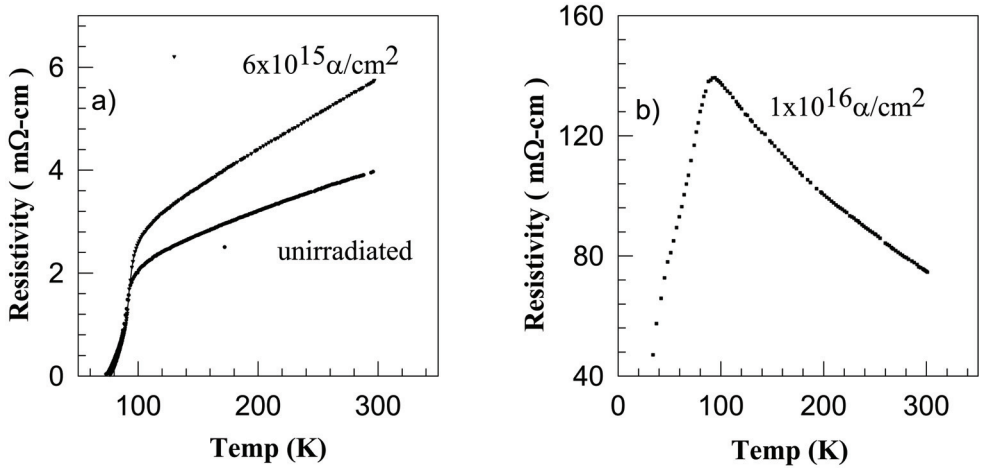

Fig. 3. (a) Resistivity of unirradiated, $6x10^{15}$ α/cm^2 and (b) highest dose ($1x10^{16}$ α/cm^2) of polycrystalline of Bi-2212 as a function of tempareture.

Dose (α/cm^2)	Tc(R=0) (K)	Tc(Onset) (K)	Excess Oxygen (x)
Bi-2212:			
0	73.1	90.5	0.204
$2x10^{15}$	74.3	92.3	0.190
$4x10^{15}$	75.8	94.8	0.150
$6x10^{15}$	76.3	92.7	0.100
$1x10^{16}$	<10.0	-	0.055
Bi-2223:			
0	112.0	122.0	0.100
$1x10^{15}$	111.0	122.0	0.100
$2x10^{15}$	108.0	122.0	0.100
$3x10^{15}$	105.8	121.8	0.100
$4x10^{15}$	103.6	121.6	0.096
$1x10^{16}$	64.0	94.0	0.096

Table I. Variation of Tc, Excess Oxygen and other parameters with dose for polycrystalline Bi-2212 and Bi-2223 irradiated with 40MeV α-particles.

Tc(onset) is the temperature at which grains become superconducting. The granular Tc is controlled by the lattice oxygen content. Hence, Tc(onset) is affected by x, the excess oxygen, whereas Tc(R=0) is controlled by the intergranular links too. In polycrystalline samples, grain boundaries are regions of the highest energy and most vulnerable for radiation damage like enhanced formation of defects, outdiffusion of oxygen etc., which lead to destruction of weak intergranular links and depression of Tc(R=0) even at lower doses of irradiation, whereas the granular Tc i.e. Tc(onset) is not affected.

It is the radiation induced destruction of weak intergranular links in polycrystalline samples that causes an increase in the transition width and fast decrease in Tc(R=0) of 40Mev α-irradiated Bi-2212 sample at higher dose where it is underdoped with respect to oxygen. This is reflected in the overdoped region too. In the overdoped region, irradiation induced knock-out of oxygen increases Tc on one hand and the destruction of intergranular links causes a decrease in Tc. Hence, Tc(R=0) versus excess oxygen curve is less sharp than that of Allgeier et al. [13], i.e. the increase of Tc (R=0) with dose is less compared to Tc (onset) in the overdoped region. It is because of this intergranular effects that the peak of Tc (R=0) corresponds to oxygen content of 0.10 and not 0.15 where the peaking of Tc(onset) occurs.

Unlike polycrystalline Bi-2212, there has been no increase in Tc(onset) and no change in oxygen content in particle irradiated Bi-2223. The irradiation induced knock-out of oxygen is absent in Bi-2223. In most cases (both proton and α-irradiation on Bi-2212 and Bi-2223), there are increases of transition widths (ΔTc).

The resistivity changed from metallic to insulating behavior by α-irradiation at a dose of $1x10^{16}\alpha/cm^2$ and higher for both Bi-2212 and Bi-2223. The nonlinear behavior of resistivity is indicative of localization of charge carriers caused by irradiation induced disorder. We analysed the non linear behavior of resistivity in the framework of variable range hopping (VRH). Normally, the resistivity in the insulating region is given by

$$\rho = \rho_0 \exp [(T_0 /T)^{1/(d+1)}] \quad (2)$$

where the hopping conduction of carriers occurs in d-dimension. Here, T_0 and ρ_0 are constants.

Thus, for 2-dimensional VRH, $\rho = \rho_0 \exp [(T_0 /T)^{1/3}$,

and for 3-dimensional VRH, $\rho = \rho_0 \exp [(T /T)^{1/4}]$.

In our case, the best fit was obtained in the case of Ln(ρ) vs. $(T)^{-1/4}$ plot in the temperature range of 256K to 115K for Bi-2212 and 190K to 120K for Bi-2223. Thus, the conduction in the non-metallic region proceeds through 3-Dimensional VRH. Similar metal to insulator transition was observed in $Bi_2Sr_2Ca_{1-x}Y_xCu_2O_{8+x}$ at x>0.5 [15,16]. Substituting Y(III) in Ca(II) site causes a lowering of carrier concentration. From the general phase diagram for these systems, it is now evident that, they are Mott-Hubbard insulators at very low carrier concentration and become superconducting as the carrier concentration is increased to a certain extent and the normal state behavior changes from insulator to metallic [17-20]. For the carrier concentration corresponding to the cross-over region from metal to insulator, the conduction is generally seen to occur through 3D-VRH [21].

The reasons for transition from metal to insulator behavior of the irradiated sample at the highest dose may be two fold: 1) lowering of carrier concentration due to the knock-out of oxygen, 2) generation of localisation caused by irradiation induced disorder [22]. There is a difference between the irradiation induced localizations in Bi-2212 and Bi-2223. In α-

irradiated Bi-2223, the change of carrier concentration due to change in oxygen content is not significant which is dominant in α-irradiated Bi-2212 as evident from iodometry. Rather localisation caused by the radiation induced disorder plays a major part in case of Bi-2223.
We have estimated the localisation length denoted as α^{-1}. For 3D VRH, α^{-1} is derived from T_0 using the following expression:
$T_0 = (16\alpha^3)/[k_B N(E_F)]$; $N(E_F)$ is the density of states at Fermi level and k_B is Boltzmann constant. For Bi-2212, the values of $N(E_F)$ obtained from specific heat data range from 1.25-5.62x10^{-2} states/eV/Å^3 (for three dimensions) [23,24]. We have taken the value ~1.8x10^{-2}states/eV/Å^3 [20]. The localisation length (α^{-1}) comes ~10.7Å. This value of α^{-1} is quite low compared to that (60-80Å) in the case of $Bi_2Sr_2Ca_{1-x}Y_xCu_2O_{10+x}$ in 3D-VRH regime at the cross-over of metal to insulator transition (for x=0.55) [21]. Our value is comparable to that for x=0.6. In case of Bi-2223, the localisation length (α^{-1}) comes 10.6Å, around five times the Cu-O bond length in CuO_2 plane.
The Cu-O bond in CuO_2 sheet is the strongest bond and it controls the lattice constants [25]. The other layers in the crystal structure are constrained to match the CuO_2 sheet and thus internal stress is generated within the crystal structure. The lattice stability in these cuprates is governed by a tolerance factor defined as:[26]

$$t=(A\text{-}O)/[2^{1/2}(B\text{-}O)]$$

In Bi-2212, A-O and B-O are bond lengths of Bi-O in rock salt block and Cu-O in perovskite block respectively. In perovskites, for stable structure, value of 't' should be as $0.8 < t < 0.9$ [36]. If the bond lengths are taken to be the sum of the ionic radii of the respective ions, then with $r_{(Bi^{3+})}$ =0.93 Å, $r_{(O^{2-})}$ =1.4 Å, $r_{(Cu^{2+})}$ =0.72 Å , 't' comes out to be 0.78 in Bi-2212, and is less than the value needed for structural stability and an internal strain is developed. Since the Cu-O bond is rigid, the strain due to lattice mismatch can be relieved by the increase of A-O bond length which can be attained either by substitution of Bi^{3+} by larger ion or by accommodating excess oxygen in the Bi-O layer. In undoped Bi-2212, the latter process occurs, whereby the Bi-O bond distance increases to 2.6 Å and the tolerance factor comes within proper range. This excess oxygen resides in Bi-O layer because of the repulsion of the lone pair of electrons in Bi^{3+}ion and oxygen along c-axis. The extra oxygen atoms form rows along a-axis and cause incommensurate modulation along b-axis [27]. They are not valence bound. The binding energy of these extra oxygen atoms is very low and hence they are vulnerable to be knocked out by energetic α-particles and protons depending on the amount of energy deposited by the projectile.
The decrease in oxygen content (or the knock-out of oxygen) caused by irradiation with charged particles from Bi-2212 sample can be understood to occur through following steps: 1) Appreciable oxygen vacancies are created by charged particle irradiation induced displacement at a dose > 1x10^{15} particles/cm^2; 2) These displaced oxygen atoms occupy pores which are energetically favourable to them; 3) These 'free' or labile oxygen molecules diffuse from pores to outside (of the sample) which is in vacuum (~10^{-6}torr) during irradiation [28]. This is the driving force for migration. The rate of oxygen atoms/molecules diffusing out is proportional to the atoms/molecules of oxygen present in pores. At room temperature, there is no reabsorption of oxygen by Bi-2212 as oxygen absorption needs activation energy and hence a net decrease in oxygen content occurs.
In Bi-2223 synthesised by partially doping Pb in Bi-site, the tensile stress in Bi-O layer is relieved by substitution of larger Pb^{2+} ion (1.2Å) in Bi^{3+} (0.93Å) site. So, Pb doped Bi-2223

does not accommodate excess oxygen significantly. Pb(II) substituting Bi(III) provides holes to CuO layer, thereby relieving its compressive stress. Hence there is no loosely bound oxygen to be knocked out. In Bi-2223, because of absence of loosely bound oxygen, only strong lattice bound oxygen comes into picture for being knocked out. TRIM-95 calculations show the number of oxygen atoms displaced by 40 MeV α-particles is ~5/ion in case of Bi-2223, whereas the same in case of Bi-2212 containing loosely bound oxygen is around 110/ion [28]. This gives rise to the difference in Bi-2212 and Bi-2223 with respect to oxygen knock-out. Manifestation of this difference was reflected in their behaviour in Tc and resistivity and also in Jc and pinning potential, as the irradiation induced knocked out oxygen vacancies play the role of flux pinning centres. Thus, Bi-2212 and Bi-2223 behave differently with respect to the enhancement of Jc and pinning potential, as will be revealed in the following section 4.

3. Jc and pinning potentials for irradiated BSCCO superconductors

The most important aspects of defects governing the physical properties of superconductors, in particular Jc and pinning, are their size and concentration. Pinning is intimately related to the size of defects and is maximum when the size of the defects is nearly same as vortex core. Hence to assay the pinning due to defects, it is essential to have an idea of concentration and size of defects. We are highlighting studies of defects and their pinning in proton irradiated BSCCO (Bi-2212 and Bi-2223) superconductors

Positron Annihilation Lifetime (PAL) study is a probe for assaying defect size and concentration. Positron annihilates with electrons of atoms. Absence of atoms or, vacancies causes trapping of positrons and hence enhancement of lifetime. More the size of vacancies, the more will be the lifetime of positrons. Moreover, there is some broadening of the annihilated γ spectra due to the angular momentum of the electrons with which the positron annihilation takes place. Thus, Doppler Broadened Positron Annihilation Radiation technique (DBPARL) also highlights about defects.

The positron lifetime spectra of Bi-2212 and Bi-2223 revealed three lifetimes – the longest one designated as τ_3 of 1.6-2.0 ns being the pick-off annihilation lifetime of ortho-positronium atoms, formed at the intergranular space. Among other life times, the shorter one τ_1 represents the combined effects of positrons annihilating in the bulk and those with free Bloch state residence time. Longer one τ_2 is the result of trapping of positrons in vacancy type defects with which we are mostly concerned regarding the size of defects. For unirradiated Bi-2212 and Bi-2223, the values of τ_2 are 284 and 274 ps respectively. These values indicate that the unirradiated Bi-2212 and Bi-2223 consist of defects essentially in form of divacancy and monovacancy respectively [29]. τ_2 increases for Bi-2212 up to the dose of $5x10^{15}$ proton/cm^2 and then decreases (Fig. 11). But, in case of Bi-2223, there is no significant change in τ_2 up to this dose compared to the unirradiated sample. From Table-II, we see that there is no significant change in the concentration of defects in Bi-2223, which is higher than Bi-2212 in unirradiated stage.

Increase in τ_2 and defect size of Bi-2212 are manifestations of irradiation induced knock-out of oxygen, creating thereby oxygen vacancies. These oxygen vacancies agglomerate with each other increasing the defect size and τ_2. Increase in defect size causes a decrease in concentration of defects in Bi-2212 with increasing dose, as evident from Table-II. In Bi-2223, the knock-out of oxygen is absent and hence there is no change in size of defects. Because of increase in size, there is a reduction in concentration of defects in Bi-2212 up to the dose of $5x10^{15}$ protons/cm^2 as seen from Table-II.

Irradiation dose (Protons/cm^2)	N (number of vacancies per vacancy cluster)	C (ppm)
Bi-2212		
Unirradiated	2	2.63
1x10^{15}	2	2.57
2x10^{15}	2	1.76
5x10^{15}	3	1.06
8x10^{15}	1	4.26
1x10^{16}	1	6.37
Bi-2223		
Unirradiated	1	5.10
1x10^{15}	1	5.25
2x10^{15}	1	5.25
5x10^{15}	1	5.30
8x10^{15}	1	5.45
1x10^{16}	1	5.55

Table II. Defect Size (N) and Concentration (C) in Bi-2212 and Bi-2223 as a function of dose.

Increase in defect size causes a decrease in concentration of defects in Bi-2212 with increasing dose, as evident from Table-II. At high dose of irradiation however, there will be appreciable generation of cationic vacancies too by displacement of either of Bi, Sr, Ca, Cu. There is a possibility of combination of a fraction of these cationic atoms with oxygen vacancies. This process can reduce the size of oxygen vacancies, which is reflected at a dose higher than 5x10^{15} protons/cm^2. In Bi-2223, the knock-out of oxygen is absent and hence there is no change in size of defects.

In the mixed state of a Type II superconductor with transport current, Lorentz force is exerted on magnetic flux lines which causes flux motion and energy dissipation. There are two categories of flux motion- flux flow and flux creep. In the former case, Lorentz force dominates and drives the flux lines. In the latter case, the flux pinning is strong and the flux lines move only by thermally activated jump from one pinning site to another. Magnetoresistance under high field in the superconducting state is a manifestation of this dissipation. Thus, the systematic study of the influence of an external magnetic field on resistive transition is an important source of information for Jc and pinning potential. So, DC electrical resistivity of irradiated as well as unirradiated BSCCO samples were measured in magnetic field.

The conventional Lorentz force induced dissipation plays a minor role in the high temperature part of resistive transition (i.e. near Tc(onset)) due to fluctuation of the superconducting order parameter which is very dominant in case of HTSC materials [30]. Only, in case of low temperature part of the resistive transition temperature (i.e. near Tc(R=0), dissipation energy due to motion of vortices by thermally activated flux creep plays an important role in pinning [31,32]. Hence, thermally activated flux creep model [48] was used to analyse the magnetoresistance of irradiated and unirradiated BSCCO samples in the temperature regime Tc(onset) to Tc(R=0). According to this model, the resistivity in this temperature regime is given as:

$$\rho(T,H) = \rho_0 \exp [-U(T,H)/(K_B T)] \quad (3)$$

where prefactor ρ_0 is a coefficient related to the vortex volume, the average hopping distance of vortices and the characteristic frequency with which vortices try to escape the potential well. Usually, ρ_0 is of the order of normal state resistivity near Tc(onset) [33]. ρ_0 in our case has been taken as the normal state resistivity at 100K and 125K for Bi-2212 and Bi-2223 respectively. The activation energy U(T,H) for various fields H has been extracted by using Arrhenius type equation (3) in the form:
$U(T,H) = (K_BT)\ln[\rho_0 / \rho(T,H)]$ based on $\rho(T)/\rho_0$. Finally, U(0,H) was determined from the plots of U(T,H) versus temperature fitted with the equation:

$$U(T,H) = U(0,H)\,[1-T/Tc(H)]^n \quad (4)$$

We have done the analysis in low temperature regime corresponding to flux creep, i.e. where $U(T,H) >> K_BT$ [34]. The best fit was obtained for n=2.
In Bi-2212, the pinning potential U(0,H) has increased with dose up to $5x10^{15}$ protons/cm^2. This is in tune with the increase in positron lifetime τ_2 in PAL studies and hence the increase in defect size from divacancy to trivacancy and thereby defects acting as more effective pinning centre. Beyond this dose, U(0,H) values have decreased with reduction in vacancy size from trivacancy to monovacancy. In Bi-2223, U(0,H) does not show any significant change with the dose of irradiation as seen in PAL studies. U(0,H) of unirradiated Bi-2223 is significantly higher than Bi-2212. The defect concentration of unirradiated Bi-2223 was also higher than Bi-2212 as revealed from Table-II.
Jc of proton irradiated as well as unirradiated BSCCO samples were evaluated from DC magnetisation studies at fields up to 1 Tesla. At the field higher than Hc_1, magnetic flux enters into the grain and hence the intragranular critical current density Jc can be evaluated using Clem-Bean formula [36,37]:

$$Jc = [30\Delta M] / a$$

where M is the magnetisation and 'a' is the average grain size of the samples taking into account the granularity in polycrystalline samples.
Jc versus H shows a clear exponential relation as:

$$Jc = Jc_0 \exp(-H/H_0),$$

where Jc_0 and H_0 are fitting parameters [38].
Jc_0 is defined as the critical current density at zero magnetic field. In Bi-2212, Jc and Jc_0 increase with dose up to $5x10^{15}$ protons/cm^2 and then decreases. But, in Bi-2223, there is no significant change up to this dose, though in the unirradiated stage, Jc and Jc_0 are higher for Bi-2223 owing to high defect concentration in the unirradiated stage, as discussed earlier.
At doses higher than $5x10^{15}$ protons/cm^2, there is a possibility of occupancy of cationic atom at the site of oxygen vacancies causing a decrease in defect size in Bi-2212. The smaller defects are less effective in pinning causing a reduction in pinning potential and Jc. On the other hand, in Bi-2223, there is a reduction in positron lifetime τ_2 implying the formation of vacancy loops acting as a weak trapping centre. This defect configuration might be deleterious in pinning, whereby there is a drastic fall in Jc in Bi-2223 above the dose of $5x10^{15}$ protons/cm^2.
Thus, there is one to one correspondence between defect size, pinning potential and Jc in Bi-2212 and Bi-2223. Moreover, difference in these two systems with respect to abovementioned properties is due to the difference with respect to the irradiation induced knock-out of oxygen.

5. Particle irradiation on MgB_2

In MgB_2, the irradiation studies with heavy ions on thin films [39] and protons on bulk materials [40] have not reflected any significant changes in T_c and other superconducting properties. Hence we employed heavy ions like Neon with large deposition energy and high values of displacements per atom (dpa) to bring about changes in bulk samples. There has not been significant change in Tc up to the dose of $1x10^{15}$Neon/cm^2. The plots of resistivity versus temperature for all the four samples are shown in Fig. 4. We observe that there is no significant change in Tc indicative of rather insensitivity of MgB_2 towards particle irradiation. There is slight decrease in Tc for the sample with the highest dose. The values of Tc and room temperature resistivity (ρ_{300}) are listed in Table III. There is almost no increase in ΔTc excepting at the highest dose. ρ_{300} of the polycrystalline samples increased with dose except for the lowest dose. The decrease in resistivity for the sample irradiated with the dose of $1x10^{13}$ Neon/cm^2 may be due to thermal annealing of the defects, which were initially present in the sintered sample leading to a decrease in the residual resistivity. At low dose of irradiation, mobile defects are also seen to increase the long-range ordering in partly ordered metallic alloys [41]. The depth of 160 MeV Neon ion implantation is 106μ, as obtained from Monte Carlo simulation using the code TRIM [6]. Displacement energy of both Mg and B has been 25eV with lattice binding energy of 3eV. The high binding energy of B is an outcome of strong sp^2 hybrid σ bonding between in-plane B atoms. The number of displacements/ion is 2734 as obtained from TRIM simulations. The dpa in the range of 106μ obtained thereby is $8.2x10^{-18}$/ion/cm^2. Energy loss here is larger by a factor of 10^2 than that caused by 6 MeV protons in MgB_2. Defect concentration at the highest dose is around 0.1% in the range of the projectile with fairly bulk damage.

As already stated, in MgB_2, the grains are strongly coupled which are not disturbed even after irradiation, as noticed by inappreciable change in ΔTc in contrast to HTSC cuprates. MgB_2 is a strongly coupled phonon mediated superconductor. The decrease in resistivity is

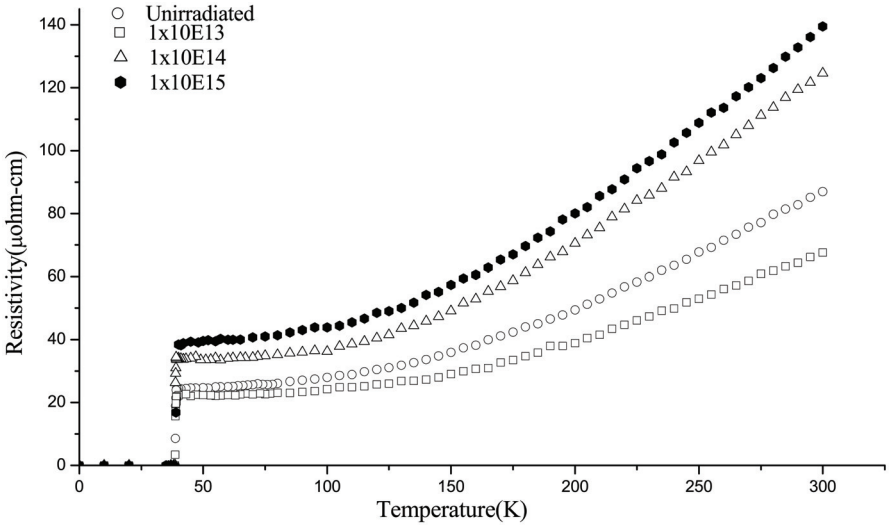

Fig. 4. Resistivity versus temperature. Though it is metallic, the resistivity is nonlinear.

Dose (ions/cm²)	Tc (K)	ρ_0 (μΩ-cm)	ρ_{300} (μΩ-cm)	ρ' (μΩ-cm/K)	$\rho_{300} - \rho_0$ (μΩ-cm)
Zero	38.7	25.01	86.94	0.32	61.93
1X10¹³	38.6	22.47	67.57	0.26	45.10
1X10¹⁴	38.7	33.71	124.60	0.48	90.89
1X10¹⁵	38.0	39.94	139.46	0.52	99.52

Table III.

linear with temperature from 300K up to a certain point (~ 200 K) and then it deviates from linearity. This shows that resistivity can be explained from phonon scattering mechanism. We have fitted the experimental curve to Bloch-Grüneisen expression [42],

$$\rho(T) = \rho_0 + (m-1)\rho'\Theta\left(\frac{T}{\Theta}\right)^m \int_0^{\frac{\Theta}{T}} \frac{x^m \exp(x)}{\left(\exp(x)-1\right)^2} dx \tag{5}$$

Here, ρ_0 is the residual resistivity, ρ' the temperature coefficient of resistivity and Θ the Debye temperature. ρ_0, ρ' and Θ are the fitting parameters. ρ(T) varies as T^5 at low temperature. The increase in resistivity has contributions from ρ_0 and ρ'. The increase of ρ_0 can be related to the increase in defect concentration and the damage at grain boundaries with irradiation. The decrease in ρ_0 at the lowest dose can be understood from annealing of the defects as already mentioned. Debye temperature did not vary much with irradiation and was from 903K to 909K (variation is within the error range of the fit).

We have obtained the EPC constant λ about 0.84 for the unirradiated sample using the experimentally obtained Tc and the fitted Θ value in the McMillan equation

$$T_c = \frac{\Theta}{1.45}\exp\left[\frac{-1.04(1+\lambda)}{\lambda-(1+0.62\lambda)\mu^*}\right] \tag{6}$$

with the value of Coulomb pseudopotential μ^* taken as 0.1 [43]. λ also has not changed significantly with irradiation due to insignificant variation of T_c and Θ.

The increase in ρ' can be understood from bonding nature of MgB_2. As mentioned earlier, strong covalent σ-bonding within B-B layer gives rise to σ bands. The carriers of the σ bands are strongly coupled with the in-plane B E_{2g} stretching modes, giving rise to superconductivity [44,45]. Electron- phonon coupling constant along σ bands (λ_σ) governs Tc. The contribution to the conductivity is expected to be low in σ bands due to strong EPC. In two band system, the conductivity can be considered arising from the parallel network of the σ and π bands [43]. As compared to σ bands, conductivity would be large in π bands due to low EPC constant. The density of states around the Fermi surface ($N(E_F)$) of π band is 56% and that of σ bands is 44% [46]. So the normal state conductivity is mainly governed by the carriers of the metallic π bands.

Particle irradiation causes vacancies in both B and Mg layers. Irradiation induced B vacancies would damage both σ and π bonding network. π bonding network extends towards Mg ions as there is an interaction between them. Irradiation induced vacancies in both Mg and B sites affect the π bonding and hence $N(E_F)$ due to π-bonding. As ρ' is inversely proportional to $N(E_F)$, decrease in $N(E_F)$ with irradiation causes an increase in ρ'.

There is no role of Mg ions with σ bonding hence no role in EPC and Tc. Irradiation induced B vacancies up to the dose of $1x10^{15}$ ions/cm^2 do not cause significant change in λ_σ and hence tc.

6. Upper critical field

Upper critical field $H_{c2}(T)$ was extracted from the magneto transport measurements from the intersection of the slopes at the points of resistivity at 40K (ρ_{40}) and at the point corresponding to $0.9\rho_{40}$. In Fig. 5, $H_{c2}(T)$ for samples A and B (A: Unirradiated & B: Irradiated) are plotted as a function of temperature. There has been only an appreciable increase in upper critical field with lowering of coherence length, which has got some significance in application.

$H_{c2}(0)$ was extracted using the formula:

$$H_{c2}(T) = H_{c2}(0)\left\{1-\left(\frac{T}{T_c}\right)^{\alpha}\right\}^{\beta} \tag{7}$$

with $\alpha = 2$ and $H_{c2}(0)$ and β as fitting parameter. β was found to be ~ 1.67 for unirradiated sample and 1.78 for irradiated sample. In MgB_2 single crystal $\mu_0 H_{c2}(0)$ is around 3.5T along *c* axis and around 15 to 17 T along *ab* direction [47, 48]. In polycrystalline sample where the grains are randomly oriented, $H_{c2}(0)$ is governed by the higher value of the $H_{c2}c$ and H_{c2}^{ab}. $\mu_0 H_{c2}(0)$ of the unirradiated sample is 18.7T and for the irradiated sample, it increases to 20.4T due to disorder introduced by Ne ion irradiation. There is a positive curvature of the H_{c2}–T near T_c. In MgB_2 single crystal this positive curvature is observed in $H_{c2}^{ab}(T)$ [47]. The positive curvature is believed to be characteristic of layered superconductors [49]. It seems that both the two-gap and the anisotropic gap model [50] can qualitatively explain the positive curvature of MgB_2 near T_c. But this feature is also observed in single gap superconductor or in isotropic $(K,Ba)BiO_3$ systems [51]. The curvature of the irradiated sample is greater than the unirradiated sample.

Using Ginzburg-Landau (GL) expression for B_{c2}:

$$\mu_0 H_{c2} = \left[\frac{\phi_0}{\left(2\pi\xi^2\right)}\right] \tag{8}$$

where, ϕ_0 is the quanta of flux *h*/2*e*, we obtain $\xi(0)$ = 4.2 nm for the unirradiated sample A and 3.9 nm for B-slight reduction due to irradiation.

7. Critical current density

The magnetisation critical current density (J_c) was extracted using Bean's critical state model. J_c of the unirradiated sample A at 15K and 1.0T is around 10^5 Amp/cm^2. The value is quite high as compared to HTS like bismuth cuprate superconductor. However, there is a sharp fall of J_c with increasing B for the unirradiated sample like HTS. In case of the irradiated sample B, the magnetisation measurement shows J_c to be lower than the unirradiated sample A at low field but higher than A at high field as evident from Fig. 6.

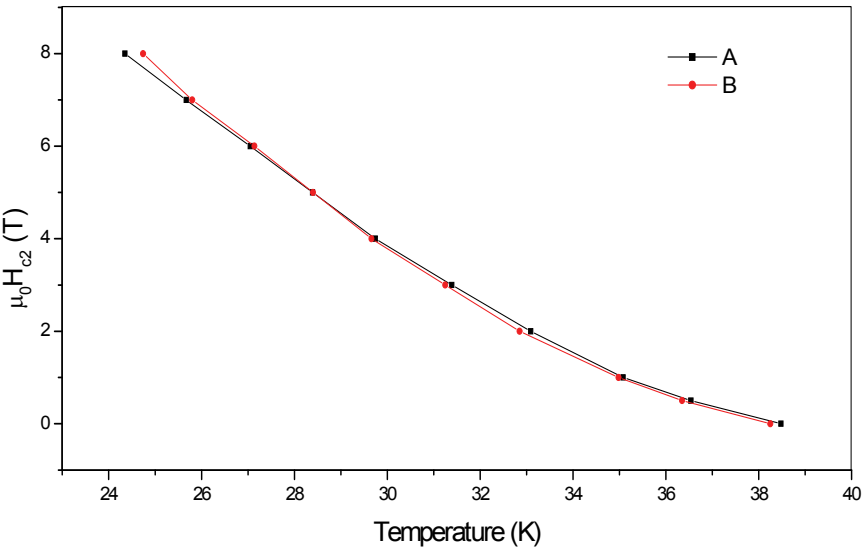

Fig. 5. Temperature variation of upper critical field for A & B.

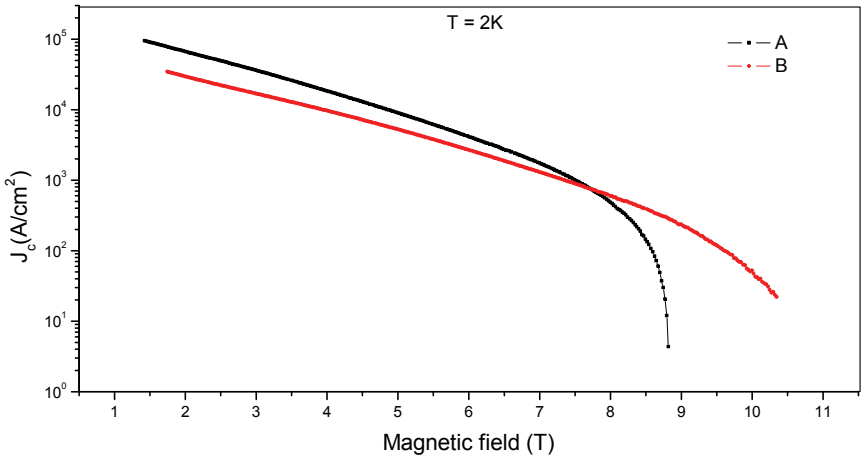

Fig. 6. Jc as a function of field. Jc for B is lower at low field but higher at high field .

$J_c(B)$ is governed by the nature of pinning and pinning force density. In order to see the effect of irradiation on pinning force density F_p ($F_p = J_c x H$), we have plotted $F_p(H,T)$ versus H in reduced scale. It is known that such curves form universal scaling at different temperatures [52]. In fig. 7, we have plotted fp ($f_p = F_p/F_p^{max}$) versus h ($h = H/H_{irr}$); F_p^{max} is the maximum value of F_p and H_{irr} is the irreversibility field at that particular temperature being explained as follows. In high temperature superconductors there exist a large region below the thermodynamic upper critical field (H_{c2}) line in H-T phase diagram (high T high H region) where the motion of the flux lines is reversible [53]. The lower boundary of this region is marked by a line called irreversibility line (IL). This region occurs in H-T phase

diagram due to some dissipative effects. In low temperature superconductors there is little or insignificant difference between IL and H_{c2} line. However, in HTS, IL is found to lie much below H_{c2} line. IL is attributed to a line above which the temperature enhances the classical Kim-Anderson flux creep or phase transition of flux line (like vortex-glass to liquid phase transition, melting of flux line lattice etc) [54, 55]. HTS has high critical temperature and at the same time they are highly anisotropic. Hence there is a large gap between IL and H_{c2} in HTS.
We have demonstrated a representative plot of fp versus h at 20 K (figure 7). There is a slight change between irradiated and unirradiated sample. We have fitted the curve using the generalized function:

$$f = ah^k (1-h)^m \tag{9}$$

The exponents k and m are 0.89 and 3.14 respectively for sample A and 0.61 and 2.22 respectively for sample B. Fig. 8 shows the 3D plot of F_p^{max}-H-T relation for the sample A. This shows that the pinning mechanism is somewhat altered due to Neon ion irradiation. The lower value of pinning force density F_p^{max} for irradiated sample B causes J_c to be lower than that of A at low field. But the lower values of the exponents for B in equation (9) show that F_p is higher for sample B than that of A at high field and hence J_c. This indicates that F_p decreases with applied magnetic field more slowly in case of B implying lower slope of J_c-B curve for sample B. The lower values of the exponents k and m of the irradiated sample show that there is reduction of the distance of the pinning centers (though to a low extent).

8. Conclusion

High temperature Cuprate superconductors (HTSC) are nonstoichimetric based on defects and disorders, which play a great role as carrier concentration and hence control Tc, Jc, resistivity etc. Particle irradiation induced defects modulate the carrier density through change in oxygen stoichiometry. In particular, irradiation induced oxygen vacancies act as flux pinning centres causing enhancement in Jc, pinning potential. Other cationic defects and disorder manifest,

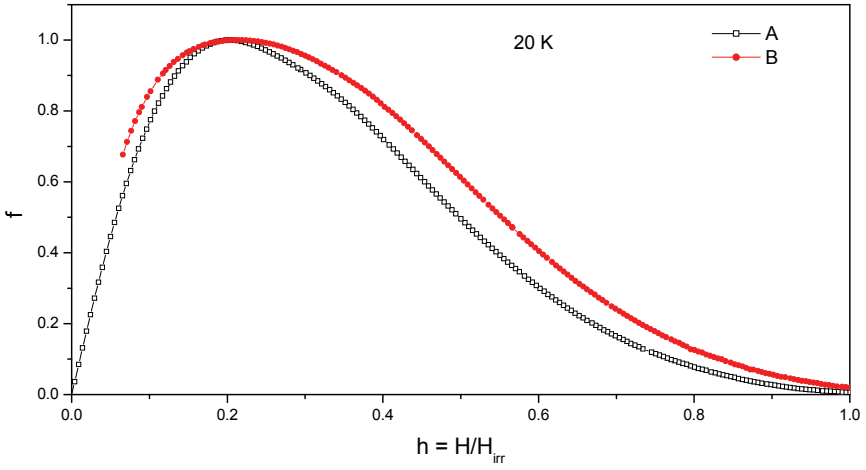

Fig. 7. Normalised pinning force versus magnetic field normalized with H_{irr}.

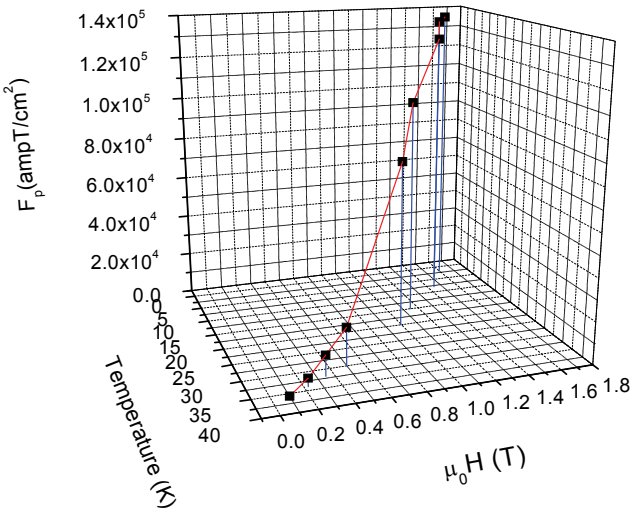

Fig. 8. 3D plot of pinning force density as function of temperature, magnetic field.

where this irradiation induced oxygen knock out is absent. We studied particle irradiation effects on Bi-based superconductors- Bi-2212 and (Bi,Pb)-2223. In Bi-2212 containing loosed excess oxygen needed for structural stability, particle irradiation causes knock-out of loose oxygen. In these systems, this excess oxygen plays the role of hole carrier. Hence, change of excess oxygen content due to particle irradiation causes a change in Tc (increase in the overdoped Bi-2212) and resistivity. Moreover, knocked out oxygen vacancies act as flux pinning centre for the enhancement of Jc. But, in Bi-2223, the presence of larger Pb(II) minimizes the presence of loose excess oxygen, and the irradiation induced oxygen knock-out is not the scenario. Hence there is no significant enhancement of Jc owing to irradiation. There is decrease in Tc and increase in resistivity. In both systems, there is a metal to insulator transition above the fluence of $1x10^{16}$α/cm², but, the reasons are different. Lowering of oxygen carrier concentration is the cause in Bi-2212 and in Bi-2223, localization due to irradiation induced disorder is the prime factor. Thus, HTSC's are in general very much sensitive to particle irradiation, whether by lowering of carrier concentration or, by generation of irradiation induced disorder. On the other hand, MgB_2, which is an intermediary between conventional superconductors and HTSC's is fairly insensitive to irradiation. It is a multiband BCS type phonon mediated superconductor. Strong covalent σ-bonding within B-B layer gives rise to σ bands and carriers of σ bands are strongly coupled with the in-plane B E_{2g} stretching modes, giving rise to superconductivity. Electron- phonon coupling constant along σ bands (λ_σ) governs Tc, which is not significantly affected by heavy ion like neon irradiation, even at the fluence of $1x10^{15}$ ions/cm². In two band system, the conductivity can be considered arising from the parallel network of the σ and π bands. As compared to σ bands, conductivity would be large in π bands due to low EPC constant. Particle irradiation affects the π band network. Hence, there is an appreciable increase in resistivity without any significant decrease in Tc and also, the role of irradiation induced defects in intragranular pinning is insignificant. The grain boundary pinning is the dominant scenario in case of MgB_2 as evident from magnetization and

magnetoresistance measurements. We also studied the enhancement of Jc by doping Mg with Hf (1%). The enhancement was enormous! The contribution was from other borides precipitating at the grain boundary.

9. References

[1] S.K.Bandyopadhyay, P.Barat, S.K.Kar, U. De, A.Poddar, P.Mandal, B.Ghosh, and C.K.Majumdar, Solid State Communications 82 (1992) 397.
[2] S.K.Bandyopadhyay, P.Barat, Pintu Sen, A.K.Ghosh, A.N.Basu and B.Ghosh, Phys. Rev. B58 (1998) 15135.
[3] G.Linker, J.Geerk, T.Kroener, O.Meyer, J.Remmel, R.Smithey, B.Strehlau, and X.X.Xi, Nucl. Inst. Meth. in Phys. Res.B59-60 (1991) 1458.
[4] O.Meyer, in Studies of High Temperature Superconductors, ed. A.V.Narlikar, V. 1. (Nova Science Publishers, New York, 1989); p. 139 and. the references therein.
[5] P. Sigmund, Radiation Effects 1 (1969) 15; M.J.Norgett, M.T.Robinson and I.M.Torrens, Nucl. Eng. De sign 33 (1974) 50.
[6] J.P.Biersack and L.G.haggmark, Nucl. Inst. & Meth. 174 (1980) 257.
[7] R.Viswanathan and R.Certon, Phys. Rev. B18 (19780 15.
[8] L.R.Testardi and L.F.Matthews, Phys. Rev. Lett. 41 (1978) 1612.
[9] B.D.Weaver, E.M.Jackson, G.P.Summers and E.A.Burke, Phys. Rev. B46 (1992) 1134; and references therein.
[10] G.P.Summers, D.B.Chrisley, W.G.Maisch, G.H.Strauss, E.A.Burke, M.Nastasl and J.R.Tesmer, IEEE Trans. On Nucl. Sci. 36 (1989) 1840.
[11] G.C.Xiong, H.C.Li, G.Linker and O.Meyer, Phys. Rev. B38 (1988) 1; Physica C153-155 (1988) 1447.
[12] G.J.Russell, H.B.Sun and K.N.R.Taylor, Physica C241 (1995) 219.
[13] C.Allgeier and J.S.Schilling, Physica C168 (1990) 499.
[14] J.M.Tarascon, Y.LePage, P.Bardoux, B.G.Bagley, L.H.Greene, W.R.McKinnon, G.W.Hull, M.Giroud and D.M.Hwang, Phys. Rev. B37 (1988) 9382.
[15] T.Tamegai, K.Koga, K.Suzuki, M.Ichimara, F.sakai and Y.Iye, Jpn. J. Appl.Phys. 28 (1989) L112.
[16] R.Yoshizaki, Y.Saito, Y.abe and H.Ikeda Physica C152 (1988) 408.
[17] J.B.Torrance, Y.Tokura, A.I.Nazzal, A.Bezinge, T.C.Huang and S.S.P.Parkin, Phys. Rev. Lett. 61 (1988) 1127.
[18] Y.Shimakawa, Y.Kubo, T.Manako and H.Igarashi, Phys. Rev. B40, (1989)11400.
[19] A.Matsuda, K.Kinoshita, T.Ishii, H.Shibata, T.Watanabe and T.Yamada, Phys. Rev. B38 (1988) 2910.
[20] Z.Z.Wang, J.Clayhold, N.P.Ong, J.M.Tarascon, L.H.Greene, W.R.McKinnon and G.W.Hull, Phys. Rev. B36 (1987) 7222.
[21] P.Mandal, A.Poddar, B.Ghosh and P.Choudhury, Phys. Rev B43 (1991)13102 .
[22] P.W.Anderson, Phys. Rev. 109 (1958) 1492.
[23] R.A.Fisher, S.Kim, S.E.Lacy, N.E.Phillips, D.E.Morris, A.G.Markelz, J.Y.T.Wei and D.S.Ginley, Phys. Rev. B 38 (1988) 11942.
[24] N.Okazaki, T.Hasegawa, K.Kishio, K.Kitazawa, A.Kishi, Y.Ikeda, M.Takano, K.Oda, H.Kitaguchi, J.Takada and Y.Miura, Phys. Rev.B 41 (1990) 4296.
[25] H.Zhang and H.Sato, Physica C214 (1993) 265.
[26] F.S.Galasso, Structure, Properties and Preparation of Perovskite-Type Compounds (Pergamon. , New York, 1969) p. 4

[27] S.B.Samanta, P.K.Dutta, V.P.S.Awana, E.Gmelin and A.V.Narlikar, Physica C178 (1991) 171.
[28] S.K.Bandyopadhyay, Pintu Sen, P.Barat, P.Mukherjee, S.K.Das and B.Ghosh, Pramana, Journal of Physics 47, 309 (1996); S.K.Bandyopadhyay, A.K.Ghosh, P.Barat, Pintu Sen, A.N.Basu and B.Ghosh, Phys. Stat. Sol. A162 (1997) 701.
[29] M.J.Puska and R.M.Nieminen, J.Phys. F : Metal Phys 13 (1983) 333.
[30] D.H.Kim, D.J.Miller, J.C.Smith, R.A.Holoboff, J.H.Kang and J.Talvacchio, Phys. Rev. B44 (1991) 7607.
[31] R.Ikeda, T.Ohmi and T.Tsuneto, Phys. Rev. Lett. 67 (1991) 3874.
[32] O.Brunner, L.Antognazza, J.M.Triscone, L.Miévelle and Ø.Fisher, Phys. Rev. Lett. 67 (1991) 1354.
[33] T.T.M.Palstra, B.Batlogg, R.B.van Dover, L.F.Schneemeyer and J.V.Waszczac, Phys. Rev. B41 (1990) 6621.
[34] C.Attanasio, C.Coccorese, V.N.Kushnir, L.Maritato, S.L.Prischepa and M.Salvato, Physica C255 (1995) 239.
[35] M.D.Lan, J.Z.Liu, Y.X.Jia, L.Zhang, Y.Nagata, P.Klavins and R.N.Shelton, Physica C218 (1993) 69.
[36] Shin-Pei Matsuda, T.Doi, A.Soeta, T.Yuasa, N.Inoue, K.Aihara and T.kamo, Physica C185-189 (1991) 2281.
[37] W.M.Chen, S.S.Jiang, Y.C.Guo, J.R.Jin, X.S.Wu, X.H.Wang, X.Jin, X.N.Xu, X.X.Yao and S.X.Dou, Physica C 299 (1998) 77.
[38] J.Fontcuberta, S.Pinol, X.Obradors, F.Lera and C.Rillo, Cryogenics 30 (1990) 656.
[39] A Gupta, H. Narayan, D. Astil, D. Kanjilal, C. Ferdeghini, M. Paranthaman and A.V. Narlikar, Supercond. Sci. Technol. 16 (2003) 951-955.
[40] E. Mezzeti, D. Botta, R. Cherubini, A. Chiodoni, R. Gerbaldo, G. Ghigo, G. Giunchi, L. Gozzeline and B. Minetti, Physica C 372-376 (2002) 1277.
[41] E.M. Schulson, J Nucl. Mater. 83 (1979) 239.
[42] Y. Kong, O.V. Dolgov, O. Jepsen and O.K. Anderson, Phys. Rev. B 64 (2001) 020501(R).
[43] I.I. Mazin and V.P. Antropov, Physica C 385 (2003) 49.
[44] A.Y. Liu, I.I. Mazin and J. Kortus, Phys. Rev. Lett. 87 (2001) 087005.
[45] J.Kortus, I.I. Mazin, K.D. Belashchenko, V.P. Antropov and L.L.Boyer, Phys. Rev. Lett. 86 (2001) 4656.
[46] H.J. Choi, M.L. Cohen and S.G. Louie, Physica C 385 (2003) 66.
[47] M. Zehetmayer, M. Eisterer, J. Jun, S.M. Kazakov, J. Karpinski, A. Wisniewski, and H. W. Weber, Phys. Rev. B 66 (2002) 052505.
[48] L. Lyard, P. Samuely, P. Szabo, T. Klein, C. Marcenat, L. Paulius, K.H.P. Kim, C.U. Jung, H.S. Lee, B. Kang, S. Choi, S.I. Lee, J. Marcus, S. Blanchard, A.G.M. Jansen, U. Welp, G. Karapetrov and W. K. Kwok, Phys. Rev. B 66 (2002) 180502.
[49] J.A. Woollam, R. Somoano and P.O'Connor, Phys. Rev. Lett. 32 (1974) 712.
[50] A.I. Posazhennikova, T. Dahm and K. Maki, Europhys. Lett., 60 (2002) 134.
[51] S. Blanchard, T. Klein, J. Marcus, I. Joumard, A. Sulpice, P. Szabo, P. Samuely, A. G. M. Jansen, and C. Marcenat, Phys. Rev. Lett. 88 (2002) 177201.
[52] D. Dew-Hughes, Phil. Mag. 55, (1987) 459.
[53] Y. Yeshurun and A.P. Malozemoff, Phys. Rev. Lett. 60 (1988) 2202.
[54] M.P.A. Fisher, Phys. Rev. Lett. 62 (1989) 1416.
[55] A. Houghton, R.A. Pelcovits and S. SudbØ, Phys. Rev. B, 40 (1989) 6763.

9

Application of Optical Techniques in the Characterization of Thermal Stability and Environmental Degradation in High Temperature Superconductors

L. A. Angurel[1], N. Andrés[2], M. P. Arroyo[2], S. Recuero[2],
E. Martínez[1], J. Pelegrín[1], F. Lera[1] and J.M. Andrés[3]
[1]*Instituto de Ciencia de Materiales de Aragón, CSIC-University of Zaragoza*
[2]*Instituto de Investigación en Ingeniería de Aragón, I3A, University of Zaragoza*
[3]*Instituto de Carboquímica, CSIC*
Zaragoza,
Spain

1. Introduction

The possibility of applying non-destructive techniques is important in the characterization of different problems that are associated with the use of high temperature superconducting materials in diverse technological applications. In this context, optical characterization techniques are being implemented in the analysis of several properties of solid materials due to their non-destructive nature. In particular, in some optical techniques the sample is illuminated with a coherent light and the recorded images present a granularity. This granularity is called speckle and its origin comes from the interference of the light scattered by the different points of the surface (Goodman, 1975b; Andrés et al., 2008). In consequence, any change taking place in the surface is immediately transferred to the speckle. Some speckle techniques that use digital recording have been developed. In this work, we present the applicability of Digital Speckle Pattern Interferometry (DSPI) and Digital Speckle Photography (DSP) in the study of two important problems associated with high temperature superconducting materials: the thermal stability and the environmental degradation (Recuero et al., 2005a; Angurel et al., 2006).

Thermal stability is a great challenge in the development of applications. In comparison with low-T_c superconductors, thermal properties of High Temperature Superconductors combine higher specific heat values and lower thermal conductivity ones. With these properties, the normal zone propagation velocities in these materials are several orders of magnitude lower than in the classical superconductors (Wang et al., 2007). Due to these properties, usually a hot spot appears in these materials and an important heat amount is generated leading to local temperature increases. Several stabilizing strategies have been used in order to facilitate heat dissipation in higher volumes and to reduce the possibility of local thermal degradation of the material. In addition, a great amount of work is being performed in order to obtain information about quench generation and propagation in High

Temperature Superconductors. Usually, a local transition to the normal state is induced in the sample while the temporal evolution of the temperature or/and the electric field along the sample is recorded. Other experimental techniques that have been proposed are acoustic noise detection (Lee et al., 2004), dynamic magneto-optical imaging (Song et al., 2009) or fluorescent paints, which provide a two-dimensional temperature distribution during quench propagation (Ishiyama et al., 2007).
Digital Speckle Pattern Interferometry (DSPI) has also been proposed as an adequate technique to obtain valuable information about quench generation in different high temperature superconductors (Recuero et al., 2005b, Lera et al., 2005, Angurel et al., 2008). DSPI allows us to measure small displacements in diffusively reflecting objects (Rastogi, 2001). In this technique, a fringe pattern is obtained after having compared two specklegrams, one recorded in a reference state and the second one after having produced a deformation in the object. This fringe pattern has the information associated with the displacement of each surface point. DSPI is adequate due to several of its properties: non-contact nature, digital recording, high sensitivity and the possibility of obtaining information of large surfaces. In the case of superconducting materials, the surface deformation is associated with thermal expansion that is originated when a transition to the normal state takes place in any point of the sample and its temperature increases. One of the most important features of this technique is the ability for visualizing where a hot spot will appear before it causes severe damage, thus marking the defective area where further microstructural analyses are to be made looking for the associated defects (Lera et al., 2005).
The second problem that will be analysed is the environmental degradation of high temperature superconductors in atmospheres with a high humidity (Argyropoulou et al., 2007). These materials have a strong chemical reactivity with water and for this reason environmental degradation plays an important role in the design of new applications in which effective protective methods have to be considered. Speckle Photography is a technique that has been proposed to study the surface degradation that takes place during corrosion (Fricke-Begemann et al., 1999). The technique analyses the decorrelation that takes place in the speckle images due to surface degradation. In this work, we show that Digital Speckle Photography (DSP) is an adequate tool to obtain qualitative and quantitative information about the surface degradation of different materials in different conditions, and, in particular, textured $Bi_2Sr_2CaCu_2O_{8+\delta}$ (Bi-2212) monoliths (Andrés et al., 2008, Recuero et al., 2008).
In this chapter, section 2 summarises the fundamentals of speckle techniques. Section 3 shows several examples of DSPI applied to the analysis of thermal stability on superconductors: Bi-2212 monoliths and 2G HTS wires. Section 4 analyses the environmental degradation of textured bulk Bi-2212 samples using DSP technique.

2. Fundamentals of speckle optical techniques

2.1 Introduction

Speckle techniques rely on a basic phenomenon that arises when an optically rough surface is illuminated with a laser. Thus, a granular structure appears over it. These randomly distributed spots are called speckles. The intensity of each speckle is the superposition of many scattered waves with random intensities and phases, coming from different points of the object surface. The specific pattern is related to the microstructure. Changes in the shape or structure of the surface can be measured by comparing scattered speckle fields, which are obtained at different states of the object. Two types of deformations are distinguished: Macroscopic

deformations, which lead to a bulk movement on the speckle pattern, and changes in the microscopic structure of the surface, which induce modifications in the speckle pattern or decorrelation. Depending on the case, different techniques can be used (Vest, 1979).
Speckle Interferometry is a technique that determines displacements or deformations. An initial image of the object is taken as the reference state. The object is imaged on the sensor of a CCD camera where it is superimposed to a reference beam. New images are taken by the camera after a change in the object is produced. The subtraction of both images produces an image with bright and dark fringes which represent iso-lines of equal deformation. The technique is sensitive to out of plane displacements. It has been used in solids to determine the out of plane deformation (Jones & Wykes, 1989) and, in fluids, to determine velocities (Andrés et al., 1999; Andrés et al., 2001).
Speckle photography is a technique that compares intensities of the speckle fields and determines alterations on the surface through movements or changes of the speckle pattern. No reference wave is used in these images. Thus, phase information is lost but the method is very simple and easy to use. Traditionally, this technique has been applied to measure the in-plane displacements in solids (Archbold & Ennos, 1972), deformations (Fricke-Begemann, 2003) and roughness (Yamaguchi et al., 2004).

2.2 The speckle

The image recorded when a rough surface is illuminated with white light is different from that obtained when a coherent laser beam is used. An example of a metallic surface sanded with emery paper of 400# is presented in Fig. 1. In the image obtained with white light (Fig. 1.a) the scratched structure produced by sand paper is distinguished. When the same object is illuminated with a laser beam the image presents a granularity called speckle (Fig. 1.b).
The origin of this granularity is the coherent superposition of many scattered waves with random intensities and phases, coming from different points of the object surface. This process takes place when the sample surface is optically rough, that is, if the surface height variations are greater that the optical wavelength (in this case $\lambda \sim 6 \times 10^{-7}$ m). Thus, a coherent addition of the scattered waves from different object points is obtained. The intensity of each speckle changes from 0 to a maximum value depending on the interference state.

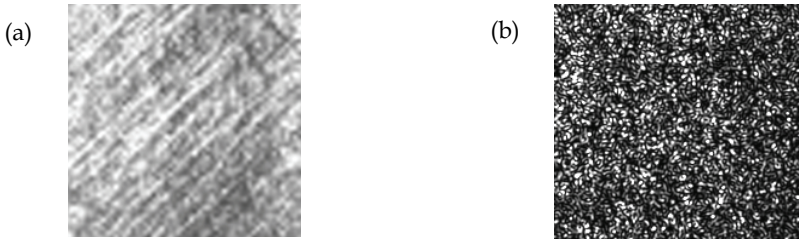

Fig. 1. Recorded images of a metallic sample sanded with emery paper of 400# and illuminated: (a) with white light and (b) with a coherent laser beam.

A statistical analysis (Goodman, 1975b) is done by assuming that the phases of the small contributions are uniformly distributed over a complete 2π-interval, that the amplitude and phases are statistically independent variables, and that the number of contributions is sufficiently large. This analysis leads to probability density functions of the intensity I and of the phase of a fully developed, polarized speckle field as follows:

$$p(I)=\frac{1}{I}e^{-\frac{I}{\langle I\rangle}} \qquad p(\theta)=\frac{1}{2\pi} \tag{1}$$

where p(I)dI is the probability for a speckle to have an intensity value between I and I+dI and p(θ)d θ is the probability for the phase to have a value between θ and θ+dθ.
There are two main geometries to observe the speckles. A freely propagating field, called objective speckle, and the imaged speckle, called subjective speckle, when the object is recorded by means of a lens system. In the techniques described in this section, speckles are recorded on the image plane (subjective speckle). Thus, the speckle mean size d_s is determined by the following equation:

$$d_s=1.22\frac{(1+M)\lambda f}{D} \tag{2}$$

where f is the focal length, M the magnification, λ the wavelength and D the aperture diameter of the recording system.

2.3 Digital speckle photography (DSP)

In digital speckle photography, the object is illuminated with a laser beam under an angle θ and the scattered light is imaged onto a CCD sensor (Fig. 2.a). The lens of the recording system is determined by the required magnification. The speckle size must be bigger than the pixel dimensions. The purpose of this technique is the comparison of two different speckle patterns, corresponding to two object states. The first one is considered as the reference state, and is recorded before the object modification process starts, while the second one is recorded after the surface has been modified.

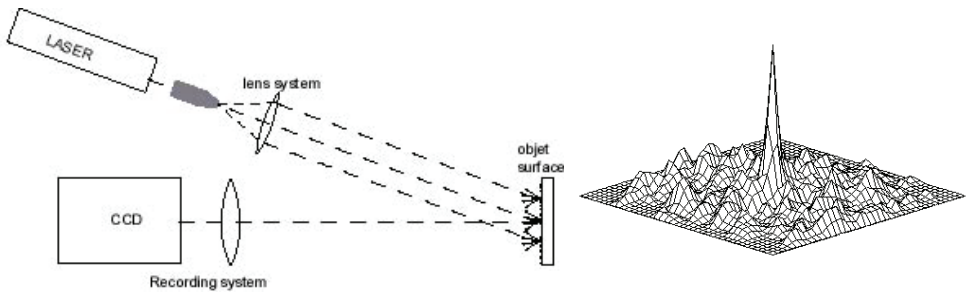

Fig. 2. (a) Digital Speckle Photography recording setup. (b) Plot of a 2D cross correlation function.

As it is a digital recording, each speckle image is a matrix of intensity values, I(r), associated with the intensity of the interference at each point of the image. The characteristics of the CCD camera determine the intensity level range and the matrix dimensions. Due to the random nature of the speckle fields, changes in the object surface cannot be inferred from each individual speckle. The information has to be extracted through an averaging process. Correlation functions are used to quantify the variation between the intensity fields in two speckle images. The normalized 2D cross correlation function has been used. It is defined as:

$$CC_{I_1 I_2}(\Delta\vec{r}) = \frac{\left\langle I_1(\vec{r}) I_2(\vec{r}+\Delta\vec{r})\right\rangle - \left\langle I_1(\vec{r}) I_2(\vec{r})\right\rangle}{\left[\left(\left\langle I_1^2(\vec{r})\right\rangle - \left\langle I_1(\vec{r})\right\rangle^2\right)\left(\left\langle I_2^2(\vec{r})\right\rangle - \left\langle I_2(\vec{r})\right\rangle^2\right)\right]^{1/2}} \quad (3)$$

where $I_1(\mathbf{r})$ and $I_2(\mathbf{r})$ are the intensity field of the first and second speckle images, respectively. This function has a different value for each $\Delta\mathbf{r}=(\Delta x,\Delta y)$ (Fig. 2.b), and has a maximum at a certain value. The peak position is proportional to the in-plane sample displacement and its height is related to the surface modifications. Both contributions can be analysed separately. The peak value, also known as the correlation coefficient, changes from 1, when the surface remains unchanged, to cero that corresponds to a total decorrelation.
The calculation of the 2D cross correlation function using eq. 3 is a time consuming process, it is numerically implemented with Fast Fourier Transform algorithms (Takeda, 1982). Then:

$$\left\langle I_1(\vec{r}) I_2(\vec{r}+\Delta\vec{r})\right\rangle = \left[\Im^{-1}\left[\Im[I_1]\Im[I_2]\right]\right] \quad (4)$$

where $\Im$ means Fourier Transform. The correlation coefficient can be calculated over the full image or using correlation windows of N_x x N_y pixels. In the first case, the evolution of the correlation coefficient gives a global value of surface changes. As the value at each interrogation area indicates the local changes, the second procedure allows obtaining a 2D correlation map, with information on where the surface modification process has taken place. The size of the sub-regions has to be big enough for the statistical analysis to be feasible but as small as the size of the defects to be identified.

2.4 Digital speckle pattern interferometry (DSPI)

In digital speckle pattern interferometry, the light scattered by the object is made to interfere with a reference beam (Fig. 3). This interference, called specklegram, is recorded on a CCD camera at different time states. The reference wave is obtained by diverting a small amount of the main laser beam. Due to the small spatial resolution of CCD cameras, the angle between both beams has to be very small. Then, both beams are combined in front of the CCD camera by means of a cube beam-splitter (Fig. 3). The sustration of two specklegrams, recorded for different object states, produces an image, whose intensity in each point is proportional to:

$$I(x,y) \sim (1-\cos\Delta\phi) \quad (5)$$

where $\Delta\phi$ is the phase difference in the object wave, which is related to the object local displacement as:

$$\Delta\phi = \mathbf{K}\cdot\mathbf{L} \quad (6)$$

with $\mathbf{K}=(\mathbf{k_o}-\mathbf{k_i})$ the sensitivity vector, being $\mathbf{k_i}$ and $\mathbf{k_o}$ the wave vectors of the illumination and observation beams and $\mathbf{L}$ the surface displacement vector.
Since the fringes are loci of constant phase difference, the deformation vector components can be measured using appropriate configurations. In many cases, the visual aspect of the fringes, that represent regions of equal displacement, can provide enough information in the analysis of a given experiment.
In order to know the quantitative phase difference value, spatial phase shifting (SPS) can be introduced (Burke et al., 1998; Creath, 1985). It is based on the addition of a known phase

function called phase carrier. A conventional DSPI setup can be turned into a SPS-DSPI setup by shifting the origin of the smooth divergent reference wave with respect to the lens centre an amount Δx (Fig. 4). This generates a linear phase shift in the x-direction of the sensor. The phase-shifted data are recorded simultaneously on adjacent pixels, in the same speckle. To resolve this modulation frequency, a phase shift of 2π (maximum-minimum-maximum) must be recorded in each speckle instead of the constant phase in a standard speckle of a DSPI specklegram. Thus, the speckle size is appropriately increased up to a value of around 3 pixels.

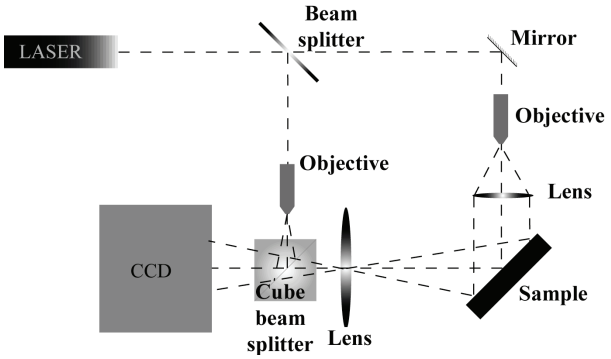

Fig. 3. Digital Speckle Inteferometry setup

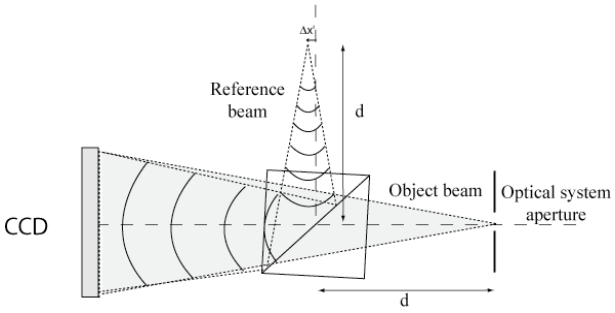

Fig. 4. Experimental setup used for introducing SPS in a DSPI system.

Phase maps are obtained using a global Fourier Transform method (FTM) (Takeda et al., 1982; Lobera et al., 2004). This analysis is based on the calculation of the Fourier transform of the specklegram. The positive frequency side lobe is isolated and translated to the origin to eliminate the carrier frequency component. The inverse discrete Fourier transform is then carried out, and the object phase at each pixel is obtained. A phase difference map, instead of a intensity map, is retrieved by subtracting two object phase maps. For visualization, the phase differences are mapped to grey levels such as that 0 is black and 2π is white, given that the phase differences are wrapped (only known in the range 0 to 2π).

Although this technique is more sensitive to out-of-plane displacements, if big changes take place on the surface the correlation between images decreases and then the visibility of the fringe pattern decreases and even disappears.

3. Analysis of quench generation in high temperature superconductors using digital speckle pattern interferometry

In this section we show several examples on the use of DSPI for the analysis of the thermal stability in High Temperature Superconductors. First, we present the experimental modifications needed to apply this technique in cryogenic conditions, as required for the study of superconducting materials, and then we show several examples of inhomogeneity along the length in the transition from superconductor to normal state in different materials.

3.1 Experimental modifications required to apply DSPI in cryogenic conditions

In this application, DSPI has to be used while the superconducting material is in the superconducting state, at temperatures close to 77 K. For this reason, it has been necessary to build a new experimental set-up (Recuero et al., 2005). A glass dewar (height of 420 mm and diameter of 200 mm) was designed with several 85 mm x 100 mm windows with optical access for different optical techniques (Fig. 5.a). This window was heated with an external manganin resistance to avoid any condensation on the external wall that could strongly disturb the DSPI observations.

Two different DSPI configurations have been used in different works. In the first one the sample was illuminated at an angle of $\varphi=45^{o}$ (Recuero et al., 2005, Lera et al., 2005). The angle between the illumination and the recording direction was 90^{o}. With this set-up two optical windows were required to illuminate and to observe the sample. The sensitivity of the technique was 0.45 μm per fringe. As can be observed in Fig. 5.b, φ can be reduced. In the case of the second configuration $\varphi =10^{o}$ (Angurel et al., 2008, Angurel et al., 2009), only one optical window was required and the sensitivity increased up to 0.28 μm/fringe. In both cases, the size of this window can be adjusted to the sample size.

One of the difficulties to overcome is the need of a stable atmosphere around the sample. In the initial experiments, the sample was fixed to an aluminium plate held at the centre from the dewar top cover and it was cooled by a conduction system, thermally anchored to the aluminium plate, which is partially immersed in liquid nitrogen. In these conditions, the sample cannot be placed inside liquid nitrogen because liquid movements induce some changes in the refraction index that create a random fringe pattern and hide any observation related to the sample deformation. For this reason, the sample was usually placed above the liquid surface and the pressure inside the dewar was reduced to approximately 0.1 atm.

Obviously it is also interesting to obtain information about quench generation with samples immersed in liquid nitrogen because in some applications these superconducting materials have to work in these conditions. A new experimental configuration, with the sample placed very close to the dewar window, was designed (Angurel et al., 2009) (Fig. 5.b). In this case, the sample was placed closer to the dewar wall in order to reduce the light path inside the liquid nitrogen from 20 cm to 1 cm. The measurement procedure consists on reducing the pressure inside the dewar and wait for approximately 15 minutes. It has been observed that during this time, the random fringe pattern transforms in a series of near horizontal fringes whose number decreases with time (Fig. 6) and finally almost disappears. This means that liquid nitrogen movement changes from a random state to a still stratified one and finally it stabilizes. In these conditions, there is a time window of approximately 10-15 minutes where the sample displacements can be visualized. The sample temperature can be controlled by changing the gas pressure inside the dewar.

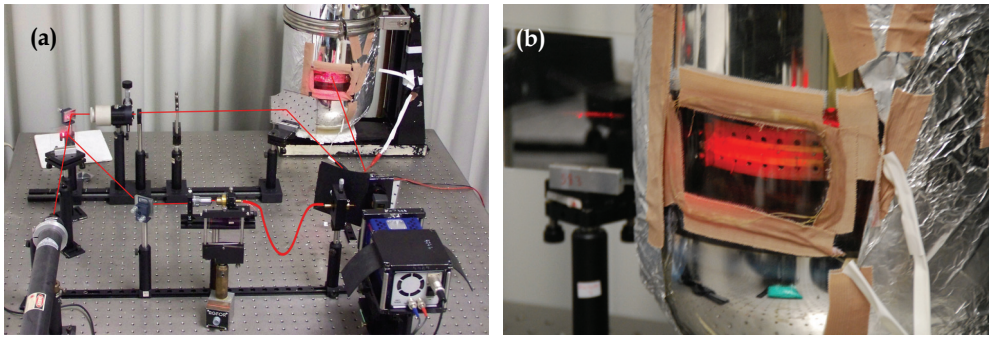

Fig. 5. (a) Experimental arrangement used to apply DSPI in cryogenic conditions. (b) Detail of the modification performed for placing the sample close to the dewar window in order to take measurements with the sample immersed in liquid nitrogen.

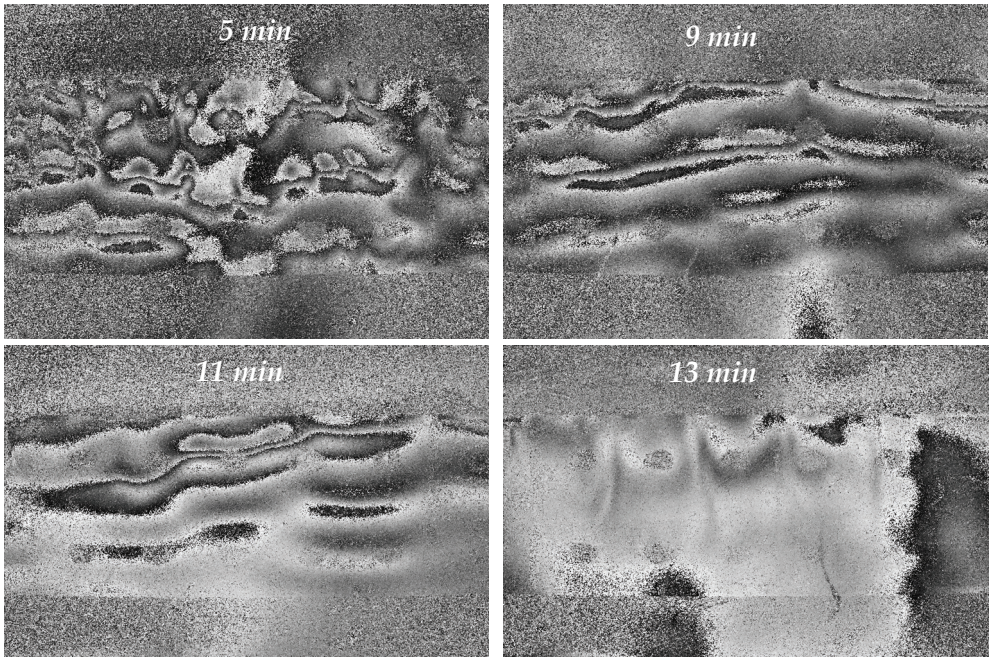

Fig. 6. Fringe patterns associated with liquid nitrogen movements at different instants after having reduced the pressure inside the dewar.

3.2 Hot spot generation in Bi-2212 monoliths

Properties of bulk Bi-2212 monoliths are determined by the quality of the intergranular junctions. Laser melting techniques were introduced as an adequate tool to texture these materials in a planar geometry and to obtain good superconducting properties (Mora et al., 2003). When the material transits to the normal state, heat dissipation starts in the points where the junctions have the poorest properties. These materials have very low thermal

conductivity values and this local heat generation induces inhomogeneous temperature increments that can deteriorate the superconductor.
Experiments were performed with the optical configuration that had a sensitivity of 0.45 μm/fringe for deformations in the direction perpendicular to the sample surface (Recuero et al., 2005; Lera et al., 2005). The sample was fixed by one point to the aluminium plate in order to avoid the movement of the sample and to have a fixed reference point (Fig. 7). The sample and the metallic support were electrically isolated.

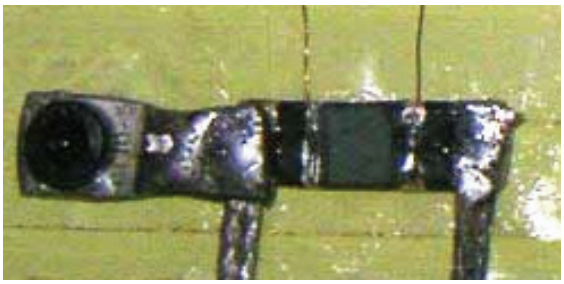

Fig. 7. Photograph of the system used to hold the Bi-2212 monoliths.

An initial characterization was performed at room temperature. In this case, small currents were applied for some seconds and the fringe pattern was recorded. At the same time, the resistance change, which is proportional to the temperature variation, was measured. Fig. 8 shows the time dependence of the resistance that was measured in a Bi-2212 monolith at room temperature for different applied current values. The observed behaviour correlates with the DSPI fringe patterns recorded at different instants (Fig. 9). The fringe pattern corresponds to a bending sample movement with fringes appearing in the image right side. In the case of 1.5 A only two fringes are observed, they appear at t=20s and they remain constant during the rest of the pulse. In the case of a current of 2.5 A, the number of fringes increases up to 6, at t=40s, remaining unchanged afterwards. As in other samples (Lera et al., 2005) the number of fringes is proportional to the resistance change and, in consequence, to the temperature variations. This confirms that the number of fringes is related to the sample deformation associated with thermal expansion.
These monoliths were also characterized at temperatures below T_c, applying current pulses higher than the critical current value (Recuero et al., 2005). Samples were cooled by conduction. A rotary pump vacuum was made in order to eliminate unwanted fringe patterns associated with gas movement. As it has been mentioned, in these materials, when a current higher than the critical current value is applied, dissipation starts at the points with the poorer superconducting properties. This is reflected on a different fringe pattern shape. Fringes arise from a point whose location coincides with the point that has the poorer properties. An example in which the applied current is approximately 3 times higher than the critical current is presented in Fig. 10. This was confirmed by applying higher currents values, with the objective of generating enough heat to melt the sample. Results showed that melting was originated in a point (Fig. 10), that coincided with the point where the fringes were originated.
In consequence, DSPI allows determining where a hot spot will be located. The main advantage is that it can be located when the temperature reached by the sample is lower that 100 K. These experimental conditions do not deteriorate the sample. For this reason, these

studies can be performed combined with microstructural analysis in order to obtain information on the defects that are responsible of the hot spot generation (Lera et al., 2005). In these materials, texture processing induces a microstructure where the grains are very well aligned to the sample axis. DSPI showed that the hot spots were located in regions where many holes, originated during the texturing process, were concentrated.

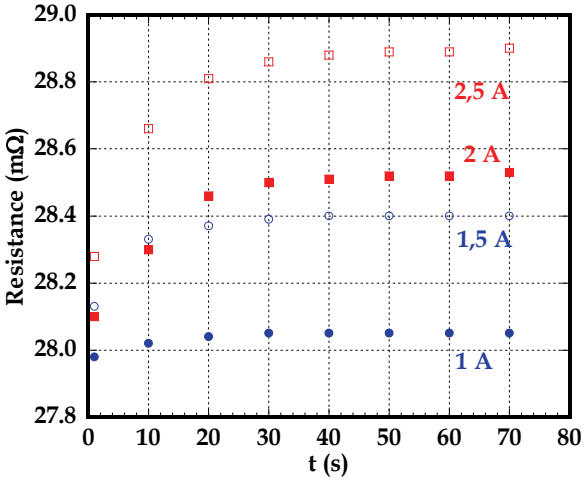

Fig. 8. Time dependence of the Bi-2212 monolith resistance at room temperature for different applied currents.

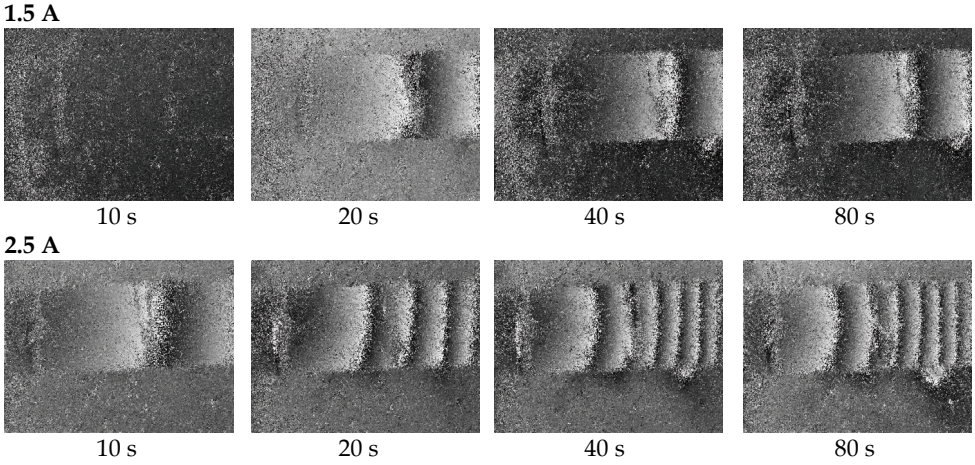

Fig. 9. Fringe patterns obtained in a Bi-2212 monolith at room temperature for two applied currents at different times.

This example shows that DSPI observations can be used to obtain information on the origin of hot spots and how the processing conditions can be modified in order to control these defects and to reduce their influence on the final properties of the superconducting material.

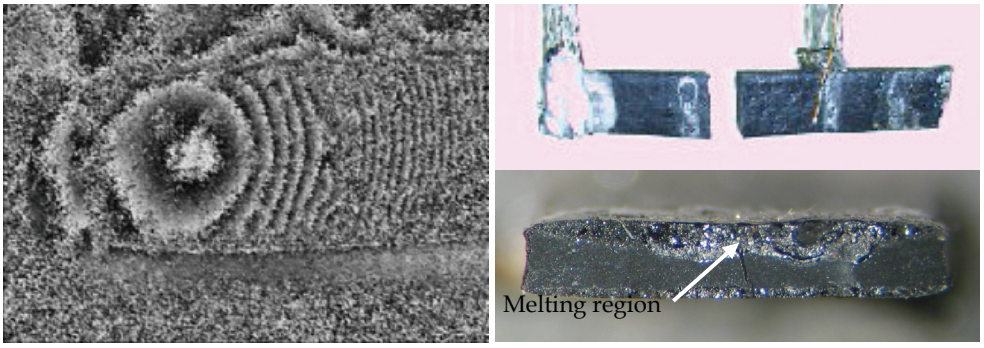

Fig. 10. Fringe pattern observed in a Bi-2212 monolith at low temperature when a current higher that the critical current is applied. Longitudinal and transverse photographs of the sample after having applied a high current pulse that melted it.

3.3 Quench generation in 2G HTS wires

Visualization of quench generation in 2G HTS wires has also been analysed using DSPI techniques (Angurel et al., 2008; Angurel et al., 2009). This work is being performed in the framework of a collaboration with SuperPower Inc.. The experiments were done in homogeneous samples as well as in samples with a controlled defect. This defect produced a local reduction of the critical current value at 77 K to values around a 20% of the average value. Experiments were performed with the sample placed both above and below the liquid nitrogen level. In the first case, two different cooling conditions were used: with the sample fixed to an isolation sample holder or fixed to a metallic holder. The main result (Angurel et al., 2008) is that quench generation does not always appears in the point with the lower critical current value and that other facts as the cooling conditions or inhomogeneities in the sample thermal stabilization can play a fundamental role.

The results presented here correspond to the case of the sample immersed in liquid nitrogen, as required in many applications of these conductors. For this reason, as it was mentioned in section 3.1, an effort was made for performing DSPI observations in these challenging experimental conditions (Angurel et al., 2009). In addition, the measuring system has been modified in order to obtain simultaneous measurements of the optical properties and of the electric field and temperature profiles during the current pulse.

Fig. 11 and Fig. 12 show the results of the DSPI technique applied to two different samples of the same batch, corresponding to a SCS4050 2G HTS wire with a width of 4 mm and a 20 μm thick stabilizing copper layer. A special sample holder was designed for allowing both sides of the sample to be in contact with liquid nitrogen or for placing the sample on a metallic support. The sample is fixed at the two ends and, for this reason, the deformation associated with the thermal stabilization leads to the bending of the sample.

Fig. 11 shows the typical behaviour of a homogeneous sample, as it is seen by the electric field and by the temperature profiles, during a pulse of 120 A for 3 s while the sample was immersed in liquid nitrogen and T=78.6K (I_c(77K)=123 A) because the pressure inside the dewar was above atmospheric pressure. Both sides of the sample are in contact with liquid nitrogen. The electric field values at the pulse end is on the order of $3x10^{-4}$ V/cm (Fig. 11.a) and temperature rises less than 0.8 K (Fig. 11.b). DSPI fringe patterns are presented in Fig. 11.c to 11.h. In this case, the reference state has been recorded before applying the pulse and

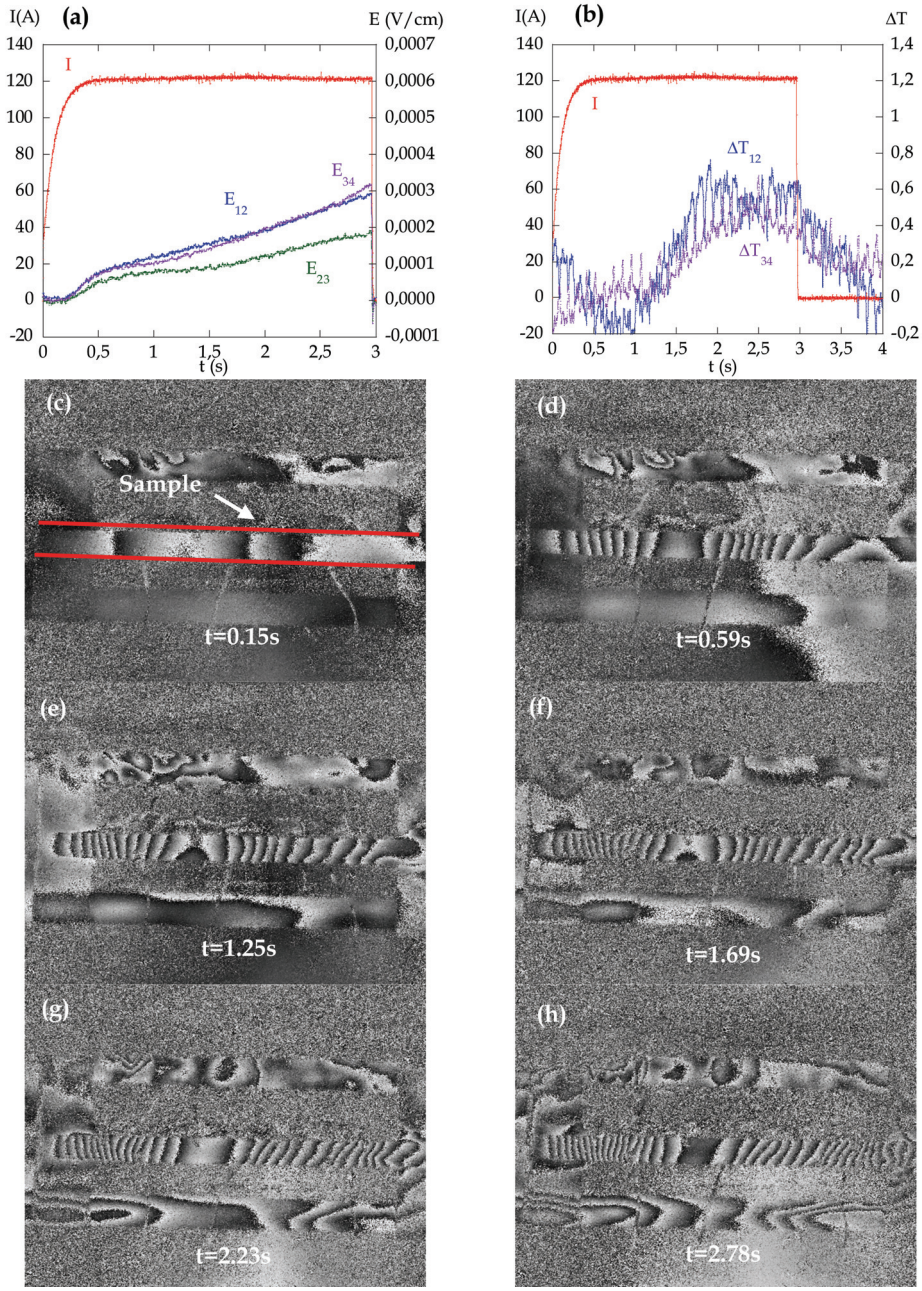

Fig. 11. (a) Electric field and (b) temperature profiles recorded in a 2G HTS wire after applying a current pulse of 120 A for 3 s at 78.6K. (c) to (h) Fringe patterns observed at different instants: 0.15s, 0.59s, 1.25s, 1.69s, 2.23s, 2.78s, taking as reference t=0s.

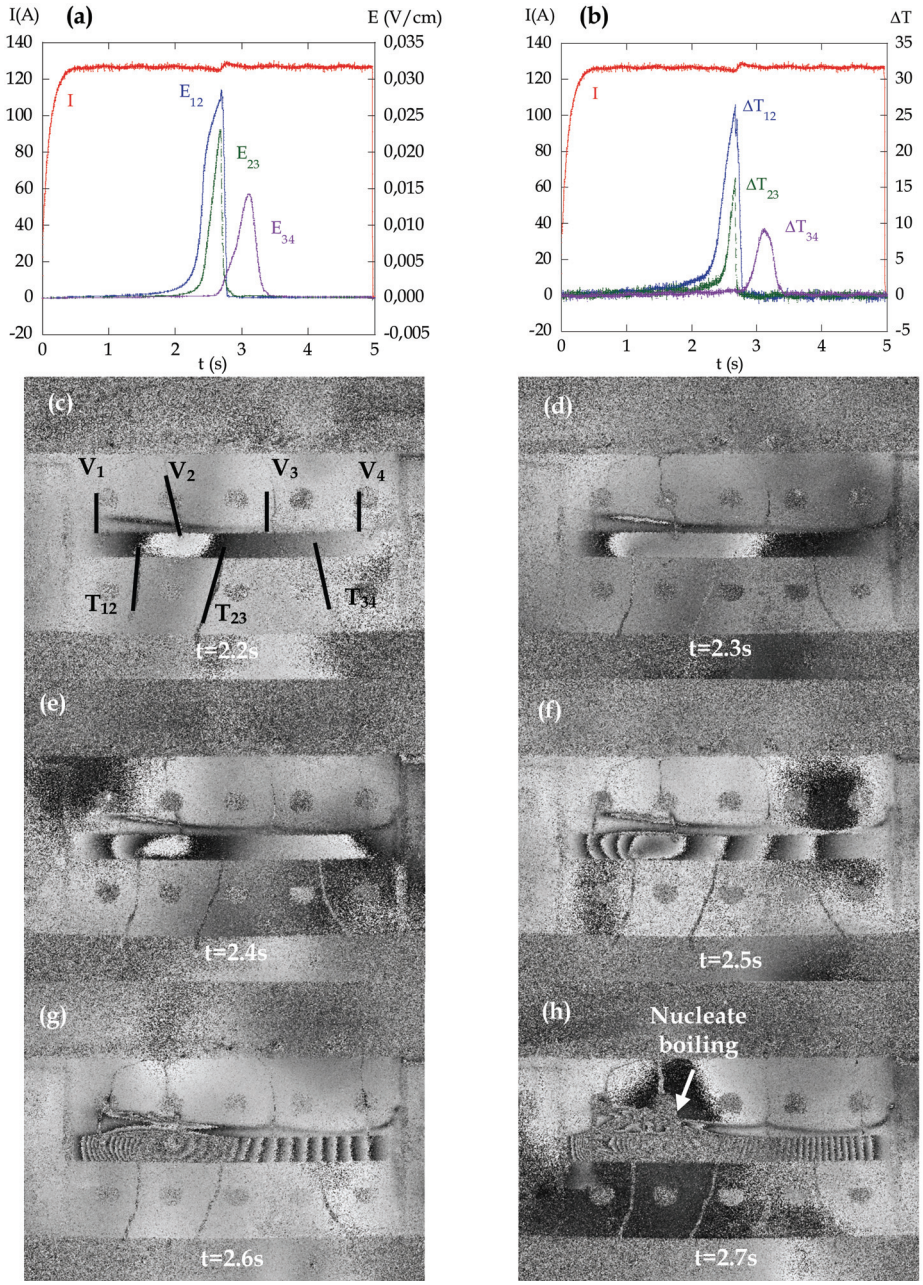

Fig. 12. Behaviour of a sample with a defect in contact V_2 after having applied a pulse current of 125 A for 3 s at 78.6 K. (a) Electric fields and (b) temperature profiles. (c)-(h) Fringes patterns obtained taking as a reference the sample situation at $t=t_0$-0.1 s.

for this reason the total deformation is being observed. The fringe patterns at t=0.15 s and t=0.59 s show that in the initial bending deformation stages, the sample takes an S-like shape with a central maximum deformation of 2.2 μm (8 fringes) and a minimum one of approximately 0.56 μm (2 fringes) in the right part of the sample. In the rest of the images, the sample deformation leads to the expected C-liked shape bending deformation of a sample fixed by the two extremes. The number of fringes increases with time in a similar way to the electric field.

DSPI also helps to detect situations in which heat is not generated in a uniform way. This can be seen in Fig 12, which shows the behaviour observed in a 2G HTS wire where a defect was unintentionally produced in the sample when soldering the voltage tap number 2 and a current pulse of 125 A was applied for 5 s. In this case, the sample was placed on the metallic plate. The electric field generation increases faster in regions 1-2 and 2-3 reaching values of the order of 0.03 V/cm, two orders of magnitude higher than in the case presented in Fig. 11. At t=2.67s the electric field in these two regions show a strong reduction that can be also observed in the temperature profiles. They are associated with the increase in the heat transfer coefficient of the liquid nitrogen when moving from the convective to the nucleate boiling regime (Angurel et al., 2008, Martínez et al., 2010). The results indicate that the electric field generation and the temperature increase in region 3-4 start later than in regions 1-2 and 2-3.

In this case, the deformation is much higher than in the previous case, the number of fringes is too high and the resolution is not enough. For this reason, deformation evolution (Fig. 12. c-h) has been visualized taking as the reference the previous image. With this configuration, the observed deformation corresponds to the deformation that took place in the sample during the previous 0.1s. At t=2.2s, deformation and, in consequence, heat generation is located in the position of voltage contact V_2. In the region between contacts V_3 and V_4 the sample does not deform. This is also consistent with the measured temperature profiles evolution. ΔT_{34} starts to increase later on. At t=2.4s the heat generated in the sample, in the left part, is enough to induce some movement of the liquid nitrogen above the sample. In the last two photographs, the nucleate boiling has started between contacts V_1 and V_3 and the fringe pattern can not be observed, while in the right part of the sample, region 3-4, the different fringes can clearly be observed.

These results indicate that DSPI observations provide information that is complementary to the electric field and temperature profiles. The main advantage is that DSPI provides precise local information and determines with a good resolution where the origin of the heat generation is placed and that this information can be inferred without anchoring any voltage tap or thermocouple on the sample.

4. Analysis of environmental degradation in textured bulk $Bi_2Sr_2CaCu_2O_{8+\delta}$ monoliths obtained by laser melting techniques.

4.1 Applicability of digital speckle photography on the analysis of local surface modifications in metallic materials.

Before studying the surface degradation in $Bi_2Sr_2CaCu_2O_{8+\delta}$ monoliths, the possibilities of the DSP technique have been explored on the analysis of well known corrosion processes of metallic samples in different conditions. First, we analysed the corrosion of Fe samples in H_2SO_4 solutions with different concentrations (Andrés et al., 2008). In this case, the corrosion process produces the generation of H_2 bubbles in the metallic surface. These bubbles are clearly observed in Fig. 13.a in the case of a Fe sample after having been immersed 40 s in a 0.1 N H_2SO_4 solution. These bubbles prevent the information about the surface state in these points from being obtained (Fig. 13.b).

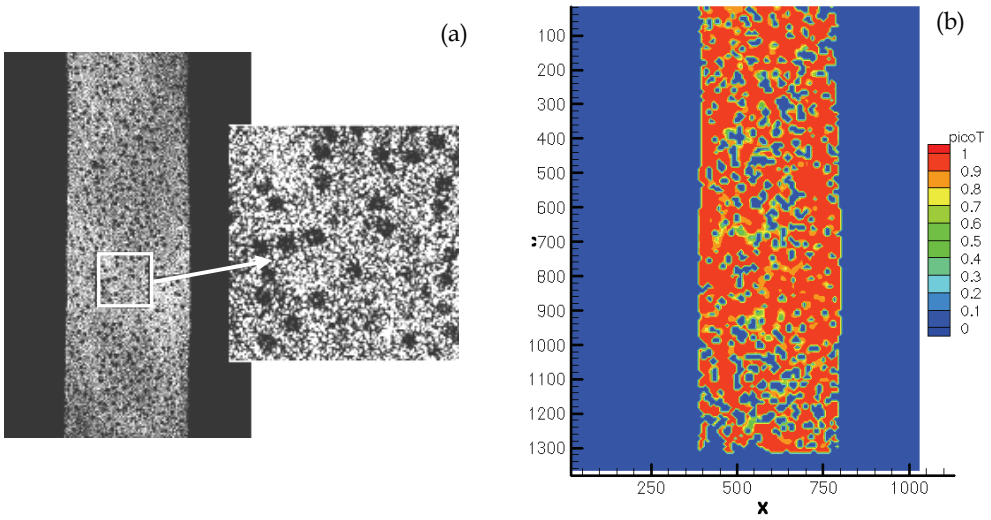

Fig. 13. (a) Image of speckle photography from a Fe sample after being immersed in a 0.1 N H_2SO_4 solution for 40 s. (b) 2-D correlation coefficient map measured in these conditions.

For this reason, when corrosion takes place in an acid solution, these studies were performed by recording the images with the sample removed from the solution. It was observed that the time dependence of the correlation coefficient is linear in the initial 250 s, when the correlation coefficient value reduces down to 0.6. It was proposed that the slope of this variation is related to the corrosion rate of Fe in these conditions. DSP observations have been compared with linear sweep voltametry measurements. This comparison showed that DSP can be used to compare corrosion rates in different conditions.

A second problem that has been analysed is when the corrosion process involves the deposition of a layer on the surface. This is the case of Fe samples immersed in $Cu(NO_3)_2$ solutions, where a copper layer is deposited on the Fe surface. Samples have been sanded with emery paper of 400# which produces a scratched structure on the surface (Fig. 14.a).

The maximum scratch depth is 1.2 μm. DSP observations (Fig. 14.b) clearly show that the corrosion is not uniform being more important in the central and right part of the sample, where the correlation coefficient has lower values.

In order to find a relation between the correlation coefficient variations and the modifications taking place on the sample surface, the topography along the line indicated in Fig 14.b has been measured using confocal microscopy. Results are compared in Fig. 15, where each image corresponds to a 1.1 mm length. In Fig. 15.a and 15.b, the left part of the region, with the highest values of the correlation coefficient, is presented. Between pixels 390 and 420, where the correlation coefficient remains close to 1, the surface was not modified. In the regions where the correlation coefficient is reduced to values between 0.8 and 0.9 the surface becomes smoother. Around pixel 430, the correlation coefficient value is close to 0.7. In this region, Cu deposition is observed with small aggregates, 1 to 2 μm thick. A region with higher variations is observed in Fig. 15.c and 15.d. The correlation coefficient reaches values between 0.2 and 0.3. In this case, the Cu layer completely covers the Fe surface reaching a layer thickness close to 8 μm.

These results clearly show that DSP is a technique that can be used to compare the corrosion rate in different experimental conditions. One of the main advantages is that it is possible to obtain local information of how the corrosion process evolves in different regions of the surface.

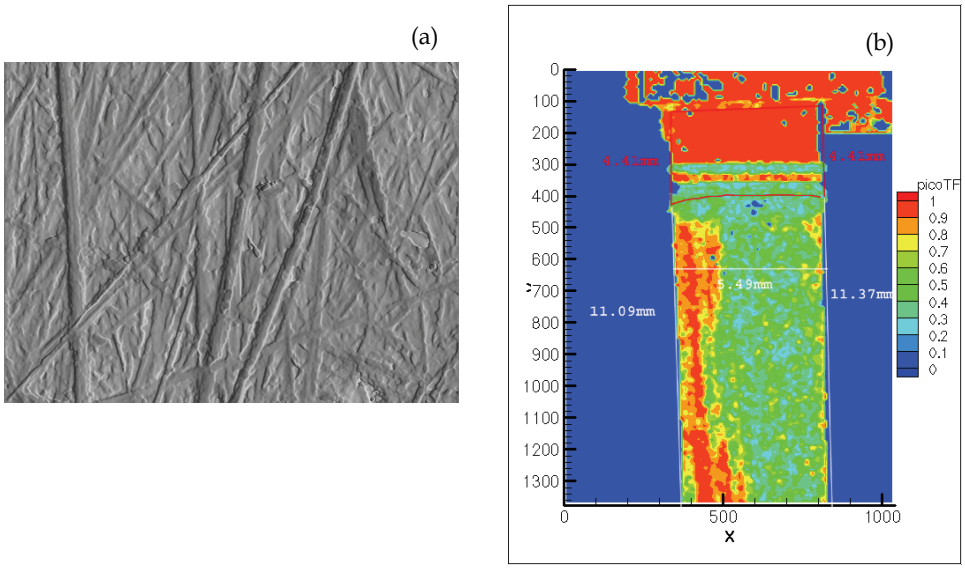

Fig. 14. (a) Confocal image of the Fe surface (255 x 190 μm²) before starting the deposition process. (b) 2D correlation map obtained in a Fe sample after being immersed in a 0.1 M $Cu(NO_3)_2$ solution for 1 h.

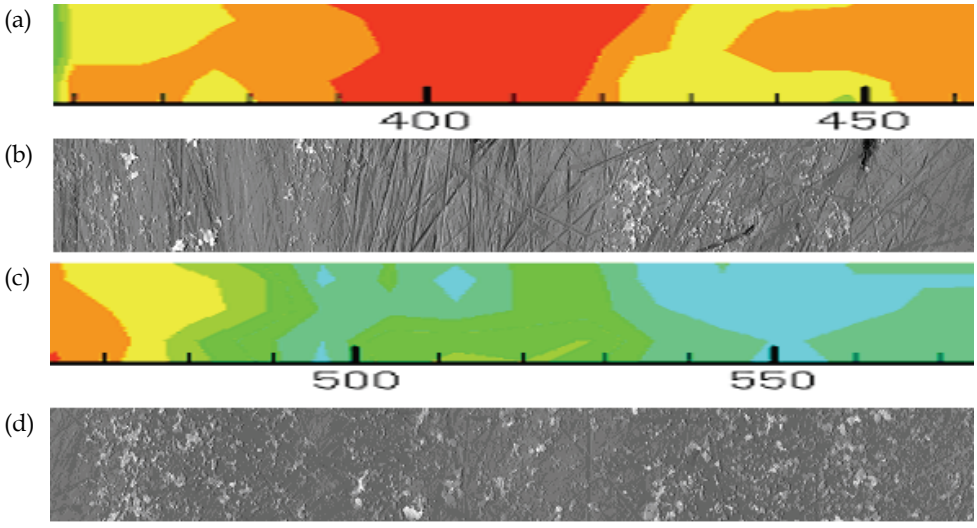

Fig. 15. Comparison of the 2D correlation coefficient map and the surface topography measured with confocal micrscopy in the line shown in Fig. 14.b.

4.2 Analysis of the environmental degradation process in textured Bi-2212 monoliths

The application of melting techniques to fabricate Bi-2212 monoliths produces a multiphase material (Mora et al., 2003). The as-grown material is composed of the $Bi_2Sr_2CuO_6$ (Bi-2201) phase as the main phase and the $(Sr,Ca)CuO_2$ oxide as the secondary one. After annealing, the Bi-2212 becomes the predominant phase but some amounts of the Bi-2201 and the $(Sr,Ca)CuO_2$ phases remain. These differences in the phase composition can affect the resistance of these materials to environmental degradation.

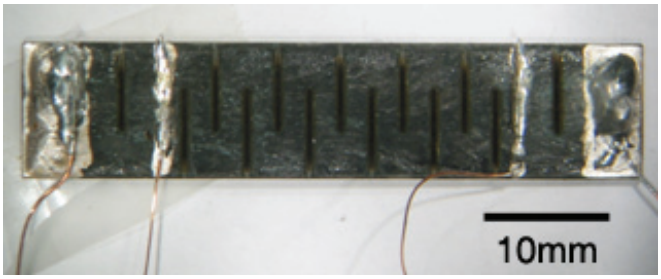

Fig. 16. Bi-2212 coating on a MgO substrate used for environmental degradation experiments with the sample immersed in water.

Initial tests were performed with the samples immersed in water. Fig. 16 shows an example of a Bi-2212 coating on a MgO substrate (Mora et al., 2004) where these initial tests were performed. The sample was machined with meander geometry in order to explore the possibility of using these materials in resistive fault current limiters (López-Gascón, 2005). DSP observations are presented in Fig. 17. A magnification of 0.61 was used, and the observation surface is 15 mm x 10 mm, that covers 5 machined lines. Fig. 17.a shows the image of the analysed surface. After 10 s, the 2D correlation map shows that some surface changes have started close to the machined lines (Fig. 17.b). This process evolves as can be observed in Fig. 17.c where the 2D correlation map after 60 s is presented. It is observed that in the regions close to the machined lines, the correlation values are lower while in the other regions, the surface has not degraded.

Immersing the samples in water is not the best procedure because surface degradation processes are too fast and in these ceramic samples some air bubbles appear on the sample surface. Thus, the next tests were performed placing the superconducting samples inside a small chamber with a relative humidity value of a 93% (Recuero et al., 2008). These experimental conditions were used to compare the resistance of as-grown and annealed samples to environmental degradation. DSP observations in textured Bi-2212 monoliths were compared with other complementary characterization techniques: diffuse reflectance infrared spectroscopy (DRIFT), X-ray diffractometry (XRD) and scanning electron microscopy (SEM). DSP observations showed that the correlation was lost faster in the as-grown sample indicating a faster surface degradation.

The $(Sr,Ca)CuO_2$ grains that are close to the surface decompose to an amorphous phase that is responsible of the swollen regions that appear in the superconductor surface (Fig. 18). This modification is responsible of the reduction in the correlation coefficient values. The amount of this phase is higher in the as-grown samples. For this reason, the observed reduction in the correlation coefficient value is 3.5 times faster in the as-grown samples than in the annealed ones. In consequence, the environmental degradation in the as-grown

samples is 3.5 times faster. One of the main advantages of the DSP measurements is that this conclusion can be obtained just 60 s after having started the experiments.

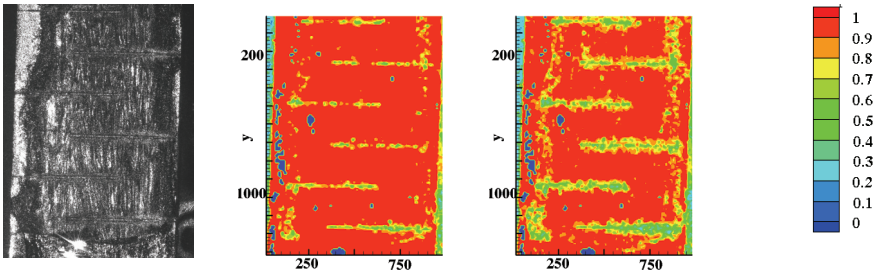

(a) (b) (c)

Fig. 17. (a) Image of the analysed surface. (b) 2D correlation map after 10 s. (c) 2D correlation map after 60 s.

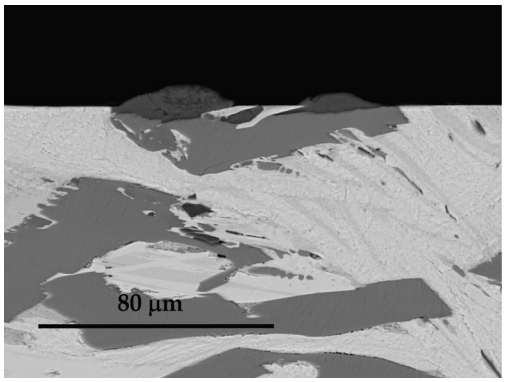

Fig. 18. SEM micrograph showing the decomposition of the (Sr,Ca)CuO_2 phase due to the reaction with moisture.

The second advantage of the DSP is that these 2D observations provide information about how the surface degradation evolves in different regions of the sample. In addition, DSP measurements allow determining how the degradation process changes with time. If the reference is taken at an instant t, the correlation maps visualize the changes that have taken place from this instant.

4.3 Influence of laser ablation machining process in the environmental degradation resistance of Bi-2212 monoliths

One of the problems associated with the ceramic nature of high temperature superconductors are the difficulties associated with machining without introducing mechanical defects in the sample. One of the alternatives is to use laser ablation techniques (López-Gascón, 2005). This technology allows obtaining samples with different geometries or to machine meander geometries in the sample (Angurel et al, 2006).

When this machining process is performed with a nanosecond pulsed laser, an amount of superconductor is melted during the ablation. Fig. 19.a shows that, in the surface of the machined regions there is a layer of melted material with a thickness of approximately 1 μm.

In consequence, the (Sr,Ca)CuO_2 phase does not reach the surface. If the environmental degradation is due to the chemical decomposition of this phase, laser ablation can modify the resistance of these materials to environmental degradation. Another factor related to the microstructure of these materials is that it is not uniform as the (Sr,Ca)CuO_2 phase is mainly concentrated close to the sample surface. In order to study these effects several 4 mm x 5 mm rectangles have been machined in 1 cm wide samples (Fig. 19.b). The depth of these machined regions increases from number 1 to 5: 60, 100, 220, 300 and 480 μm. Environmental degradation tests for both as-grown and annealed samples have been performed using the humidity chamber procedure.

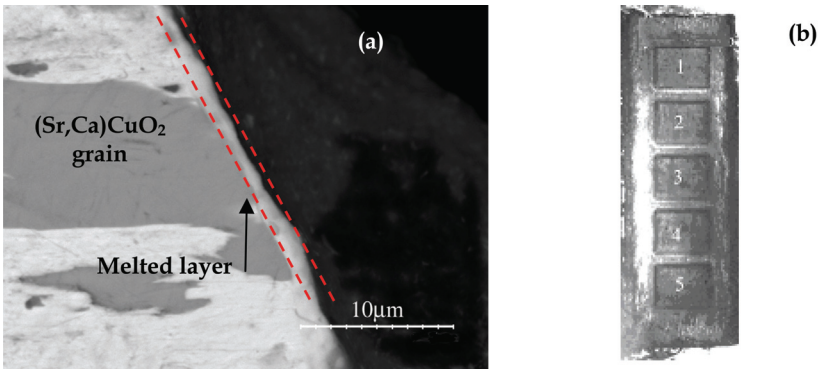

Fig. 19. (a) Detail of the surface of a machined region showing the external layer of melted material. (b) Photograph of a textured Bi-2212 sample showing the machined regions obtained with laser ablation.

Fig 20 shows the 2D correlation maps measured in the as-grown sample. It can be observed that the degradation process is slower in all the machined regions. The degradation rate increases slowly when the machined region depth increases. The behaviour observed in region 5 is similar to the non-machined regions. In consequence, the laser ablation process of as-grown Bi-2212 textured materials reduces the chemical interaction with water of the sample surface, at least in the initial instants.

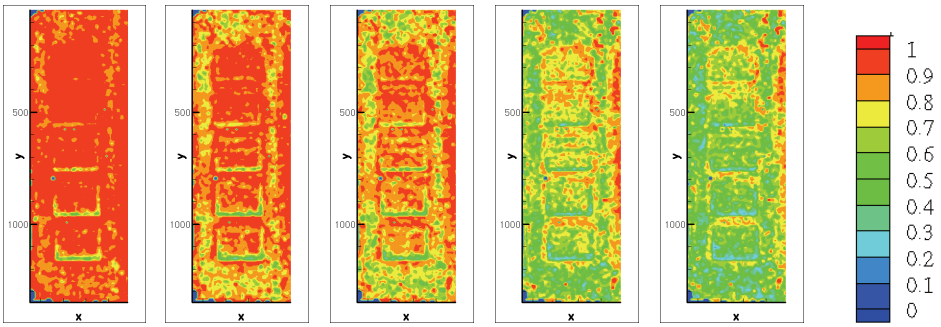

Fig. 20. 2D correlation maps of the as-gown sample with different machined regions at different instants. The reference corresponds to the surface state at t=0s.

This evolution has also been analysed by comparing the time dependence of the correlation coefficient value of a rectangle of 180 x 140 pixels in each region (Fig. 21). From the slope of this dependence it is possible to infer that the degradation rate is 2.6 times faster in the non-machined region than in region 1. But there is another interesting fact. For longer times degradation in the non-machined region seems to stabilize and it becomes faster in the machined ones. This can be confirmed looking to the time evolution of the correlation coefficient (Fig. 21.b) and the 2D correlation maps (Fig. 22) that have been obtained taking as reference the situation of the sample at t=1800 s.

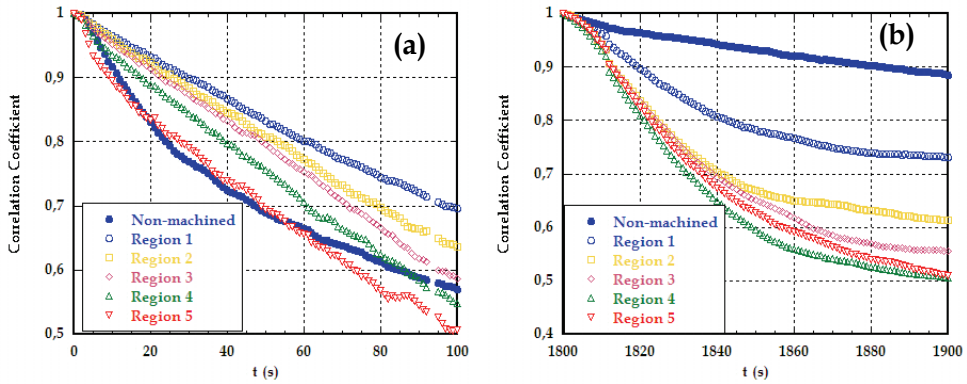

Fig. 21. Time evolution of the correlation coefficient in the different regions of the as-grown samples. The reference has been taken at (a) t=0s and at (b) t=1800s.

In the case of the annealed samples, the behaviour is slightly different. Degradation rate in the machined regions is faster (Fig. 23) than in the non-machined ones. Another difference is that the behaviour of all the machined regions is much more similar than in the as-grown samples.

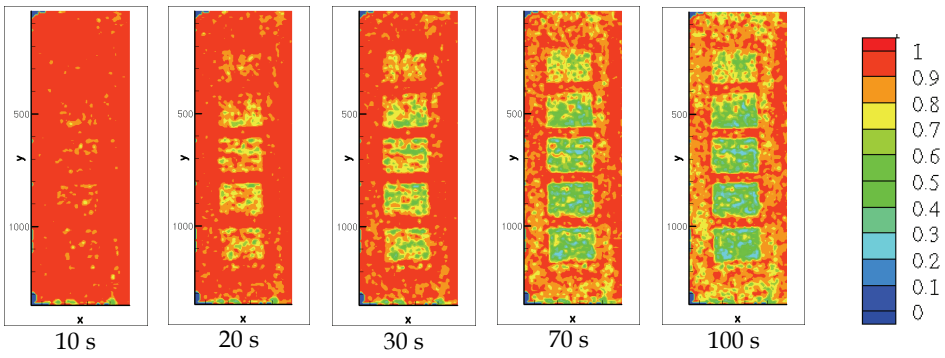

Fig. 22. 2D correlation maps of the as-gown sample with different machined regions at different instants. The reference corresponds to the sample surface at t=1800 s.

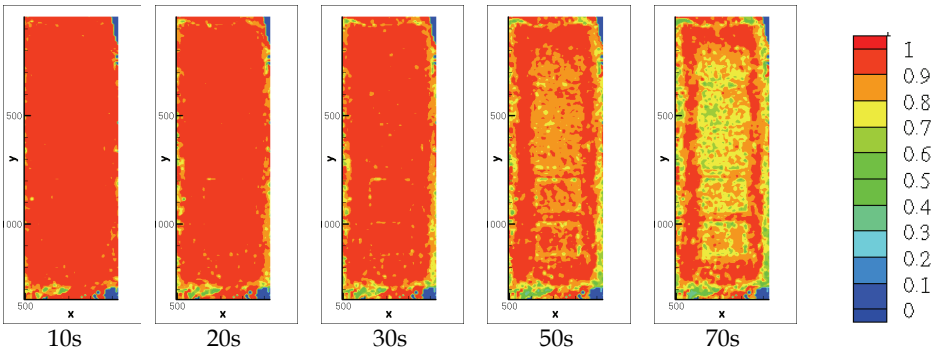

Fig. 23. 2D correlation maps of the annealed sample with different machined regions at different instants. The reference is the sample surface at t=0s.

5. Conclusions and future research

These results show that optical techniques are valuable tools to obtain information about the behaviour of superconducting materials, relevant to the design of different technological applications. In particular, problems with quench generation and environmental degradation have been studied.

DSPI can be used to visualize different heat generation processes that take place in superconducting materials depending on the cooling conditions. It can be used to detect where a hot spot will take place before damaging the sample. In consequence, it can help to find out which are the microstructural defects that are more important in heat generation and propagation. This has been applied in the analysis of bulk Bi-2212 monoliths and 2G HTS wires. In the case of bulk materials this information can be used to modify the processing parameters in order to eliminate these defects or to distribute them in the sample in order to homogenise the transition to the normal state. In the case of 2G HTS wires DSPI measurements visualize if the sample presents a homogeneous or an inhomogeneous transition to the normal state. This information has been confirmed with the direct measurement of the electric field and temperatures profiles. The main advantage is that DSPI does not require soldering voltage taps or thermocouples in the sample.

One of the objectives for the future research is to obtain quench parameters from the optical observations. This is not a simple task because the deformations that are observed also depend on the sample mechanical constraints. For this reason, in order to obtain quantitative information from these measurements, thermo-mechanical models are being developed in order to be able of determining the temperature profile from the mechanical deformation.

DSP has provided useful information about environmental degradation of bulk superconducting materials. The chemical reactions that take place modify the surface characteristics and, in consequence, reduce the correlation coefficient values. The main advantage of this technique in comparison with other experimental techniques is that it provides 2D local information in the very early stages of the degradation process. In addition, if the reference image is changed from the initial state to any other at a given time,

the evolution of the degradation processes from this instant can be determined. This allows evaluating how the degradation process rate evolves at any instant.
In the case of the Bi-2212 monoliths, it has been established that the surface degradation is associated with (Sr,Ca)CuO_2 chemical decomposition. DSP has shown that this process is faster in the as-grown samples than in the annealed ones. In addition, this optical technique has also been applied to quantify the change in the degradation rate when the samples are machined with laser ablation techniques.

6. Acknowledgments

Authors thank the Spanish Ministry of Science and Innovation (Projects MAT-2008-05983-C03-01 to -03) and the Gobierno de Aragón (Research groups T12, T61 and T76) for financial support of this research. Authors are also obliged to SuperPower, Inc and, in particular, to Dr. V. Selvamanickam and Dr. Y.-Y. Xie for their collaboration in applying these techniques in 2G HTS wires. Finally authors also thank Prof. G. de la Fuente and Dr. C. López-Gascón for their collaboration in applying laser ablation techniques in Bi-2212 monoliths.
Present address: Instituto Tecnológico de Óptica, Color e Imagen (AIDO), Spain

7. References

Andrés, N.; Arroyo, M. P.; Hinrichs, H. & Quintanilla, M. (1999). Digital speckle interferometry as a full-field fluid-velocity technique. *Opt. Lett.*, Vol. 24, No. 9, 575-577, ISSN: 0146-9592

Andrés, N.; Arroyo, M. P.; Zahn, H. & Hinrichs, H. (2001). Application of digital speckle pattern interferometry for fluid velocimetry in wind tunnel flows. *Exp. Fluids,* Vol. 30, No. 5, 562-567, ISSN: 0732-4864

Andrés, N.; Recuero, S.; Arroyo, M. P.; Bona, M. T.; Andrés, J. M. & Angurel, L. A. (2008). Fast visualization of corrosion processes using digital speckle photography. *Corrosion Science*, Vol. 50, No. 10, 2965-2971, ISSN: 0010-938X

Angurel, L. A.; Díez, J. C.; De la Fuente, G. F.; Gimeno, F.; Lera, F.; López-Gascón, C.; Martínez, E.; Mora, M.; Navarro, R.; Sotelo, A.; Andrés, N.; Recuero, S. & Arroyo, M. P. (2006). Laser technologies applied to the fabrication and characterization of bulk Bi-2212 superconducting materials for power applications. *Phys. stat. sol. (a)*, Vol. 203, No. 11, 2931-2937, ISSN: 0031-8965

Angurel, L. A.; Martínez, E.; Lera, F.; Recuero, S.; Andrés, N.; Arroyo, M. P.; Xie, Y. Y. & Selvamanickam, V. (2008). Quench detection in $YBa_2Cu_3O_{7-\delta}$ coated conductors using interferometric techniques. *J. Appl. Phys.,* Vol. 104, No. 9, 093916, ISSN: 0021-8979

Angurel, L. A.; Martínez, E.; Lera, F.; Recuero, S.; Andrés, N.; Arroyo, M. P.; Xie, Y. Y. & Selvamanickam, V. (2009). Analysis of Quench Initiation in YBCO Coated Conductors Using Optical Interferometric Techniques. *IEEE Trans. Appl. Supercond.*, Vol. 19, No. 3, 3479-3482, ISSN: 1051-8223

Archbold, E. & Ennos, A. E. (1972). Displacement measurement from double-exposure laser photographs, *Opt. Acta*, Vol. 19, No. 4, 253-271, ISSN:0030-3909

Argyropoulou, R.; Ochsenkuhn-Petropoulou, M.; Dounis, C.; Karaboulis, P.; Altzumailis, A. & Ochsenkuhn K. M. (2007). Comparison of the behaviour of the three

superconductors YBCO, Bi-2212 and MgB_2 in different environmental conditions. *J. Mat. Proc. Technol.*, Vol. 181, No. 1-3, 2-5, ISSN: 0924-0136

Burke, J.; Helmers, H.; Kunze, C. & Wilkens, V. (1998). Speckle intensity and phase gradients: influence on fringe quality in spatial phase shifting ESPI-systems. *Opt. Comm.*, Vol. 152, No. 1-3, 144-152, ISSN: 0030-4018

Creath, K. (1985). Phase-Shifting Speckle Interferometry. *App. Opt.*, Vol. 24, No. 18, 3053-3058, ISSN: 0003-6935

Fricke-Begemann, T.; Gulker, G.; Hinsch, K. D. & Wolff, K. (1999). Corrosion monitoring with speckle correlation. *App. Opt.*, Vol. 38, No. 28, 5948-5955, ISSN: 0003-6935

Fricke-Begemann, T. (2003). Three-dimensional deformation field measurement with digital speckle correlation. *App. Opt.*, Vol. 42, No. 34, 6783-6796, ISSN: 003-6935

Goodman, J. W. (1975). *Introduction to Fourier optics*, Roberts & Company Publishers, ISBN:0-07-024254-2

Goodman, J. W (1975). Static properties of laser speckle patterns, in: *Laser Speckle and Related Phenomena*, J. C. Dainty (Ed.), 9-74, Springer Verlag, ISBN: 0387074988, Berlin

Ishiyama, A.; Tsuchida, M.; Ueda, H. & Shiohara, Y. (2007). Assessment of cryogenic thermography system using commercial fluorescent paints on their applicability to visualization of normal-zone propagation in YBCO coated conductors, *IEEE Trans. Appl. Supercond.*, Vol. 17, No. 2, 3765-3768, ISSN: 1051-8223

Jones, R. & Wykes, C. (1989). *Holographic and Speckle Interferometry*, Cambridge University Press, ISBN: 0-521-34878-1

Lee, H.; Kim, H. M.; Jankowski, J. & Iwasa, Y. (2004). Detection of "hot spots" in HTS coils and test samples with acoustic emission signals. *IEEE Trans. Appl. Supercond.,* Vol. 14, No. 2, 1298-1301, ISSN: 1051-8223

Lera, F.; Angurel, L. A.; Rojo, J. A.; Mora, M.; Recuero, S.; Arroyo, M. P. & Andrés, N. (2005). Microstructure origin of hot spots in textured laser zone melting Bi-2212 monoliths. *Supercond. Sci. Technol.*, Vol. 18, No. 11, 1489-1495, ISSN: 0953-2048

Lobera, J.; Andrés, N. & Arroyo, M. P. (2004). From ESPI to Digital Image Plane Holography (DIPH): Requirements, possibilities and limitations for velocity measurements in a 3-D region, in: *Particle image velocimetry: Recent improvements*, Stanislas, M.; Westerweel, J. & Kompenhans, J. (Ed.), 363-372, Springer-Verlag, ISBN: 3-540-21423-2, Berlin

López-Gascón, C. (2005). *Procesado y mecanizado de cerámicas superconductoras de Bi-2212 con técnicas láser*. PhD Thesis, University of Zaragoza, Spain

Martínez, E.; Angurel, L. A.; Pelegrín, J.; Xie, Y.-Y. & Selvamanickam, V. (2010). Thermal stability analysis of YBCO-coated conductors subject to over-currents. *Supercond. Sci. Tecnol.*, Vol. 23, No. 2, 025011, ISSN: 0953-2048

Mora, M.; Díez, J. C.; López-Gascón, C. I.; Martínez, E. & De la Fuente, G. F. (2003). Laser textured Bi-2212 in planar geometries. *IEEE Trans. Appl. Supercond.*, Vol. 13, No. 2, 3188-3191, ISSN: 1051-8223

Mora, M.; Gimeno, F.; Angurel, L. A. & de la Fuente, G. F. (2004). Laser zone melted $Bi_2Sr_2CaCu_2O_{8+\delta}$ thick films on (100) MgO substrate. *Supercond. Sci. Technol.*, Vol. 17, No. 10, 1133-1138, ISSN: 0953-2048

Rastogi, P. K. (2001). *Digital Speckle-Pattern Interferometry and related techniques*. Willey, ISBN: 978-0-471-49052-4, Chichester, UK

Recuero, S.; Andrés, N.; Arroyo, M. P.; Lera, F. & Angurel, L. A. (2005). Superconductor ceramics behaviour analyses during service by speckle metrology, *Proceedings of the Society of Photo-Optical Instrumentation Engineers (SPIE)*, 5856, 775-785, ISBN: 0-8194-5856-2, Munich, June 2005, SPIE-International Society of Optical Engineering, Bellingham, USA.

Recuero, S.; Andrés, N.; Lobera, J.; Arroyo, M. P.; Angurel, L. A. & Lera, F. (2005). Application of DSPI to detect inhomogeneous heating on superconducting ceramics. *Meas. Sci. Technol.,* Vol. 16, No. 4, 1030-1036, ISSN: 0957-0233

Recuero, S.; Bona, M. T.; Andrés, N.; Andrés, J. M. & Angurel, L. A. (2008). Visualization of environmental degradation in ceramic superconductors using digital speckle photography. *Jour. Eur. Ceram.,* Vol. 28, No. 11, 2239-2246, ISSN: 0955-2219

Song, H. H.; Davidson, M. W. & Schwartz, J. (2009). Dynamic magneto-optical imaging of transport current redistribution and normal zone propagation in $YBa_2Cu_3O_{7-\delta}$ coated conductor. *Supercond. Sci. Technol.*, Vol. 22, No. 6, 062001, ISSN: 0953-2048

Takeda, M.; Ina, H. & Kobayashi, S. (1982). Fourier-transform method of fringe-pattern analysis for computer based topography and interferometry. *J. Opt Soc. Am.*, Vol. 72, No. 1, 156-160, ISSN: 0030-3941

Vest, C.M. (1979). *Holographic Interferometry*. John Willey and Sons, ISBN: 0471906832, New York.

Wang, X.; Trociewitz, U. P. & Schwartz, J. (2007). Near-adiabatic experiments on short $YBa_2Cu_3O_{7-\delta}$ coated conductors. *J. Appl. Phys.,* Vol. 101, No. 5, 053904, ISSN: 0021-8979

Yamaguchi, I.; Kobayashi, K. & Yaroslavsky, L. (2004). Measurement of surface roughness by speckle correlation. *Opt. Eng.*, Vol. 43, No. 11, 2753-2761, ISSN: 0091-3286

10

Nanoscale Pinning in the LRE-123 System - the Way to Applications up to Liquid Oxygen Temperature and High Magnetic Fields

Muralidhar Miryala[1], Milos Jirsa[2] and Masaru Tomita[1]
[1]*Railway Technical Research Institute (RTRI), Applied Superconductivity, Materials Technology Division, 2-8-38, Hikari-cho, Kokubuni-shi, Tokyo 185-8540*
[2]*Institute of Physics, ASCR, CZ-182 21 Praha 8*
[1]*Japan*
[2]*Czech Republic*

1. Introduction

The discovery of superconductivity in oxides (Bednorz, et al., 1986), especially in the system of $YBa_2Cu_3O_y$ "Y-123" (Wu et al., 1987), having a transition temperature well above boiling point of liquid nitrogen and capable of carrying critical current densities at a level necessary for practical use, moreover in rather high magnetic fields, placed cuprate composites into center of the present material physics and technology. Liquid nitrogen cooling has promised construction of cryogenic systems greatly simplified, more realistic and economical in operation. Note that not only the critical temperatures of the new superconductors have been much higher than those of the conventional materials. The upper critical field of the order of 100 T has been estimated and also measured, making from these materials ideal candidates for high field applications (Welp et al., 1989). On the other hand, it has also been found that high-T_c materials in a polycrystalline form carry only low critical current densities, due to grain boundary weak links and crystal anisotropy (Cava et al., 1987). Attempts to improve the critical current density of the Y-123 material by texturing substrates and identifying coupling mechanisms at interface started immediately world-wide (Jin et al., 1988; Babcock et al., 1990). U.S. Pat. No. 5,061,682, issued to Aksay et al., 1991 disclosed a process for preparing conductive and superconductive ceramics composed of Y_2BaCuO_5, $YBa_2Cu_3O_7$, and $YBa_2Cu_4O_8$. The most successful process at present is melt-texturing, which controls to a high degree lattice orientation of the crystalline material. In this way the superconducting phase ($YBa_2Cu_3O_x$) is formed by a peritectic reaction of Y_2BaCuO_5 (211) with a liquid phase. The growth process of the superconducting phase is accelerated by means of finely and homogeneously dispersed 211 phase in the liquid phase; at the same time, however, the 211 phase serves as a pinning medium dispersed in the superconducting phase. During the following slow cooling nucleation often occurs. This secondary nucleation forms parasitic grains that consume the material intended for the growth of superconducting grains. In this way high-angle grain boundaries are created that

reduce the current conducting efficiency of the polycrystalline material. The conventional procedure for fabricating a good quality 123-phase material was reported by the SRL group (Murakami et al., 1995). The material was produced by melting the raw materials for an oxide superconductor of REBaCuO, solidifying the melt, pulverizing the solidified material, and adding Pt or $PtBa_4Cu_2O_y$ to the powder, molding the mixture to a predetermined shape, and again heating the mixture to grow a superconducting phase. The process in which the 211 phase and the platinum compound were finely dispersed in the 123 crystal was patented as U.S Pat. No. 5,395,820 (Murakami et al., 1995).

By adding silver or silver oxide to the powder in this process, and preparing the precursor containing silver or a silver oxide finely dispersed therein (Vipulanandan & Salib, 1994) mechanical performance can be dramatically improved. Fabrication of single-grain Y-123 superconductors was reported in U.S. Pat. No. 6,046,139; Blohowiak et al., 2000. In the method, 1–25 wt % of 211 YBCO, 0.05–1.0 wt % Pt, and a balance of $YBa_2Cu_3O_{7-x}$ (123 YBCO material) were combined. Pt is believed to limit growth of non-superconducting 211-phase crystallites. The mixed precursor powder was pressed into the form of a compact disk or other forms. A seed crystal $NdBa_2Cu_3O_{7-x}$ or $SmBa_2Cu_3O_{7-x}$ was placed onto the top surface, parallel to it. The compact was heated to a maximum temperature around 1050° C and held at that temperature for a time sufficient to fuse the seed crystal to the compact surface. The temperature was then lowered at the rate of approximately 0.1–1.0° C per hour. As the materials cooled, growth of the 123 YBCO grain started at the seed crystal. After nucleation, the compound was cooled at the rate of about 1–10° C per hour to a temperature of approximately 950° C. The Y-123 grain growth spread from the nucleation site until the entire pellet transformed into a single 123 YBCO grain. Using a similar approach and controlling the processing conditions and cooling rate, one can produce good-quality large single-grain YBCO pellets. In these processes the initial constitution of the starting composition resides on a "123-211 tie line" of a ternary phase diagram while keeping a sufficient but not excessive mass balance to yield a superconductive phase (123 phase) and to cause micro-dispersion of the 211 phase (in cases of Y, Sm, etc.) or the 422 phase (in cases of Nd, La, etc.), functioning as magnetic flux pinning centers in the superconductive phase. It increases critical current density, J_c, and at the same time keeps mass balance to minimize a residue of unreacted Cu, Ba, etc. As a result, such melt-grown Y-123 samples trap magnetic field much higher than that supplied by best nowadays known hard magnetics (Tomita & Murakami, 2003). The enormous effort in research and development has led to growing large single crystal grains of the 123 phase with spread the fine RE-211 phase in the matrix and significantly improved critical current density for super-magnet applications. On the other hand, it was found that the high J_c due to fine RE-211 phase appeared at low magnetic fields and decreased as the field increased (Salama et al., 1994; Cardwell et al., 1998).

In parallel to the YBCO system, the LRE-123 analogues (LRE=Nd, Sm, Eu, Gd) have been extensively studied. In these superconductors the rare earth elements partially substitute for Ba and vice versa (Yoo et al., 1994). Without control, an excess of such defects can deteriorate superconducting properties of such a compound. E.g. the early $NdBa_2Cu_3O_y$ melt-textured blocks prepared in air exhibited a lower T_c than Y-123 bulks. It was found, however, that melt growth proceeded in a reduced partial pressure of oxygen reduced the mutual substitution of LRE and Ba ions and such materials were found to exhibit T_c even higher than that of Y-123 (Murakami et al., 1996). Moreover, the compositional fluctuation

on nm scale in such LRE-123 materials had a similar positive effect on the secondary peak of $J_c(B)$ as oxygen vacancies in YBCO (Egi et al., 1995; Ting et al., 1997). This fluctuation originated in solid solution of LRE atoms with Ba "LRE-123ss" (Osabe et al., 2000). In order to regulate the complex melt growth process in LRE-123 compounds, leading in general also to T_c reduction and superconducting transition broadening, a melt growth in a reduced oxygen atmosphere has been developed and optimized. In this process, the melt texturing process was decoupled from oxygenation, which enabled an independent control of both steps. The former could be optimized with respect to the LRE-123ss cluster concentration and the associated secondary peak (fishtail effect) enhancement (Pradhan et al., 2001), the latter with respect to the highest T_c. The oxygen-controlled-melt-grown (OCMG) LRE-123 materials reach typically 94-96 K with superconducting transition width below 1 K and exhibit a well developed secondary peak (Yoo et al., 1994). Materials with a slight excess of LRE or Ba can be produced but also materials with macroscopically stoichiometric composition but with composition fluctuation on a nanometer scale, in all the cases with the same positive effect on the electromagnetic performance.

The next breakthrough came with ternary $(LRE^1,LRE^2,LRE^3)Ba_2Cu_3O_y$. Combination of three light rare earth elements in the elementary cell provides an exceptional technological freedom that enables a fine variation in the inter-atomic exchange within the elementary cell and, consequently, a control of a variety of physical characteristics of the final product (Muralidhar et al., 1998). The OCMG processed $(Nd,Eu,Gd)Ba_2Cu_3O_y$ "NEG-123" system proved that mixture of three different elements is possible, without any deterioration of the electromagnetic performance (Muralidhar et al., 2000 patent). Moreover, a control of the Nd: Eu: Gd ratio in the NEG-123 matrix enabled tailoring the pinning performance according to the requirements of the specific use (Muralidhar & Murakami, 2000). One can produce materials with a high narrow secondary peak of $J_c(B)$ at moderate fields or with a rather broad moderate peak with maximum at fields as high as 4 T (77 K) (Muralidhar et al., 2001). In a certain range of the Nd:Eu:Gd ratio, a nano-scale variation in the NEG-123 matrix composition appeared, correlated with the ordinary twin boundary structure. It enhanced vortex pinning in exceptionally high fields, around 10 T at 77 K and lead to shifting the irreversibility field at 77 K up to 15 T (Muralidhar et al., 2002a; Muralidhar et al., 2003a). As in YBCO, also here externally added secondary phase particles enhance critical current density at low magnetic fields (Diko et al., 2000). Gd_2BaCuO_5 "Gd-211" proved to form the smallest particles of all other LRE secondary phases and became a standard addition in the LRE composites. The efficiency of the secondary phase precipitates is inversely proportional to their size. With the aim to further improve the low-field pinning performance, we reduced the initial size of the secondary phase particles. (Muralidhar et al., 2002b; Muralidhar et al., 2003b). The refinement of Gd-211 particles from the commercial size of about 3 μm to several tens of nm was done by ball-milling with Y_2O_3 – ZrO_2 balls. With the help of these ball-milled nanoparticles a new type of nano-scale Zr-rich NEG-Ba-Cu-O precipitates appeared in the final product, accompanied by an exceptional pinning enhancement in all high temperatures, up to vicinity of T_c. As a result, this material showed very high critical current density at 90.2 K, the boiling temperature of liquid oxygen (Muralidhar et al., 2003c). With this material we could levitate a permanent magnet at 90.2 K. As a result, a remarkable flux trapping, by order of magnitude higher than the best classical hard magnets, was achieved. These new materials can be utilized as a new class of high temperature superconducting super-magnets for a wide range of commercial and industrial applications (Jirsa & Muralidhar, 2004; Muralidhar et al., 2004a).

The present review focuses on the latest development in the field of mixed ternary LRE-123 systems. We report the results of microstructure and magnetization analyses of ternary LRE-123 compounds. Flux pinning and size effect of the initially added nanometer-sized Gd-211 and Zr-, Ti-, Mo-, and Nb-based particles is reviewed and discussed, especially from the viewpoint of applications of superconducting permanent magnets usable up to vicinity of T_c (liquid oxygen refrigeration).

2. Flux pinning in ternary $LREBa_2Cu_3O_y$ materials

Critical currents in superconductors usually rapidly decrease with increasing magnetic field. This feature, expressed e.g. by the Kim's empirical formula $J_c(B)=A/(B+B_0)$, is one of the main obstacles for sharing superconducting applications. In bulk high-T_c superconductors the fishtail effect represents some sort of exception from this rule, valid in intermediate fields. However, above the fishtail peak position, the $J_c(B)$ decay is even faster than that predicted by Kim. One can thus generalize and state that in high magnetic fields critical currents in high-T_c superconductors vary rapidly decay with increasing field. There are several factors contributing to this situation: (i) high-T_c superconductors are strong type II superconductors. The Ginsburg-Landau factor $\kappa=\lambda/\xi$, where ξ is the coherence length and λ is the magnetic penetration depth, is very high, in the range of 100. Vortex core diameter, being in HTSCs in the range of a few nm, is very small. The defects interacting with such tiny vortex cores have to be of an equal or even smaller size. The corresponding pinning and activation energies are then extremely low; (ii) the high critical temperatures encountered in these materials enable operation at rather high temperatures at which thermal activation is very high. Together with the low mean activation energy it leads to a fast vortex release from the pinning sites and so called giant magnetic relaxation. This effect is manifested by the existence of an irreversibility line $B_{irr}(T)$ above which the superconductor can no more hold a reasonable internal magnetic field gradient and carry critical current associated with this gradient. In contrast to the classical metallic type-II superconductors, in HTSCs $B_{irr}<<B_{c2;}$ (iii) high-T_c superconductors are layered structures composed of superconducting and non-superconducting planes. Therefore, the materials are highly anisotropic and the flux lines are more or less stacks of freely joined pancake vortices. Such objects are very flexible and elastic, which complicates modeling of vortex-defect interaction. The activation energies, enabling a vortex release from a defect, are here very low, especially, if the pancakes correlation becomes rather weak or if the vortex matter gets liquid of individual pancakes or their short segments.

For more than 20 years it has been a major practical objective to increase efficiency of pinning centers in high-T_c superconductors by a careful control of microstructure. An important aspect was to bring the pinning defects size up to nanoscale level, close to the material's coherence length (4.5 nm in YBCO at 77 K and similar in all LRE-123 compounds). Recently, this goal was realized in the ternary NEG-123 system produced by means of the OCMG process (Muralidhar et al., 2002c; Awaji et al., 2004). A further tuning of the nanoscale secondary phase particles with Zr, Mo, Ti, Nb additives enhanced flux pinning of these materials more than 3 times compared to a single-LRE 123 materials (Muralidhar et al., 2008a; Muralidhar et al., 2008b; Muralidhar et al., 2009). These results are systematically described below in respect of microstructure and flux pinning performance.

3. Second-phase inclusions and the associated flux pinning in NEG-123

In the melt growth process the RE-123 domain growth advances with a peritectic recombination of the RE-211 particles and the liquid phase (Ba- and Cu-rich). The rare earth ions needed for the 123 phase growth are supplied from RE-211 particles dispersed in the liquid. Moreover, as an optimum, 20-40 mol% of an additional secondary phase is usually added to the 123 powders before melt processing. These extra particles are partly utilized in the liquid phase for growth of the 123 matrix, partly are trapped in the RE-123 matrix (see Fig.1).
According to some models the interface between the RE-123/RE-211 is a good pinning medium.

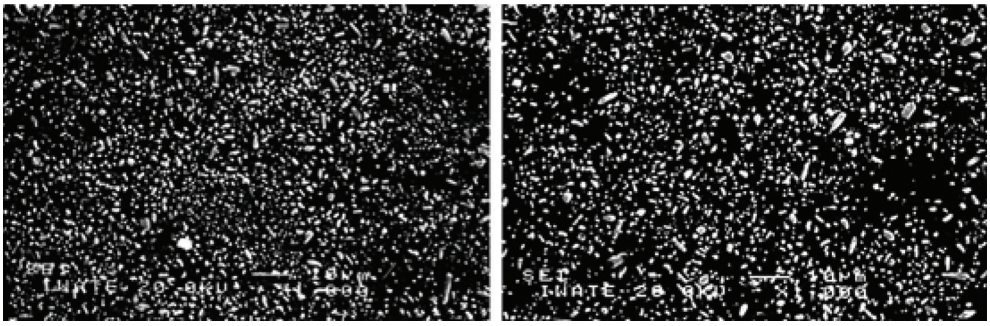

Fig. 1. Scanning electron micrographs of the NEG-123 + 30 mol% (left figure) & 40 mol% (right figure) Gd-211 composite prepared under 1% partial pressure of O_2. Note the uniform dispersion of fine 211 inclusions in the NEG-123 matrix.

In such models the critical current density increases with the V_{211}/d_{211} ratio, where V_{211} is the RE-211 volume fraction and d_{211} is the average size of the RE-211 particles (Murakami 1991), Sandiumenge et al., 1997). According to another model, this dependence is $V_{211}/\sqrt{d_{211}}$. (Zablotskii 2002). In both cases, the particle size decrease leads to a J_c enhancement.
In the mixed LRE-123 systems one can control the size, homogeneity, and dispersion of the Gd-211 particles (see Fig. 2). As the formation temperature of Gd-123 is lowest among the four LRE-123, the small Gd-211 particles cannot be consumed for the growth of Gd-123 and thus have a chance to survive (see Fig. 2). As a result, the critical current density of the samples with Gd-211 shows a remarkable J_c-B performance as compared to the "classical" melt-processed Y-123 or LRE-123 (LRE: Nd, Sm, Eu, Gd) systems without additional secondary phase. The OCMG-processed Nd-123 presents a well-developed peak effect. However, an extremely good pinning performance can be seen in the melt-processed (Nd,Eu,Gd)-123 "NEG-123" with 40 mol% NEG-211 or 30 mol% Gd-211 (see Fig. 3). The microstructure observations along with a compositional analysis showed that the extremely fine NEG-211 particles contain only Gd on the rare earth site. These particles therefore represent the effective flux pinning centers. The samples exhibit a pronounced secondary peak effect in the magnetization loops. A further improvement of the NEG-123 flux pinning was possible by an intentional size reduction of the initial Gd-211 particles to nanometer scale.

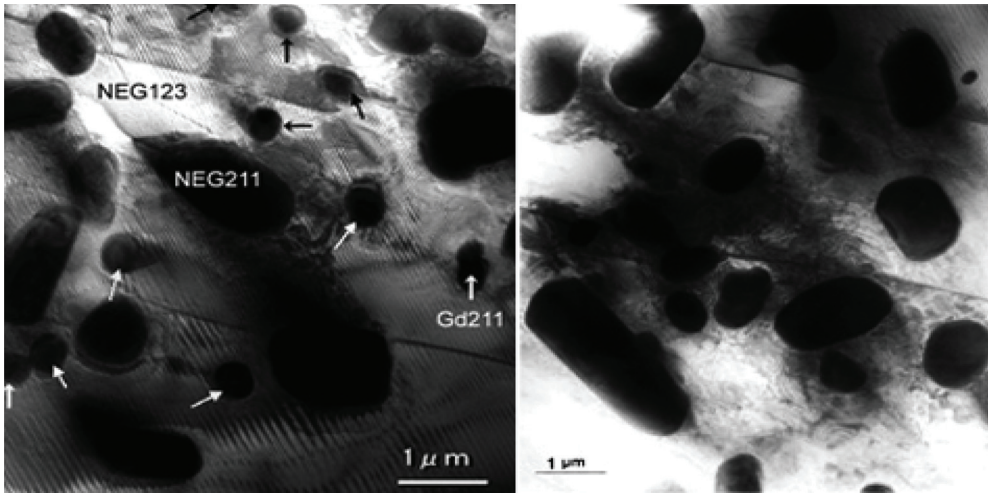

Fig. 2. Transmission electron micrograph of NEG123 with 30 mol% NEG-211 and 0.5 mol% Pt. Note the fine 211 inclusions dispersed in the matrix, which mainly comprise Gd in the rare earth site.

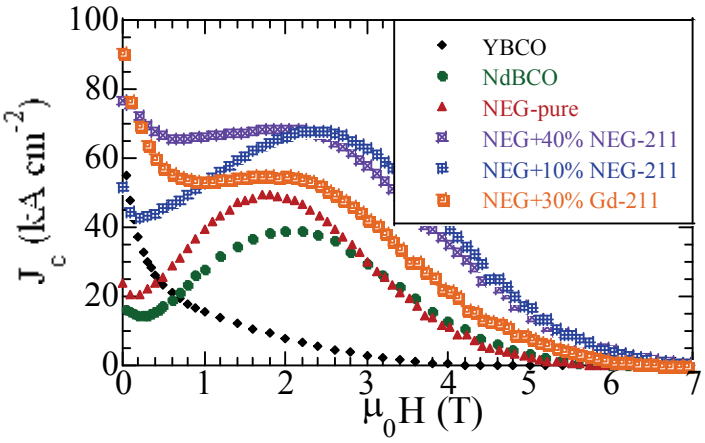

Fig. 3. Comparison of the field dependences of critical current density (T = 77 K, H_a parallel to the c axis) for melt-processed YBCO, OCMG-processed Nd-123, (Nd,Eu,Gd)-123 with 0 mol%, 10 mol%, and 40 mol% additions of NEG-211, and 30 mol% addition of Gd-211.

4. Nanometer-sized second-phase inclusions in NEG-123

Further improvement in flux pinning was obtained in NEG-123 system with a gradually reduced starting size of the Gd_2BaCuO_5 particles. The Gd- 211 powder was milled using Y_2O_3 – ZrO_3 balls in acetone, for 0.3, 2, and 4 h. The size was estimated by Brunauer-Emmerit-Teller (BET) specific area measurements (Brunauer et al., 1938). 30 and 40 mol% of the ball-milled Gd-211 were added to the sintered NEG-123. For coarsening suppression of the Gd-

211 particles during melt processing, 0.5 mol% Pt and 1 mol% CeO_2 were added. The pellets were grown by OCMG process in Ar with 1% O_2. The starting average particle size was 200 nm, 100 nm, and 70 nm, in dependence of ball-milling time 0.3 h, 2 h, and 4 h, respectively. The $J_c(H)$ dependencies of both types of NEG-123 samples with 30 and 40 mol% of differently sized Gd-211 particles are shown in Fig. 4. For comparison also a sample with commercial Gd-211 powders "CP" (< 3 μm) was measured. All measurements were performed at 77.3 K and $H//c$-axis. A clear increase of remnant J_c with decreasing size of the particles is visible. Remarkable is the record value of the remnant J_c, 140 kA/cm², reached in the sample with 30 mol% of Gd-211, with the average starting particle size of 70 nm. The same particle size dependence was observed in the composite with 40 mol% Gd-211 (squares in the figure), where the remnant J_c value for the average starting particle size of 70 nm reached even 192 kA/cm² and 110 kA/cm² at remnant state and 3 Tesla, respectively. This result is by more than 60% better than the previous record values of NEG-123 and other RE-123 materials. Simultaneously with the enhancement of the low-field pinning also the super-current density at intermediate fields significantly increased in both materials with decreasing secondary phase particle size. This might be an indication of an overlapping of the "large" particle pinning mechanism with the individual vortex pinning regime on point-like defects. However, the 70 nm particles seem to be rather large to significantly contribute to single-vortex pinning regime. Microstructure and chemical analyses enlightened the problem. DFM test of the sample with 30 mol% Gd-211 (starting size 70 nm) brought an evidence of the final particle size dispersion between 20 and 50 nm. Such small secondary phase particles have not been observed before in any RE-123 material. Figure 5 shows the TEM micrographs of this sample. Two types of nanoparticles can be seen: large irregular inclusions of about 300 to 500 nm in size and round particles of 20-50 nm in diameter. The quantitative analysis by TEM-EDX clarified that the former ones were Gd-211 and Gd-rich NEG-211 particles. Both types were evidently created or at least strongly modified during the melting process. The small 211 inclusions had a clear link to a long-term ball-milling.

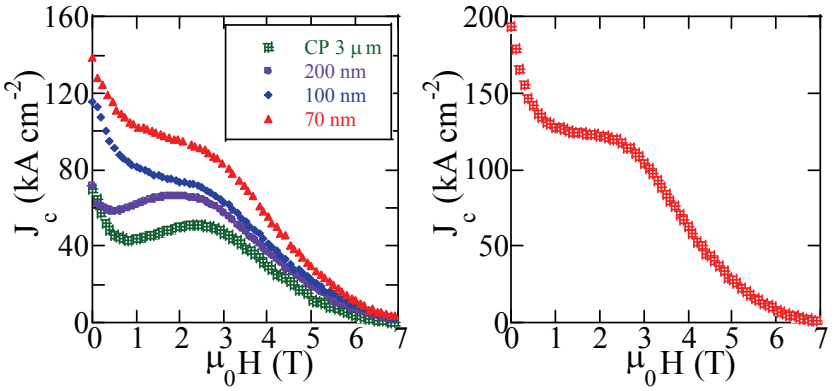

Fig. 4. Field dependence of super-current density for (Nd,Eu,Gd)$Ba_2Cu_3O_y$ samples with 30 mol% and 40 mol% Gd-211 (squares) refined by ball-milling for 0.3, 2, and 4 h (200 nm, 100 nm, and 70 nm). "CP" represents the commercial Gd-211 powders (≈3μm). All the samples were measured at T = 77 K with $H||c$-axis. The current density increased in the whole field range with decreasing particle size. Record critical current densities of 192 and 110 kA/cm² were achieved at 0 and 3 Tesla, respectively.

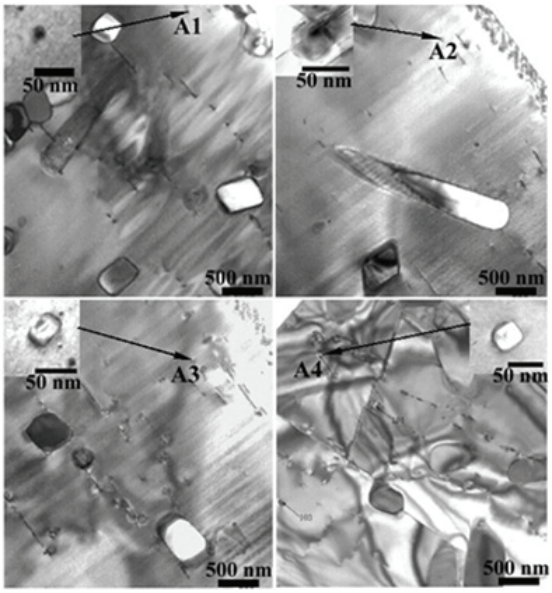

Fig. 5. Transmission electron micrographs of (Nd,Eu,Gd)$Ba_2Cu_3O_y$ samples with 30 mol% Gd-211 (average particle size was 70 nm); Insets show the new Zr-rich pinning medium in a higher magnification.

These defects, denoted as A1 - A4, are marked in figure 5 by arrows. Chemical analysis of nanoparticles with different sizes and shapes was made by energy dispersive spectroscopy (EDS) in scanning transmission electron microscopy (STEM) mode. Each analyzed spot had diameter of 2-3 nm. More than 65 nanoparticles were analyzed. We found that particles of size below 50 nm contained a significant amount of Zr. The four nanoparticles (A1 - A4) possessed different elemental ratios, always with a significant amount of Zr. A similar feature was observed in different parts of the sample. As no Zr was intentionally introduced into the system, we learned that the Gd-211 powder was contaminated with Zr from the balls used for milling. To estimate the Zr content in the Gd-211 particles, we made very precise quantitative analysis by inductively coupled plasma spectroscopy (ICP model: SPS-1700HVR). An average content of Zr was found to be 0.23 wt% for 4 hours ball-milled Gd-211 powders. Chemical composition of the particles represents a new, Zr-rich compound close to Gd-211, with yet not fully clear chemical structure.

The average size 20 – 70 nm sets these pins between point-like and "large" particles. This implies a potential of these defects to enhance material pinning in both low and intermediate fields. In comparison with another method capable of producing comparably sized artificial defects, namely fast neutron irradiation (Umezawa et al., 1997), the present technology is quite simple and can be easily adapted for mass production. Therefore, the new type of pins represents a unique economically feasible way how to enhance pinning in low and intermediate fields. This is particularly important for the applications using liquid nitrogen cooling. Note that J_c at 77 K and 3 Tesla is by about one order of magnitude higher than in high quality Nd-123 samples.

Another important consequence of the effective pinning by the new type of defects is the shift of the operating temperature from liquid nitrogen (77.2 K) to liquid oxygen (90.3 K).

For the first time the super-current density at 90 K was high enough to successfully levitate permanent magnet under liquid oxygen cooling (Muralidhar et al., 2003c).

5. Trapped magnetic field in RE-123 bulk superconductors

A strong electromagnetic suspension force can be generated by interaction of the melt-processed ternary RE-123 bulk superconductor with the stray magnetic field of a strong permanent magnet. This effect is applicable e.g. to construction of a practically lossless magnetic bearing, a contact-less liquid pump or a superconducting flywheel. The latter system has a wide range of applications, like position stabilizer, electric power storage, a high capacity, high current "fast" electric "battery", unit absorbing and compensating voltage fluctuations at solar-cell or wind power plants etc.
When the superconducting pellet is magnetized to a high magnetic field, part of this field is trapped in the pellet and we get a superconducting permanent magnet or, shortly, super-magnet. Such a name is fully justified as high-*T*c superconductors can trap magnetic field by order of magnitude higher than the best hard ferromagnets nowadays known. The major problem to solve is that the material is a ceramic, though in the state of pseudo single crystal. It is difficult in practice to prevent generation of micro-cracks and micro-pores during the melt processing. The micro-cracks are formed especially during the oxygenation process when a transformation from tetragonal to orthorhombic phase takes place, accompanied by significant atom displacements and stresses. As a result, the c-axis shrinks and b-axis is prolonged with respect to the a-axis. As the main atom displacement takes place within the a-b plane, most cracks lie just in the plane. Some, however, are also transversal to the current flow and hinder its flow. In any case, the mechanical properties are rather poor. To improve the mechanical performance of the materials, (i) addition of 20-30 wt% silver can help, when silver atoms prevent cracks proliferation, as well as (ii) reinforcement of the sample with metal ring, (iii) resin impregnation in vacuum when resin fills the pores and cracks, or (iv) resin impregnation with wrapping the material in carbon fiber. All these procedures greatly improve mechanical performance of the material. As a result, a trapped field of 14.35 T was recorded at 22.5 K (Fuchs et al., 2009). However, the samples are cracked also during the experiment, from a strong mechanical impact, thermal impact due to sudden temperature variation, a large electromagnetic force. The stress is then concentrated just in the aforesaid micro-cracks, which become a starting point of a progressive cracking of the whole sample. To overcome this problem, Tomita et al. 2003 impregnated the melt processed YBCO sample with Bi-Pb-Sn-Cd alloy along with the epoxy resin impregnation. The alloy has a high thermal conductivity at low temperatures (at 29 K) and its thermal expansion coefficient is close to the YBCO disk. To improve the thermal conductivity of the interior region of the disk, 1 mm in diameter bores were mechanically drilled in the center of the sample and filled with 0.9 mm diameter Al wires fixed by the Bi-Pb-Sn-Cd alloy. As a result, the trapped field of 9.5 T at 46 K, and 1.2 T for 78K was recoded. Until now valid record of 17.24 T was achieved at 29K, that all between two 2.65 cm in diameter discs, all without fracturing. These results opened the way to a new class of compact super magnets for various industrial applications. Note that the above experiment was done with a specially treated YBCO bulk. In the case of NEG-123 the pinning effect is considerably higher than in YBCO, both due to the LRE/Ba substitution and the capability of these materials to incorporate a rich network of various types of nanoparticles. According to resent reports, these bulk superconductors can trap magnetic field of about 1T at liquid nitrogen temperature (77 K) and several tens of Tesla even at liquid oxygen temperature

(90.2 K). The present refrigeration technique enables, however, operation at considerably lower temperatures, where the critical current and thus also the trapped field rapidly grow. Thus, in comparison to YBCO, the LRE super-magnets can trap comparable fields at much higher temperatures or at the same temperatures in pellets of much smaller diameter (the trapped field magnitude is also proportional to the pellet diameter). This opens a new class of applications, especially for space programs and medicine.

6. Flux pinning in NEG-123 due to TiO_2 nanoparticles

One should note that in these early NEG-123 materials with high pinning at high temperatures (in the range above 80 K) only the remnant critical current density was high but rather rapidly decayed with increasing magnetic field. It was desirable to extend the range of high critical current densities at high temperatures to higher magnetic fields. As the nanoparticles contaminated by Zr during ball milling appeared so effective, we also tried to introduce and to study the pinning effect of ZrO_2 (Muralidhar et al., 2004c) and other oxides of refractory metals from vicinity of Zr in the periodic table of elements. First, we tried to dope the material with TiO_2 nanoparticles. In accord with our expectations, nanometer-sized defects appeared in the final product of this kind, correlated with a significantly improved flux pining at low and medium magnetic fields. This effect was particularly significant at high temperatures. To characterize the superconducting transition of the NEG-123 samples with various contents of Ti, the temperature dependence of the dc magnetic moment was first measured (Fig. 6). The zero-field-cooled (ZFC) and field-cooled (FC) curves were measured in magnetic field of 1 mT. All studied compositions exhibited a sharp superconducting transition (around 1 K wide) with the onset T_c around 93 K. The onset T_c slightly decreased from 93.2 K to 92 K with increasing Ti content. This showed that the small quantities of Ti studied in this work only slightly affected the superconducting performance of the NEG-123 material. Several previous reports have dealt with the TiO_2 doping. It was found that the increasing content of TiO_2 from 1% to 5% in a flame-quench-melt-grown (FQMG) $YBa_2Cu_3O_{7-\delta}$ bulk caused a decrease of superconducting transition temperature, while in the range from 7 to 10 wt.% T_c slightly recovered again (Yanmaz et al., 2002). In the $YBa_2(Cu_{3-x}Ti_x)O_y$ specimens, T_c of about 80 K was observed for $0 \leq x \leq 0.9$ (Okura et al., 1988).

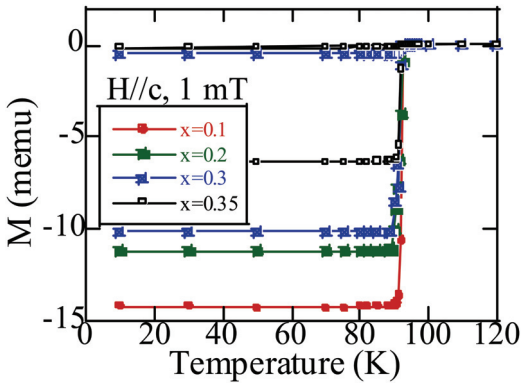

Fig. 6. Temperature dependence of the normalized DC susceptibility of the OCMG-processed NEG-123 + 35 mol% Gd-211 (70 nm) with varying content of TiO_2.

Venkataramani et al., 1988 found T_c significantly dropping with increasing x in $Y_{1-x}Ti_xBa_2Cu_3O_{7-\delta}$ (x=0.05 and 0.1), which they attributed to a site preference (Venkataramani et al., 1988). In the $DyBa_2(Cu_{1-x}Ti_x)_3O_{7-z}$ system the observed decrease of T_c with increasing Ti doping was attributed to the hole-filling mechanism (Mavani et al., 2004). In all above-mentioned cases the Ti doping was high compared to the present work. It is clear that the optimum content of Ti cannot depress T_c of the investigated RE-123 system.

In the present case small amounts of nanometer-sized TiO_2 (≤0.35 mol%) were added to the NEG-123 samples in order to improve the current-carrying capacity of the material, in particular around liquid nitrogen boiling point or at higher temperatures. Figure 7 presents the critical current densities at 77 K of the 0-0.35 mol% TiO_2-added NEG-123 composites magnetized parallel to the *c*-axis. It is evident that the self -field critical current increased for 0.1 mol% of TiO_2 as compared to the pure NEG-123 and reached at 77 K 320 kA/cm². The high-field critical current density, J_c, and the irreversibility field, H_{irr}, decreased with further increase of TiO_2 content (≥0.2 mol% of TiO_2). These results proved that the optimum amount of TiO_2 in the NEG-123 system was around 0.1 mol%.

Ti is a 3d transition metal that can be accommodated at Cu sites in the RE-123 system due to the similar ionic radius with Cu. The drop of T_c in the Dy-123 system doped by Ti was in one previous study interpreted so that Ti ions maintain their +4 normal valence state as in the starting TiO_2 (Mavani et al., 2004). Vankataramani et al., 1988 found only a slight effect of Ti-substitution. They argued that the T_c dependence on Ti substitution is slower than that arising from oxygen vacancies in the Cu(1)-O chains. The behavior of the system up to 10% of Ti did not change much and correlated much more with the concentration of the second phase when Ti was substituted for yttrium. It could mean that Ti actually did not occupy the Y-sites but the Cu- ones. On the other hand, a low Zn substitution for Cu in the Y-123 system (Krabbes et al., 2000) or Fe, Co, or Ni substitutions for Cu in Bi-2212 single crystals were found to enhance J_c (Shigemori et al., 2004). These results showed that a direct doping in superconducting CuO_2 planes is an effective method for introducing point-like pinning sites in cuprate

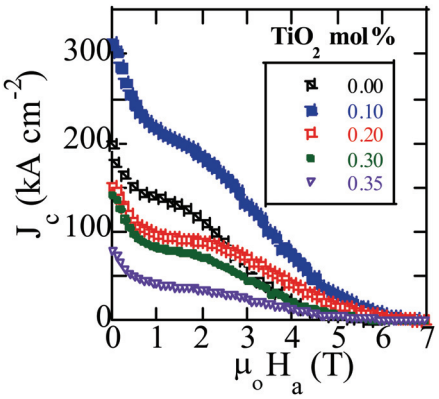

Fig. 7. Field dependence of the super-current density in NEG-123 samples with the same, 35 mol% content of Gd-211 (70 nm) but various contents of TiO_2. All the samples were measured at T = 77 K with $H \| c$-axis. The current density increased in the whole field range up to the 0.1 mol% content of TiO_2 and decreased thereafter. Note the relatively high critical current density of 320 kA/cm² at self-field and 77 K, achieved with 0.1 mol% TiO_2.

superconductors provided the doping levels stay low. Such a dilute doping technique is particularly effective when the mean distance between the impurity ions is much longer than the coherence length in the *a-b* plane (Shimoyama et al., 2005). The present results indicate that an optimum "dilute" content of Ti enhances flux pinning of the NEG-123 material.

To find more about the pinning effect of Ti nanoparticles in NEG-123, we examined the microstructure of the samples in detail using the high resolution transmission electron microscopy (HRTEM). Figure 8 shows the typical TEM images of 0.1 mol% of TiO_2-added NEG-123 viewed from the <001> direction. In the images, two types of defects could be distinguished: large irregular inclusions of about 200 to 500 nm in size, and round particles of 20-50 nm size. The energy-dispersive x-ray (EDX) spectra of the larger particles identified them as a Gd-rich NEG-211 secondary phase, spontaneously created by peritectic decomposition of LRE-123 in the partial-melted region during the melt-texturing process. On the other hand, the small round particles of 20-50 nm size contained a significant amount of Ti, similar to the samples with a Zr addition. The critical current densities of the samples with various contents of TiO_2 are presented in Figure 9 for temperatures between 65 K and 90 K. Magnetic field was applied parallel to the *c*-axis and J_c was calculated from *M-H* curves using the extended Bean model. In all samples, the remnant critical current density dramatically increased in the whole range of investigated temperatures. At 65 K the critical current density of the sample with 0.1 mol% TiO_2 reached 550 kA/cm² at 0 and 4.5 Tesla and exceeded 450 kA/cm² over the whole range up to 5 Tesla. In the case of 0.2 mol% TiO_2 doping the super-current density at 65 K reached 275 kA/cm² at 0 and 4.5 Tesla and exceeded 250 kA/cm² over the whole range up to 5 Tesla, while the sample with 0.35 mol% of TiO_2 showed J_c of only 150 kA/cm² at 0 Tesla and 100 kA/cm² over the whole range up to 5 Tesla. At 90.2 K the remnant super-current density of the sample with 0.1 mol% TiO_2 reached 50 kA/cm² and the value decreased with further increasing the TiO_2 (≥0.2 mol%) content. All these data indicate that the optimum pinning was reached for 0.1 mol% of TiO_2. The J_c values presented here are significantly higher than those of a pure NEG-123 (without TiO_2) (Fig. 8). TiO_2 addition makes the NEG-123 composite a further member of the group

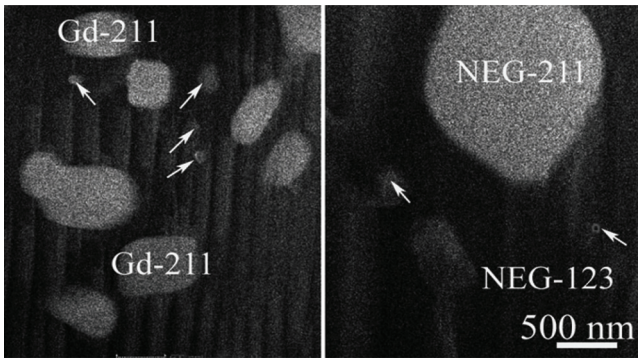

Fig. 8. Transmission electron micrograph of the NEG-123 + 35 mol% Gd-211 (70 nm) with 0.1 mol% TiO_2. Besides the rather large precipitate of NEG-211 seen in the right figure, two types of nanoparticles appear in the product, one within the size range 200-500 nm and another one of 20-50 nm size. The 200-500 nm particles are Gd-rich NEG-211 and Gd-211 secondary phase. The smallest particles are (LRE,Ti)BaCuO and LRE-Ba_2CuZrO_y. The arrows point to some of the nanometer sized Ti-based nanoparticles.

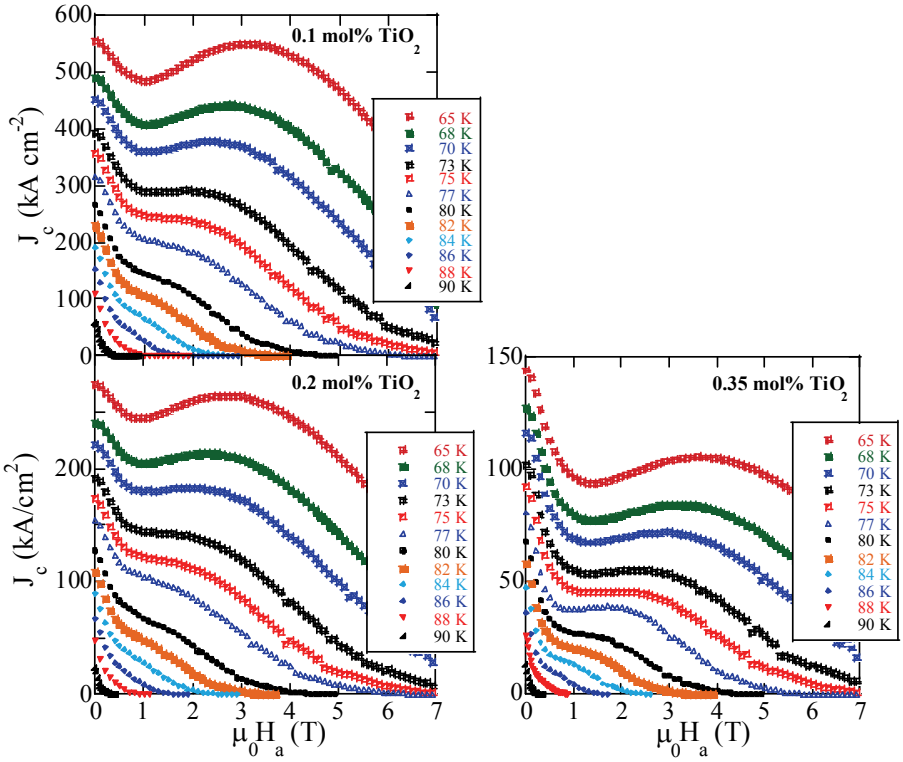

Fig. 9. Field dependence of the super-current density of the NEG-123 samples with the same, 35 mol%, content of Gd-211 (70 nm) but various contents of TiO_2, measured from 65 K to 90 K with $H||c$-axis. Note the critical current densities of 550 kA/cm² at self-field and 4.5T at 65 K and 50 kA/cm² at self-field at 90 K, achieved with 0.1 mol% TiO_2.

capable of permanent magnet levitation at 90.2 K, with liquid oxygen cooling (Muralidhar et al., 2003b).

The normalized volume pinning force density, $f_p = F_p/F_{pmax}$, as a function of the reduced field, $h = H_a/H_{irr}$, is frequently used as a measure of the pinning structure effectiveness. H_{irr} was determined from magnetization loops using the criterion of 100 A/cm². The $f_p(h)$ curves for a pure and Ti-doped NEG-123 are presented in Fig. 10. For the pure and 0.1 mol% of Ti NEG-123 samples, the $f_p(h)$ dependence peaked close to 0.42. Note that 0.5 was in classical theories associated with δT_c pinning. While even a slightly increased TiO_2 content over 0.1 mol% shifted the peak of $f_p(h)$ down to 0.36, the optimum quantity of 0.1 mol% of Ti did not affect the pinning mechanism much.

Whatever the pinning mechanism really is, a higher position of the $f_p(h)$ peak is associated with a better flux pinning. Moreover, the normalized peak position 0.5 is the highest met in literature. In this sense the $f_p(h)$ dependence confirms the conclusion that the 0.1 mol% Ti concentration is optimum. Magnetic data combined with microstructure analysis proved that TiO_2 nanoparticles belong to the agents capable to significantly improve pinning performance of the LRE-123 materials so that NEG-123 could be utilized for fabrication of superconducting super-magnets working at liquid argon and/or liquid oxygen temperatures.

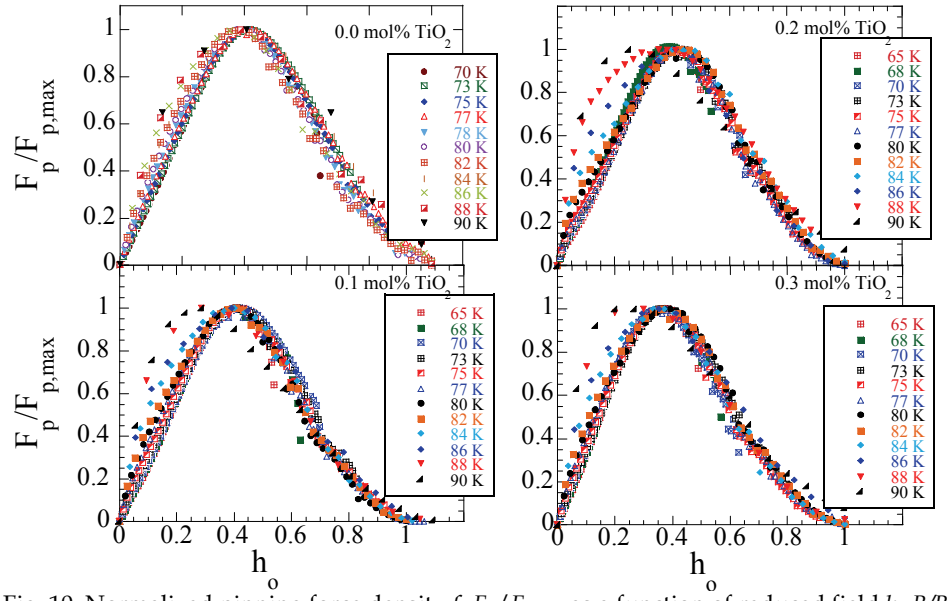

Fig. 10. Normalized pinning force density $f=F_p/F_{pmax}$ as a function of reduced field $h=B/B_{irr}$ of NEG-123 samples with the same, 35 mol%, content of Gd-211 (70 nm) but various contents of TiO_2, for temperatures from 65 to 90 K.

7. Flux pinning in NEG-123 with MoO_3 nanoparticles

The size reduction of non-superconducting pinning centers significantly below 100 nanometer range proved that mesoscopic precipitates (size of a few tens of nanometers) were able to exceptionally enhance flux pinning up to very high temperatures. Although levitation experiments at 90.2 K have already been realized with NEG-123 superconductors doped by Zr-based or TiO_2 based nanoparticles, the safety margins needed for practical applications require a further improvement in flux pinning in these materials. Recent experiments clarified that this task could be realized with MoO_3 nanoparticles.

Figure 11 shows the temperature dependence of the dc magnetic susceptibility in the ZFC and FC modes in magnetic field of 1 mT for NEG-123 + 35 mol% Gd-211, 1 mol% CeO_2, and 0.5 mol% Pt samples with varying contents of MoO_3. All the samples exhibited a sharp superconducting transition (around 1 K wide) with a high onset T_c. The onset T_c systematically decreased from 93.2 to 92 K with increasing MoO_3 content.

The critical current density at 77 K of the MoO_3 added NEG-123 composites with 35 mol% Gd-211 secondary phase is presented in Fig. 12 (left). The remnant critical current density dramatically increased for 0.1 mol% MoO_3 but decreased thereafter. The J_c-B curves of the 0.1 mol% MoO_3 sample deduced from SQUID magnetometer measurements in the temperature range around 77 K in magnetic field applied parallel to the c-axis are shown in Fig. 12. At 65 K tremendous super-currents were obtained, exceeding 700 kA/cm² at 0 and 4.5 Tesla and 610 kA/cm² over the whole range, up to 5 Tesla. These values approach the range typical for thin films. It might be promising to combine this technology with that used for fabrication of thick coated conductors. At liquid argon (87 K) and liquid oxygen (90.2 K), the super-current densities at zero field reached 175 kA/cm² and 50 kA/cm², respectively.

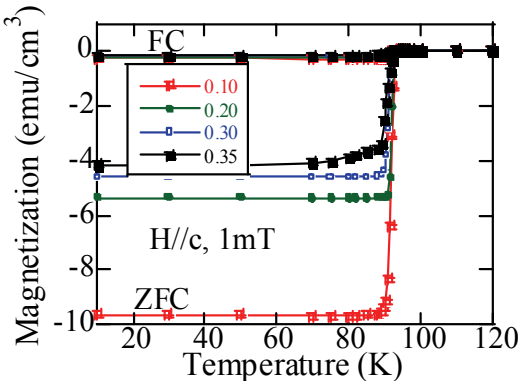

Fig. 11. Temperature dependence of the normalized susceptibility of the OCMG-processed NEG-123 + 35 mol% Gd-211 (70 nm) with varying contents of MoO_3.

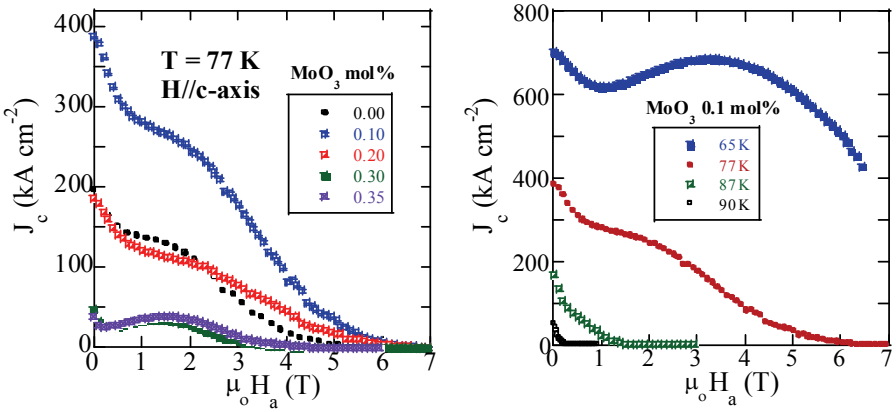

Fig. 12. Left: $J_c(B_a)$ plots for NEG-123 samples with 35 mol% Gd-211 (70 nm), 1 mol% CeO_2, 0.5 mol% Pt, and various contents of MoO_3 at 77 K and B_a | | c-axis. Note the relatively high critical current density of 390 kA/cm² at self-field at 77 K achieved with 0.1 mol% MoO_3. Right: The $J_c(H)$ curves of the sample with 0.1 mol% MoO_3 under liquid nitrogen pumping (65 K), at liquid nitrogen (77 K), liquid argon (87 K), and liquid oxygen (90.2 K) (H | | c-axis). Note the very high critical current density of 700 kA/cm² at self-field and 4.5T at 65 K (right figure).

The MoO_3-based nanoparticles thus represent an effective pinning medium, appropriate for moderate magnetic fields and high temperatures, going up to boiling point of liquid oxygen. In order to evaluate the nanoparticle dispersion and its chemical analysis in the NEG-123 sample with 0.1 mol% MoO_3, TEM-EDX observations were performed on it. Figure 13 shows the TEM viewed from the <001> direction. Three types of defects can be seen: large irregular inclusions of about 150 to 500 nm in size, round particles of 20-50 nm size, and clouds of spots less than 10 nm in diameter. We note that in the partial-melted region there are two different kinds of LRE-211 inclusions: one (ball-milled) added to the initial powders and another one being created by peritectic decomposition of LRE-123. The large particles (over 150 nm in size) are Gd-rich NEG-211 or NEG-211 ones of the latter origin.

The chemical composition of the precipitates was studied by scanning TEM-EDX analysis. The quantitative analysis clarified that the large particles were Gd-211/Gd-rich-NEG-211, in agreement with our earlier studies of the NEG-123 system. In contrast, the defects with size below 50 nm always contained a significant amount of Mo. For the particles less than 10 nm, marked by the white arrows, it was difficult to estimate the exact composition. Anyway, just these particles are considered to be responsible for the high *Jc* observed at high temperatures. We succeeded in finding the appropriate processing parameters for their creation. The pinning enhancement due to the new type of defects is so profound that it extends up to temperatures above 90 K. This means that the limiting operating temperature for levitation experiments and other applications shifts from liquid nitrogen (77.3 K) to liquid oxygen (90.2 K) temperature.

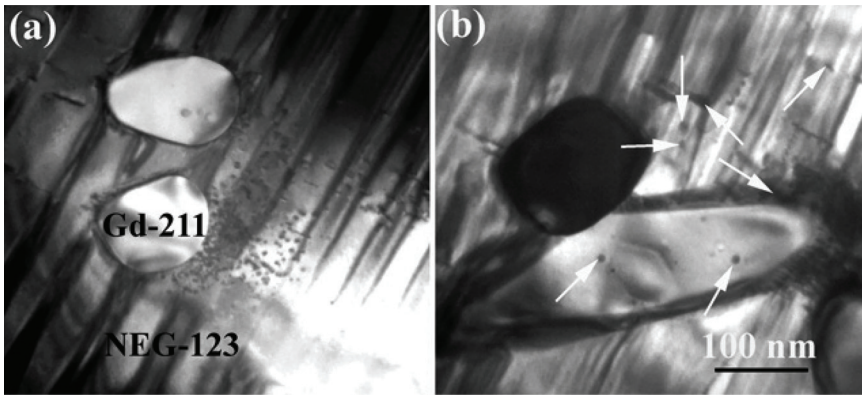

Fig. 13. Transmission electron micrograph of NEG-123 sample with 35 mol% Gd-211 (the initial average particle size 70 nm) and 0.1 mol% MoO_3 the arrows point to some of the smallest nanoparticles, of size below 10 nm.

8. Flux pinning in NEG-123 due to Nb_2O_5 nanoparticles

An optimum content, size, and dispersion of the nanoparticles play the crucial role in improving vortex pining in the melt-textured LRE-123 materials. Different physical/chemical properties are certainly equally important. This conclusion follows from the fact that the refractory metals of the same group as Zr give so different results, even if added in the same amount and same size. The best results in this direction were so far achieved with Nb_2O_5 nanoparticles added to the NEG-123 material. The critical current densities at 77 K of the NEG-123 composites with 35mol% Gd-211 doped by various contents of Nb_2O_5 are presented in Fig. 14. The low-field super-current density in the sample with 0.1 mol% of Nb_2O_5 was more than factor three higher than that of the standard NEG-123. The remnant J_c values of 640 kA/cm^2 and 400 kA/cm^2 were achieved at zero and 2 Tesla, respectively. This result was by more than 50% better than the previous record values of NEG-123 and by more than order of magnitude better than in other RE-123 materials. With further increase of Nb content the super-current density and irreversibility already dropped. The super-currents in the sample with 0.1 mol% of Nb_2O_5 in temperatures around 77 K are presented in the in Fig. 15. The remnant J_c value reached 925 kA/cm^2 at 65K. In liquid argon (87 K) and liquid oxygen (90.2 K) the super-current densities at zero field reached 300 kA/cm^2 and 100 kA/cm^2, respectively. These J_c values are the highest reported so far for bulk RE-123 materials at the respective temperatures, approaching nearly the thin film limit.

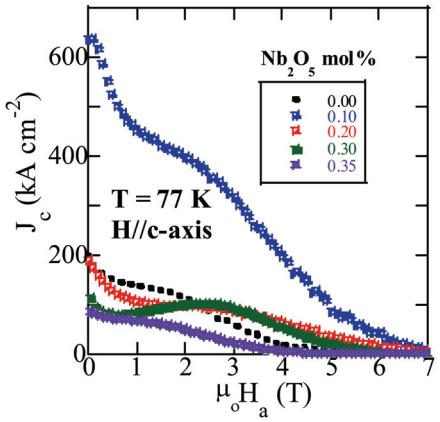

Fig. 14. Field dependence of the super-current density in NEG-123 samples with the same, 35 mol% content of Gd-211 (70 nm) but various contents of Nb_2O_3. All the samples were measured at T = 77 K with $H||c$-axis. The current density increased in the whole field range up to the 0.1 mol% content of Nb_2O_5 and decreased thereafter. Note the critical current density of 640 kA/cm² at self-field and 77 K, achieved with 0.1 mol% Nb_2O_5.

In Fig. 16 we show the TEM images of the sample with 0.1 mol% Nb_2O_5, viewed from the <001> direction. Three types of defects can be seen: large irregular inclusions of about 150 to 500 nm in size, round particles of 20-50 nm size, and clouds of spots less than 10 nm in diameter. We note that in the partial-melted region there are two different kinds of LRE-211 inclusions: one (ball-milled) added to the initial powders and another one being created by peritectic decomposition of LRE-123. The large particles (over 150 nm in size) are Gd-rich NEG-211 or NEG-211 ones.

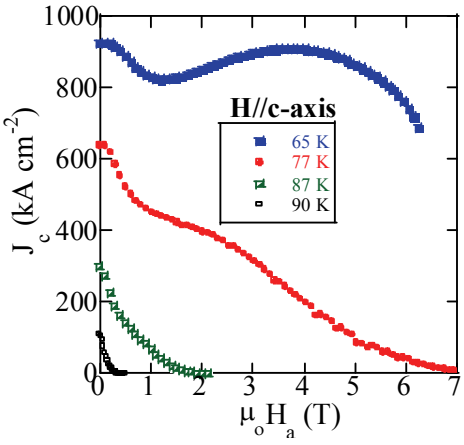

Fig. 15. The $J_c(H)$ curves of the sample with 0.1 mol% Nb_2O_5 under liquid nitrogen pumping (65 K), at liquid nitrogen (77 K), liquid argon (87 K), and liquid oxygen (90.2 K) ($H||c$-axis). Note the record critical current density of 925 kA/cm² at self-field and 4.5T at 77 K.

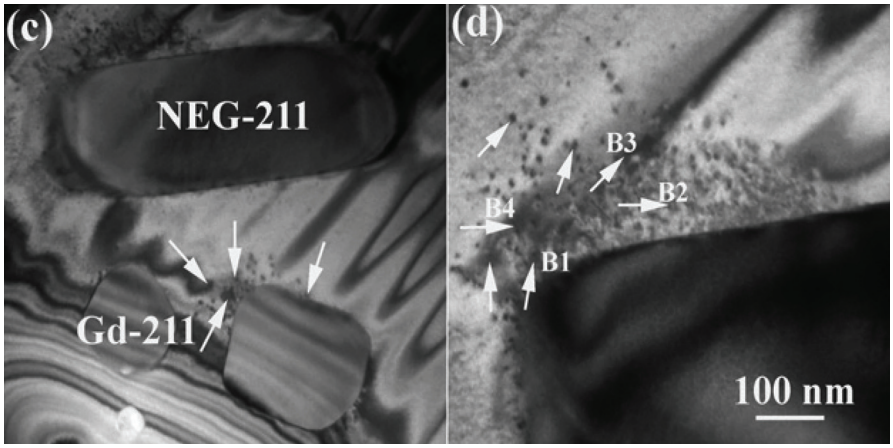

Fig. 16. Transmission electron micrograph of NEG-123 sample with 35 mol% Gd-211 (the initial average particle size 70 nm) and 0.1 mol% Nb_2O_5 the arrows point to some of the smallest, Nb-based, nanoparticles.

The small Gd-211 nanoparticles (≈20 nm) were found to be those contaminated by Zr during the ball milling process. As Nb and Mo just follow Zr in the periodic table of elements, they possess similar properties as Zr, in particular chemical inactivity with respect to the constituents of the perovskites under study.

The chemical structure identification of the precipitates was made by scanning TEM-EDX analysis. The analyzed spot of 2-3 nm in diameter enabled to unambiguously analyze even the smallest clusters. The quantitative analysis clarified that the large particles were Gd-211/Gd-rich-NEG-211, while the defects with size below 50 nm always contained a significant amount of Zr, in agreement with our earlier studies of the NEG-123 and SEG-123 systems (Muralidhar et al., 2003c; Muralidhar et al., 2004a). Recently, the exact chemical composition of these particles was determined as $LREBa_2CuZrO_y$ (Muralidhar et al., 2003). The new class of precipitates of less than 10 nm in size contained a detectable amount of Nb incorporated in the NEG secondary phase. Some of these defects are marked in Fig. 16 by white arrows but these defects were distributed over the whole sample. Four such defects are denoted as B1 - B4 in figure 16. The four nanoparticles possessed different elemental ratios but always a significant amount of Nb atoms (see Fig. 17). The appearance of such small defects correlates with the super-current enhancement in a wide temperature range, spread up to liquid oxygen temperature.

The decreasing average particle size resulted in a critical current density enhancement at low and intermediate magnetic fields. Although the size of the smallest particles came close to the vortex core size, 2ξ, (in YBCO $2\xi_{ab}(77\ K) \approx 4.5$ nm) and thus the limit of single-vortex interaction has been approached for these particles, no sign of a crossover to the secondary peak enhancement was observed. Note that a similar behavior was observed in the studies of [Werner et al., 2000] and [Sauerzopf et al., 1995; Sauerzopf et al., 1998] done on various RE-123 and Y-124 single crystals irradiated by fast neutrons. The explanation might be still a broad distribution of defect sizes, the largest ones having the strongest pinning energy, governing thus the overall behavior of the sample. Another possibility is that the crossover

between multiple- and single-vortex pinning is rather sharp and we are still not close enough. Or, the present defects are in some sense different from the typical point-like defects (oxygen vacancies and/or the LRE-123 matrix chemical fluctuation (Werner et al., 2000; Ting et al., 1997; Osabe et al., 2000).

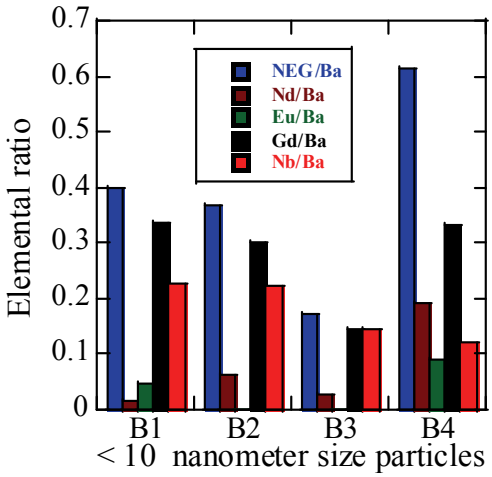

Fig. 17. The elemental content in the new nanoparticles in the material from Fig. 16. Note the significant amount of Nb in all nanoparticles.

The last NEG-123 material features the highest flux pinning performance of all bulk RE-123 compounds developed in SRL-ISTEC and to our knowledge in the world. To control pinning performance of the NEG material in a broad low-field range, various second phase precipitates have been tested in various contents. Gd-211 was found to produce always the highest flux pinning. Its optimum content was established to be around 35mol%. In each further step we have used the optimum composition obtained in the previous step. Thus, the Gd-211 content was also here just 35 mol%. Also the oxygen partial pressure has been chosen in accord with the best previous experience. The only variable in the present work was the varying content of the nanometer-sized TiO_2, MoO_3, and Nb_2O_5. As a result, critical current density was enhanced by factor 2, 3, and 4, respectively, in comparison with the best our previous results, in all cases extended up to high temperatures. This record electromagnetic performance was always accompanied by appearance of clouds of exceptionally small precipitates (10 nm in size) in the NEG-123 matrix. Although this cannot be taken as a direct proof of causality, a similar coincidence observed previously in the case of Zr-contaminated 20 nm in size particles and the previous significant enhancement of the low- and medium-field critical currents (Muralidhar et al., 2005) supports this conclusion. In fact, it correlates with predictions of various models of vortex interaction with "large" normal particles (Campbell et al., 1991; Dew-Hughes et al., 1974; Zablotskii et al., 2002) suggesting $j_c \propto d^{-n}$, where d is the average particle diameter and n=1 [2] or 1/2. These facts are strong indications that the enhanced pinning is due to a collaborative pinning by the operative pinning assemble, the result being exceptionally sensitive to the smallest nanoparticles, in our work especially those containing Mo and Nb, 10 nm in size.

9. Trapped-field distribution in the NEG-123 samples calculated using the J_c-B data at 77 K and 90 K.

In the NEG system, we can now for the first time create a particles distribution of the size less than 10 nm. As a result, the critical current density is very high, even at the boiling point of liquid oxygen. Trapped field measurements at 90.2 K for sample with Zr-contaminated nanoparticles (Muralidhar et al., 2004b) showed two peaks the higher of which reached 0.16 T. It indicated a crack in the sample created during magnetization process. Evidently, the mechanical performance was not good enough and a reinforcement was needed by adding silver oxide, resin impregnation (Tomita & Murakami, 2003), and/or an external metal ring (Kita et al., 2006).

We calculated TF values using experimental J_c-B data and with help of a numerical simulation. NEG-123 with 30 mol% Gd-211 (70 nm particles) was selected for this purpose, the J_c-B data from Fig. 4. Based on these data we calculated trapped field profile for disks of 40 mm and 50 mm diameters and thicknesses of 10 mm and 20 mm, respectively. Figure 18 shows the result for the disk of 50 mm in diameter and 20 mm thick, giving 0.45 T at 90 K. So far a standard NEG-123 sample of 32 mm diameter was able to trap in remnant state at 77 K maximum of 1.4 T (Yamada et al., 2003). Using the same J_c-B data, trapped field profiles for 77 K and samples of 50 mm in size and 10 and 20 mm thick were calculated in the same manner as above. The results are presented in Fig. 19. The trapped field reached more than 4 T in remnant state at 77 K. A summary of the calculated TF values at 77 K and 90 K is presented in the right Fig. 19. It is clear that the NEG-123 samples can generate more than 5T at 77 K with increasing the sample size to 60 mm diameter. The simulation results proved that the new material enables construction of non-contact pumps for transport of liquid gases including liquid oxygen. Thus, these results represent a significant step forward in the technology of bulk high-T_c superconductors towards novel engineering applications.

10. Levitation experiments at liquid oxygen temperature (90.2 K) and its new application potential

When speaking about applications of bulk high-temperature superconductors, superconducting levitation should be mentioned in the first place. Several years after the discovery of high temperature superconductivity, we developed a NEG-123 disk capable of levitation with liquid oxygen cooling. Although Y-123 has also critical temperature above boiling point of oxygen (90.2 K), levitation with this coolant has not yet been possible. The reason is that the pinning performance of Y-123 rapidly drops when coming close to the critical temperature. Thus, Y-123 can be used so far only for levitation at 77.3 K. The superconductors with T_c higher than 100 K, like $Bi_2Sr_2Ca_2Cu_3O_{9+\delta}$ and others, exhibit a poor pinning performance already at intermediate temperatures and thus they cannot be used for levitation even with liquid nitrogen cooling. The new LRE-123 materials reach critical temperatures 93-96 K, not significantly above those typical for Y-123, but the best of them possess an exceptionally good pinning at high temperatures, super-current density being in the range of several tens of kA/cm^2 at 90 K (Fig. 15). This enabled levitation experiments with liquid oxygen cooling. Superconducting materials working at 90.2 K might have an important impact in industrial applications as magnet levitation at this temperature is a direct link to construction of non-contact pumps for liquid oxygen. Note that the industrial use of liquid oxygen is quite broad. It is commonly used in hospitals or as an oxidizer for liquid hydrogen fuel for launching rockets.

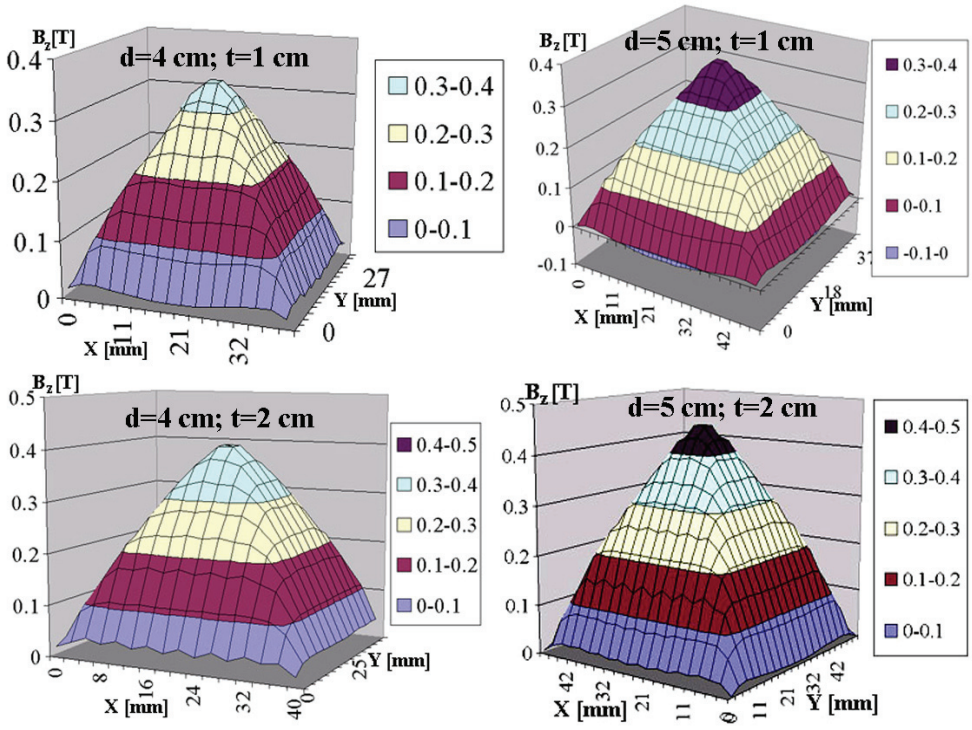

Fig. 18. The calculated trapped field distribution in the sample NEG-123 + 30 mol% Gd-211 (70 nm in size), melt processed in Ar-1% O_2, at liquid oxygen temperature (90.2 K). Dimensions and thicknesses of the sample were assumed 40&50 mm and 10&20 mm, respectively. The high trapped field of 0.45 T was achieved in the remnant state at 90.2 K.

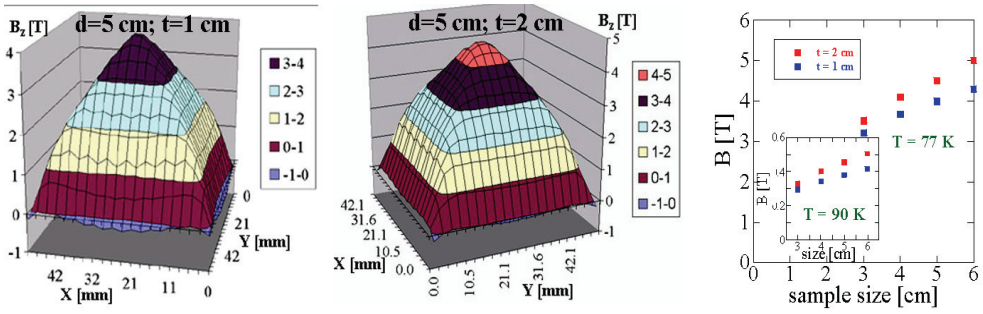

Fig. 19. The calculated trapped field distribution in the sample NEG-123 + 30 mol% Gd-211 (70 nm in size), melt processed in Ar-1% O_2, calculated for the liquid nitrogen temperature. Dimensions and thicknesses of the sample were assumed 50 mm and 10&20 mm, respectively. Trapped field as high as 4.5 T was achieved in the remnant state at 77.3 K. The summary for the sample size vs trapped field at 77 K and 90 K in the remnant state is in the right figure.

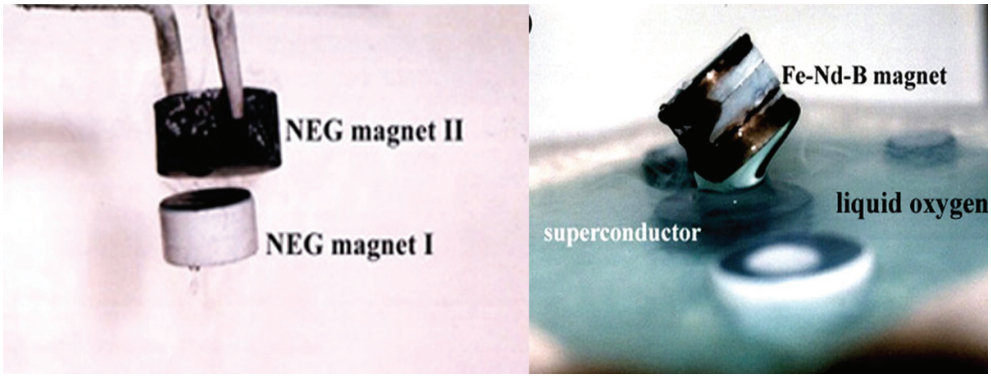

Fig. 20. (left) NEG-123 + 40 mol% Gd-211 superconductor suspended below another NEG-123 + 40 mol% Gd-211 superconducting magnet. Both NEG super-magnets were before cooled by liquid oxygen; (right) Levitation of a tilted Fe-Nd-B magnet over the NEG-123 + 40 mol% Gd-211 superconductor cooled by liquid oxygen. Note that liquid oxygen is attracted to the magnet due to its paramagnetism.

Fig. 20 (left) is a proof, how effective is the potential well created in this way: a NEG-123 magnet can be suspended *below* another NEG-123 magnet when both are kept cool enough. That liquid oxygen is really used as a coolant, it is seen in figure 20 (right): since liquid oxygen is paramagnetic (in contrast to the diamagnetic liquid nitrogen), it is attracted to a tilted Fe-Nd-B magnet hanging over the superconductor immersed in liquid oxygen. Hospitals need comprehensive medical gas distribution systems to meet increasing demands of the life support technologies and emergency help. Medical gases have to be distributed in a clean, safe, and reliable manner. Gases in liquid form can be transported in a sophisticated network, which would supply either medical air and/or oxygen for patient breathing support or nitrous oxide for anesthesia. For such systems, the new superconductors represent a basic construction material for design of non-contact liquid oxygen pumps.

11. Summary

Over the past 20 years, remarkable progress in the area of melt-grown LRE-123 systems processing has been made. Improved processing techniques like oxygen controlled melt growth (OCMG) have been used for $LREBa_2Cu_3O_y$ bulks processing and then ternary $LREBa_2Cu_3O_y$ systems have been developed. Ternary $LREBa_2Cu_3O_y$ composites feature typical T_c onset around 94 K, critical current density at 65 K in the self-field and 5 T at the level of 10^5 A/cm^2 ($H//c$-axis), and irreversibility field at 77 K ($H//c$-axis) up to 15 T. This performance, highly exceeding that of YBCO, makes from these materials an excellent option for utilization in practical applications. A very important aspect is the possibility to control the pinning defects size up to nanoscale level and to bring it close to the material's coherence length (4.5 nm in YBCO at 77 K and similar in the LRE-123 compounds). A further tuning of the nanoscale secondary phase particles and Zn, Mo, Ti, Nb etc. additives enhance flux pinning of these materials up to 3 times compared to a single-LRE 123 material. As a result, pinning in these materials is very strong up to liquid oxygen temperature (90.2 K), leading to impressive levitation forces and extending thus the

application range of 123 compounds by about 13 K. In another direction, these materials can be utilized as a new type of bulk superconducting magnets, in particular for liquid oxygen pumps for various purposes.

12. Acknowledgements

The authors would like to record thanks to Prof. S. Tanaka, the former Director of ISTEC-SRL for his encouragement. We also acknowledge the stimulating discussions with Dr. U. Balachandran (Argonne), Prof. David A Cardwell (University of Cambridge), Dr. Shunichi KUBO (RTRI), Prof. M. Murakami (SIT), Prof. V. Hari Babu (Osmania University), Dr. A. Das (Canada), Dr. M. R. Koblischka (Germany), Dr. N. Sakai (ISTEC-SRL) and Dr. P. Diko (SAS,Slovakia). This work was supported by Grants-in-Aid for Science Research from the Japan Society for the Promotion of Science (JSPS). One of the authors, MJ, acknowledges support from grants MEYS CR No. ME 10069 and AVOZ 10100520.

13. References

Aksay, I.; Han, C.; Maupin, G. D.; Martin, C. B.; Kurosky, R. P.; & Stangle, G. C. (1991). Ceramic precursor mixture and technique for converting the same to ceramic, *United states patent* No. 5061682, October 1991.

Awaji, S.; Isono, N.; Watanabe, K.; Murakami, M.; Muralidhar, M.; Koshizuka, N.; & Noto, K. (2004). Bose glass state in (Nd,Eu,Gd)$Ba_2Cu_3O_x$ bulk with high irreversibility field, *Phys. Rev. B,* Vol.69, No.21, (214522, 4p).

Brunauer, S.; Emmett, P.; & Teller, E. (1938) Adsorption of Gases in multimolecilar layers. *J. Am. Chem. Soc.* Vol. 60, No. 2, (309-319).

Bednorz, J. G.; & and Mueller, K. A. (1986). Possible high T_c superconductivity in the Ba-La-Cu-O system, *Z. Phys. B,* Vol. 64, No. 2, (189-193).

Babcock, S. E.; Cai, X. Y.; Kasier, D.L.; & Larbalestier, D.C. (1990). Weak-link-free behaviour of high-angle $YBa_2Cu_3O_y$ grain boundaries in high magnetic fields, *Nature* Vol. 347, 13 September 1990, (167-169).

Blohowiak, K. Y.; Garrigus, D. F.; Luhman, Thomas S.; Mccrary, K. E.; Strasik, M.; Aksay, I.; Dogan, F.; Hicks, W. C.; & Martin, C. B. (2000). Making large, single crystal, 123 YBCO superconductors, *United states patent* No. 6046139, April 2000.

Campbell, A. M.; Evetts, J. E.; & Dew-Hughes, D. (1968). Pinning of flux voritices in type II superconductors, *Philos. Mag*. Vol. 18, (313-343).

Cava, R. J.; Batlogg, B.; van Dover, R. B.; Murphy, D. W.; Sunshine, S. ; Siegrist, T.; Remeika, J. P.; Rietman, E. A.; Zahurak, S.; & Espinosa, G. P. (1987). Bulk superconductivity at 91 K in single phase oxygen-deficient perovskite $Ba_2YCu_3O_{9-\delta}$, *Phys. Rev. Lett*. Vol.58, Issue 16, (1676-1679).

Cardwell, D. A. (1998). Processing and properties of large grain (RE)BaCuO. *Mater. Sci. Eng.B,* Vol. 53, No.1 (1-10).

Dew-Hughes, D. (1974). Flux pinning mechanisms in type II superconductors, *Philos. Mag*. 30, Issue 2, (293-305).

Diko, P.; Muralidhar, M.; Koblischka, M. R. & Murakami, M. (2000). Homogeneous distribution of 211 secondary-phase particles in single-grain melt-grown (Nd,Eu,Gd) $Ba_2Cu_3O_7$ bulk, *Physica C*, Vol.339, No. 3, (143-147).

Egi, T.; Wen, J. G.; Kurada, K.; Koshizuka, N.; & Tanaka, S. (1995). High critical-current density of Nd (Ba,Nd)2Cu3O7-δ single crystals. *Appl. Phys. Lett.* Vol. 67, No. 16, (2406-2408).

Fuchs, G. (2000). Trapped magnetic fields larger then 14T in bulk $YBa_2Cu_3O_y$. *Appl. Phys. Lett.* Vol. 76, No. 15, (2107-2109)

Jirsa, M.; & Muralidhar, M. (2004). Superconducting permanent magnets for high temperature operation, *Czech J. Phys.*, Vol.54, No. 1, (441-444).

Jin, S.; Fastnacht, R. A.; Tiefel, T. H.; & Sherwood, R. C. (1988). Transport critical current in rare-earth-substituted superconductors $RBa_2Cu_3O_{7-\delta}$, (R=Gd, Dy, Sm, Ho,Y), *Phys. Rev. B*. Vol. 37, Issue 10, (5828-5830).

Koblischka, M. R.; van Dalen, A.J.J.; Higuchi, T.; Yoo, S. I.; & Murakami, M. (1988). Analysis of pinning in $NdBa_2Cu_3O_{7-\delta}$ superconductors, *Phys. Rev. B,* Vol. 58, Issue 5, (2863-2867).

Krabbes, G.; Fuchs, G.; Schatzle, P.; GruB, S.; Park, J. W.; Hardinghaus, F.; Stover, G.; Hayn, R.; Dreshsler, S-L.; & Fahr, T. (2000). Zn doping of $YBa_2Cu_3O_y$ in melt textured materials: peak effect and high trapped fields, *Physica C*. Vol. 330, No. 3, (181-190).

Kita, M., Nariki, S.; Sakai. N.; & Hirabayashi, I. (2006). Characteristics of metal impregnated bulk Gd-Ba-Cu-O superconductors cooled down in a magnetic field, *Supercond. Sci. Technol*., Vol. 19, Issue 7, (S491-S493).

Mavani, K.R., Rana, D.S., Nagarajan, R.; & Kuberkar, D.G. (2004). Effect of Sc and Ti doping on superconducting and magnetic properties in $DyBa_2Cu_3O_{7-\delta}$, *J. Mag. and Mag. Mat*., Vol. 272, (E1067-E1069).

Murakami, M.; Gotoh, S.; Fujimoto, H.; Yamaguchi, K.; Koshizuka, N.; Tanaka, S. (1991). Flux pinning and critical currents in melt processed YBCO superconductors, Supercond. Sci. Technol. Vol. 4, No. 1S, (S43-S50).

Murakami, M.; Takata, T.; Yamaguchi, K.; Kondoh, A.; & Koshizuka, N. (1995). Oxide superconductor and preocess for producing the same, *United states patent* No. 5395820, May 1995.

Murakami, M.; Sakai, N.; Higuchi, T.; & Yoo, S. I. (1996). Melt-processed light rare earth element -Ba-Cu -O. *Supercond. Sci. Technol.* Vol. 9, Issue 12, pp.1015-1032.

Muralidhar, M.; Chauhan, H. S.; Saitoh, T.; Kamada, K.; Segawa, K.; & Murakami, M. (1997). Effect of Mixing Three Rare Earth Elements on the superconducting properties of $REBa_2Cu_3O_y$, *Supercond. Sci. Technol*., Vol. 10, Issue 9, (663-668).

Muralidhar, M.; Murakami, M.; Segawa, K.; Kamada, K.; & Saitho, T. (2000). Oxide Superconductor of high critical current density, *United states patent* No. 6063736, May 2000.

Muralidhar, M.; & Murakami, M. (2000). Effect of matrix composition on the flux pinning in (Nd,Eu,Gd)$Ba_2Cu_3O_y$ superconductors, *Phys. Rev. B*., Vol. 62, No.21, (13911-13914).

Muralidhar, M.; Jirsa, M.; Sakai, N.; & Murakami, M. (2001). Optimization of Matrix chemical ratio for high flux pinning in ternary (Nd-Eu-Gd)$Ba_2Cu_3O_y$, *Appl. Phys. Lett.*, Vol.79, No.19, (3107-3109).

Muralidhar, M.; Wu, Y.; Sakai, N.; Murakami, M.; Jirsa, M.; Nishizaki, T.; & Kobayashi, N. (2002a). Excess of Eu in the $(Nd_{0.33}Eu_{0.66-x}Gd_x)Ba_2Cu_3O_y$ system-the way to high irreversibility field at 77 K, *Supercond. Sci. Technol*., Vol. 15, No. 9, (1357-1363).

Muralidhar, M.; Nariki, M.; Jirsa, M.; Wu, Y.; & Murakami, M. (2002b). Strong pinning in ternary (Nd-Sm-Gd)$Ba_2Cu_3O_y$ superconductors, *Appl. Phys. Lett.,* Vol. 80, No. 6, (1016-1018).

Muralidhar, M.; Sakai, N.; Chikumoto, N.; Jirsa, M.; Machi, T.; Wu, Y.; & Murakami, M. (2002c). New type of vortex pinning structure effective at very high magnetic fields, *Phys. Rev. Lett.,* Vol.89, No.23, (237001-1-237001-4)

Muralidhar, M.; Sakai, N.; Nishiyama, T.; Jirsa, M.; Machi, T.; & Murakami, M. (2003a). The pinning characteristics in chemically modified (Nd,Eu,Gd)-Ba-Cu-O superconductors, *Appl. Phys. Lett.,* Vol. 82 , No. 6, (943-945).

Muralidhar, M.; Sakai, N.; Jirsa, M.; Murakami, M.; & Koshizuka, N. (2003b). Levitation of NEG-123 at the temperature of liquid oxygen (90.2K), *Supercond. Sci. Technol*., Vol. 16, No. 11, (L46-L48).

Muralidhar, M.; Sakai, N.; Jirsa, M.; Koshizuka, N.; & Murakami, M. (2003c). Vertex pinning by mesoscopic defects – a way to levitation at liquid oxygen, *Appl. Phys. Lett.,* Vol. 83, No. 24, (5005-5007).

Muralidhar, M.; Sakai, N.; Jirsa, M.; Koshizuka, N.; & Murakami, M. (2004a). Direct observation and analysis of nanoscale precipitates in (Sm,Eu,Gd)$Ba_2Cu_3O_y$, *Appl. Phys. Lett.,* Vol. 85, No. 16, (3504-3506).

Muralidhar, M.; Sakai, N.; Jirsa, M.; Murakami, M.; & Koshizuka, N. (2004b). Pinning centers in NEG-123 active at liquid oxygen temperature (90.2 K), *Supercond. Sci. Technol*., Vol. 17, No. 2, S66-S69.

Muralidhar, M.; Sakai, N.; Jirsa, M.; Murakami, M.; & Koshizuka, N. (2004c). Effect of nanoscopic ZrO_2 particles on flux pinning in (Nd,Eu,Gd)-123/Gd-211 composites, *Supercond. Sci. Technol*., Vol.17, (1129-1132).

Muralidhar, M.; Sakai, N.; Jirsa, M.; Machi, T.; & Murakami, M. (2008a). Levitation at 90.2 K and its applications, *International Journal of Condensed Matter,* Vol.6, (269-292).

Muralidhar, M.; Sakai, N.; Jirsa, M.; Murakami, M.; & Hirabayashi, I. (2008b). Highly enhanced flux pinning in melt-textured NEG-123 doped Nb and Mo nano partices, *Appl. Phys. Lett.,* Vol. 92, Issue 16, (162512-3p).

Muralidhar, M.; Tomita, M.; Jirsa, M.; Sakai, N.; Murakami, M.; & Hirabayashi, I. (2009). Observation of record flux pinning in melt-textured NEG-123 superconductor doped by Nb, Mo, and Ti nano particles, *Physica C,* Vol.469, (1196-1199).

Okura, K.; Ohmatsu, K.; Takei, H.; Hitotsuyanagi, H.; & Nakahara, T. (1988). Superconductivity of $Ba_2Y(Cu, Ti)_3O_y$ oxide, *Jpn. J. Appl. Phys*. Vol. 27, No. 4, (L655-L657).

Osabe, G.; Yoo, S. I.; Sakai, N.; Higuchi, T.; Takizawa, T.; Yasohama K.; & Murakami, M. (2000). Confirmation of Ba-rich $Nd_{1+x}Ba_{2-x}Cu_3O_{7-\delta}$ solid solutions *Supercond. Sci. Technol.* Vol. 13, No. 6, (637-640).

Pradhan, A. K.; Muralidhar, M.; Feng, Y.; Shibata, S.; Murakami, M.; Nakao, K.; & Koshizuka, N. (2001). Flux pinning in melt-processed ternary (Nd-Eu-Gd) and Nd-based superconductors, *IEEE Appl. Supercond*. Vol. 11, No. 1, (3706-3711).

Salama, K.; & Lee, F. D. (1994). Progress in melt texturing of $YBa_2Cu_3O_x$ superconductor, *Supercond. Sci. Technol*. Vol.7, No. 4, (177-193).

Sandiumenge, F.; Martinez, B.; & Obradors, X. (1997). Tailoring of microstructure and critical current in directionally solidified $YBa_2Cu_3O_{7-x}$, *Supercond. Sci. Technol*., Vol. 10, No. 7A, (A93-A119).

Sauerzopf, F. M.; Wiesinger, H. P.; Weber, H. W.; Crabtree, G.W. (1995). Analysis of pinning effectrs in $Yba_2Cu_3O_y$ single crystals after fast neutron irradiation, *Phys. Rev. B.* Vol. 51, (6002-6012).

Sauerzopf, F. M. (1998). Anisotropic flux pinning in single crystals: The influence of defect size and density as determined from neutron irradiation, *Phys. Rev. B*, Vol. 57, (10959-10971).

Shigemori, M.; Okabe, T.; Uchida, S.; Sugioka, T.; Shimoyama, J.; Horii, S.; & Kishio, K. (2004). Enhanced flux pinning properties of Bi(Pb)2212 single crystals, *Physica C,* Vol. 408-412, (40-45).

Shimoyama, J.; Maruyama, T.; Shigemori, M.; Uchida, S.; Yamamoto, A.; Katsura, Y.; Hori, S.; & Kishio, K. (2005). Generic positive effects of low level impurity doping on flux pinning properties of HTSC and MgB_2, *IEEE Trans. Appl. Supercond.* Vol. 15, (3778-3781).

Ting, W.; Egi, T.; Kurada, K.; Koshizuka, K.; & Tanaka, S. (1997). Evidence of a new magnetic flux pining center in $Nd_1Ba_2Cu_3O_y$ single crystals. *Appl. Phys. Lett.*, Vol. 70, Issue 6, (770-772).

Tomita, M.; & Murakami, M. (2003). High-temperature superconductor bulk magnets that can trap magnetic fields of over 17 tesla at 29 K, *Nature.* Vol. 421, (517-520).

Umezawa, A.; Crabtree, G. W.; Liu, J. Z.; Weber, H. W.; Kwok, W. K.; Nunez, L. H.; Moran, T. J.; Sowers, C. H.; & Claus, H. F. (1997). Enhanced critical currents due to fast neutron irradiation in single crystal $YBa_2Cu_3O_{7-d}$. *Phys. Rev. B.* Vol.36, (7151-7154).

Vipulanandan, C,; & Salib, S. (1994). Mechanical and Physical properties of sintered YBCO melt bulk composites with silver powder and fibres, *J. Mat. Sci.*, Vol. 30, (763-769).

Venkataramani, N.; Muraleedharan, K.; Datta, A.; Bhatia, S. N.; Prakash, O.M.; & Srivastava, C. M. (1988). Effect of Zr, Ti, substitutions on T_c in superconducting $YBa_2Cu_3O_{7-\delta}$ system, *Pramana J.Phys*.Vol. 30, (L455-L457).

Wu, M. K.; Ashburn, J. R.; Torng, C. J.; Hor, P. H.; Meng, R. L..; Gao, L.; Huang, Z. J.; Wang, Y.Q.; & Chu, C. W. (1987). Superconductivity at 93 K in a new mixed-phase Y-Ba-Cu-O compound system at ambient pressure, *Phys. Rev. Lett.*, Vol. 58, (908-910).

Welp, U.; Kwok, W. K.; Crabtree, G. W.; Vandervoort, K. G.; & Liu, J. Z. (1989). Magnetic measurements of the upper critical field of $YBa_2Cu_3O_{7-\delta}$ single crystals, *Phys. Rev. Lett.*, Vol. 62, (1908-1911).

Werner, M.; Sauerzopf, F.M.; Weber, H. W.; & Wisniewski, A. (2000). Fishtail effect in the magnetization of superconducting $RBBa_2Cu_3O_{7-d}$ (R= Y,Nd,Yb) and $YBa_4Cu_8O_{16}$ single crystals, *Phys. Rev. B.* Vol. 61, (14795-14803).

Yoo, S. I.; Sakai, N.; Takaichi, H.; & Murakami, M. (1994). Melt processing for obtaining $NdBa^2Cu_3O_y$ superconductors with high T_c and large J_c, *Appl. Phys. Lett.* Vol. 65, (633-635).

Yanmaz, E.; Bali, B., & Kucukometoglu, T. (2002).Magnetic properties of melt textured $YBa_2Cu_3O_{7-\delta}$ with TiO_2 dopent, *Materials Lett.*, Vol. 54, No. 2, (191-199).

Yamada, T.; Ikuta, H.; Yoshikawa, M.; Yanagi, Y.; Itoh, Y.; & Mizutani, U. (2003). Field trapping capability of melt processed (Nd-Eu-Gd)-Ba-Cu-O bulk superconductors, *Physica C*, Vol. 392-396, (623-627).

Zablotskii, V.; Jirsa, M.; & Petrenko, P. (2002). Vortex pinning by large normal particles in high T_c superconductors, *Phys. Rev*. B. Vol. 65, (224508, 4p).

11

X-ray Micro-Tomography as a New and Powerful Tool for Characterization of MgB_2 Superconductor

Gheorghe Aldica[1], Ion Tiseanu[2], Petre Badica[1],
Teddy Craciunescu[2] and Mattew Rindfleisch[3]
[1]*National Institute of Materials Physics, Magurele, Ilfov, 077125*
[2]*National Institute for Lasers, Plasma and Radiation Physics, Magurele, Ilfov, 077125*
[3]*Hyper Tech Research, Inc. Troy, OH 45373*
[1,2]*Romania*
[3]*USA*

1. Introduction

Applied superconductivity is virtually important for all human activities solving different problems in the fields such as power and energy, electronics, computing and communications, medical equipment and sensors, fast transportation and so on. However, the progress in this field is relatively slow when compared to other young industries. The reasons are diverse, and among them are the prohibitive prices vs. performance of the superconducting technologies. In this regard, superconducting-based materials or products with improved working characteristics at constant or lower prices are always of interest.

One superconductor of practical interest is MgB_2. This superconductor has several advantages as follows:

1. Critical temperature T_c = 39 K of MgB_2 [1] is the highest among simple superconducting compounds. This is a unexpectedly high T_c and, although MgB_2 can be considered a s-wave classical Bardeen-Cooper-Schriffer (BCS) superconductor, it shows elements of unconventional superconductivity: two-gap superconductivity was observed with gap values of Δ_σ = 7.4 meV and Δ_π = 2.1 meV at 4.2 K corresponding to critical temperatures of 15 K and 45 K, with σ and π being the bands of the boron electrons [2]. In fact, there are two hole-type quasi-two-dimensional σ bands (σ1 and σ2), an electron-type (π 1) and a hole-type (π 2) three-dimensional π bands [3,4]. Such situation generates new physical effects with markedly different behaviors in many properties some of them of practical meaning when compared with single band superconductors.
2. It is a simple compound composed of only two elements.
3. It is a cheap compound composed of relatively cheap and available elements.
4. It is not toxic and it is considered stable in the air.
5. It is a light compound with low theoretical density of 2.63 g/cm^3. Crystal structure is relatively simple of layered hexagonal type.
6. It has anisotropy, but it is not as high as in high temperature superconductors.

7. Ginzburg-Landau coherence length along the ab-plane is ξ_{ab} = 10 nm, while along c-axis is ξ_c = 5 nm [5]. These values are significantly higher than for the HTS resulting in transparent grain boundaries for the supercurrent passing. Moreover, grain boundaries are recognized to act as strong pinning centers in this superconductor enhancing critical current in high magnetic fields.
8. MgB_2 has in dirty C-alloyed MgB_2 thin films H_{c2} and J_c above the values for the practical superconductors Nb_3Sn and NbTi.
9. Films of MgB_2 were shown to grow on single crystal substrates, but also on metallic ones, e.g. on stainless steel [6 and therein refs]. This is important for fabrication of coated conductors.

Despite significant advantages, MgB_2 has several problems in the growth and properties control. Among them we shall mention the fact that Mg is a highly volatile element. High volatility of Mg, according to general ceramic principles does not allow synthesis of high-density bulks. This is a serious and difficult-to-remove limitation and, as a consequence, it requires much effort to improve connectivity, to produce a high-density uniformity and finally to improve critical current density J_c, that is the key parameter for applications of superconductors. Challenging difficulties are amplified because microscopy techniques such as optical microscopy or SEM, in many cases, cannot provide useful information on specifics of the MgB_2 nanostructure, on local density, local density distribution and connectivity, while TEM is very local and is applied to few selected regions. It is important to mention in this context that most of the practical MgB_2 samples are composed of nanoparticles usually less than 20-30 nm. The requirement of nanostructuring in MgB_2 is due to point 7, above introduced: smaller grain in the material means more grain boundaries with a positive effect on pinning increase, and, hence, on J_c enhancement. Another limitation is that typical microscopy techniques are not suitable for 3D observations. On the other hand, 3D observations are extremely useful in analysis of composite complex 3D objects such as wires, tapes, cables, joints, coils and so on of superconductors and in particular of MgB_2. X-ray microtomography as it will be shown in this chapter can fill the gap and solve some of the presented problems, bringing new and very useful information about MgB_2. At the same time X-ray microtomography cannot replace existing microscopy techniques.

2. Principles of X-ray micro-tomography method

Computed tomography (CT) is widely used in the medical community and is receiving increased attention from industrial users including electronics, aviation, advanced materials research, casting and other manufacturing. Computed tomography systems are usually configured to take many views of the object in order to build a 3-D model of its internal structure. 2-D slices through this volume can be viewed as images, or the 3-D volume may be rendered, sliced, thresholded and measured directly. Amplitudes of the volume elements (or voxels) are proportional to the X-ray linear attenuation of the material at that position and are therefore dependent only on material properties and not on the shape of the object as in case of plain radiography.

The principle of most common transmission tomography configurations is depicted in Fig 1. Traditionally, volumetric image reconstruction is achieved through scanning a series of cross-sections (slices) with a fan-shaped X-ray beam, and by stacking these slices. Recently, with the introduction of planar detectors, computed tomography began a transition from fan-beam to cone-beam geometry. In cone-beam geometry the entire object is irradiated with

a point-shaped X-ray source, and the radiation attenuation is measured on a detector plane behind the object. The primary advantages of cone-beam geometry include reduced data acquisition time, improved image resolution, and optimized photon utilization. Cone-beam X-ray microtomography is used in this work to characterize MgB_2 superconducting objects.

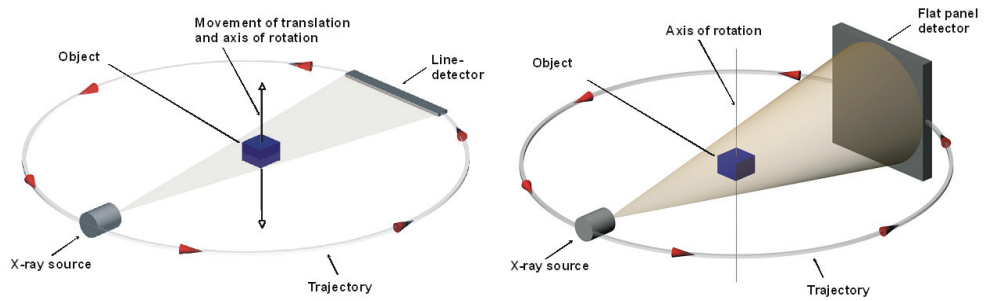

Fig. 1. Fan beam (left) versus cone beam (right) tomography configurations.

Despite progress in exact cone-beam reconstruction, approximate cone-beam reconstruction remains the 3-D CT main solution, especially in the cases of incomplete scanning and partial detection. Furthermore, approximate reconstruction is usually associated with higher computational efficiency, and may produce less image noise and ringing. The Feldkamp (FDK) cone-beam algorithm [7], which is an ingenious adaptation of the weighted filtered backprojection algorithm for equispatial rays, represents the most reliable approach for solving the cone-beam reconstruction problem. The unknown distribution function at position *(t,s,z)* is given by:

$$f(t,s,z)=\frac{1}{2}\int_0^{2\pi}\frac{D_{SO}^2}{\left(D_{SO}-s\right)^2}\int_{-\infty}^{\infty}P_\beta(Y,Z)h\left(\frac{D_{SO}t}{D_{SO}-s}-Y\right)\frac{D_{SO}}{\sqrt{D_{SO}^2+Y^2+Z^2}}d\beta dY$$

where: $t=x\cos\beta+y\sin\beta$, $s=-x\sin\beta+y\cos\beta$, *(Y, Z)* are the detector pixel coordinates in a plane translated such that the q-axis is superimposed on the z-axis (Fig. 2).

The cone beam reconstruction algorithm can be conveniently broken into the following steps:

1. Weighting projections: multiply projection data, $P_\beta(Y,Z)$, by the function $Dso/(Dso^2+Y^2+Z^3)$ to find the weighted projections.
2. Filtering projections: convolute the weighted projection with the ramp filter h by multiplying their Fourier transforms with respect to Y. Note this convolution is done independently for each elevation Z.
3. Backprojection: each filtered weighted projection is backprojected over the three-dimensional reconstruction grid. The two arguments of the weighted projection represent the transformation of a point in the object volume into the coordinate system of the tilted fan.

The FDK algorithm is highly parallelizable and hardware supported. The FDK is an approximate method because only those points of the object that are illuminated from all directions can be properly reconstructed. In a cone-beam system this region is a sphere of radius $D_{SO}\sin(\Gamma_m)$ where Γ_m is half the horizontal cone angle. Outside this region a point

will not be included in some of the projections and thus will not be correctly reconstructed. The main limitation occurs at relatively large cone angles.

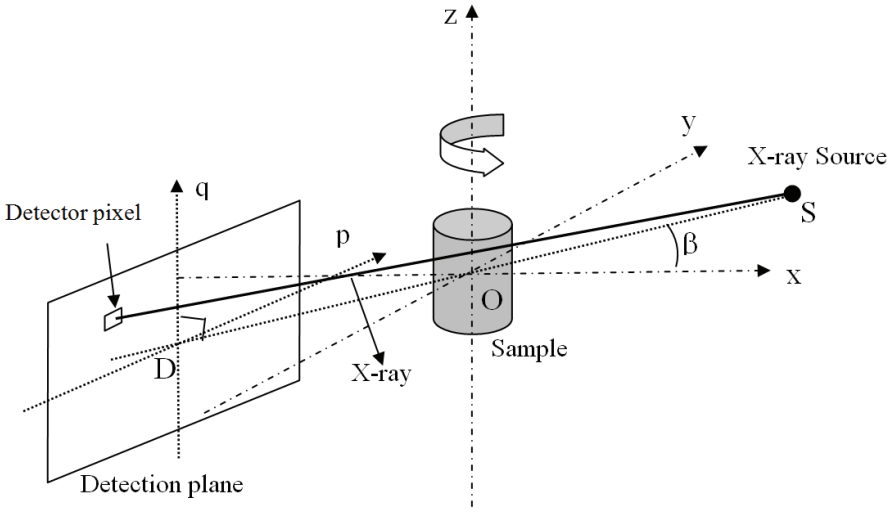

Fig. 2. Feldkamp algorithm cone-beam geometry

Oxyz - reconstruction coordinate system; sample rotates around z-axis
Dpq - planar detector coordinate system
SO - source-object distance
SD - source-detector distance
β - angle of rotation of sample (equivalent picture – angle of synchronous rotation of source-detector assembly)

The application of X-ray tomography for non-destructive analysis of superconducting materials was recently reported. Synchrotron tomography [8-9], but also micro-tomography based on conventional X-ray tubes [10, 11] proved to provide useful information on the internal structure of superconducting materials. X-ray micro-tomography (XRT) was initially used and tested to reveal in a non-invasive and convenient way [11], the architecture of the superconducting composite wires. The method can also reveal at macro local scale the occurrence, distribution and shape of the regions with a different density [12]. The results presented here were obtained using a high resolution X-ray micro-tomography facility constructed at NILPRP Bucharest, Romania with European Community support. The main component is an open type microfocus X-ray source (W target, maximum high voltage of 160 kVp at 20 W maximum power). X-rays are detected by means of a high-resolution image intensifier (Siemens Medical Solutions) or an amorphous silicon flat panel sensor (Hamamatsu). The detection system is placed on a precise motorized stage (Sigma-Koki) additionally provided with vertical and transversal adjustable tables. The investigated sample is placed on a four axes motorized manipulator to assure a high degree of freedom in accurate sample positioning. The micro-radiography analysis is guaranteed for feature recognition down to 1 micron. Due to the ability to work with magnifications over 1000, it has been demonstrated that for miniaturized samples the micro-tomography analysis is valid for feature recognition down to few microns. The 3D tomographic image

reconstructions are obtained by a proprietary highly optimized computer code based on a modified Feldkamp algorithm.

The reconstruction software also incorporates efficient techniques for beam hardening reduction and ring artifacts elimination. Beam hardening effects are the main challenge for the application of the microtomography technique to the analysis of high density metallic samples. Beam hardening artifact consists of an elevated density displayed on the perimeter of a uniform density object and a corresponding density depression in the object's core region. It is caused by the polychromatic structure of the energy spectrum of the X-ray generators. Several experimental techniques have been reported for beam-hardening correction [13-15]. However, the optimization of the tomographic measurement by experimental selection of a large set of parameters is a very laborious procedure and the result is not always guaranteed. Therefore, in our approach [15], a numerical simulation procedure-time-independent multimaterial and multidimensional-coupled electron/photon Monte Carlo transport - was developed. Any important element, such as: target material, pre and post-filters and X-ray energy spectra have been studied. The optimisation procedure requires pre-filtering the X-ray beam for narrowing the energy spectra, at the same time monitoring the spectra evolution into the probe structure for maximum absorption contrast. High performance microtomography on fusion material samples of advanced steel alloys would require, in addition to beam parameters optimization, the application of active methods of beam hardening reduction. This means the determination of the non-linear dependence between investigated object thickness and log ratio of intensities in the radiographic views, followed by the corresponding processing of the radiographic data. Obviously, determination of the non-linearity of the line integrals by accurate Monte Carlo simulation instead of laborious experiments is always desirable. Reducing beam hardening effects means, consequently, reducing the need for employing highly sophisticated post-processing methods.

3. Application of XRT on MgB_2 superconductors

3.1 MgB_2 synthesis using mechanical alloying method and X-ray microtomography observations

First attemps to apply X-ray microtomography were performed on MgB_2 ceramic obtained by conventional solid state reaction between powder of boron and magnesium. Mixtures of Mg (99.5%, 45 μm), B (0.85 μm, amorphous, 95% purity and impurities are: 3% Mg, 0.5% water soluble, 1% insoluble in H_2O_2 and 0.5% moisture) and SiC (99.3%, 20 nm) powders with composition $(Mg + 2B)_{0.95}(SiC)_{0.05}$ were prepared by hand mixing under Ar (glove-box) and by mechanical milling in a planetary ball mill (Fritsch P7, Cr-steel pot and 20 balls of 7 mm diameter; composition of the Cr-steel used for the pot and balls is: 85.3%Fe, 12%Cr, 2.1%C, 0.3%Si, 0.3Mn) [16, 17]. Mechanical milling was done for 0.5, 1, and 3 h at 400 rpm under Ar gas introduced into an evacuated milling pot. As-prepared powders, after pressing into pellets, were heat treated in Ar using a tube furnace with a quartz tube. Pellets were wrapped into Mo and Zr-foils together with chunks of Mg to prevent significant evaporation of this element from the samples during heating. Samples and processing conditions are gathered in Table. 1.

Samples were characterized by x-ray diffraction (PANalytical, CuKα radiation) and SEM (JEOL JSM 6400F). Measurements of M-H loops at 4.2 K and 20 K were conducted using a

SQUID magnetometer (Quantum Design, 5T). Same equipment was used to determine critical temperature, T_c taken as the onset of the diamagnetic signal in the zero-field-cooled M(T) curves measured for a *dc* magnetic field of 20 Oe. X-ray microtomography measurements were performed as presented in second part of this section.

Sample	Mixing/milling	Heat treatment temp. (°C)	Heat treatment time (h)
A	Manual in Ar	700	1h
B	Mechanical milling in Ar, 0.5h	700	1h
C	Mechanical milling in Ar, 1h	700	1h
D	Mechanical milling in Ar, 3h	700	1h
Tape	Powder in tube MgB_2 tape [18]	750	1h

Table 1. Samples and processing conditions

SEM images (not presented) taken on the A-D Ar-as-milled (un-reacted) powders consist of large agglomerates up to 30-50 μm and no other significant differences can be observed. On the other hand, XRD patterns for the same precursor powders A-D show that enhancement of milling time produces patterns with Mg diffraction-lines of lower intensity and larger *full width at half maximum* (FWHM). For A-D mixtures FWHM was estimated at 0.16, 0.23, 0.25 and 0.27°, respectively. The result suggests occurrence of smaller particles with a lower degree of crystal perfection for Mg vs. milling time. A relatively short milling time leads to a relatively fast decrease of the intensity and a fast increase of FWHM, while for longer milling time variation of the intensity and of FWHM is slower. B cannot be observed in the XRD patterns since this element was used in the amorphous state.

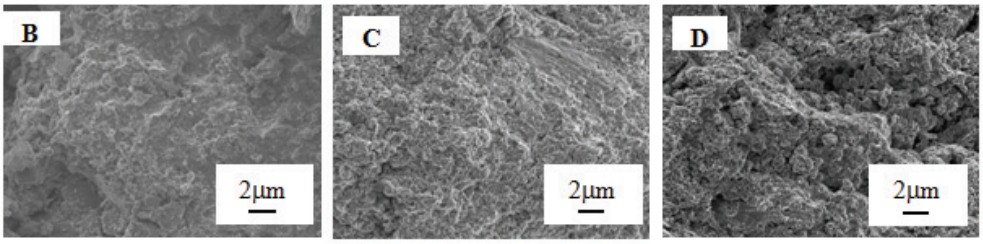

Fig. 3. SEM images for the reacted B-D samples. Sample notation is the same as in Table 1.

Bulk samples prepared from the powders A-D for the same heat treatment conditions are showing roughly very similar XRD and SEM (Fig. 3) results with some small differences. In the XRD the crystal quality is decreasing with the milling time, but the ratio between different phases is approximately constant. Low level of MgB_4 in the samples indicates that Mg-losses during heat treatment are relatively low, while the decrease in *a*-axis of the MgB_2 (from 0.3084 to 0.3074 nm) with the increase in the milling time (from 0 to 3 h, respectively) of the precursor mixtures suggests introduction into the lattice of MgB_2 of C coming from the milling pot and balls.

SEM images (Fig. 3) on the reacted B-D samples are showing small grains and agglomerates of 1-3 μm. The appearance is of a glassy bulk where the grains cannot be easily observed, and the connectivity between the grains is likely decreasing from sample A to D. The

decrease of the connectivity and the decrease of the crystal quality can be the reasons for the decrease of the superconducting properties. Carbon presence should be also considered and it is probably the main reason for the observed decrease of the critical temperature (37.4, 34.8, 32.2 and 32 K for A-D samples, respectively). The presence of other impurities is also of interest and some aspects are addressed in the next paragraphs. The decrease in T_c with the milling time is accompanied by the decrease in the magnetization loop width, ΔM, which is proportional to J_c through the Bean formula [19] (Fig. 4).

Our results indicate that milling and milling time are important and are producing different states for Mg and a different level of carbon in the precursor. This likely influences the further growth processes leading to a different quality of the MgB_2 samples. Changes in the superconducting properties are logically correlated with the changes observed in SEM and XRD data, but the details are missing and the mechanism and the key factors controlling this relationship cannot be satisfactorily revealed. It is also questionable if this is the full picture and one problem is that the changes in the T_c and J_c are significant, while in the XRD and SEM are much lower. This discrepancy leads to the idea that XRD and SEM are not sensitive enough or are not the most appropriate to reveal the differences. Complementary techniques to check and expand the available data are needed.

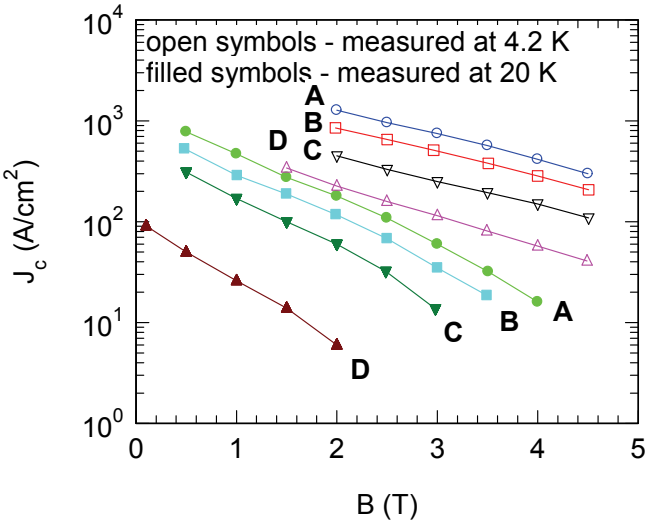

Fig. 4. Magnetization loop width (proportional to J_c) for the samples A-D at 4.2 K and 20 K.

X-ray microtomography (XRT) was applied for characterization of the reacted bulk samples AD (Fig. 5). This technique can display images of microstructure in the sense that the dark regions are of low density. Pores in the material will be black and they will have the shape and size as visualized through microscopy. Grains will have in the XRT images different gray tones and the whiter they are the higher density they have. What is remarkable about this technique is that, in fact, we do not depend on the clear observation of the grains to construct a 3D image showing macroscopic regions of the material with a different density.

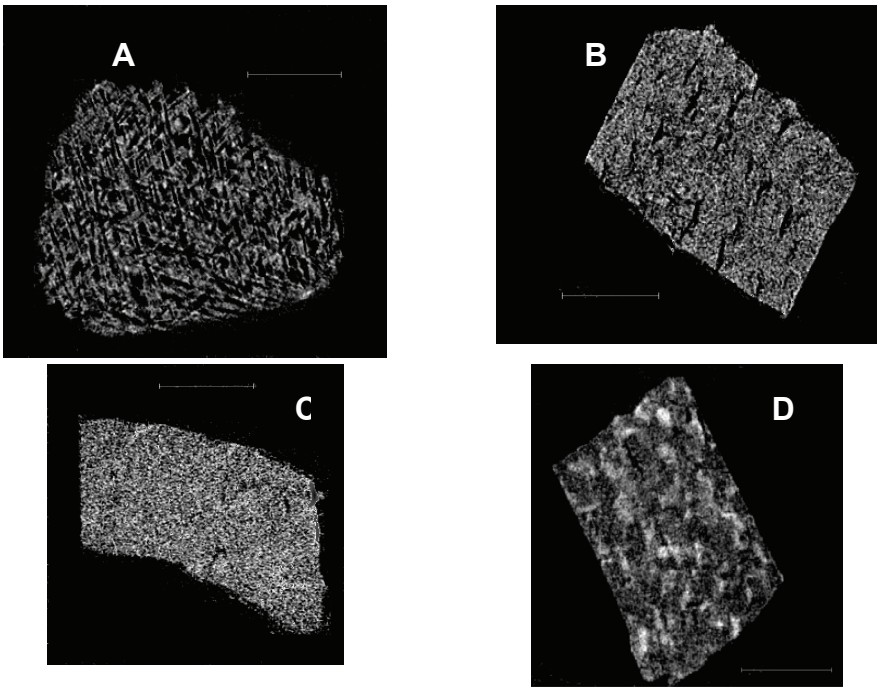

Fig. 5. Representative XRT images of the heat treated bulk samples A-D (Table 1). Images were taken for a voltage of 40 kV and a current of 100 μA. Scale bar is 100 μm.

This is advantageous because even a relatively low XRT resolution (of few μm in our case) when compared to SEM or TEM and when measuring materials composed of small-size grains (for our samples less than 50-100 nm and significantly less than the XRT resolution), can reveal useful information on local density distribution and uniformity or on the shapes, packing and alignment of the regions and/or pores of the size larger than the resolution. Further development of the technique and improvement of the resolution is expected to show more details inside the macroscopic regions and also to identify the phases based on their density. One interesting aspect related to the last part of the previous statement is that our MgB_2 samples contain a relatively low level of impurities. By XRD the impurities in the reacted A-D samples were Mg_2Si, MgO, MgB_4 and some unreacted Mg. The densities, d, of different phases in the material and of the raw materials are: d_{SiC} = 3.22 g/cm^3, $d_{C\text{-graphite or amorphous}}$=1.8-2.3 g/cm^3, d_{Mg} = 1.738 g/cm^3, $d_{B\text{-amorphous or crystalline}}$ = 1.74-2.44 g/cm^3, d_{MgB2} = 2.63 g/cm^3, d_{MgO} = 3.58 g/cm^3, d_{Mg2Si} = 2.56 g/cm^3 and d_{MgB4} = 2.50 g/cm^3. The highest density is for MgO or SiC. The two phases should have the whitest colour on the XRT images. The amount of the XRT white regions in the A-D superconducting samples is much larger than a few percent of residual MgO or SiC phases estimated from XRD. Hence, the white regions in the XRT images do not reflect a certain phase and mainly show regions with a very different local density. However, contribution of a certain phase to the colour nuance of a region cannot be totally excluded. It is also necessary to discuss some other issues related to the limitations of different measurement techniques. It is generally recognized that solid and liquid phases are present during the reaction to form MgB_2.

Hence, glassy phases, phases with poor crystal quality or nanoscale grains can easily occur and can be hardly detected by XRD leading to underestimated values of the impurity-phases amounts. Following the same idea, a special attention deserves MgO or more general the presence of oxygen in the material. Sometimes, a fine mixture of MgB_2 with oxygen is mentioned (more often for thin films), and even by high resolution techniques such as TEM it is very difficult to observe grains of MgB_2 and MgO and to make a separation between them. Since the role and behaviour of the oxygen in MgB_2 is not clear and also considering the above limitations from the different measuring techniques it is wise to keep in mind the oxygen impurification during milling and the following scenario can be imagined: with the increase in the milling time, the amount of oxygen impurification in the precursor powders may increase. This might be related to the behaviour of Mg and its reactivity influenced by the milling conditions. It is thought that longer milling time, generating lower Mg crystal quality and smaller grains, leads to more reactive powders including with residual oxygen. It is noteworthy that, during milling, other processes relevant for the XRT images may take place such as the transfer of the material from the milling-pot-walls and balls into the precursor powder. Impurities are also present in the raw materials, especially in the boron amorphous raw powder of relatively low purity. Milling can change their behaviour so that they can influence processes. However, EDS and XRD investigations could not detect impurity elements (except the presence of C entering the lattice of the MgB_2 phase) or phases (such as Fe_2B) in the MgB_2 final bulk meaning that, if they are present, these elements are below the detection limit of these techniques. From XRT point of view changes in the particle size and particle size distribution can influence agglomeration and rheological properties of the powder mixtures so that packing and density distribution in the bulk can be very different.

Although, at present, it is not possible to significantly advance the understanding of the milling-properties relationship, XRT can reveal clear differences between the samples and the details are addressed in the next paragraphs.

For the reacted samples milled in Ar-atmosphere (Fig. 5), XRT microstructure is changing from a vermicular in A to a layered structure with long oriented pores in B (up to 50 μm in length), to a relatively uniform distribution of the regions of higher and lower density and containing many small pores as well as few large pores of irregular shape in sample C. Finally, a 'leopard'-3D-spot-like structure is observed for the sample D. The white 'spots' of the high density material in this sample are of regular sphere- and ellipsoidal- like or of the irregular shape. One can appreciate from the Fig. 5 that the amount of the brighter regions is likely to enhance from A to D and, hence, the amount of the high density regions in the material is enhancing. At the same time the homogeneity of the samples is getting lower. Furthermore, the tendency of the XRT patterns is likely preserved for the case when precursor powders are milled in H_2 atmosphere [12], but the evolution of the XRT microstructure towards the 'leopard'-like structure is slower. This might be because Ar is an inert atmosphere while H_2 is a highly reducing one, so that the reacted samples in the same conditions may contain different amounts of the residual oxygen, as it was discussed above.

3.2 Observation of MgB_2 tapes and wires by XRT

Powder-in-tube fabrication of the tape observed by X-ray microtomography was reported in [18].

XRT structure of the tape can be visualized in (Fig. 6). Tape shows relatively uniform XRT microstructure, when compared with the patterns taken on bulk samples A-D (Section 3.1),

but one can easily observe regions with different nuances of gray. There are regions in the center of the MgB_2 core from the tape that are darker (e.g. see Fig. 6c) suggesting a lower density, and meaning, from a practical point of view, that that there is room for improvements even for tapes with record high level of J_c in high magnetic fields [18] as measured in this tape investigated here by XRT.

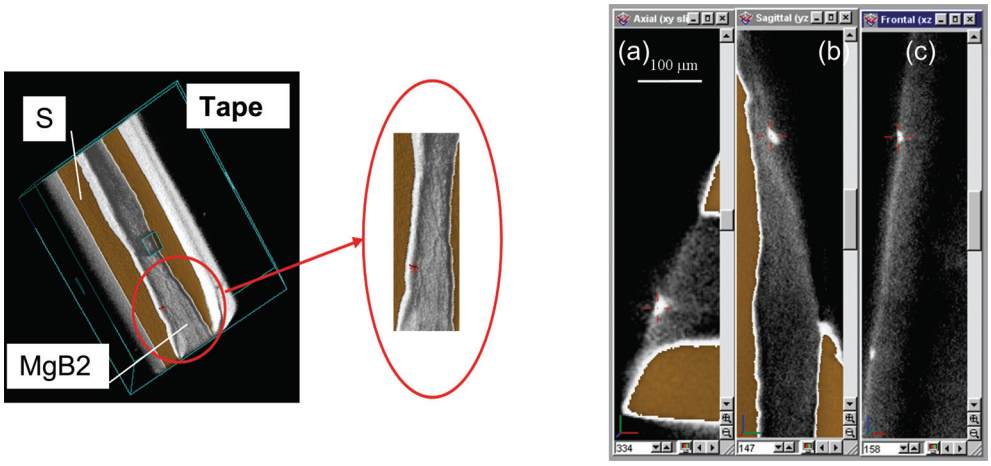

Fig. 6. 3D XRT image reconstruction of an MgB_2 tape (S = metal sheath) and representative images of the (a)- axial, (b)-sagital and (c)-frontal (from left to right) sections. The cross identifies the same point in all images. Images were taken for a voltage of 60 kV and a current of 80 μA.

Apart from the local density information, 3D images and selected sections can also give valuable information on the architecture and geometrical perfection of the composite tapes or wires as well as on some macro defects such as cracks and pores.

3D visualisation is particularly important for complex multifilamentary MgB_2 wires. This is because for real applications (e.g. fabrication of the superconducting coils) wires are more suitable than tapes. This situation, and the necessity to test the 3D geometrical quality and defects of the wires for their further improvement and for development of new types of wires, motivated us to apply XRT visualization to commercial wires produced by HyperTech Inc, US. These round-shape wires of MgB_2 were produced by Hypertech Inc. by continuous tube forming and filling process [20].

The significant advantage of XRT in the case of wires is that it works on extended 3D volumes vs. 2D SEM or optical microscopy. The 3D reconstructed images can reveal hidden defects that can easily go unnoticed with traditional microscopy methods. For example, in Fig. 7, from the SEM images taken in SE and BSE regimes on a HyperTech wire with 7 sub-elements, one can observe regions with possible defects. The nature, shape and, hence, importance of such defects cannot be assesed from the 2D images. At the same time, 3D navigation (Fig. 8 left) inside the same wire shows macrodefects. In particular, defects of interruption of the Nb barrier material or voids are clearly visible. Similar 3D defects were visualised for another HyperTech wire with 18 sub-elements (Fig. 8 right). Macrodefects, such as e.g. voids, can have extended, irregular shape and, not rarely, a hidden part. It

means that XRT is valuable not only because it is possible to detect the defect in a highly reliable way, but it can reveal their 3D shape details.

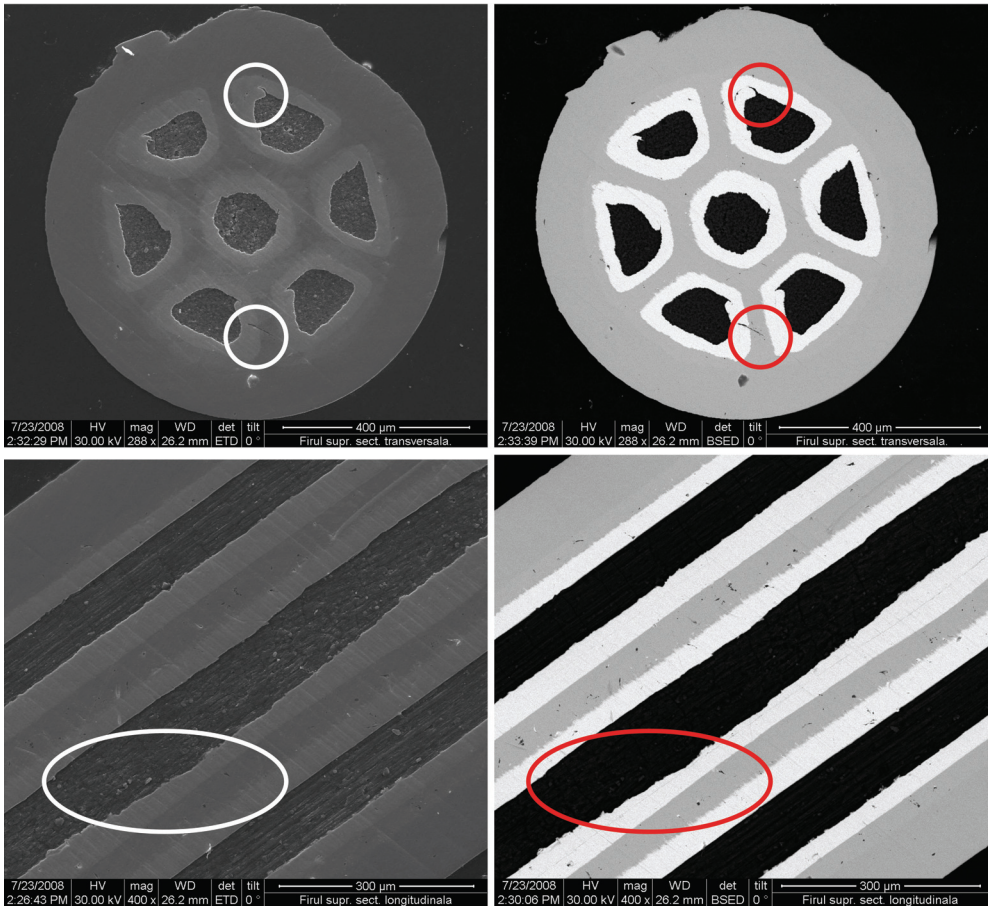

Fig. 7. SEM images of the polished Hypertech MgB_2 wires (7 sub elements): upper panels – transversal SE and BSE modes; bottom panels - longitudinal SE and BSE modes. Defects are identified by the circles. The outer diameter of the wire is 0.83 mm.

It is expected that different architecture of the wires will result in different non-uniformities leading to different overall quality. Non-uniformity is expressed in uniformity of the phase quality (crystal, morphological, structural defects, impurities, grain boundaries) density distribution quality (variation of the local density as discussed for tapes), geometrical perfection. It is a complex system and indicated parameters are not independent. Architecture of the wire vs. processing should be investigated and optimized. XRT can help in understanding the geometrical quality of a sample produced by different technological conditions or it allows comparative analysis between different wires for the same technology. For example, the two wires already mentioned (Fig. 8 left and right colums) from the geometrical perfection viewpoint, even in the absence of the macrodefects are very

different. For each wire there is a difference in the quality of the superconducting sub-elements if the sub-element is located in the outer or inner part of the wire. Namely, interface roughness (R) between Nb and MgB_2 sub-element for the inner sub-elements is higher, while cylinder-shape perfection (CSP) is worse for the same sub-elements. Furthermore, this difference between inner and outer sub-elements is higher for the wire with 18 than for the wire with 7 sub-elements. A closer look also suggests that the worst quality from the R and CSP viewpoints is for the inner sub-elements from the wire with 18 sub-elements. These representative results show that XRT analysis can play an important role in explaining the differences in superconducting properties of MgB_2 samples. However, at present, the relationship between XRT and the superconducting properties of the wires is not established and more research is required.

3.3 MgB_2 consolidation by Spark Plasma Sintering method and XRT observations

One promising method to obtain a dense MgB_2 superconductor is the Field Assisted Sintering Technique (FAST), also known as Spark-Plasma-Sintering (SPS) that was successfully used to consolidate different kinds of difficult-to-sinter powders [e.g. 21]. In this technique, the sample is submitted to a pulsed electric field during the compression process. Although the physics involved is not completely understood, this method provides an excellent way to obtain high density MgB_2 [22-24], while preventing the increase of the grain size. Both, high density and reduced grain size, as already noted above, are very important features for maximization of the properties in MgB_2. Also, doping with various elements or compounds into MgB_2 has been found to enhance the critical current properties [25-27]. In this respect, best results were obtained by using nano-SiC [28], SiC whiskers, nanometer Si/N/C [29] and B_4C [30], that showed a positive influence on irreversibility field (H_{irr}) and critical current density J_c under magnetic fields. In this regard detailed study of the XRT microstructure of MgB_2 samples is of interest.

Polycrystalline samples of MgB_2 (MB), C-doped MgB_2 (MBBC), and SiC-doped MgB_2 (MBSC) were prepared from commercially available powders of MgB_2 (2.3 μm, Alpha Aesar), SiC (45 nm, Merck), and B_4C (0.8 μm, HC Starck Grade HS). For each experiment about 3 g of MgB_2 powder without or with doping compound was loaded into a graphite die with 1.9 cm diameter punches. Prior to powder loading, MgB_2 and SiC or B_4C were mixed in a 0.95:0.05 molar ratio using a mortar and pestle in argon atmosphere for 30 min. After loading the powder into the die (also in argon atmosphere), samples were processed using a "Dr Sinter" (Sumitomo Coal Mining Co, Japan) sintering machine. Sintering was performed in vacuum (6-15 Pa). The temperature was measured by a thermocouple (type K) placed at half of the thickness of the die wall. A uniaxial pressure of 63 MPa was applied during sintering for all samples. In the SPS apparatus, we used a default 12:2 (on:off) current pulsed pattern. The waveform is not square and, in fact, is composed of several spikes (pulses) separated by a current-free interval [31]. Regardless of the pattern, each pulse has the same period of about $3 \cdot 10^{-3}$ s. Thus, the pattern of 12:2 has a sequence of 12 pulses "on" and 2 pulses with no current (off). The total time of one sequence (cycle) is about 0.04 s. The operating voltage and the peak current were below 10 V and 1000 A, respectively.

The SPS-processed pellets have bulk densities (Table 2) above 90 % of the theoretical value (2.63 g/cm^3) [32, 33]. For $0.95MgB_2+0.05B_4C$ a smaller density is observed probably due to the limited chemical reaction between two components, and to a lower sintering temperature. Maximum sintering temperature was selected to be about 40-45 °C higher then the temperature T_d where sample's densification starts.

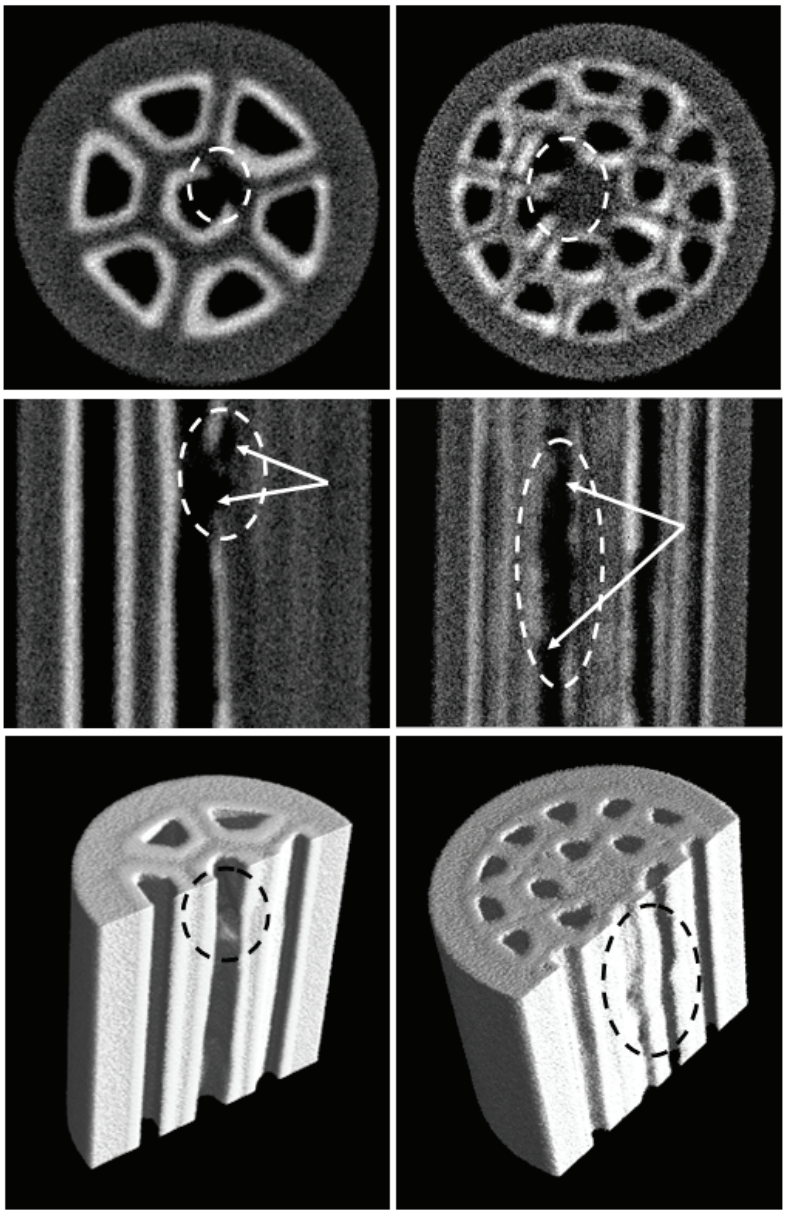

Fig. 8. X-ray microtomography images of the Hypertech MgB_2 wires: left panels - 7 sub elements; right panels - 18 sub elements. Defects are identified on transversal (top) and longitudinal (middle) cross sections and on the associated 3D reconstructions. The outer diameter of the wires was constant at 0.83 mm.

Sample	T (°C)	Density (g/cm^3)	T_d (°C)
MB	960	2.39	920
MBSC	1000	2.37	955
MBBC	1000	2.08	960

Table 2. Samples, the maximum SPS-processing temperature, final density and T_d data.

The tomographic inspection was performed using the following operation parameters: U = 50 kV, I = 40 mA, voxel size = 5 μm. Representative results on the pristine MgB_2 sample are presented in Figs. 9-11. Figure 9 illustrates the identification of high density regions inside the investigated sample. By filtration and thresholding techniques the distribution of these high density regions inside the volume of the sample is revealed in Fig. 10. The identification of macroscopic low density regions is illustrated in Fig. 11.

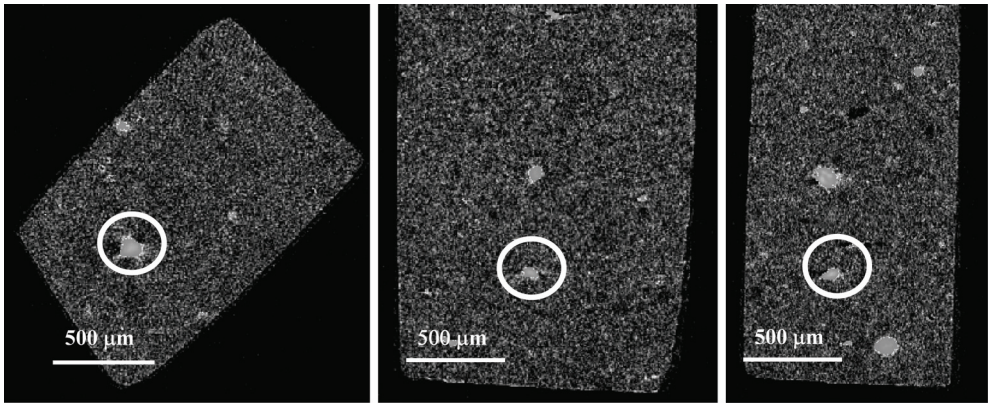

Fig. 9. Transversal, sagital and longitudinal cross-sections revealing high density regions; high density region size (inside circles) is of about 160 μm.

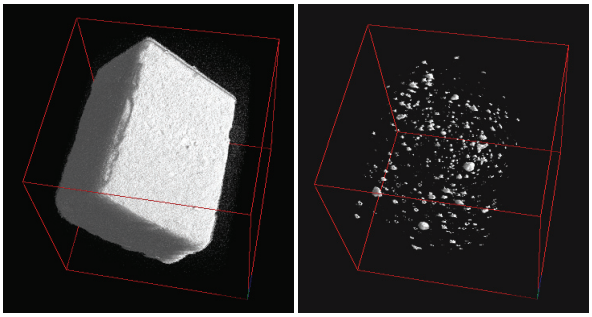

Fig. 10. 3-D reconstruction (left) and the distribution of the high density regions inside the volume of the sample of about 0.8 mm^3.

To identify what represent the dense regions, the high resolution X-ray digital radiography analysis was performed on the raw powder sample. The result is presented in Fig. 12. In order to have a dimensional/density reference, a wolfram wire of 5 μm diameter, was

placed on the sample. The radiography reveals high density regions, of above 2-3 μm diameter-size, spreaded in the sample. Same intensity of the W-wire and of the high density regions suggests that in the commercial as-received MgB_2 raw powder this element is present, most probably in the form of WC. We suppose that impurification occured during powders milling in the process of commercial MgB_2 raw powder preparation.

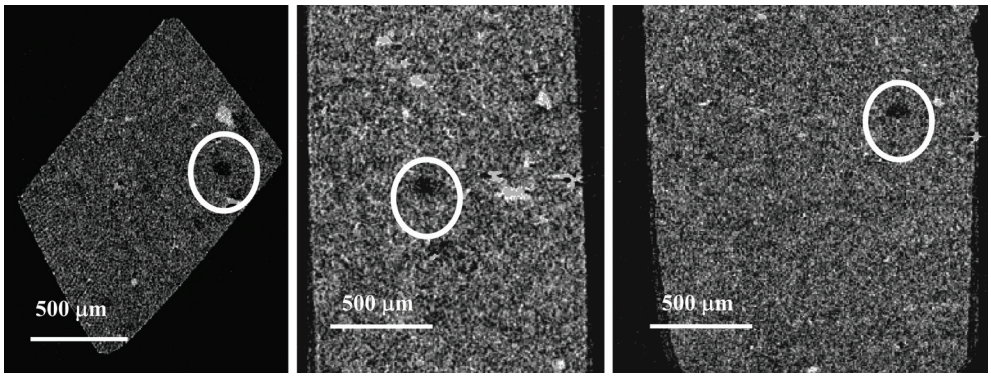

Fig. 11. Transversal, sagital and longitudinal cross-sections revealing low density region; low density region size (inside circles) is of about 130 μm.

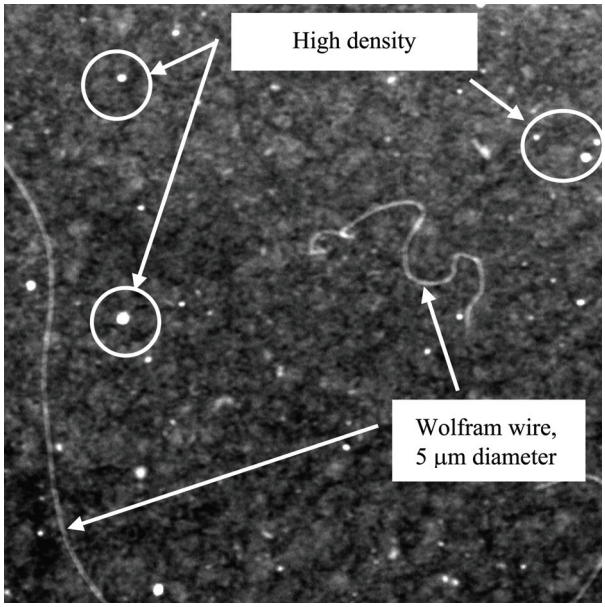

Fig. 12. Digital radiography of a MgB2 sample and a W-wire.

For the studies by SEM, for a comparative analysis with micro-tomographic experiments, the samples have been fractured to reveal their grains structure and morphology. Selected secondary electron image is shown in Fig. 13. One can observe dense polycrystalline pristine

SPS-processed MgB2 material with pores and grains of different form and size (Fig. 13). The pores of micrometer order are located at the grain boundaries. Apparently the observable size of the grains or sintered aggregates is of 0.2 – 2.5 μm. There are no significant differences that can be revealed by SEM among the 3 SPS-processed samples.

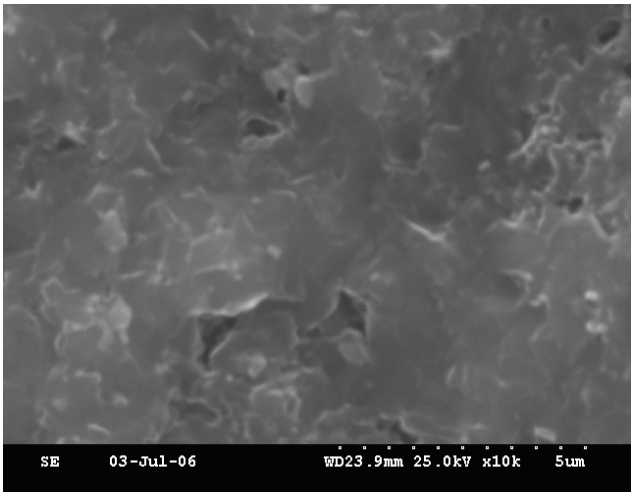

Fig. 13. Polycrystalline MgB_2 sample (×10.000).

Images of 3D tomographic reconstructions were observed in SiC- and B_4C- doped MgB_2 samples. In Fig. 14 it can be observed the diference of the local densities between three samples. Samples show some clear differences, but, they are not as large as in the case of the samples A-D presented in Section 3.1. Remarkable is that although the local density uniformity is much improved for the SPS-processed samples, this is not perfect and a lower quality is likely obtained for the samples with additions. Indeed, some superconducting parameters were superior for the pristine MgB_2 SPS-sample and detailed results were reported in [34].

4. Discussions and future trends

XRT is a useful and powerful technique to observe MgB_2 superconducting samples. Remarkable is that although the resolution is at the level of micrometers we investigated nanostructured MgB_2-based materials, and we got very useful information. We shall emphasize that one important limitation of the XRT is that it cannot give any information on crystal quality and composition. Therefore, this method is providing additional information, but it cannot replace the data from other measurements such as, e.g. structural ones (x-ray or electron diffraction) or those giving quantitative data on local composition (EDS, other). It is expected that with the improvement of the resolution more details can be observed. This is especially important for more uniform samples such as SPS-processed MgB_2-bulks. Such developments are expected also to help in advancing the understanding of the relationship between processing, XRT, conventional microscopy techniques and superconducting properties. Based on this, a new generation of MgB_2 tapes/wires for various applications with optimum, controlled or improved working parameters will be produced.

In this work we show that XRT can reveal in a non-invasive and convenient way the architecture of 3D MgB_2 composite objects (e.g. wires). This is an important advantage saving time and energy.

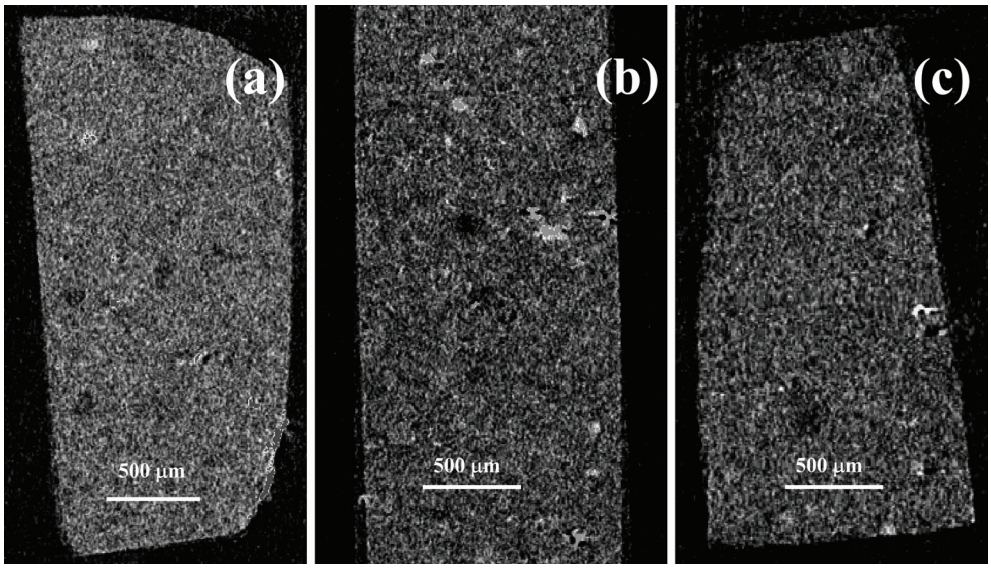

Fig. 14. Sagital cross-sections: (a) MgB_2 (MB), (b) SiC-doped MgB_2 (MBSC) and (c) C-doped MgB_2 (MBBC).

XRT is envisioned as a continuous and in-situ testing method of the quality of the MgB_2 bulks, wires, tapes (and in the future of thin films) and their products. For example, XRT will provide direct and real-time information during processing, fabrication or exploatation of a MgB_2-based product (e.g. fabrication of composite superconducting wires/tapes, formation of joints, coils winding, coils exploatation and so on).
XRT will bring also information on local chemical and phase composition and some positive results are already in progress.
XRT is not limited to MgB_2 and many other classes of materials can be investigated by this method. There is no doubt that XRT will become a key characterization technique in materials science and technology.

5. Conclusion

In summary, we applied XRT vizualization to MgB_2 bulks, tapes and wires. XRT provides powerful and unmached information by the conventional microscopy techniques on the local 3D density uniformity and distribution, connectivity, search and identification of the macrodefects, 3D-shape details of the macro defects and of the components from the composite MgB_2 wires or tapes, on the roughness and perfection of the intefaces between the components. Advantages, limitations and future development trends are discussed. We have also shown that XRT allows to evaluate at least qualitatively the architectural integrity and geometrical quality of the samples and this information can be related to

superconducting quality of the products. However, the details of this complex relationship remains unrevealed and the expectations are that with the improvement in the 3D XRT method one may understand more in this direction with much benefit in designing and fabrication of improved MgB_2 superconducting products.
The importance of pioneering the application of 3D non-invasive XRT on MgB_2 is general, i.e. XRT is expected to be applied with much success for many other materials, processing and fabrication processes, and to monitor the work of different products/systems.

6. Acknowledgements

Authors would like to acknowledge Prof. J. Groza from UC, Davis, US for SPS use, Dr. P. Nita from METAV CD, Romania for SEM measurements on wires, Prof. K. Togano from NIMS, Japan for the use of a SQUID (Quantum Design 5T) magnetometer, and J. Jaklovszky for the samples preparation for XRT. Prof. Y. Ma, Electrotechnical Institute, Chinese Academy of Science kindly provided MgB_2 tapes investigated in this work. Work at INCDFM was supported by ANCS-CNCSIS-UEFISCSU (CEEX 27/2005, PNII PCE 513/2009 and PNII PCCE 239/2008).

7. References

[1] Nagamatsu J, Nakagawa N, Muranaka T, Zenitani Y, Akimitsu J, *Superconductivity at 39 K in magnesium diboride*, Nature 410 (2001) 63.
[2] Picket W, *Mind the the double gap*, Nature 418 (2002) 733.
[3] Yang H, Liu Y, Zhuang C, Shi J, Yao Y, Massidda S, Monni M, Jia Y, Xi X, Li Q, Liu ZK, Feng Q, W HH, *Fully band-resolved scattering rate in MgB_2 revealed by nonlinear Hall effect and magnetoresistance measurements*, Phys. Rev. Lett. 101 (2008) 067001.
[4] Kortus J, Mazin II, Belashchenko KD, Antropov VP, Boyer LL, *Superconductivity of metallic boron in MgB_2*, Phys. Rev. Lett. 86 (2001) 4656.
[5] Caplin AD, Bugoslavsky Y, Cohen LF, Cowey L, Driscoll J, Moore J, Perkins GK, *Critical fields and critical currents in MgB_2*, Superconductor Science and Technology 16 (2003) 176.
[6] Xi XX, *MgB_2 thin films*, Superconductor Science and Technology 22 (2009) 043001 (review).
[7] Feldkamp LA, Davis LC, Kress JW, *Practical cone-beam algorithm*, J. Opt. Soc. Am. A 1-6 (1984) 612.
[8] Haibel A, Scheuerlein C, Synchrotron Tomography for the Study of Void Formation in Internal Tin Nb_3Sn Superconductors, IEEE Transactions on Applied Superconductivity 17(1) (2007) 34.
[9] Scheuerlein C, di Michael M, Haibel A, *On the formation of voids in internal tin Nb_3Sn superconductors,* Appl. Phys. Lett. 90 (2007) 132510.
[10] Tiseanu I, Craciunescu T, Mandache NB, *Non-destructive analysis of miniaturized samples and irradiation capsules by X-ray microtomography*, Fus. Eng. Des. 75–79 (2005) 1005.
[11] Tiseanu I, Craciunescu T, Petrisor P, della Corte A, *3D X-ray micro-tomography for modelling of Nb_3Sn multifilamentary superconducting wires*, Fus. Eng. Des. 82 (2007) 1447.
[12] Badica P, Aldica G, Craciunescu T, Tiseanu I, Ma Y Togano K, *Microstructure of MgB_2 samples observed by x-ray microtomography*, *Supercond. Sci. Technol.* 21 (2008) 115017

[13] Hammersberg P, Mangard M, *Correction for beam hardening artefacts in computerised tomography*, Journal of X-ray Science and Technology 8 (1998) 5.

[14] Van Geet M, Swennen R, Wevers M, *Quantitative analysis of reservoir rocks by microfocus x-ray computerised tomography*, Sedimentary Geology 132 (2000) 25.

[15] Tiseanu I, Simon M, Craciunescu T, Mandache BN, Volker Heinzel C, Stratmanns E, Simakov SP, Leichtle D, *Assessment of the structural integrity of a prototypical instrumented IFMIF high flux test module rig by fully 3D X-ray microtomography*, Fus. Eng. Des. 82 (2007) 2608.

[16] Kondo T, Badica P, Nakamori Y, Orimo S, Togano K, Nishijima G, Watamabe K, *MgB_2/Fe superconducting tapes using mechanically milled powders in Ar and H_2 atmospheres*, Physica C 426-431 (2005) 1231.

[17] Badica P, Kondo T, Togano K, Aldica G, *Superconducting MgB_2 ceramics and tapes prepared from mechanically milled powders*, J. Optoelec. Adv. Mater. 10 (2008) 2753.

[18] Ma Y, Zhang X, Nishijima G, Watanabe K, Awaji S, Bai XD, *Significantly enhanced critical current densities in MgB_2 tapes made by a scaleable nanocarbon addition route*, Appl. Phys. Lett. 88 (2006) 072502.

[19] Bean CP, *Magnetization of Hard Superconductors*, Phys. Rev. Lett. 8, (1962), 250

[20] Homepage of Hypertech Inc, USA: http://www.hypertechresearch.com/.

[21] Groza JR, ASM Handbook Vol. 7: *Powder Metal Technologies and Applications*, eds. Lee PW, Eisen WB, German RM (ASM International Handbook Committee, Ohio), pp. 583-589 (1998).

[22] Lee SY, Yoo SY, Kim YW, Hwang NM, Kim DY, *Preparation of Dense MgB_2 Bulk Superconductors by Spark Plasma Sintering*, J. Am. Ceram. Soc. 86, 1800 (2003).

[23] Song KJ, Park C, Kim SW, Ko RK, Ha HS, Kim HS, Oh SS, Kwon YK, Moon SH, Yoo S-I, *Superconducting properties of polycrystalline MgB_2 superconductor fabricated by spark plasma sintering,* Physica C 426-431 (2005) 588.

[24] Locci AM, Orru R, Cao G, Sanna S, Congiu F, Concas G, *Simultaneous Synthesis and Densification of Bulk MgB_2 Superconductor by Pulsed Electric Current, AIChE* Journal 52(7) (2006) 2618.

[25] S. Ueda, J. I. Shimoyama, A. Yamamoto, S. Horii, K. Kishio, *Enhanced Critical Current Properties Observed in Na_2CO_3 Doped MgB_2*, Supercond. Sci. Technol. 17 (2004) 926.

[26] Perner O, Eckert J, Hassler W, Fischer C, Muller KH, Fuchs G, Holzapfel B, Schultz L, *Microstructure and impurity dependence in mechanically alloyed nanocrystalline. MgB_2 superconductors*, Supercond. Sci. Technol. 17 (2004) 1148.

[27] Senkowicz BJ, Giencke JE, Patnaik S, Eom CB, Hellstrom EE, Larbalestier DC, *Improved upper critical field in bulk-form magnesium diboride by mechanical alloying with carbon*, Appl. Phys. Lett. 86 (2005) 202502.

[28] Dou SX, Soltanian S, Horvat J, Wang XL, Zhou SH, Ionescu M, Liu HK, Munroe P, Tomsic M, *Enhancement of the critical current density and flux pinning of MgB_2 superconductor by nanoparticle SiC doping*, Appl. Phys. Lett. 81 (2002) 3419.

[29] Jiang X, Ma Y, Gao Z, Yu Z, Nishijima C, Watanabe K, *The effect of different nanoscale material doping on the critical current properties of in situ processed MgB_2 tapes*, Supercond. Sci. Technol. 19 (2006) 479.

[30] Yamamoto A, Shimoyama J, Ueda S, Iwayama I, Horii S, Kishio K, *Effects of B_4C Doping on Critical Current Properties of MgB_2 Superconductor*, Supercond. Sci. Technol. 18 (2005) 1323.

[31] Chen W, Anselmi-Tamburini U, Garay JE, Groza JR, Munir ZA, *Fundamental investigations on the spark plasma sintering/synthesis process: I. Effect of dc pulsing on reactivity*, Mater. Sci. Eng. A 394 (2005) 132.

[32] Aldica G, Badica P, Groza JR, *Field-assisted-sintering of MgB_2 superconductor doped with SiC and B_4C*, J. Optoelec. & Adv. Mater. 9(6) (2007) 1742.

[33] Aldica Gh. –V., Nita P, Tiseanu I, Craciunescu T, Badica P, *High density MgB_2 superconductor: structure and morphology through microtomography and SEM investigations,* J. Optoelec. & Adv. Mater. 10(4) (2008) 929.

[34] Sandu V, Aldica G, Badica P, Groza JR, Nita P, *Preparation pure and doped MgB_2 by field-assisted-sintering technique and superconducting properties*, Supercond. Sci. Technol. 20 (2007) 836.

12

Synthesis and Thermophysical Characterization of Bismuth based High-T_c Superconductors

M. Anis-ur-Rehman[1] and Asghari Maqsood[2]
[1]*Applied Thermal Physics Laboratory, Department of Physics, COMSATS Institute of Information Technology, Islamabad 44000*
[2]*Thermal Transport Laboratory, SCME, National University of Sciences and Technology (NUST), Islamabad*
Pakistan

1. Introduction

Dissipation phenomena in high temperature superconductors are directed by the microstructure that builds up during the preparation process. Therefore, detailed investigations of the electrical and thermal transport and ac magnetic susceptibilities in superconductors prepared either in the form of single crystals, thin films or polycrystalline are important for understanding superconductivity as well as for useful applications.
The effect of elements (Pb, Fe, Co, Ni, V, Zn) doping in Bi-based superconducting materials has been extensively investigated (Remschnig et al., 1991; Awana et al., 1992; Maeda et al., 1990; vom Hedt et al., 1994; Pop et al., 1997; Mori et al. 1992; Kim et al., 1992; Gul et al., 2008; Maqsood et al., 1992). It was reported that the superconducting properties of these materials are affected with increase of the amount of doping, regardless of the nature of the dopants. The repression of superconductivity was concluded to be due to local disorder induced by the amount of doping. However, the details of the current limiting means in the Bi-2223 system are not well established. Consequently, it is of interest to try these doping elements in the Bi-2223 system with a different nominal composition, of which we intend to investigate $Bi_{1.6}Pb_{0.4}Sr_{1.6}Ba_{0.4}Ca_2Cu_3O_y$ in order to provide additional observations to contribute further understanding of their role on the superconductivity of the system.
It is well established that ceramic high-*T*c superconductors include a collection of tiny, randomly oriented anisotropic grains which are connected to each other by a system of so called 'weak links' or 'matrix'. The linear temperature dependence of the electrical resistivity is one of the most important characteristics of the normal phase kinetics of high-T_c layered cuprates (Batlogg, 1990).
In superconductors where the dc electrical resistivity diverges to zero below T_c, the thermal conduction is almost a unique measurement to study the transport properties below T_c. The magnitude and temperature dependence of the thermal conductivity are parameters which have an impact on a broad spectrum of devices. In high-T_C superconductors, such information is even more valuable to know how the free carriers and lattice vibrations contribute to the transport of heat. Transient Plane Source (TPS) technique is a well

developed and a well known method (Gustafsson, 1991; Maqsood, 1994; Maqsood, 1996) to study the thermal transport properties. For TPS method a single transition phase will be of great help to study such properties. Multiple phases, in the material, will make the situation more complicated and an increase in measurement errors also. The TPS technique is modified and improved for the measurements of thermal transport properties of high-T_c superconductors. The modified arrangement is referred to as the Advantageous Transient Plane Source (ATPS) technique (Rehman, 2002). The circuit components are reduced with this new arrangement as compared to the bridge used earlier (Maqsood, 2000). The modified bridge arrangement is already calibrated with fused quartz, carbon steel and AgCl crystals (Rehman, 2002; Rehman, 2003).

Peltier refrigerators use the thermoelectric materials for refrigeration. Peltier thermoelectrics are more reliable than compressor based refrigerators, and are used in situations where reliability is critical like deep space probes. Thermoelectric material applications include refrigeration or electrical power generation. Thermoelectric materials used in the present refrigeration or power generation devices are heavily doped semiconductors. The metals are poor thermoelectric materials with low Seebeck coefficient and large electronic contribution to the thermal conductivity. Insulators have a large Seebeck coefficient and a small contribution to the thermal conductivity, but have too few carriers, which result in a large electrical resistivity. The Figure of merit is the deciding factor for the quality of thermoelectric materials. In order to increase the whole Figure of merit, it is of interest to replace the p-type leg of the Peltier junction by a thermoelectrically passive material with a Figure of merit close to zero (Fee, 1993). This is why it is interesting to study the Figure of merit of the ceramic superconductors.

One of the important thermomagnetic transport quantities is the electrothermal conductivity and is shown to be one of the powerful probes of high-temperature superconductors. Cryogenic bolometers are sensitive detectors of infrared and millimeter wave radiation and are widely used in laboratory experiments as well as ground-based, airborne, and space-based astronomical observations (Richards, 1994). In many applications, bolometer performance is limited by a trade off between speed and sensitivity. Superconducting transition-edge bolometer can give a large increase in speed and a significant increase in sensitivity over technologies now in use. This combination of speed with sensitivity should open new applications for superconducting bolometric detectors (Leea et al., 1996).

Other potent applications for electrothermal conductivity of superconductors is actuators in MEMS technologies, electrothermal rockets etc (Microsoft Encarta Encyclopedia, 2003).

The temperature dependence of the dc electrical resistivity, along with low field ac magnetic susceptibility, X-ray diffraction, thermal transport, electrothermal conductivity and thermoelectric power studies and calculations of Figure of merit factor are reported here.

2. Experimental

2.1 Preparation and characterization

In the Bi-based high-T_c superconductors the Bi-2223 phase is stable within a narrow temperature range and exhibits phase equilibrium with only a few of the compounds existing in the system (Majewski, 2000). Precise control over the processing parameters is required to obtain the phase-pure material (Balachandran et al., 1996). All samples were prepared from 99.9% pure powders of Bi_2O_3, PbO, $SrCO_3$, $BaCO_3$, $CaCO_3$ and CuO. The powders were mixed to give nominal composition of $Bi_{1.6}Pb_{0.4}Sr_{1.6}Ba_{0.4}Ca_2Cu_3O_y$ and were thoroughly ground in an

agate mortar to give very fine powder. The grind powder was calcined for 21 hours in air at 800°C. A series of pellets was produced in two sizes, from this well mixed material and controlled heating and cooling carried out, in air, using a horizontal tube furnace. Poly Vinyl Alcohol (PVA) was used as binder in the samples. PVA is one of the few high molecular weight polymers, which is water soluble and is dry solid, commercially available in granular or powder form. The properties of Poly Vinyl Alcohol vary according to the molecular weight of the parent poly vinyl acetate and the degree of hydrolysis. Fully hydrolyzed form with medium viscosity grade PVA was used in our case. Samples were in the shape of cylindrical disks having diameters 13mm and 28mm, and lengths 3mm and 11mm respectively. These samples were sintered at 830°C for the intervals of 24 hours in each sintering step as sintering procedures do affect the properties (Rehman et al., 1998).

The superconducting properties were characterized electrically by using standard four probe method. Contacts were made by high quality silver paste. The temperature was measured by using a calibrated Pt-100 thermometer.

Low field ac susceptibility measurements are very important for the characterization of high-temperature superconductors (Chen et al., 1989; Muller, 1989; Ishida & Goldfarb, 1990; Celebi, 1999). The sharp decrease in the real part χ' (T) below the critical temperature T_c is a manifestation of diamagnetic shielding. Ac susceptibility of the sample was measured after each sintering step. The low field ac susceptibility properties were studied by the use of mutual inductance bridge method. The measurements were taken from room temperature down to 80K.

X-ray diffractograph (XRD) of sample was taken after the final sintering. The radiation used for XRD was CuK_α and the measurements were made at room temperature. Measurements were done at room temperature since there is no change in the structure of the superconducting materials before and after transition (Rehman et al., 1998; Jasiolek et al. 1990).

2.2 Thermal transport properties

Thermal transport measurements, i.e. thermal conductivity, thermal diffusivity and heat capacity per unit volume were performed using the Advantageous Transient Plane Source (ATPS) Technique (Rehman & Maqsood, 2002; Rehman & Maqsood, 2003). Circuit diagram for the method is shown in Fig. 1. Simultaneous measurement of thermal conductivity and thermal diffusivity is the foremost advantage of this technique. Heat capacity per unit volume is then calculated using the idea that, if all heat is transported via solid specimen then the thermal conductivity (λ), thermal diffusivity (κ) and heat capacity per unit volume (ρC_p) are expressed by;

$$\kappa = \frac{\lambda}{\rho C_p} \tag{1}$$

A detailed description of this experimental technique can be found elsewhere (Gustafsson, 1991). The ideal model presupposes that the double spiral sensor, assumed to consist of a set of equally spaced, concentric, and circular line heat sources, is sandwiched in specimens of infinite dimensions. In practice all real specimens do have finite dimensions. However, by restricting the time of the transient, which relates to the thermal penetration depth of the transient heating, a measurement can still be analyzed as if it was performed in an infinite medium. This means that the ideal theoretical model is still valid within a properly selected

time window for the evaluation. The scatter in thermal conductivity measurements is about 0.14% and is 0.66% and 0.52% in thermal diffusivity and volumetric heat capacity respectively (Rehman & Maqsood, 2002; Rehman & Maqsood, 2003). Taking into consideration the limitations of the theory of the technique and the experimental sampling errors, the thermal conductivity and thermal diffusivity data contain errors of 4% and 7% respectively. The errors in volumetric heat capacity are around 10% (Rehman & Maqsood, 2002; Maqsood et al., 2000; Rehman & Maqsood, 2003).

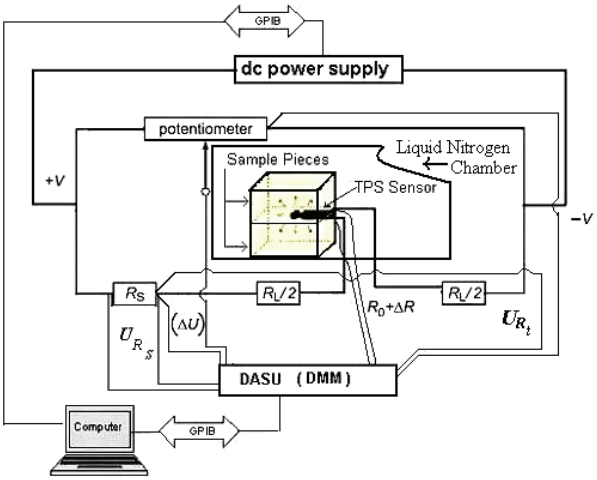

Fig. 1. Circuit diagram for the Advantageous Transient Plane Source (ATPS) technique

2.3 Thermoelectric power measurements

An easy to use and simple apparatus was designed and developed for thermoelectric power (S) measurements. Circuit diagram along with the sample holder assembly is shown in Fig. 2. The sample is subjected to a temperature difference ΔT using a heating resistor and corresponding voltage difference ΔV across the sample is measured. Thermoelectric power is obtained by taking ratio of the voltage difference to the temperature difference. Chromel-alumel thermocouples are used for measuring the temperature difference, ΔT. The thermocouples are electrically isolated from the sample and thermally connected to the sample. Heat losses through the electrical connections are minimized using long leads wrapped around a Teflon tube. The voltage leads are then silver pasted to the sample in the vicinity of thermocouples to assure that the voltage and temperature gradients are measured at the same locations on the sample for accurate thermoelectric power measurements. The next step includes loading the sample assembly into the sample chamber and evacuation of the chamber. The chamber is evacuated to eliminate any water vapour condensation on the sample, which can result in erroneous measurements. Dry nitrogen gas is then filled in the chamber as a conducting media between chamber walls and the sample. This sample chamber is then inserted in liquid nitrogen container for cooling. Data are collected under the computer control. By incorporating multiple measurements in a single run, considerable time is saved by avoiding remounting, and recooling of the samples. In this technique the surface mount resistor (50Ω) was used to heat one end of the sample to establish a measured temperature gradient of approximately 1K.

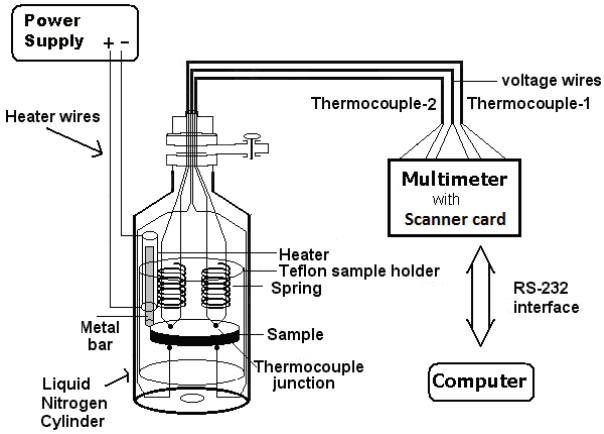

Fig. 2. Block diagram of the apparatus developed for thermoelectric power measurements. Scanner card is used with the multimeter for simultaneous measurements at different points as shown. RS-232 is the standard serial interface of the computer

3. Experimental results and discussion

3.1 Dc electrical resistivity

Variation of resistivity with change in temperature is recorded for after each sintering step and the plots are given in Fig. 3.

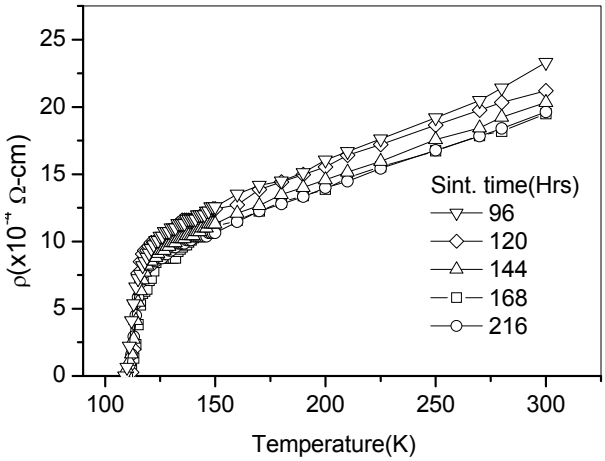

Fig. 3. DC electrical resistivity as a function of temperature for the sample after each sintering step

One of the most striking features about the cuprate superconductors is the behavior of the resistivity of the normal state that is found above the transition temperature of the optimally doped materials. After the final sintering the measured density of the sample was 3.48 gcm^{-3} and $T_{c,0}$ was 110 ± 1K. The added barium (Ba) has increased the $T_{c,0}$. Residual resistivity was

0.19 mΩ-cm and the intrinsic resistivity was 5.9 μΩ-cmK^{-1}. The ratio ρ(273K)/ρ(4.2K) is the residual resistivity ratio (RRR), an important parameter in the design of superconductive applications. In the case of a superconductor, the denominator has to be taken at a temperature slightly above the critical temperature (Seeber, 1998). RRR in our case was in the range 23-33.

3.2 Ac susceptibility

Ac susceptibility measurements were done after each sintering step (Fig. 4).

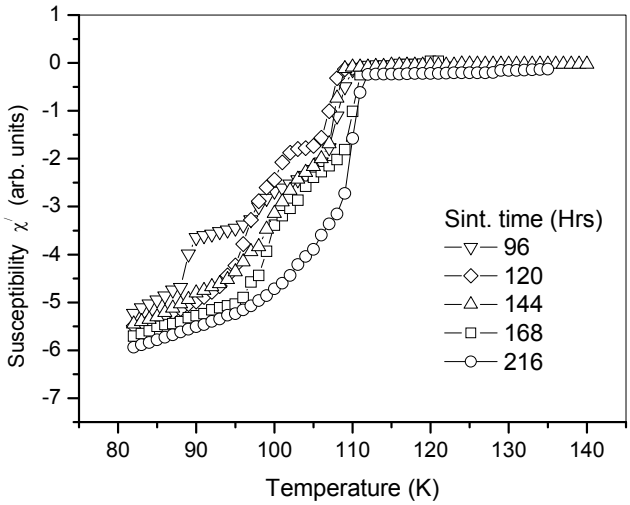

Fig. 4. Variation of ac susceptibility (real part), with temperature after each sintering step

Initially two transition phases were present. One of the identified phases is the Bi-2212(low T_c) phase and the other Bi-2223(high T_c) phase. With sintering, the low T_c phase was smoothed out and only phase left is the Bi-2223(high-T_c) phase. Although the resistivity variation with temperature was smoothed out after the third sintering but slight kinks were observed in the susceptibility against temperature plot showing the more sensitivity of the measuring method.

3.3 X-ray diffraction studies

Almost all the peaks are indexed. The only phase is the orthorhombic high-T_c Bi-2223 phase. Lattice parameters were calculated from the (h k l) values of the indexed peaks. The lattice parameters are a = 5.42 (1) Å, b = 5.37 (1) Å and c = 37.12 (8) Å. No peaks were found matching the Bi-2212 low T_c phase. Indexed X-ray diffractograph is shown in Fig. 5.

The lattice constants agreed with the previous reports (Maqsood et al., 1996). The size of the grains in polycrystalline materials has pronounced effects on many of its properties. Using Scherrer's equation [29];

$$B = \frac{0.9\lambda}{t\cos\theta} \tag{2}$$

where;
B = Broadening of diffraction line measured at half its maximum intensity (radians), λ = Radiation source wavelength and t = Diameter of crystal particle,
particle sizes are determined and the diameter of the crystal particles lies between 172 – 512 Å.

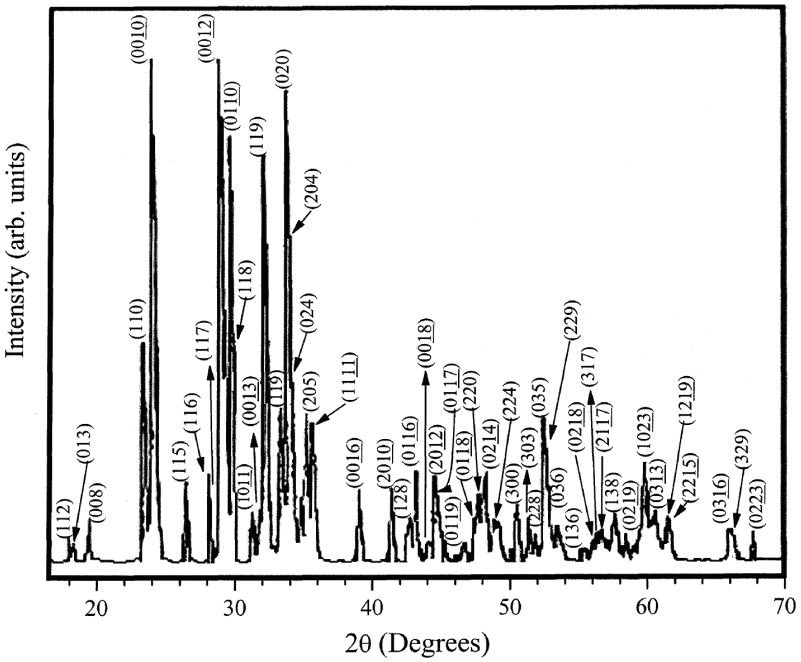

Fig. 5. Indexed x-ray diffraction pattern of the sample after the final sintering at room temperature

3.4 Thermal properties measurements

After the preliminary characterization of the samples and existence of almost a single phase, large disc-shaped samples (28 mm diameter and 11 mm thickness) were used for the thermal measurements. Fig. 6 shows the temperature dependence of the thermal conductivity λ. As the temperature decreases, the conductivity gradually decreases down to near T_c then remarkably increases below T_c. Further decrease in temperature was not possible, due to limitation of the cryostat used, to take the maximum in λ. This temperature dependence agrees with the widely observed behavior of λ for the oxide superconductors (Uher & Kaiser, 1987; Peacor & Uher, 1989; Mori et al., 1989; Crommie & Zettle, 1990; Cohn et al., 1992).

Comparing the results between different laboratories, one notes that the thermal conductivity depends on a particular sample preparation process. The temperature dependence of the conductivity is really similar for all the samples (Ginsberg, 1992; Ikebe et al. 1994) . So the order of magnitude of thermal conductivity (measured by non-steady state

method in our case) is comparable to the results obtained by different authors (measured by steady state methods).

Fig. 6 also shows the variation of measured thermal diffusivity κ with temperature for the sample. Between 294K and T_c, κ increases very gradually with decreasing temperature. The increase of κ becomes very large around T_c and become very steep.

The heat capacity per unit volume, ρC_p, calculated from the thermal conductivity measurements and thermal diffusivity measurements using equation 1 is shown in Fig. 6. ρC_p decreases with decrease in temperature and near T_c a sizeable kink is observed. This jump is mostly due to the improved sharpness of the transition related to the reduction of

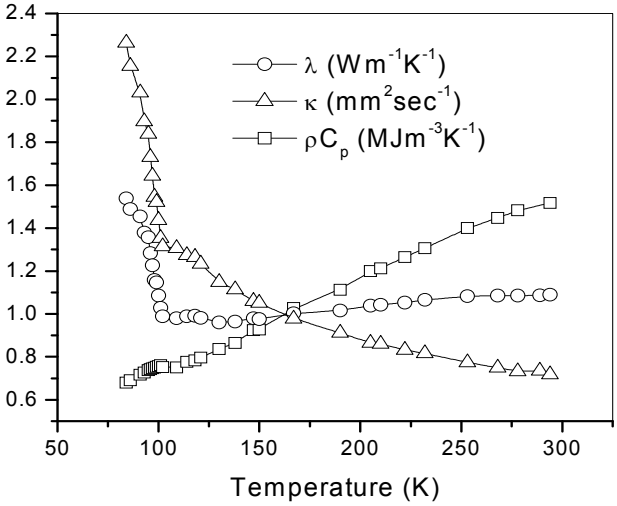

Fig. 6. Variation in thermal transport properties with temperature for the sample $^{Bi}_{1.6}{}^{Pb}_{0.4}{}^{Sr}_{1.6}{}^{Ba}_{0.4}{}^{Ca}_{2}{}^{Cu}_{3}{}^{O}_{y}$

intergrowth structure by adding Pb (Okazaki et al., 1990) and is improved by adding Ba in our case. Since the calculated lattice constants of our sample are similar to Bi-2223 composition so it is assumed that oxygen is 10, and then the composition becomes $Bi_{1.6}Pb_{0.4}Sr_{1.6}Ba_{0.4}Ca_2Cu_3O_{10}$. Also there is no change in the density of the superconducting sample in the studied temperature range so the value of specific heat C_p is calculated. The absolute value of C_p is 320 $Jmol^{-1}K^{-1}$ at 180K and that is similar to already reported value of a similar composition (Okazaki et al. 1990; Gordon et al. 1991). Because the phonon contribution is by far dominant than the electronic contribution in the temperature range studied, the specific heat data fitted to the following Debye formula,

$$C_{p-ph} = 9nR\frac{T^3}{\Theta_D^3}\int_0^{\Theta_D/T}\frac{x^4 e^x}{(e^x-1)^2}dx \tag{3}$$

where $C_{p\text{-}ph}$ is molar specific heat, x is the reduced phonon frequency, n (= 19) the number of atoms composing Bi(Ba) 2223 molecules, R the gas constant and Θ_D is the Debye temperature. Although a single Θ_D fitting fails to give a unified strict fitting over the entire temperature range, but Θ_D = 510 K gives a satisfactory fitting between T = 120 to 230 K as is shown in Fig. 7.

3.5 Thermoelectric power

To check the calibration of this new apparatus (Fig. 2), thermoelectric power of copper was measured in the temperature range 85-310K. Results of our measurements are shown in Fig. 8 indicating an agreement with the already published data (Barnard, 1972).

The standard deviation in the data was between 0.01-0.22 μVK^{-1} and the difference between measurements done in this work and the already published (Barnard, 1972) data were within 5%.

The thermoelectric power of the high-T_C superconducting sample was measured in temperature range 85-300K. The thermoelectric power (S) reached zero within experimental uncertainty in superconducting state. The thermoelectric power increased with decrease in temperature and after reaching T_c value, thermoelectric power decreased strongly to zero value (Fig. 9).

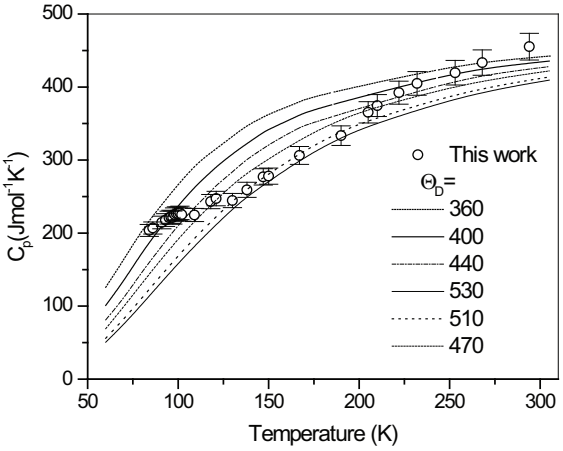

Fig. 7. The specific heat estimated from thermal conductivity (λ) and thermal diffusivity (κ). Calculated values for different values of Θ_D are also shown.

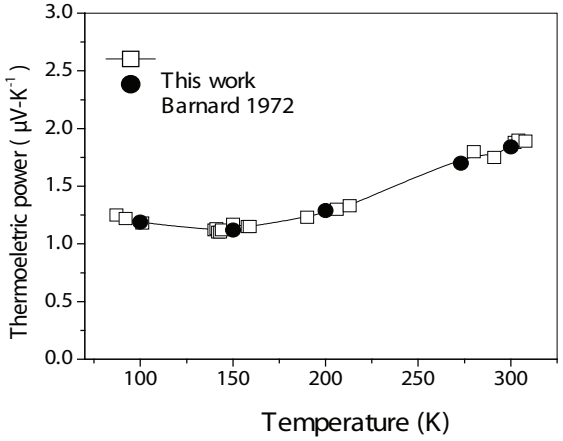

Fig. 8. Thermoelectric power of the copper sample with temperature.

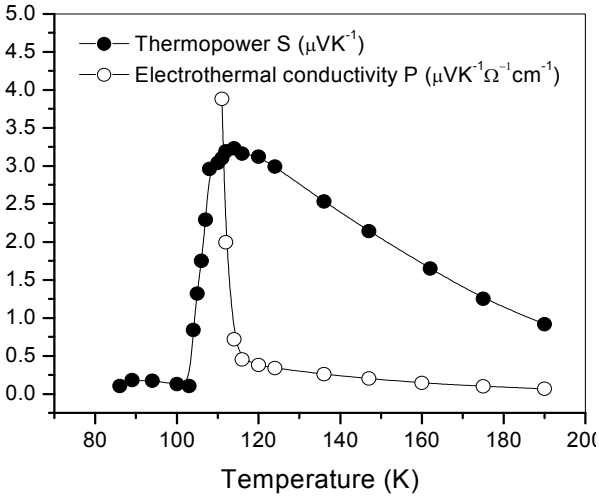

Fig. 9. Variation of thermoelectrical power (S) and electrothermal connductivity (P) with temperature for the sample

At high temperatures the thermoelectric power is almost linear. Thus we can use the Mott expression to determine the Fermi level (Barnard, 1972; Bougrine et al., 1998):

$$S = S_0 - \frac{\pi^2 k_B^{\,2}}{3 \mid e \mid E_F} T \tag{4}$$

where S_0 is a constant. From the slope (-0.03145 μV / K²) estimated by a linear extrapolation we have found the Fermi level to be 0.78 eV.

Similar profile for the same kind of superconductors is reported (Mitra et al., 1998; Chen et al., 1989; Laurent et al., 1989; Lopez et al., 1991; Naqvi et al., 1997; Pekala et al. 1996).

3.6 Electrothermal conductivity

The electrothermal conductivity (P) is the thermoelectric power divided by the dc electrical resistivity and is given as,

$$P = \frac{S}{\rho} \tag{5}$$

Where S is the thermoelectric power and ρ is the dc electrical resistivity.

In the mixed state of a superconductor, the electrothermal conductivity is also defined as the measure of the electrical current density produced by a thermal gradient and is supposed to be independent of the magnetic field. We have utilized the former definition to calculate electrothermal conductivity as shown in Fig. 9.

3.7 Figure of merit

Using the data of electrical resistivity, thermal conductivity and thermoelectric power, Figure of merit factor is calculated and is plotted in Fig. 10.

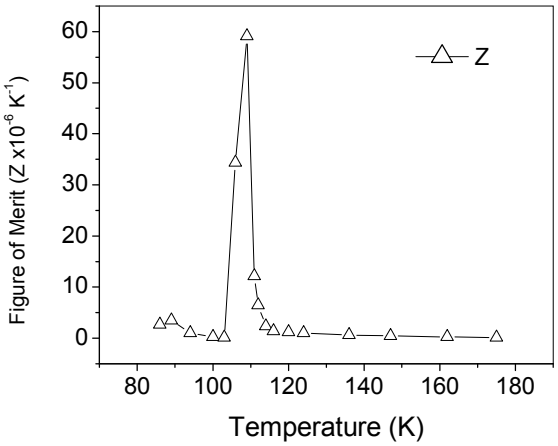

Fig. 10. Variation of Figure of Merit Factor (Z), with temperature.

The Figure of merit is calculated from the expression (Bougrine et al., 1998),

$$Z(T) = \frac{S^2(T)}{\lambda(T)\rho(T)} \tag{6}$$

Where: Z(T) is the Figure of merit factor, S(T) is the thermoelectric power, λ(T) is the thermal conductivity and ρ(T) is the electrical resistivity.

Near critical temperature the Figure of merit present a remarkable peak for the samples. This peak is due to a quick drop in the electrical resistivity which occurs about 3K before the drop in thermoelectric power. Outside the critical temperature region one can see that the curves of the Figure of merit and thermoelectric power are characterized by a similar behaviour near T_c. Similar trend of the Figure of merit is observed in the Bi-based high-T_c superconductors (Bougrine et al., 1998).

4. Summary and conclusions

The samples with nominal composition $Bi_{1.6}Pb_{0.4}Sr_{1.6}Ba_{0.4}Ca_2Cu_3O_Y$ were synthesized by a solid state reaction method with controlled synthesis process to get the preferred single phase. This composition was chosen on the basis of experiments conducted by the authors with a similar composition (Maqsood et al., 1992). The samples were almost a single phase with Bi-2223 high-T_c phase recognized. All the three types of tests i.e. dc electrical resistivity, ac magnetic susceptibility and x-ray diffraction are in conformity with each other, all validating almost a single Bi-2223 high-T_c phase. Single transition phase in the material and fabrication of homogenous samples in large sizes favored the Advantageous Transient Plane Source (ATPS) technique for thermal transport measurements. Thermal transport properties include thermal conductivity, thermal diffusivity and heat capacity per unit volume. Synchronized measurement of thermal conductivity and thermal diffusivity makes it possible to estimate specific heat and the Debye temperature Θ_D. The simultaneous measurement also provides a useful check on the consistency and the reliability of the analyses. Thermal conductivity variation with temperature shows slight decrease initially

and then a pronounced increase around T_c. A similar behaviour is observed in all hole-type CuO_2-plane superconductors and in all their structural forms. This effect is due to phonon (Tewordt & Wolkhausen, 1988) or quasiparticle scattering (Houssa and Ausloos, 1994). Thermal diffusivity shows a similar tendency as that of the thermal conductivity. Heat capacity per unit volume decreases with decrease in temperature. Assuming density of the sample to be constant in the studied temperature range molar specific heat is also calculated. Specific heat jump around T_c is also very prominent. These results indicate a good crystalline structure and the most favorable doping. Thermoelectric power was positive in the studied bismuth-based superconductor. The behavior of thermoelectric power of the sample was approximately linear with temperature as observed in other bismuth-based high-T_C superconductors. The superconducting transition started at 114±1K and after that, thermoelectric power reduced almost to zero value at 103±1K. The known value of the transition temperature of this sample measured from electrical resistivity was 110±1K. Therefore, the difference between thermoelectric transition temperature and resistivity transition temperature were almost in agreement within experimental errors. Electrothermal conductivity increases sharply near the transition temperature. A maximum in the Figure of merit, of this ceramic superconductor, is around the superconducting transition temperature. It is then reduced to zero below critical temperature. This system can be valuable for application in low-temperature Peltier devices in order to reach temperatures lesser than the temperature of liquid nitrogen.

5. References

Awana V.P.S., Agarwal S.K., Kumaraswany B.V., Singh B.P., Narlikar A.V. (1992). *Supercond. Sci. Technol.* 5 376.

Balachandran U., Iyer A.N., Haldar P., Hoehn J.G., Motowidlo L.R., H Maeda, Togano K. (1996). (Eds.), *Bi-Based High-T_c Superconductors*, Marcel Decker Inc., New York

Barnard R.D. (1972) *Thermoelectricity in metals and alloys*, Taylor & Francis Ltd., London,

Batlogg B. (1990). *High temperature superconductivity*, Addison-Wesley, Redwood city, CA

Bougrine H., Ausloos M., Cloots R., Pekala M. (1998) Proc. 17th International conference on thermoelectrics, IEEE

Celebi S. (1999). *Physica C* 316 251

Chen G.H., Yang G., Yan Y.F., Jia S.L., Ni Y.M., Zheng D.N., Yang Q.S., Zhou Z.X. (1989). *Mod. Phy. Lett. B* 3 1045

Chen D.X., Nogues J., Rao K.V.(1989). *Cryogenics* 29 800

Cohn J.L., Wolf S.A., Vanderah T.A. (1992). *Phys. Rev. B* 45 511.

Crommie M.F., Zettle A. (1990). *Phys. Rev. B* 41 10978.

Cullity B.D. (1967). *Elements of X-ray diffraction* 3rd ed., Addison-Wesley Publishing Company, Inc., London

Fee M. (1993). *Appl. Phys. Lett.* 62 1161

Ginsberg D.M. (1992). *High Temperature Superconductivity*, World Scientific Publishing Co. Pte. Ltd.

Gordon J.E., Prigge S., Collocott S.J. , Driver R. (1991). *Physica C* 185-189 1351

Gul I.H., Maqsood A. (2008). *J. Supercond. Nov. Magn.* 399-407 21.
Gustafsson S.E. (1991). *Rev. Sci. Instrum.* 62 797
Houssa M., Ausloos M. (1994). *Physica C* 235 1483
Ikebe M., Fujishiro H., Naito T., Noto K. (1994). *J. Phys. Soc. Japan.* 63 3107
Ishida T., Goldfarb R.B. (1990). *Phys. Rev. B* 41 8937
Jasiolek G., Gorecka J., Majewski J., Yuan S., Jin S., Liang R. (1990). *Supercond. Sci. Technol.* 3 194
Kim S.H., Kim H.S., Lee S.H., Kim K.H. (1992). *Solid State Commun.* 83 127
Laurent C., Patapi S.K., Green S.M., Luo L., Politis C., Durczewski K., Ausloos M. (1989). *Mod. Phy. Lett. B* 3 241.
Leea A.T., Richards L.P., Nam S.W., Cabrera B., Irwin K.D. (1996). *Appl. Phys. Lett.* 69 12
Lopez A.J., Maza J., Yadava Y.P., Vidal F., Garcia-Alvarado F., Morán E., Senaris-Rodriguez M.A. (1991). *Supercond. Sci. Technol.* 4 S292
Maeda A., Yabe T., Takebayashi S., Hase M., Uchinokura K. (1990). *Phys. Rev. B* 41 4112
Mitra N., Trefny J., Yarar B., Pine G., Sheng Z.Z., Hermann A.M. (1988). *Phys. Rev. B* 38 7064.
Majewski P. (2000). J. *Mater. Res.* 15 4.
Maqsood A., Amin N., Maqsood M., Shabbir G., Mahmood A., Gustafsson S.E. (1994). *Int. J. Energy Res.* 18 777.
Maqsood M., Arshad M., Zafarullah M., Maqsood A. (1996). *J. Supercond. Sci. Technol.* 9 321.
Maqsood A., Khaliq M., Maqsood M. 1992). *J. Mat. Sci.* 27 5330
Maqsood A., Rehman M.A., Gumen V., Haq A. (2000). *J. Phys D: Appl. Phys.* 33 2057.
Microsoft Encarta Encyclopedia. (2003). Microsoft Corporation, USA
Mori N., Wilson J.A., Ozaki H. (1992). *Phys. Rev. B* 45 10633.
Mori K., Sasakawa M., Igarashi T., Isikawa Y., Sato K., Noto K., Muto Y. (1989). *Physica C* 162 512.
Muller K.H. (1989). *Physica C* 159 717.
Naqvi S.M.M.R., Rizvi S.D.H., Rizvi S., Raza S.M. (1997). Proc. *5th International Symposium on Advanced Materials*, Islamabad
Okazaki N., Hasegawa T., Kishio K., Kitazawa K., Kishi A., Ikeda Y., Takano M., Oda K., Kitaguchi H., Takada J., Miura Y. (1990). *Phys. Rev. B* 41 4296
Peacor S.D. , Uher C. (1989). *Phys. Rev. B* 39 11559
Pekala M., Tampieri A., Celotti G., Houssa M., Ausloos M. (1996). *Supercond. Sci. Technol.* 9 644.
Pop A.V., Deltour R., Harabor A., Ciurchea D., Ilonca Gh., Pop V., Todica M. (1997) . Supercond. Sci. Technol. 10 943.
Rehman M.A., Maqsood A. (2002). *J. Phys D: Appl. Phys* 35 2040.
Rehman M.A., Maqsood A. (2003). *Int. J. of Thermophys.* 24 867.
Rehman M.A., Maqsood M., Ahmad N., Maqsood A., Haq A. (1998). *J. Mat. Sci.* 33 1789.
Remschnig K., Tarascon J.M., Miceli P.F., Hull G.W. (1991). *Phys. Rev. B* 43 5481
Richards P.L. (1994). *J. Appl. Phys.* 76 1.
Seeber B. (1998). *Handbook of Applied Superconductivity* vol. 1, Institute of Physics Publishing, Bristol and Philadelphia
Tewordt L., Fay D., Wolkhausen Th. (1988). *Solid State Commun.* 67 301.

Uher C., Kaiser A.B. (1987). *Phys. Rev. B* 36 5680.
vom Hedt B., Lisseck W., Westerholt K., Bach H. (1994). *Phys. Rev. B* 49 9898.

13

Development of Large Scale $YBa_2Cu_3O_{7-x}$ Superconductor with Plastic Forming

Makoto Takahashi[1], Sadao Ohkido[2] and Kouichi Wakita[3]
[1]*Department of Applied Chemistry, College of Engineering,*
[2]*Department of Natural Science and Mathematics, College of Engineering,*
[3]*Department of Electronic Engineering, College of Engineering,*
Chubu University, Matsumoto-cho 1200, Kasugai, Aichi 487-8501, Japan

1. Introduction

As superconducting oxides with a critical temperature above 77 K were discovered in 1986[1], subsequent developments and research into superconducting materials such as $YBa_2Cu_3O_{7-x}$ and $Bi_2Sr_2CaCu_2O_x$ have been widely carried out. Depending on the application, superconducting materials have been prepared as pellets, wires, or films. In order to synthesize products, numerous approaches have been tried using a variety of synthesis technologies, such as melt-powder-melt growth (MPMG)[2], and quench and melt growth (QMG)[3]. In order to produce a large bulk sample with these methods, the equipment must be remodeled to fit the sample size. This limits the size of the samples that can be produced. For thin films, several methods have been used such as the sol–gel method[4], metalorganic chemical vapor deposition (MOCVD)[5], pulsed laser deposition[6]. However, it is difficult to produce thick and large samples with various three-dimensional structures by these methods. Large bulk superconducting materials for making magnetic shielding for use in magnetic resonance imaging (MRI) cannot be produced by the above techniques. Therefore, a technique for easily and inexpensively making a large bulk superconductor is highly desired.

Plastic forming is very simple method and has been widely used for producing ceramics. However, there have been few papers about the preparation of bulk superconductor with using plastic forming. In the plastic forming, the slurry is prepared with kneading the mixture of ceramic powder, binder, dispersant and solvent. Polyvinyl alcohol (PVA), poly ethylene glycol, clay, sodium silicate and alumina colloid are used as the organic or inorganic binder. The addition of several % these binders to the slurry improves the forming performance of the green body and the homogenization properties of the sintered sample. Surfactants or sodium diphosphate are used as organic or inorganic dispersant. After firing, the organic binder and dispersant above described may be left in the sample as some kind of impurity. It is also known that the residual carbon and other impurities exist along the grain boundary and influence the electrical and mechanical properties. It was reported that the residual carbon decreased the superconducting properties, especially the critical current density [7]. Therefore, the plastic forming has not been used to make the bulk superconductor sample, because the used slurry includes many impurities.

When the large bulk superconductor samples are made by the plastic forming, we think next matters are important.

1. Making the particle size of ceramic powders the same size.
2. Making the particle size of inorganic binder the same size.
3. Removing useless materials (act as impurities) from the slurry.

In this book, we introduce how to make the large scale $YBa_2Cu_3O_{7-x}$ superconductor with plastic forming.

2. Preparation and characterization

2.1 Preparation process for $YBa_2Cu_3O_{7-x}$ slurry and bulk $YBa_2Cu_3O_{7-x}$ sample and measurements.

Figure 1 shows the preparation procedure for the $YBa_2Cu_3O_{7-x}$ bulk sample. Calcined $YBa_2Cu_3O_{7-x}$ powder was prepared by firing a mixture of Y_2O_3 (purity 99.99%), $BaCO_3$ (purity 99.9%), and CuO (purity 99.99%) at 1223 K in air. The $YBa_2Cu_3(OH)_x$ precursor was synthesized by hydrolyzing an ethanol solution containing $Y(OC_3H_7)_3$ (purity 99.9%), $Ba(OC_3H_7)_2$ (purity 99.9%), and $Cu(CH_3COO)2$ (purity >95%) at a molar ratio of 1:2:3. The precursor was refined with absolute ethanol after precipitation and filtration. Sol solutions were prepared by suspending the refined precursor in the solution at various PVA concentrations using an ultrasonic cleaner. PVA with an average molecular weight of 22 000 (degree of polymerization5500) was dissolved in warm water (at 40 – 45°C) and the solution was equilibrated to room temperature[8].

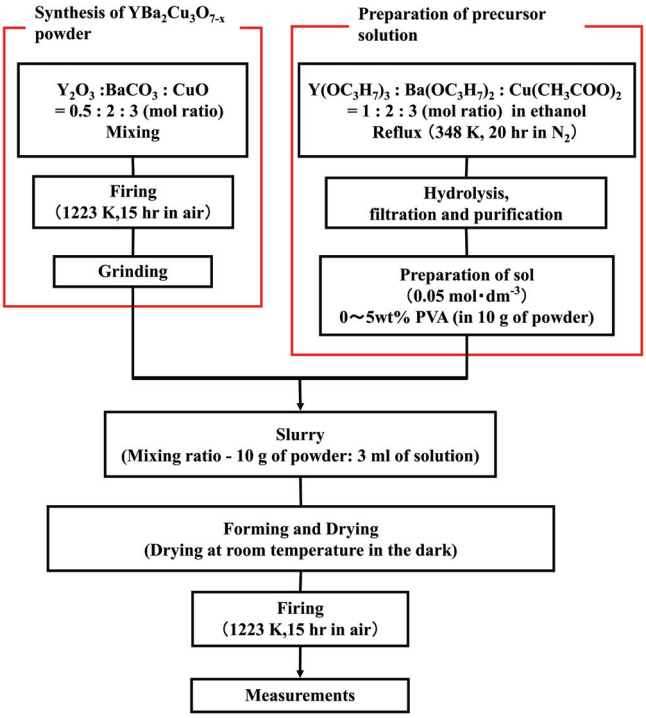

Fig. 1. Preparation procedure for YBa2Cu3O7-x slurry and bulk sample.

Green sheet samples (about 80 mm x 80 mm x 3 mm) were made using the slurry prepared by mixing 10 g of $YBa_2Cu_3O_{7-x}$ powder (average diameter 0.15 mm) and 3 ml of 0.05 mol/dm^3 precursor solution (average diameter of precursor particle: 380 nm) (kneading time: 50–60 min). After being dried in the shade at room temperature for 6 days, the sample was fired in an electric furnace at 1223 K for 15 h in air. The heating rate was set to about 50 K/h and the cooling rate to about 90 K/h up to about 440 K.

The crystal structures of the samples were measured by the X-ray diffraction (XRD) method (Rigaku Co., Ltd., Mini Flex, Tokyo, Japan) using CuKα1(0.154 nm) radiation. The surface morphology and composition of the samples were examined using a scanning electron microscope (SEM) (Hitachi High-Technologies Corporation, S-3500N, Tokyo, Japan) at an accelerating voltage of 15 kV. Standard four-probe DC electrical measurements using a 10 mA constant current were carried out in a flow cryostat operated over a temperature range of 50–300 K in a vacuum of 10^{-4} Torr. The degrees of dependence of the Jc on the magnetic field strength were evaluated using magnetization curves (M–H curves) and the Bean equation [Jc=30(⊿MH/d), in which ⊿MH is the width of M–H hysteresis and d is the sample thickness]. M–H curves were measured using a vibrating sample magnetometer (VSM) at 77 K[9]. The magnetic field was changed from -1.0 to +1.0 T. The values plotted in the figure are the average values for at least three and up to five samples that were grown under the same set of conditions.

2.2 The effect of PVA on the shaping of samples

Figure 2 shows photographs of green sheets and sintered samples prepared from the slurry with (1) 0 and (2) 1 wt% PVA.

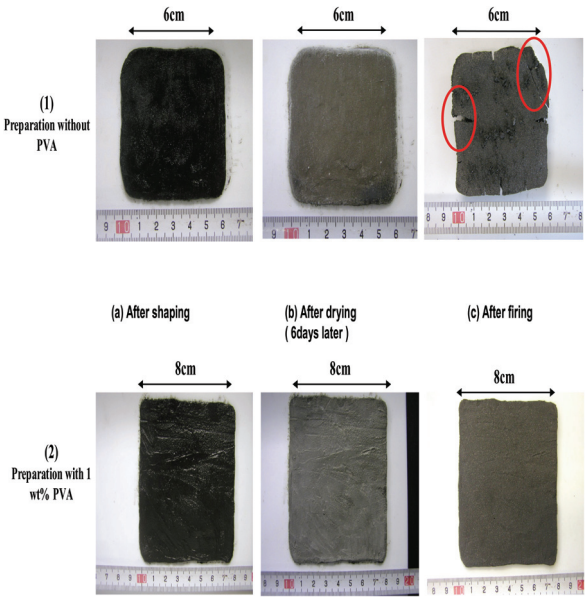

Fig. 2. The effect of PVA on the shaping of sample. Photographs of the samples prepared from the slurry containing (1) 0 and (2) 1 wt% PVA at (a) after shaping, (b) after drying (6 days later) and (c) after firing.

From photographs in Fig. 2(1), many crazes were observed on the surface of the dry green sheet (see in Fig. 2(1)(b)). After firing(see in Fig. 2(1)(c)), many large cracks were observed on the surface and near peripheral region.
On the other hand, in Fig. 2(2), no crazes and no cracks were seen with the naked eye for the dry green sheet(see in Fig. 2(2)(b)) and the sintered sample(see in Fig. 2(2)(c)).
These results indicate that crack generation can be considerably reduced by adding a small amount of PVA to the slurry.

2.3 The effect of PVA on the product

Figure 3 shows the X-ray diffraction patterns of samples prepared from the slurry with (a) 0 wt% and (b) 1 wt% PVA. In these X-ray diffraction patterns, 18 diffraction peaks are observed at 2θ= 22.81, 27.71, 27.91, 30.61, 32.51, 32.81, 38.51, 40.31, 46.51, 47.51, 51.41, 52.51, 54.91, 58.21, 58.71, 62.71, 68.11 and 68.71, corresponding to the (030), (120), (021), (040), (130), (031), (050), (131), (200), (002), (151), (160), (070), (161), (132), (241), (260), and (081) planes of orthorhombic $YBa_2Cu_3O_{7-x}$, respectively[10]. These results indicate that adding a small amount of PVA to the slurry has no marked influence on the final product in X-ray resolution.

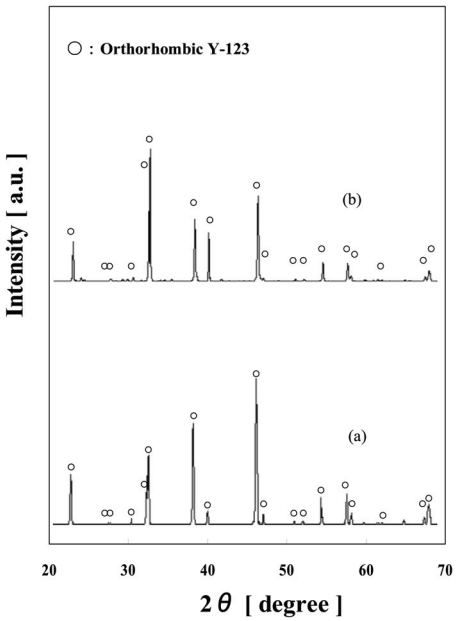

Fig. 3. X-ray diffraction patterns of the sheet samples prepared from the slurry with various PVA concentrations: (a) 0 and (b) 1 wt%.

2.4 Effect of adding PVA on the superconducting properties

Figure 4 shows the temperature dependence of electrical resistance for the samples prepared from the slurry with (a) 0 wt% and (b) 1 wt% PVA concentration. It can be seen that, for both samples, the electrical resistance first decreases linearly with temperature and then begins to decline sharply near 92 K and reaches zero near 89 K. In both samples, the T_{con} (onset

transition temperature) was about 92 K and T_{coff} (offset transition temperature)(T_c) at which the electric resistance becomes zero was about 89 K. There is no visible effect of PVA addition on T_c. The distribution of T_c values in the large samples prepared from the slurry with (a) 0 wt% and (b) 1 wt% PVA concentration shows in Fig. 5 (a) and (b), respectively. These results indicated that the whole of both samples would be superconductors under 85 K. Average T_c of samples prepared from the slurry with (a) 0 wt% and (b) 1 wt% PVA was 87.6±2 K and 88.6±2 K, respectively.

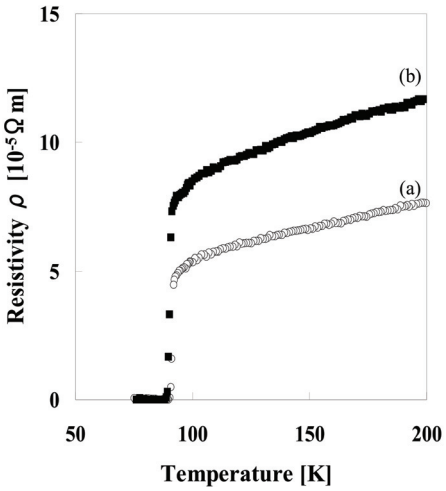

Fig. 4. Dependence of resistivity on temperature. The samples were prepared from the slurry with various PVA concentrations: (a) 0 and (b) 1 wt%.

The difference of average T_c for both samples was small within 1 K. The average T_c did not depend on the PVA concentration, which was in the range between 0 and 5 wt%, and the average T_c of all samples was 88.3±3 K.

89.5 K	86.2 K	86.3 K	
	88.3 K	88.5 K	
	88.3 K		
85.4 K			88.5 K

(a)

88.4 K	89.4 K	87.5 K	88.4 K
	88.0 K	89.5 K	
87.0 K	87.5 K	89.5 K	
		89.0 K	90.0 K

(b)

Fig. 5. The distribution of Tc values in the samples prepared from the slurry with (a) 0 wt% and (b) 1 wt% PVA concentration.

Figure 6 shows the dependence of current density on the magnetic flux density measured at 77K for the samples prepared from the slurry with the PVA concentrations of (a) 0 wt% and

(b) 1 wt%. The samples used were the same as those in Fig. 4. The current density of the sample prepared from the slurry with 1 wt% PVA is larger than that of the sample without PVA for the magnetic field range between -1.0 and +1.0 T. It can be seen that with the addition of PVA, the critical current density (***Jc***) increased from 370 to 713 A/cm^2. This ***Jc*** of 713 A/cm^2 was about 35% of the reported ***Jc*** (about 2000 A/cm^2) of the$YBa_2Cu_3O_{7-x}$ polycrystalline sample produced by the Bridgman method. The distributions of ***Jc*** values, which were observed at 77 K at 0.018T, on the large samples used in Fig. 6(a)0% and (b)1% are shown in Fig. 7(a) and (b), respectively. From Fig. 7(a), ***Jc*** values of the sample prepared without PVA were distributed in the range from 253 to 443 A/cm^2, and that the average ***Jc*** of this sample was 340±70 A/cm^2 (except maximum and minimum ***Jc***). From Fig. 7(b), ***Jc*** values of the sample prepared from the slurry containing 1% PVA were distributed in the range from 587 to 890 A/cm^2, and that the average ***Jc*** of this sample was 755±135 A/cm^2 (except maximum and minimum ***Jc***).

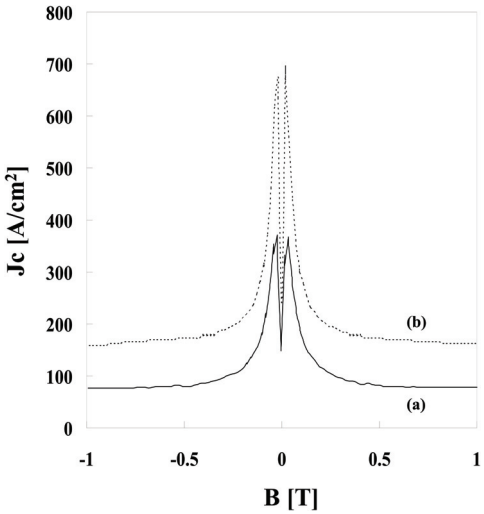

Fig. 6. Dependence of current density on magnetic flux density. The samples were prepared from the slurry with various PVA concentrations: (a) 0 and (b) 1 wt%. Measurement was performed at 77 K.

Comparing with Fig. 7(a) and (b), it is found that the average ***Jc*** value of the sample prepared from the slurry containing 1 wt% PVA was about two times larger than that of the sample without PVA. This fact can be explained by the difference of the density. The average density of the sample without PVA and with 1 wt% PVA was 4.6±0.3 g/cm^3 and 5.4±0.4 g/cm^3, respectively. Since our samples consist of polycrystalline samples, the number of the superconducting path in the sample increases with increase in the density of the sample so that ***Jc*** value of the sample prepared with 1 wt% PVA became larger than that of the sample without PVA. In our studies, over 1 wt% PVA, Jc values decreased with increases in PVA concentration. The reason for this decrease of Jc was thought that when the amount of PVA included in the sample increased, after firing, the amount of the residual carbon and related impurities, which exist along the grain boundary, increased so that the decrease of ***Jc*** was observed. In our studies, the optimum PVA concentration was 1 wt%.

Figure 8 is the photograph that Meissner effect is observed by the sample used in Fig. 7(b). In this picture, sample was cooled at 77 K with liquid nitrogen. This figure indicates that our sample made by the plastic forming method was a superconducting material.

			270
370	334		
	366	443	357
	345		253

(a)

730		740	880
	887	713	751
890	670	790	
		630	587

(b)

Fig. 7. The distribution of Jc values in the samples prepared from the slurry with (a) 0 wt% and (b) 1 wt% PVA concentration. Jc measurement was done at 0.018 T.

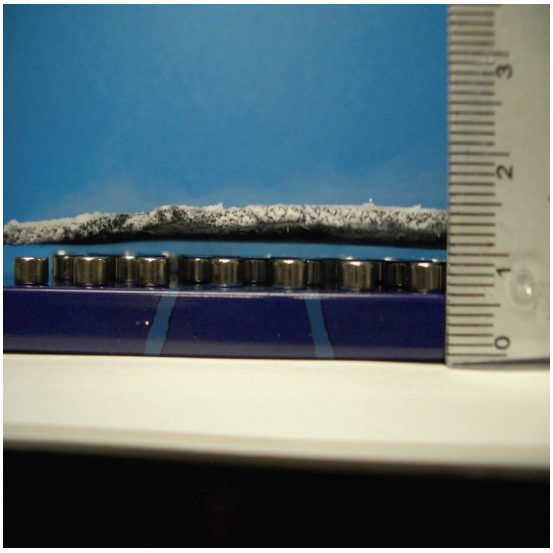

Fig. 8. The photograph of Meisser effect of the sample used in Fig. 7(b)

3. Improvement of the superconducting properties

The maximum average ***Jc*** observed in this study was about 755 A/cm^2, which is much smaller than the reported maximum ***Jc*** of the bulk $YBa_2Cu_3O_{7-x}$ sample (>10^4 A/cm^2). The main reasons why ***Jc*** is much smaller than the reported value are as follows:

1. The density of samples prepared from the slurry containing 1 wt% PVA (5.4±0.4 g/cm^3) is about 86 % of the theoretical density (d=6.36 g/cm^3).

2. The sample is a polycrystal in which the degree of orientation to the c-axis is low.
3. Non-superconducting materials exist among grain boundaries.
4. The degree of oxygen deficiency is large.
5. The degree of crystallinity of used $YBa_2Cu_3O_{7-x}$ powder/particle was of no high quality.

We tried to improve the superconducting properties of our samples.

(1) Oxygen annealing

It has been well known that the oxygen defect strongly affects the crystal structure and the superconducting properties of HTS. Therefore, we tried to improve the superconducting properties of samples by the oxygen annealing.

Figure 9 shows the dependence of current density on magnetic flux density of (a) non-heat-treated sample and (b) heat treated sample[11]. Heat treatment was done at 773 K, 10 h, under oxygen gas flow condition. It is found that by the heat treatment in an oxygen atmosphere, the current density increased about three or four times more than that of non-heat-treated sample and especially ***Jc*** value at 0.018 T was about 1500 A/cm^2 and this value was about 70% of the reported value for under doped $YBa_2Cu_3O_{7-x}$ prepared with Bridgman method[12]. And this fact implies that the superconducting properties can be improved by the heat treatment in the oxygen atmosphere.

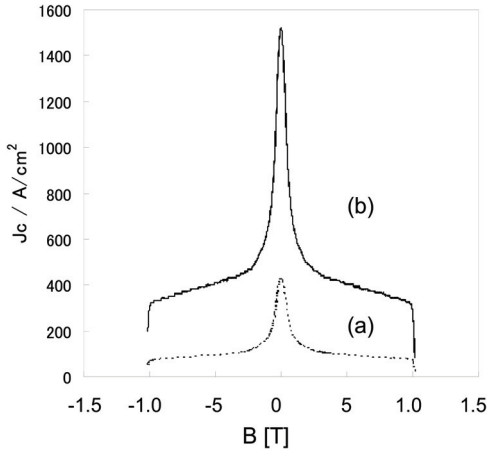

Fig. 9. The dependence of current density on magnetic flux density of (a) non-heat-treated sample and (b) heat treated sample. Heat treatment was done at 773 K, 10 h, under oxygen gas atmosphere.

(2) Changing of $YBa_2Cu_3O_{7-x}$ powder/particles

In general, the degree of crystallinity of the $YBa_2Cu_3O_{7-x}$ powder/particles prepared with conventional sintering method was of poorer quality than that prepared with other methods such as MPMG method, Bridgman method, etc, so that near 0 T, superconducting properties of $YBa_2Cu_3O_{7-x}$ samples made by conventional sintering method became of less quality inhomogeneos than those prepared with other methods. Changing of $YBa_2Cu_3O_{7-x}$ powder/particles prepared with conventional sintering method to $YBa_2Cu_3O_{7-x}$ powder/ particles prepared with MPMG method, we tried to improve superconducting properties.

Figure 10 shows the dependence of current density on magnetic flux density of (a) the sample prepared with $YBa_2Cu_3O_{7-x}$ powder/particles made by convenience sintering

method and (b) the sample prepared with powder/particles made by MPMG method [2]. ***Jc*** value and ***Tc*** of $YBa_2Cu_3O_{7-x}$ powder/particles made by convenience sintering method was about 700 A/cm² and 89 K, respectively. On the other hand, ***Jc*** value and ***Tc*** of $YBa_2Cu_3O_{7-x}$ powder/particles made by MPMG method was about 2000 A/cm² and 89 K, respectively. From results in Fig. 9, ***Jc*** values of samples prepared with $YBa_2Cu_3O_{7-x}$ powder/particles made by (a) convenience sintering method and (b) MPMG method were about 900 and about 2900 A/cm², respectively. It is also found that ***Jc*** value of the sample prepared with powder/particles made by MPMG method is about three times larger than that of the sample prepared with powder/particles made by convenience sintering method. And it is found that using powder/particles made by MPMG method, the superconducting properties near 0 T were improved. This fact indicates that if the $YBa_2Cu_3O_{7-x}$ powder/particle, which has larger ***Jc*** value, will be used, the ***Jc*** value of the sample made by plastic forming will be larger than those of our reported samples.

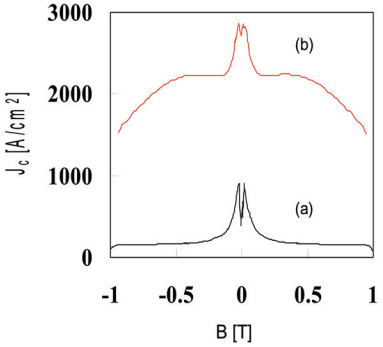

Fig. 10. The dependence of current density on magnetic flux density. Sample (a) was prepared with $YBa_2Cu_3O7_{-x}$ powder made by conventional sintering method. Sample (b) was prepared with $YBa_2Cu_3O7_{-x}$ powder made by MPMQ method.

4. Conclusion

In this work, we have described that large $YBa_2Cu_3O_{7-x}$ superconductor samples can be easily prepared with the plastic forming which is the preparation method for large scale ceramics samples with simple, easy and reproductive processes. Used slurry was prepared by mixing $YBa_2Cu_3O_{7-x}$ particles which were prepared with the sintering method, the inorganic binder and polyvinyl alcohol (PVA). In this method, fine $YBa_2Cu_3(OH)_x$ colloid particles (average particle diameter : 380±70 nm) prepared with the sol-gel method was used as inorganic binder and polyvinyl alcohol (PVA) was used as protective colloid and also acted as flocculant (aggregation agent). Adding a small amount of PVA into the slurry, the clack generation was reduced and so that large scale bulk $YBa_2Cu_3O_{7-x}$ superconductor (about 100 mm x 100 mm x 2 mm) could be produced. The sample became superconducting at 88.3±3 K and had the average ***Jc*** of 755±135 A/cm².

To improve superconducting properties, we changed the $YBa_2Cu_3O_{7-x}$ powder/particles prepared with conventional sintering method to $YBa_2Cu_3O_{7-x}$ powder/particles prepared with MPMG method. So that the samples became superconducting at 91.5±0.5 K and had average critical current density 2900±200 A/cm² (at 77 K under H=0.018 T). This result indicates that superconducting properties, especially ***Jc*** value, of samples made with plastic

forming are determined by those of used $YBa_2Cu_3O_{7-x}$ powder/particles. Therefore, superconducting properties of sample prepared with plastic forming will be improved by both optimizations of $YBa_2Cu_3O_{7-x}$ powder/particles and $YBa_2Cu_3(OH)_x$ colloid particles.

5. Acknowledgments

We would like to thank Dr. Hirosi Terada and Dr. Shoji Sato for their valuable discussions and suggestions. We are grateful to Asami Murai, Kengo Sawada, Hiroyuki Ishikawa, Tatsunosuke Omi for their assistance with the sample production and characterization.

6. References

[1] R. J. Cava, B. Batlogg, R. B. van Dover, D. W. Murphy, S. Sunshine, T. Siegrist, J. P. Remeika, E. A. Reitman, S. Zahurak, and G. P. Espinosa, ''Bulk Superconductivity at 91 K in Single-Phase Oxygen-Deficient Perovskite Ba2YCu3O9-δ'', Phys. Rev. Lett., 58, pp.1676–9 (1987).

[2] M. Murakami, T. Oyama, H. Fujimoto, T. Taguchi, S. Gotoh, Y. Shiohara, N. Koshizuka, and S. Tanaka, ''Large Levitation Force due to Flux Pining in YBaCuO Superconductors Fabricated by Melt-Powder–Melt–Growth Process", Jpn. J. Appl. Phys., 29, L1991–4 (1990).

[3] M. Murakami, M. Morita, and N. Koyama, ''Magnetization of a YBa2Cu3O7 Crystal Prepared by the Quench and Melt Growth Process'', Jpn. J. Appl. Phys., 28, L1125–7 (1989).

[4] A. A. Hussain and M. Sayer, ''Fabrication, Characterization and Theoretical Analysis of High-Tc Y–Ba–Cu–O Superconducting Films Prepared by a Chemical Sol–Gel Method'', J. Appl. Phys., 70, pp.1580–90 (1991).

[5] S. Yamamoto, A. Kawaguchi, S. Oda, K. Nakagawa, and T. Hattori, ''Atomic Layer-by-Layer Epitaxy of Oxide Superconductors by MOCVD'', Appl. Surf. Sci., 112, pp.30–7 (1997).

[6] C. Belouet, ''Thin Film Growth by Pulsed Laser Assisted Deposition Technique'', Appl. Surf. Sci., 96/98, pp.630–42 (1996).

[7] K. Maiwa, K. Honda, K. Kamihira, K. Goto, and T. Fujii, ''Effects of Impurity Contents of the Starting Materials of YBa2Cu3Ox on Superconducting Characteristics'', J. Jpn. Soc. Powder Powder Metall, 41, pp.436–40 (1993).

[8] M. Takahashi, T. Miyauchi, K. Sawada, H. Ishikawa, S. Sato, M. Tahashi, K. Wakita, S. Okido, M. Honda, A. Murai, M. Kamiya, and M. Matubara, "Preparation and Characterization of a Large-Scale $YBa_2Cu_3O_{7-x}$ Superconductor Prepared by Plastic Forming without a High-Pressure Molding: Effect of Polyvinyl Alcohol (PVA) Addition on Superconducting Properties", J Am. Ceram. Soc., 92, pp.578-584(2009)

[9] M. Senda and O. Ishii, ''Critical Current Density of Screen Printed YBa2Cu3O7_x Sintered Thick Film',' J. Appl. Phys., 69, pp.6586–9 (1991).

[10] JCPDS Card No. 38-1433

[11] M. Takahashi, Y. Tomioka, T. Miyauchi, S. Sato, A. Murai, T. Ido, K. Wakita, H. Terada, S. Ohkido, and M. Matsubara, ''Characterization of a Large-Scale Nondoped YBa2Cu3O7_x Superconductor Prepared by Plastic Forming without High-Pressure Molding'', J. Am. Ceram. Soc., 90, pp.2032–7 (2007).

[12] E. Mendoza, T. Puig, X. Granados, X. Obrados, L. Porcar, D. Bourgault, and P. Tixador, ''Extremely High Current-Limitation Capability of Underdoped YBa2Cu3O7_x Superconductor'', Appl. Phys. Lett., 83, pp.4809–11 (2003).

14

Some Chaotic Points in Cuprate Superconductors

Özden Aslan Çataltepe
Anatürkler Educational Consultancy and Trading Company
Bağdat Cad. No: 258 3/6 Göztepe, İstanbul
Turkey

1. Introduction

The aim of this chapter is to determine the chaotic points of cuprate layered superconductors by means of magnetization data and the concept of the Josephson penetration depth based on Bean Critical State and Lawrance-Doniach Models, respectively. In this chapter, the high temperature mercury based cuprate superconductors have been examined by magnetic susceptibility (magnetization) versus temperature data, X-Ray Diffraction (XRD) patterns and Scanning Electron Microscope (SEM) outputs. Thus by using these data, a new method has been developed to calculate the Josephson penetration depth precisely, which has a key role in calculating various electrodynamics parameters of the superconducting system. The related magnetization versus temperature data have been obtained for the optimally oxygen doped virgin (uncut) and cut samples with the rectangular shape. By means of the magnetization versus temperature data of the superconducting sample, taken by Superconducting Quantum Interference Device (SQUID), the Meissner critical transition temperature, T_c, and the paramagnetic Meissner temperature T_{PME}, called as the critical quantum chaos points, have been extracted. In superconductors, the second order phase transition occurs at Meissner transition temperature, T_c, that is considered as the first chaotic point in the system, since the normal state of being is transformed into another state of being called as "superconducting state" that has been driven by temperature. The XRD measurements have been performed in order to calculate the lattice parameters of the system. The crystallographic lattice parameters of superconducting samples, determined by the XRD patterns, have been used to estimate the extent of the Josephson penetration depth. The SEM outputs have been used to determine the grain size of the optimally oxygen doped polycrystalline superconducting samples. The average grain size of the $HgBa_2Ca_2Cu_3O_{8+x}$ (Hg-1223) samples, t, is a crucial parameter, since the critical current density value, J_c, is inversely proportional to "t", whereas it is directly proportional to the difference in magnetization. It has been concluded that the grain size of the superconductors and the length of the c-axis of the unit cell of the system are highly effective on both of the first and second chaotic points of the superconducting system.

2. The mercury based copper oxide layered superconductors

It is well known that, the superconducting materials have a phase transition from normal state to superconducting state at the Meissner transition temperature, T_c. The most common

property of the superconductivity is the diamagnetic response to the applied magnetic field. In addition to diamagnetic response, some superconductors exhibit a simultaneous paramagnetic behaviour under a weak applied magnetic field (Braunish et al., 1992; Braunish et al., 1993; Onbaşlı et al., 1996; Nielsen et al., 2000). This paramagnetic behavior is called as Paramagnetic Meissner Effect (PME) and it can be observed within a specific temperature interval with the maximum paramagnetic signal **at the paramagnetic Meissner temperature, T_{PME}**. At this temperature, **the direction of the orbital current changes its direction in the momentum space**. Since both temperatures represent the transition from one state of being to another, T_c and T_{PME} are considered as the critical quantum chaos points of the superconducting specimens (Aslan et al., 2009; Onbaşlı et al., 2009). The superconducting system is considered as the best material media displaying the chaotic behavior (Waintal et al., 1999; Bogomolny et al., 1999; Evangelou, 2001). The determination of the critical chaotic points is very important in order to decide about the operating temperatures for the high sensitive advanced technological applications. In this context, the determination of the critical chaotic points of T_c and T_{PME} on both a.c. (alternative current) and d.c. (direct current) magnetic susceptibility versus temperature data of the mercury based superconductors have been realized (Onbaşlı et al., 1996; Aslan et al., 2009; Onbaşlı et al., 2009).

The mercury based copper oxide layered superconductor investigated , which is one of the high temperature superconductors, has the highest critical parameters such as Meissner transition temperature, T_c, the critical current density, J_c, etc. (Onbaşlı et al., 1996; Aslan et al., 2009). Due to the highest critical parameters of the bulk superconducting Hg-1223 samples, the determination of some electrodynamics parameters such as Josephson penetration depth, plasma frequency and the anisotropy factor has also a great importance for both theoretical and various advanced technological applications. To calculate these electrodynamics parameters, the average spacing of copper oxide bilayers, s, and the grain size of the superconductor are required to be measured. The average spacing of copper oxide bilayers, s, is seen in the primitive cell of the mercury cuprate superconductors given in Fig. 1.

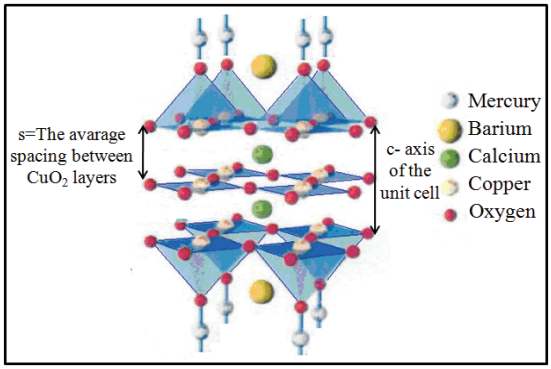

Fig. 1. The primitive cell of Hg-1223 superconductor at the normal atmospheric pressure (Aslan, 2007).

The primitive cell of the mercury cuprates contains three superconducting copper oxide planes separated by insulating layers and this structure is considered as an intrinsic Josephson junction array (Fig. 1).

As is known, the superconductivity occurs in the copper oxide planes which form intrinsic structural layers. **The origin of the superconductivity is based on the harmony which is extended to all copper oxide layers along the c-axis via electromagnetic coupling at the Josephson plasma frequency, ω_p (Lawrance & Doniach, 1971).** However, the Josephson penetration depth, λ_j, being the most important electrodynamics parameters, is given in Eq. (1)

$$\lambda_j = \sqrt{\frac{\Phi_o c}{2\pi J_c \mu_o s}} \tag{1}$$

where Φ_o=2.0678×10^{-15}($T.m^2$) represents the flux quantum, c is the velocity of light, $\mu_o = 4\pi \times 10^{-7} \left(\frac{N}{A^2}\right)$ is the permeability of free space, J_c is the critical current density and s is the average spacing of copper oxide bilayers. According to the scientific literature, the Josephson penetration depth, λ_j, is considered as a measure of the magnetic penetration depth of the field induced by super current (Gough, 1998; Ketterson & Song, 1999; Tinkham, 2004; Fossheim & Sudbo, 2004). It has been previously determined that the Josephson penetration depth, λ_j increases with temperature for the mercury cuprate superconducting family (Özdemir et al., 2006; Güven Özdemir et al, 2007).

In the next section, both the required lengths and quantum chaotic points mentioned above for the bulk superconducting Hg-1223 samples will be examined by means of XRD patterns, SEM outputs and magnetic moment versus temperature data.

3. Determination of the chaotic points

3.1 The analysis of temperature dependence of magnetization

The concept of chaos can be defined as the transition from one state of being to another state of being where the probability density of the system, which is sensitive to the initial conditions, changes via temperature (Gleick, 1987; Panagopoulos & Xiang, 1998). In this point of view, the superconducting system is one of the best examples to understand the unexpected chaotic transitions via magnetic measurements. Superconducting systems, which exhibit the second order phase transition, possess some critical chaotic points as defined above. According to many researchers, the phenomenon of the critical quantum chaos have been observed in the quasi periodic systems, the systems with two interacting electrons and the fractal matrices (Evangelou & Pichard, 2000; Evangelou, 2001). Furthermore, the superconductors investigated, in which phonon mediated attractive electron-electron interaction leads to form quasi-particles, namely Cooper pairs (Aoki et al, 1996; Egami et al., 2002; Tsudo & Shimada, 2003), constitute a natural laboratory for searching and observing quantum critical chaotic points (Onbaşlı et al., 2009).

In this section, the optimally oxygen doped superconducting samples have been investigated by referring to T_c and T_{PME} temperatures extracted from the magnetic susceptibility versus temperature data taken by Quantum Design SQUID susceptometer model MPMS-5S. In all of the magnetization measurements, the magnetic field has been applied to the superconducting bulk specimen along the c-axis.

The optimally doped virgin (uncut) samples have been obtained by pressing under 1 ton of weight. Hg-1223 samples, which have been kept in air for several months after being synthesized, were still mechanically very hard, dense and stiff (Onbaşlı et al., 1996; Onbaşlı et al., 1998; Güven Özdemir et al., 2009). Afterwards, the virgin samples have been cut by

diamond saw in the rectangular shape of 4x2x1 mm. Hence the magnetic susceptibility of the Hg based cuprate superconducting samples has been investigated under both a.c. and d.c. magnetic fields (Onbaşlı et al., 1996; Onbaşlı, 2000).
The related a.c. data for the optimally doped virgin (uncut) and cut samples, which belong to the same virgin batch, are given in Fig. 2. Both data have been taken under a.c. magnetic field of 1 Gauss with 1 kHz frequency.
As seen in Fig. 2, the paramagnetic Meissner and the critical Meissner chaotic temperatures of the uncut samples have been determined as 126K and 137K, respectively. However, for the cut samples with rectangular shape, T_{PME} and T_c have been found as 122K and 140K, respectively. As is known that the paramagnetic Meissner effect can also be observed on very cleanly prepared polycrystalline samples under d.c. magnetic fields. Magnetic moment versus temperature curve for the uncut sample has been taken under zero and 1 Gauss of d.c. magnetic field. The paramagnetic Meissner effect has been observed under d.c. field cooled data of the uncut (virgin) specimen (Fig. 3).

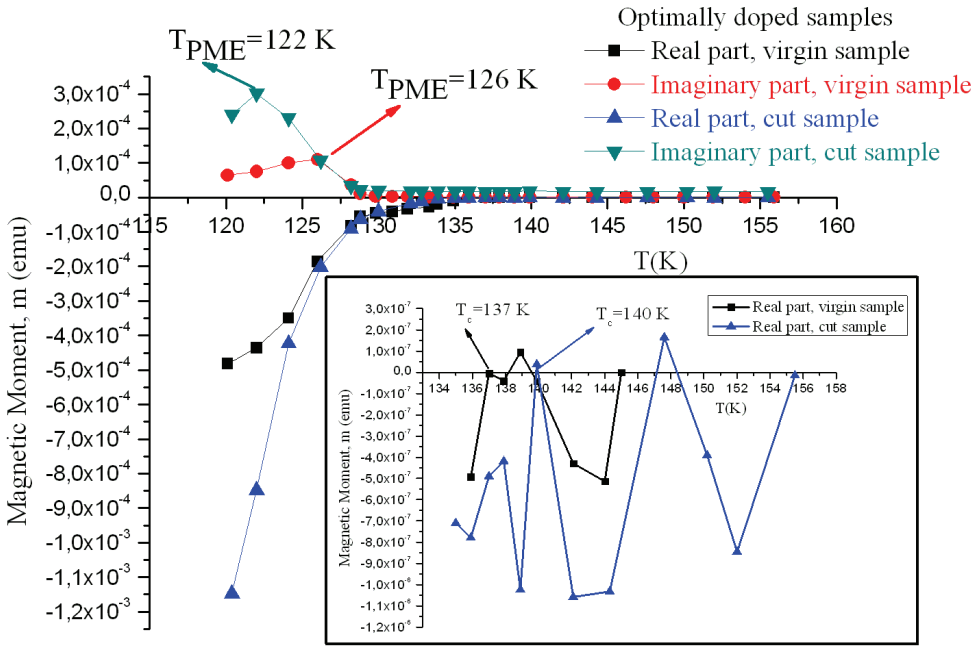

Fig. 2. Magnetic moment versus temperature curves of the virgin (uncut) Hg-1223 and cut samples under a.c. magnetic field of 1 Gauss. The inset shows the real part of the magnetic moment and indicates the Meissner critical temperatures for both of the virgin and cut specimens.

3.2 The symmetries and symmetry breakings in Hg-1223 superconductors

The concepts of the symmetries and symmetry breakings are accepted as one of the most unsolved problems of the 21st century. The symmetries have a crucial role in giving information about the present forces in a system considered and that symmetries can be broken in various ways such as variation of density, temperature, etc. (Nambu & Pascual, 1963; Smolin, 2006).

The concept of symmetry breakings has been discussed by the phenomenon of the critical quantum chaos in the mercury cuprates by means of the magnetic susceptibility versus temperature graphics.

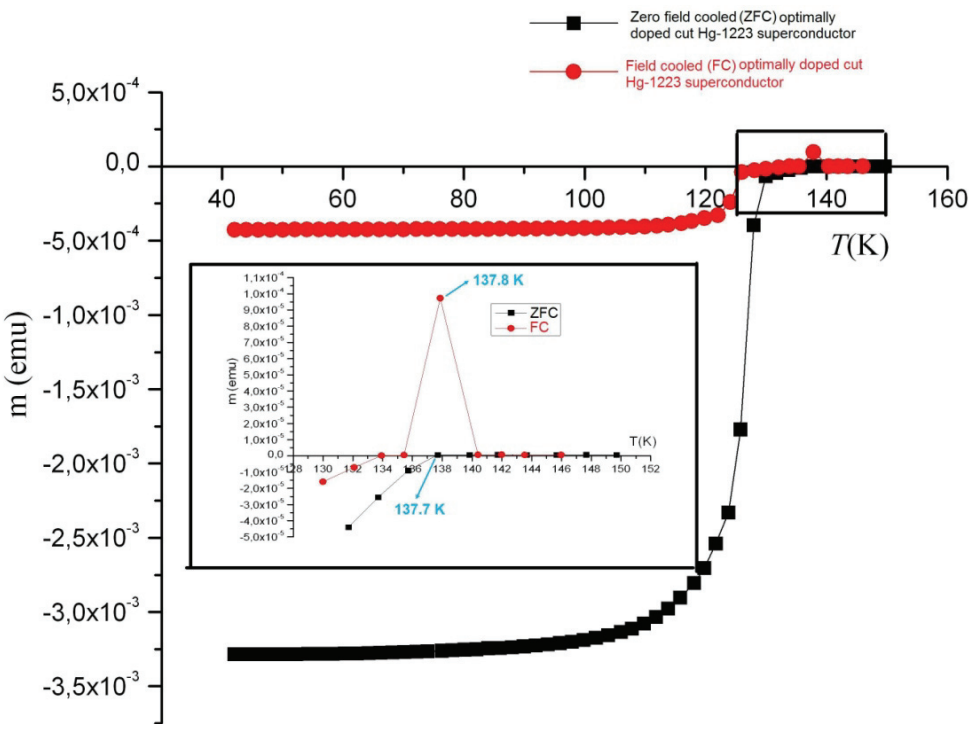

Fig. 3. Magnetic moment versus temperature curves of the optimally doped uncut (virgin) Hg-1223 superconductors under zero and 1 Gauss d.c. magnetic field cooled. The inset shows that only the field cooled specimen displays PME.

The global gauge symmetry is broken at Meissner transition temperature, T_c, in high temperature superconductors (Zhang, 2001; Li, 2003; Roman, 2004; Onbaşlı et al., 2009). Accompanying the global gauge symmetry breaking, the symmetry of the order parameter undergoes a transition from s-wave to d-wave at T_c, as well. Furthermore, due to the fact that the system exhibits spatial Bose-Einstein condensation (Güven Özdemir et al., 2007), the superconducting system can be considered to display f-wave symmetry, as well. The schematic representations of the s-wave, d-wave and f-wave symmetries are given in Fig. 4.
Moreover, Weinberg states that "A superconductor is simply a material in which electromagnetic gauge invariance is spontaneously broken." With this statement, Weinberg means that the electromagnetic gauge field acquires a mass due to the Higgs mechanism in a superconductor. In other words, the particle physicists often speak of gauge invariance interchangeably with the Higgs mechanism (Weinberg, 1996; Greiter, 2005).
In addition to this symmetry breaking at T_c, the time reversal symmetry breaking phenomenon becomes observable on paramagnetic Meissner effect at T_{PME} in mercury cuprates. In the unconventional (high temperature) superconductors, the breaking of the

time reversal symmetry is related to the orbital magnetism. The origin of the PME has been estimated by the reversion mechanism of the direction of the orbital current (Li, 2003; Onbaşlı et al., 2009). According to Sigrist et al., the time reversal symmetry can be destroyed by application of magnetic field and that addition of magnetic impurities (Sigrist et al., 2006). In scientific literature, it has been predicted that the time reversal symmetry breaking occurs below Meissner transition temperature, T_c in superconductors (Horovitz & Golub, 2002).

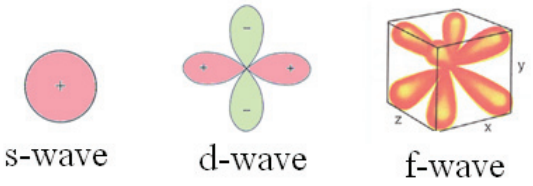

Fig. 4. The schematic representation of s-wave, d-wave and f-wave.

The PME phenomenon has been suggested as a reliable method for determining broken time reversal symmetric state in superconductors instead of very complicated experimental methods such as the angle resolved photoelectron spectroscopy (ARPES) (Onbaşlı et al., 2009). Using ARPES for detecting time reversal symmetry breaking phenomenon may bring the possibility of having the order parameter to be collapsed. So that the magnetic method introduced in this chapter will be a reliable tool to detect the symmetry breaking points of the high T_c superconductors (Onbaşlı et al, 2009).

In recent years, it has been suggested that the copper oxide layered superconductors are considered as a perfect prototype for the electroweak theory and electroweak symmetry breaking due to Higgs mechanism in superconductors (Quigg, 2008). The Higgs mechanism in layered superconductors has been explained by Josephson plasma excitations. In weakly Josephson coupled layered superconductors, the main Josephson plasma excitation modes consist of the longitudinal and transversal modes. The transversal Josephson plasma excitation is an electromagnetic wave, propagating perpendicular to the polarization vector (a-Tachiki et al., 1996; b-Tachiki et al., 1996). On the other hand, the longitudinal mode known as Nambu–Goldstone (Anderson–Bogalibov) mode is an elementary excitation mode accompanying with the superconducting phase transition due to the symmetry breaking (Anderson, 1958; Rickazyen, 1958; Nambu, 1960). However, the zero energy gap at k = 0, does not obey to the Goldstone theorem. Therefore, an additional mechanism, which is known as Higgs mechanism, has been suggested to obtain the finite energy gap. In this point of view, the longitudinal plasma waves should be massive since Higgs bosons have finite mass (Kadowaki et al., 1998). As is known that, all the electroweak force particles are massless in the electroweak symmetry. On the other hand, the breaking of the electroweak symmetry gives mass to the electroweak force particles $W^{\pm}$ and Z^0 (namely weak gauge bosons) leaving the photon massless (Quigg, 2006). According to Veltman, if the space is filled with a type of superconductor, it gives mass to $W^{\pm}$ and Z^0 bosons (Goldstone bosons). This superconductor can be considered as consisting of Higgs bosons (Veltman, 1986). It has been proposed that Higgs boson has zero spin and zero angular momentum. It has been predicted that, the time reversal symmetry breaking at PME temperature, in which the angular momentum is zero, can be considered as the emerging of Higgs boson in the superconducting state (Onbaşlı et al., 2009).

Anderson discovered the physical principle underlying the formation of mass mechanism in the context of superconductivity. The boson, which appears as a result of the Goldstone theorem, has zero unrenormalized mass, which is converted into a finite mass plasmon by interaction with electromagnetic gauge field (Anderson, 1963). The effective mass of the quasi particles, (m^*), introduced in the following chapter, corresponds to the three dimensional (spatial) net effective mass, which is neither attributed to Goldstone boson nor plasmon. In the following chapter, the third quantum chaotic point will be introduced. The third quantum chaotic point called as, quantum gravity point, T_{QG}, where the net effective mass of the quasi-particles (m^*) in the superconducting system has the maximum value, corresponds to the quantum gravity peak for the optimally oxygen doped mercury cuprate superconductors, at which the plasma frequency shifts from microwave to infrared region at the T_{QG} temperature (Aslan Çataltepe et al., 2010).

3.3 Relevant distribution functions of the mercury based superconductors

At T_c, the distribution functions of the system differs from one to another while the transition from normal state to superconducting state occurs. Hence, the system includes both Fermi Dirac (F-D) and Bose-Einstein (B-E) distribution functions depending on the normal state and superconducting state, respectively. As the temperature is higher than the Meissner transition temperature, T_c, the system is in its normal state that obeys to F-D distribution. So that the partition function yields to (e^A+1). The shorter presentation of the exponential term contained by both of the distribution functions is abbreviated by $A=(E-\mu)/\kappa_B T$, where E is the energy of the system, μ is the chemical potential, κ_B is the Boltzmann constant and T is the temperature. At normal state, where $T>T_c$, the spin quantum number (S) is ½ and angular momentum quantum number (L) is zero.

At the critical transition temperature, $T=T_c$, the exponential term becomes equal to 1 (unity) that yields to $e^A=1$.The illustration of the distribution function at the vicinity of the critical Meissner transition temperature is given in Fig. 5.

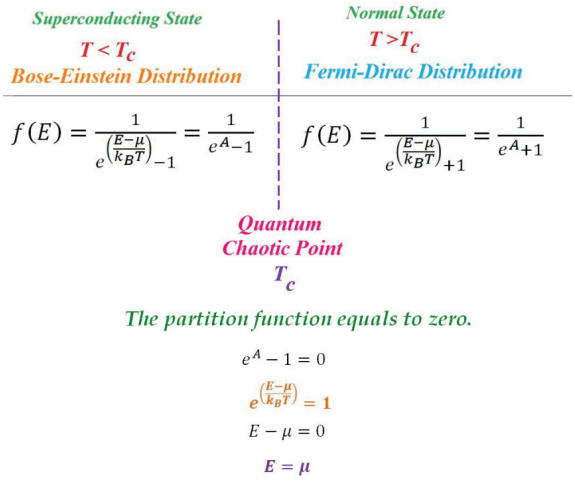

Fig. 5. The repsentative illustration of the distribution function at the vicinity of the critical Meissner temperature T_c. At the Meissner transition temperature, the partition function equals to zero that results in the equality of the chemical potential to the total energy of the system.

At T_c, the absolute value of the chemical potential, μ equals to the total energy of the system, *E*. Hence, the partition function approaches to zero, so that the distribution function diverges to infinity.
Below T_c, the distribution function obeys to B-E distribution where the angular momentum and spin quantum numbers are L=2 and S=0, respectively.
In short, the exponential terms of the partition functions both have the same magnitude that reaches the unity at $T=T_c$. So that the ±1 interval has a crucial role for determining the distribution functions and that of the order parameters of the superconducting system, as well (Onbaşlı et al., 2006).

3.4 The quantum mechanical analysis of mercury cuprate superconductors

The quantum mechanical interpretation of PME is based on the development of a conceptual relationship between the time reversal symmetry and the magnetic quantum number of the system. It is known that, reversing the time (*t*) not only replaces *t* by -*t* in equations, but also it reverses momentums defined by the time derivatives of spatial quantities such as angular momentum, L. Furthermore, magnetic quantum number, m, refers to the projection of the angular momentum, L_z. This component of angular momentum in z direction is defined by the well known formula:

$$L_z = m\hbar \tag{2}$$

where $\hbar(=h/2\pi)$ is the reduced Planck constant. Since, there is a relationship between the magnetic moment and the magnetic quantum number, inverting the direction of the time flow will affect the sign of the z component of the angular momentum, the magnetic quantum number, and magnetic moment of the system. For this reason, the magnetic moment (susceptibility[1]) versus temperature data has been re-examined in the context of magnetic quantum numbers as illustrated in Fig. 6. In this respect, alternative current magnetic susceptibility versus temperature data of the optimally oxygen doped Hg-based cuprate had been previously suggested to explain the time reversal symmetry breaking phenomenon (Onbaşlı et al., 2009). In Fig. 6, magnetic susceptibility versus temperature curve of Hg-1223 has been divided into three regions with respect to magnetic quantum number, m. Since the system investigated is represented by the d-wave symmetry with the orbital quantum number, ℓ, equals to 2, the m values will vary from minus two to plus two ($\ell = 2$, $m = \pm2, \pm1, 0$).
In the non-superconducting region III, the superconducting system has the room temperature symmetry (s-wave symmetry). The temperature region, at which the d-wave symmetry is valid, has been divided into two parts. In region II, magnetic quantum number, m, equals to ±1. Since the imaginary component of the magnetic susceptibility is related to the losses of the system, the imaginary component of magnetic susceptibility in region II corresponds to the m =-1 domain. Hence the real component of magnetic susceptibility in region II corresponds to m = +1 domain. Furthermore, m is equal to minus and plus two in region I. By reducing the temperature, the magnetic quantum number of the system experiences a change from ''-" to ''+" and vice versa. This means that the projection of the

[1]Magnetic measurements have been performed under 1 Gauss of magnetic field.

angular momentum in z direction, L_z, passes through "*zero*" at T_{PME}. From this point of view, T_{PME} is attributed to the breaking point of the time reversal symmetry.

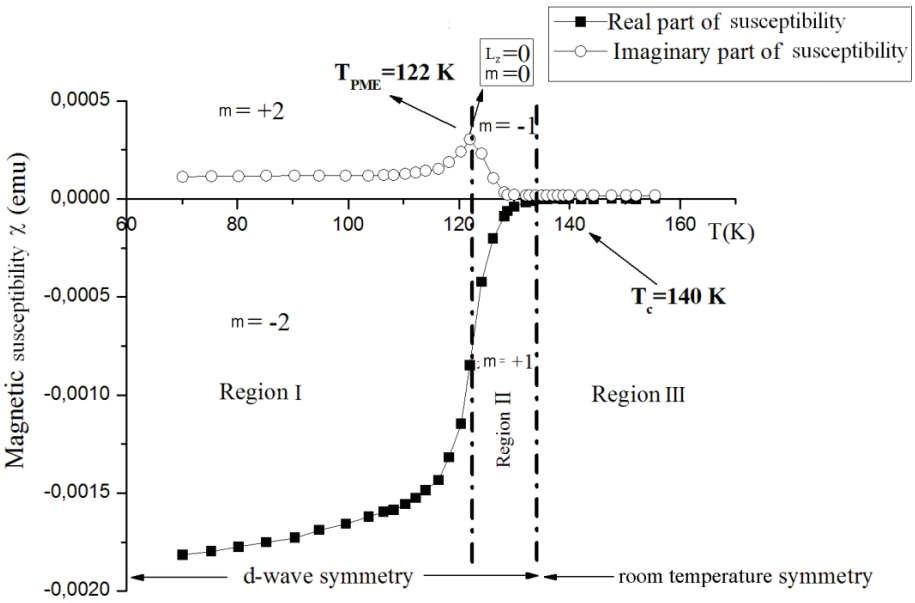

Fig. 6. Magnetic susceptibility (magnetic moment) versus temperature for the optimally oxygen doped Hg-1223 sample at 1 Gauss of a.c. magnetic field. The d-wave and room temperature symmetry regions together with the related magnetic quantum numbers (m) are indicated for three distinguished regions (Onbaşlı et al., 2009).

Related to the quantum mechanical analysis, the concept of the parity should be taken into account. For $T>T_{PME}$ temperatures, the superconducting system has the odd parity. In the other words, the wave function of the system is anti-symmetric, so there is 2-dimensional degree of freedom. For the temperatures lower than T_{PME}, the superconducting system has the even parity and the symmetric wave function with 1-dimensional degree of freedom. Moreover, it has been determined that, the quantum gravity point, T_{QG}, which emphasized in the following chapter, appears at region I at which the superconducting system has one dimensional degree of freedom with the even parity.

4. X-Ray Diffraction (XRD) pattern analysis and the lattice parameters of the mercury cuprates

In this work, the crystal structure of the mercury based copper oxide layered high temperature superconductors is determined by the XRD measurements. The first motivation of performing the XRD measurements is to determine the "s" parameter, which has a crucial importance in calculating the Josephson penetration depth electrodynamics parameter. The second motivation is to investigate the effects of the crystal structure of the superconducting sample on the critical quantum chaos points. As is known, the crystal structure is directly affect the critical quantum chaos point temperatures, such as T_c and T_{PME} (Aslan et al., 2009).

The XRD patterns have been extracted from a Cu/40kV /40kA Rigaku Model XRD device. The XRD patterns of the optimally doped and under oxygen doped samples have been shown in Fig. 7 and Fig. 8, respectively.
According to Fig. 7 and Fig. 8, the lattice parameters of both the optimally and under doped Hg-1223 superconductors have been calculated and the results are given in Table 1 and Table 2, respectively (Aslan, 2007; Aslan et al., 2009).

a-axis	b-axis	c-axis
3.8684 *Å*	3.8684 *Å*	15.7182 *Å*

Table 1. The lattice parameters of the optimally doped sample calculated from the XRD data given in Fig. 7 (T_c=140 K).

a-axis	b-axis	c-axis
3.8328 *Å*	3.8328 *Å*	15.7452 *Å*

Table 2. The lattice parameters of the under doped sample calculated from the XRD data given in Fig. 8 (T_c=135 K).

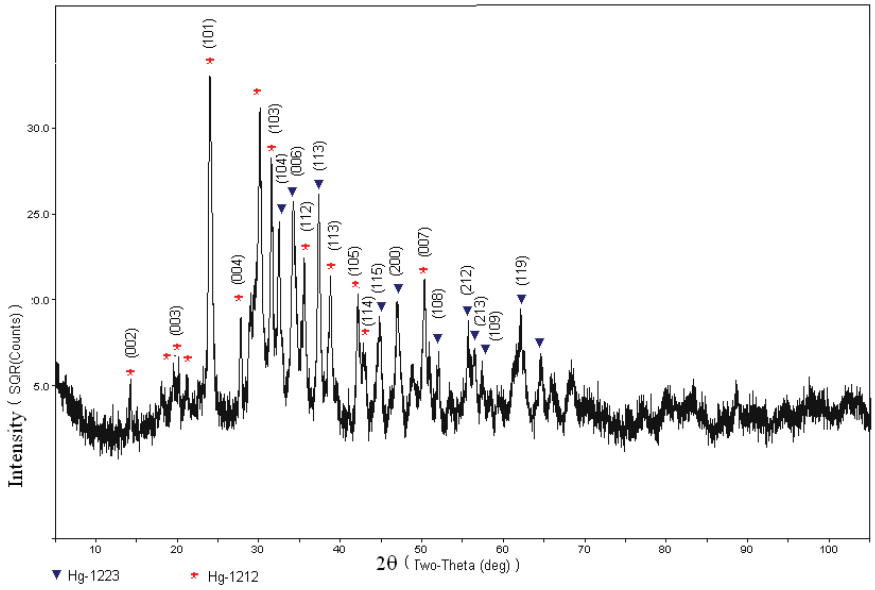

Fig. 7. XRD Pattern and (hkl) planes (Miller indices) of the optimally doped sample in 50 minutes counting. * indicates Hg-1212 and ▼ indicates Hg-1223 phases, respectively.

The X-ray data taken on the optimally and under-doped samples have been clearly shown a mixed phase of $HgBa_2CaCu_2O_{6+x}$ (Hg-1212) and $HgBa_2Ca_2Cu_3O_{8+x}$ (Hg-1223). According to the data taken on both samples, the crystal symmetries have been found to be tetragonal structure with a space group of P4/mmm. This result is also consistent with the previous scientific literature on the crytal symmetry of mercury cuprate family superconductors. As is known,

that the crystal structure of cuprates can generally be divided into two categories; tetragonal and orthorhombic lattices. Some cuprates such as $La_{2-x}Sr_xCuO_4$, $Tl_2Ba_2CaCu_2O_8$, $HgBa_2CaCu_2O_6$ (Hg-1212), and $HgBa_2Ca_2Cu_3O_{8+x}$ (Hg-1223) and some others have the tetragonal crystal structure (Wagner et al., 1995; Gough, 1998; Tsuei & Kirtley, 2000; Li, 2003).

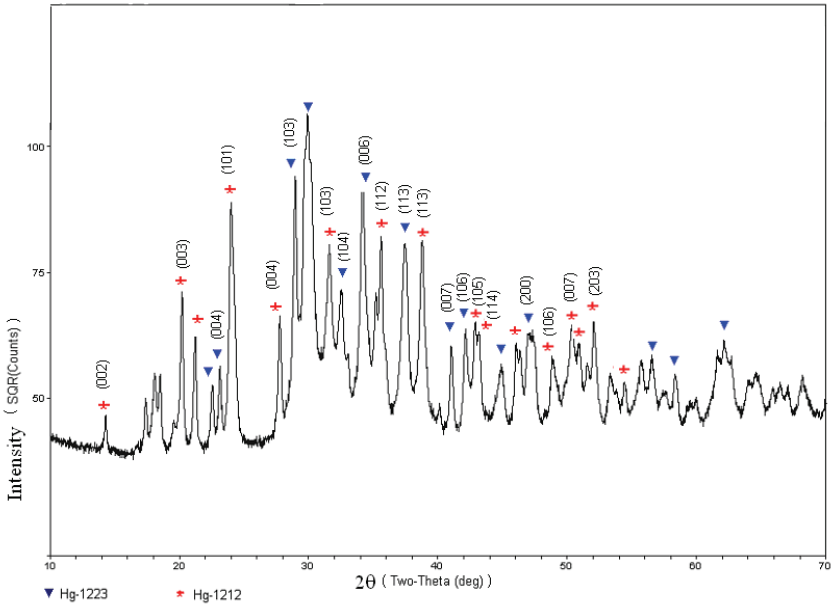

Fig. 8. XRD Pattern and (hkl) planes (Miller indices) of the under doped sample in 7 hours counting. * indicates Hg-1212 and ▼ indicates Hg-1223 phases, respectively.

The average spacing between the copper oxide layers of the mercury based sample, "s" has been determined from the translation vector along the c-direction of the unit cell[2].

The average spacing between copper oxide layers of the optimally and the under oxygen doped samples have been calculated as 7.8591 $\dot{A}$ and 7.8726 $\dot{A}$, respectively. Both of the average spacing values will be used to determine the Josephson penetration depth of the superconductors in further works.

Moreover, it has been determined that the superconducting plane (ab-plane) of the optimally doped sample is larger than that of the under-doped sample. However, the lattice parameter along the c-axis of the optimally doped sample is 0.027 $\dot{A}$ shorter than the other one. Recalling the fact that the reduction in c-axis parameter increases the quantum tunnelling probability between the superconducting CuO_2 ab-planes, so that the T_c of the optimally doped sample is higher than that of the under-doped sample. According to our experimental studies, it has been determined that the deficiency of oxygen doping reduces the T_c by few Kelvin degree for bulk mercury based sample (Onbaşlı et al., 1996). Also, it has been observed that the critical quantum chaos points of the optimally doped sample are higher than that of non-doped samples.

[2]The schematic representation of the unit cell of Hg-1223 superconductors was given in Fig. 1.

Furthermore, as is known, the existence of the intrinsic Josephson effect in superconductors indicates the formation of natural super lattices of Josephson junctions in the crystal structure. According to Ustinov, the spatial period of the super lattices is only 15 $\dot{A}$ so that Josephson junctions are densely packed in the intrinsic structure (Ustinov, 1998). From this point of view, the mercury based copper oxide layered superconductors also include a natural super lattice with the translation vector magnitude of 15.71 $\dot{A}$ and 15.74 $\dot{A}$ for the optimally and under doped samples, respectively.

5. The Scanning Electron Microscope (SEM) analysis and the average grain size of the superconducting samples

In this work, the average grain size "t" of the mercury based copper oxide layered high temperature superconductors is determined by the SEM measurements. The motivation of performing the SEM measurements is to determine the "t" parameter, which has a crucial importance in calculating the critical current densities, J_c and the interrelated parameter of Josephson penetration depth, λ_j.
The critical current density of the mercury cuprates is calculated by the Bean Critical State Model (Bean, 1962; Bean, 1964) below the lower critical magnetic field[3],

$$J_c = 30\frac{4\pi\Delta M}{t} \tag{3}$$

where ΔM is the magnetization difference between the increasing and decreasing field branches of the M-H curves and t is the average grain size of the specimen (Onbaşlı et al., 1998). The dynamic hysteresis measurements of the optimally oxygen doped Hg-1223 samples for various temperatures have been performed by the Quantum Design SQUID susceptometer, model MPMS-5S (Fig. 9). The magnetic field of 1 Gauss has been applied parallel to the c-axis and the critical currents flowed in the ab-plane of sample.

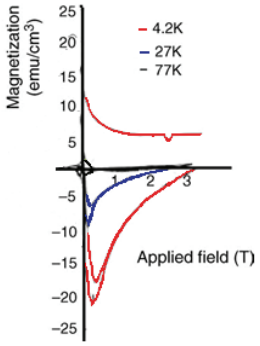

Fig. 9. Magnetization versus applied magnetic field (M–H) for the optimally oxygen doped Hg-1223 samples at 4.2, 27 and 77 K.

[3]Since the calculations have been made below the lower critical magnetic field, H_{c1}, the whole magnetic flux has been totally expelled from the sample.

The SEM measurements have been performed by JSM-5910 LV and ESD X350 model SEM devices. The related SEM images are given in Fig. 10 and Fig. 11.

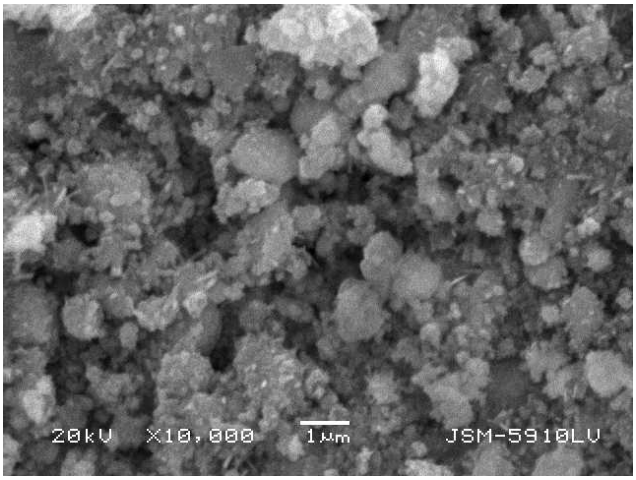

Fig. 10. The optimally oxygen doped Hg-1223 sample with rectangular shape. The SEM output has been taken at 20 kV and JSM-5910 LV (T_c=140 K, t=1.098 μm)

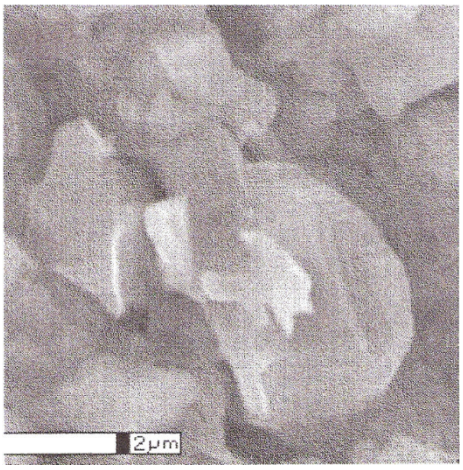

Fig. 11. The optimally oxygen doped uncut (virgin) Hg-1223 sample. The SEM output has been taken at 20 kV, ESD X350. (T_c=136 K, t=1.5 μm) (Onbaşlı et al, 1998).

The average grain sizes of the Hg-1223 samples have been found by using the intercept method and the results are given in Table 3.

According to the SEM outputs, the grain size of the superconductors affects the Meissner transition temperature which is the one of the critical quantum chaos points. In experimental studies, it has been found that the smaller the grain size the higher the Meissner transition temperature (Table 3) (Aslan et al., 2009; Özdemir et al., 2006; Onbaşlı et

al., 1998). Also, the effect of the shape of the superconductors has been investigated by the magnetic moment versus temperature data by which the critical quantum chaos points have been determined (Table 3) (Aslan et al., 2009).

	The grain size, t (μm)	The Meissner transition temperature, T_c (K)	The paramagnetic Meissner temperature, T_{PME} (K)
Cut sample	1.098	140	122
Virgin sample	1.5	137	126

Table 3. The grain size and the Meissner transition temperatures of cut and virgin samples

By using Eq. (3) and the grain sizes determined by SEM, the critical current densities for the optimally doped Hg-1223 superconductors have been calculated to vary 10^{12} A/m^2 to 10^{10} A/m^2 . Ultimately, according to our new method, the Josephson penetration depth have been calculated by Eq. (1) via the "s" parameter determined in the previous section and the critical current density. The Josephson penetration depth values have been obtained to be in the order of micrometers.

6. Conclusion

In this chapter, the investigation of the variation of the tunneling probability in high temperature superconductors depending on the oxygen content and that of the geometry of the sample has been realized. Moreover, a new magnetic method to calculate the Josephson penetration depth reliably has been introduced. It is also shown that this work displays a correlation between SEM, XRD data and quantum chaos points of the superconducting sample establishing a bridge between the momentum and Cartesian spaces.

The determination of chaotic points has a crucial importance for technological applications of the superconductors. Hence, the prediction of the quantum chaotic points of a superconducting system enables the technologists to figure out the reliable working temperature interval for construction of superconducting devices such as bolometers, MRS and all the magnetically sensitive detectors.

Moreover, the appropriately oxygen doped and cut mercury cuprate samples have the highest Meissner transition temperature of 140K ever obtained among the other superconductors prepared under the normal atmospheric pressure. Furthermore, the stability has been confirmed by SQUID measurements performed on the mercury based cuprate samples which have been kept in air for several months after being synthesized. From this point of view, the high stability and durability of the superconducting system with the highest Meissner transition temperature make the mercury cuprate family superconductors as a convenient candidate for the advanced and sensitive technological applications

7. References

Anderson, PW. (1958). Coherent excited states in the theory of superconductivity: Gauge invariance and the Meissner effect. *Physical Review*, Vol. 110, Issue. 4 827–835, ISSN: 1094-1622 (online), ISSN:1050-2947(print).

Anderson, P.W. (1963). Plasmons, gauge invariance, and mass, *Physical Reviews*, Vol. 130, Issue 1 439-442, ISSN:1050-2947(print).

Aoki, R.; Murakami, H.; Kita, T.; Shirai. M.; Nishio, Y.; Svistunov, VM.; Dyachenko, A.I. & Afanassyev, D.N. (1996). Phonon Contribution on the high T_c cooper pairing investigated by tunneling spectroscopy. *Physica B,* Vol. 219, Issue 1-4 172-174, ISSN: 0921-4526.

Aslan, Ö. (2007). Investigation of the symmetries and the breakages in relativistic and non-relativistic regions in high temperature superconductors. PhD Thesis Marmara University Institute of Pure and Applied Sciences.

Aslan, Ö.; Güven Özdemir, Z.; Keskin, S.S. & Onbaşlı, Ü. (2009). The chaotic points and xrd analysis of Hg-based superconductors". *Journal of Physics: Conference Series,* Vol 153, Number. 1/ 012002 1-9, ISSN:1742-6596 (online), ISSN:1742-6588 (print),

Aslan Çataltepe Ö.; Güven Özdemir, Z.; Arık, M. & Onbaşlı Ü. (2010). Strong-electroweak unification and quantum gravity achieved in chaotic regime. submitted to Chaos Solitons & Fractals ISSN:0960-0779 (online)

Bean, C.P. (1962). Magnetization of hard superconductors. *Physical Review Letters*, Vol.8, Issue 6 250-253, ISSN:1079-7114 (online), ISSN:0031-9007 (print).

Bean, C.P. (1964). Magnetization of high field superconductors. *Review of Modern Physics*, Vol. 36 Issue 1 31-39, ISSN:1539-0756 (online), ISSN:0034-6861 (print).

Bogomolny, E.; Gerland, U. & Schmit, C. (1999). Models of intermediate spectral statistics. *Physical Review E,* Vol. 59, Issue 2, R1315-R1318, ISSN:1550-2376 (online), ISSN:1539-3755 (print).

Braunish, W.; Knauf, N.; Kataev, V.; Neuhausen, S.; Grutz, A.; Kock, A.; Roden, B.; Khomskii, D. & Wohlleben, D. (1992). Paramagnetic Meissner effect in Bi high-temperature superconductors. *Physical Review Letters*, Vol. 68, Issue 12 1908-1911, ISSN:1079-7114 (online), ISSN:0031-9007 (print).

Braunish, W.; Knauf, N.; Bauer, G.; Kock, A.; Becker, A.; Freitag, B.; Grutz, A.; Kataev, V.; Neuhausen, S.; Roden, B.; Khomskii, D. & Wohlleben, D. (1993). Paramagnetic Meissner effect in high-temperature superconductors. *Physical Review B, V*ol. 48, Issue 6 4030-4042, ISSN:1550-235X (online), ISSN:1098-0121 (print),

Egami, T.; Chung, J.H.; McQueeney, R.J.; Yethiraj, M.; Mook, H.A.; Frost, C.; Petrov, Y.; Dogan, F.; Inamura, Y.; Arai, M.; Tajima, S. & Endoh, Y. (2002). Electron–phonon interactions in HTSC cuprates. *Physica B* Vol. 316-317, 62-68, ISSN: 0921-4526.

Evangelou, S.N. & Pichard J.L. (2000). Critical quantum chaos and the one dimensional harper model, *Physical Review Letters*, Vol. 84, Number 8 1643-1646, ISSN: 1079-7114 (online), ISSN: 0031-9007 (print)

Evangelou, S.N. (2001). Critical quantum chaos, *Physica B*, Vol. 296, 62-65, ISSN: 0921-4526.

Fossheim, K. & Sudbo, A. (2004). *Superconductivity: Physics and Applications*, John Wiley & Sons Ltd, ISBN-10: 0-470-84452-3, Great Britain.

Horovitz, B. & Golub, V. (2002). Spontaneous magnetization and Hall effect in superconductors with broken time-reversal symmetry. *Europhys Lett.* Vol. 57, Number 6 892–897, ISSN:1286-4854 (online), ISSN:0295-5075 (print).

Gleick, J. (1987). *Chaos: Making a New Science*, Viking, ISBN: 0140092501, New York.

Gough, C.E. (1998). C-axis conductivity and the role of d-wave superconductivity and fluctuations on anisotropic high temperature superconductors. In: *The Gap Symmetry and Fluctuations in High- Tc Superconductors Nato ASI Series, Series B:*

Physics vol 371, J. Bok, G. Deutscher, D. Pavuna & S.A. Wolf (Eds.), 465-485, Plenum Press, ISBN:978-0-306-45934-4, New York.

Greiter, M. (2005). Is electromagnetic gauge invariance spontenously violated in superconductors? Annals of Physics Vol. 319, Issue 1 217-249, ISSN:0003-4916.

Güven Özdemir, Z.; Aslan, Ö. & Onbaşlı, Ü. (2007). Calculation of microwave plasma oscillation in high temperature superconductors. In: *The Seventh International Conference on Vibration Problems ICOVP 2005 Springer Proceedings in Physics*, E. İnan & E. Kırış (Eds.), 377-382, Springer, ISBN: 978-1-4020-5400-6, Dordrecht, The Netherlands.

Güven Özdemir, Z.; Aslan, Ö.& Onbaşlı, Ü. (2009). Terahertz oscillations in mercury cuprates superconductors, *Pramana-Journal of Physics*, Vol. 73, No. 4 755- 763. ISSN: 03044289.

Kadowaki, K.; Kakeya, I. & Kindo, K.(1998). Observation of the Nambu–Goldstone mode in the high-temperature superconductor $Bi_2Sr_2CaCu_2O_{8+d}$. *Europhys Lett.,* Vol. 42, 203–208, ISSN: 1286-4854 (online), ISSN: 0295-5075 (print).

Ketterson, J. B. & Song S. N. (1999) *Superconductivity*, Cambridge University Press, ISBN:0-521-56295-3 , United Kingdom.

Lawrence, W.E. & Doniach S. (1971). Theory of Layer Structure Superconductors. In: *Proceedings of the 12th International Conference on Low Temperature Physics*, E. Kanda (Ed.), 361-362, Academic Press of Japan, Kyoto.

Li, M.S. (2003). Paramagnetic Meissner effect and related dynamical phenomena. *Physics Reports*, Vol. 376,Iissue 3 133-223, ISSN: 0370-1573.

Nambu Y. (1960). Quasi-particles and gauge invariance in the theory of superconductivity. *Phys Rev.,* Vol. 117 Issue 3 648–663, ISSN:1536-6065 (online).

Nambu, Y. & Pascual, N. (1963). Self-Consistent Models Of Strong Interaction With Chiral Symmetry, *Nuovo Cimento* Vol. 30, 354-365.

Nielsen, A. P.; Cawthorne, A.B.; Barbara, P.; Wellstood, F.C.; Lobb, C.J.; Newrock, R.S. & Forrester, M.G. (2000). Paramagnetic Meissner effect in multiply-connected superconductors, *Physical Review B*, Vol. 62, No.21 14380-14383, ISSN: 1550-235X (online).

Onbaşlı, Ü. ; Wang, Y.T.; Naziripour, A.; Tello, R.; Kiehl, W. & Hermann, A.M. (1996). Transport properties of high Tc mercury cuprates. *Physica Status Solidi B* Vol. 194, 371-382, ISSN: 0370-1972.

Onbaşlı, Ü.; Öztürk, S.; & Hasçiçek, Y. (1998). Magnetic measurement of critical currents on mercury cuprates. *Applied Superconductivity Conference* California, September 1998, USA.

Onbaşlı, Ü. (2000). Oxygen post-annealing at the crirtical parameters of mercury cuprates, *Physica C,* Vol. 332, 333-336, ISSN 0921-4534.

Onbaşlı, Ü.; Aslan, Ö. & Güven Özdemir, Z. (2006). The super logic in the concept of probability density. In: *Logic, Mathematics and Probability IV National Symposium on Probability 5-8 September 2006, Foça İzmir*, 77-87, İstanbul Kültür Üniversitesi Yayınları, Yayın No: 3, ISBN: 978-975-6957-74-5, İstanbul, Turkey.

Onbaşlı , Ü. ; Güven Özdemir, Z. & Aslan, Ö.(2009). Symmetry breakings and topological solitons in mercury based d-wave superconductors. *Chaos, Solitons & Fractals* Vol. 42, No. 4, (30 November 2009) 1980-1989, ISSN:0960-0779 (online).

Özdemir, Z.G.; Aslan Ö. & Onbaşlı Ü. (2006). Determination of c-axis electrodynamics parameters of mercury cuprates. *Journal of Physics and Chemistry of Solids*, Vol. 67 No. 1-3 (January-March 2006) 453-456 ISSN:0022-3697.

Panagopoulos, C. & Xiang, T. (1998). Relationship between the superconducting energy gap and the critical temperature in high-Tc superconductors. *Physical Review Letters*, Vol. 81, 2336–2339, ISSN: 1079-7114 (online), ISSN: 0031-9007 (print).

Quigg, C. (2008). The coming revolutions in particle physics. *Scientific American* February 2008,46-53, ISSN:0036-8733.

Quigg, C. (2006). Particles and the standard model. In: *The New Physics For The Twenty-First Century*, F. Gordon (Ed.), 86-118, Cambridge University Press, ISBN-10:0-521-81600-9, New York.

Rickazyen, G. (1958). Meissner effect and gauge invariance. *Physical Review* Vol. 111 Issue 3 817–821, ISSN: 1094-1622 (online), ISSN:1050-2947(print).

Roman, P. (2004). Why symmetry?, In: *Symmetries in Science XI*, B. J. Gruber, G. Marmo & N. Yoshinaga (Eds.), 1-12, Kluwer Academic Publisher, ISBN:1-4020-2633-1 (HB), Netherlands.

Sigrist, M.; Agterberg, D.F.; Frigeri, P.A.; Hayashi, N.; Kaur, R.P.; Koga, A.; Milat, I. & Wakabayashi, K. (2006). Unconventional superconductivity in non-centrosymmetric materials In: *Effective Models for Low Dimensional Strogly Correlated Systems AIP Conf Proc Vol. 816*, G.G. Batrouni & D. Poilblanc (Eds.), 124-135, American Institute of Physics, ISBN: 0-7354-0309-0, New York.

Smolin, L. (2006). *The trouble with physics, the rise of string theory, the fall of a science and what come next*, Houghton Mifflin Company, ISBN-10:0-618-55105-0, Boston/New York.

Tachiki, M.; Koyama, T. & Takahashi, S. (1996)-(a). Some exotic phenomena related to vortices in high-Tc and heavy fermion superconductors. *Physica C* Vol. 263, Number 1 May 1996 1–11, ISSN: 0921-4534.

Tachiki, M.; Koyama, T. & Takahashi, S. (1996) –(b). Josephson plasma in high temperature superconductors. In: *Coherence in Superconductors*, G. Deutscher & A. Revcolevschi (Eds.), 371-392, World Scientific Publishing Company Inc., ISBN-10:9810226500, Singapore.

Tinkham, M. (2004). *Introduction to Superconductivity*, (Second Edition) Dover Publications, ISBN-10: 0486435032 New York.

Tsudo, N. & Shimada, D. (2003). Layer number dependence of superconducting critical temperature of cuprates: consequence of a phonon contribution to the pairing. *Physica C* Vol. 390, Issue 2 (15June 2003) 95-100, ISSN: 0921-4534.

Tsuei, C.C. & Kirtley, J.R. (2000). Pairing symmetry in cuprate superconductors. *Reviews of Modern Physics*, Vol. 72, Issue 4 969-1016, ISSN: 1539-0756 online), ISSN: 0034 6861(print).

Ustinov, A.V. (1998). Solitons in Josephson junctions. *Physica D* Vol. 123, Issue 1-4 (15 November 1998) 315-329, ISSN: 0167-2789 (print).

Veltman, M.J. (1986). The Higgs bosons. *Scientific American* November 1986, 88-94, ISSN:0036-8733.

Waintal, X.; Weinmann, D. & Pichard, J. L. (1999). Two interacting particles in a disordered chain II: Critical statistics and maximum mixing of the one body state. *The European Physical Journal B* Vol. 7 Februaury I 451-456, ISSN: 1434-6036 (online), ISSN: 1434-6028 (print).

Wagner, J.L.; Hunter, B.A.; Hinks, D.G. & Jorgensen, J.D. (1995). Structure and superconductivity of HgBa2Ca2Cu3O8+δ. *Physical Review B* Vol. 51, Issue 21 15407-15414, ISSN: 1550-235X (online), ISSN: 1098-0121 (print).

Weinberg, S. (1996). *The Quantum Theory of Fields Volume II*, Cambridge University Press, ISBN:0-521-55002-5 (hardback), USA.

Zhang, W. (2001). Nontrivial gauge symmetry in high Tc superconductivity. *Physica C*, Vol. 364-365, (November 2001) 147-150, ISSN: 0921-4534.

15

Superconductors and Quantum Gravity

Ülker Onbaşlı[1] and Zeynep Güven Özdemir[2]
[1]*University of Marmara, Physics Department*
[2]*Yıldız Technical University, Physics Department*
[1,2]*Turkey*

1. Introduction

The high temperature oxide layered mercury cuprate superconductor is a reliable frame of reference to achieve a straitforward comprehension about the concept of quantum gravity. The superconducting order parameter, ψ, that totally describes the superconducting system with the only variable of the phase difference, φ of the wave function, will be the starting point to derive the net effective mass of the quasi-particles of the superconducting system. The calculation procedure of the net effective mass, m^*, of the mercury cuprate superconductors has been established by invoking an advanced analogy between the supercurrent density J_s, which depends on the Josephson penetration depth, and the third derivative of the phase of the quantum wave function of the superconducting relativistic system (Aslan et al., 2007; Aslan Çataltepe et al., 2010). Moreover, a quantum gravity peak has been achieved at the super critical temperature, T_{sc} for the optimally oxygen doped samples via the first derivative of the effective mass of the quasi-particles versus temperature data. Furthermore, it had been determined that the plasma frequency shifts from microwave to infrared at the super critical temperature, T_{sc} (Özdemir et al., 2006; Güven Özdemir et al., 2007). In this context, we stated that the temperature T_{sc} for the optimally oxygen doped mercury cuprates corresponds to the third symmetry breaking point so called as T_{QG} of the superconducting quantum system. As is known that the first and second symmetry breaking points in the high temperature superconductors are the Meissner transition temperature, T_c, at which the one dimensional global gauge symmetry $U(1)$ is broken, and the Paramagnetic Meissner temperature, T_{PME}, at which the time reversal symmetry (TRS) is broken, respectively (Onbaşlı et al., 2009).

2. $HgBa_2Ca_2Cu_3O_{8+x}$ mercury cuprate superconductors

Hg-based cuprate superconductors exhibit the highest superconducting Meissner transition temperature among the other high temperature superconducting materials (Fig. 1).
The first mercury based high temperature superconductor was the $HgBa_2CuO_{4+x}$ (Hg–1201) material with the T_c=98K, which was synthesized by Putilin et al. in 1993 (Putilin et al, 1993). In the same year, Schilling et al. reached the critical transition temperature to 134K for the $HgBa_2CaCu_2O_{7+x}$ (Hg–1212) and $HgBa_2Ca_2Cu_3O_{8+x}$ (Hg–1223) materials at the normal atmospheric pressure (Schilling et al., 1993). Subsequent to this works, Gao et al., achieved to increase the critical transition temperature to 153K by applying $150.10^8 Pa$ pressure to the

$HgBa_2Ca_2Cu_3O_{8+x}$ superconductor (Gao et al., 1993). Ihara et al. also attained the T_c=156K by the application of 250.10^8P pressure to the superconducting material contains both Hg–1223 and Hg–1234 phases (Ihara et al., 1993). Afterwards, in 1996, Onbaşlı et al. achieved the highest critical transition temperature of 138K at normal atmospheric pressure in the optimally oxygen doped mercury cuprates which contain Hg-1212 /Hg-1223 mixed phases (Onbaşlı et al., 1996). Recently, the new world record of T_c at the normal atmospheric pressure has been extended to 140K for the optimally oxygen doped mercury cuprate superconductor by Onbaşlı et al. (Onbaşlı et al., 2009).

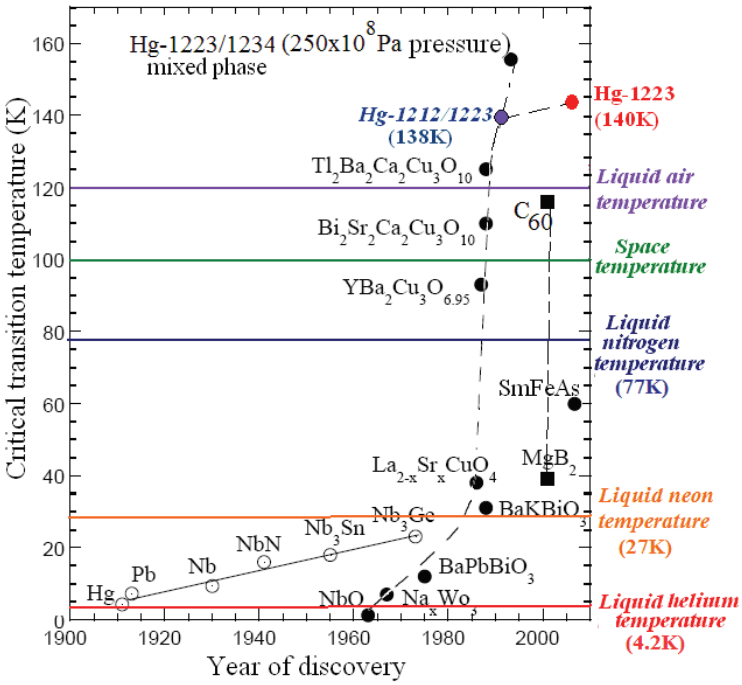

Fig. 1. Illustration of the years of discovery of some superconducting materials and their critical transition temperatures.

In general, layered superconductors such as Bi-Sr-Ca-Cu-O, are considered as an alternating layers of a superconducting and an insulating materials namely intrinsic Josephson junction arrays (Helm et al., 1997; Ketterson & Song, 1999). As is known that Josephson junction comprises two superconductors separated by a thin insulating layer and the Josephson current crosses the insulating barrier by the quantum mechanical tunnelling process (Josephson, 1962). The schematic representation of the superconducting-insulating-superconducting layered structure is illustrated in Fig. 2.

In the Lawrence-Doniach model, it is assumed that infinitesimally thin superconducting layers are coupled via superconducting order parameter tunnelling through the insulating layers in layered superconductors (Lawrence & Doniach, 1971). Recent work on the optimally oxygen doped mercury cuprate superconductors has shown that the Hg-1223 superconducting system is also considered as an array of nearly ideal, intrinsic Josephson junctions which is placed in a weak external field along the *c*-axis (Özdemir et al., 2006).

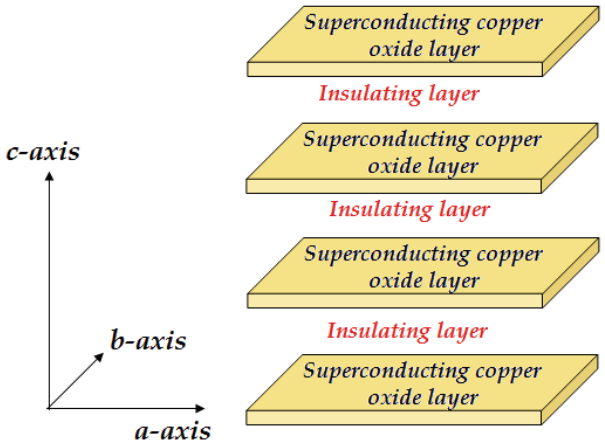

Fig. 2. The schematic representation of the intrinsic Josephson structure in the layered high temperature superconductors.

Moreover, the Hg-1223 superconducting system verifies the Interlayer theory, which expresses the superconductivity in the copper oxide layered superconductors in terms of the occurrence of the crossover from two-dimensional to three-dimensional coherent electron pair transport. The realization of the three dimensional coherent electron pair transport can be achieved by the Josephson-like or Lawrence-Doniach–like superconducting coupling between the superconducting copper oxide layers (Anderson, 1997; Anderson, 1998). In other words, if the Josephson coupling energy equals to superconducting condensation energy, the superconducting system exhibits the perfect coupling along the *c*-axis (Anderson, 1998). With respect to this point of view, we have analyzed the mercury cuprate system by comparing the formation energy of superconductivity with the Josephson coupling energy and the equality of these energies has been achieved at around the liquid helium temperature for the system (Özdemir et al., 2006; Güven Özdemir et al., 2009).

Since the mercury cuprates justify the Interlayer theory at the vicinity of the liquid helium temperature, the mercury cuprate Hg-1223 superconducting system acts as an electromagnetic wave cavity (microwave and infrared) with the frequency range between 10^{12} and 10^{13} Hz depending on the temperature (Özdemir et al., 2006; Güven Özdemir et al., 2007). Moreover, the optimally oxygen doped $HgBa_2Ca_2Cu_3O_{8+x}$ (Hg-1223) superconductor exhibits three-dimensional Bose-Einstein Condensation (BEC) via Josephson coupling at the Josephson plasma resonance frequency at the vicinity of the liquid helium temperature (4.2K-7K) (Güven Özdemir et al., 2007; Güven Özdemir et al., 2009). In this context, mercury based superconductors have a great interest for both technological and theoretical investigations due to the occurrence of intrinsic Josephson junction effects and the three dimensional BEC. In this context, the mercury cuprate superconductors have a great potential for the advanced and high sensitive technological applications due to their high superconducting critical parameters, the occurrence of the intrinsic Josephson junction effects and, the three dimensional BEC. Due to that reasons, the importance of the determination of the concealed physical properties of the mercury cuprates becomes crucial. To avow the fact, the effective mass of the quasi-particles, which describes the dynamics of the condensed system, has been investigated in details in the following sections.

3. Derivation of the effective mass equation of quasi particles via order parameter in the $HgBa_2Ca_2Cu_3O_{8+x}$ mercury cuprate superconductors

In our previous works, the effective mass equation of quasi-particles in the mercury cuprate superconductors has already been established by invoking an advanced analogy between the supercurrent density J_s, which depends on the Josephson penetration depth, λ_J, and the third derivative of the phase of the quantum wave function of the superconducting relativistic system (Aslan et al., 2007; Aslan Çataltepe et al., 2010). In this section, the logic of the derivation process of the effective mass equation has been expressed in details.

Since the mercury cuprate system exhibits three dimensional BEC, the system is represented by the unique symmetric wave function, ψ, and all quasi-particles occupy the same quantum state. In this context, the superconducting state is represented by the superconducting order parameter[1], ψ, which is defined by the phase differences, φ between the superconducting copper oxide layers of the system.

$$\psi = |\psi| \exp(i\varphi) \tag{1}$$

In this context, in order to derive the effective mass equation, our starting point is the universally invariant parameter of φ by means of Ferrel & Prange equation (Ferrell & Prange, 1963). As is known, the Ferrel & Prange equation (Eq. 2) predicts how the screening magnetic field penetrates into parallel to the Josephson junction

$$\frac{d^2\varphi}{dx^2} = \frac{1}{\lambda_J^2} \sin\varphi \tag{2}$$

where λ_J is the Josephson penetration depth (Ferrell & Prange, 1963, Schmidt, 1997). ***The Josephson penetration depth represents the penetration of the magnetic field induced by the supercurrent flowing in the superconductor***[2]. The Josephson penetration depth is defined as

$$\lambda_J = \sqrt{\frac{c\phi_0}{8\pi^2 J_c d}} \tag{3}$$

where, c is the speed of light, J_c is the magnetic critical current density, ϕ_0 is the magnetic flux quantum, and d is the average distance between the copper oxide layers. The solution of the Ferrel & Prange equation gives the phase difference distribution over the junction. If the external magnetic field is very weak, both the current through the Josephson junction and the phase difference become small. In these conditions, the Ferrel & Prange equation has an exponential solution as given in Eq. (4) (Schmidt, 1997; Fossheim & Sudbo, 2004)

$$\varphi(x) = \varphi_0 \exp\left(-\frac{x}{\lambda_J}\right) \tag{4}$$

[1]The superconducting order parameter, ψ is the hallmark of the phenomenological Ginzburg & Landau theory that describes the superconductivity by means of free energy function.

[2]The italic and bold representation intends to prevent the confusion from the concept of London penetration depth.

where φ_0 is phase value at x=0. Eq. (4) represents the invariant quantity of the phase of the quantum system, φ, as a function of distance, x for low magnetic fields (lower than H_{c1}) (Fig. 3(b)-1).

According to Schmidt, the first and second derivatives with respect to distance correspond to the magnetic field, $H(x)$ at any point of the Josephson junction and the supercurrent density, J_s, respectively (Schmidt, 1997). The related $H(x)=f(x)$ and $J_s=f(x)$ graphics for low magnetic fields are illustrated in Fig. 3(b)-2 and 3, respectively. Since the supercurrent density, J_s, is related to the velocity of the quasi-particles, we have made an analogy between the velocity versus wave vector schema and the super current density versus distance schema in Fig. 3. As is known in condensed matter physics, the effective mass of the quasi-particles is derived from the first derivative of the velocity with respect to wave vector. Like this process, the effective mass of the quasi-particles in the mercury cuprate superconductors can be determined by the first derivative of the J_s with respect to distance x. From this point of view, in order to achieve the effective mass of the quasi-particles, the first derivative of the supercurrent with respect to distance has been taken. The first derivative of the supercurrent density, $\frac{dJ_s}{dx}$, is proportional to third derivative of the phase, $\frac{d^3\varphi(x)}{dx^3}$.

$$\frac{dJ_s}{dx} = \frac{c\phi_0}{8\pi^2 d}\frac{d^3\varphi(x)}{dx^3} = \frac{c\phi_0}{8\pi^2 d}\left(-\frac{1}{\lambda_J}\right)^3 \varphi_0 \exp\left(-\frac{x}{\lambda_J}\right) \tag{5}$$

Consequently, we have calculated the inverse values of m^* via the first derivative of the supercurrent density of the system.

$$\frac{1}{\varphi_0 m^*} = \frac{c\phi_0}{8\pi^2 d}\left(-\frac{1}{\lambda_J}\right)^3 \exp\left(-\frac{x}{\lambda_J}\right) \tag{6}$$

We have called Eq. (6) as "Ongüas Equation" that gives the relationship between the m^* and the phase of the superconducting state (Aslan et al., 2007; Aslan Çataltepe et al., 2010). This effective mass equation also confirms the suggestion, proposed by P.W. Anderson, that the effective mass is expected to scale like the reverse of the supercurrent density (Anderson, 1997). The derivation of the effective mass equation are summarized in Fig. 3.

Let us examine the signification of the effective mass determined by the Ongüas Equation. As is known, the effective mass of the quasi-particles is classified as the in-plane (m_{ab}^*) and out off-plane (m_c^*) effective masses in the anisotropic layered superconductors, like mercury cuprates (Tinkham, 1996). On the other hand, as the mercury cuprate superconducting system is represented by a single bosonic quantum state due to the occurrence of the spatial i.e. three dimensional Bose-Einstein condensation, there is no need to consider the in-plane (m_{ab}^*) and out off-plane (m_c^*) effective masses, one by one . In this context, the effective mass of the quasi-particles, m^*, calculated by the Eq. (6), is interpreted as the ***"net effective mass of the quasi-particles"*** for the superconductor which exhibits the spatial resonance. Hence, the quasi-particles, described by the net effective mass, cannot be attributed to the Bogoliubov quasi-particles in the Bardeen-Cooper-Schrieffer (BCS) state. We have proposed that the generation of the mentioned net effective mass of the quasi-particles is directly

related to the Higgs mechanism in the superconductors, which will be discussed in Section 5. (Higgs, 1964 (a), (b)).

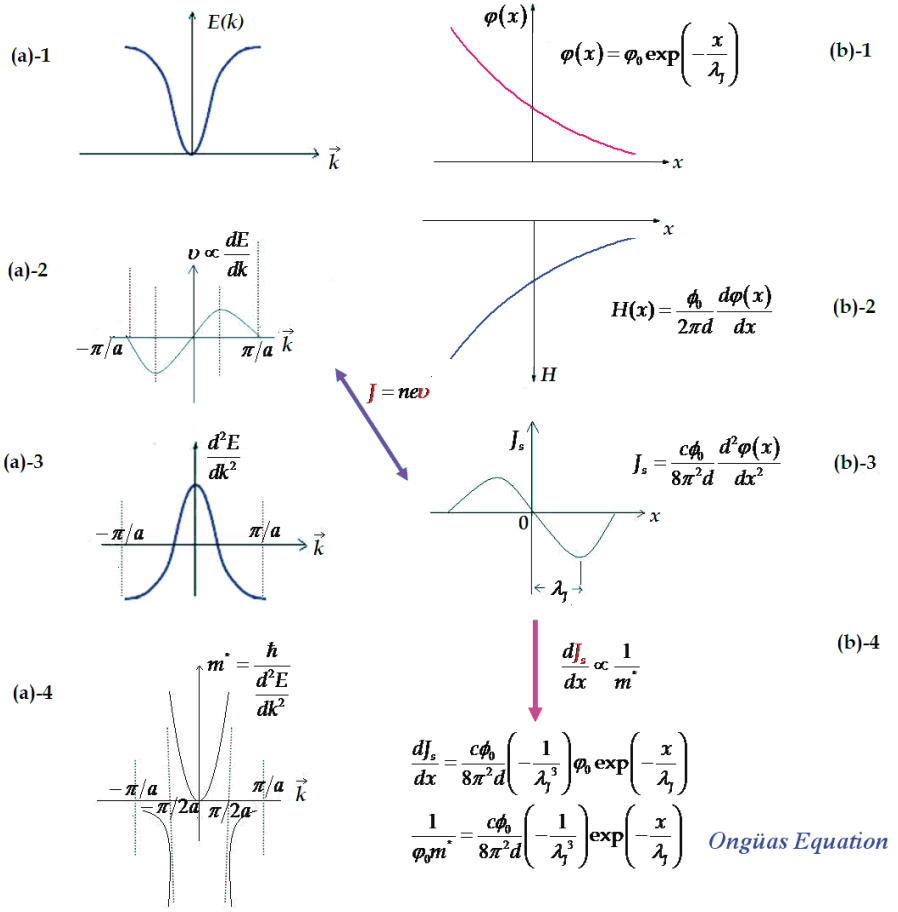

Fig. 3. The derivation procedure of the effective mass equation of the quasi-particles in the condensed matter physics and the mercury cuprates are given in (a)-1,2,3,4 and (b)-1,2,3,4, respectively. (b)-1 The phase versus length graphic for the low magnetic fields in the Josephson junction. (b)-2 The distance dependence of the magnetic field in the Josephson junction. (b)-3 The super current in the Josephson junction versus distance graph. (b)-4 The effective mass equation of the quasi-particles has been derived from the relation of the supercurrent density versus distance.

4. The net effective mass of the quasi particles in the optimally and over oxygen doped mercury cuprate superconductors

In our previous works, the effect of the rate of the oxygen doping on the mercury cuprates has been investigated in the context of both the superconducting critical parameters, such as

the Meissner critical transition temperature, lower and upper critical magnetic fields, critical current density and the electrodynamics parameters by means of Josephson coupling energy, Josephson penetration depth, anisotropy factor etc. In this section, the effect of the oxygen doping on the effective mass of the quasi-particles has been examined on both the optimally and over oxygen doped mercury cuprates from the same batch. The net effective mass values have been calculated via the magnetization versus magnetic field experimental data obtained by the SQUID magnetometer, Model MPMS-5S. During the SQUID measurements, the magnetic field of 1 Gauss was applied parallel to the *c*-axis of the superconductors and the critical currents flowed in the *ab*-plane of the sample. The magnetic hysterezis curves for the optimally and over oxygen doped Hg-1223 superconductors at various temperatures are given in Fig. 4 and Fig. 5, respectively.

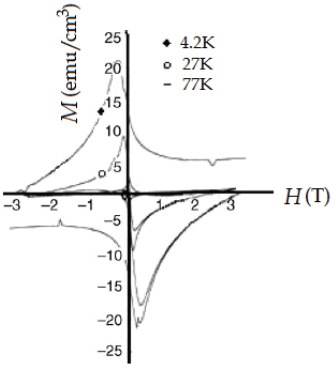

Fig. 4. The magnetization versus applied magnetic field curves of the optimally oxygen doped mercury cuprates at 4.2, 27 and 77K (Özdemir et al., 2006).

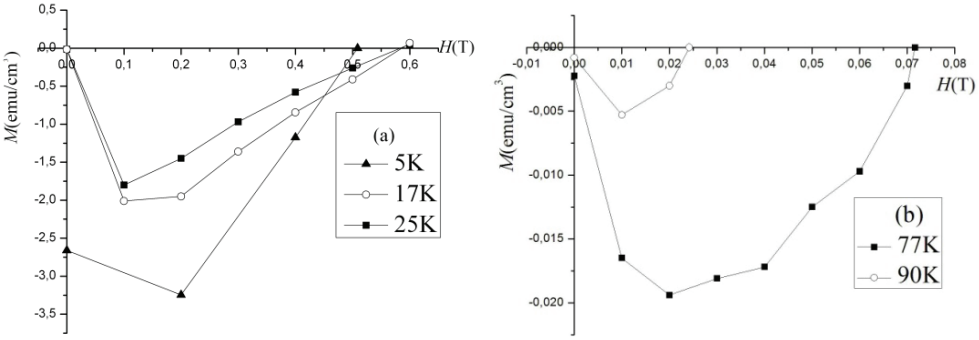

Fig. 5. The magnetization versus applied magnetic field of the over oxygen doped mercury cuprates at 5, 17, 25, 77 and, 90K are seen in Figure 5(a) and (b), respectively. (Aslan Çataltepe, 2010).

According to the Bean critical state model, the critical current densities of the Hg-1223 superconductors have been calculated at the lower critical magnetic field of, H_{c1} (Bean, 1962; Bean, 1964). In this context, the system does not have any vortex. The magnetization difference between the increasing and decreasing field branches, ΔM, has been extracted

from magnetization versus magnetic field curves and the average grain size of the sample has been taken as 1.5μm (Onbaşlı, 1998). The Josephson penetration depth values, which have a crucial role in determining the net effective mass, have been calculated by Eq. (3). In Eq. (3), the average distance between the superconducting layers, d, has been obtained by XRD data that reveals to $7.887 \times 10^{-10}\, m$ (Özdemir et al., 2006).
The critical current densities (J_c) have been calculated at the lower critical magnetic field and the corresponding Josephson penetration depths are given in Table 1 for the optimally and over oxygen doped Hg-1223 superconductors (Özdemir et al., 2006; Güven Özdemir, 2007).

Material	Temperature (K)	J_c (A/m^2) at H_{c1}	$\lambda_J(\mu m)$
Optimally oxygen doped Hg-1223 superconductor	4.2	1.00×10^{12}	0.575
	27	1.62×10^{11}	1.430
	77	1.00×10^{10}	5.75
Over oxygen doped Hg-1223 superconductor	5	1.58×10^{11}	1.449
	17	6.88×10^{10}	2.195
	25	5.71×10^{10}	2.410
	77	5.07×10^{8}	25.581
	90	3.44×10^{8}	31.055

Table 1. The critical current density and Josephson penetration depth values for the optimally and over oxygen doped mercury cuprates.

Variations of the Josephson penetration depth with temperature for the optimally and over oxygen doped Hg-1223 superconductors have been obtained by the Origin Lab 8.0® program (Fig. 6-(a) and (b)).

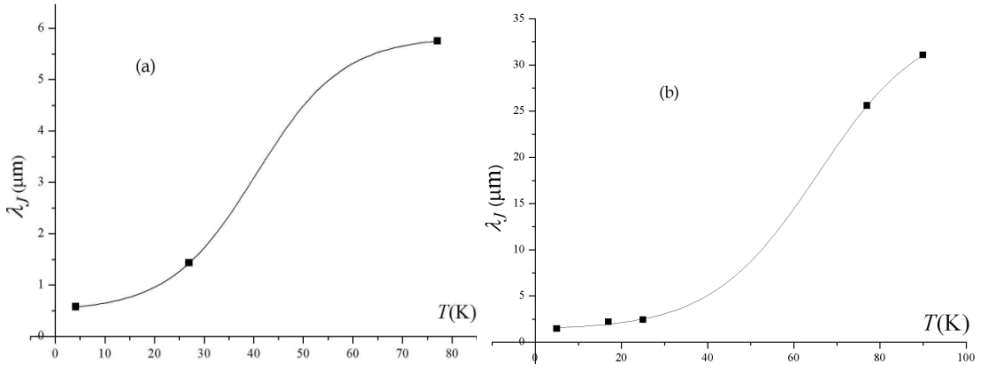

Fig. 6. The temperature dependence of the Josephson penetration for (a) the optimally (b) the over oxygen doped Hg-1223 superconductors.

The temperature dependences of the Josephson penetration depth for the optimally and over doped samples both satisfy the Boltzmann equations which are given in Eqs. (7-a) and (7-b), respectively.

$$\lambda_J(\mu m) = 5.82915 + \frac{(0.49346 - 5.82915)}{1 + \exp\left(\frac{T - 40.46878}{8.70652}\right)} \quad \text{for the optimally doped Hg-1223} \tag{7a}$$

$$\lambda_J(\mu m) = 35.08815 + \frac{(1.33383 - 35.08815)}{1 + \exp\left(\frac{T - 65.54345}{12.24175}\right)} \quad \text{for the over doped Hg-1223} \tag{7b}$$

In addition to experimental data, some λ_J values for various temperatures have been calculated by using Eqs. (7-a) and (7-b).
The net effective mass values for the optimally and over oxygen doped superconductors have been calculated by Eq. (6). The phase value at x=0 has been taken as a constant parameter in all calculations. In order to investigate the temperature dependence of the net effective mass, the distance parameter, x in Eq. (6) has been chosen as 0.3 μm which is smaller than the lowest λ_J values for both the optimally and over oxygen doped samples.
The net effective mass values for the optimally and over oxygen doped Hg-1223 superconductors are given in Table 2.

The optimally oxygen doped Hg-1223		The over oxygen doped Hg-1223	
T(K)	m^* (kg)	T(K)	m^* (kg)
4.2	-3.20×10^{-20}	5	-3.76×10^{-19}
10	-4.35×10^{-20}	10	-5.79×10^{-19}
17	-8.24×10^{-20}	17	-1.21×10^{-18}
20	-1.20×10^{-19}	20	-1.20×10^{-18}
25	-2.57×10^{-19}	25	-1.59×10^{-18}
27	-3.76×10^{-19}	27	-2.26×10^{-18}
30	-6.14×10^{-19}	30	-3.26×10^{-18}
40	-3.26×10^{-18}	40	-1.38×10^{-17}
50	-9.72×10^{-18}	50	-6.92×10^{-17}
60	-1.596×10^{-17}	60	-3.09×10^{-16}
70	-1.91×10^{-17}	70	-9.76×10^{-16}
77	-2.00×10^{-17}	77	-1.70×10^{-15}
90	-2.07×10^{-17}	90	-3.03×10^{-15}
100	-2.08×10^{-17}	100	-3.70×10^{-15}

Table 2. The net effective mass values for the optimally and over oxygen doped mercury cuprates.

According to the data in Table 2, the temperature dependences of the net effective mass of the quasi-particles for the optimally and over oxygen doped mercury cuprates from the same batch both satisfy Boltzmann fitting (Fig. 7 and Fig. 8).

5. The relativistic interpretation of the net effective mass

In this section, we have developed a relativistic interpretation of the net effective mass of the quasi-particles in the mercury cuprate superconductors. Let us review the origin of mass in the context of Higgs mechanism to construct a relativistic bridge between condensed matter and high energy physics.

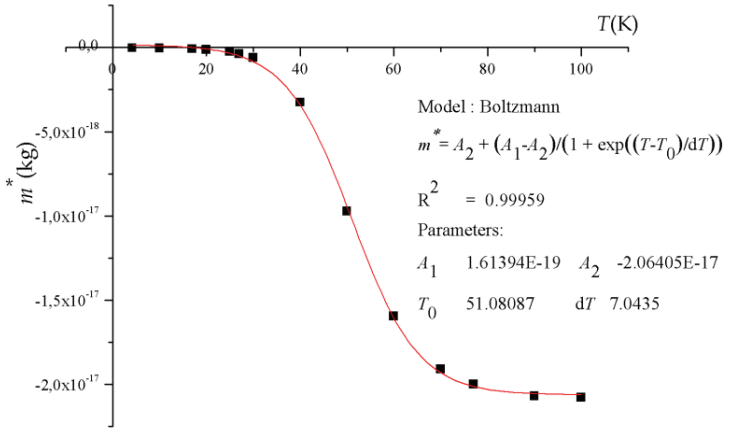

Fig. 7. The m^* versus temperature for the optimally O_2 doped Hg-1223 superconductor.

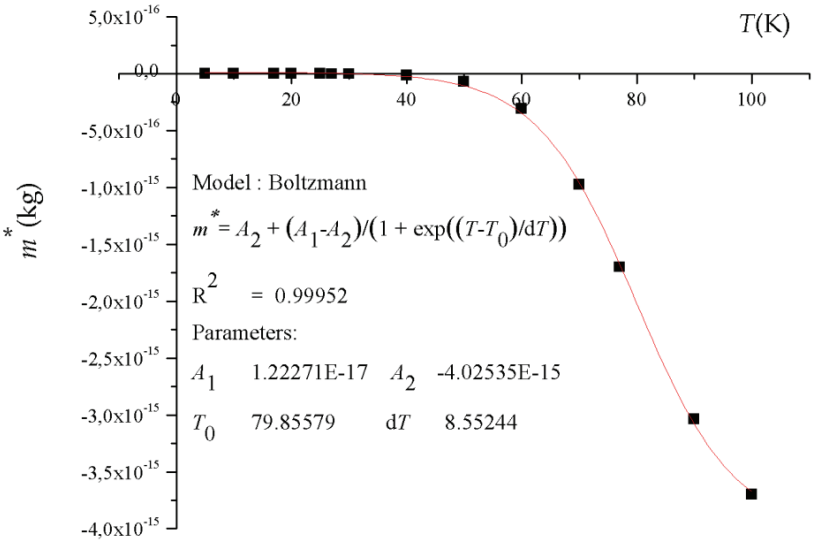

Fig. 8. The m^* versus temperature for the over O_2 doped Hg-1223 superconductor.

As is known, the superconducting phase transition generally offers an instructive model for the electroweak symmetry breaking. The weak force bosons of $W^{\pm}$ and Z^0 become massive when the electroweak symmetry is broken. This phenomenon is known as the Higgs mechanism which can be considered as the relativistic generalization of the Ginzburg-Landau theory of superconductivity (Ginzburg & Landau, 1950; Higgs (a),(b), 1964; Englert & Brout, 1964; Guralnik et al., 1964; Higgs, 1966; Kibble, 1967; Quigg, 2007). **Y. Nambu, who was awarded a Nobel Prize in physics in 2008** for his valuable works on spontaneous symmetry breakings in the particle physics, had also **stated that "the plasma and Meissner effect" had already established the general mechanism of the mass generation for the**

gauge field. So that he suggested a superconductor model for the elementary particle physics on the concept of mass generation in 1960's (Nambu, Y. & Jona-Lasinio, 1961 (a); Nambu, Y. & Jona-Lasinio, 1961 (b); G.; Nambu, 2008). In this context, **superconductors can be accepted as the most convenient and reliable candidate frame of reference to extend the comprehension to understand the emerging procedure of mass.**

The suggestion already made by Quigg that the superconductors can be utilized as the perfect prototype for the electroweak symmetry breaking (Quigg, 2008) has been realized by the mercury cuprate superconductor via Paramagnetic Meissner effect (PME) (Onbaşlı et al., 2009). As is known, contrast to the Meissner effect, superconductors acquire a net paramagnetic moment when cooled in a small magnetic field in the PME (Braunisch et al., 1992; Braunisch et al., 1993; Schliepe et al., 1993; Khomskii et al., 1994; Riedling et al., 1994; Thompson et al., 1995; Onbaşlı et al., 1996; Magnusson et al., 1998; Patanjali et al., 1998; Nielsen et al., 2000). The PME leads to develop spontaneous currents in the opposite direction with the diamagnetic Meissner current in superconductors that results in the breaking of time reversal symmetry. In other words, at the T_{PME} temperature the orbital current changes its direction. In this context, the T_{PME} point is considered as the second quantum chaotic point of the system. (Onbaşlı et al., 2009). The first chaotic point of the system is the critical transition temperature, T_c, at which the one dimensional global gauge symmetry is broken. Furthermore, it has been determined that the process of inverting the direction of the time flow in the PME also affects the z component of angular momentum, magnetic quantum number, and magnetic moment as has been pointed out in the previous chapter. Moreover, the fact that the spin-orbit coupling process occurs at the T_{PME} temperature reveals to the relativistic effects in the mercury cuprate superconducting system, as well. According to our quantum mechanical investigations on PME, it has been determined that T_{PME} temperature, at which the angular momentum is zero, can be considered as the emerging of Higgs bosons in the superconducting state (Onbaşlı et al., 2009).

In addition to electroweak symmetry breaking phenomenon, there is another remarkable relativistic effect in the mercury cuprate system. It had been already determined that the plasma frequency of the mercury cuprate system shifts from microwave to infrared region at the vicinity of 55.5 K (Özdemir et al., 2006; Güven Özdemir et al., 2007).

Both the occurrence of the electroweak symmetry breaking and the frequency shifting phenomenon in the mercury cuprate system lead us to discuss the net effective mass in terms of relativistic manner. The momentum of the quasi-particles in the superconducting system is to be neglected, since the $p = m * \frac{d\vartheta}{dt}$ momentum term of the general relativity vanishes due to the fact that there is practically no acceleration term in the sense of temperature rate of change of velocity of the system (Feynmann, 1963). In this context, the corresponding relativistic energies for the net effective mass of the quasi-particles have been calculated by the relativistic energy-mass equation $E=m^*c^2$ where c is the velocity of the light. The related relativistic energy values vary from 10^7 GeV/c^2 to 10^{13} GeV/c^2 which coincide with the unexplored energy gap of the particle physics' hierarchic GeV/c^2 energy scale (Fig. 9) (Aslan Çataltepe et al., 2010).

6. The negative effective mass in the mercury cuprates

In this section, the concept of negative effective mass will be discussed in the context of both condensed matter physics and the concept of anti-gravity.

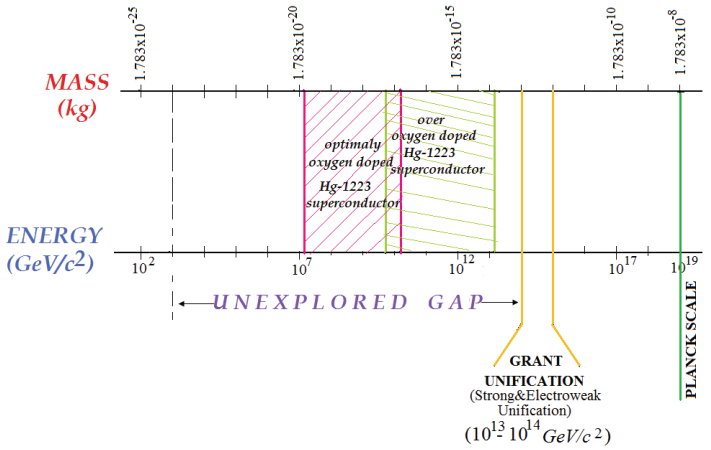

Fig. 9. The representative illustration of the net effective mass values for the optimally and over oxygen doped mercury cuprates in the hierarchic GeV/c^2 energy scale of high enegy physics.

- In condensed matter physics, the negative sign of the effective mass indicates that the charge carriers are holes. As is known, the Hall measurements show that the Hg-based high temperature superconductors are hole-type i.e. the charge carries are holes (Adachi et al., 1997; Smart & Moore, 2005). Moreover, it has been already observed that the Hg-1223 mercury cuprate superconductor displays hole-type of conductivity (Onbaşlı et al., 1996). In this context, the negative sign of the net effective mass verify the hole-type of conductivity in the mercury cuprates.
- The Meissner effect, which is the occurrence of the flux expulsion below T_c and the resulting diamagnetic response to the applied magnetic field, causes a magnetic levitation. In addition to magnetic levitation process, superconductors display the magnetic suspension effect as shown in Fig. 10.

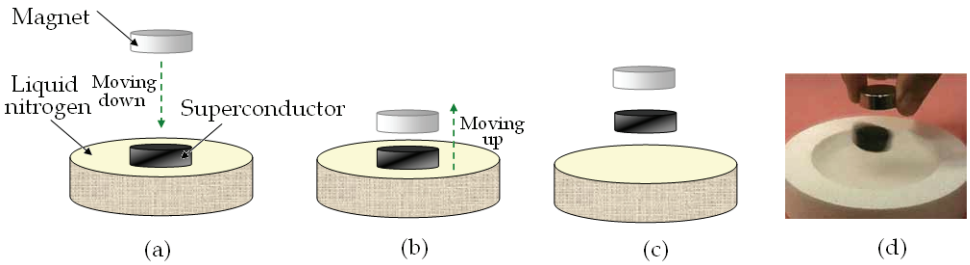

Fig. 10. The schematic representation and the photography of the magnetic suspension effect of the superconductors. (a)- The magnet moves down to the superconductor which is cooled in the liquid nitrogen (b),(c)- When the magnet is lifted up, the superconductor holds its magnetic lines and follows the magnet (www.images.com/articles/superconductors/superconduction-suspension-effect.html) (d)- The photography of the magnetic suspension effect of the superconductor. (Web site of the Superconductivity Laboratory of the University of Oslo, http://www.fys.uio.no/super/levitation/)

In the magnetic suspension effect, the superconductor is suspended by magnetic fields. Magnetic pressure is used to counteract the effects of the gravitational and any other accelerations. From this point of view, it is possible to deduce that the negative net effective mass values can be interpreted as the formation of an anti-gravitational force which has the reverse sign to the gravitational field of the Earth.

7. Quantum gravity in the mercury cuprate superconductors

This section is devoted to investigate the quantum gravitational effects in the mercury cuprate superconductors. In order to get knowledge about the quantum gravitational effect in the system, the net force acting on the system has to be determined. The net force is calculated by

$$F = m^* \frac{d\vartheta}{dt} + \frac{dm^*}{dt}\vartheta \tag{8}$$

for the relativistic systems. In Eq. (8), ϑ represents the velocity of the quasi-particles. Since there is no entropy propagation in the superconducting system, the only variable is the temperature. In this context, the derivatives with respect to time can be considered as the derivatives with respect to temperature in Eq. (8). According to the relativity, "there is practically no acceleration term in the sense of a change velocity under application of a constant force" (Feynmann, 1963). From this point of view, if the acceleration term ($\frac{d\vartheta}{dt}$) goes to zero, the second term in Eq. (8) will describe the net force of the system. Hence, the net force of the system is proportional to the term of $\frac{dm^*}{dT}$.

Consequently, the temperature rate of change of the net effective mass of the quasi-particles for the optimally and over oxygen doped Hg-1223 superconductors are given in Figure 11-(a) and Figure 12-(a), respectively.

According to Figure 11-(a) and Figure 12-(a), the temperatures of 55.5K and 82K, which correspond to the maximum value of the $\frac{dm^*}{dT}$, have been considered as the super critical temperature, T_{SC} for the optimally and over doped samples, respectively.

Moreover, since the plasma frequency shifts from microwave to infrared region at the T_{SC} for the optimally oxygen doped mercury cuprate superconductors (Fig. 11-(b)), the net effective mass of the quasi-particles at T_{SC} corresponds to the quantum gravity peak. However, it is a remarkable point that the plasma frequency shifting phenomenon hasn't been detected for the over doped Hg-1223 superconductor (Fig. 12-(b)).

As is known that the electromagnetic wave shifts to infrared region under gravitational field in a relativistic system (Pound & Rebka, 1959; Pound & Rebka, 1960). Moreover, since the temperature variable can be considered as the time variable of the system in the derivation process as mentioned above, the quantum gravitational effect manifests itself by the variation of temperature in this frame of reference. This phenomenon is consistent with the El Naschie's quantum gravity (Cantorian gravity). According to El Naschie's quantum gravity, the speed at which time flows could be slowed down by a gravitational field. In the other words, by changing the speed of the passing time (temperature), one can create a gravitational effect. Hence, the fluctuation in time creates a fluctuation in gravity and vice versa (El Naschie et al., 1995; El Naschie, 2005 (a); El Naschie, 2005 (b); Agop & Cracuin, 2006).

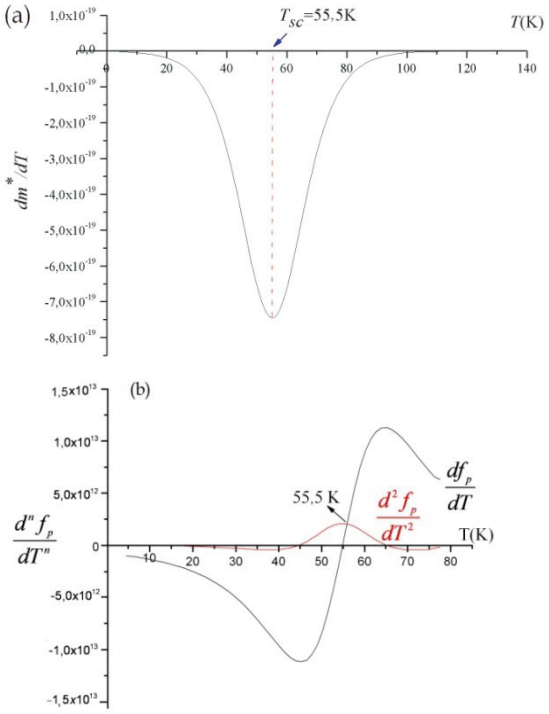

Fig. 11. (a)- The first derivative of the net effective mass with respect to temperature (time). (b)- The plasma frequency shifts from microwave to infrared at the T_{SC}. (Özdemir et al., 2006).

In this point of view, the phenomenon is attributed to the intrinsic gravitational field of the superconducting system that appears at a particular temperature of 55.5 K for the optimally oxygen doped sample (Fig. 11-(a)). Hence it is clear that, the occurrence of the quantum gravitational effect is strongly depending on the initial conditions especially the oxygen content of the system. In this point of view, we have named the net effective mass of the quasi-particles at T_{SC} for the optimally oxygen doped superconducting system mentioned as the "***super critical effective mass***".

8. Force unification in the mercury cuprate superconductors

In this section, the conceptual correspondence of the third symmetry breaking point, T_{QG} to the quantum gravity in high temperature cuprate superconductors will be discussed. As is known that the symmetry breakings give some reliable information about the present forces in a system. In this context, the appearance of the quantum gravitational effects in the mercury cuprate superconductors as a condensed matter media, for sure will give a new insight to the comprehension of the grand unification of the fundamental forces i.e. strong and nuclear forces, electromagnetic force and gravity. Up till now, the grand unification force process has been explained by the Big Bang of the Universe and the four fundamental forces are assumed to be unified up to 10^{-43} s after the Big Bang (Fig. 13).

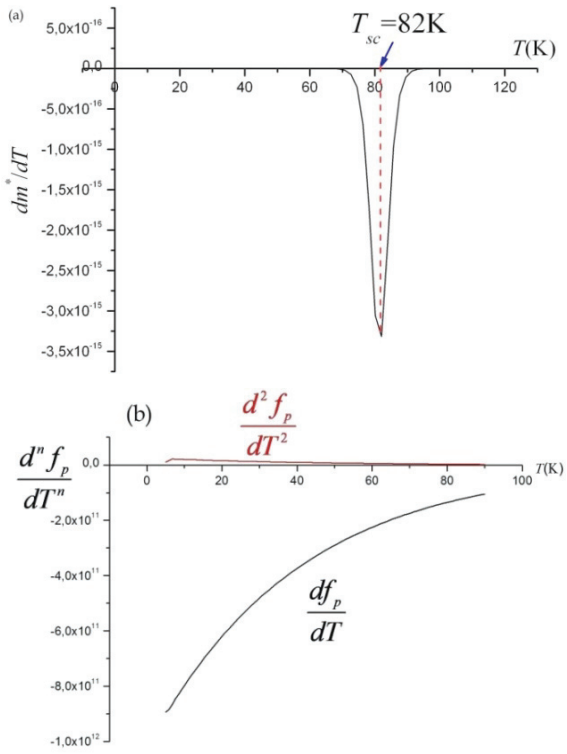

Fig. 12. (a)-The first derivative of the net effective mass with respect to temperature (time). (b)-The plasma frequency does not shift from microwave to infrared at the T_{SC}.

On the other hand, by dealing with the magnetic susceptibility data, it can be easily realized that a kind of mini-Big Bang is driven in the mercury cuprate high temperature superconductors by the variation of the temperature. The related temperature variation causes some symmetry breakings in the system as is summarized in Fig. 14.

As is known that the Meissner critical transition temperature, T_c corresponds to the second order phase transition in the superconductors. At this temperature, the one-dimensional global gauge symmetry is broken and due to that reason the critical Meissner temperature represents the first quantum chaotic transition point. Since the system exhibits the three dimensional BEC via Josephson coupling process with non-zero coupling coefficient, all entities can be represented by a unique, symmetric wave function, ψ with the phase, φ. Hence, the system can be attributed to a giant molecule which inevitably contains the fundamental strong forces at T_c. Moreover, since the mercury cuprate system behaves as an electromagnetic wave cavity, the T_c also marks the presence of the electromagnetic force in the superconducting media.

If the temperature is cooled down to T_{PME}, the time reversal symmetry and the electroweak symmetry are both broken. So that the T_{PME} point indicates the second quantum chaotic transition point. Moreover, towards the lower temperatures, we have observed a peak value on the temperature rate of change of the net effective mass of the quasi-particles at the

T_{QG} temperature, which has been attributed to **the third quantum chaotic transition point**. Obviously, the system undergoes a quantum transition that **can be observed via the fourth derivative of the phase of the order parameter of the superconductor**.

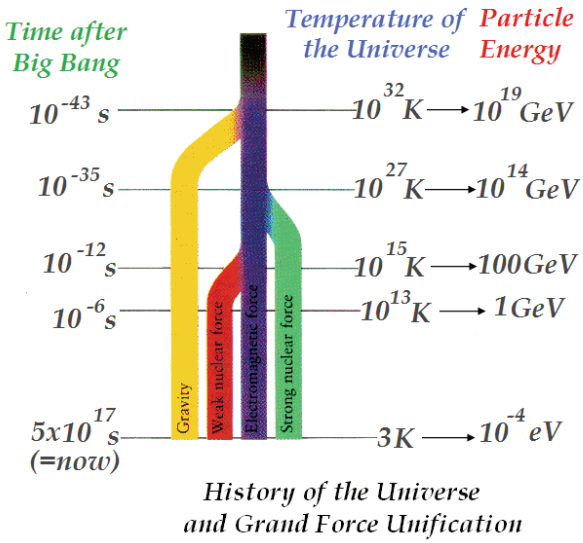

Fig. 13. The schematic representation of the history of the Universe and Grand force unification (http://ircamera.as.arizona.edu/NatSci102/NatSci102/lectures/eraplanck.htm).

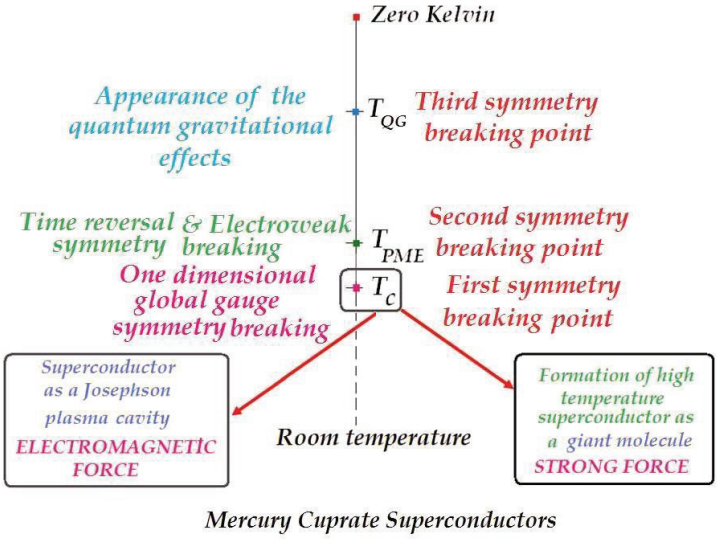

Fig. 14. The schematic representation of the symmetry breakings and the force unification in the optimally oxygen doped mercury cuprate superconductors.

According to Fig. 14, we have concluded that the high temperature superconducting system is a reliable frame of reference for the condensed matter physicists as well as the high energy physicists to get know about the controllable existence of the field particles, such as gluons, photons, weak force particles (W±and Z^0 bosons) and gravitons.

9. Conclusions

In this chapter, the concept of the phase, φ of the order parameter, which is the unique invariant parameter in the universe, has been utilized to derive the net effective mass equation "Ongüas Equation" of the quasi-particles. The net effective mass of the quasi-particles has been reinterpreted in the relativistic manner. The corresponding relativistic energy values for the net effective mass coincide with some part of the unexplored energy gap of high energy physics, which lies between 10^3 GeV/c^2 -10^{13} GeV/c^2. Hence, the unexplored energy gap of the GeV/c^2 hierarchic scale of high energy physics finds an opportunity to be investigated by the superconducting frame of reference for the first time. In this context, we hope that, this method enlightens the secret reality behind the origin and the formation of mass.

Moreover, in this work, the influence of the quantum gravity has been made clear without any doubt in the superconducting condensed matter media. Furthermore, we believe that the discussion of the symmetry breakings in the context of force unification procedure may also give a positive feedback about the dilemma about the force unification efforts that has been going on for many decades.

Ultimately, we hope that this work will unveil the mystery about the universal realities in nature such as the origin of having a mass, force unification process which have been accepted as some of the unsolved problems in physics in 21st century.

10. References

Adachi, S.; Tokiwa-Yamamato, A.; Fukuoka, A.; Usami, R.; Tatsuki, T.; Morikawaki, Y. & Tanabe, K. (1997). Hg-base homologous series of superconductors, Hg-12(n-1)n (Hg-Tl)-22(n-1)n. *Studies of High Temperature Superconductors (Advances In Research & Applications) Hg-Based High T_c Superconductors Part I Volume 23* Anant Narlikar (Ed.) Nova Science Publishers, INC., 163-191, ISBN: 1-56072-472-2, New York.

Agop, M. & Craciun, P. (2006). El Naschie's Cantorian gravity and Einstein's quantum gravity. *Chaos, Solitons & Fractals* Vol. 30 No.1 (October 2006) 30-40 ISSN:0960-0779.

Anderson, P.W. (1997). *The Theory of Superconductivity in the High-Tc Cuprates*, Princeton University Press, ISBN: 0-691-04365-5, Princeton, New Jersey.

Anderson, P.W. (1998). C-Axis electrodynamics as evidence for the interlayer theory of high temperature superconductivity. *Science*, Vol. 279, No. 5354, (20 February 1998) 1196-1198, ISSN:0036-8075 (Print version).

Aslan, Ö.; Güven Özdemir, Z. & Onbaşlı, Ü. (2007). Correlation between the anisotropy and the effective mass of the quasi-particles in oxide superconductors, In: *The VI.th International Conference of The Balkan Physical Union, 22-26 August 2006 American Institue of Physcis Conf. Proc. 899*, S.A. Çetin & İ. Hikmet (Eds.), 271-272, Springer-Verlag, ISBN:978-07354-0405-2, New York.

Aslan Çataltepe Ö.; Güven Özdemir, Z.; Arık, M. & Onbaşlı Ü. (2010). Strong-electroweak unification and quantum gravity achieved in chaotic regime. submitted to Chaos Solitons & Fractals ISSN:0960-0779 (online)

Bean, C.P. (1962). Magnetization of hard superconductors. *Physical Review Letters*, Vol. 8, No. 6, 250-253, ISSN:1079-7114 (Online version).

Bean, C.P. (1964). Magnetization of high field superconductors. *Review of Modern Physics*, Vol. 36, No. 1, 31-39, ISSN:1539-0756 (Online version).

Braunisch, W.; Knauf, N.; Kataev, V.; Neuhause, S.; Grütz, A.; Kock, A.; Roden B.; Khomskii, D. & Wohlleben, D. (1992). Paramagnetic Meissner effect in Bi high temperature superconductors. *Physical Review Letters*, Vol. 68, No.12, 1908-1911, ISSN:1079-7114 (Online version).

Braunisch, W.; Kanuf, N.; Bauer, G.; Kock, A.; Becker, A.; Freitag, B.; Grütz, A.; Kataev, V.; Neuhausen, S.; Roden, B.; Khomskii, D.; Wohlleben, D.; Bock, J. & Preisler, E. (1993). Paramagnetic Meissner effect in high temperature superconductors. *Physical Review B* Vol. 48, No. 6, 4030-4042, ISSN:1550-235X (Online version).

El Naschie, M.S. (a). (2005). From experimental quantum optics to quantum gravity via a fuzzy Kähler manifold. *Chaos, Solitons & Fractals*, Vol. 25 No. 5, (September 2005) 969-977, ISSN:0960-0779 (Online version).

El Naschie, M.S. (b). (2005). Non-Euclidean spacetime structure and the two-slit experiment. *Chaos, Solitons & Fractals*, Vol. 26, No. 15, (October 2005) 1-6, ISSN:0960-0779 (Online version).

El Naschie, M.S.; Rossler, O.E. & Prigogine, I. (1995). Quantum *Mechanics, Diffusion and Chaotic fractals*, Pergamon, ISBN: 0080420273, Oxford.

Englert, F. & Brout, R. (1964). Broken symmetry and the mass of gauge vector bosons. *Physical Review Letters*, Vol. 13, No. 9 321–323, ISSN:1079-7114 (Online version).

Ferrell R. & Prange R. (1963). Self field of Josephson tunneling of superconducting electron pairs. *Physical Review Letters*, Vol. 10, No. 11, 479-481, ISSN:1079-7114 (Online version).

Feynman, R. (1963). *Lectures on Physics vol 1*, Addison Wesley Publishing, ISBN-10: 0201021161/0-201-02116-1 Massachusetts.

Fossheim, K. & Sudbo, A. (2004) *Superconductivity: Physics and Applications*, John Wiley & Sons, Ltd, ISBN-10: 0-470-84452-3, Great Britain.

Gao, L.; Huang, J.Z.; Meng, R.L.; Lin, G.; Chen, F.; Beauvais, L.; Sun, Y.Y.; Xue, Y.Y. & Chu, C.W. (1993). Study of superconductivity in the Hg-Ba-Ca-Cu-O system. *Physica C*, Vol. 213, No.3-4, (15 August 1993) 261-265, ISSN:0921-4534.

Ginzburg, V. L. & Landau, L. D. (1950) Zh. Eksp. Teor. Fiz. 20 1064–1082. Translated into English in *Collected Papers of L. D. Landau,* D. Ter Haar (Ed.), Intl Pub Distributor Inc., ISBN-10: 0677205503 (June 1965), 546.

Guralnik, G. S.; Hagen, C.R. & Kibble, T.W.B. (1964). Global conservation laws and massless particles. *Physical Review Letters*, Vol. 13, No. 20 585–587, ISSN:1079-7114 (Online version).

Güven Özdemir, Z.; Aslan, Ö. & Onbaşlı, Ü. (2009). Terahertz oscillations in mercury cuprate superconductors. *Pramana-Journal of Physics* Vol. 73, No.4 755-763, ISSN: 03044289.

Güven Özdemir Z.; Onbaşlı, Ü. & Aslan, Ö. (2007). Calculation of microwave plasma oscillation in high temperature superconductors. In: *The Seventh International Conference on Vibration Problems ICOVP 2005 Springer Proceedings in Physics*, E. İnan

& E. Kırış (Eds.), 377-382, Springer, ISBN: 978-1-4020-5400-6, Dordrecht, The Netherlands.

Helm, Ch.; Preis Ch.; Forsthofer, F.; Keller J.; Schlenga, K.; Kleiner, R. & Müller P. (1997). Coupling between phonons and intrinsic Josephson oscillations in cuprate superconductors. *Physical Review Letters*, Vol.79, No. 4 737-740, ISSN:1079-7114 (Online version).

Higgs, P. W. (a). (1964). Broken symmetries and the masses of gauge bosons. *Physical Review Letters* Vol. 13 No. 16 508–509, ISSN:1079-7114 (Online version).

Higgs, P. W. (b). (1964). Broken symmetries, massless particles and gauge fields. *Physics Letters*, Vol. 12, No. 2, (15 September 1964) 132–133, ISSN:0375-9601.

Higgs, P. W. (1966). Spontaneous symmetry breakdown without massless bosons. *Physical Review,* Vol. 145, No. 4 1156–1163, ISSN:1536-6065 (Online version).

Ihara, H.; Hırobayashi, M.; Tanino, H.; Tokiwa, K.; Ozawa, H.; Akahana, Y. & Kawamura, H. (1993). The resistivity measurements of $HgBa_2Ca_2Cu_3O_{8+x}$ and $HgBa_2Ca_3Cu_4O_{10+x}$ superconductors under high pressure. *Japanese Journal of Applied Physics*, Vol. 32, No: 12A L1732-L1734, ISSN:1347-4065 (Online version).

Josephson, B.D. (1962). Possible new effects in superconducting tunneling. *Physics Letters*, Vol. 1 No. 7, (1 July 1962) 251-253, ISSN: 0375-9601.

Ketterson, J. B. & Song S. N. (1999) *Superconductivity*, Cambridge University Press, ISBN:0-521-56295-3 , United Kingdom.

Khomskii, D. I. (1994). Wohlleben effect (Paramagnetic Meissner effect) in high-temperature superconductors, *Journal of Low Temp. Physics*, Vol. 95, No. 1-2 205-223, ISSN: 0022-2291.

Kibble T.W.B. (1967). Symmetry Breaking in Non-Abelian Gauge Theories. *Physical Review* Vol. 155 No.5 1554–1561, ISSN:1536-6065 (Online version).

Lawrence, W.E. & Doniach S. (1971). Theory of Layer Structure Superconductors. In: *Proceedings of the 12th International Conference on Low Temperature Physics*, E. Kanda (Ed.), 361-362, Academic Press of Japan, Kyoto.

Magnusson, J. ; Papadopoulou, E.; Svedlindh, P. & Nordblad, P. (1998). Ac susceptibility of a paramagnetic Meissner effect sample, *Physica C*, Vol. 297, No:3-4, (10 March 1998) 317-325, ISSN:0921-9601 .

Nambu, Y. & Jona-Lasinio, G. (a). (1961). Dynamical model of elementary particles based on an analogy with superconductivity I. *Physical Review* Vol. 122, No. 1 345-358, ISSN: 1536-6065 (Online version).

Nambu, Y. & Jona-Lasinio, G. (b). (1961). Dynamical model of elementary particles based on an analogy with superconductivity II. *Physical Review* Vol. 124, No. 1 246-254, ISSN: 1536-6065 (Online version).

Nambu, Y. Nobel Prize Lecture Slides. (2008). http://nobelprize.org/nobel_prizes/physics/laureates/2008/nambu-slides.pdf

Nielsen, A. P.; Cawthorne, A.B.; Barbara, P.; Wellstood, F.C.; Lobb, C.J.; Newrock, R.S. & Forrester, M.G. (2000). Paramagnetic Meissner effect in multiply-connected superconductors, *Physical Review B*, Vol. 62, No.21 14380-14383, ISSN: 1550-235X (Online version).

Onbaşlı, Ü.; Wang, Y.T.; Naziripour, A.; Tello, R.; Kiehl, W. & Hermann, A.M. (1996). Transport properties of high Tc mercury cuprates. *Physica Status Solidi B* Vol. 194, 371-382, ISSN: 0370-1972.

Onbaşlı, Ü.; Öztürk, S.; & Hasçiçek, Y. (1998). Magnetic measurement of critical currents on mercury cuprates. *Applied Superconductivity Conference* California, September 1998, USA.

Onbaşlı, Ü.; Güven Özdemir, Z. & Aslan, Ö. (2009). Symmetry breakings and topological solitons in mercury based d-wave superconductors. *Chaos, Solitons & Fractals* Vol. 42, No. 4, (30 November 2009) 1980-1989, ISSN:0960-0779 (Online version).

Özdemir, Z.G.; Aslan Ö. & Onbaşlı Ü. (2006). Determination of c-axis electrodynamics parameters of mercury cuprates. *Journal of Physics and Chemistry of Solids*, Vol. 67 No. 1-3 (January-March 2006) 453-456 ISSN:0022-3697.

Pound, R.V. & Rebka, G.A. (1959). Gravitational red-shift in nuclear resonance. *Physical Review Letters* Vol. 3, No. 9 439-441, ISSN: 1079-7114 (Online version).

Pound, R.V. & Rebka, G.A. (1960). Apparent Weight of Photons. *Physical Review Letters* Vol. 4, No. 7 337-341, ISSN: 1079-7114 (Online version).

Patanjali, P. V.; Seshu Bai, V.; Kadam, R.M. & Sastry, M.D.(1998). Anomalous microwave absorption in GdBCO powder: π-junctions and the paramagnetic Meissner effect. *Physica C*, Vol. 296, No. 3-4, (20 February 1998) 188-194, ISSN:0921-4534.

Putulin, S.N.; Antipov, E.V.; Chmaissem, O. & Marezio, M. (1993). Superconductivity at 94 K in HgBa2Cu04+δ. *Nature* Vol. 362, No. 6417, (18 March 1993) 226-228 ISSN:0028-0836.

Quigg, C. (2007). Spontaneous symmetry breaking as a basis of particle mass. *Reports On Progress In Physics*, Vol. 70, No. 7, (July 2007) 1019–1053, ISSN: 0034-4885.

Quigg C. (2008). The coming revolutions in particle physics. *Scientific American* February 2008, 46-53, ISSN:0036-8733.

Riedling, S.; Brauchle, G.; Lucht, R.; Röhberg, K.; Löhneysen, H.V.; Claus, H.; Erb, A.& Müler-Vogt, G.(1994). Observation of the Wohlleben effect in YBa2Cu3O7-δ single crystals. *Physical Review B*, Vol. 49, No.18 13283-13286, ISSN: 1550-235X (Online version).

Schilling, A.; Cantoni, M.; Guo, J.D. & Ott, H.R. (1993). Superconductivity above 130 K in the Hg–Ba–Ca–Cu–O system. *Nature* Vol. 363, No. 6424, (6 May 1993) 56-58, ISSN:0028-0836.

Schliepe, B.; Stindtmann, M.; Nikolic, I. & Baberschke, K. (1993). Positive field-cooled susceptibility in high-Tc superconductors. *Physical Review B*, Vol. 47, No. 13 8331-8334, ISSN: 1550-235X (Online version).

Schmidt V. V. (1997). *The Physics of Superconductors, Introduction to Fundamentals and Applications*. P. Müller & A.V. Ustinov (Eds.), 81-86, Springer, ISBN-10: 3540612432, Erlangen, Germany.

Smart, L. E. & Moore, E.A. (2005*). Solid State Chemistry: An Introduction*, Taylor and Francis Group, CRC Press ISBN: 0-7487-7516-1, USA

Thompson, D.J.; Minhaj, M.S.M.; Wenger, L.E. & Chen, J.T. (1995). Observation of paramagnetic Meissner effect in niobium disks. *Physical Review Letters* Vol. 75, No.3 529-532, ISSN: 1079-7114 (Online version).

Tinkham M. (2004). *Introduction to Superconductivity*, (Second Edition) Dover Publications, ISBN-10: 0486435032, New York.

16

Phase Dynamics of Superconducting Junctions under Microwave Excitation in Phase Diffusive Regime

Saxon Liou and Watson Kuo
Department of Physics, National Chung Hsing University, Taichung
Taiwan

1. Introduction

Superconductivity exhibits elegant macroscopic quantum coherence in such a way that the many-body physics can be understood in a one-body way, described by the superconducting phase, and its quantum conjugate variable, the charge. When two superconductors are connected to each other through a tunnel junction, the charge tunneling can be controlled by the phase difference ϕ, leading to many interesting phenomena. For decades, because of the robustness of phase coherence in large junctions, a simple classical approach by modeling the system by a damped pendulum to the problem is successful and overwhelmed.(Tinkham 1996) However, as the sub-micro fabrication techniques had emerged in the 1990's, ultra small junctions were found exhibiting stronger quantum fluctuations in phase due to charging effect, which cannot be overlooked. For exploring the novel phenomena in the opposite limit, people have made devices with robust charging effect. These phenomena can be well understood by treating the charge tunneling as a non-coherent perturbation to the quantum states described by charge. However, in the case when the Josephson energy and charging energy are competing, neither approach gives a satisfactory description. One of the attempts is to include the coherent nature in the charge tunneling processes by introducing a phase correlation function in time, which quantifies the robustness of the phase coherence.(Ingold & Nazarov 1991) The correlation function, which has been studied in many other fields, has a universal relation to the dissipation of the system, called fluctuation-dissipation theorem. Taken in this sense, dissipation is an important controlling parameter in the phase coherence robustness. If the environment impedance of the junction is much smaller than the quantum resistance (for Cooper pairs) $R_Q=h/4e^2$, the phase fluctuation is strongly damped, leading to pronounced phase coherence.(Devoret, Esteve et al. 1990) Indeed, why the classical model is so successful? The pioneer work done by Cadeira and Leggett(Caldeira & Leggett 1983) has pointed out that the environment impedance plays an important role. Their work stimulated many studies in dissipation-driven phase transitions in various systems including Josephson junctions.(Leggett, Chakravarty et al. 1987; Schon & Zaikin 1990)

In this article, we will focus on the responses of Josephson junctions under microwave irradiation. Theoretically the phenomenon can be explained by the phase dynamics under an ac driving. In section 2, we will start from a classical picture by considering a Langevin

equation for phase to explore different regimes for phase dynamics.(Koval, Fistul et al. 2004) In certain condition the phase demonstrates the mode locking of the internal and external frequencies, namely the phenomenon of Shapiro steps. In section 3, we will focus on the phase diffusive regime and begin with the phase correlation so as to derive the resulting charge tunneling rate.(Liou, Kuo et al. 2008) In section 4, we briefly introduce the approach by using the Bloch waves as the quantum sate basis. In section 5, the photon-assist tunneling(Tucker & Feldman 1985) will be briefly addressed and in section 6, we review some experiment works. Possible microwave detection application based on the above phenomena will be discussed.

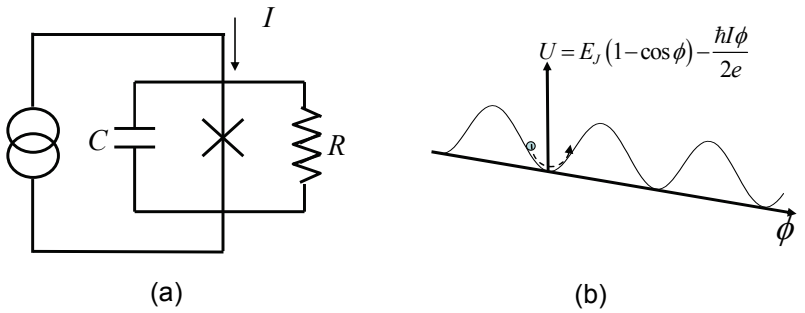

Fig. 1. (a) The model circuit of the resistively(*R*) and capacitively(*C*) shunted junction. (b) The phase dynamics in a junction under a dc current bias can be modeled with a particle of a mass *C* moving in a tilted washboard potential.

2. Langevin equation for superconducting phase

The celebrated resistively and capacitively shunted junction(RCSJ) is a classical way to describe the phase dynamics from a circuit point of view(see Fig. 1(a)). In this model, a model capacitance *C* and a model resistor *R* are connected in parallel to the junction under consideration. We note that a Josephson junction obeys the so-called voltage-phase relation and the current-phase relation that

$$V = \frac{\hbar}{2e}\dot{\phi}$$
$$I_S = I_C \sin\phi$$

in which I_C is the junction critical current. Therefore, the phase ϕ obeys an equation of motion as

$$\frac{\hbar}{8E_C}\ddot{\phi} + \frac{R_Q}{2\pi R}\dot{\phi} + \frac{I_C}{2e}\sin\phi = \frac{I(t)}{2e}, \tag{1}$$

in which $E_C = \frac{e^2}{2C}$ is the charging energy, and *I* is the total bias current. The critical current is related to Josephson energy E_J through $I_C = 2e\frac{E_J}{\hbar}$.

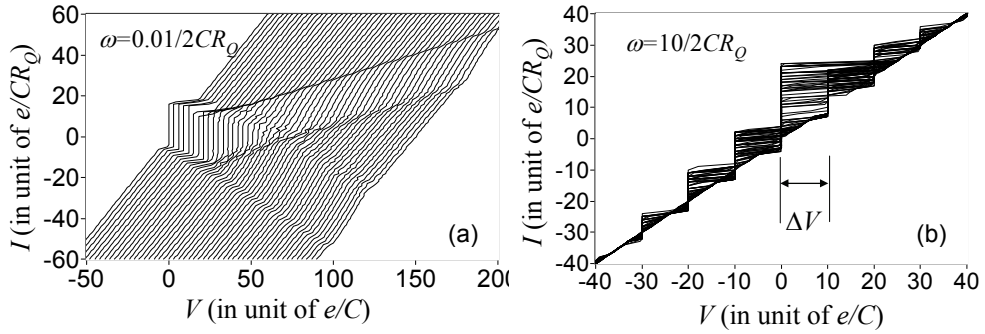

Fig. 2. The calculated current-voltage(*IV*) characteristics of an RC-shunted junction under the ac current driving of various amplitudes at a low frequency(a) and a high frequency(b). Note that the curves in (a) are shifted for clarity. With high frequency driving, the junction exhibits a mode-locking for superconducting phase at certain voltages with an equal spacing $\Delta V=\hbar\omega/2e$.

A dimensionless time scale, $\tau=\omega_p t$, in which $\omega_p=\frac{\sqrt{8E_C E_J}}{\hbar}$ is the plasma frequency, can be introduced further in such a way to yield a reduced equation, namely

$$\ddot{\phi}+\alpha\dot{\phi}+\sin\phi=f(\tau)\,. \tag{2}$$

Here $\alpha=\frac{2}{2\pi}\sqrt{\frac{2E_C}{E_J}}\frac{R_Q}{R}$ and $f=\frac{I}{I_C}$ is the bias current in unit of I_C. It can be clearly seen that expression (2) is of the form of Langevin equation describing a particle in a washboard potential as depicted in Fig. 1(b) with dimensionless dissipation α and a (dimensionless) driving force *f*. Also it resembles the dynamics of a damped simple pendulum, in which ϕ describes the angle of the pendulum to the vertical direction. When this system is kept in equilibrium with a heat bath, the heat bath provides thermal fluctuations which can be modeled as random forces to the system. In this sense, the right-hand side of the equation should be written as $f+\xi(\tau)$, in which $\xi(\tau)$ describes the random force and should obeys the fluctuation-dissipation theorem that $\langle\xi(\tau)\xi(0)\rangle=k_B T\alpha$ in which $\langle\cdots\rangle$ denotes ensemble average.

When the junction is excited by the microwaves, an external force periodic in time will be exerted to the particle, namely, $f(\tau)=f_0+f_1\sin\tilde{\omega}\tau$. Here $\tilde{\omega}=\omega/\omega_p$ is the dimensionless microwave frequency. By inputting all ingredients, one can solve equation (2) to get a distribution of particle in phase space $(\phi,\dot{\phi})$. The results can be compared to those from current-voltage (*IV*) measurement by calculating the average particle velocity $v=\langle\dot{\phi}\rangle=2eV/\hbar\omega_p$ as a function of f_0 at various ac forces and dissipations. Intuitively speaking, when the junction when the junction is dc biased, it undergoes a periodic motion like the vertical circular motion

of a pendulum with an intrinsic angular frequency of $v = \langle \dot{\phi} \rangle$. Whenever there is an ac driving of which the frequency matches the intrinsic frequency, the junction exhibits interesting mode-locking phenomenon in such a way that the junction voltage is locked to the resonant condition. It turns out the mode-locking can occur at $V_n = n\hbar\omega/2e$, producing step structures in *IV* curves equally spaced in the voltage, called the Shapiro steps (see Fig. 2).
The above phenomenon is analyzed in a naïve way without dissipation consideration. Kovel et al (Koval, Fistul et al. 2004) explicitly derived the result without ac driving ($f_1 = 0$) analytically in the diffusive regime and found that at small voltage ranges, $I_S^0 = \frac{I_C}{\alpha}\frac{v}{v^2+\delta^2}$ in which δ quantifies the diffusion of the phase by $\langle \cos[\phi(\tau)-\phi(0)] \rangle = \exp(-\delta\tau)$. One can clear see that the dissipation gives rise to a finite voltage drop even in the "coherent" Cooper-pair tunneling branch. The supercurrent would be peaked at $v = \delta$, which can be verified by experiments.
With the presence of the ac driving, the current can be expressed by the summation of incoherent multi-photon absorption and emissions:

$$I_S = \sum_{n=-\infty}^{\infty} J_n^2\left(\frac{f_1}{\alpha\tilde{\omega}}\right) I_S^0(v - n\tilde{\omega}) = \sum_{n=-\infty}^{\infty} J_n^2\left(\frac{f_1}{\alpha\tilde{\omega}}\right) I_S^0\left(V - n\frac{\hbar\omega}{2e}\right) \tag{3}$$

Here $J_n(x)$ denotes the Bessel functions. We note that this result is similar to that derived by Tien and Gordon (Tien & Gordon 1963) for the single charge tunneling.

3. Spectral function theory

The incoherent Cooper-pair tunneling can be analyzed by the theory of spectral function $P(E)$, in which the tunneling rate can be expressed by

$$\Gamma(E) = \frac{\pi}{2\hbar} E_J{}^2 P(E), \tag{4}$$

from which the net supercurrent can be obtained $I_s(V) = 2e[\Gamma(2eV) - \Gamma(-2eV)]$ (Schon & Zaikin 1990). The spectral function is given by the Fourier transform of the correlation function(Devoret, Esteve et al. 1990; Ingold & Nazarov 1991)

$$P(E) = \frac{1}{2\pi\hbar}\int_{-\infty}^{\infty} \left\langle e^{i\varphi(t)} e^{-i\varphi(0)} \right\rangle e^{iEt/\hbar} dt .$$

In thermal equilibrium, the phase fluctuation is Gaussian so the Wick's theorem yields $\left\langle e^{i\phi(t)} e^{-i\phi(0)} \right\rangle = \exp K(t)$, in which $K(t) = \langle [\varphi(t) - \varphi(0)]\varphi(0) \rangle$. Applying the fluctuation-dissipation theorem, one can express $K(t)$ by using the environment impedance $Z(\omega)$ in unit of R_Q [10]:

$$K(t) = 2\int_{-\infty}^{\infty} \frac{d\omega}{\omega} \frac{\mathrm{Re}\, Z(\omega)}{R_Q} \frac{e^{-i\omega t} - 1}{1 - e^{-\hbar\omega/k_B T}} . \tag{5}$$

In the case of an Ohmic dissipation, $K(t)$ follows a square law in a short time scale. Whereas it linearly decreases with time $K(t) = -\left(R/R_Q\right)\left(\pi k_B T/\hbar\right)t$ beyond the RC time $\tau_{RC} \simeq \left(RC\right)^{-1}$ and inverse of Matsubara frequency $1/\nu_M = 2\pi k_B T/\hbar$, in which R and C are respectively the environmental impedance and capacitance. Here we can refer to the phase-diffusion result in previous section that $\delta \simeq \left(R/R_Q\right)\left(\pi k_B T/\hbar\omega_p\right)$. Also the RC time can be viewed as a mean-free time for the phase motion. One can see that this effect results in a finite resistance around zero-bias either in thermal fluctuation regime, $k_B T \gg \hbar\omega_p$ or in quantum fluctuation regime $R >\approx R_Q$.

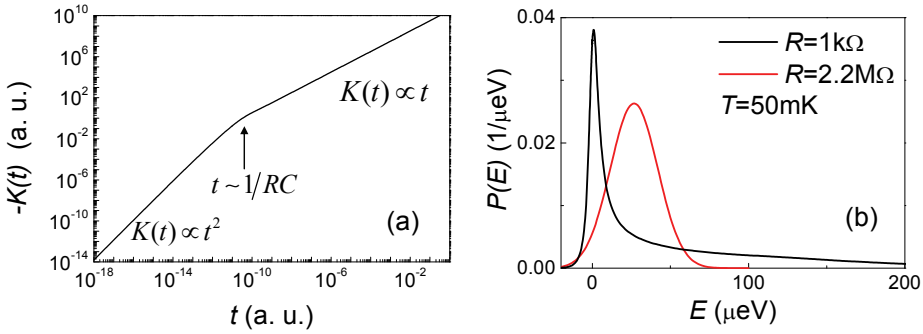

Fig. 3. (a) $K(t)$ function for an RC-shunted junction. When $t \ll 1/RC$, it follows a square law, describing a free particle moving under a constant driving force. In the long time limit, the particle moves in a diffusive way so as to yield a correlation function linear in time. (b)The calculated $P(E)$ function for $R<R_Q$ (black) and $R>R_Q$(red). For $R<R_Q$, the function is peaked at $E=0$ while for $R>R_Q$, the peak will be at $E=E_C$, signify a Coulomb-blockaded charge tunneling. Adopted from (Kuo, Wu et al. 2006)

In order to find the microwave influence to the supercurrent via the correlation function, we turn to the classical equation of motion of superconduting phase under an ac driving force by applying the model of a tilted-washboard potential. When the ac-bias frequency is much smaller than the plasma frequency, the system is in the linear response regime. It can be shown that the correlation function should have the following form, $K(t) = K_0(t) + K_{ac}(t)$, in which $K_0(t)$ is the correlation function in absence of microwave while $K_{ac}(t)$ represents the contribution due to ac-driving under different initial conditions. Since the superconducting phase obeys an equation of motion of $\dot{\varphi} = 2eV/\hbar$, for the ac-driving part, the phase would in general have a sinusoidal motion with an amplitude of $x = 2eV_{ac}/\hbar\omega$ and a frequency the same as the ac-driving one. Substitute the result into the correlation function, we have

$$\left\langle e^{i\varphi(t)} e^{-i\varphi(0)} \right\rangle \simeq \left\langle e^{i\varphi_0(t)} e^{-i\varphi_0(0)} \right\rangle \left\langle e^{ix\cos(\omega t+\theta) - ix\cos\theta} \right\rangle_\theta ,$$

in which θ is the initial phase constant, and $\varphi_0(t)$ is the part of high frequency fluctuations. The latter average on the right-hand side is taken on the initial condition, θ. Now the $P(E)$ reads

$$P(E) = \lim_{T\to\infty} \frac{1}{2\pi\hbar T} \int_{-\infty}^{\infty}\int_{0}^{T} \left\langle e^{i\varphi_0(t)} e^{-i\varphi_0(0)} \right\rangle e^{ix\cos\omega(t+t')} e^{-ix\cos\omega t'} e^{iEt/\hbar} dt'dt$$
$$= \sum_{n=-\infty}^{\infty} J_n^2(x) P_0(E - n\hbar\omega) \tag{6}$$

Here $P_0(E)$ is the spectral function in absence of the microwave influence, and satisfies the detailed balance $P_0(-E) = \exp(-E/k_BT)P_0(E)$, a consequence of thermal equilibrium. We note that equation (6) is an expression of multiple photon absorption and emission with the amplitude of Bessel function $J_n(x)$.

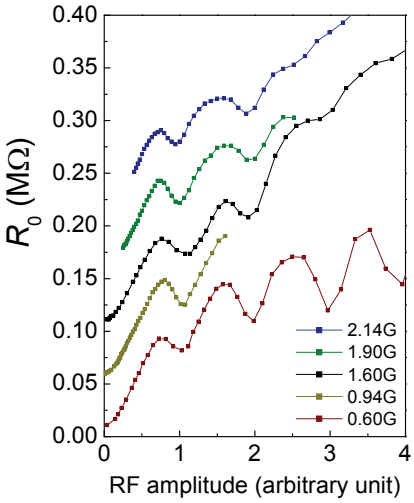

Fig. 4. The zero-bias resistance as a function of irradiating microwave (or RF) amplitude at various frequencies. Here the resistances are shifted and the microwave amplitude is rescaled to its period for each curve. The oscillation period is related to the superconducting gap of the electrodes. Adopted from (Liou, Kuo et al. 2008)

Expression (6) gives a supercurrent

$$I_s(V) = \sum_{n=-\infty}^{\infty} J_n^2(x) I_s^0\left(V - n\frac{\hbar\omega}{2e}\right). \tag{7}$$

Here $I_s^0(V)$ is the Cooper-pair tunneling current in absence of the microwaves. When the environmental impedance is much smaller than the quantum resistance, the spectral function becomes Delta-function so as to yield a coherent supercurrent, I_C at zero bias voltage. In turn, the microwave-induced supercurrent becomes $I_s(V_n) = I_C J_n^2(x)$ at a voltage $V_n = n\frac{\hbar\omega}{2e}$, leading to the structure of Shapiro steps. Ideally, each step in IV curves represents a constant-voltage state, labeled by n, featuring a "coherent" charge tunneling generated by the mode-locking. When the bias voltage is ramped, the junction would switch

from one constant-voltage state to another, and eventually jumps to the finite-voltage state. It is noteworthy that in the analogy of a driven pendulum described in the previous section, the mode-locking should yield $I_s(V_n) = I_C \left| J_n(x) \right|$, a different result from the incoherent square dependence.

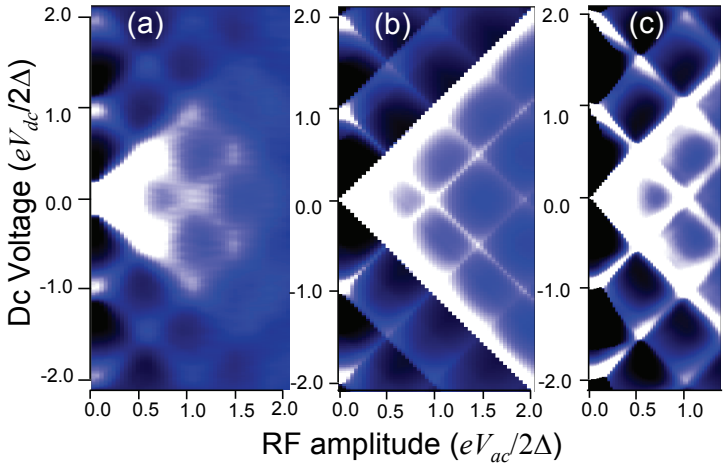

Fig. 5. The intensity plots of the dynamical conductance as a function of dc bias voltage V_{dc} and microwave amplitude V_{ac} of a long array(a) and a short array(c). According to the model described in text, the conductance peaks evolve into a "mesh" structure with the same period in V_{dc} and in V_{ac} of $2\Delta/e$. Adopted from(Liou, Kuo et al. 2008)

When the microwave frequency ω is small, argument x and n large, the summation over n can be replaced by an integration of $u = \cos^{-1}(n/x)$:

$$I_s = (2\pi)^{-1} \int_0^{2\pi} I_s^0 (V_{dc} + V_{ac} \cos u) \mathrm{d}u \,. \tag{8}$$

This expression is quite simple: It follows the same result as in the classical detector model. We note that Eq. (8) gives a general description for mesoscopic charge tunneling processes and should be applicable to both Cooper-pair tunneling and quasiparticle tunneling in the superconductive junction system.

4. Bloch wave formalism

Previous results are classical in nature. In a quantum point of view, the phase is not a function of time, but time-evolving quantum states. The un-biased single junction Hamiltonian can be expressed by

$$H_0 = 4E_C n^2 - E_J \cos\phi \,. \tag{9}$$

Here n is the charge number, obeying the commutation relation $[n, \phi] = i$. Because the potential is periodic in ϕ, the wavefunctions have the form of Bloch waves in lattices:

$$\Psi(\phi) = u_{k,s}(\phi)e^{ik\phi}$$

In which $u_{k,s}(\phi)$ is the envelope function for lattice momentum k and band index s. When there is a bias, an interaction term $H_I = (\hbar/2e)I\phi$ is added to the Hamiltonian, rendering the change of the lattice momentum and inter-band transitions.

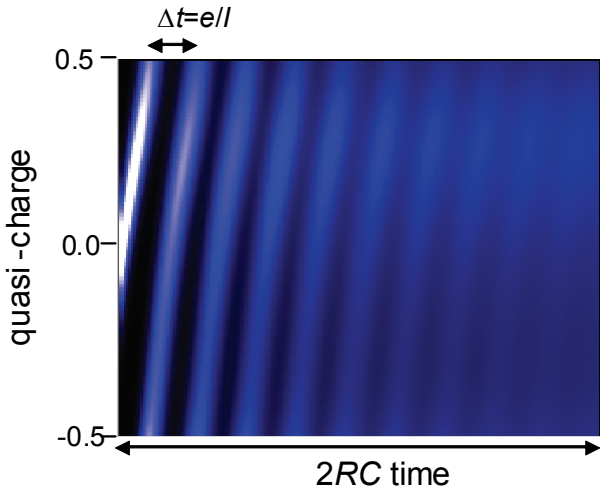

Fig. 6. The calculated diagonal elements of the single band density matrix for the junction under a dc-current bias. The expectation value of the lattice momentum (also called quasi-charge) linearly increases in time. This results in an oscillatory response with a period in time of e/I.

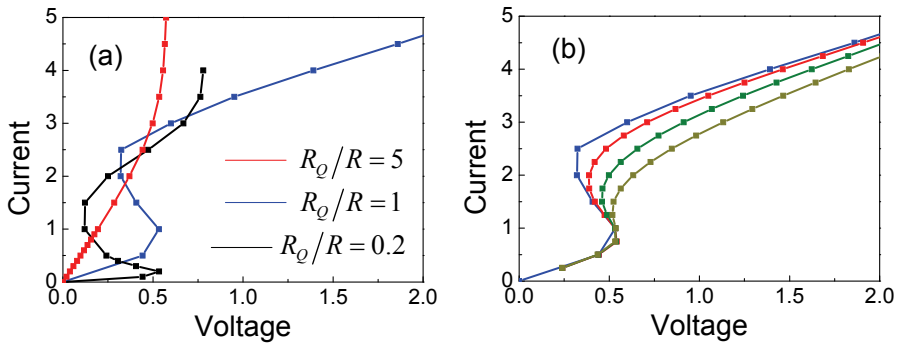

Fig. 7. (a) The calculated current-voltage characteristics of a junction with different dissipation strengths using the Bloch wave formalism. A Coulomb gap appears when the dissipation which quantified as R_Q/R is weak, featuring a relative stable quasi-charge. When the bias current is larger than $I_x = e/RC$, the quasi-charge starts to oscillate, turning the IV curve to a back-bending structure. (b) The IV curves of a R=R_Q junction under the ac driving of various amplitudes, I_1. In both figures the voltage is presented in unit of e/C while the current is presented in unit of e/R_QC.

It has been shown that in quantum dissipative system, the effect of environment can be introduced through a random bias and an effective damping to the system.(Weiss 2008) These effects would be better considered by using the concept of density matrix, ρ in stead of wavefunctions $\Psi(\phi)$:

$$\frac{\partial \rho}{\partial t} = \frac{i}{\hbar}[\rho, H].$$

Especially, when dropping the contributions from the off-diagonal elements, one can write down the differential equations for the diagonal parts:

$$\frac{\partial \sigma_s}{\partial t} = -\frac{I}{e}\frac{\partial \sigma_s}{\partial k} + \frac{1}{eR}\frac{\partial}{\partial k}(\sigma_s V_s) + \frac{k_B T}{e^2 R}\frac{\partial^2 \sigma_s}{\partial k^2} + \sum_{s'}\left\{-\left(\Gamma^Z_{ss'} + \Gamma^E_{ss'}\right)\sigma_s + \left(\Gamma^Z_{s's} + \Gamma^E_{s's}\right)\sigma_{s'}\right\} \qquad (10)$$

Here $\sigma_s(k) = \rho_{kk,ss}$ denotes the diagonal element of the density matrix for quasi-momentum *k* and band *s*. Also called master equation, expression (10) describes the time evolution of the probability of state $|k,s\rangle$. The terms describe the effect of the external driving force, the resistive force, the random force, and interband transitions due to Zener tunneling($\Gamma^Z_{ss'}$-terms) and energy relaxation($\Gamma^E_{ss'}$-terms). Also, $V_s = \frac{1}{e}\frac{\partial E_{k,s}}{\partial k}$ describes the dispersion relation of the Bloch waves in band *s*.

By calculate the time-evolution of the density matrix elements, one can obtain the corresponding junction voltage $V = \sum_s \int V_s \sigma_s dk$ under a driving current *I*, yielding a comparison to the *IV* measurement results(Watanabe & Haviland 2001; Corlevi, Guichard et al. 2006). The most important feature of this approach is the Bloch oscillation under a constant bias current, $I = 2e\omega/2\pi$ as illustrated in Fig. 6. In the *IV* calculations, a Coulomb gap appears when $R_Q/R < 1$, featuring a relative stable quasi-charge. When the bias current is larger than $I_x = e/RC$, the driving force is large enough for the quasi-charge to oscillate. The Bloch oscillation features a back-bending structure in the *IV* curve which cannot be explained by previous approaches(see Fig. 7 for calculation results and Fig. 8 for experimental results).

When the junction is driven by the ac excitation, namely $I(t) = I_0 + I_1 \cos\omega t$, a mode-locking phenomenon may be raised at specific dc current $I_n = 2ne\omega/2\pi$. This mode-locking can be viewed as a counterpart of the Shapiro steps, which gives characteristic voltages $V_n = n\hbar\omega/eV$. The master equation approach, although more accurate than the classical ways, involves complicate calculations so a numerical method is un-evitable.

5. Photon-assisted tunnelling

The method introduced in previous section is a perturbative approach which may not be appropriate when the bias current is large. Alternatively, one may consider the eigen-energy problem for a periodically driven system describe by the Hamiltonian:

$$H = H_0 + H_I(t),$$

in which $H_0 = 4E_C n^2 - E_J \cos\phi$, and H_I is a periodic function with frequency ω, satisfying $H_I\left(t + \frac{2\pi}{\omega}\right) = H_I(t) = \sum_n H_{I,n} e^{in\omega t}$. Here $H_{I,n}$ is the n-th Fourier component in the frequency domain.

In general, it can be solved by applying the Floquet's theorem, which is similar to the Bloch theorem, in the following way:

$$\Psi(t) = \sum_n \psi_n e^{in\omega t} e^{-\frac{i}{\hbar}Et}. \tag{11}$$

The result can be viewed as a main level at energy E with sideband levels spaced by $\hbar\omega$. To determine the coefficients Ψ_n, one needs to solve the eigen equation:

$$H_0\psi_n + \sum_m H_{I,m}\psi_{n+m} = E\psi_n.$$

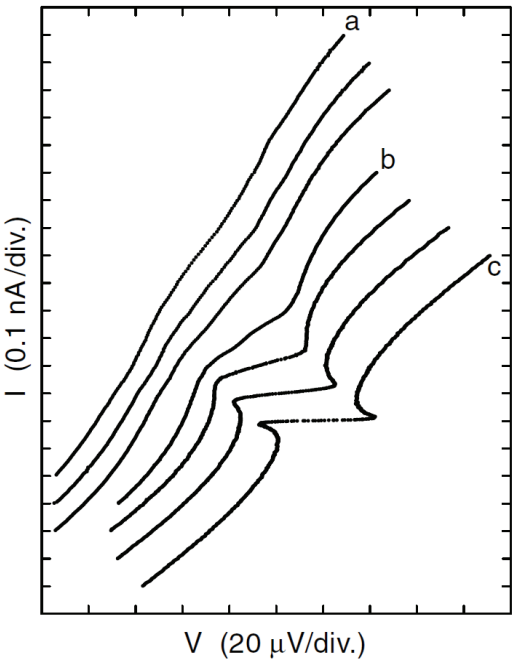

Fig. 8. The *IV* curves of the single junction in tunable environment of different impedances. From top left to bottom right, the environment impedance increases. Origin of each curve is offset for clarity. Adopted from (Watanabe & Haviland 2001)

Tien and Goldon (Tien & Gordon 1963) gave an simple model to describe the charge tunneling in the presence of microwaves. Suppose the ac driven force produces an ac

modulation in the state energy that $E = E_0 + eV_{ac}\cos\omega t$ for an unperturbed wavefunction φ_0. Then the change in wavefunction is simply on the dynamical phase such that,

$$\begin{aligned}\Psi(t) &= \varphi_0 \exp\left[\frac{i}{\hbar}\int_0^t (E_0 + eV_{ac}\cos\omega t')dt'\right] \\ &= \varphi_0 \sum_n J_n(x) e^{in\omega t} e^{-\frac{i}{\hbar}E_0 t}\end{aligned} \quad . \tag{12}$$

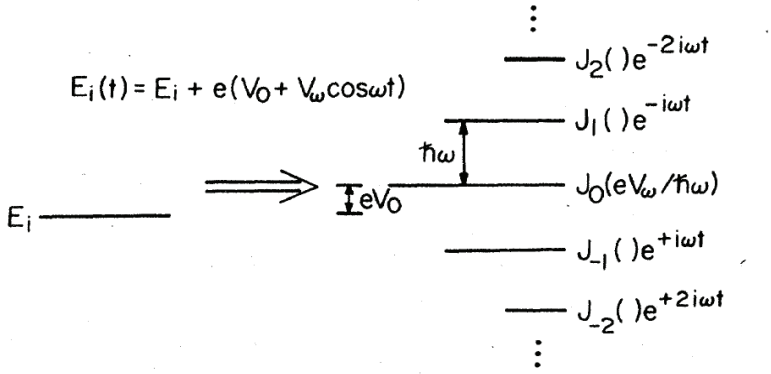

Fig. 9. The energy levels generated according to Eq. (12) in the presence of a microwave field. Adopted from (Tucker & Feldman 1985).

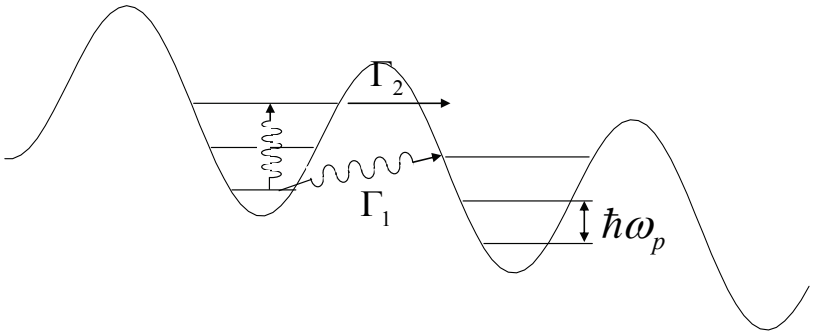

Fig. 10. A schematic of the enhanced macroscopic quantum tunneling in a single Josephson junction due to photon excitation. In each potential valley, the quantum states may form a harmonic oscillator ladder with a spacing of $\hbar\omega_p$. The absorption of photon energy may lead to an inter-valley resonant tunneling Γ_1, and a tunneling followed by an inner-valley excitation, Γ_2. The enhancement in macroscopic quantum tunneling results in a reduction of junction critical current.

Again $x = 2eV_{ac}/\hbar\omega$ as defined before. This expression is useful in the tunneling-Hamiltonian formalism applicable to the high-impedance devices such as single electron

transistors and quantum dots. One may include additional tunneling events through the side-band states with energies of $E_0 \pm n\hbar\omega$, namely the photon-assisted tunneling(PAT).
The PAT is a simple way to probe the quantum levels in the junctions. For example, if the Josephson coupling energy E_J is relatively large, a single potential valley of the washboard potential can be viewed as a parabolic one. In this case the system energy spectrum has a structure of simple harmonic ladder as shown in Fig. 10. The microwave excitation enhances the tunneling of the phase to adjacent valleys, also called macroscopic quantum tunneling when the photon energy matches the inter-level spacing. This can be observed in the reduction of junction critical current.

6. Experiments on ultra-small junctions

The Josephson junction under the microwave excitation has been studied for decades and much works have contributed to the topic, however mostly on low impedance junctions. (Tinkham 1996) Here the main focus is the junctions with small dissipation, namely, with environmental impedance $\mathrm{Re}\,Z \geq R_Q$. Although a large junction tunneling resistance as well as small junction capacitance can be obtained by using advanced sub-micron lithography, the realization of the high impedance condition remains a challenge to single junctions because of large parasitic capacitance between electrodes. Tasks have been made by using electrodes of high impedance to reduce the effective shunted resistance and capacitance.(Kuzmin & Haviland 1991) Another approach to this problem can be made by using systems in a moderate phase diffusive regime by thermal fluctuation, namely, $E_J \simeq k_B T$. Koval et al performed experiments on sub-micron $Nb/AlO_x/Nb$ junctions and found a smooth and incoherent enhancement of Josephson phase diffusion by microwaves. (Koval, Fistul et al. 2004) This enhancement is manifested by a pronounced current peak at the voltage $V_p \propto \sqrt{P}$. Recently experiments on untrasmall Nb/Al/Nb long SNS junctions have found that the critical current increases when the ac frequency is larger than the inverse diffusion time in the normal metal, whereas the retrapping current is strongly modified when the excitation frequency is above the electron-phonon rate in the normal metal. (Chiodi, Aprili et al. 2009)
Double junctions, also called Bloch transistors and junction arrays are much easier for experimentalists to realize the high impedance (low dissipation) condition. The pioneer work by Eiles and Martinis provided the Shapiro step height versus the microwave amplitude in ultra-small double junctions.(Eiles & Martinis 1994) Several works found that the step height satisfies a square law, $I_s(V_n) = I_C J_n^2(x)$ instead of the RCSJ result, $I_s(V_n) = I_C \left| J_n(x) \right|$.(Eiles & Martinis 1994; Liou, Kuo et al. 2007) In the one-dimensional(1D) junction arrays, the supercurrent as a function of microwave amplitude can be found to obey $I_s(0) = I_C J_0^2(x)$ at high frequencies, $\hbar\omega > k_B T$, although no Shapiro steps were seen. At low frequencies, the current obeys the classical detector result as in expression (8) even for quasi-particle tunneling. (Liou, Kuo et al. 2008) Therefore a direct and primary detection scheme was proposed by using the 1D junction arrays.
In single junctions with a high environmental impedance, people has reported observation of structures in IV curves at $I = 2e\omega/2\pi$, featuring the Bloch oscillations due to pronounced charge blockade. (Kuzmin & Haviland 1991) The 1D arrays also demonstrate similar

interesting behavior signifying time-correlated single charge tunneling when driven by external microwaves. This behavior yields a junction current of $I_n = 2ne\omega/2\pi$ as what was found in the single junctions.(Delsing, Likharev et al. 1989; Andersson, Delsing et al. 2000) Recently, the Bloch oscillations are directly observed in the "quantronium" device and a current-to-frequency conversion was realized. (Nguyen, Boulant et al. 2007)

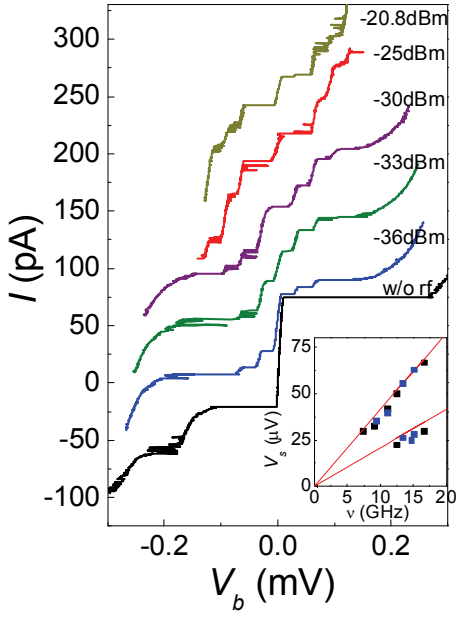

Fig. 11. The *IV* curves of a double junction under microwave irradiation clearly show Shapiro steps. Inset illustrate the step voltages obey the theoretical prediction. Adopted from (Liou, Kuo et al. 2007)

PAT is an ideal method to probe the quantum levels or band gaps in a quantum system. For the charge dominant system($E_C > E_J$, $R > R_Q$) as an example, Flees et al. (Flees, Han et al. 1997) studied the reduction of critical current of a Bloch transistor under a microwave excitation. The lowest photon frequency corresponding to the band gap in the transistor was found to reduce as the gate voltage tuned to the energy degeneracy point for two charge states. In another work, Nakamura et al. biased the transistor at the Josephson-quasiparticle (JQP) point. The irradiating microwaves produced a photon-assisted JQP current at certain gate voltages, providing an estimation of the energy-level splitting between two macroscopic quantum states of charge coherently superposed by Josephson coupling.(Nakamura, Chen et al. 1997) For the phase dominant systems, enhanced macroscopic quantum tunneling were observed in system of single Josephson junction (Martinis, Devoret et al. 1985; Clarke, Cleland et al. 1988) and superconducting quantum interference devices(SQUIDs)(Friedman, Patel et al. 2000; van der Wal, Ter Haar et al. 2000). Recently, devices based on Josephson junctions, such as SQUIDs, charge boxes, and single junctions have been demonstrated as an ideal artificial two-level system for quantum computation applications by using the microwave spectrometry.(Makhlin, Schon et al. 2001)

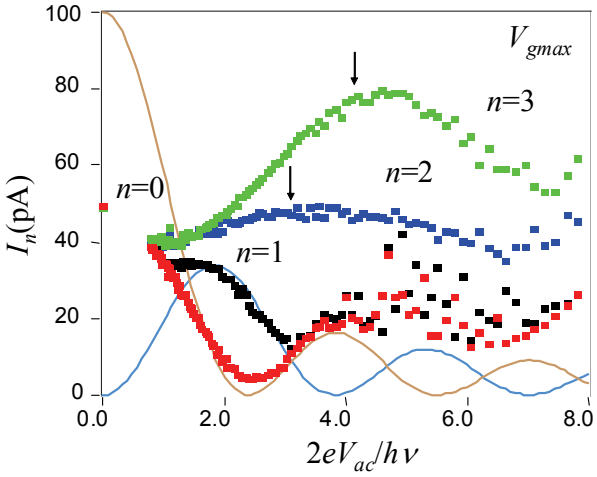

Fig. 12. The Shapiro height as a function of the microwave amplitude V_{ac} observed in a double junction system obeys the square law, a feature of incoherent photon absorption in this system. Adopted from(Liou, Kuo et al. 2007).

7. Conclusion

We have discussed the dc response of a Josephson junction under the microwave excitation in the phase diffusion regime theoretically as well as summarized recent experimental findings. In relative low impedance cases, the classical description (in phase) is plausible to explain the observed Shapiro steps and incoherent photon absorption. The quantum mechanical approaches may provide a more precise description for the experimental results of higher impedance cases such as Bloch oscillations and photon-assisted tunneling. In extremely high impedance cases, single charge tunneling prevails and a classical description in charge, such as charging effect can be an ideal approach.

8. Acknowledgement

The authors thank National Chung Hsing University and the Taiwan National Science Council Grant NSC-96-2112-M-005-003-MY3 for the support of this research.

9. References

Andersson, K., P. Delsing, et al. (2000). "Synchronous Cooper pair tunneling in a 1D-array of Josephson junctions." Physica B: Physics of Condensed Matter 284: 1816-1817.

Caldeira, A. and A. Leggett (1983). "Dynamics of the dissipative two-level system." Ann Phys 149: 374.

Chiodi, F., M. Aprili, et al. (2009). "Evidence for two time scales in long SNS junctions." Physical Review Letters 103(17): 177002.

Clarke, J., A. Cleland, et al. (1988). "Quantum mechanics of a macroscopic variable: the phase difference of a Josephson junction." Science 239(4843): 992.

Corlevi, S., W. Guichard, et al. (2006). "Phase-Charge Duality of a Josephson Junction in a Fluctuating Electromagnetic Environment." Physical Review Letters 97(9): 096802.

Delsing, P., K. K. Likharev, et al. (1989). "Time-correlated single-electron tunneling in one-dimensional arrays of ultrasmall tunnel junctions." Physical Review Letters 63(17): 1861.

Devoret, M., D. Esteve, et al. (1990). "Effect of the electromagnetic environment on the Coulomb blockade in ultrasmall tunnel junctions." Physical Review Letters 64(15): 1824-1827.

Eiles, T. M. and J. M. Martinis (1994). "Combined Josephson and charging behavior of the supercurrent in the superconducting single-electron transistor." Physical Review B 50(1): 627.

Flees, D. J., S. Han, et al. (1997). "Interband Transitions and Band Gap Measurements in Bloch Transistors." Physical Review Letters 78(25): 4817.

Friedman, J. R., V. Patel, et al. (2000). "Quantum superposition of distinct macroscopic states." Nature 406(6791): 43-46.

Ingold, G.-L. and Y. V. Nazarov (1991). *Single Charge Tunneling*. H. Grabert and M. H. Devoret. New York, Plenum. 294.

Koval, Y., M. Fistul, et al. (2004). "Enhancement of Josephson phase diffusion by microwaves." Physical Review Letters 93(8): 87004.

Kuo, W., C. S. Wu, et al. (2006). "Parity effect in a superconducting island in a tunable dissipative environment." Physical Review B 74(18): 184522-184525.

Kuzmin, L. S. and D. B. Haviland (1991). "Observation of the Bloch oscillations in an ultrasmall Josephson junction." Physical Review Letters 67(20): 2890.

Leggett, A., S. Chakravarty, et al. (1987). "Dynamics of the dissipative two-state system." Reviews of Modern Physics 59(1): 1-85.

Liou, S., W. Kuo, et al. (2007). "Shapiro Steps Observed in a Superconducting Single Electron Transistor." Chinese Journal of Physics 45: 230.

Liou, S., W. Kuo, et al. (2008). "Phase diffusions due to radio-frequency excitations in one-dimensional arrays of superconductor/ insulator/superconductor junctions." New Journal of Physics(7): 073025.

Makhlin, Y., G. Schon, et al. (2001). "Quantum-state engineering with Josephson-junction devices." Reviews of Modern Physics 73(2): 357.

Martinis, J. M., M. H. Devoret, et al. (1985). "Energy-Level Quantization in the Zero-Voltage State of a Current-Biased Josephson Junction." Physical Review Letters 55(15): 1543.

Nakamura, Y., C. Chen, et al. (1997). "Spectroscopy of energy-level splitting between two macroscopic quantum states of charge coherently superposed by Josephson coupling." Physical Review Letters 79(12): 2328-2331.

Nguyen, F., N. Boulant, et al. (2007). "Current to Frequency Conversion in a Josephson Circuit." Physical Review Letters 99(18): 187005.

Schon, G. and A. Zaikin (1990). "Quantum coherent effects, phase transitions, and the dissipative dynamics of ultra small tunnel junctions." Physics Reports 198: 237-412.

Tien, P. and J. Gordon (1963). "Multiphoton process observed in the interaction of microwave fields with the tunneling between superconductor films." Physical Review 129(2): 647-651.

Tinkham, M. (1996). *Introduction to Superconductivity*. New York, McGraw-Hill.

Tucker, J. and M. Feldman (1985). "Quantum detection at millimeter wavelengths." Reviews of Modern Physics 57(4): 1055-1113.

van der Wal, C., A. Ter Haar, et al. (2000). "Quantum superposition of macroscopic persistent-current states." Science 290(5492): 773.

Watanabe, M. and D. Haviland (2001). "Coulomb Blockade and Coherent Single-Cooper-Pair Tunneling in Single Josephson Junctions." Physical Review Letters 86(22): 5120-5123.

Weiss, U. (2008). Quantum dissipative systems, World Scientific Pub Co Inc.

17

Determination of the Local Crystal-Chemical Features of Complex Chalcogenides by Copper, Antimony, and Arsenic NQR

R.R. Gainov[1,2], A.V. Dooglav[1], I.N. Pen'kov[2], A.Yu. Orlova[1], I.A. Evlampiev[1], N.N. Mozgova[3], and R.R. Khasanov[2]

[1]*Department of Physics, Kazan Federal University, Kazan, Kremlevskaya str. 18, 420008,*
[2]*Department of Geology, Kazan Federal University, Kazan, Kremlevskaya str. 4/5, 420111,*
[3]*Institute of geology of ore deposits, petrography, mineralogy and geochemistry of the Russian Academy of Science, Staromonetny per. 35, Moscow 109017, Russian Federation*

1. Introduction

In recent years, a number of reviews have appeared in scientific literature on the application of different physical methods in the structural-chemical and physical studies of solid state materials, for example, high-temperature superconductors (HTSC). An important place among them is occupied by nuclear-resonance methods, particular, nuclear magnetic resonance (NMR), nuclear quadrupole resonance (NQR), nuclear gamma resonance (NGR or Mössbauer spectroscopy) and other. Particularly, this article shows the feasibility of using the NQR method, in some instance, in the study of those features of material structure and chemistry, which are difficult or impossible to attack by conventional methods. The key advantage of NQR is a possibility to probe directly the electric (quadrupole) interactions between nuclei and their local environment. In general, the quadrupole interaction describes the coupling of the nuclear quadrupole moment to the electric field gradient (EFG). The EFG is determined by bond directions and electronic charge distribution, therefore the quadrupole interaction is a very sensitive tool for structural-chemical studies of condensed matter. Notably, it is possible to analyze NQR data (both the spectroscopic and the relaxation) in materials containing different structural copper (^{63,65}Cu), arsenic (^{75}As), and antimony (^{121,123}Sb) complexes. This circumstance is especially important in the light of existence of two types of HTSC: Cu-oxide materials (cuprates) (Rigamonti et al., 1998) and As- and Sb-bearing pnictides (Wilson, 2009).

Our article is devoted to brief review of some important spectroscopic experimental results obtained during the studies of binary chalcogenide CuS (also known as covellite), representing the unusual low-temperature superconductor, and ternary material Ag_5SbS_4 (referred to as a stephanite). Examples are taken mainly from the studies of the authors' research group.

The article is organized as follows. Section I contains necessary NQR background for ^{63,65}Cu, ^{75}As, ^{121,123}Sb nuclei. In Section II we report our results concerning the covellite CuS and

some related materials with subsequent discussions. Section III is devoted to studies of stephanite Ag_5SbS_4 in connection with other related compounds. The paper concludes with a summary in Section IV.

2. NQR background

The NQR background will be reviewed only for the sake of clarity (Grechishkin, 1973). The nuclear spins I interact with their electronic environment through quadrupole (i.e. electric) and magnetic hyperfine couplings. In general, the NQR spectrum is described by the following Hamiltonian:

$$H_Q = \frac{eQV_{ZZ}}{4I(2I-1)}\{3I_Z^2 - I(I+1) + \frac{1}{2}\eta(I_+^2 + I_-^2)\} \quad (1)$$

Hamiltonian H_Q refers to as the coupling of nuclear quadrupole moment eQ to the local crystal electric field gradient (EFG) with V_{ZZ} the largest component of the crystal EFG tensor, $\eta = |V_{XX} - V_{YY}|/V_{ZZ}$ the asymmetry parameter showing the deviation of the EFG symmetry from the axial one, i.e. the value of η lies in the range [0,1]. The EFG components satisfy Laplace equation: $V_{XX} + V_{YY} + V_{ZZ} = 0$.

The pure NQR spectrum is observed in the case of absence of the external ($H_0=0$) and internal ($H_{int} = 0$) static magnetic fields. The number of NQR lines is defined (i) by the amount of crystallographically nonequivalent positions of quadrupole nucleus ($I > ½$) in the crystal structure, (ii) by the local geometry (i.e. symmetry) of quadrupole nucleus surrounding, (iii) by the magnitude of nuclear spin I and (iv) by the number of naturally available isotopes of quadrupole nucleus.

In case of copper, only two naturally available isotopes exist: ^{63}Cu (69.2% natural abundance, $\gamma/2\pi$=1.128 kHz/Oe, Q=-0.22 barn) and ^{65}Cu (30.8% natural abundance, $\gamma/2\pi$=1.209 kHz/Oe, Q=-0.204 barn) both having spin I=3/2 and thus two doubly degenerate ±1/2 and ±3/2 energy levels. Thus, for each isotope a transition between these levels yields a single NQR signal at a frequency:

$$^{63,65}\nu_Q = \frac{e \cdot {}^{63,65}QV_{ZZ}}{2h} \cdot \sqrt{1 + \frac{1}{3}\eta^2}\ . \quad (2)$$

Arsenic has a single total-lot isotope ^{75}As (I = 3/2, 100% natural abundance, $\gamma/2\pi$=0.729 kHz/Oe, Q=0.3 barn), therefore the single arsenic crystal-chemical position gives only one NQR signal at a frequency:

$$^{75}\nu_Q = \frac{e \cdot {}^{75}QV_{ZZ}}{2h} \cdot \sqrt{1 + \frac{1}{3}\eta^2}\ . \quad (3)$$

Antimony has two naturally occurring isotopes ^{121}Sb (I = 5/2, 57.3% natural abundance, $\gamma/2\pi$=10,188 MHz/T, Q=-1.3 barn) and ^{123}Sb (I = 7/2, 45.7% natural abundance, $\gamma/2\pi$=5,517 MHz/T, Q=-0.18 barn). The ^{121}Sb exhibits two NQR signals at frequencies ($\eta < 0.2$):

$$^{121}\nu_{Q(\pm 3/2 \leftrightarrow \pm 1/2)} = \frac{3e \cdot {}^{121}QV_{ZZ}}{20h} \cdot (1 + \frac{59}{54} \cdot \eta^2)\,, \quad (4a)$$

$$^{121}\nu_{Q(\pm5/2\leftrightarrow\pm3/2)} = \frac{6e\cdot {}^{121}QV_{ZZ}}{20h}\cdot\left(1-\frac{11}{54}\cdot\eta^2\right). \tag{4b}$$

The ^{123}Sb with I=7/2 has three NQR signals at frequencies ($\eta < 0.2$):

$$^{123}\nu_{Q(\pm3/2\leftrightarrow\pm1/2)} = \frac{e\cdot {}^{123}QV_{ZZ}}{14h}\cdot\left(1+\frac{109}{30}\cdot\eta^2\right), \tag{4c}$$

$$^{123}\nu_{Q(\pm5/2\leftrightarrow\pm3/2)} = \frac{2e\cdot {}^{121}QV_{ZZ}}{14h}\cdot\left(1-\frac{17}{30}\cdot\eta^2\right), \tag{4d}$$

$$^{123}\nu_{Q(\pm7/2\leftrightarrow\pm5/2)} = \frac{3e\cdot {}^{121}QV_{ZZ}}{14h}\cdot\left(1-\frac{1}{10}\cdot\eta^2\right). \tag{4e}$$

Thus, the single antimony crystal-chemical position in the structure of material under study yields five NQR signals.

As one can see, NQR frequency ν_Q depends on the certain arrangement of the surrounding ions through the parameters V_{ZZ} and η. The value of ν_Q is defined by two parameters in Eq.(4): V_{ZZ} and η; so it is impossible to obtain both parameters experimentally from the NQR spectra consisting of only one line for I=3/2 (copper and arsenic). Usually it is done from the angular dependence of the NMR spectrum taken for a single crystal or from numerical simulations of NMR spectrum for the unaligned powder. In some cases, for determination of η the 2D nutation NQR studies also could help.

In a semi-empirical approach (Kaufmann & Vianden, 1979), it is assumed that components of EFG tensor at Cu nuclei site can be written as the sum of two terms – lattice and valence contributions:

$$V_{ZZ} = (1-\gamma_\infty)\cdot V_{latt} + (1-R_{val})\cdot V_{val} \tag{5}$$

The parameters γ_∞, R_{val} are the Sternheimer antishielding factors. The first contribution arises from all ion charges outside the ion under consideration and can be calculated using the model of point-charges (MPC):

$$V_{latt} = \sum_i \frac{q_i\cdot(3\cdot\cos^2\theta_i - 1)}{r_i^3}, \tag{6}$$

where q_i and r_i are the charge and the position of the i-th ion, respectively, θ_i – angle between main axis of symmetry and direction into the neighboring ion.

The computation of valence contribution V_{val} (and, as consequence, total V_{ZZ}) constitutes a complex problem, since it requires a detailed knowledge of the structure and electronic density distribution. On the other hand, the comparison of ν_Q and V_{ZZ}, deduced from theoretical calculations on the basis of different structural models and approaches (see Eq.(5)), with experimental values (Eq.(4)) permits to determine the individual features of local electronic arrangement and peculiarities of chemical bonds. Actually, the lattice contribution V_{val} is defined by crystal symmetry, whereas the valence contribution V_{val} is determined by the local symmetry of nearest environment, i.e. according to NQR frequencies and line-widths it is possible to investigate the following EFG characteristics: the

electronic density distribution inside of different coordination complexes and their symmetry, the extent of ionic (covalent) bonds and angles between them. Every factor, which is connected with reorganization of atomic or molecular group, can change significantly the EFG value on the nucleus inside of a such group and, as consequence, NQR is very sensitive to different crystal-chemical transformations in crystal lattice. Therefore, the studies of temperature dependences of NQR spectroscopic parameters give the possibility to find phase transitions and investigate their nature.

3. Towards to electronic structure of binary copper chalcogenides

There is a great number of compounds in the system of binary copper chalcogenides Cu-S, Cu-Se, and Cu-Te. In particular, materials eleven natural minerals and two unstable synthetic phases among only binary copper-sulfide have been discovered up to date (Goble, 1985; Gablina, 1997). Many of them are widely used in optoelectronics (Abrikosov et al., 1975; Isac et al., 2007) and some of them represent the industrial mineral specimens in copper-ore deposits (Izoitko, 1997). The more significant involving of these compounds into the practical application is stopped by the fact that currently available standard instrumental techniques for studying crystal-chemical problems such as X-ray structural diagnosis, optical spectroscopy, and electronic microscopy have inherent limitations (Gablina, 1997). These manifest themselves in being unable to characterize the chalcogenides samples fully, especially if they are polycrystalline. These methods are mainly ineffective and little informative in case of multiphase natural samples (minerals) (Gablina, 1997).
This Section describes briefly the spectroscopic studies of layered low-temperature superconductor CuS (covellite, originally published in (Gainov et al., 2009)) and related, potentially perspective, but insufficiently known compounds: non-stoichiometric sulfide $Cu_{1.6}S$ (naturally occurring as geerite) and selenium analog of CuS – α-CuSe (klockmannite). The description of experimental methodic and synthesis conditions can be found in (Gainov et al., 2009).

3.1 Crystal-chemistry of CuS, $Cu_{1.6}S$, and α-CuSe

Covellite CuS represents the metal with excellent hole conductivity, which becomes anisotropically superconducting below T_C = 1.6 K (Meissner, 1929; Buckel & Hilsch, 1950; Saito et al., 1997; Di Benedetto et al., 2006). The elementary cell of CuS at room-T has a hexagonal symmetry (space group $P6_3/mmc$) (Berry, 1954; Evans & Konnert, 1976; Ohmasa et al., 1977). The structure of CuS can be described as a "sandwich", which consists of three alternating layers A_1-B-A_2 (Fig. 1). The layer B represents the net of [Cu(1)-$S(1)_3$]–triangles, whereas the layers A_1 and A_2 are made up of [Cu(2)-S(1)$S(2)_3$]–tetrahedra. The units A_1-B-A_2 are connected together along the c-axis by S(2)-S(2) bonds. It was revealed that the second-order phase transition (PT) is occurred at about T_{PT} = 55 K (Fjellvåg et al., 1988). This transition can be presented as a little shift of the layer B with respect to the layers A_1 and A_2 perpendicular to the c-axis with the change of the Cu(2)-S(1)-Cu(2) bonding angle from 180° at room-T to 170° below T_{PT}.
The crystal structure of klockmannite α-CuSe is not identified in detail up to date. As a first approach, it is assumed that the structure of α-CuSe is somewhat similar to those in CuS (Berry, 1954; Peiris et al., 1998; Milman, 2002): there are the same space group and layered motive A_1-B-A_2 with the $CuSe_3$, $CuSe_4$, and Se-Se complexes. At the same time, it is proposed the occurrence of CuS-based superlattice in klockmannite (Berry, 1954).

The structure of geerite $Cu_{1.6}S$ is unsolved. It was suggested only that $Cu_{1.6}S$ can have a structure with the blende-like subcell (Goble, 1985).

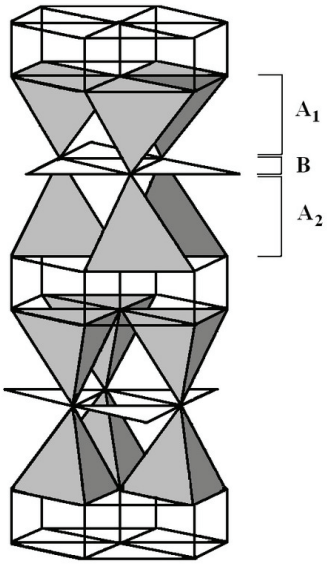

Fig. 1. Crystal structure of the covellite CuS above T_{PT} = 55 K. For details, see text

3.2 NQR spectra of CuS, $Cu_{1.6}S$, α-CuSe

In Table I the NQR frequencies observed for the title materials together with previously published data are listed. As one can see, the values of NQR frequencies are quite different. However, their comparison and analysis can allows us to reveal some unique features of compounds studied.

Let us start from the covellite CuS. It was found that copper NQR spectra of both synthetic and natural samples of CuS contain two copper pairs (Gainov et al., 2009). The presence of two spectral pairs permits us to assert that NQR spectra reflect the occurrence of two crystallographically non-equivalent sites of copper nuclei in CuS. The first pair, attributed to three-coordinated Cu(1), is placed at 14.88 (^{63}Cu, 4.2 K) and 13.77 MHz (^{65}Cu, 4.2 K) (Fig. 2(a)), whereas the second pair, assigned to four-coordinated Cu(2) site (not shown here, see (Gainov et al., 2009)), is located at 1.87 (^{63}Cu, 4.2 K) and 1.73 MHz (^{65}Cu, 4.2 K). In general, there is no EFG at the sites with cubic local symmetry (Slichter, 1996). This case is takes place for the tetrahedral Cu(2) sites in layers A_1 and A_2 (Fig. 1). However, significant deformations of the CuS_4 tetrahedrons break the cubic symmetry and, as consequence, EFG on the copper nucleus in this position becomes nonzero. The appearance of low-frequency NQR signals points that this case is realized actually for the tetrahedral Cu(2) sites in CuS. Therefore, our NQR spectra prove strongly the crystallographic data (Fjellvåg et al., 1988) concerning the occurrence of low-symmetry distortions around Cu(2) sites below T_{PT} = 55 K. Other words, NQR spectra can serve as an independent confirmation of the low-*T* model of the CuS structure.

Material	**Positions**	**^{63}Cu NQR frequencies [1], MHz (T = 4.2 K)**
CuS (covellite)	Site 1	14.89
	Site 2	1.87
$Cu_{1.6}S$ (geerite)	Site 1	16.95
	Site 2	16.20
	Site 3	15.25
	Site 4	11.95
	Site ?	Below 2 MHz?
α-CuSe (klockmannite)	Site 1	12.17
	Site 2	11.89
	Site 3	9.49
	Site 4	9.39
	Site 5	8.27
	Site 6	6.60
	Site 7	6.50
	Site 8	4.49
	Site 9	4.01
	Site 10	3.75
	Site 11	3.29
	Site 12	2.83
	Site 13	2.09

[1] The values of NQR frequencies for ^{65}Cu isotope can be calculated in accordance with ratio $\nu_Q(^{63}\text{Cu})/\nu_Q(^{65}\text{Cu}) = 1{,}081$.

Table I. NQR frequencies for CuS and some related compounds.

High-frequency NQR spectra, corresponding to triangular Cu(1), are also intriguing (Fig. 2(a)). It is notable that these NQR signals are placed at lower frequency range in comparison with the region of 20-25 MHz, in frame of which NQR signals of majority of other copper sulfides lie (Abdullin et al., 1987). In case of copper sulfides EFG is mainly formed by the lattice term and a quite narrow range of the ν_Q changes can be explained by insignificant variations of the Cu-S distances, S-Cu-S angles and the polarity of chemical bonds. In fact, such conclusion was checked by theoretical calculations according to Mulliken-Wolfsberg-Helmholtz method (Abdullin et al., 1987). This result indicates directly that the valence contribution for the EFG at the Cu(1) site in CuS is more considerable than in case of triangular units CuS_3 of other sulfides. Analysis shows that the more probable reason of this unusual ν_Q lowering is connected with anomalously short Cu(1)-S distances in CuS (2.19 Å) compared to those in other sulfides (≈ 2.33 Å). It seems, however, that due to Bayer's influence of thermal-induced lattice vibrations, NQR frequency ν_Q must increase with decreasing distances as it takes place in most compounds (Semin et al., 1975): according to MPC model (Eq.(6)), EFG is inversely proportional to the distance between metal and ligand. On the other hand, the shortening of metal–ligand distances can lead to charge transfer with subsequent redistribution on the different orbitals (Semin et al., 1975). In our case this process can be related to the charge transfer between valency Cu-4p,3d and S-3p orbitals (Gainov et al., 2009). Indeed, in frame of the semi-empirical approach (Section I), the valence contribution to the EFG, V_{val}, is related particularly to the various electronic hole densities as follows:

$$V_{val}^{(4p)} = A \cdot \langle r^{-3} \rangle_{4p} \cdot [N_{4p(z)} - \frac{1}{2} N_{4p(x)} - \frac{1}{2} N_{4p(y)}], \quad (7)$$

where A is a constant, $N_{3d(x,y,z)}$ and $N_{4p(x,y,z)}$ are the numbers of electronic holes in different Cu-4p orbitals, the charge of an electron is given by $-e$. In this way, the hole concentration can be estimated from the change of ν_Q. It was pointed that the shortening of Cu-S distances in Cu(1)S_3 complexes in CuS can lead to decreasing electronic density of the Cu-4p_z orbital and increasing population of Cu-4p_x and Cu-4p_y orbitals. According to Eq.(7) this factor can play a vital role in the lowering of the total EFG value at the Cu site by about 5 MHz. Thus, the experimentally observed shift of the high-frequency ^{63}Cu(1) NQR signal from the frequency range of 20–25 MHz typical for three-coordinated Cu by S atoms in other copper sulfides can serve as an indication of the strong hybridization of Cu(1)–S chemical bonds in Cu(1)S_3 complexes. Remarkably, this conclusion was confirmed later by studies of copper nuclear spin-lattice relaxation (Gainov et al., 2009).

Let us compare now the ^{63}Cu NQR spectra of covellite CuS and geerite $Cu_{1.60}S$ (Fig. 2(b)-2(d), Table I). As one can see, the samples studied are multiphase and contain two structural phases (CuS and $Cu_{1.60}S$).

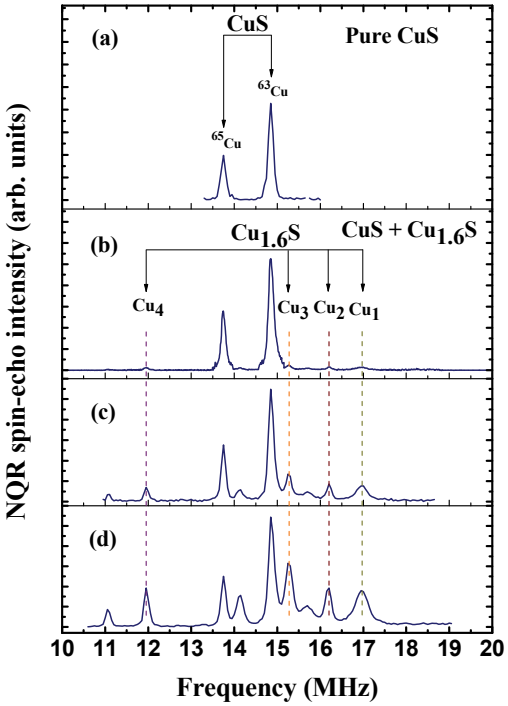

Fig. 2. High-frequency copper NQR spectra for covellite, CuS, and geerite, $Cu_{1.6}S$. Arrows point to the positions of ^{63,65}Cu(1) NQR signals of CuS. The vertical dashed lines point to the positions of ^{63}Cu NQR signals of $Cu_{1.6}S$ phase For details, see text.

The principle difference between samples is a variation of quantitative proportion of CuS and $Cu_{1.60}S$. The NQR spectra of such samples are convenient for detailed discussion. As indicated in Fig. 2, at high-frequency range (10.00-17.00 MHz) there are five copper NQR pairs, one of them corresponds to covellite CuS (exact coincidence of Cu line frequencies); the additional four Cu pairs belong to another structural phase – geerite $Cu_{1.60}S$. Notably, the NQR spectra, which pertain to this phase, coincide in all multiphase samples and include the following lines: 16.95, 16.20, 15.25, 11.95 MHz for ^{63}Cu and 15.67, 14.98, 14.11, 11.06 MHz for ^{65}Cu. It should be noted that our results prove fully the previous data for $Cu_{1.6}S$ (Anashkin et al., 1994), according to which these eight Cu NQR lines have been observed at the same frequencies. It is interesting that the NQR signal intensities of $Cu_{1.6}S$ phase increase with increasing amount of $Cu_{1.6}S$ and, simultaneously, the signals intensities of CuS decrease according to the same proportion (Fig. 2). We not here that this fact can in general serve as supplementary striking evidence for the possibility to use NQR method in qualitative and quantitative phase-analytical diagnostics of different chalcogenides.

As it was pointed above (Section I), the number of NQR centers in the structure of material studied is not less than the amount of crystallographically non-equivalent positions of resonant nuclei. At least four centers exist in case of geerite $Cu_{1.6}S$ (four pairs of ^{63}Cu and ^{65}Cu lines). Hence, the total number of different crystal-chemical sites of copper in this compound is not less than four. This circumstance reflects the serious distinction in symmetry of CuS and $Cu_{1.6}S$ electronic structures. On the other hand, we can see that the range of 10.00-17.00 MHz, in frame of which eight $^{63,65}Cu$ lines of $Cu_{1.6}S$ are located, is also not typical for NQR signals exhibited by most of copper sulfides. Moreover, NQR lines of $Cu_{1.6}S$ are grouped around the high-frequency Cu NQR signal of covellite CuS. Taking into account these two aspects, it is possible to claim that the electronic structures of CuS and $Cu_{1.60}S$ are still different, but they have the same crystal-chemical motive. In principle, our NQR results suggest that the structure $Cu_{1.60}S$ can be interpreted as the derivative of covellite CuS structure with the strong deformations. To our knowledge, this conclusion is a first experimental argument in favor of crystallographical proximity between CuS and $Cu_{1.60}S$ phases.

We turn now to the ^{63}Cu NQR spectrum for CuS and the ^{63}Cu NQR spectrum for selenium analog of CuS – klockmannite, α-CuSe (Table I). Their comparative analysis can also introduce new information concerning their electronic structure as well as highlight some reasons for low-temperature phase transitions in these materials (Section II.1). In general, the copper selenide CuSe undergoes two phase transitions upon cooling: from γ-CuSe into β-CuSe modification near 398 K and to α-CuSe at 323 K (Nozaki et al., 1995; Milman, 2002). It was proposed that α-CuSe has the same structure as CuS (Berry, 1954) and the β–γ transformation of CuSe is similar to that in CuS at T_{PT}=55 K (Nozaki et al., 1995). Notably, Raman spectroscopy and powder X-ray diffratometry shows that in the system of $CuS_{1-x}Se_x$ ($0 \le x \le 1$) compounds T_{PT} increases from 55 K for x=0 up to 398 K for x=1 (Nozaki et al., 1995). However, it was found that α-CuSe is characterized by 13 lines in the spectrum with NQR frequencies in the range of 13–2 MHz at 4.2 K. First, this aspect points strongly to the presence of strong deformations of the α-CuSe crystal and gives evidence that CuS and α-CuSe are not isostructural as it was supposed earlier (Berry, 1954). It is clearly seen that α-CuSe has at least 13 non-equivalent Cu positions. These data point that α-CuSe can be considered as distorted version of CuS-based structure. Second, ^{63}Cu NQR frequencies in α-CuSe are rather low as compared with that in CuS. This indicates that insertion of Se atoms

instead of S in CuS results in the conversion of Cu(1) threefold units (Fig. 1) into distorted fourfold ones in $CuS_{1-x}Se_x$. However, such a substitution mechanism implies basically the preservation of layered structural motive in $CuS_{1-x}Se_x$ (as in CuS). The preferential occupation of Se at the S(2) sites (Nozaki et al., 1995) leads to the approaching of some Se(2) atoms to Cu(1) sites and to the formation of distorted tetrahedrons $Cu(1)Se(1)_3Se(2)_1$ in α-CuSe instead of triangular units $Cu(1)S(1)_3$ in CuS (Fig. 1). In this case such deformations would promote the approaching of Cu(1) and Cu(2) ions to each other and creation of an effective interaction between them, as it was proposed for CuS and α-CuSe earlier (Fjellvåg et al., 1988; Milman, 2002). Upon cooling this interaction can stimulate the phase transition. Such scenario is supported by the dependence of the T_{PT} value on the Se amount in mixed samples $CuS_{1-x}Se_x$ ($0 \le x \le 1$) (Nozaki et al., 1995). Actually, since the Cu(1)-Cu(2) bonds in CuS are longer than that in $CuS_{1-x}Se_x$, this phase transition in CuS occurs at lower T. Thus, NQR spectra signify that α-CuSe material is related crystal-chemically to CuS and have a somewhat similar layered structure, but either of $Cu(1)Se_3$ and $Cu(2)Se_4$ complexes in this compound are strongly distorted and this aspect leads again to layered A_1-B-A_2 structure, as in CuS, but with different and uncertain structures of layers A_1, A_2, and B (Fig. 1).

3.3 Temperature dependences of NQR spectra of CuS, $Cu_{1.6}S$, α-CuSe

The dependence of the high-frequency ^{63}Cu(1) NQR line of CuS on temperature is shown in Fig. 3. As one can see, the quadrupole frequency ν_Q decreases with increasing temperature without significant anomalies. However, there exist two weak effects: the change of the slope in the temperature dependence of ν_Q at 65 K (near T_{PT}) and 210 K. In order to describe an approximate behavior of ν_Q in the region of 65–290 K we applied the following equation (Kaufmann & Vianden, 1979):

$$\nu_Q(T) = \nu_Q(0) \cdot (1 - a \cdot T^b), \tag{8}$$

where $\nu_Q(0)$, a and b are the fitting parameters. The best result of fitting depicted in Fig. 3 by solid curve was obtained for $\nu_Q(0)$ = (14.95 ± 0.02) MHz, a = (1.7 ± 0.5)*10^{-4} MHz/K and b = (0.98 ± 0.05). It has been argued that the dependence of the NQR frequency in CuS on temperature can be understood in terms of charge fluctuations in Cu(1)-S(1)-Cu(2) bonds. It is known that a lot of non-cubic metals $\nu_Q(T)$ can be well reproduced by the empirical Eq. (8) with b=1.5; this relation is often referred to as the "$T^{3/2}$ law" (Kaufmann & Vianden, 1979). No reliable explanation of the $T^{3/2}$ temperature dependence of ν_Q has been presented in the literature (Kaufmann & Vianden, 1979; Torumba et al., 2006). However, it is proposed that thermal vibrations of the host lattice atoms are regarded as responsible for such universal relation. CuS shows another relation – parameter b is close to 1 and, as consequence, $\nu_Q(T)$ does not follow the $T^{3/2}$ law. Such unusual behavior of ν_Q is observed in mixed-valence metals, for example, in $EuCu_2Si_2$ (Sampathkumaran, et al., 1979). The principle distinction of mixed-valence metals from "simple" ones is a variable number of conduction electrons (holes), which can "stick" temporary to ionic orbitals as valence electrons (holes). This valence instability initiated by Eu ions influences indirectly the Cu quadrupole interactions (V_{ZZ}) and, as it was shown experimentally, the $T^{3/2}$ law becomes not valid. Since in the range of 60–290 K there are no structural changes in CuS ($\eta \approx 0$), the dependence of ν_Q on temperature is determined only by V_{ZZ}. In a similar manner, the bridging S(1) ion in CuS can provide a minor charge transfer between Cu(1) and Cu(2) in some fluctuating regime. The strong hybridization of Cu(1) and Cu(2) conduction bands via S(1) atom, which was

revealed by means of analysis of NQR spectra and nuclear relaxation (Section II.2), should allow this transfer.

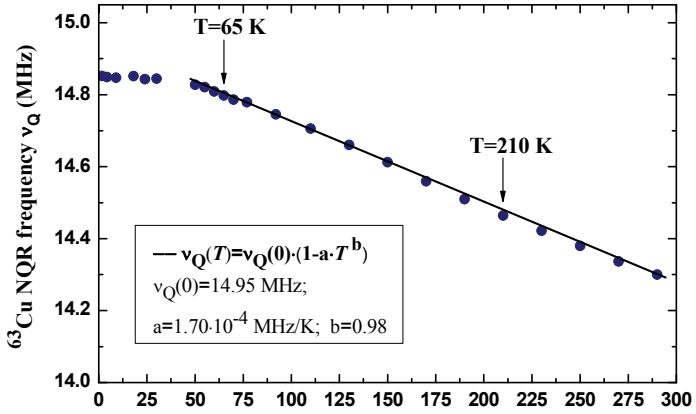

Fig. 3. The temperature dependence of ^{63}Cu(1) NQR frequency for CuS (points) with the fit of data by Eq. (8) within 65–290 K (curve) and extracted fitting parameters. Arrows point to the positions of the change of slope in the $\nu_Q(T)$ dependence at 210 K and at 65 K. For details, see text.

Remarkably that the temperature dependences of NQR frequencies in geerite $Cu_{1.6}S$ (Section II.2) have the same linear character, as it takes place in case of case covellite CuS (results will be published in forthcoming paper). This experimental feature can also serve as indication of the similarity of CuS and $Cu_{1.6}S$ structures. Furthermore, the proximity of NQR spectra for CuS and $Cu_{1.6}S$ materials and their analogous temperature dependences provide evidence that the main structural block of geerite was inherited from covellite CuS. The temperature dependences of some NQR frequencies in α-CuSe were also monitored in the range of 4.2-77 K (Anashkin et al., 1994). It was found that the temperature gradient of NQR frequencies is rather small, although the dispersion of NQR frequencies is substantial. These data are also point that CuS and α-CuSe have the similar features in lattice dynamics, where the layered structural motive and comparable coordination complexes play the essential role.

4. Towards to electronic structure of antimony chalcogenides Sb_2S_3, As_5SbS_4, Ag_3SbS_3

The binary and ternary chalcogenide compounds of As, Sb, and Bi have the structures, which are closely related to zinc blende or wurtzite materials. As copper chalcogenides, some of them are used in optoelectronics (Abrikosov et al., 1975) and these compounds also represent the economically important minerals, which serve, for example, as sources of silver. From "scientific" position, these materials are interesting due to the fact that many of them undergo phase changes at low temperatures from ordered states to cation-disordered ones. The disordered states in these materials have potentially useful unique physical properties. For example, proustite Ag_3AsS_3 and pyrargyrite Ag_3SbS_3 appear to be excellent model crystals for studies of commensurate and incommensurate ferroelectric properties (Blinc & Zeks, 1974). Experience has proved that NQR in combination with X-ray analysis

can be as an effective tool for studies of detailed aspects of such phases (Blinc & Zeks, 1974). In spite of this fact, some related materials (for instance, phase of stephanite, Ag_5SbS_4) are little known from crystal-chemical and physical point of views. In order to highlight the electronic features of Ag_5SbS_4, we present here some modern NQR data concerning this compound and comparative analysis in the context of associated materials, such as stibnite (antimonite) Sb_2S_3 and pyrargyrite Ag_3SbS_3.

4.1 Crystal-chemistry of Sb_2S_3, As_5SbS_4, Ag_3SbS_3

Stibnite (Sb_2S_3), pyrargyrite (Ag_3SbS_3), proustite (Ag_3AsS_3), stephanite (Ag_5SbS_4), and other Sb(As)-bearing sulfides and sulfosalts belong to the group of the complex chalcogenides with universal formula $A_xB_yS_n$, where A = Ag, Cu, Pb, etc., and B = As, Sb Bi. Some structural units in materials mentioned above are the same; hence the chalcogenides are rather similar. In particular, all of them consist of infinite one-dimensional chains, extended along the c-axis. One of the basic unit elements are the trigonal group BS_3, referred also to as umbrella-like complexes (Povarennykh, 1972). The differences between them, however, are substantial and are caused by different combinations of structural units, mechanisms of their connection and, of course, different kind of crystal-chemical distortions. However, these data are not always determinable with the desired accuracy by the methods of X-ray diffraction: the patterns usually obtained are averaged for all elementary cells.

The elementary cell of stephanite, Ag_5SbS_4, at room temperature corresponds to orthorhombic symmetry with the space group $Cmc2_1$ (Fig. 4). The parameters of the unit cell are the following: a =7.830 Å, b = 12.450 Å, c = 8.538 Å (Petrunina et al., 1970). The structure can be presented as chains formed by SbS3 complexes. These chains organize the pairs and they are oriented along the c-axis. Atoms of Ag are located between the SbS3 units of adjacent chains. According to X-ray analysis, stephanite contains a single crystal-chemical position of Sb in the structure.

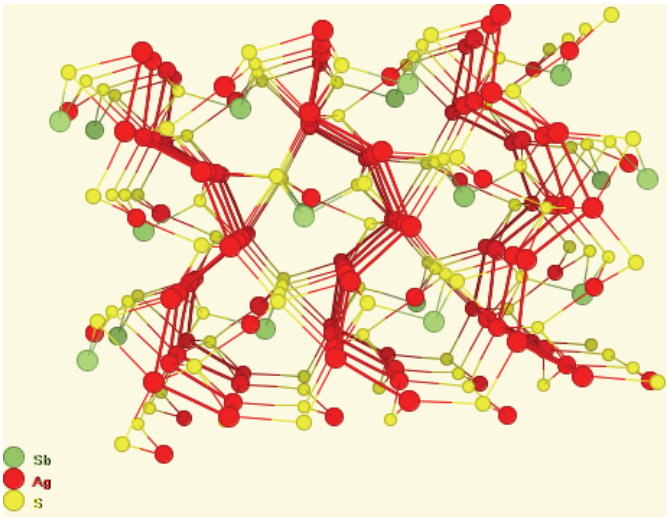

Fig. 4. Crystal structure of the stephanite, Ag_5SbS_4 at room temperature. Green circles – antimony atoms, red circles – silver atoms, yellow circles – sulfur atoms.

The space group of stibnite (antimonite), Sb_2S_3, is *Pbnm*, the lattice constants are the following: a =11.20 Å, b = 11.28 Å, c = 3.83 Å (Povarennykh, 1972). The lattice is constructed on the base of Sb-S-Sb zigzag-like chains, which form the double tapes $(Sb_4S_6)_n$. The unit cell contains two crystallographically non-equivalent Sb-postions: site *A* and site *B*.
Pyrargyrite, Ag_3SbS_3, and proustite, Ag_3AsS_3, are isostructural compounds with limited substitution between As and Sb (Povarennykh, 1972). Umbrella complexes (BS_3) are turned by vertexes to one direction and jointed by means of Ag atoms, which form together with S atoms the helical chains elongated along the cell axis. Their space groups at room temperature are *R3c* with cell dimensions a =10.78 Å, c = 8.682 Å for proustite and a =11.05 Å, c = 8.74 Å for pyrargyrite. All of them have at room temperature the single crystal-chemical position of Sb(As) in the structure.

4.2 NQR spectra of Sb_2S_3, As_5SbS_4, Ag_3SbS_3

In Table II the NQR frequencies of the compounds mentioned above are reported. NQR spectrum of stephanite is shown in Fig. 5. In general, it was found that antimony NQR spectra of Sb_2S_3 at 77 K consist of 10 lines (Safin & Pen'kov, 1962; Abdullin et al., 1977). This fact points that stibnite have two crystallographically non-equivalent sites of antimony nuclei (Section I). Such NQR data are in good agreement with X-ray analysis studies (Section III.1), according to which there exist two antimony positions noted as site *A* and site *B*. As it should be noted from NQR spectra, *A* complexes are axially-symmetrical; asymmetry parameter of EFG tensor closes to zero (η = 0.8 %). In contrast, *B* complexes are strongly distorted ($\eta \approx$ 40 %). As one can see from Table II and Fig. 5, ^{121,123}Sb NQR spectra of stephanite, Ag_5SbS_4, at 77 K consist of 5 lines. This information indicates that all positions of antimony in stephanite lattice are structurally equivalent (there is a single antimony site). Non-zero value of asymmetry parameter signifies that the perceptible distortions of SbS_3 pyramids take place in Ag_5SbS_4. Analogous situation happens in case of isostructural pyrargyrite, Ag_3SbS_3, and proustite, Ag_3AsS_3 (Pen'kov & Safin, 1966a). For both chalcogenides, the NQR signals at 77 K are observed from one structural Sb(As) site (Table II). Analysis of NQR spectra shows that asymmetry parameters at these temperatures are not far from zero (Pen'kov & Safin, 1966a).

Material	Position	^{121,123}Sb NQR frequencies, MHz (T = 77 K)					η, %	Ref.
		^{121}Sb		^{123}Sb				
		1/2↔3/2	3/2↔5/2	1/2↔3/2	3/2↔5/2	5/2↔7/2		
Sb_2S_3 (stibnite)	Site *A*	47.71	95.41	28.96	57.90	86.86	0.8	Safin & Pen'kov, 1962
	Site *B*	42.98	73.29	32.27	43.13	67.45	38.1	
Ag_3SbS_3 (pyrargyrite)	Single	49.84	99.70	30.28	60.52	90.78	≈ 0	Pen'kov & Safin, 1964
Ag_5SbS_4 (stephanite)	Single	54.942	108.280	34.265	65.462	98.700	10.7	This work; Pen'kov & Safin, 1966a

Table II. NQR frequencies for Ag_5SbS_4 and some related compounds.

The construction of umbrella $Sb(As)S_3$ complexes, in contrast to some complexes with transition metals (as it occurs, for example, for CuS_4 units in copper chalcogenides, see Section II) suggests the presence of non-cubic local crystal fields. This circumstance shows that EFG on the Sb(As) nuclei is not caused by structural distortions (particularly, X-Sb(As)-

X angles have little changes in equitype coordination complexes AsS_3-SbS_3-BiS_3-AsO_3). As consequence, it is obvious that *sp*-hybridization does not play a substantial role in creation of EFG. In this case the EFG is formed primarily due to redistribution of electronic density. It was demonstrated specially that the main factor influenced on the EFG value in NQR spectra of Sb(As)-bearing chalcogenides is a change of Sb(As)-S bond polarity (Pen'kov & Safin, 1966b), i.e. the extent of bond ionicity. Analysis of the EFG nature in a number of structural motives allows one to take into account the following aspects in distribution of electronic density: 1) ionicity-covalency of Sb(As)-S bonds, in frame of which the donor-acceptor type of bonds are also become apparent; 2) occurrence of Sb(As)-Sb(As) interactions; 3) influence of Me-S (Me is a metal element, such as Cu, Pb, Ag, and other). The donor-acceptor bonds can be realized owing to transfer of electrons from atoms-"donors", which either contains the essential number of electrons on the external *p*- and *d*-orbitals or have "unshared" s^2-electrons, to atoms-"acceptors" with the little number of electrons. Sulfur atoms (S, $3s^23p^4$) can serve as donors due to both the unshared s^2-electrons and the *p*-electrons.

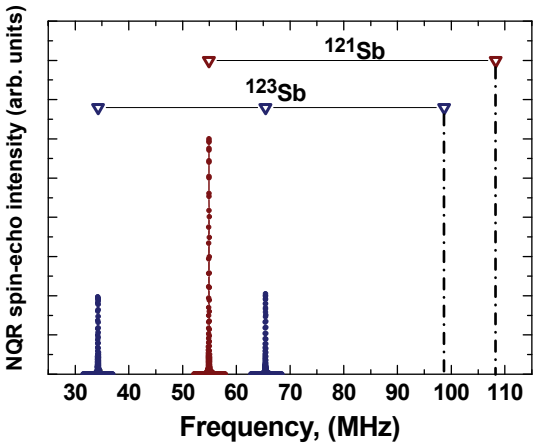

Fig. 5. Antimony NQR spectra for Ag_5SbS. Triangular symbols point to the positions of ^{121,123}Sb NQR signals. The vertical dashed lines point to the positions of two Sb NQR signals, which were not studied. For details, see text.

In this context, let us discuss at first the EFG origin in stibnite, Sb_2S_3 (Safin & Pen'kov, 1962; Abdullin et al., 1977). Interestingly, the values of NQR frequencies for antimony in *B* site are notably less that NQR frequencies for this element in *A* site. As it was proposed, Sb-S bonds in case of *B* site appear to be more covalent as compared with bonds, corresponding to *A* site. The increasing of covalent effect is explained by manifestation of additional bonds, having the donor-acceptor nature. These contacts should decrease the value of effective charge on the antimony atom. Taking into account these aspects, the coordination number of Sb atoms located in *B* position increases up to 5. Corresponding coordination polyhedron can be visualized as a distorted semi-octahedron SbS_5.

In case of "metallic" chalcogenides situation is more complex. In contrast to binary Sb(As)-bearing compounds, the crystal electric fields, caused by Sb(As)-S bonds in frame of SbS_3(SbS_5) complexes, are influenced also by the fields created by metallic atoms (Cu, Ag

and other). These interactions lead to appearance of twofold consequence. First factor is a so-called steric effect: Sb(As) and S atoms are repulsed. Second factor is an induction effect, according to which the metallic atoms "remove" part of electronic density. These effects are closely associated and usually coexist. As a result, Sb(As)-S bonds are "loosened" and they become more polar. This leads, as a rule, to increase of NQR frequencies. The pyrargyrite-proustite phases $Ag_3[Sb(As)]S_3$ may serve as an excellent example of such behavior (Pen'kov & Safin, 1966a). As it was found, the natural samples of pyrargyrite, Ag_3SbS_3, can contain a little number of As impurity; these substitution atoms occupy the positions of Sb. The resonance frequency shift for As impurities indicates the existence of more ionic nature for the As-S bonds in Ag_3SbS_3 matrix than for those in the etalon samples of proustite, Ag_3AsS_3. The increasing of ionicity is explained by steric inconsistency: actually, the covalent radiuses of As and Sb atoms are 1.21 and 1.41 Å, respectively. In this case, the impurity atoms are forced to accommodate themselves into the structural positions and dimensions of "native" matrix atoms.

Now, it is easier to discuss the EFG nature in stephanite, Ag_5SbS_4. Indeed, ^{121,123}Sb NQR frequencies for Ag_5SbS_4 are higher than that for binary stibnite, Sb_2S_3. This fact provides evidence that the "metallic" twofold factor, in addition to "standard" donor-acceptor bonds, also exists in Ag_5SbS_4. Moreover, the values of NQR frequencies for Ag_5SbS_4 exceed the values of resonance frequencies exhibited by pyrargyrite, Ag_3SbS_3. Therefore, Sb-S bonds in stephanite appear to be more polar than in stibnite and pyrargyrite. This circumstance implies also that the higher NQR frequencies (as compared with pyrargyrite) are associated with a higher coordination number of the Ag atoms (in other words, with stronger induction interaction of the Sb-S and Ag-S bonds).

4.3 Temperature dependences of NQR spectra of Sb_2S_3, As_5SbS_4, Ag_3SbS_3

The study of spectroscopic parameters (NQR frequencies, ν_Q, NQR line-widths, $\Delta\nu_Q$, and asymmetry parameter, η,) as a function of temperature (T) immediately provides important information since the components of EFG tensor are very sensitive to small atomic displacements or modifications of charge distribution.

Let us describe at first the recent data for stephanite phase, Ag_5SbS_4. As it was noted above, ^{121,123}Sb NQR spectrum of Ag_5SbS_4 at T =77 K consists of five lines (Fig. 5). It is quite enough to observe only three of five NQR lines in order to detect any possible anomalies in temperature dependences of spectroscopic characteristics and calculate asymmetry parameter, η (Section I). In general, we studied the temperature dependences (4.2–300 K) of the following resonance frequencies and their line-widths: $\nu_{Q1}(\pm1/2\leftrightarrow\pm3/2)$, $\nu_{Q2}(\pm3/2\leftrightarrow\pm5/2)$ for ^{123}Sb, and $\nu_{Q3}(\pm1/2\leftrightarrow\pm3/2)$ for ^{121}Sb. The Sb NQR line shapes were well fitted by Lorentzian function at all temperatures studied (corresponding line-widths were taken as a full width at half maximum). The temperature dependence of ν_{Q1} is presented in Fig. 6.

On the whole, the quadrupole frequency ν_{Q1} decreases with increasing temperature without any significant anomalies. Thus, it is possible to exclude the major structural transitions. At the same time, we point out on the weak change in the slope of the ν_{Q1} versus T dependence at about 145 K. The temperature dependences of line-widths $\Delta\nu_{Q1}$ and $\Delta\nu_{Q2}$ are displayed in Fig. 7. It is important that the line-widths at all temperatures studied are not larger than 90 kHz. Such values, taking into account the stephanite complexity, imply this compound represents a high-ordered structure. As one can see, the NQR line-widths decrease rather weakly with decreasing of temperature in the range of 4.2–145 K, but it seems that one of the lines ($\Delta\nu_{Q2}$) narrows more drastically above 145 K.

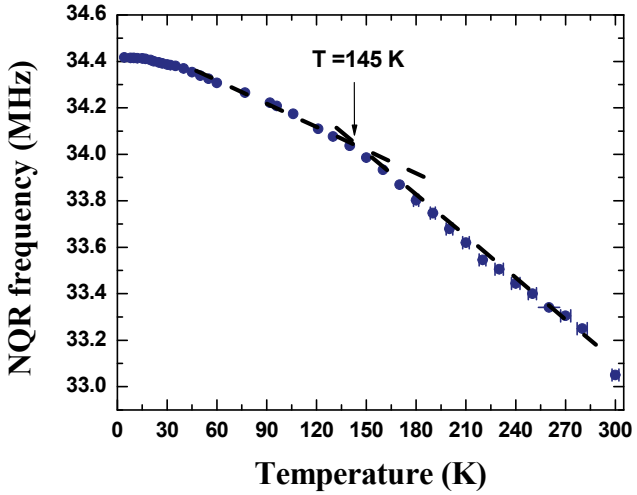

Fig. 6. The temperature dependence of ^{123}Sb NQR frequency ν_{Q1} (transition ±1/2↔±3/2) for Ag_5SbS_4. Arrow points to the positions of the change of slope in the $\nu_{Q1}(T)$ dependence at 145 K, curves are guides for eyes. For details, see text.

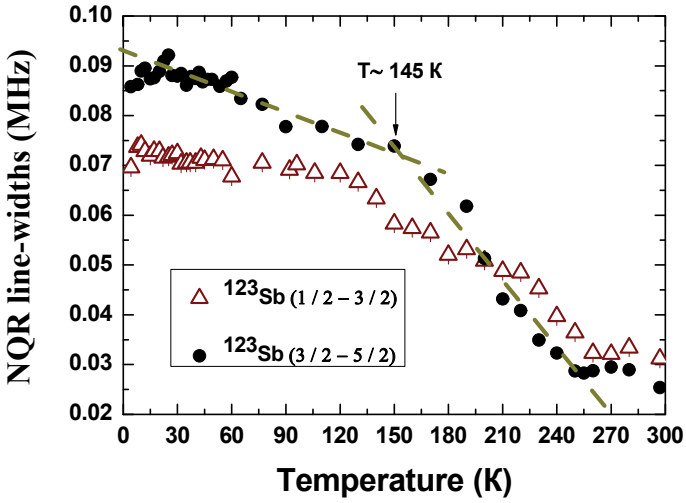

Fig. 7. The temperature dependence of ^{123}Sb NQR line-widths $\Delta\nu_{Q1}$ (transition ±1/2↔±3/2) and $\Delta\nu_{Q2}$ (transition ±3/2↔±5/2) for Ag_5SbS_4. Arrow points to the positions of the change of slope in the $\Delta\nu_{Q2}(T)$ dependence at 145 K, curves are guides for eyes. For details, see text.

More accuracy and detailed information can be extracted on the base of temperature dependence of asymmetry parameter (Fig. 8). In general, the value of η changes in frame of a small range (in the vicinity of 10 %). This aspect indicates about noticeable, but not large distortions of umbrella SbS_3 complexes, which can be interpreted in character as deviation of the local symmetry for SbS_3 unit from the axial one. More exciting aspect is an intelligible

bend, which takes place at 145 K. Such changes in spectroscopic characteristics (in our case about 145 K) represent the characteristic features of phase transitions (Grechishkin, 1973). The lack of NQR frequency jumps and/or changes of number of lines in NQR spectrum prove the absence of dramatic structural transformations near 145 K.

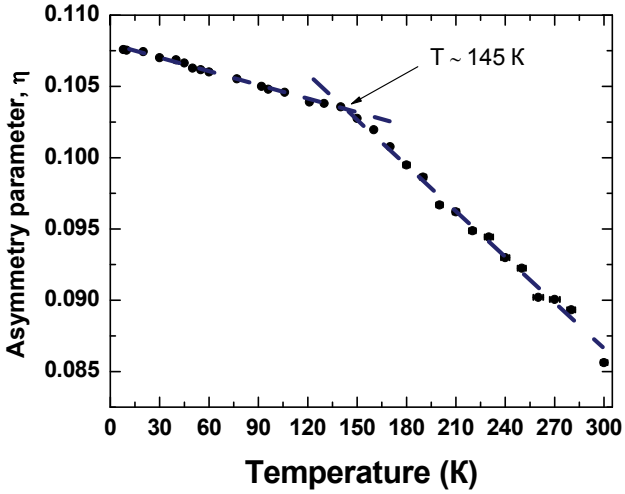

Fig. 8. The temperature dependence of asymmetry parameter, η, for Ag_5SbS_4. Arrow points to the positions of the change of slope in this dependence at 145 K, curves are guides for eyes. For details, see text.

Let us compare the NQR features that characterize the phase transition in stephanite, Ag_5SbS_4 with those for stibnite, Sb_2S_3, and pyrargyrite-proustite series, $Ag_3[Sb(As)]S_3$ (more detailed analysis will be presented in forthcoming paper). Actually, both the stibnite and the pyrargyrite-proustite have the ferroelectric properties, but these properties become apparent by different ways. In particular, it is known that the single ^{75}As NQR line for proustite, Ag_3AsS_3, at $T > 60$ K and $T < 24$ K splits into 8 lines at least, in spite of the fact that no structural transformation in this critical region was found by X-ray diffraction investigation (Bondar' et al., 1983). Analysis of NQR data shows that such anomalies can be understood in terms of existence in crystal under study of so-called incommensurate phase, which is caused by interacting oscillating modes of the crystal (modern data can be found, for instance, in (Apih et al., 2000)). Notably, similar slitting was observed also in case of $^{121,123}Sb$ NQR lines for pyrargyrite phase, Ag_3SbS_3, (Baisa et al., 1977). Obviously, stephanite sample, Ag_5SbS_4, related to pyrargyrite-proustite series from crystal-chemical point of view does not follow the similar mechanism. Instead of this, NQR measurements on single antimony site in Ag_5SbS_4 resemble in some extent the NQR studies performed on both antimony sites (*A* and *B*) in stibnite, Sb_2S_3 (Abdullin et al., 1977). Indeed, there is no any splitting of NQR lines, but a number of weak anomalies were observed at 140, 225, ≈ 300, 355, and 420 K. As it was found, these anomalies correspond to phase transitions of second order, which are accompanied by slight structural reorganizations of antimony coordination spheres, leading to transformations of ferroelectric properties. It seems that stephanite, Ag_5SbS_4, and stibnite, Sb_2S_3, have several common features in lattice dynamics that emphasize in some extent their relationship in electronic properties. In this context, our NQR results can be considered as the probing studies and, simultaneously, as a basis for further studies Ag_5SbS_4 with application of more specific methods.

5. Conclusions

Our examples of NQR spectroscopic studies of copper, antimony, and arsenic chalcogenides show that rather broad and diverse information may be obtained. There are themes typical to many solid state investigations, i.e. phase transitions, the relation of electric field gradients to electronic structure. NQR has proven to be an indispensable tool in this field.

6. Anknowledgment

This work is partly supported by the Grant RNP-2.1.1/6183 from the Ministry of Education and Science, Russian Federation.

7. References

Abdullin, R.S.; Pen'kov, I.N.; Nizamutdinov, N.M.; Grigas, I. & Safin, I.A. (1977). Temperature dependence of NQR spectra of $^{121,123}Sb$ in Sb_2S_3. *Physics of the Solid State,* 19, 1632-1635.

Abdullin, R.S.; Kal'chev, V.P.; Pen'kov, I.N. (1987). Investigation of copper minerals by NQR: crystallochemistry, electronic structure, lattice dynamics. *Phys. Chem. Minerals,* 14, 258–263.

Abrikosov, N.K.; Bankina, V.F.; Poretskaya, L.V.; Skudnova, E.V. & Chizhevskaya, S.N. (1975). *Semiconducting chalcogenides and their alloys*, Publishing House Nauka, Moscow.

Anashkin, V.N.; Kalinina, T.A.; Matukhin, V.L.; Pen'kov, I.N. & Safin, I.A. (1994). NQR spectra of $^{63,65}Cu$ in coexisting covelline (CuS) and geerite ($Cu_{1,6}S$). *Proceedings Rus. Mineral. Soc.*, 5, 59-63.

Apih, T.; Mikac, U.; Dolinšek, J.; Seliger, J. & Blinc, R. (2000). Unique 1-*q* and 3-*q* incommensurate phases in proustite: ^{75}As NQR line-shape and spin-lattice relaxation study. *Phys. Rev. B,* 61, 1003-1013.

Baisa, D.F.; Bondar', A.V. & Gordon, A.Ja. (1977). The phase transition "order-disorder" in pyrargyrite. *Physics of the Solid State,* 19, 1273-1276.

Berry, L.G. (1954). The crystal structure of covellite, CuS, and klockmanite, CuSe. *Am. Mineral.*, 39, 504-509.

Blinc, R. & Zeks, B. (1974). *Soft modes in ferroelectrics and antiferroelectrics*, Elsevier, New York.

Bondar', A. V.; Vihnin, V. S.; Rjabchenko, S. M. & Jachmenov, V. E. (1983). Incommensurate phase near the second-order phase transition in proustite. *Physics of the Solid State,* 25, 2602-2609.

Buckel, W. & Hilsch, R. (1950). Zur Supraleitung von Kupfersulfid. *Z. für Physik,* 128, 324-346.

Di Benedetto, F.; Borgheresi, M.; Caneschi, A.; Chastanet, G.; Cipriani, C.; Gatteschi, D.; Pratesi, G.; Romanelli, M. & Sessoli R. (2006). First evidence of natural superconductivity. *Eur. J. Mineral.,* 18, 283-287.

Evans, H. T. Jr. & Konnert, J. A. (1976). Crystal structure refinement of covellite. *Am. Mineral.*, 61, 996-1000.

Fjellvåg, H.; Grønvold, F.; Stølen, S.; Andresen, A.F.; Müller-Käfer, R. & Simon, A. (1988). Low-temperature structural distortion in CuS. *Z. für Kristallogr.*, 184, 111-121.

Gainov, R. R.; Dooglav, A. V.; Pen'kov, I. N.; Mukhamedshin, I. R.; Mozgova, N. N.; Evlampiev, I. A. & Bryzgalov, I. A. (2009). Phase transition and anomalous electronic behavior in the layered superconductor CuS probed by NQR. *Phys. Rev. B.*, 79, 075115.

Grechishkin, V.S. (1973). *Nuclear quadrupole interactions in solids*, Nauka (in Russian), Moscow.

Goble, R.J. (1985). The relationship between crystal structure, bonding and cell dimensions in the copper sulfides. *Can. Mineral*., 23, 61-76.

Gablina, I.F. (1997). Copper sulfides as indicators of the ore-forming environment. *Transactions RAS*. 357, 1133-1137.

Izoitko, V.M. (1997). *Technological mineralogy and estimation of ore*, Nauka, St. Petersburg.

Isac, L.A.; Duta, A.; Kriza, A.; Enesca, I.A. & Nanu, M. (2007). The growth of CuS thin films by Spray Pyrolysis. *J. Phys.: Confer. Series,* 61, 477-481.

Itoh, Y.; Hayashi, A.; Yamagata, H.; Matsumura, M.; Koga, K. & Ueda, Y. (1996). Cu NMR and NQR study of CuS. *J Phys Soc Japan (letters),* 65, 1953-1956.

Kaufmann, E.N. & Vianden, R.J. (1979). The electric field gradient in non-cubic metals. *Rev. Mod. Phys*., 51, 161-214.

Meissner, W. (1929). Messungen mit Hilfe von fliissigem Helium. V. Supraleitfahigkeit von Kupfersulfid. *Z. für Physik,* 58, 570-572.

Milman, V. (2002). Klockmannite, CuSe: structure, properties and phase stability from ab initio modeling. *Acta Cryst. B*., 58, 437-447.

Nozaki, H.; Shibata, K.; Ishii, M. & Yukino, K. (1995). Phase transition of $CuS_{1-x}Se_x$ ($0 \le x \le 1$) studied by X-ray diffractometry. *J. Solid State Chem.,* 118, 176-179.

Ohmasa, M. ; Suzuki, M. & Takeuchi, Y. (1977). A refinement of the crystal structure of covellite, CuS. *Mineral. J. (Japan),* 8, 311-319.

Peiris, S.M.; Pearson, T.T. & Heinz, D.L. (1998). Compression of klockmannite, CuSe. *J. Chem. Phys*., 109, 634-636.

Pen'kov, I.N. & Safin, I. A. (1964). Nuclear quadrupole resonance in proustite and pyrargyrite. *Physics of the Solid State,* 6, 2467-2470.

Pen'kov, I.N. & Safin, I. A. (1966a). NQR study of stephanite (Ag_5SbS_4). *Dokl. Akad. Nauk SSSR,* 168, 1148-1150.

Pen'kov, I.N. & Safin, I. A. (1966b). Application of nuclear quadrupole resonance in study of minerals. *Izv. Akad. Nauk SSSR (Geol. Ser),* 12, 41-52.

Petrunina, A.A.; Maksimov, B.M. & Iljuhin, V.V. (1970). Crystal Structure of Stephanite Ag_5SbS_4. *Sov. Phys. Dokl*., 188, 342-346.

Povarennykh, A.S. (1972). *Crystal chemical classification of minerals*, Plenum Press, New York.

Rigamonti, A.; Borsa, F. & Carretta, P. (1998). Basic aspects and main results of NMR-NQR spectroscopies in high-temperature superconductors. *Rep. Prog. Phys.,* 61, 1367-1439.

Safin, I. A. & Pen'kov, I.N. (1962). NQR in stibnite. *Dokl. Akad. Nauk SSSR,* 147, 2, 410-413.

Saito, S.-H.; Kishi, H.; Nie, K.; Nakamaru, H.; Wagatsuma, F. & Shinohara, T. (1997). ^{63}Cu NMR studies of copper sulfide., *Phys. Rev. B* 55, 14527-14535.

Sampathkumaran, E.V.; Gupta, L.C. & Vijayaraghavan, R. (1979). Valence fluctuation and the temperature dependence of copper nuclear quadrupole interaction in $EuCu_2Si_2$ and $YbCu_2Si_2$. *Phys. Rev. Lett.,* 43, 1189-1192.

Semin, G.K.; Babushkina, T.A. & Yakobson, G.G. (1975). *Nuclear quadrupole resonance in chemistry*, John Wiley & Sons, New York.

Slichter, C.P. (1996). *Principles of magnetic resonance (3rd enriched and updated edition)*, Springer-Verlag, Berlin.

Torumba, D.; Parlinski, K.; Rots, M. & Cottenier, S. (2006). Temperature dependence of the electric-field gradient in hcp-Cd from first principles. *Phys. Rev. B*., 74, 144304.

Wilson, J.A. (2009). A perspective on the pnictide superconductors. Cornell University Library (http://arxiv.org/abs/0809.0560)